2019

Development of biomarker-based proxy methods for reconstructing the late Quaternary sea ice history in the Barents Sea

Koseoglu, Deniz Can

UNIVERSITY OF PLYMOUTH

DEVELOPMENT OF BIOMARKER-BASED PROXY METHODS FOR RECONSTRUCTING THE LATE QUATERNARY SEA ICE HISTORY IN THE BARENTS SEA

by

DENIZ CAN KÖSEOĞLU

A thesis submitted to the University of Plymouth

in partial fulfilment for the degree of:

DOCTOR OF PHILOSOPHY

School of Geography, Earth and Environmental Sciences

August 2019

To the greatest of friends and family.

“An expert is one who has made every mistake possible in a narrow field.”

(Niels Bohr)

Development of biomarker-based proxy methods for reconstructing the late Quaternary sea ice history in the Barents Sea

Deniz Can Köseoğlu

ABSTRACT

Application of the sympagic diatom-produced, C_{25} highly branched isoprenoid (HBI) termed IP_{25} to paleo-sea ice reconstruction has confirmed its utility as a qualitative seasonal sea ice proxy. Combination of IP_{25} and a pelagic biomarker into the Phytoplankton-IP_{25} index (PIP_{25}) has facilitated more detailed, semi-quantitative descriptions of sea ice conditions. Further work is motivated by challenges inherent to univariate methods (such as PIP_{25}), and the availability of multiple HBIs characteristic of ice algal and pelagic production within sedimentary archives. This study investigated the potential of incorporating multiple biomarkers to characterise contrasting sea ice and productivity conditions in the contemporary Barents Sea, applying the findings for paleo-reconstructions encompassing both abrupt and gradual climate change.

Multivariate analysis of HBIs in Barents Sea surface sediments characterised by contrasting overlying sea ice conditions revealed the potential of classification trees (CTs) as a robust method of biomarker-based sea ice reconstruction. Thus, IP_{25} and a $C_{25:2}$ analogue produced by sea ice diatoms were characteristic of extensive spring sea ice cover, while pelagic $C_{25:3}$ isomers defined marginally ice-covered and ice-free areas in both surface and downcore sediments. Further, CT models did not require a correction factor and allowed systematic selection of a pelagic counterpart to IP_{25}, thereby alleviating some inherent limitations of PIP_{25}. In addition to the CT model, an association between a ratio of HBI $C_{25:3}$ isomers and spring diatom blooms in the Barents Sea was tentatively identified, characterised by distinct relative abundances of these pelagic HBIs in regions of different productivity regimes. Further work is needed to determine biological and/or community-driven controls on this HBI triene ratio as a potential diatom bloom indicator.

Finally, complementary application of CT and PIP_{25} methods to marine sediment cores spanning the last ca. 26 cal kyr BP at the northern and western Barents Sea continental margins resulted in reconstruction of both sea ice conditions and diatom productivity trends. At the western continental slope, extensive sea ice conditions and high sympagic production during the Last Glacial Maximum (LGM) definitively confirmed the presence of productive polynya throughout this glacial interval. After perennial sea ice and near-zero productivity resulted from the collapse of the Barents Sea Ice Sheet (BSIS) at the onset of Heinrich Stadial 1 (HS1), the ecosystem eventually recovered after rapid ice retreat as a consequence of increased Atlantic Water (AW) and reduced meltwater surges. At the northern margin, conditions during the subsequent Younger Dryas stadial were significantly ameliorated relative to the western Barents Sea at this time, possibly indicating the absence of a proximal Svalbard ice sheet, with warm AW influence. Such inferences of sea ice and productivity dynamics accompanying massive, abrupt climate change during glacial-interglacial cycles are key prerequisites for improved comprehension of current and future climate change.

Table of Contents

ABSTRACT i
Acknowledgements xvi
Author's declaration xvii
Publications xviii
Presentations xviii
List of common abbreviations xix

CHAPTER ONE 1
1. Introduction 1
1.1 Sea Ice 2
1.1.1 Ice within the Arctic ecosystem 2
1.1.2 Current trends of sea ice extent and physical properties 5
1.1.3 Causes and implications of sea ice decline 10
1.2 The Barents Sea 16
1.2.1 Paleoceanographic setting since the last glacial advance to the shelf 16
1.2.2 Contemporary oceanographic setting and sea ice conditions 21
1.3 Paleoclimate proxies in the Arctic Ocean 29
1.3.1 Common micropaleontological and geochemical proxy measures 29
1.3.2 Highly-Branched Isoprenoid (HBI) alkenes 32
1.4 Aim and objectives of the current study 42

CHAPTER TWO 45
2. General laboratory, analytical, and statistical methods 45
2.1 Storage and freeze drying 45
2.2 Sediment extraction and purification 46
2.2.1 Internal standard addition 46
2.2.2 Total organic extract 46
2.2.2.1 The DCM-methanol method 46
2.2.2.2 The KOH saponification method 47
2.2.3 Removal of elemental sulphur 48
2.2.4 Partial purification by silica chromatography 50
2.2.5 Removal of saturated hydrocarbons by silver-ion chromatography 50
2.3 Sample analysis, identification, and quantification 51
2.3.1 Sample preparation and derivatisation 51
2.3.2 Gas Chromatography-Mass Spectrometry 52
2.3.3 Identification and quantification of HBIs 53
2.3.4 Identification and quantification of sterols 58
2.4 Calculations and statistical procedures 63
2.4.1 Calculation of $P_{III}IP_{25}$ indices 63
2.4.2 Classification trees 64
2.4.2.1 An overview of decision tree methodology 64
2.4.2.2 Application of CT models in the current study 67
2.5 Biomarker extraction with and without KOH saponification 67

CHAPTER THREE 72
3. Biomarker-based multivariate classification of recent sea ice and productivity conditions in the Barents Sea 72
3.1 Introduction 72
3.2 Materials and methods 75
3.2.1 Surface sediment material 75
3.2.2 Downcore sediment material 76
3.2.3 Analysis of HBI biomarkers 77
3.2.4 Statistical procedure 77
3.2.4.1 Satellite data processing 77
3.2.4.2 $P_{III}IP_{25}$, HBI triene ratio, and data transformation for CT models 79
3.2.4.3 CT induction from sedimentary HBI composition 80
3.3 Results 82
3.3.1 Classification tree models and $P_{III}IP_{25}$ 82
3.3.1.1 CTs in surface sediments 82
3.3.1.2 CT and $P_{III}IP_{25}$–based sea ice estimates in downcore records 85
3.3.2 HBI triene ratio 86
3.4.2.1 Comparisons with satellite-derived parameters in surface sediments 86
3.4.2.2 HBI triene ratio-based productivity inferences in downcore records 86
3.4 Discussion 87
3.4.1 Evaluation of HBI variable importance for sea ice classification 87
3.4.2 Rationalising CT model outcomes in surface sediments 94
3.4.3 Downcore CT predictions and comparison to PIP_{25}-based SpSIC 100
3.4.4 General comparison between CT and PIP_{25} methods 103
3.4.5 The HBI triene ratio as a spring bloom indicator 107
3.4.5.1 Triene ratio comparisons with surface oceanography and productivity 107
3.4.5.2 Spring bloom occurrence and intensity in downcore records 116
3.5 Conclusions 119

CHAPTER FOUR 121
4. Further assessment and application of CT models, the $P_{III}IP_{25}$ index, and the HBI triene ratio for millennial-scale paleo sea ice and productivity reconstruction 121
4.1 Introduction 121
4.2 Materials and methods 123
4.2.1 Downcore sediment material 123
4.2.2 HBI lipid extraction and analysis 125
4.2.3 Proxy and statistical methods 126
4.3 Results and discussion 128
4.4.1 Comparison of CT and $P_{III}IP_{25}$-based sea ice inferences since the YD 128
4.3.1.1 Core 70 (northern Barents Sea) 128
4.3.1.2 Core 1200 (southwestern Barents Sea) 133
4.3.1.3 Core KA11 (western Barents Sea) 138
4.3.1.4 Core GC11 (Kvitøya Trough proximal to the northern Barents Sea shelf) 143
4.3.1.4.1 Paleo-sea ice variability throughout the last 13 cal kyr BP 143
4.3.1.4.2 Critical comparison between $P_{III}IP_{25}$- and CT-based sea ice inferences 154
4.3.2 Millennial-scale HBI triene ratio variability as a bloom indicator 162
4.4 Conclusions 168

CHAPTER FIVE 171
5. Multi-proxy characterisation of seasonal sea ice and productivity regimes at the western Barents Sea continental slope during the late Weichselian glaciation 171
5.1 Introduction 171
5.2 Biomarker interpretation rationale 175
5.3 Materials and methods 177
5.3.1 Sediment material 177
5.3.2 Lipid extraction and analysis 178
5.3.3 Statistical analysis 180
5.4 Results 181
5.4.1 LGM (ca. 25.8–18.0 cal kyr BP) 181
5.4.2 HS1 (ca. 18.0–16.3 cal kyr BP) 184
5.4.3 Deglaciation (after 16.3 cal kyr BP) 184
5.4.4 Surface sediment biomarker distributions 186
5.5 Discussion 187
5.5.1 BSIS-adjacent productive SIZ during the LGM (25.8–18 cal kyr BP) 187
5.5.2 Productivity termination during the HS1 (18–16.3 cal kyr BP) 193
5.5.3 Ice retreat and productivity recovery after 16.3 cal kyr BP 196
5.6 Conclusions 204

CHAPTER SIX 206
6. Conclusions and future work 206
6.1 Conclusions 206
6.1.1 CT model development and comparison to the $P_{III}IP_{25}$ approach 207
6.1.2 Association between the HBI triene ratio and spring bloom dynamics 209
6.1.3 A distributional approach to paleo-reconstruction in the Barents Sea 210
6.2 Future work 213
Appendix A 215
Appendix B 215
Appendix C 216
Spatial averaging of daily-resolution satellite data 222
Example calculations of CT model performance metrics 223
Appendix D 225
Appendix E 235
References 245

List of Figures

Figure 1.1: Arctic sea ice extent (>15% ice cover) for March (a) and September (b) of 2017, shown as white polygons. Solid red lines represent mean ice extent (1981–2010). Data from: National Snow and Ice Data Centre (Fetterer et al., 2017).....2

Figure 1.2: Areas of the Arctic used for reginal calculations. Polygon shapefiles from: National Snow and Ice Data Centre (Fetterer et al., 2010). Abbreviations denote Baffin Bay (BB), Barents Sea (BS), Beaufort Sea (BeaS), Bering Sea (BerS), Canadian Arctic Archipelago (CAA), Central Arctic (CA), Chukchi Sea (CS), East Siberian Sea (ESS), Greenland Sea (GS), Hudson Bay (HB), Kara Sea (KS), Laptev Sea (LS), Sea of Okhotsk (SofO). The software used to analyse satellite data and create Fig. 1.2, 1.4, 1.6 and Tables 1.1, 1.2, was developed for the purposes of this research using the R version 3.5.0 (R Core Team, 2018), and the source code made available in Appendix A.....7

Figure 1.3: Trends of average September (red), March (blue), and annual (grey) pan-Arctic sea ice extent for the 1979–2017 period (Peng et al., 2013; Meier et al., 2017). All trends were significant at a 99% confidence level, with the greatest decline observed for the September sea ice minimum.....9

Figure 1.4: (a), (c) and (e) show, respectively, the pan-Arctic Melt Onset (MO; day of year), Freeze Onset (FO; day of year), and Melt Season Length (MSL; days) averaged for the 1979–2017 period; corresponding trends (in days) are illustrated in (b), (d), and (f). Satellite data from: NASA Cryosphere (Stroeve et al., 2014).....13

Figure 1.5: Map of the Barents Sea illustrating the main currents and bathymetry. Abbreviations include the Norwegian Atlantic Current (NAC), Norwegian Coastal Current (NCC), North Cape Current (NCaC), West Spitsbergen Current (WSC), East Spitsbergen Current (ESC), Persey Current (PC). 23

Figure 1.6: (a) and (c) illustrate the average spring (April–June) and winter (January–March) % sea ice concentration (SpSIC and WinSIC, respectively) in the Arctic for the 1988–2017 period. Solid lines represent contours. Corresponding least-squares trends for SpSIC and WinSIC, in % per decade, are shown in (b) and (d), respectively. Note the extensive spatial gradients in the central Barents Sea and around Svalbard. 24

Figure 1.7: Trends of sea ice extent decline in the Barents Sea for the 1979–2017 period. Data from: National Snow and Ice Data Centre (Meier et al., 2017). 26

Figure 1.8: Structures of C_{25} Highly-Branched Isoprenoid (HBI) biomarkers utilised in the current study: I – IP_{25} (with carbon numbering shown); II – $C_{25:2}$ 6(17) (i.e. $IPSO_{25}$); III – $C_{25:3}$ 9(10), *Z* isomer; IV – $C_{25:3}$ 9(10), *E* isomer; V – $C_{25:3}$ 6(17); VI – $C_{25:2}$ 7(20).....34

Figure 1.9: Maps showing presence and absence, in both surface sediments and downcore records, of: (a) IP_{25}; (b) III and IV in the Arctic. Solid white lines denote median April sea ice extent for the 1981–2010 period (Fetterer et al., 2017). 37

Figure 1.10: Maps showing presence and absence, in both surface sediments and downcore records, of: (a) $IPSO_{25}$; (b) III and IV in the Antarctic. Solid white lines denote median April sea ice extent for the 1981–2010 period (Fetterer et al., 2017).....38

Figure 2.1: displayed formulae of internal standards used for analyte quantification: (a) 9-octylheptadec-8-ene (9-OHD); (b) 5α-androstan-3β-ol. 46

Figure 2.2: a scheme illustrating the method used for obtaining TOEs from marine sediments via the DCM/MeOH extraction procedure. 47

Figure 2.3: a schematic representation of the KOH saponification-based method of obtaining TOEs from marine sediments. 48

Figure 2.4: Removal of sulphur (S_8) from dry TOEs after DCM/methanol extraction. 49

Figure 2.5: Schematic showing partial purification of sediment TOEs via silica column chromatography. 50

Figure 2.6: schematic representation of the Ag-Ion chromatography method used for fractionation of saturated and unsaturated hydrocarbons. 51

Figure 2.7: GC-MS SIM chromatograms showing the elution order, observed and previously reported retention indices of $C_{25:1}$ (*m/z* 350.3), $C_{25:2}$ (*m/z* 348.3), and $C_{25:3}$ (*m/z* 346.3) HBIs. The integration technique is shown (dashed red lines). Black lines correspond to the CAA reference sediment; green lines are SIM chromatograms of Barents Sea surface sediment extracts added to better illustrate V and VI (Fig. 1.8). 54

Figure 2.8: Background-corrected TIC mass spectra of: (a) 9-OHD; (b) IP_{25}; (c) II; (d) III; (e) IV; (f) V; (g) VI. 55

Figure 2.9: Background-corrected TIC mass spectra and structures of internal standard and sterol TMS ethers in sediment extracts: (a) 5α-androstan-3β-ol; (b) Cholesterol; (c) Brassicasterol; (d) 24-methylenecholesterol; (e) Campesterol; (f) β-sitosterol; (g) Dinosterol. 59

Figure 2.10: EICs of sterols, showing the elution order of cholesterol (A), brassicasterol (B), 24-methylenecholesterol (C), campesterol (D), β-sitosterol (E), and dinosterol (F). 61

Figure 2.11: (a) A typical nodal structure of a binary classification tree. Left and right branches represent cases where the splitting condition is true and false, respectively; (b) An example of a cost-complexity analysis used to select the optimal tree size based on the relative misclassification error from *k*-fold cross validation. Red and green points represent the appropriate number of splits chosen based on the minimum cross-validated classification error (where +1SD is represented by the dashed line) and the 1-SE rule, respectively (Breiman et al., 1984). 65

Figure 2.12: A comparison of HBI concentrations obtained via the DCM-MeOH and KOH methods for core JR142-11GC (Chapter 4): (a) IP_{25}; (b) II; (c) III; (d) IV.....69

Figure 2.13: Brassicasterol (a) and cholesterol (b) concentrations in core JR142-11GC obtained via direct extraction into DCM-MeOH or KOH saponification. 70

Figure 3.1: Barents Sea maps showing: (a) Surface sediments characterised by marginal (<10% SpSIC), intermediate (10–50% SpSIC), and extensive (>50% SpSIC) satellite-based sea ice conditions (Cavalieri et al., 1996); (b) Downcore records (numbered black squares) and a representation of surface currents carrying major water masses (NAC: North Atlantic Current; WSC: West Spitsbergen Current; NCaC: North Cape Current; ESC: East Spitsbergen Current; PC: Persey Current; NCC: Norwegian Coastal Current). The average April–June 1988–2007 sea ice extent (≥15% SpSIC) and the ice edge (>0% SpSIC) are shown by solid and dashed black lines, respectively. 74

Figure 3.2: Complete linkage agglomerative hierarchical clustering of satellite-derived spring sea ice concentrations (SpSIC) estimates for surface sediment samples. Ice-free locations did not provide information about the SpSIC distribution and were excluded. ...79

Figure 3.3: Confusion matrices for CT models A–D created from percentage HBI abundances. Rows and columns represent known and model-predicted classes of sea ice conditions (MAR = marginal, INT = intermediate, EXT = extensive) after repeated cross-validation. Off-diagonal values highlighted in red represent misclassified samples. 83

Figure 3.4: Classification of marginal, intermediate, or extensive sea ice conditions by CT models A–D for the surface sediment training set (left); white circles denote misclassified samples. The best (center) and worst (right) performance after 10-fold cross-validation is also shown. 84

Figure 3.5: Pruned classification tree (CT) structures obtained using the absolute HBI concentrations (ng g^{-1}) in surface sediments (n = 198) and following application of the 1-SE rule to HBI assemblage: (a) A; (b) B; (c) C; (d) D. Abbreviations denote CT-assigned classes of marginal (MAR), intermediate (INT) and extensive (EXT) sea ice conditions (Fig. 3.1a).89

Figure 3.6: Pruned classification tree (CT) structures obtained using HBI percentage abundances (Eq. 3.2–3.5) in the surface sediment training dataset (n = 198) and following application of the 1-SE rule to: (a) Model A; (b) Model B; (c) Model C; (d) Model D. For (a), bracketed values represent ranges of splitting rule thresholds within ±1 standard deviation estimated using the method of Quinlan (1993).....90

Figure 3.7: Relative HBI importance for models built using absolute concentrations (ng g^{-1}) and compositional abundances (%) within assemblages A–D after cross-validation (Breiman et al., 1984). 91

Figure 3.8: Relative HBI importance for models built using absolute concentrations (ng g^{-1}) and compositional abundances (%) within assemblages A–D using the Random Forest algorithm (n = 300 trees; Breiman, 2001). 92

Figure 3.9: Deconstructed HBI importance for models built using absolute concentrations (ng g^{-1}) and compositional abundances (%) within assemblages A–D. Values including or excluding secondary splits (i.e. competing and surrogate variables) are shown by solid blue and shaded green bars, respectively.....93

Figure 3.10: Scatter plot showing the distribution of surface sediments within the data space of CT model A. Classes of marginal, intermediate, and extensive sea ice conditions determined using satellite SpSIC data (Fig. 3.1a) are shown by red circles, yellow squares,

and green triangles, respectively. The coloured regions represent areas within the data space classified by CT model A as marginal (red), intermediate (yellow), and extensive (green) sea ice conditions. The regions are separated by model-determined decision boundaries (annotated black lines), which show the chosen HBI biomarkers and corresponding relative abundance thresholds used for splitting rules. Misclassified samples (n = 12) are represented by diamond symbols and mostly correspond to sites from west Svalbard and the central Barents Sea MIZ. 95

Figure 3.11: Daily-resolution annual development of Chl *a* (mg m^{-3}), SIC (%), PAR (E m^{-2} d^{-1}), and SST (°C) in the Barents Sea based on satellite data from MODIS Aqua (NASA, 2018a–d) and NSIDC (Peng et al., 2013; Meier et al., 2017). 97

Figure 3.12: Satellite Chl *a* (2003–2017; mg m^{-3}) for the north-western (A), north-eastern (B), south-western (C), and south-eastern (D) Barents Sea. 99

Figure 3.13: (A) Comparison of $P_{III}IP_{25}$- and CT-based sea ice conditions from four dated short cores (cores 1, 8, 43 and 712) from the study region representing contrasting modern-day sea ice cover (Fig. 3.1b). The magnitude of each data point (left-hand axis) corresponds to the $P_{III}IP_{25}$-derived SpSIC and associated standard error estimates based on the regional calibration of Smik et al. (2016). The colours of each data point indicate the CT model A predictions of marginal (red), intermediate (yellow) and green (extensive) sea ice conditions (Fig. 3.1a); (B) A magnification of plot A, where pie charts show the estimated probability of classification (Quinlan, 1993) into the marginal and intermediate sea ice class for samples where percentage abundances of IP_{25} and IV were within the SD boundaries of CT model A (Fig. 3.6a). 101

Figure 3.14: Scaled factor loadings of various primary (red lines) and secondary (blue lines) variables with the HBI triene ratio III/(III+IV) at surface sediment locations. Red labels denote months of averaged (2003–2017) satellite-derived Chl *a* (mg m^{-3}). Blue labels represent average (2003–2017) sea surface temperature (SST; °C), photo-available radiation (PAR; E m^{-2} d^{-1}), particulate inorganic carbon (PIC; mol m^{-3}),1955–2012 sea surface salinity (SSS; psu), as well as 1988–2017 sea ice concentration (SIC; %); prefixes "Su" and "Sp" denote summer (July–September) and spring (April–June). $P_{III}IP_{25}$ index and the HBI triene ratio are shown in green. 109

Figure 3.15: Quartile distributions of: (A) III; (B) IV; (C) HBI triene ratio. (D)–(I) show complete linkage AHC of the HBI triene ratio, where red and white circles represent two clusters, overlaid onto averaged (2003–2017) satellite data for: (D) May Chl *a*; (E) April–May Chl *a*; (F) July–September PIC; (G) July–September PAR; (H) July–September SST; (I) shows mean July–September SSS for 1955–2012. The thin (thicker) black lines represent the 0% (15%) contours of average SIC spanning 1988–2017 in all maps; 2 mg m^{-3} contours for Chl *a* are shown as solid white lines in (D), (E). 110

Figure 3.16: Temporally averaged (2003–2017) satellite-derived parameters and associated results of complete linkage AHC clustering at surface sediment locations for: (A) April Chl *a*; (B) May Chl *a*; (C) April–May Chl *a*; (D) April–June Chl *a*; (E) April–June PIC; (F) July–September PIC. Crossed-out sample locations represent AHC cluster memberships mismatching those of the HBI triene ratio III/(III+IV) in Fig. 3.15. The total number of such

mismatches is shown in red at the bottom-right corner of each map. The thin (thicker) black lines represent the 0% (15%) contours of average SIC spanning 1988–2017 in all maps. 111

Figure 3.17: Temporally averaged satellite-derived parameters and associated results of complete linkage AHC clustering at surface sediment locations for: (A) April–June SST; (B) July–September SST; (C) April–June SSS; (D) July–September SSS; (E) April–June PAR; (F) July–September PAR. Crossed-out sample locations represent AHC cluster memberships mismatching those of the HBI triene ratio III/(III+IV) in Fig. 3.15. The total number of such mismatches is shown in red at the bottom-right corner of each map. The thin (thicker) black lines represent the 0% (15%) contours of average SIC spanning 1988–2017 in all maps. 112

Figure 3.18: Distance (km) of surface sediment locations from the nearest coastline, highlighting matched (black dots) and mismatched (red diamond markers) AHC cluster memberships between the III/(III+IV) triene ratio and: (A) April Chl *a*; (B) May Chl *a*; (C) April–May Chl *a*; (D) April–June Chl *a*; (E) April–June PIC; (F) July–September PIC. The total number of cluster mismatches (Fig. 3.16, 3.17) is shown in the bottom left corner of each plot. Proximity of each triene ratio value to the dataset median (*ca.* 0.57 or 57%) is shown on the ordinate axis. 113

Figure 3.19: Distance (km) of surface sediment locations from the nearest coastline, highlighting matched (black dots) and mismatched (red diamond markers) AHC cluster memberships between the HBI triene ratio and: (A) April–June SST; (B) July–September SST; (C) April–June SSS; (D) July–September SSS; (E) April–June PAR; (F) July–September PAR. The total number of cluster mismatches (Fig. 3.16, 3.17) is shown in the bottom left corner of each plot. Proximity of each triene ratio value to the dataset median (*ca.* 0.57 or 57%) is shown on the ordinate axis. 114

Figure 3.20: HBI triene ratio trends at core sites 1, 8, 43, and 712 throughout the last 250 years. The dashed line represents a tentative threshold value of 0.62 separating the spring phytoplankton bloom from reduced productivity conditions in the Barents Sea..... 117

Figure 3.21: Map of the Barents Sea showing the locations of cores 1, 8, 43, and 712 overlaid onto a 2003–2017 average May Chl *a* grid. The surrounding setting of core 1 is magnified, with a suggested NCaC pathway shown. Thin and thick solid black lines represent the average ice edge (0% SpSIC) and ice extent (15% SpSIC) boundaries for the 1988–2017 period. The 2 mg m^{-3} Chl *a* contour is shown by a solid white line. 119

Figure 4.1: Map of the Barents Sea showing locations of downcore records 1200, KA11, GC11, and 70 (black squares). Solid and dotted black lines represent the average April–June sea ice extent (1988–2007) corresponding to SpSIC thresholds of 15% and 0%, respectively. A simplified representation of surface Atlantic Water (AW; red arrows), Arctic Water (ArW; blue arrows) and Coastal Water (CW; green arrows) currents is also shown, with abbreviations analogous to those in Fig. 3.1 (Chapter 3). 122

Figure 4.2: Age model for core GC11, showing median calibrated ^{14}C AMS dates (orange markers) and corresponding 2σ standard error ranges (black bars). 125

Figure 4.3: Sea ice proxy data for core 70 showing the $P_{III}IP_{25}$-based % SpSIC profile (black line) with: (A) An RMSE error of ca. 11% (blue bands; Smik et al., 2016) and superimposed CT predictions of marginal (red circles), intermediate (yellow squares), and extensive (green diamonds) sea ice cover. Dashed horizontal lines represent the 10% and 50% satellite SpSIC boundaries separating sea ice classes in the CT model (Fig. 3.1a, Chapter 3); (B) The probabilities of classification estimated from SD boundaries of CT model splitting rules (Quinlan, 1993) shown as pie charts for samples where the probability of classification into a single class was not certain (i.e. not =100%). Colours within pie charts correspond to the red, yellow, and green colours of SpSIC classes in plot A. The portion of plot B contained within the red square was magnified in plot C. 129

Figure 4.4: HBI concentrations and correlations for core 70 (northern Barents Sea), where black lines (with circle markers) and red lines correspond to primary (left) and secondary (right) colour-coded y-axes: (a) Concentrations of IP_{25} and II; (b) Concentrations of III and IV; (c) Running correlations (window of 9 horizons) for IP_{25} versus II (black line with circle markers) and III versus IV (red line). Grey diamonds represent significant correlations (p = 0.05). The dashed line separates positive (r > 0) and negative (r < 0) correlations. 130

Figure 4.5: Pearson's correlations of IP_{25} versus II (panels A–C) and III versus IV (panels D–F) in Barents Sea surface sediments with marginal (<10% SpSIC; red circles), intermediate (10–50% SpSIC; yellow triangles), and extensive (>50% SpSIC; green squares) overlying sea ice conditions. Only surface sediments (Fig. 3.1a, Chapter 3) where holistic data for IP_{25}, II, III and IV was available were used to avoid influencing the best-fit line towards zero. 131

Figure 4.6: Sea ice proxy data for core 1200, where plots A, B, and C are analogous to those presented in Fig 4.3. Diagonal crosses represent horizons where any discrepancy between CT predictions and $P_{III}IP_{25}$ estimates (c=0.63) was observed. 136

Figure 4.7: HBI concentrations and correlations for core 1200 (southwestern Barents Sea). The illustrated profiles are analogous to those shown in Fig 4.4. The light blue vertical bar highlights the YD (12.95–11.70 cal kyr BP). 137

Figure 4.8: Sea ice proxy data for core KA11 analogous to that shown for cores 70 and 1200 in Fig. 4.3 and 4.6, respectively. In plot A, crossed light-blue circle markers represent horizons where the discrepancy between CT predictions and $P_{III}IP_{25}$-based SpSIC estimates exceeded the $P_{III}IP_{25}$ versus SpSIC calibration RMSE of ca. 11% (Smik et al., 2016) irrespective of the c-factor used to calculate $P_{III}IP_{25}$. 140

Figure 4.9: HBI concentrations and correlations for core KA11 (western Barents Sea). The illustrated profiles are analogous to those shown in Fig. 4.4, 4.7. The light blue vertical bar highlights the YD (12.95–11.70 cal kyr BP). 141

Figure 4.10: Biomarker profiles and correlations for core KA11: (a) Concentrations of IP_{25} and II represented by black (with circle markers) and green lines, respectively; (b) Running correlation of first relative (%) differences, with a sampling window of 9 horizons. Positive and negative correlations are separated by a dashed horizontal line, while grey diamonds show correlations significant at a 95% confidence level. In both (a) and (b), crossed red

squares represent samples for which CT model predictions significantly differed from $P_{III}IP_{25}$-derived % SpSIC values, with a discrepancy exceeding the RMSE of the $P_{III}IP_{25}$–SpSIC calibration (ca. ±11% SpSIC) irrespective of the *c*-factor used to calculate $P_{III}IP_{25}$. The light blue vertical bar highlights the YD (12.95–11.70 cal kyr BP). 142

Figure 4.11: Proxies of core GC11, and modelled climate data spanning the last 13 cal. kyr BP: (A) Modelled AMOC anomaly describing the global oceanic overturning (Ritz et al., 2013), and average May insolation values (Laskar et al., 2004) at several latitudes; (B) Sympagic IP_{25} and II concentrations (ng g^{-1}); (C) Pelagic HBI III and IV concentrations (ng g^{-1}); (D) $P_{III}IP_{25}$-based SpSIC profile with CT model classification of core horizons analogous to Fig. 4.3a, 4.6a, 4.8a. Periods of distinct climate conditions are delineated by black lines. Abbreviations denote: YD – Younger Dryas; PB – Preboreal; PBO – Preboreal Oscillation; HCO – Holocene Climatic Optimum. 145

Figure 4.12: Proposed spatio-temporal development of sea ice conditions at core sites examined herein (black squares) and in previous investigations (white circles), where black numbering represents the timing of: (A) The YD (ca. 13.0–11.7 cal. kyr BP) onset. The extent of Svalbard and Fennoscandian ice sheets at ca. 13 cal kyr BP is shown in red (Bradley and England, 2008); (B) The YD–Preboreal transition (ca. 11.7–10.8 cal. kyr BP); (C) The onset of increased AW inflow during the Early Holocene and HCO (ca. 10.8–10.4 cal. kyr BP); (D) The Mid-Holocene Cooling onset (MHC; ca. 9.4–6.5 cal. kyr BP). Southward ice expansion from 9.4 cal. kyr BP to ca. 6.5 cal. kyr BP is shown by solid black and white lines, respectively; (E) Continued cooling (i.e. Neoglaciation) and ice expansion over the last ca. 6.0 cal. kyr BP. Bracketed numbers denote data sources, summarised in (F). In maps A–E, the suggested annual maximum and minimum sea ice extent is shown by solid and dotted white lines, respectively. 147

Figure 4.13: HBI concentrations and correlations for core GC11 (north-eastern Barents Sea margin). The illustrated profiles are analogous to those shown in Fig. 4.4, 4.7, and 4.9. The light blue vertical bar highlights the YD (12.95–11.70 cal kyr BP). 156

Figure 4.14: Sea ice proxy data for core GC11 analogous to that shown for other cores in Fig. 4.3, 4.6, and 4.8. 157

Figure 4.15: A comparison of the number of discrepancies of at least 1% between CT model predictions and $P_{III}IP_{25}$-based SpSIC estimates obtained using *c*-factor values of 0.63 (A), 1 (B), and 1.17 (C), where the latter was obtained by optimising the $P_{III}IP_{25}$–SpSIC regression of Smik et al. (2016) for a maximum correlation coefficient *r*. 158

Figure 4.16: Biomarker composition and CT model output for cores 70, 1200, KA11, and GC11 using different RF combinations: (a) Averaged relative abundances of IP_{25} and HBIs II, III and IV in surface sediments and cores using calibrated and arbitrarily equated (uncalibrated) RFs; (b) Percentage distribution of core horizons classified into three categories of sea ice conditions by the CT model. "Correct RFs" are those calibrated externally, whereas "mismatched RFs" denotes the use of calibrated and uncalibrated RFs (equated to 1) for the CT training set and downcore records, respectively. Values within white circles correspond to the number of horizons classified into a given category of sea

ice conditions where a discrepancy with $P_{III}IP_{25}$-based SpSIC estimates was observed. No samples were misclassified into the extensive (>50% SpSIC) sea ice category..... 161

Figure 4.17: $P_{III}IP_{25}$-based SpSIC estimates (black line; left-hand y-axis) with overlaid CT predictions of sea ice conditions, and HBI triene ratios (blue line; right-hand y-axis) for core: (a) 70; (b) 1200; (c) KA11; (d) GC11. The dashed blue line is a tentative HBI triene ratio threshold (Chapter 3) separating areas of phytoplankton blooms in well-stratified waters (>0.62) from areas of reduced production due to slower development of weaker stratification (<0.62), such as the contemporary western Barents Sea. 165

Figure 5.1: Maps of the Barents Sea showing: (a) The main inflow currents carrying AW (via the NAC, NCaC, and WSC), ArW (PC and ESC), and CW (NCC); (b) Surface and downcore sample locations. Green and white circles correspond to surface sediment locations where HBI data (Chapter 3) were available with and without additional sterol data, respectively. Both the investigated site and referenced downcore locations are shown by numbered diamond markers: (1) GS14-190-PC01 (this study); (2) JM11-F1-19PC (Ezat et al., 2014; Hoff et al., 2016); (3) MD95-2010 (Marcott et al., 2011); (4) JM05-85-GC (Aagaard-Sørensen et al., 2010; Junttila et al., 2010); (5) JM02-460 GC/PC (Rasmussen et al., 2007); (6) MSM5/5-712-2 (Müller and Stein, 2014); (7) PS93/006-1 (Kremer et al., 2018a); (8) PS2837-5 (Wollenburg et al., 2004; Müller et al., 2009); (9) PS92/039-2 (Kremer et al., 2018b); (10) HH11-09GC (Chauhan et al., 2016); (11) PS2138-1 (e.g. Knies and Stein, 1998; Nørgaard-Pedersen et al., 2003). In both maps, dashed and solid black lines correspond to averaged SpSIC contours (April–June; 1988–2017) of 0% and 15%, respectively. 175

Figure 5.2: HBI concentration profiles for core GS14: (a) IP_{25} and II, indicative of sympagic diatom productivity; (b) III and IV, showing pelagic diatom productivity; (c) $P_{III}IP_{25}$-based SpSIC (%) estimates with confidence limits (grey lines) corresponding to the standard error of calibration (ca. ±11%; Smik et al., 2016), and superimposed categorical CT predictions of marginal (ca. <10% SpSIC), intermediate (ca. 10–50% SpSIC), and extensive (>50% SpSIC) sea ice regimes denoted by red diamonds, yellow triangles, and green circles, respectively. The threshold for summer sea ice occurrence is shown by the horizontal dashed line. In all plots, coloured background bands constrain the LGM, HS1 and Deglacial time intervals. Changepoints significant at a 99.5% confidence level ($p < 0.005$) are shown by vertical red lines, where upward-pointing dashed arrows apply to the left y-axis only, while a solid line applies to both the left and right y-axes. 182

Figure 5.3: Sterol concentration profiles for core GS14: (a) Brassicasterol and chalinasterol; (b) Campesterol and β-sitosterol; (c) Dinosterol; (d) Cholesterol. In all plots, coloured background bands constrain the LGM, HS1 and Deglacial time intervals. Changepoints significant at a 99.5% confidence level ($p < 0.005$) are shown by vertical red lines, where upward or downward pointing dashed arrows apply to the left and right y-axis, respectively, while a solid line applies to both left and right y-axes. 183

Figure 5.4: Concentration distributions during the LGM, HS1 and Deglacial for: (a) HBIs; (b) Sterols. Error bars denote ± 1 sample SD in each case. Blue and red boxes with

outgoing arrows show plot areas zoomed in for clarity for HBIs and sterols, respectively. 185

Figure 5.5: Relative abundance distributions during the LGM, HS1 and Deglaciation for: (a) HBIs, with comparisons to modern distributions reported in Barents Sea surface sediments characterised by contrasting sea ice regimes (Fig. 5.1b); (b) Sterols, with comparisons to surface sediments within and south of the MIZ. Error bars denote ± 1 sample SD for each biomarker, while the sample size *n* is shown in red above each distribution. 186

Figure 5.6: Comparison of GS14 data with other paleo-reconstructions: (a) GS14 IP_{25} and IV concentrations; (b) GS14 dinosterol and cholesterol concentrations; (c) $P_{III}IP_{25}$-derived SpSIC with CT predictions of sea ice conditions (as in Fig. 5.2c); (d) $\delta^{18}O$ of *N. pachyderma* (sin.) for GS14 (Knies et al., 2018) and the Norwegian Sea core J11-F1-19PC (Hoff et al., 2016), with the modelled North Atlantic AMOC anomaly on the right y-axis (Ritz et al., 2013); (e) Foraminiferal Mg/Ca-based bottom water temperature (BWT) at Norwegian Sea sites MD95-2010 (Marcott et al., 2011) and J11-F1-19PC (Ezat et al., 2014), with paleoproductivity north off Svalbard (Wollenburg et al., 2004). 189

Figure 5.7: Conceptual representation of sea ice and productivity conditions at the southwestern Barents Sea continental slope throughout: (A) The LGM (25.8–18.0 cal kyr BP); (B) The HS1 (18.0–16.3 cal kyr BP); (C) The Deglacial (16.3 cal kyr BP onwards). Seasonal sea ice conditions inferred from SpSIC (%) and the CT model are illustrated during winter (October–March), spring (April–June) and summer (July-September). Red and blue arrows correspond to AW and meltwater fluxes, respectively, where line width increases with flow strength. Orange arrows represent solar insolation. 198

Figure C.1: quadrants used to derive daily time-series of satellite data for the north-western (A), north-eastern (B), south-western (C), and south-eastern (D) Barents Sea. 222

Figure E.2: Absolute sterol concentrations before (A) and after (B) normalisation to TOC during the Deglacial period (after 16.3 cal kyr BP) of the GS14 record, and in surface sediments characterised by <50% SpSIC in the modern Barents Sea (Chapter 5). 244

List of Tables

Table 1.1: Regional decline of spring (April–June), winter (January–March), and annual mean sea ice extent for the 1979–2017 period. Abbreviations denote: SpSIE – spring sea ice extent; WinSIE – winter sea ice extent. Regions used for calculations are shown in Fig. 1.2. Satellite data from: Sea Ice Index, National Snow and Ice Data Centre (Peng et al., 2013; Meier et al., 2017). 8

Table 1.2: Interannual development of the melt season length for 13 Arctic regions spanning the 1979–2017 period. Abbreviations denote: MO – Melt Onset; FO – Freeze Onset; MSL – Melt Season Length. Regions used for calculations are shown in Fig. 1.2. Satellite data updated from: NASA Cryosphere (Stroeve et al., 2014). 11

Table 1.3: A summary of paleoclimate proxies described in the text.....36

Table 2.1: GC-MS instrumental parameters used for analysis of HBIs and sterols. 53

Table 2.2: GC-MS RFs for HBIs, with associated percentage deviations. Red asterisks denote $RF_{estimate}$ values (Eq. 2.4) estimated using RRFs calculated via Eq. 2.3. 58

Table 2.3: example calculation steps to obtain RF estimates for sterols in the absence of an authentic standard calibration.....62

Table 2.4: Comparison of HBI concentrations in two reference surface sediments extracted in triplicate directly into DCM-MeOH or via KOH saponification.....68

Table 2.5: Comparison of HBI concentrations in downcore sediments (JR142-11GC core; Chapter 4) following DCM-MeOH extraction and KOH saponification (M_A and M_B, respectively); factor difference between concentrations is denoted by Δ_{rel}. 68

Table 2.6: Sterol concentrations in surface sediments extracted via the DCM-MeOH and KOH saponification methods (analogous to data in Table 2.4). Factor differences between concentrations (Δ_{rel}) are also shown. 69

Table 2.7: Sterol concentrations in core JR142-11GC (Chapter 4) obtained via the DCM-MeOH (M_A) and KOH (M_B) methods; Δ_{rel} denote factor differences, with mean and standard deviation calculated across all horizons (analogous to data in Table 2.5). A comparison of 5α-androstan-3β-ol peak areas (PA) is also shown.....70

Table 3.1: Summary of performance metrics for classification tree (CT) models obtained using percentage HBI abundances with assemblages A–D. Abbreviations represent classes of sea ice conditions (Fig. 3.1a): MAR = marginal; INT = intermediate; EXT = extensive. Kappa and F1 score were 0.8 ± 0.1 and 0.9 ± 0.1 for models A, C, and D; model C exhibited values of 0.7 ± 0.2 and 0.8 ± 0.1, respectively.....83

Table 3.2: Top competing variables and surrogate splits corresponding to splitting rules (in %) for derived from relative abundance-based1SE-pruned CT models A–D (Fig. 3.6). The classification improvement and agreement metrics represent a relative performance measure of competing variables and level of similarity (scaled from 0–1) between surrogate and primary splitting rules, respectively.....85

Table 3.3: Top competing variables and surrogate splits corresponding to splitting rules (in ng g^{-1}) for 1SE-pruned CT models derived from absolute HBI concentrations of assemblages A–D (Fig. 3.5). The top two primary splits were common to all assemblages.....85

Table 3.4: Summary of advantages and limitations of PIP_{25}- and CT-based methods for estimating spring sea ice conditions.....103

Table 3.5: Descriptive statistics of April–May Chl *a* (mg m^{-3}) averaged for the 2003–2017 period at core sites 1, 8, 43, and 712. Note the small sample size for core site 8. 118

Table 4.1: Mean absolute concentrations of HBIs (ng g^{-1} ± 1 SD) and relative abundances (%) calculated from these in surface sediments used to build the CT model, as well as in downcore records 70, 1200, KA11, and GC11.....133

Table 5.1: A list of HBI and sterol lipids utilized as biomarkers of sea ice and primary productivity regimes in the current study, with associated uses and potential limitations...174

Table 5.2: RF_{est} values for chalinasterol, campesterol, β-sitosterol, and dinosterol estimated using Eq. 2.6 (Chapter 2) with both externally calibrated reference sterols (brassicasterol and cholesterol). The final averaged RF_{est} values used for sterol quantification in core GS14 are highlighted in bold. 179

Table B.1: Absolute concentrations (ng g^{-1} sed.) of HBIs (Fig. 1.8, Chapter 1) in the CAA reference sediment. Red asterisks denote values derived using $RF_{estimate}$ values (Eq. 2.4) calculated from RRFs (Eq. 2.3). 215

Table B.2: Absolute concentrations (µg g^{-1} sed.) of sterols (Fig. 2.9, Chapter 2) in the CAA reference sediment. Red asterisks denote values obtained using RF estimates calculated via Eq. 2.6 (Chapter 2) and shown in Table 5.2 (Chapter 5). Abbreviations denote brassicasterol (A), chalinasterol (B), campesterol (C), β-sitosterol (D); dinosterol (E), and cholesterol (F). 216

Table C.3: HBI concentrations (ng g^{-1} sed.), $P_{III}IP_{25}$-based SpSIC estimates (%), HBI triene ratios (abbreviated to TRa), and classes of marginal (M), intermediate (I), or extensive (E) sea ice conditions assigned using CT models A–D (Fig. 3.7, Chapter 3) in Barents Sea surface sediments. 216

Table C.4: HBI concentrations (ng g^{-1} sed.), $P_{III}IP_{25}$-based SpSIC estimates (%), HBI triene ratios (abbreviated to TRa), and classes of marginal (M), intermediate (I), or extensive (E) sea ice conditions assigned using CT model A (Fig. 3.7a, Chapter 3) in Barents Sea cores 1, 8, 43, and 712. 221

Table C.5: Confusion matrix results for CT model A obtained using the training set. Abbreviations represent classes of sea ice conditions based on satellite SpSIC (Fig. 3.1a): MAR = marginal; INT = intermediate; EXT = extensive. 223

Table D.6: Age model data for core GC11 (Katrine Husum, personal communication), including ^{14}C AMS-dated core depths, carbonate sources, ^{14}C (yr BP ± SD) and calibrated (cal yr BP) ages with associated 2σ error ranges. 226

Table D.7: HBI concentrations (ng g^{-1} sed.), $P_{III}IP_{25}$-based SpSIC estimates (%), HBI triene ratios (abbreviated to TRa), and classes of marginal (M), intermediate (I), or extensive (E) sea ice conditions assigned using CT model A (Fig. 3.7a, Chapter 3) in Barents Sea cores 70, 1200, KA11, and GC11. 226

Table E.8: HBI concentrations (ng g^{-1} sed.), $P_{III}IP_{25}$-based SpSIC estimates (%), and classes of marginal (M), intermediate (I), or extensive (E) sea ice conditions assigned using CT model A (Fig. 3.7a, Chapter 3) in Barents Sea core GS14. 235

Table E.9: Sterol concentrations (µg g^{-1} sed.) in core GS14. Abbreviations denote brassicasterol (A), chalinasterol (B), campesterol (C), β-sitosterol (D), dinosterol (E), and cholesterol (F). 238

Table E.10: Sterol concentrations (µg g^{-1} sed.) in Barents Sea surface sediments. Abbreviations are analogous to those in Table E.9. 240

Acknowledgements

It is a privilege to thank all the brilliant people who have transformed this journey into something extraordinary.

Firstly, my eternal gratitude to my supervisors, Prof Simon Belt and Dr Jochen Knies, for their infectious enthusiasm towards the work coupled with truly unrelenting encouragement and guidance (both moral and technical) throughout the project. None of this would have been possible without all your help. Thank you.

I would also like to say a heartfelt “Thank You!” to Darren Denslow, who has been the greatest (and most patient) of friends anyone could wish for. Your fantastic company and unconditional support have kept me afloat.

Needless to say, it has been an absolute pleasure to work with world-class researchers as part of the BGC group. Truly, the value of hard work is learned from the best, and by example. A very special thanks to Lukas Smik, who has trained and guided me throughout and answered what must have been a million of my questions.

Many thanks go out to Andrew Tonkin, Andy Arnold, Andy Fisher, and Claire Williams, who were always there with helpful and encouraging advice.

I am indebted to Dr Katrine Husum and all the participants of MOSJ-2016 for inviting and welcoming me to the (rather cold!) world of Arctic research cruises. Heavy cloud cover and barren landscapes have never (and will never) look this beautiful again.

Financial support for the project from the University of Plymouth and the Centre for Arctic Gas Hydrate, Environment and Climate (Norway) is gratefully acknowledged.

Last but by no means least, my love and admiration to my family. Both have always been reciprocated, million-fold.

Author's declaration

At no time during the registration for the degree of *Doctor of Philosophy* has the author been registered for any other University award without prior agreement of the Doctoral College Quality Sub-Committee.

Work submitted for this research degree at the University of Plymouth has not formed part of any other degree either at the University of Plymouth or at another establishment.

This study was jointly financed with the aid of a studentship from the University of Plymouth and the Research Council of Norway through its Centre of Excellence funding scheme at the Centre for Arctic Gas Hydrate, Environment and Climate (CAGE; project number 223259).

A programme of advanced study was undertaken, with relevant scientific seminars and conferences attended, at which work was often presented.

Word count of main body of thesis: 55434

Signed 

Deniz Can Köseoğlu

Date: August 2019

Publications

Köseoğlu, D., Belt, S.T., Smik, L., Yao, H., Panieri, G., Knies, J. (2018a), 'Complementary biomarker-based methods for characterising Arctic sea ice conditions: A case study comparison between multivariate analysis and the PIP_{25} index', *Geochimica et Cosmochimica Acta* **222**, pp. 406–420. DOI: https://doi.org/10.1016/j.gca.2017.11.001.

Köseoğlu, D., Belt, S.T., Husum, K., Knies, J. (2018b), 'An assessment of biomarker-based multivariate classification methods versus the PIP_{25} index for paleo Arctic sea ice reconstruction', *Organic Geochemistry* **125**, pp. 82–94. DOI: https://doi.org/10.1016/j.orggeochem.2018.08.014.

Knies, J., Köseoğlu, D., Rise, L., Baeten, N., Bellec, V.K., Bøe, R., Klug, M., Panieri, G., Jernas, P.E., Belt, S.T. (2018), 'Nordic Seas polynyas and their role in preconditioning marine productivity during the Last Glacial Maximum', *Nature Communications* **9**, article 3959. DOI: https://doi.org/10.1038/s41467-018-06252-8.

Belt, S.T., Smik, L., Köseoğlu, D., Knies, J., Husum, K. (2019), 'A novel biomarker-based proxy for the spring phytoplankton bloom in Arctic and sub-arctic settings – HBI T_{25}', *Earth and Planetary Science Letters* **523**, article 115073. DOI: https://doi.org/10.1016/j.epsl.2019.06.038.

Köseoğlu, D., Belt, S.T., Knies, J. (2019), 'Abrupt shifts of productivity and sea ice regimes at the western Barents Sea slope from the Last Glacial Maximum to the Bølling-Allerød interstadial', *Quaternary Science Reviews* **222**, article 105903. DOI: https://doi.org/10.1016/j.quascirev.2019.105903.

Presentations

POLAR-2018: A SCAR & IASC Conference, 19–23 June 2018, Davos Congress Centre, Davos, **Switzerland**. Poster presentation.

9th Annual Biogeochemistry Centre Conference, 14 December 2017, Plymouth Marine Station, Plymouth, **U.K.** Oral presentation.

28th International Meeting on Organic Geochemistry, 17–22 September 2017, Florence, **Italy**. Poster presentation.

8th Annual Biogeochemistry Centre Conference, 19 December 2016, Plymouth Marine Station, Plymouth, **U.K.** Oral presentation.

27th Annual meeting of the British Organic Geochemical Society, 13–14 July 2016, Imperial College London, London, **U.K.** Poster presentation.

4th International Palaeo-Arctic and Temporal Gateways meeting, 23–27 May 2016, Geological Survey of Norway, Trondheim, **Norway**. Poster presentation.

7th Annual Biogeochemistry Centre Conference, 16 December 2015, Plymouth Marine Station, Plymouth, **U.K.** Oral presentation.

List of common abbreviations

AHC – Agglomerative Hierarchical Clustering

AMOC – Atlantic Meridional Overturning Circulation

ArW – Arctic Water

AW – Atlantic Water

Chl *a* – Chlorophyll α

CT – Classification Tree

CW – Coastal Water

GC-MS – Gas Chromatography-Mass Spectrometry

HBI – Highly-Branched Isoprenoid

HS1 – Heinrich Stadial 1

LGM – Last Glacial Maximum

MIZ – Marginal Ice Zone

SIZ – Seasonal Ice Zone

PAR – Photosynthetically Available Radiation

PIC – Particulate Inorganic Carbon

$P_{III}IP_{25}$ – Phytoplankton-IP_{25} index using HBI triene III as the pelagic biomarker

RF – Response Factor

RMSE – Root-Mean-Square Error

SIM – Selected Ion Monitoring

SpSIC – Spring (April-June) Sea Ice Concentration

SSS – Sea Surface Salinity

SST – Sea Surface Temperature

TIC – Total Ion Current

TOE – Total Organic Extract

YD – Younger Dryas

CHAPTER ONE

1. Introduction

The Arctic Ocean is an area of global research focus due to the symbiotic relationship between its extensive sea ice cover and the unprecedented climate warming observed in recent decades (Dickson, 1999; Parkinson et al., 1999; Stroeve et al., 2007, 2012b; Steele et al., 2008). Continuous monitoring of sea ice extent and concentration became possible in 1978 with the introduction of satellite-mounted passive microwave sensors (Sandven et al., 2006) and subsequent emergence of comprehensive databases (Peng et al., 2013; Walsh et al., 2017). However, resolving the underlying causes of recent ice decline and, more generally, better prediction of potential consequences of a warming Arctic requires paleo-climate reconstruction of critical parameters, such as sea ice concentration and the associated response of marine biota (e.g. primary producers and grazers) to significant climate change throughout the geological record. Amongst a multitude of biogenic proxies developed to this end (e.g. Eglinton and Eglinton, 2008; Lea, 2014), C_{25} Highly Branched Isoprenoid (HBI) alkenes show promise when both reconstructing seasonal sea ice concentration and the occurrence of highly-productive Marginal Ice Zone (MIZ) conditions (Belt and Müller, 2013; Belt, 2018). This thesis investigates the potential of multivariate HBI distributions to better predict changes in sea ice conditions and decouple ice- (sympagic) and surface ocean-controlled (pelagic) productivity regimes in both contemporary and paleo-settings. The following sections introduce sea ice as a driver and indicator of global climate change (section 1.1), and the Barents Sea as a key study region where associated consequences are readily apparent (section 1.2). Marine paleoclimatological proxies and current development of HBIs, in particular, are introduced in section 1.3, and specific aims of this project are presented in section 1.4.

1.1 Sea Ice

1.1.1 Ice within the Arctic ecosystem

The average ice cover in the Arctic Ocean ranges between ca. 5–16 million km^2 (1–3% of the Earth's surface area) at its annual minimum (September) and maximum (February–March) respectively, making it the most expansive biome on the planet (Zwally and Gloersen, 2008; Peng et al., 2013). Seasonal ice extent variability largely occurs in shallow-shelf areas of the Arctic, most of which are completely ice-covered during winter and ice-free during summer (Johannessen et al., 2004). The majority of the Arctic Basin is therefore ice-covered at the winter maximum, whilst only the Central Arctic and northwest Greenland retains its ice cover in September (Perovich and Richter-Menge, 2009). The seasonal amplitude of sea ice extent (SIE) for 2017 is illustrated in Figure 1.1.

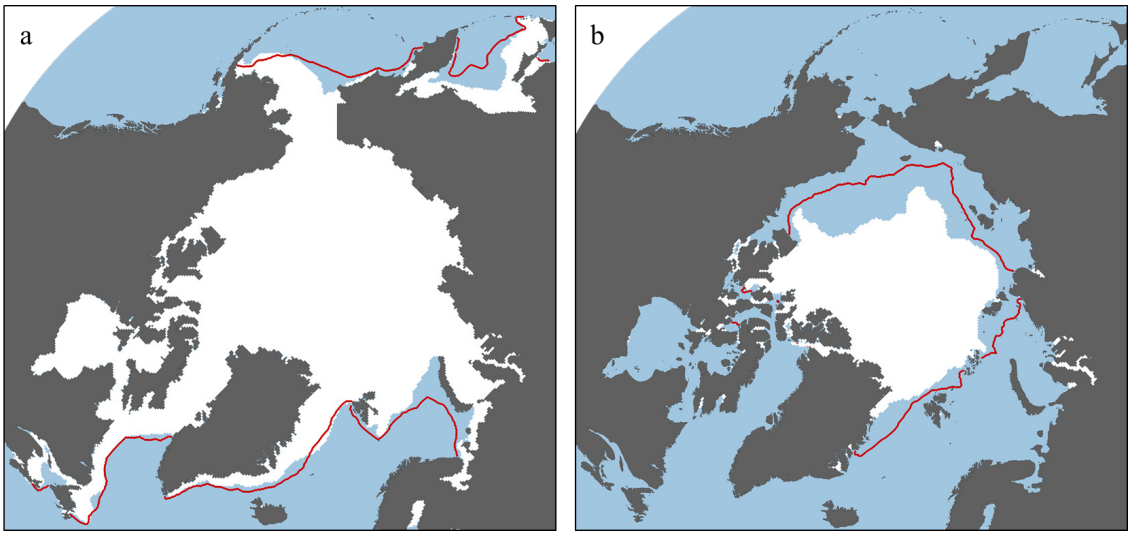

Figure 1.1: Arctic sea ice extent (>15% ice cover) for March (a) and September (b) of 2017, shown as white polygons. Solid red lines represent mean ice extent (1981–2010). Data from: National Snow and Ice Data Centre (Fetterer et al., 2017).

In addition to thinner, more saline first-year ice, the Arctic Ocean is characterised by thicker, less saline perennial ice, which is most abundant in September (when only a proportion of first-year ice survives the melt season) and comprises 30–

50% of the total minimum ice extent (Weeks and Ackley, 1986; Tschudi et al., 2016). Conversely, perennial ice declines over the winter through export via the Fram Strait, driven by wind and oceanic currents, most notably the Beaufort Gyre and Transpolar Drift (TPD) circulation modes (Colony and Thorndike, 1984). Over 0.6–1.0 million km^2 of the total sea ice area is exported annually to the North Atlantic (Polyak et al., 2010; Smedsrud et al., 2017). Such considerable annual variability of sea ice cover in the Arctic stems from the complex interactions between sea ice, ocean and the atmosphere. Rather than an isolated element, sea ice is pivotal for the Arctic ecosystem. Ice formation when the surrounding water reaches its freezing point (0°C to -1.9°C depending on salinity; Thomas and Dieckmann, 2010) expels brine and increases surface water salinity and density. The resulting oceanic convection affects the water column to a depth of 4000 m (Broecker, 1998) and facilitates the cooling and sinking of incoming warm waters from the Southern Hemisphere, forming North Atlantic Deep Water (NADW) and therefore directly influencing the Thermohaline Circulation (Perovich and Richter-Menge, 2009; Meier et al., 2014). Inversely, melting of ice introduces freshwater to the top layers of the water column, inducing strong stratification and limiting convection to 50–100 m (i.e. the Arctic Halocline). A crucial factor controlling the heat budget of the ocean-ice-atmosphere interface, and therefore influencing changes in ice extent, is the relatively high albedo (reflectivity) of sea ice. Ice is opaque and reflects up to 85% of incoming solar shortwave radiation whereas open water reflects 7–10% (Pegau and Paulson, 2001; Perovich and Polashenski, 2012). Sea ice therefore acts as an insulator and regulates the thermodynamic ice-ocean-atmosphere interactions and the oceanic heat budget, as well as exchange of gases such as CO_2, O_2 and dimethylsulphide (Vihma, 2014). An example is the reduction of poleward atmospheric heat flux during colder seasons due to effective turbulent heat loss from the ice and ocean surface (Serreze et al., 2007). Albedo is sensitive to the

physical properties of ice, and reduces with the presence of melt ponds/polynya (20–40%) and the absence of snow cover (ca. 65%), as well as changes in ice thickness (Warren et al., 1999; Perovich et al., 2002; Perovich and Polashenski, 2012). Cloud cover also affects the surface heat budget and ice albedo, regulating the radiative fluxes to the ice/ocean (Makshtas et al., 2007); longwave radiation is trapped in winter and its influx is augmented during the warmer seasons. Denser cloud cover can also prevent shortwave radiation (sunlight) from reaching the ice in the summer. Therefore, high and dense clouds cool the ice surface, while low clouds warm it (Uttal et al., 2002; Francis and Hunter, 2006; Palm et al., 2010). Overall, thermodynamics governing the surface heat budget are a key factor in controlling physical properties of ice (thus influencing ice dynamics) and the melt-freeze cycle.

Sea ice also governs many of the biochemical processes in the Arctic (Vancoppenolle et al., 2013; van Leeuwe et al., 2018). It is a global site of primary productivity and serves as a habitat for rich and diverse populations of species ranging from microorganisms (e.g. phytoplankton) to apex predators (e.g. the polar bear). Ice algal production contributes ca. 10% and 55% to total primary production in seasonal shelf seas and the multi-year ice covered Central Arctic, respectively (Gosselin et al., 1997; Søreide et al., 2013). Food webs associated with sea ice are closely tied to localized seasonal primary productivity blooms, which take place at both the ice-ocean interface along the receding ice edge – in highly productive areas known as Marginal Ice Zones (MIZs; Smith and Sakshaug, 1990) – and directly under the ice (Strass and Nöthig, 1996; Mundy et al., 2009; Arrigo et al., 2012; Assmy et al., 2017). Such blooms are highly reliant on sea ice thickness and presence/absence of snow cover, which affect light availability for photosynthesis, as well as the rate and timing of the sea ice melt, which influences stratification and hence controls nutrient upwelling to the photic zone (Meier et al., 2014). Higher up the food web, critically important ice-associated fish,

such as arctic cod, serve as prey to a myriad of other species (Bluhm and Gradinger, 2008). Many mammals at higher trophic levels rely on sea ice as grounds for hunting, as well as birthing and raising offspring (Derocher et al., 2011; Kovacs et al., 2011; Brown et al., 2018). Conversely, areas without sea ice are dominated by almost entirely different floral and faunal assemblages; changes in sea ice extent and other properties could therefore influence the balance between ice-obligate and other species, and hence their survivability (Hegseth and Sundfjord, 2008; Søreide et al., 2013; Bhatt et al., 2014).

Overall, it is evident that sea ice melting, freezing and movement dynamics are closely related to global atmospheric and oceanic circulation of moisture and heat (and the associated shifts in temperature). However, while the short-term variability of sea ice cover is largely governed by the seasonal changes within the Arctic, long-term trends of ice properties (extent, thickness, age) and dynamics (e.g. ice export) are crucial for understanding the causes and implications of global climate change (Bhatt et al., 2014; Meier et al., 2014; Vihma, 2014).

1.1.2 Current Trends of sea ice extent and physical properties

The unprecedented global temperature warming observed in the last few decades and associated implications for the Earth's climate are a subject of ongoing discussion. The average annual temperature has increased by ca. 1.0°C from the 1950–1980 mean, with 2016 ranking as the warmest year to date – among the 10 in record high annual temperatures since 2000 (Hansen et al., 2010). The warming trend is accompanied by an increase of atmospheric greenhouse gas concentrations – most notably CO_2 – to unprecedented levels due to anthropogenic forcing, such as fossil fuel combustion (Solomon et al., 2009; Notz and Marotzke, 2012). Other greenhouse gases, such as

methane, also contribute to the continuous surface warming trend (Montzka et al., 2011). Elevated CO_2 concentrations have been linked to previous warming events, such as the last deglaciation (Shakun et al., 2012). Overall, radiative forcing is a prime contributor to the recent temperature trend.

As discussed in section 1.1.1, Arctic sea ice is highly sensitive to changes in heat input, and is therefore an important indicator of climate change. In accordance with the global temperature increase, Arctic sea ice extent, thickness and the perennial ice fraction are decreasing since the emergence of satellite measurements in 1978, without precedent within the instrumental record; the negative trend is clear despite the large seasonal variability of ice cover (Walsh et al., 2017). The steepest decline in ice extent was recorded in September, where values lower than the 1981–2010 average of 6.5 million km^2 were consistently observed since 2002 (Fetterer et al., 2017; Onarheim et al., 2018). The most precipitous decreases occurred in 2007 and 2012, with corresponding extents of 4.29 and 3.62 million km^2 (Kerr, 2007; Stroeve et al., 2012a). Additionally, the rate of summer sea ice retreat has continuously accelerated, reaching ca. 13% per decade by 2016 (Meier et al., 2007, 2014; Stroeve et al., 2014; Fetterer et al., 2017); the average September extent is now at least 40% lower than in 1979 (Onarheim et al., 2018). The trend persists to a lesser extent throughout the year, with average decreases of ca. 6% per decade in early autumn and 3% per decade in winter (Meier et al., 2014; Stroeve et al., 2014). While the long-term ice retreat is pan-Arctic in nature (Polyak et al., 2010), regional variability is even more apparent; for example, ice extent in the Chukchi Sea has dropped so precipitously that the area has been almost ice-free every September since 2007 (Walsh et al., 2017). Overall, over 75 record low values of ice extent have been recorded on a monthly scale since the last sea ice maximum of 1986 (Parkinson and DiGirolamo, 2016). Mean values of regional and

pan-Arctic sea ice extent spanning the satellite record are shown in Table 1.1 (with regions identified in Fig. 1.2) and Figure 1.3, respectively.

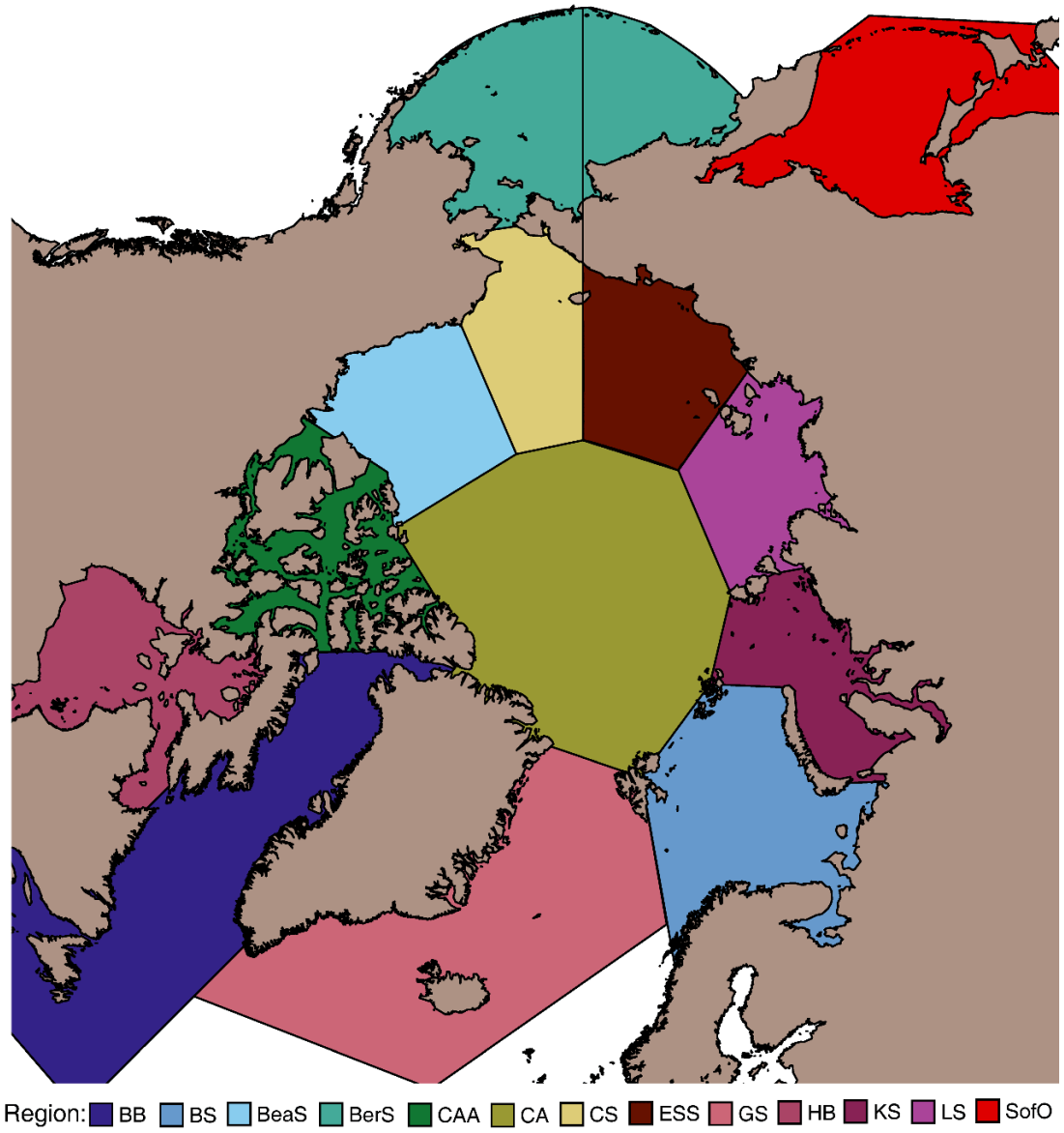

Figure 1.2: Areas of the Arctic used for reginal calculations. Polygon shapefiles from: National Snow and Ice Data Centre (Fetterer et al., 2010). Abbreviations denote Baffin Bay (BB), Barents Sea (BS), Beaufort Sea (BeaS), Bering Sea (BerS), Canadian Arctic Archipelago (CAA), Central Arctic (CA), Chukchi Sea (CS), East Siberian Sea (ESS), Greenland Sea (GS), Hudson Bay (HB), Kara Sea (KS), Laptev Sea (LS), Sea of Okhotsk (SofO). The software used to analyse satellite data and create Fig. 1.2, 1.4, 1.6 and Tables 1.1, 1.2, was developed for the purposes of this research using the R version 3.5.0 (R Core Team, 2018), and the source code made available in Appendix A.

Table 1.1: Regional decline of spring (April–June), winter (January–March), and annual mean sea ice extent for the 1979–2017 period. Abbreviations denote: SpSIE – spring sea ice extent; WinSIE – winter sea ice extent. Regions used for calculations are shown in Fig. 1.2. Satellite data from: Sea Ice Index, National Snow and Ice Data Centre (Peng et al., 2013; Meier et al., 2017).

	Average values for 1979–2017 (10^4 km^2)			Trends (10^4 km^2 decade^{-1})		
Region	SpSIE	WinSIE	Annual SIE	SpSIE	WinSIE	Annual SIE
BB	103.6 ± 12.0	128.3 ± 18.1	75.9 ± 10.5	-5.6 ± 1.5**	-7.1 ± 2.3*	-5.6 ± 1.2**
BS	64.0 ± 22.1	76.1 ± 19.4	45.9 ± 14.6	-14.7 ± 2.1**	-13.2 ± 1.8**	-10.5 ± 1.2**
BeaS	92.1 ± 2.5	94.0 ± 0.0	85.9 ± 5.4	-0.8 ± 0.3*	0.0 ± 0.0	-3.1 ± 0.6**
BerS	35.0 ± 9.5	67.7 ± 11.2	29.2 ± 5.2	-0.6 ± 1.4	0.2 ± 1.6	-0.5 ± 0.7
CAA	75.1 ± 0.8	76.1 ± 0.0	69.1 ± 2.3	-0.2 ± 0.1	0.0 ± 0.0	-1.0 ± 0.3*
CA	322.1 ± 0.7	321.6 ± 1.5	319.6 ± 3.0	0.0 ± 0.0*	-0.8 ± 0.2**	-1.7 ± 0.3**
CS	79.0 ± 2.5	83.0 ± 0.0	65.9 ± 5.9	-1.3 ± 0.3**	0.0 ± 0.0	-4.3 ± 0.5**
ESS	129.9 ± 1.4	130.4 ± 0.0	118.6 ± 8.1	0.0 ± 0.2	0.0 ± 0.0	-5.1 ± 0.8**
GS	75.2 ± 8.4	80.4 ± 13.6	62.5 ± 8.6	-5.1 ± 0.9**	-9.2 ± 1.3**	-5.9 ± 0.8**
HB	115.8 ± 4.5	123.0 ± 0.7	77.0 ± 5.3	-2.5 ± 0.5**	-0.1 ± 0.1	-3.2 ± 0.6**
KS	88.9 ± 4.0	91.0 ± 1.8	71.9 ± 7.9	-2.1 ± 0.5**	-0.8 ± 0.2**	-5.2 ± 0.7**
LS	85.9 ± 1.4	87.2 ± 0.0	76.5 ± 5.3	-0.5 ± 0.2*	0.0 ± 0.0	-3.0 ± 0.6**
SofO	37.1 ± 10.1	98.4 ± 17.8	37.3 ± 6.9	-4.6 ± 1.2**	-9.0 ± 2.1**	-3.6 ± 0.8**

*Trends significant at a 95% confidence level

**Trends significant at a 99.9% confidence level

Other physical properties that are critical for maintaining the distribution and integrity of sea ice cover have also been declining. Considerable thinning of perennial sea ice cover was inferred from data obtained by nuclear submarine campaigns during the 1950s–1990s (Rothrock et al., 2008; Wadhams et al., 2011), Upward Looking Sonar (ULS) stations (Hansen et al., 2013), satellite measurements from relatively recent ICESat and CryoSat-2 missions (Laxon et al., 2013; Kwok and Cunningham, 2015), and combinations of these data (Kwok and Rothrock, 2009; Lindsay and Schweiger, 2015). Although ice thickness data is more sporadic and less reliable than that of sea ice extent due to various sources of uncertainty (Zygmuntowska et al., 2014), there is a clear negative trend. According to Rothrock et al. (1999), the mean ice draft (thickness of underwater ice) had decreased by 1.3 m (from 3.1 m to 1.8 m) between 1958–1976 and 1993–1997. Subsequently, a loss of 1.75 m (from 3.64 m to 1.89 m) was inferred for the

1980–2008 period; over 0.5 m of this decline occurred between 2003–2008 (Kwok and Rothrock, 2009). A further study found summer ice volume had reduced by 4.39 × 10^3 km^3 between 2003–2008 and 2010–2012, with a lesser change of 1.48 × 10^3 km^3 in winter (Laxon et al., 2013).

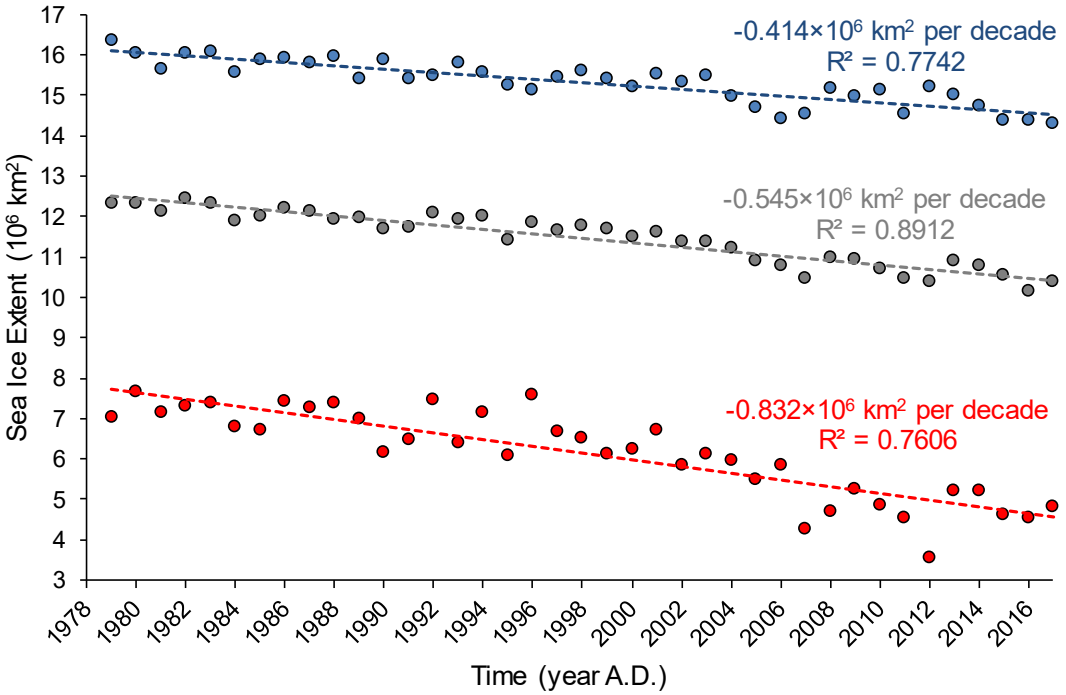

Figure 1.3: Trends of average September (red), March (blue), and annual (grey) pan-Arctic sea ice extent for the 1979–2017 period (Peng et al., 2013; Meier et al., 2017). All trends were significant at a 99% confidence level, with the greatest decline observed for the September sea ice minimum.

A property of sea ice directly affected by the thickness and volume decline is the perennial ice cover (Polyakov et al., 2012; Tschudi et al., 2016; Ye et al., 2016). Previous studies evaluated the trend of sea ice export via the Fram Strait (e.g. Comiso, 2012; Kwok et al., 2013; Krumpen et al., 2016). Recently, Smedsrud et al. (2017) concluded that the area of ice exported annually out of the Arctic Basin was consistently higher than the 1935–2014 mean value of 0.88 million km^2 since 2007, often exceeding 1.00 million km^2. A similar trend of increasing ice cover export since 1979 (ca. 3% per decade and 11% per decade for winter and summer months, respectively) was also inferred from satellite data. Such a depletion has led to considerable decreases of

summer perennial ice cover over relatively short timescales, such as the reduction from 3.0 million km^3 for the 2000–2006 period to 2.0 million km^3 in 2008 (Kwok and Rothrock, 2009). An overall decrease of perennial ice cover by 3.2 million km^2 since the late 1950s was noted by Nghiem et al. (2007); thus, only ca. 30% of the Arctic Basin is now covered by multi-year ice, in stark contrast to over 60% in the late 1970s (Maslanik et al., 2007; Kwok and Untersteiner, 2011). The shift in oldest ice that survived at least 4 melt seasons is even more severe, with a decrease from 2 million km^2 in the mid-1980s to a mere 106,000 km^2 in September of 2016 (Tschudi et al., 2016).

The unprecedented pan-Arctic trend of sea ice decline is the primary motivation for modelling endeavours, which aim to estimate future sea ice conditions in a warming climate. While there is a large spread of data associated with these predictions (Stroeve et al., 2015), the widely observed ice decline is attributed to anthropogenic forcing from increasing concentrations of greenhouse gases (Kay et al., 2011; Notz and Marotzke, 2012; Mueller et al., 2018). Under current conditions, the Arctic is projected to become seasonally ice-free by mid-21st century (Overland and Wang, 2013).

1.1.3 Causes and implications of sea ice decline

The recent sea ice decline (Table 1.2) is thought to be caused by a combination of external anthropogenic warming, which induces initial melting and thinning of the ice cover, and a series of interconnected positive feedback mechanisms that amplify and accelerate the decline over time (Perovich and Richter-Menge, 2009; Smedsrud et al., 2013; Meier et al., 2014; Zhang et al., 2018).

Table 1.2: Interannual development of the melt season length for 13 Arctic regions spanning the 1979–2017 period. Abbreviations denote: MO – Melt Onset; FO – Freeze Onset; MSL – Melt Season Length. Regions used for calculations are shown in Fig. 1.2. Satellite data updated from: NASA Cryosphere (Stroeve et al., 2014).

	Average values for the 1979–2017 period			Trends (days decade^{-1})		
Region	MO (day of year)	FO (day of year)	MSL (days)	MO	FO	MSL
BB	125.2 ± 28.8	332.4 ± 29.2	212.7 ± 64.5	-2.4 ± 0.8*	1.8 ± 0.8*	5.0 ± 1.7*
BS	129.9 ± 17.9	327.3 ± 23.9	214.3 ± 49.1	-8.1 ± 1.5**	6.1 ± 1.5**	17.6 ± 2.9**
BeaS	159.9 ± 5.5	264.5 ± 16.0	97.0 ± 20.3	-3.5 ± 0.7**	7.9 ± 1.3**	12.3 ± 1.7**
BerS	111.1 ± 17.4	340.3 ± 24.2	240.6 ± 50.8	-1.7 ± 0.8*	2.7 ± 1.2*	5.3 ± 2.2*
CAA	157.8 ± 7.7	264.1 ± 12.4	97.4 ± 15.9	-2.5 ± 0.6**	4.3 ± 0.9**	6.8 ± 1.3**
CA	168.3 ± 7.6	256.3 ± 14.6	80.5 ± 20.4	-3.9 ± 0.7**	5.4 ± 0.9**	9.9 ± 1.5**
CS	159.1 ± 8.3	286.9 ± 28.1	120.6 ± 34.0	-2.3 ± 0.7*	12.3 ± 1.4**	16.2 ± 1.6**
ESS	164.6 ± 4.9	267.3 ± 12.4	96.2 ± 16.4	-0.7 ± 0.7	10.6 ± 1.5**	12.5 ± 1.7**
GS	122.4 ± 27.1	315.3 ± 34.6	205.5 ± 77.6	-2.2 ± 1.0*	2.8 ± 1.5	3.8 ± 2.4
HB	148.3 ± 10.9	322.8 ± 20.8	168.0 ± 26.0	-4.3 ± 1.0**	5.6 ± 0.8**	11.5 ± 1.7**
KS	159.5 ± 11.9	291.3 ± 19.1	128.0 ± 27.5	-6.9 ± 0.9**	9.4 ± 1.4**	20.4 ± 2.3**
LS	167.3 ± 7.6	270.4 ± 9.5	96.9 ± 15.3	-3.5 ± 1.0*	7.3 ± 1.2**	12.1 ± 2.1**
SofO	110.1 ± 22.9	340.3 ± 29.0	246.4 ± 58.3	2.3 ± 1.0*	-1.6 ± 1.0	-5.1 ± 2.5

*Trends significant at a 95% confidence level

**Trends significant at a 99.9% confidence level

As the ice melts in response to increased air temperatures (Johannessen et al., 2004; Rothrock and Zhang, 2005), a greater inflow of warm Atlantic Water (Årthun et al., 2012; Ivanov et al., 2012), and increased cloud cover which amplifies the air-surface flux of longwave radiation (Francis and Hunter, 2006), the onset of the melt season is hastened and a larger area of the Arctic Ocean is left exposed. As a result, more heat is absorbed by the expansive area of open water due to its lower albedo, increasing the heat budget of the Arctic and the ocean-atmosphere moisture transfer. This leads to a delay in ice re-advance during Autumn and, over time, causes extension of the summer melt season (Fig. 1.4); this has led to melt onset that is ca. 10 days earlier than in 1979 (Stroeve et al., 2014), although a much greater hastening of 9 days per decade for the period of 1979–2008 was also reported (Maksimovich and Vihma, 2012). The

associated delay of autumn ice advance causes long-term cumulative thinning of the ice, making the cover more susceptible to deformation, wind forcing, increasing temperatures and radiative fluxes as a result of decreasing albedo (Rampal et al., 2009; Meier et al., 2014; Kwok and Cunningham, 2015). An overall positive trend in solar radiation absorbed by the ocean is prevalent over most of the Arctic (Steele et al., 2008). Furthermore, thinner, lighter ice travels at an increased drift speed (up to 20 ms^{-1}), leading to accelerated export of perennial ice through the Fram Strait (Polyak et al., 2010; Smedsrud et al., 2017). The decrease in albedo is further amplified by a reduction in summer snowfall and its replacement by rain, which increases the incidence of polynya (Screen and Simmonds, 2012; Willmes and Heinemann, 2016). The combined contribution of these factors leads to a pre-disposition of ice cover to accelerated melting through a positive feedback mechanism known as the ice-albedo feedback (Pegau and Paulson, 2001; Perovich and Polashenski, 2012; Smedsrud et al., 2013; Zhang et al., 2018), which also drives the augmentation of global temperature increase from ca. 0.9° to 1.4° in the Arctic – a phenomenon first termed Arctic Amplification (Bekryaev et al., 2010; Kumar et al., 2010; Miller et al., 2010a; Serreze and Barry, 2011). Potentially irreversible and rapid loss of sea ice (a 'tipping point') was proposed as a consequence of further long-term weakening of ice cover due to strengthening positive feedback and external forcing mechanisms (Lindsay and Zhang, 2005; Eisenman and Wettlaufer, 2009).

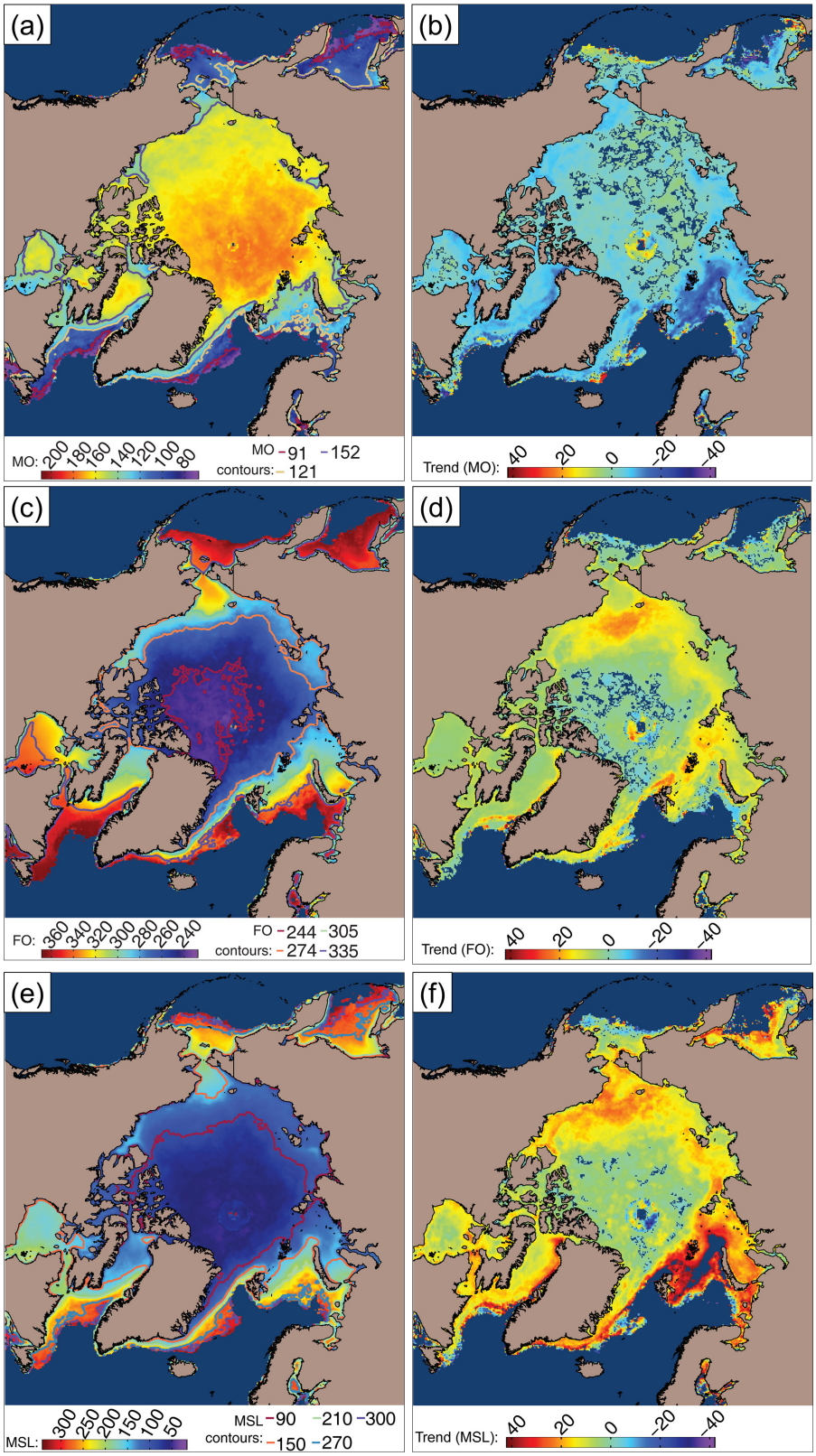

Figure 1.4: (a), (c) and (e) show, respectively, the pan-Arctic Melt Onset (MO; day of year), Freeze Onset (FO; day of year), and Melt Season Length (MSL; days) averaged for the 1979–2017 period; corresponding trends (in days) are illustrated in (b), (d), and (f). Satellite data from: NASA Cryosphere (Stroeve et al., 2014).

The trends in ice extent, thickness and variability have important implications for global oceanographic regimes, atmospheric heat circulation, Arctic food webs, and human activities. Lesser ice extent and ongoing warming of surface waters facilitates permafrost thawing in shelf areas, releasing large volumes of methane – a potent greenhouse gas (Montzka et al., 2011); additionally, local human communities may suffer from coastal erosion (Mioduszewski et al., 2018). Ice melting releases large volumes of freshwater and has been linked to considerable freshening of the North Atlantic (e.g. Peterson et al., 2006), potentially limiting convection and hindering deep water formation by virtue of increased stratification (Broecker, 1998; Thomas and Dieckmann, 2010). Large-scale atmospheric circulation patterns, such as the Arctic Oscillation (Oziel et al., 2016), are also affected by changes in sea ice cover. Current trends favour a negative phase of the Arctic Oscillation, which leads to weakening of westerly winds and strengthening of easterly winds at mid-latitudes (Francis and Vavrus, 2012) and to shifts within the normal flow of atmospheric waves. These abnormalities within the atmospheric circulation have been linked to the incidence of cold winters in Eurasia (Cohen et al., 2010; Petoukhov and Semenov, 2010; Eden, 2011; Osborn, 2011; Yang and Christensen, 2012; Mori et al., 2014), though this is still under debate (Ogawa et al., 2018). Snow precipitation in mid-latitudes has also increased as a result of more effective ocean-atmosphere moisture transfer during the summer melt season (Cohen et al., 2012; Liu et al., 2012).

The Arctic Ocean serves as a habitat to a variety of species, and consequences of changing climate on Arctic biology are apparent at all trophic levels (Vancoppenolle et al., 2013; van Leeuwe et al., 2018). The receding ice cover, extended melt season, and increased radiative heat fluxes to the ocean surface have resulted in a ca. 30% increase in primary productivity and hastened phytoplankton blooms throughout the Arctic Ocean (Bhatt et al., 2014; Arrigo and van Dijken, 2015; Kahru et al., 2016). However,

Arctic freshening and associated strong stratification of the upper water column could hinder deep-water upwelling of nutrients necessary for primary production, shifting the phytoplankton distribution to favour low-energy, smaller species (Arrigo et al., 2008; Hoppe et al., 2018). At increased water depths of the Central Arctic, a progressive shift of the ice cover towards first-year ice as a result of thinning and perennial ice export is likely to hinder sympagic production during the ice algal bloom by limiting the seeding potential of ice algae in ice that survives the melt season (e.g. Olsen et al., 2017). Thus, at all trophic levels, species reliant on ice cover and sympagic algae as an energy source are likely to suffer as a consequence of sea ice loss, while others will prosper. Examples include the northward expansion of temperate (i.e. sub-Arctic) species of phytoplankton (Hegseth and Sundfjord, 2008; Hoppe et al., 2018) and copepods (Ji et al., 2012; Assmy et al., 2017). Higher trophic species, such as polar bears and harp seals, are highly reliant on sea ice (Brown et al., 2018) and have experienced habitat loss (Derocher et al., 2011; Kovacs et al., 2011) and population decline (Stenson and Hammill, 2014). A further issue is increased competition for ice-associated prey, such as polar cod (Bluhm and Gradinger, 2008). With a larger area of the Arctic accessible to ship traffic, exploration (e.g. by natural resource industries) may contaminate natural habitats (Meier et al., 2014).

It is clear that the influence of climate change on sea ice cover is both amplified and reciprocated via a complex system of physical and thermodynamic processes which occur at the ocean-ice-atmosphere interface. The sensitivity of sea ice to changes in environmental conditions facilitates the application of ice cover as a prime indicator of climate change. However, several uncertainties remain as to the causes of recently accelerated sea ice decline – most notably, the relative influence of anthropogenic forcing and natural variability (Perovich and Richter-Menge, 2009; Meier et al., 2014). The ≈40-year record of continuous, satellite-derived sea ice extent (Fetterer et al., 2017)

does not allow for assessment of natural climate variability over geologically-significant timescales (Polyak et al., 2010). Therefore, reconstruction of past sea ice variability is crucial for understanding the causes and implications of modern trends (Harada, 2016; Onarheim et al., 2018) and for improving sea ice forecasts (Stroeve et al., 2015).

1.2 The Barents Sea

The seasonally ice-covered Barents Sea (Fig. 1.5) is the deepest Arctic shelf area, with an average depth of 230m, ranging from 50–500m at Spitsbergen bank and western Bear Island, respectively. Areal constraints include the continental shelf break to the west (between Norway and Spitsbergen) and Novaya Zemlya to the east, while the northern and southern boundaries are defined by the Svalbard shelf break and northern Norwegian coast, respectively (Loeng, 1991; Smedsrud et al., 2010, 2013). The following sections outline the current knowledge of the paleoceanographic and sea ice history of the Barents Sea since the late Weichselian glaciation, and contextualise the critical role of the contemporary region as an Atlantic Water inflow pathway into the Arctic Ocean in light of recent warming and sea ice retreat.

1.2.1 Paleoceanographic setting since the last glacial advance to the shelf

Extensive geomorphological evidence indicates that an ice sheet (Barents Sea Ice Sheet, or BSIS) covered the entirety of the Barents Sea, with at least four major advances to the western continental shelf break throughout the last 150 cal kyr BP (e.g. Mangerud et al., 1998), the last of which peaked at ca. 26–19 cal kyr BP and was designated the Last Glacial Maximum (LGM; e.g. Peltier and Fairbanks, 2006). Reconstructions of major changes in sea ice dynamics and primary productivity associated with ice sheet advance and retreat is crucial for understanding current climate change. For example, the late Weichselian marine-based BSIS is considered a viable

analogue for the contemporary West Antarctic Ice Sheet (WAIS; Andreassen and Winsborrow, 2009; Bjarnadóttir et al., 2014), the projected debuttressing of which (e.g. Hulbe et al., 2017) is potentially accompanied by a meltwater-fueled equatorward expansion of sea ice with a catastrophic impairment of deepwater circulation and primary production in the Southern Ocean (Menviel et al., 2010; Bakker et al., 2017).

Early reports provided contrasting interpretations as to the maximum extent and dynamics of the BSIS, with both the absence (e.g. Boulton, 1979) or presence of a grounded ice sheet throughout the LGM (Patton et al., 2015, 2016, 2017; Hughes et al., 2016, and references therein). A wealth of morphological, chronological, seismic and stratigraphic evidence now indicates that the BSIS was proximal to the western Barents Sea margin by ca. 29–26 cal kyr BP (Clark et al., 2009; Jessen et al., 2010; Hughes et al., 2016), and had reached the western continental shelf edge and joined the Fennoscandian Ice Sheet (FIS) between ca. 24–22.7 cal kyr BP (Landvik et al., 1998; Clark et al., 2009; Jessen et al., 2010; Chauhan et al., 2016) since pan-Arctic ice sheet growth commenced ca. 33–32 cal kyr BP (e.g. Eldevik et al., 2014). The ice sheet reached the northern margin slightly earlier at ca. 27 cal kyr BP (Knies et al., 2000, 2001). The circum-Arctic duration of the LGM (ca. 26–19 cal kyr BP; Peltier and Fairbanks, 2006; Clark et al., 2009; Pope et al., 2016) is further supported by the occurrence of consistently low eustatic sea level during this period (Peltier and Fairbanks, 2006). Throughout the LGM, AW was present at the western and northern margins as both a surface and sub-surface current, facilitating recurrent seasonally open-water conditions across both the western (e.g. Rasmussen et al., 2007; Müller et al., 2009; Jessen et al., 2010; Junttila et al., 2010; Müller and Stein, 2014) and northern (e.g. Knies and Stein, 1998; Knies et al., 1999; Nørgaard-Pedersen et al., 2003; Chauhan et al., 2016) Svalbard margins and providing a moisture supply crucial for sustained ice sheet growth. Most recently, a multiproxy geochemical study by Knies et al. (2018)

revealed almost uninterrupted primary productivity at the western Barents Sea shelf edge adjacent to the BSIS throughout ca. 32–16 cal kyr BP, and attributed this to the presence of coastal polynya sustained by katabatic winds and nutrient upwelling via inflowing AW. Less productive, largely perennial sea ice conditions were inferred for a Fram Strait sedimentary record further north (Müller et al., 2009; Müller and Stein, 2014), which nonetheless exhibited periods of increased sympagic and pelagic primary production. The initial destabilisation of the BSIS occurred as early as 20.5–18.5 cal kyr BP off western and northern Svalbard (e.g. Jessen et al., 2010; Junttila et al., 2010; Chauhan et al., 2016). This coincided with a meltwater pulse at ca. 20–19 cal kyr BP and an associated rise of sea level was recorded (Clark et al., 2004; Clark et al., 2009), as well as increasing summer insolation (Berger and Loutre, 1991; Laskar et al., 2004) and mean annual temperatures (Siegert and Dowdeswell, 2002), all of which likely triggered the initial retreat of Northern Hemisphere ice sheets (e.g. Clark et al., 2009). Hormes et al. (2013) additionally argued for the continued thinning of the BSIS throughout the LGM as a consequence of aridification driven by shifting atmospheric circulation patterns. Following destabilisation, continued sea level rise, increasing insolation, and ice outflow through ice streams, including the major Bjornoyrenna Ice Stream (e.g. Winsborrow et al., 2010), caused a final collapse of the BSIS at ca. 18–17.6 cal kyr BP, which was accompanied by a massive meltwater discharge marking the onset of Heinrich Stadial 1 (HS1; Hemming, 2004) reflected by depleted $\delta^{18}O$ values of planktic foraminifera (e.g. Jessen et al., 2010; Chauhan et al., 2016). The meltwater pulse caused a significant weakening of the AMOC at ca. 17.5 cal kyr BP (e.g. McManus et al., 2004; Ritz et al., 2013), and strong water column stratification caused prevalence of perennial sea ice cover with near-zero primary productivity (e.g. Müller and Stein, 2014) throughout the Nordic Seas until ca. 16 cal kyr BP. Around this time, the BSIS and FIS separated ca. 17–14 cal kyr BP (e.g. Newton and Huuse, 2017), with

recent model results suggesting a date of ca. 15.5 cal kyr BP (Patton et al., 2017). Following AMOC recovery at ca. 16–15 cal kyr BP (Ritz et al., 2013), increasing insolation and renewed intrusion of warm, sub-surface AW into the Nordic Seas caused a return to seasonally open water conditions (e.g. Lubinski et al., 2001; Ślubowska et al., 2005; Ślubowska-Woldengen et al., 2007, 2008; Łącka et al., 2015), which coincided with significant increases in primary productivity exceeding current values in the northern Barents Sea (Wollenburg et al., 2004) and marked the onset of the Bølling-Allerød.

Following the Barents Sea Ice Sheet (BSIS) collapse between ca. 18.5–16 cal kyr BP (e.g. Patton et al., 2016, 2017), and the warm Bølling-Allerød interstadial (BA; ca. 14.5–12.9 cal kyr BP) characterised by cool, sub-surface AW inflow (Koç et al., 2002; Ślubowska-Woldengen et al., 2008) and high sedimentation rates fuelled by turbid meltwater (Jessen et al., 2010) from BSIS remnants (Hormes et al., 2013; Klitgaard-Kristensen et al., 2013), the YD (ca. 13.0–11.7 cal kyr BP) manifested as a cold stadial throughout the Arctic Ocean and the Northern North Atlantic (e.g. Broecker, 2006; Bakke et al., 2009). The YD is thought to be caused by a vast meltwater outflow from the deglaciating Laurentide ice sheet ca. 12.9–13.0 cal. kyr BP (LIS; e.g. Tarasov and Peltier, 2005; Rasmussen et al., 2006). Sea level rise contributed to Transpolar Drift-controlled deglacial meltwater and pack ice transport through the Fram Strait (FS) into the Northern North Atlantic (NNA; Bradley and England, 2008). Thus, long-term freshening and stratification hampered the AMOC by ca. 30% (McManus et al., 2004; Condron and Winsor, 2012; Ritz et al., 2013) and caused a southward ice expansion. In the Barents Sea, this was reinforced by the melting Barents and Kara Sea ice sheets (e.g. Matthiessen and Knies, 2001; Hormes et al., 2013), with meltwater from the Laptev Sea (Spielhagen et al., 2005; Fahl and Stein, 2012).

Gradual AMOC recovery from ca. 12.2 cal kyr BP (Ritz et al., 2013) increased northward AW advection towards the Fram Strait. Together with decreasing meltwater influence from waning glaciers (e.g. Hormes et al., 2013) and peak solar insolation (Laskar et al., 2004), the resumption of warm AW transport by ca. 12 cal kyr BP rejuvenated primary productivity in the Barents Sea by ca. 12–11.5 cal kyr BP (Rasmussen et al., 2007; Bakke et al., 2009; Müller and Stein, 2014; Eilertsen, 2016) and coincided with generally ameliorated Preboreal (PB) conditions. The warming was punctuated by a cooling termed the Preboreal Oscillation (PBO; e.g. Hald and Hagen, 1998; Husum and Hald, 2002), a consequence of a short-lived (ca. 1.5–3 yr) meltwater outburst into the Arctic Ocean from the northwest outlet of Lake Agassiz (Fisher et al., 2002). This freshwater discharge via the FS at 11.25 cal. kyr BP decreased northward AW inflow via surface stratification, cooling the Barents Sea for the next ca. 300 years (e.g. Hald et al., 2007). Warmer conditions mediated by surface and sub-surface AW returned at ca. 10.9–10.8 cal kyr BP, with peak primary productivity and SSTs throughout the Norwegian coast (e.g. Knies et al., 2003; Risebrobakken et al., 2010; Risebrobakken et al., 2011), south of Spitsbergen (e.g. Rasmussen and Thomsen, 2015), and along the continental margins of Svalbard (e.g. Sarnthein et al., 2003; Ebbesen et al., 2007; Ślubowska-Woldengen et al., 2007; Skirbekk et al., 2010; Aagaard-Sørensen et al., 2013; Rasmussen et al., 2014; Werner et al., 2016). The AMOC (Ritz et al., 2013) and northward AW transport peaked between ca. 10.8–10.0 cal. kyr BP around Svalbard (Risebrobakken et al., 2010, 2011). Together with maximum summer insolation (Berger and Loutre, 1991; Laskar et al., 2004), this likely increased summer SSTs beyond modern values in the Arctic (e.g. Miller et al., 2010b) during an interval termed the Holocene Climatic Optimum (HCO).

Surface ArW returned to the Svalbard margin between ca. 9.0–8.8 cal. kyr BP (e.g. Ebbesen et al., 2007; Spielhagen, 2012; Werner et al., 2016), and a decrease of

summer insolation (Laskar et al., 2004), corresponding to generally cooler conditions around Svalbard (e.g. Risebrobakken et al., 2010, 2011) and decreased surface salinity (e.g. Lubinski et al., 2001). Meltwater from the collapsing LIS at ca. 8.2 cal kyr BP (Rasmussen et al., 2006) further contributed to the cooling (Hald and Korsun, 2008; Klitgaard-Kristensen et al., 2013). This culminated in the so-called Neoglacial (ca. 6 cal kyr BP–present) period previously characterised in the Barents Sea by weakened AW advection (Klitgaard-Kristensen et al., 2013; Ritz et al., 2013; Rasmussen et al., 2014; Werner et al., 2016), decreasing summer insolation (Laskar et al., 2004), with widespread sea ice and glacier advances in northern Norway (e.g. Hald et al., 2007; Balascio and Bradley, 2012; Rasmussen and Thomsen, 2015) and the Svalbard margins (e.g. Ślubowska-Woldengen et al., 2007; Jessen et al., 2010; Müller et al., 2012; Berben et al., 2017). Additional freshwater from the Laptev Sea could have further enhanced ice export via the FS after ca. 5.2 cal. kyr BP, promoting autumn ice expansion (Werner et al., 2013) and leading to the establishment of contemporary oceanographic and sea ice regimes in the Barents Sea, with seasonally extensive sea ice cover observed at the northern Svalbard margin (Fetterer et al., 2017).

1.2.2 Contemporary oceanographic setting and sea ice conditions

The modern Barents Sea (Fig. 1.5) holds a key position within the Arctic Continental Shelf and represents the main pathway of Atlantic Water (AW) inflow into the central Arctic Ocean, which interacts with the seasonal ice cover further north (Smedsrud et al., 2013) and originates from the Norwegian Atlantic Current (NAC). At the western entrance to the Barents Sea, the current bifurcates into an extension flowing towards and along western Svalbard to become the West Spitsbergen Current (WSC), and an eastern branch travelling along the northern coast of Norway as the North Cape Current (NCaC; Ingvaldsen et al., 2004). A part of the WSC flows westward to the

Nordic Seas (Manley, 1995), while the NCaC eventually splits into two further branches directed towards Novaya Zemlya and northwards into the Hopen Trench. The NAC and WSC provide over half of the ocean-atmosphere winter heat flux in the Arctic Ocean (Serreze et al., 2007). In addition to AW, Barents Sea hydrography is mainly influenced by Coastal Water (CW) and Arctic Water (ArW; Sakshaug et al., 2009). The influx of CW takes place inshore of the NAC, where the Norwegian Coastal Current (NCC) carries brackish (<34.4 psu) water from the Baltic Sea. Riverine input and water from the North Sea also contribute to CW. Like the NAC, the NCC is strongly topographically steered eastward into the Barents Sea, flowing along the Norwegian coast towards Novaya Zemlya (Sætre, 2007). Less saline (<34.7 psu), cold (<0°C) ArW travels southward and enters the Barents Sea via two main pathways. The East Spitsbergen Current (ESC) flows along eastern Spitsbergen between Svalbard and Franz Josef Land, while the Persey Current (PC) travels westward along the northern boundary of the Barents Sea, entering between Franz Josef Land and Novaya Zemlya. The two cold water currents converge near eastern Svalbard to form the Bear Island Current (BIC), which is topographically steered around the southern Spitsbergen margin and continues inshore of the WSC (Loeng, 1991; Loeng et al., 1997).

A sharp temperature and salinity gradient forms across the boundary where AW and ArW meet, known as the Polar Front (PF). The position of the PF is relatively stable in the western Barents Sea (Loeng and Drinkwater, 2007), but exhibits considerable seasonal and inter-annual variability to the east. Indeed, separate temperature and salinity gradients form two distinct frontal zones (Oziel et al., 2016). Additionally, several water masses are locally formed as a result of mixing AW, ArW and CW (e.g. Schauer et al., 2002). A key water mass is the cold (ca. -1.9°C) and saline (ca. 35.2 psu) Barents Sea Deep Water (BSDW), formed primarily at the shelf of Novaya Zemlya through cooling of AW followed by increasing salinity due to brine

rejection associated with formation of sea ice. Most of the resulting bottom water is exported into the Arctic Ocean between Novaya Zemlya and Franz Josef Land and facilitates ventilation of the central Arctic (Aagaard and Woodgate, 2001; Schauer et al., 2002).

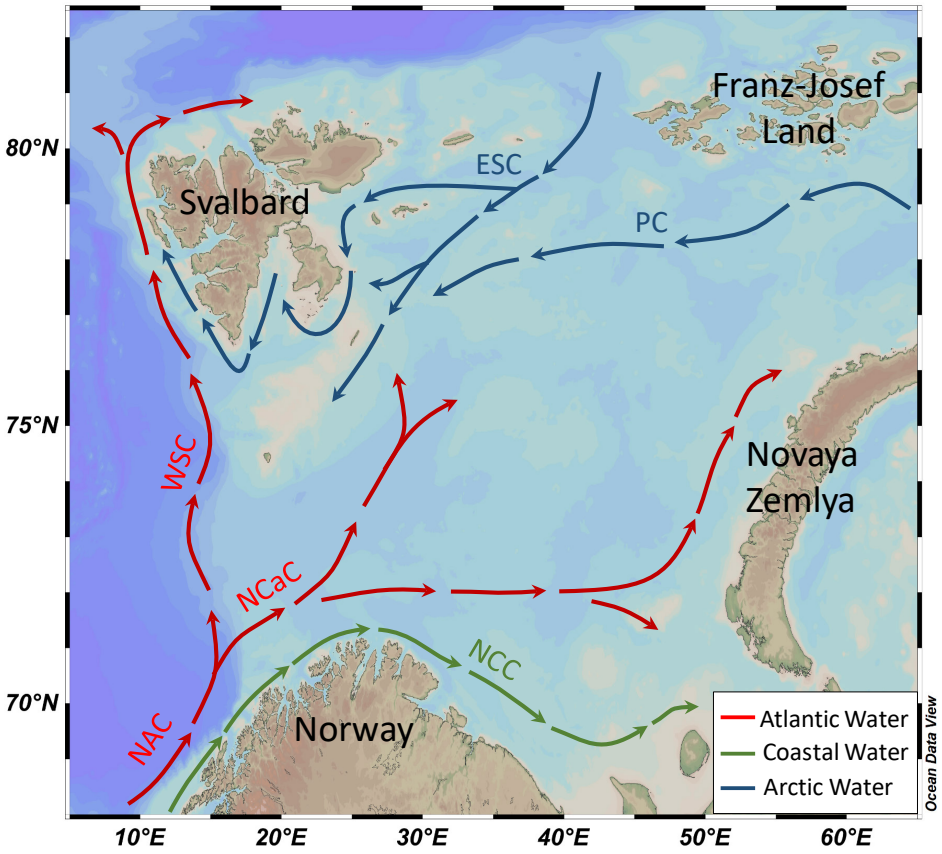

Figure 1.5: Map of the Barents Sea illustrating the main currents and bathymetry. Abbreviations include the Norwegian Atlantic Current (NAC), Norwegian Coastal Current (NCC), North Cape Current (NCaC), West Spitsbergen Current (WSC), East Spitsbergen Current (ESC), Persey Current (PC).

Direct annual inflow of ca. 2 Sv of AW (Loeng et al., 1997) supplies a large amount of heat to the Barents Sea (Smedsrud et al., 2010), over ca. 70×10^{12} W of which is lost to the atmosphere (Smedsrud et al., 2013), decreasing NAC temperature by ca. 5°C (Knies et al., 2007). The influence of AW profoundly affects the sea ice variability (Sorteberg and Kvingedal, 2006). Effective turbulent mixing of warm AW towards the surface by wind currents during the winter (October–March) facilitates selective thinning of the ice cover along the path of inflowing AW and keeps a

significant portion of western and northern Svalbard shelves ice-free (Walczowski and Piechura, 2011; Ivanov et al., 2012). Ice formation begins in October (Fig. 1.6), reaching maximum extent in March-April, while the melt season starts with increasing solar insolation in April (Sakshaug et al., 2009).

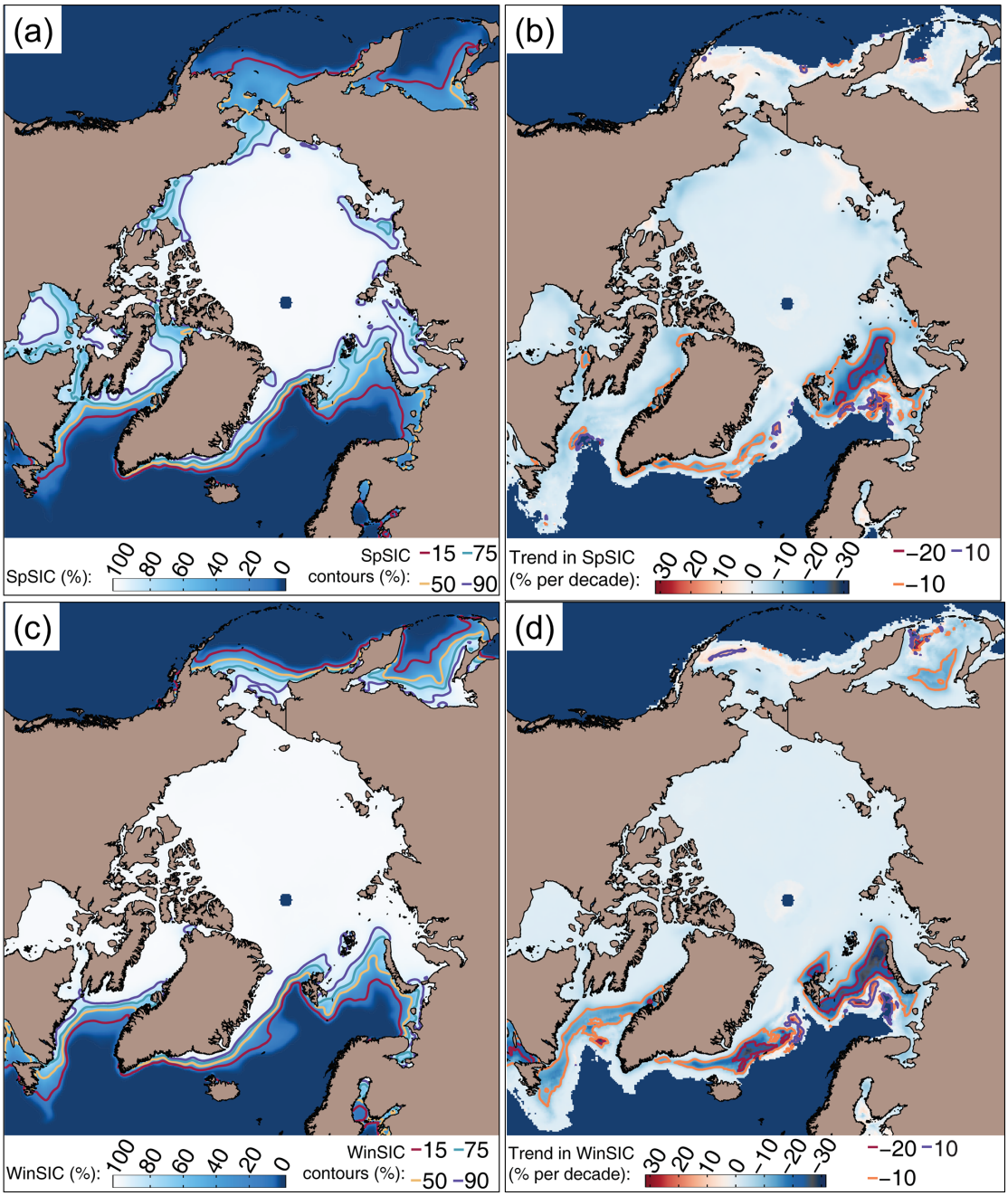

Figure 1.6: (a) and (c) illustrate the average spring (April–June) and winter (January–March) % sea ice concentration (SpSIC and WinSIC, respectively) in the Arctic for the 1988–2017 period. Solid lines represent contours. Corresponding least-squares trends for SpSIC and WinSIC, in % per decade, are shown in (b) and (d), respectively. Note the extensive spatial gradients in the central Barents Sea and around Svalbard.

Inter-annual sea ice variability reveals a strong negative trend similar to the pan-Arctic ice retreat, and correlated to that of the surrounding shelf seas (Onarheim et al., 2015; Table 1.2). The accelerated decline was linked to increasing inflow of AW, which has nearly doubled since 1980, resulting in a larger heat flux (Årthun et al., 2012; Johannesen et al., 2012; Lind and Ingvaldsen, 2012; Screen and Simmonds, 2012; Oziel et al., 2016). The 'Atlantification' of the Barents Sea has been linked to variability of several atmospheric circulation modes, such as the North Atlantic Oscillation (Loeng et al., 1997) and Arctic Oscillation (Ingvaldsen et al., 2004), which drive the increased volume transport, and – more recently – the Atlantic Multi-decadal Oscillation, which is correlated with the temperature of AW (Yashayaev and Seidov, 2015). The decreasing sea ice extent causes a larger ocean-atmosphere heat flux as a result of expansive area of open water, potentially strengthening the aforementioned atmospheric forcing mechanisms by maintaining a lower atmospheric pressure over the region (Smedsrud et al., 2013). Additionally, sea ice decline is likely to cause increased water temperatures as a function of solar heat flux (Sando et al., 2010). The area most affected by the sea ice decline and increasing AW inflow is the eastern Barents Sea, with potentially negative implications for deep water formation (Oziel et al., 2016). The decline of annual minimum and maximum sea ice extent for the 1979–2017 period is shown in Figure 1.7.

The Barents Sea serves as a habitat for a variety of flora and fauna, including various types of microalgae (Signorini and McClain, 2009), fish communities (Sakshaug et al., 2009), and marine mammals such as pinnipeds, cetaceans (Planque et al., 2014), and the polar bear (Brown et al., 2018). The region exhibits the highest primary productivity among the Arctic shelf seas, annually contributing an average of ca. 100 g C m^{-2} to the total primary production, ranging from <20–80 g C m^{-2} north of the Polar Front to over 300 g C m^{-2} in the well-stratified, shallow Spitsbergen shelf.

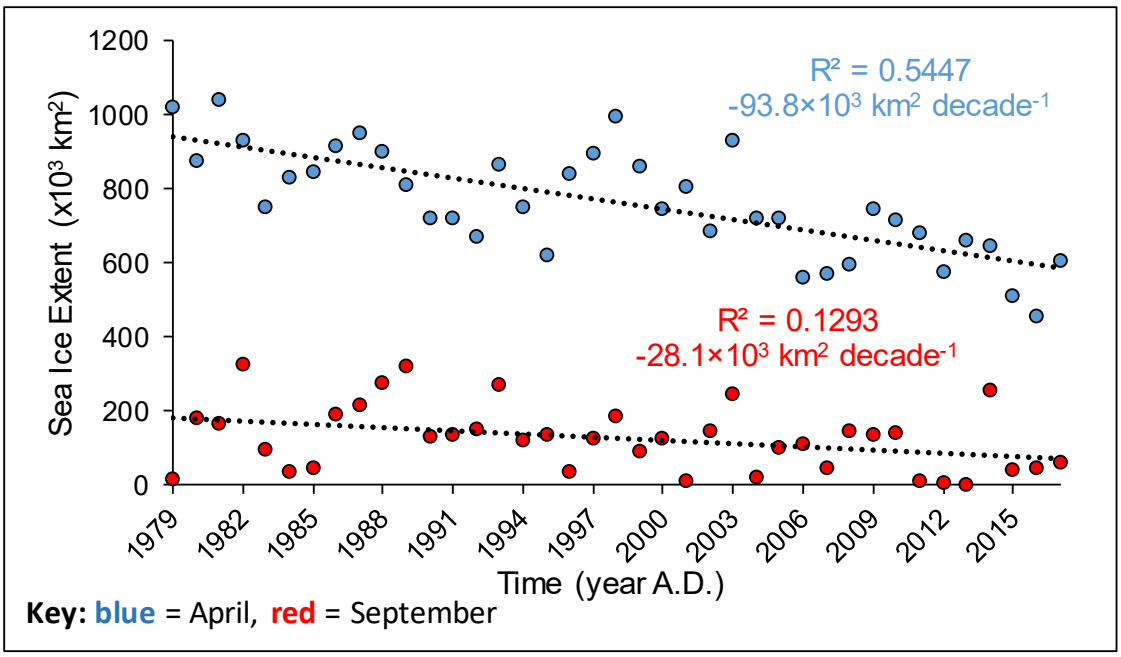

Figure 1.7: Trends of sea ice extent decline in the Barents Sea for the 1979–2017 period. Data from: National Snow and Ice Data Centre (Meier et al., 2017).

The mean primary production exhibits a large inter-annual variability of up to ca. 20% (Sakshaug et al., 2009), and is dominated by diatoms (Wassmann et al., 1999, 2006), with contributions from other types of microalgae, including haptophytes (e.g. coccolithophorids), dinoflagellates, and various picoplankton (Sakshaug and Slagstad, 1992; Hodal and Kristiansen, 2008). First, sympagic blooms of ice algae develop up to 2 months prior to seasonal ice retreat and are triggered by increasing solar insolation reaching the ice underside in March (Signorini and McClain, 2009). Ice algal biomass provides a fresh food source to the benthos, and triggers the maturation and reproduction of certain zooplankton, such as copepods (Søreide et al., 2010, 2013). Subsequently, region-wide ice recession towards the northern shelf break occurs at the onset of the solar insolation-triggered melt season during spring and summer (late April–September). The interplay of freshwater input and increased light penetration due to melting sea ice stabilises free-floating phytoplankton and AW-carried nutrients within the euphotic zone, developing extensive, but nutrient-limited (and therefore ephemeral) pelagic blooms in the MIZ within 20–50 km of the retreating ice margin

(Wassmann et al., 1999, 2006). The resulting algal biomass is initially dominated by diatoms (Signorini and McClain, 2009), which fuel energy transfer and growth of zooplankton (Tamelander et al., 2008; Leu et al., 2011), eventually reaching the ocean floor and aiding the survivability of benthic life (Søreide et al., 2010, 2013). Further, the development of leads and polynyas coupled with weak stratification from AW-induced melting of sea ice may trigger under-ice pelagic blooms even prior to the melt season (Strass and Nöthig, 1996; Arrigo et al., 2012; Assmy et al., 2017). Nitrate and silica depletion eventually allows phosphate-dependent algae, such as coccolithophores, to take over primary production in the summer (June–September), with clearly traceable blooms defined by high particulate inorganic carbon concentrations (Hopkins et al., 2015; Mikaelyan et al., 2015). Due to the complex zonal hydrography and seasonal sea ice cover in the Barents Sea, the timing of the pelagic diatom-driven spring bloom exhibits considerable spatial variability. In areas directly influenced by AW, such as the southwestern Barents Sea, the phytoplankton bloom is delayed due to slower stabilisation of the water column, which is mainly controlled by the warming of the water surface and forms a 10 m stratified top layer over the summer months. Earlier blooms can occur in some areas due to southward transport of melting ice via the Fram Strait (Kwok et al., 2005). The annual productivity in regions characterised by AW is up to twice as high relative to ice edge blooms due to wind-induced upwelling of nutrient-rich water (Sakshaug and Slagstad, 1992; Wassmann et al., 2006). Blooms in coastal water occur earlier due to a stronger salinity gradient hastening stratification (Loeng, 1991; Olsen et al., 2003). Overall, pelagic productivity constitutes over 80% of the total algal biomass in the Barents Sea (Leu et al., 2011; Søreide et al., 2013). Increasing temperature and volume of inflowing AW (Spielhagen et al., 2011; Spielhagen, 2012) and atmospheric warming associated with greenhouse gases (GHGs) have already increased primary productivity by ca. 30% since the 1990's (Arrigo and van Dijken,

2015) by reducing sea ice extent, expanding the width of the MIZ (Strong and Rigor, 2013), as well as prolonging and hastening the pelagic bloom season (Stroeve et al., 2014). Given the strong correlation between open water area and phytoplankton biomass in the Barents Sea (Dalpadado et al., 2014; Oziel et al., 2017), an increasingly earlier ice melt is likely to shorten the ice algal productivity season, with potentially serious consequences for primary consumers, such as the copepod *Calanus glacialis*, which depend on ice algae (Kohlbach et al., 2016), including for ontogenesis (Søreide et al., 2010). Reduced sympagic bloom duration and ice algal stocks may destabilise the reproductive cycle of such ice-obligate grazers in favour of pelagic-feeding boreal species (Leu et al., 2011). Thus, whether the observed increase in pelagic production (Arrigo and van Dijken, 2015) at the expense of sympagic algae benefits trophic energy transfer in Arctic food webs remains uncertain, despite recent indications of accelerated grazing in a warming climate (Richardson, 2008; Kvile et al., 2016).

In summary, the Barents Sea acts as a buffer by cooling the inflowing warm water to ca. 0°C and preventing warming of the central Arctic. Additionally, approximately 60% of inflowing AW is converted into BSDW (Aagaard and Woodgate, 2001; Schauer et al., 2002; Smedsrud et al., 2010), associated with efficient cooling and vertical mixing that helps transport atmospheric CO_2 to the ocean (Kaltin et al., 2002; Smedsrud et al., 2013). The recent increase in volume and temperature of the AW inflow (Årthun et al., 2012), and the associated decline in sea ice cover (Sorteberg and Kvingedal, 2006) may hinder deep water formation (Oziel et al., 2016) and further destabilize the timing of sympagic and pelagic algal blooms, potentially affecting the ecosystem at all trophic levels (Wassmann et al., 2006; Signorini and McClain, 2009; Derocher et al., 2011; Dalpadado et al., 2014). Such concerns provide incentive for further investigations in the region aimed at paleo-reconstruction of oceanographic and sea ice conditions in an effort to understand contemporary climate change.

1.3 Paleoclimate proxies in the Arctic Ocean

The need to reconstruct past climate variability over geologically significant timescales has facilitated development of paleo-proxies (Table 1.3) for temperature, productivity, and sea ice reconstruction (among others), based on assemblages and stratigraphic studies of micropaleontological fossils, in addition to biogenic geochemical biomarkers (for reviews, see Eglinton and Eglinton, 2008; Polyak et al., 2010; de Vernal et al., 2013a; Sachs et al., 2013; Lea, 2014). These are introduced in the following sections.

1.3.1 Common micropaleontological and geochemical proxy measures

At the high latitudes of the Arctic Ocean, micropaleontological proxies are largely encompassed by microscopic detrital matter (microfossils) originating from photo- and heterotrophic unicellular protists and crustaceans inhabiting various water depths and flourishing during particular seasons of the annual cycle. Depending on the producer taxa, such microfossils may be composed of various calcium carbonate polymorphs (Mortyn and Martínez-Botí, 2008), opal silica (Hopkinson et al., 2011; Not et al., 2012), or biopolymeric substances (de Vernal and Marret, 2007). For example, auto- and heterotrophic microprotists known as foraminifera produce calcareous tests (Kucera, 2007), while ostracodes (small crustaceans) possess a calcium carbonate exoskeleton (Cronin et al., 2002, 2013). Diatoms, the most prominent microalgal primary producers in the global ocean, produce a silica-based compound cell wall (i.e. frustule; Miettinen et al., 2013; Miettinen, 2018), while *ca.* 10–20% of pelagic protists known as dinoflagellates encase their diploid cells within a cyst made of polymeric dinosporin highly resistant to taphonomic processes and dissolution (Bogus et al., 2012). Upon death, such microfossils are deposited to the seafloor and contribute to the marine sedimentary record, where their distinctive physical properties (e.g. shell morphology),

and census data (e.g. presence/absence, relative abundances, and biodiversity) driven by different environmental tolerance ranges of species serve as sources of various proxy-based estimates in paleoclimatology. For instance, foraminiferal (Risebrobakken et al., 2011; Rüther et al., 2012; Hald et al., 2004, 2007; Ebbesen et al., 2007), diatom (Mietthinen et al., 2015; Miettinen, 2018) and dinocyst (de Vernal et al., 2013b) assemblages and their combination with mathematical transfer functions have been used to infer sea surface and sub-surface temperatures, as well as sea ice concentration in the Arctic, where high biodiversity of dinoflagellates and diatoms relative to foraminifera (Matthiessen et al., 2005) yields itself well to sea ice reconstruction (de Vernal and Rochon, 2011; de Vernal et al., 2013b), albeit with a competing temperature influence in case of the latter (Miettinen, 2018). A more straightforward, qualitative approach to paleo-inferences involves observation of high relative abundances of selected species characteristic of certain settings, with examples including foraminifera *Neogloboquadrina pachyderma* (sin.), *Melonis lobatulus*, and *Nonionellina labradorica* abundant in cold Arctic, warm Atlantic, and highly-productive waters near oceanic fronts, respectively (see e.g. Kucera, 2007; Chauhan et al., 2016 for summaries). Similarly, the parasitic pelagic ostracode *Acetabulastoma arcticum* (Cronin et al., 2010) and dinocysts of *Islandinium* and *Selenopemphix* sp. (e.g. de Vernal and Marrett, 2007) have been used to infer seasonal sea ice conditions, such as annual duration. Additional proxies, such as Ice-Rafted Debris (IRD) indicating input of iceberg and/or sea ice-entrained material to the seafloor (Andrews, 2000; Polyak et al., 2010; Stuart and Long, 2011) are often used to confirm such indirect inferences. Total counts or fluxes of microfossils may also be characteristic of seasonal productivity, with diatoms blooming in the spring (Wassmann et al., 1999; von Quillfeldt, 2000), followed by summer and autumn production of dinoflagellates and calcareous species (Signorini and McClain, 2009; Hopkins et al., 2015; Skirbekk et al., 2016). Transfer function-based quantitative

estimates of productivity in polar settings have also been attempted using dinocyst assemblages (Radi and de Vernal, 2008).

In addition to census data, stable isotope analyses of foraminifera (e.g. Ebbesen and Hald, 2004; Ravelo and Hillaire-Marcel, 2007; Bakke et al., 2009; Jessen et al., 2010) and, much less frequently, diatoms (Shemesh et al., 1992, 1995; Crosta and Koç, 2007) have been used for paleotemperature and paleosalinity estimates; for instance, meltwater injections from melting ice sheets have been detected across the Arctic and sub-Arctic as abrupt planktic $\delta^{18}O$ depletions associated with significant input of $H_2{}^{16}O$ into the surface waters (e.g. Bauch et al., 2001; Knies et al., 2018). Microfossil-based surface and bottom water temperature estimates have also been obtained from trace metal ratios, such as calcite Mg/Ca, using both foraminifera (Barker et al., 2005; Aagaard-Sørensen et al., 2013; Vázquez Riveiros et al., 2016) and ostracodes (Cronin et al., 2012) and based on the endothermic nature of Mg substitution into $CaCO_3$ (Lea et al., 2014, and references therein).

Despite their utility, both census-based and geochemical methods described above require detectable microfossils in the sedimentary record, and thus exhibit several common caveats. These include unavailability of intact microfossils in sufficient quantity for analysis, due to either dissolution of both siliceous (Nelson et al., 1995; Ragueneau et al., 2000; Stickley et al., 2009) and calcareous (Pfuhl and Shackleton, 2004; Zamelczyk et al., 2014; Werner et al., 2016) species under acidic conditions, presence of cryptic genetic species that are either not represented in contemporary oceans (Kucera, 2007) or difficult to identify reliably (Kucera et al., 2005; Brown et al., 2014c), and the inability of certain pelagic protists, such as diatoms and many dinoflagellates (Matthiessen et al., 2005; Crosta and Koç, 2007), to bloom under harsh (e.g. perennially ice-covered) conditions. Further, the indirect paleo-inferences based on species assemblages and morphology are often region-dependent and not applicable

globally – an issue potentially exacerbated by selective dissolution of less resistant microfossils and undocumented changes between the proxy-parameter relationship through geological time. One approach to circumvent such limitations involves the analysis of organic biomarker molecules indicative of their producer species (Eglinton and Eglinton, 2008; de Vernal et al., 2013a, and references therein), which are often resistant to post-depositional degradation and dissolution affecting microfossils. Notable examples include several ratio-based methods for geochemical paleothermometry that have emerged since the 1980s and include indices such as U^{K}_{37} (Brassell et al., 1986; Prahl and Wakeham, 1987), TEX_{86} (Schouten et al., 2002, 2003, 2013), and LDI (Rampen et al., 2007, 2012) based on fractional abundances of differently unsaturated long-chain C_{37} ketones (i.e. alkenones), relative cyclicity of C_{86} glycerol alkyl glycerol tetraethers (GDGTs), and isomers of long chain diols (LCDs), respectively. However, despite their extensive calibration (e.g. Müller et al., 1998; Conte et al., 2006; Kim et al., 2008, 2010; Tierney and Tingley, 2014, 2015) and application for paleotemperature investigations in temperate and sub-polar settings (e.g. Risebrobakken et al., 2010; Jenkyns et al., 2012; Lattaud et al., 2018), the limited temperature range of polar oceans hinders the applicability of these proxies (e.g. Bendle and Rosell-Melé, 2004), prompting development of specialised indices for low temperature ranges (e.g. TEX^{L}_{86} for <15°C) to variable success (Kim et al., 2010, 2012). In addition to such difficulties with obtaining accurate paleo-temperature estimates, none of the aforementioned proxies provide direct and unambiguous proxy evidence of seasonal sea ice cover in the polar oceans as another leading driver and indicator of climate (section 1.1).

1.3.2 Highly-Branched Isoprenoid (HBI) alkenes

Highly-branched isoprenoid alkenes are biogenic unsaturated hydrocarbons produced by a relatively narrow range of marine and lacustrine diatoms belonging to the

Haslea (e.g. Volkman et al., 1994; Belt et al., 1996; J. Wraige et al., 1997, 1999), *Pleurosigma* (e.g. Belt et al., 2000, 2001a; Grossi et al., 2004), *Rhizosolenia* (e.g. Sinninghe Damsté et al., 1999; Belt et al., 2017), *Navicula* (Belt et al., 2001b), *Berkeleya* (Brown et al., 2014b; Belt et al., 2016), and *Pseudosolenia* (Kaiser et al., 2016) genera. While HBIs may contain 20, 25, and 30 carbon atoms, C_{25} HBIs (termed haslenes; Fig. 1.8) containing 2–5 carbon-carbon double bonds are most commonly reported (Belt et al., 1996, 2000). The initial identification of naturally-occurring C_{25} hydrocarbons in sediments was carried out by Gearing et al. (1976) and was followed by characterisation of the highly-branched C_{25} carbon 'skeleton' and various unsaturated analogues (Robson and Rowland, 1986). Subsequent investigations identified marine and freshwater diatoms as HBI producers (e.g. Volkman et al., 1994; Belt et al., 2001b) and focused on determining individual producer species, associated HBI distributions (Belt et al., 2000), and the effect of environmental variables, such as salinity and temperature, on diatom survivability and HBI biosynthesis (Wraige et al., 1998). In a study of laboratory cultures of a marine diatom, *Rhizosolenia setigera*, Rowland et al. (2001) discovered a trend of increasing HBI unsaturation with increasing temperature; at 25°C, 15°C and 5°C, a respective majority of tetra-, tri- and di-unsaturated haslenes was observed. Despite the failure of *Rhizosolenia setigera* to grow at 0°C, the natural occurrence of mono-unsaturated HBIs at similar temperatures was hypothesized. Such a monoene, designated IP_{25} (Ice Proxy with 25 carbon atoms; Belt et al., 2007), was indeed detected in three sea ice cores from the Canadian Arctic Archipelago (CAA). Structural confirmation of IP_{25} via large-scale extraction of marine sediment was eventually carried out (Belt et al., 2012b), and a robust analytical procedure developed (Belt et al., 2012a). Investigations of the source-specificity, selectivity towards seasonal sea ice cover, and stability of IP_{25} within environmental matrices confirmed its potential as an ice proxy (Belt and Müller, 2013; Belt, 2018).

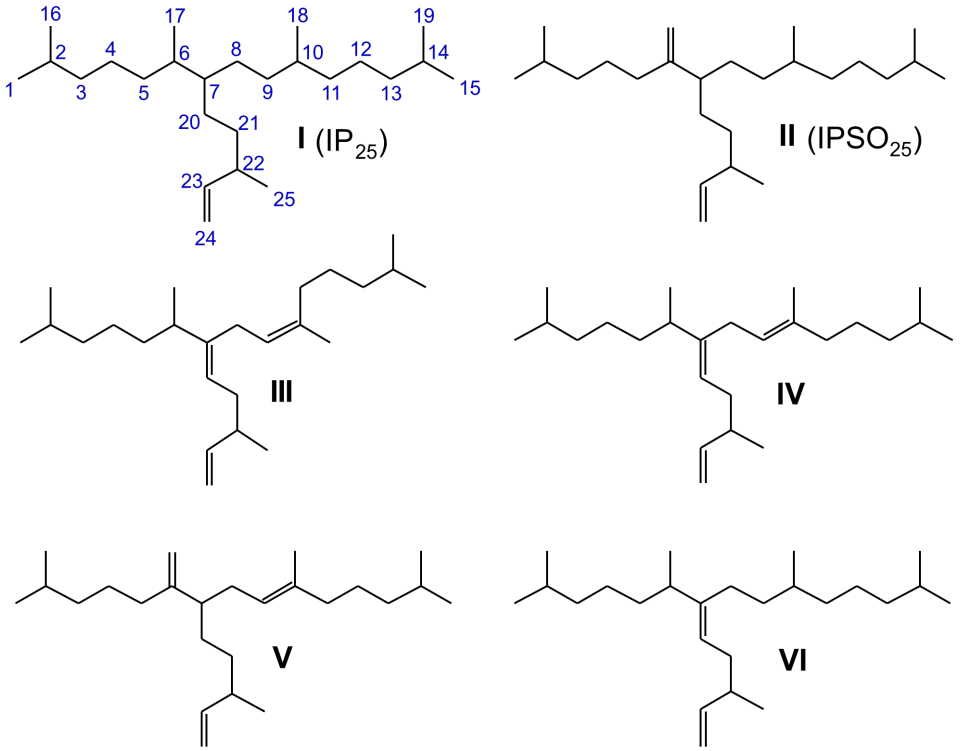

Figure 1.8: Structures of C_{25} Highly-Branched Isoprenoid (HBI) biomarkers utilised in the current study: I – IP_{25} (with carbon numbering shown); II – $C_{25:2}$ 6(17) (i.e. $IPSO_{25}$); III – $C_{25:3}$ 9(10), *Z* isomer; IV – $C_{25:3}$ 9(10), *E* isomer; V – $C_{25:3}$ 6(17); VI – $C_{25:2}$ 7(20).

IP_{25} is produced at the underside of the ice cover, given a sufficient brine volume fraction of >5%, by a few relatively minor (1–5% of total population) *Haslea* and *Pleurosigma* spp. (Brown et al., 2014c) during the insolation-driven ice algal bloom in spring, and is released from the ice matrix throughout the melt season, peaking in late May-early June, at least in the Canadian Arctic (Brown et al., 2011, 2016; Belt et al., 2013). Consequently, various analyses of surface sediments spanning the Arctic Ocean showed ubiquitous presence of IP_{25} in seasonally ice-covered locations, and nearly universal absence in open waters (e.g. Méheust et al., 2013; Navarro-Rodriguez et al., 2013; Stoynova et al., 2013; Weckström et al., 2013; Xiao et al., 2013, 2015a; Belt et al., 2015), which supported its selectivity towards seasonal sea ice (Fig. 1.9). The stability of IP_{25} is evidenced by its exceptional resistance to chemical alteration by photodegradation, autoxidation (Rontani et al., 2011, 2014a, b) and clay-induced isomerisation (Belt and Cabedo-Sanz, 2015), which allows it to achieve deposition relatively unaltered. Although potential concerns with aerobic bacterial degradation in

oxic near-surface sediments remain (Rontani et al., 2018a, b), IP_{25} is detectable and responsive to changes in sea ice conditions within the sedimentary record at time scales spanning recent centuries to millions of years (e.g. Stein and Fahl, 2013; Stein et al., 2016; Clotten et al., 2018; Detlef et al., 2018; Lo et al., 2018) and has been extensively used for reconstructing past sea ice variability throughout the Arctic Ocean and the Nordic Seas (for a recent review, see Belt, 2018).

In addition to IP_{25}, an HBI diene with a double bond at the 6(17) position (hereafter II; Fig. 1.8 and 1.10) has been reported in previous investigations in both the Antarctic (Nichols et al., 1988; Johns et al., 1999; Collins et al., 2013; Barbara et al., 2016; Belt et al., 2016) and the Arctic (alongside IP_{25}). A remarkable correlation of II to IP_{25} in Arctic sediments was revealed (Belt et al., 2007; Vare et al., 2009; Cabedo-Sanz et al., 2013; Xiao et al., 2013) and a common diatom source was inferred (Brown et al., 2014c), further supported by similarly enriched $\delta^{13}C$ values of diene II and IP_{25} (Belt et al., 2008). However, the presence of II in temperate freshwater settings (He et al., 2016) potentially suggests a less source-specific and sea ice-selective nature than that of IP_{25}. Nevertheless, due to the significant correlation of IP_{25} and II in the Arctic environment, the Diene/IP_{25} ratio, termed DIP_{25} (Cabedo-Sanz et al., 2013) was reported. Variability in the DIP_{25} values has been interpreted as a qualitative indicator of both temperature changes (Stein and Fahl, 2012; Xiao et al., 2013; Müller and Stein, 2014) – an unlikely scenario given the isothermal conditions within sea ice – and a rapidly changing or fluctuating sea ice regime (Cabedo-Sanz, 2013; Ruan et al., 2017). In the Antarctic, diene II was recently identified as a potential proxy of Antarctic platelet ice, labelled $IPSO_{25}$ (Ice Proxy for the Southern Ocean with 25 carbon atoms) based on its source, the tube-dwelling Antarctic sea ice diatom *Berkeleya adeliensis* (Belt et al., 2016). Sedimentary and water column distributions of $IPSO_{25}$ highlight its potential as an Antarctic sea ice proxy (Massé et al., 2011; Collins et al., 2013; Schmidt et al., 2018).

Table 1.3: A non-exclusive summary of paleoclimate proxy advantages and limitations

Proxy measure	Advantages	Disadvantages	References
Foraminifera (heterotrophic protists)	Qualitative inferences of pelagic and benthic marine productivity in the summer based on census data; Semi-quantitative estimates of summer SST via transfer functions.	Indirect paleo-inferences that are not applicable globally; Risk of calcite dissolution, such that foraminifera are undetectable or important species are removed from the assemblage.	Kucera, 2007; Pearson et al., 2012
Diatoms (microalgae)	Transfer function-based quantitative estimates of SST and spring SIC in parts of the Arctic Ocean; Qualitative inferences of temperature ranges and water masses based on census data.	Poor preservation in the Arctic Ocean and its shelf seas due to extensive dissolution of biogenic silica frustules; Quantitative SIC reconstruction hindered by significant SST overprint.	Miettinen et al., 2015, 2018; Oksman et al., 2017
Dinoflagellates (auto- and heterotrophic protists)	Diverse polar populations with species characteristic of both ice-obligate and ice-distal settings, and good preservation of dinosporin cysts allow for quantitative reconstruction of sea ice conditions and productivity.	Not always abundant, especially under harsh conditions (e.g. perennial ice cover) and in offshore settings farther away from continental shelves; Occurrence of cryptic species.	De Vernal and Marrett, 2007; Mudie et al., 2001; Matthiessen et al., 2005
Ostracodes (small crustaceans)	*A. arcticum* a pelagic species associated with perennial sea ice cover. Several other characteristic taxa as qualitative indicators of various bottom water masses and surface productivity.	Unknown ecological requirements and depth habitats of many species, and potential for calcite dissolution (albeit not as high as that of foraminifera).	Cronin et al., 2002, 2010, 2012, 2013
$\delta^{18}O$ of foraminifera & diatoms	Provides information on surface and benthic salinity changes and can trace meltwater input (e.g. from melting ice sheets during glacial-interglacial transitions).	Competing effects from calcite precipitation temperature and $\delta^{18}O$ of surrounding water, requiring additional data for definitive assessment.	Ravelo and Hillaire-Marcel, 2008; Pearson et al., 2012
Carbonate shell Mg/Ca ratio of foraminifera and ostracodes	Quantitative estimates of both surface (planktic foraminifera), sub-surface, and bottom (benthic foraminifera and ostracodes) water temperatures.	Temperature estimates require careful calibration at species level; Dissolution may significantly affect the ratio.	Hastings et al., 1998; Lea et al., 2000, 2014
U^{K}_{37} & $U^{K'}_{37}$ TEX_{86} & TEX^{L}_{86} LDI	Quantitative estimates of sea surface and sub-surface water temperatures via core-top calibrations.	Poorly applicable to polar settings due to the limited oceanic temperature range; LDI requires further phenological study.	Brassell et al., 1986; Schouten et al., 2002; Rampen et al., 2012
IP_{25}, other HBIs & the PIP_{25} index	IP_{25} and $IPSO_{25}$ produced by sea ice diatoms are indicative of seasonal sea ice; HBIs III and IV produced exclusively by pelagic diatoms and flourish in MIZ diatom blooms near the ice edge; Combination of IP_{25} and HBI III into the $P_{III}IP_{25}$ index provides semi-quantitative SIC estimates grounded in the opposing relationship between ice algal and pelagic diatom productivity.	The applicability of a regional *c*-factor to downcore records is uncertain; Difficult to objectively select a pelagic biomarker counterpart to IP_{25}, as the PIP_{25} is limited to two biomarkers; Calibration is regionally applicable and assumes the relationship remains stationary downcore; further calibrations required for spatial coverage.	Belt et al., 2007, 2013, 2015, 2017; Müller et al., 2011; Smik et al., 2016

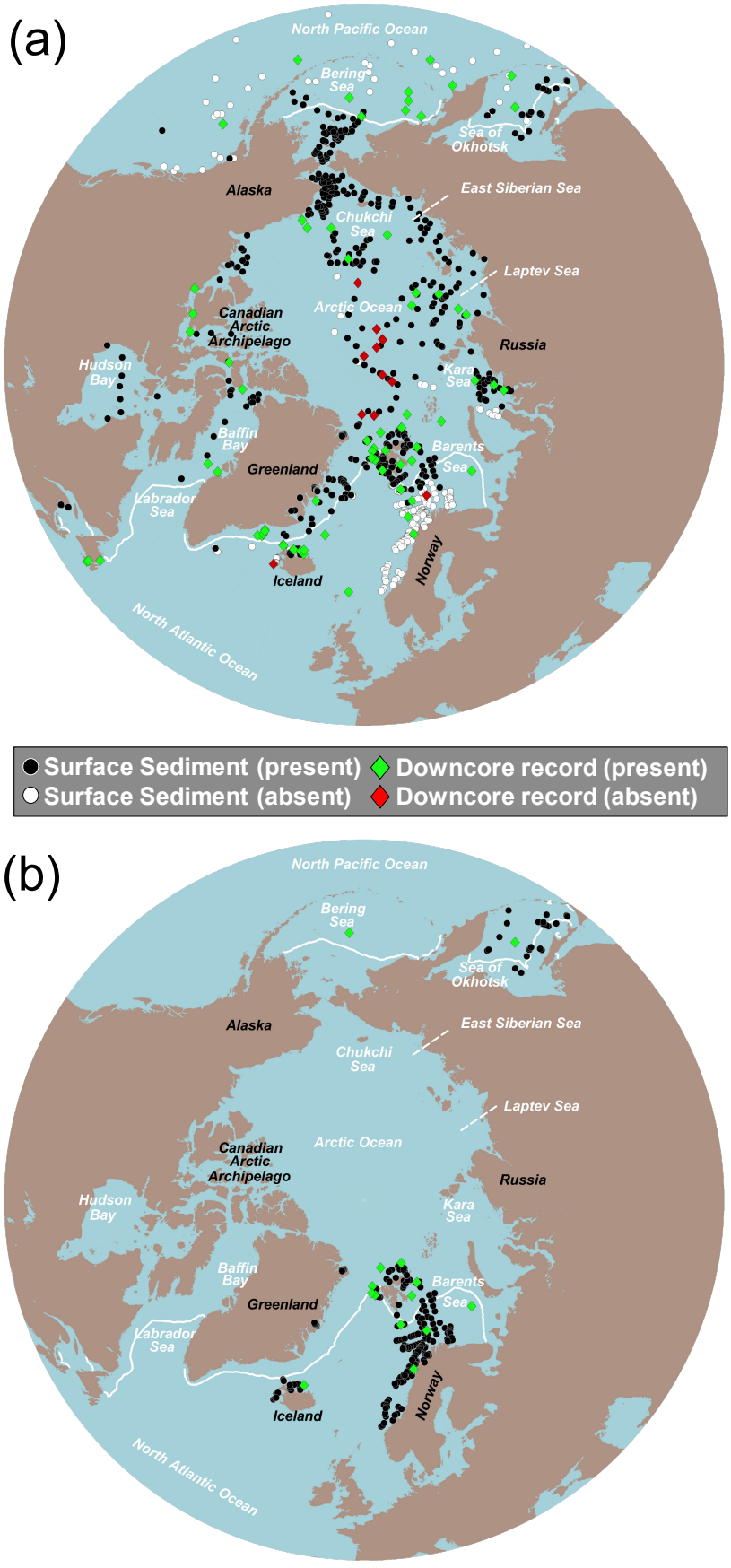

Figure 1.9: Maps showing presence and absence, in both surface sediments and downcore records, of: (a) IP_{25}; (b) III and IV in the Arctic. Solid white lines denote median April sea ice extent for the 1981–2010 period (Fetterer et al., 2017).

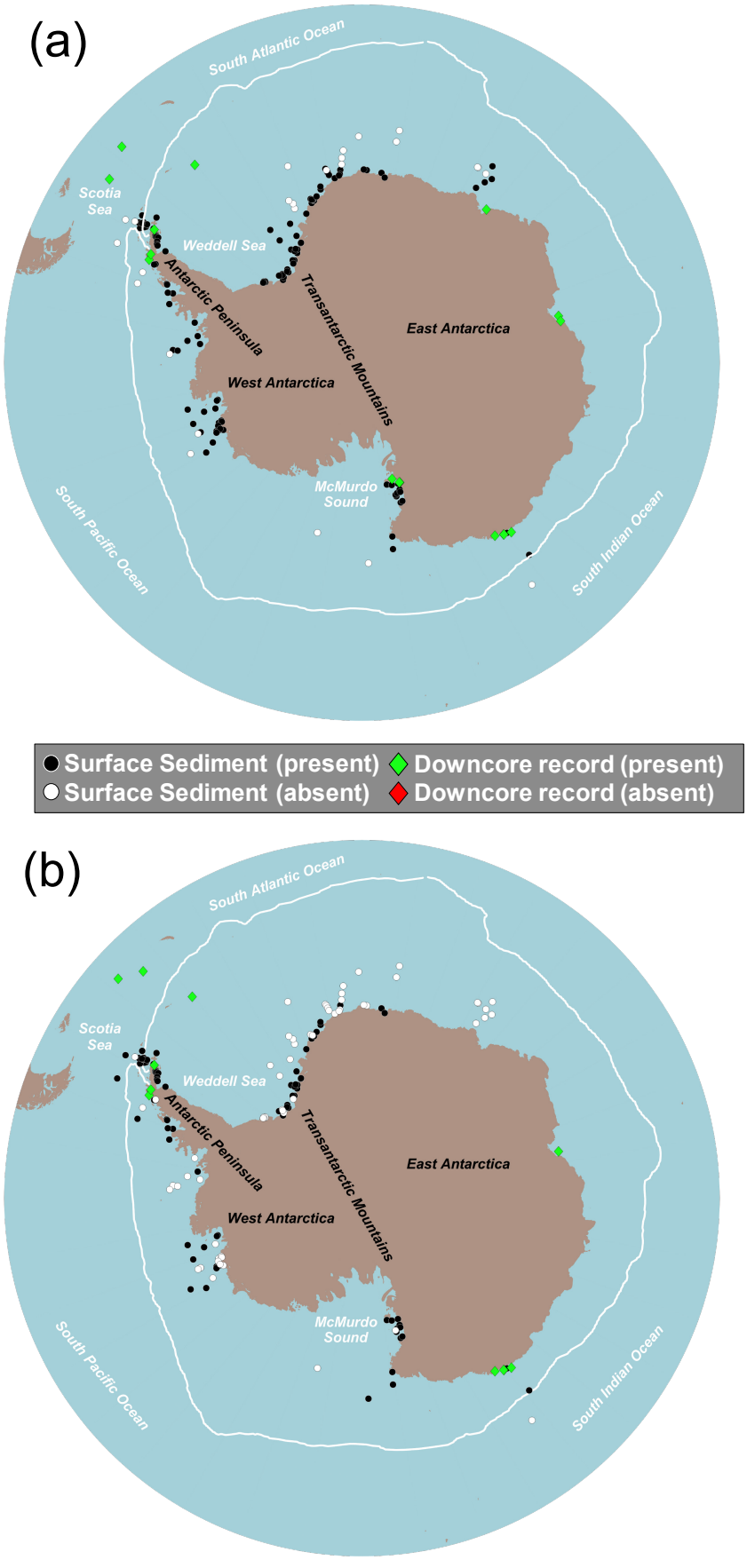

Figure 1.10: Maps showing presence and absence, in both surface sediments and downcore records, of: (a) $IPSO_{25}$; (b) III and IV in the Antarctic. Solid white lines denote median April sea ice extent for the 1981–2010 period (Fetterer et al., 2017).

A limitation of sea ice reconstructions based on IP_{25} alone is the difficulty in distinguishing between perennial sea ice cover and ice-free conditions, as it is usually absent in the latter scenario (Belt and Müller, 2013; Belt, 2018), but is often present at comparably low concentrations in otherwise contrasting sea ice conditions, such as the near-permanent sea ice cover of the central Arctic (Xiao et al., 2015a) and regions of limited annual sea ice duration, such as the Barents Sea MIZ (Navarro-Rodriguez et al., 2013; Belt et al., 2015). Consequently, the combining of phytoplankton biomarker and IP_{25} concentrations to calculate a Phytoplankton–IP_{25} index (PIP_{25}) was used to obtain semi-quantitative descriptions of sea ice conditions (Müller et al., 2011). Sterol-based PIP_{25} indices have since been utilised in several studies of both surface and downcore sedimentary records (e.g. Fahl and Stein, 2012; Müller et al., 2012; Cabedo-Sanz et al., 2013; Navarro-Rodriguez et al., 2013; Stoynova et al., 2013; Weckström et al., 2013; Xiao et al., 2013, 2015a, b; Berben et al., 2014, 2017; Müller and Stein, 2014; Belt et al., 2015; Hoff et al., 2016; Pieńkowski et al., 2016; Polyak et al., 2016; Hörner et al., 2017). The adoption of a uniform scale (0–1) with the PIP_{25} index allows for more consistent comparisons of inferred sea ice conditions from different datasets, especially considering the variability of sedimentary IP_{25} concentration for regions of similar sea ice cover (Stoynova et al., 2013; Xiao et al., 2015a). However, several challenges are associated with sterol-based PIP_{25} indices. First, despite sterol diversity among microalgae and plankton (Volkman, 2003) and their use as chemotaxonomic biomarkers of marine versus terrigenous organic matter sources (e.g. Hudson et al., 2001; Ternois et al., 2001; Knies, 2005; Belt et al., 2013), they are not particularly source-specific and few are considered unambiguous biomarkers of specific algal groups, many of which contribute the same sterols to the sedimentary budget (Volkman, 1986; Yunker et al., 2005; Rampen et al., 2010). Sterols are also produced by sympagic algae (Belt et al., 2013, 2018), which likely adds bias to PIP_{25} values in some settings and underlines the

need to consider more source-specific pelagic biomarkers when decoupling ice-covered and open water conditions in paleo-records. Second, a consequence of sterol ubiquity is a considerable discrepancy between the typical concentration ranges of sterols and IP_{25}, necessitating the use of a concentration balance factor, or *c*-factor, which can be adversely affected by, amongst other things, downcore concentration distributions and potential differential degradation of biomarkers in paleo-records (Belt and Müller, 2013; Belt, 2018).

In an attempt to alleviate these limitations, Belt et al. (2015) compared the spatial distribution of IP_{25} in Barents Sea surface sediments to that of a tri-unsaturated HBI (hereafter III; Fig. 1.8), to date only identified in certain open-water diatoms belonging to the *Pleurosigma* and *Rhizosolenia* genera (Belt et al., 2000; Rowland et al., 2001) – including some species present in mixed phytoplankton communities from western Svalbard (Belt et al., 2017) – and thus likely to provide a more selective representation of the pelagic environment than many other biomarkers. Since the contribution of *Pleurosigma* spp. and *Rhizosolenia* spp. to many pelagic diatom assemblages and the proportion of IP_{25}-producing sympagic diatoms in sea ice are generally similar (ca. 1–5%; von Quillfeldt, 2000; Ratkova and Wassmann, 2005; Brown et al., 2014c), it was also hypothesized that sedimentary concentration ranges of III and IP_{25} would be comparable. Consistent with this background, an inverse relationship between IP_{25} and III was found for regions of contrasting sea ice cover, while $P_{III}IP_{25}$ indices (i.e. PIP_{25} based on IP_{25} and III) exhibited a vastly reduced influence of the c-factor on downcore profiles compared to those of P_BIP_{25} (i.e. PIP_{25} based on IP_{25} and brassicasterol), due to similar sedimentary concentrations of IP_{25} and III, as predicted (Belt et al., 2015). Using the same dataset, Smik et al. (2016) demonstrated a positive linear correlation between $P_{III}IP_{25}$ and spring sea ice concentration (SpSIC), thus providing a regional calibration, which has since been used

to obtain semi-quantitative SpSIC estimates in downcore records spanning the Holocene (Cabedo-Sanz and Belt, 2016; Berben et al., 2017) and MIS6–MIS2 (Kremer et al., 2018a). Notably, the *E*-diastereoisomer of HBI III (HBI IV; Fig. 1.8), also exhibits remarkable correlation with HBI III, at least in the Barents Sea (Cabedo-Sanz, 2013; Navarro-Rodriguez, 2014), and both have been co-produced in laboratory diatom cultures (Belt et al., 2000; Rowland et al., 2001); however, IV has also been detected in sea ice (Belt et al., 2007; Brown, 2011; Ringrose, 2012). Although the sources of III and IV are not yet comprehensively known, their recent detection in the pelagic diatom *Rhizosolenia setigera* near western Svalbard (Belt et al., 2017) and clear enhancement near the receding spring sea ice edge (Belt et al., 2015) support their use as indicators of pelagic diatom productivity, at least in the Barents Sea MIZ, and potentially other regions. Further, in a study of HBI III *E*/*Z* isomer distributions in Barents Sea surface sediments, a potential link to Arctic and sub-Arctic (e.g. Atlantic) water mass distribution was hypothesized (Navarro-Rodriguez, 2014), with the *E*-isomer relatively more abundant in latter settings; such findings encourage further investigation.

More recently characterised HBIs, the responses of which to climate change have not, thus far, been investigated in any detail, include the $C_{25:2}$ 7(20) (hereafter VI; Fig. 1.8) identified solely in the *Berkeleya rutilans* diatom abundant in coastal and brackish waters (Brown et al., 2014b). An additional $C_{25:3}$ 6(17) (hereafter V; Fig. 1.8) has also been identified in both sea ice (Belt et al., 2007) and temperate regions (He et al., 2016). Overall, the presence of a multivariate HBI biomarker set (Fig. 1.8) provides a foundation to explore and develop combinative approaches, which may either provide new insights into HBI-based inferences of paleoclimate, or supplement and improve upon existing univariate proxies, such as PIP_{25} indices. To date, combinations of multiple HBIs have been utilized to trace the contribution of ice-derived and pelagic organic carbon in Arctic food webs, using the so-called H-Print approach of analysing

relative abundances of HBIs in polar and sub-polar heterotrophs (Brown et al., 2014d, 2015). Various investigations have detected HBIs at a multitude of trophic levels, from Arctic pelagic zooplankton (Brown et al., 2012) and benthic fauna (Brown and Belt, 2012; Brown et al., 2015) to mammals, such as ringed seals (Brown et al., 2014a) and polar bears (Brown et al., 2018), where HBI distributions were generally representative of, and unique to, sympagic and pelagic feeding. Such responses of HBI distributions to different organic matter sources have since been linearly calibrated in the brine shrimp *Artemia* spp. and various Arctic amphipods (Brown et al., 2017; Brown and Belt, 2017). Considering the previously suggested metabolic stability of the H-print irrespective of trophic level (Brown et al., 2014a), as well as within appropriately-stored preserved animals (Brown, 2018), it is a promising method of differentiating sympagic and pelagic feeding in both polar oceans (e.g. Schmidt et al., 2018). However, while the H-print highlights the potential of combinative approaches using multiple HBIs (and, more generally, multiple biomarkers), it is still a ratio method which ultimately results in a univariate measure of sympagic versus pelagic contribution to polar food webs (Brown et al., 2017; Brown and Belt, 2017), not unlike the principle of $P_{III}IP_{25}$-based SpSIC estimates. In contrast, multivariate methods involving simultaneous analysis of multiple HBIs have not been investigated for paleo sea ice reconstruction, in particular. Such analyses could provide new insights into Arctic sea ice and productivity regimes.

1.4 Aim and objectives of the current study

The overall aim of this project was to investigate new HBI-based proxy methods for reconstructing the development of sea ice and primary productivity dynamics in the Barents Sea throughout both rapid and gradual climate change. To this end, the main objectives included:

- Development and testing of both HBI-derived multivariate and ratio-based proxy measures that would incorporate some of the more recent and less utilized HBIs (such as III–VI; Fig. 1.8) for reconstructing sea ice conditions and other critical climate-controlled parameters, such as phytoplankton bloom dynamics.
- Alleviation of some limitations of the PIP_{25} index, such as the spatial variability of the *c*-factor and the difficulty of selecting an appropriate biomarker of pelagic production (Belt et al., 2015; Smik et al., 2016), using the developed approaches.
- Application of the new method(s) described above in tandem with PIP_{25} and additional biomarkers (e.g. sterols) to derive novel insights into the sea ice and sympagic/pelagic primary productivity regimes governing the Barents Sea over millennial timescales.

These objectives are described, and outcomes presented in the following chapters:

Chapter 2: *General laboratory, analytical, and statistical methods*.
A detailed description of laboratory, analytical, and statistical methods.

Chapter 3: *Biomarker-based multivariate classification of contemporary sea ice and productivity conditions in the Barents Sea*.
The development of a multivariate statistical classification procedure for reconstructing Barents Sea ice conditions is described, based on the comparison of satellite-derived sea ice conditions with several HBI biomarkers (Fig. 1.8) in 198 surface sediments, using the Classification and Regression Trees (CART) algorithm. A comparative assessment between the resulting classification tree (CT) model and $P_{III}IP_{25}$-based SpSIC estimates is provided for four centennial downcore records with contrasting overlying sea ice conditions. The same surface sediments and downcore records are also utilised to investigate the association between an HBI triene ratio of $C_{25:3}$ 9(10) diastereoisomers and satellite-derived oceanographic and productivity indicators. The outcomes are

partially published in: Köseoğlu, D., Belt, S.T., Smik, L., Yao, H., Panieri, G., Knies, J. (2018a), "Complementary biomarker-based methods for characterising Arctic sea ice conditions: A case study comparison between multivariate analysis and the PIP_{25} index", *Geochimica et Cosmochimica Acta* **222**, pp. 406–420.

Chapter 4: *Further assessment and application of CT models, the $P_{III}IP_{25}$ index, and the HBI triene ratio for millennial-scale paleo sea ice and productivity reconstruction*

Further testing of the CT model (Chapter 3) and associated comparisons to the $P_{III}IP_{25}$ index are provided for four millennial-scale Barents Sea paleo records extending to the Younger Dryas and Bølling-Allerød interstadial (*ca.* 13–15 cal kyr BP). The outcomes are published in: Köseoğlu, D., Belt, S.T., Husum, K., Knies, J. (2018b), "An assessment of biomarker-based multivariate classification methods versus the PIP_{25} index for paleo Arctic sea ice reconstruction", *Organic Geochemistry* **125**, pp. 82–94.

Chapter 5: *Multi-proxy characterisation of seasonal sea ice and productivity regimes at the western Barents Sea continental slope during the late Weichselian glaciation.*

In this chapter, the sea ice and sympagic/pelagic primary productivity regimes spanning the late Weichselian glaciation (*ca.* 25.5–15.5 cal kyr BP) are reconstructed at the south-western Barents Sea continental slope using a multiproxy approach incorporating the $P_{III}IP_{25}$ index, CT model, HBI and sterol concentrations, as well as sedimentological and inorganic geochemical proxies. The outcomes form part of: Knies, J., Köseoğlu, D., Rise, L., Baeten, N., Bellec, V.K., Bøe, R., Klug, M., Panieri, G., Jernas, P.E., Belt, S.T. (2018), "Nordic Seas polynyas and their role in preconditioning marine productivity during the Last Glacial Maximum", *Nature Communications* **9**, article 3959.

Chapter 6: *Conclusions and future work.*

Outcomes and potential for future work are summarised in context of the project aims.

CHAPTER TWO

2. General laboratory, analytical, and statistical methods

This Chapter lists the general and additional analytical procedures used for the extraction, purification, analysis (including analytical instrumentation operating parameters), as well as routine and statistical processing of HBI biomarker data in marine sediment samples from the Barents Sea. The majority of described procedures focusing on biomarker extraction, quantification, and interpretation have been described previously (Belt et al., 2012a; Cabedo-Sanz, 2013; Navarro-Rodriguez, 2014; Belt and Cabedo-Sanz, 2015). However, an initial reproducibility assessment of KOH saponification versus direct DCM/methanol extraction of HBIs and sterols is also provided (section 2.5). While most of the sediment samples analysed for the purposes of this research were provided by the Geological Survey of Norway (courtesy of Dr Jochen Knies), the reader is referred to dedicated methodology sections of Chapters 3–5 for detailed descriptions of sediment materials and their sources.

2.1 Storage and freeze drying

Bulk marine surface and downcore sediments were sub-sampled at ca. 5–10 g per surface location or core horizon, and stored in sealed plastic bags in a dark environment at ca. -20°C until extraction; the bulk sediments were previously stored in similar conditions at the Geological Survey of Norway. Of the sediments received, certain fresh samples were freeze-dried at the University of Plymouth laboratories using a Christ Alpha 2-4 LD Plus freeze drier. Samples were kept in glass vials at -20°C for at least 24 hours, and were subsequently freeze-dried (0.001 mbar; -80°C) in batches of 50 for approximately 24–48 hours per batch of ca. 30–40 samples. Samples were protected from light during drying to maintain integrity.

2.2 Sediment extraction and purification

2.2.1 Internal standard addition

Two internal standards (IS) were added to sediment samples before extraction to permit quantification; 9-octyl-8-heptadecene (9-OHD, 0.1 μg) and 5α-androstan-3β-ol (0.1 μg) were added for HBI and sterol quantification, respectively (Fig. 2.1).

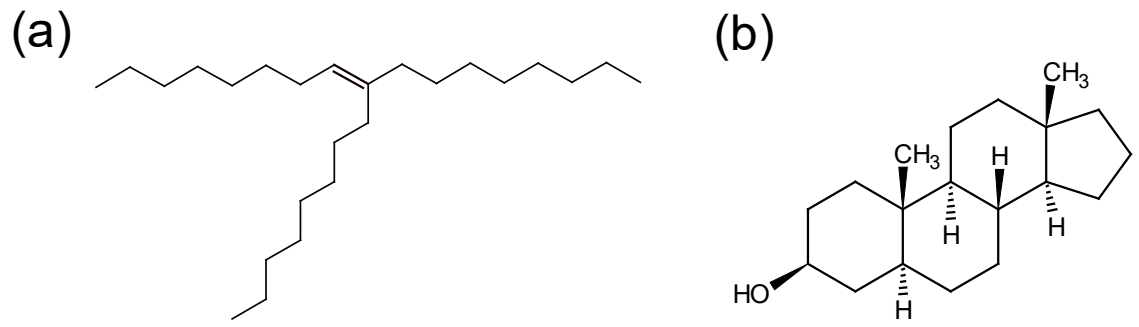

Figure 2.1: displayed formulae of internal standards used for analyte quantification: (a) 9-octylheptadec-8-ene (9-OHD); (b) 5α-androstan-3β-ol.

2.2.2 Total organic extract

Dry sediments were extracted and analysed in batches of 15–20 samples, weighing approximately 1.5–2.5 g of each sediment into 7 mL glass vials. The extraction procedure for obtaining the Total Organic Extracts (TOEs) differed for HBIs and sterols. Thus, HBIs were extracted using DCM/methanol (section 2.2.2.1), while direct saponification with KOH was used for sterols (section 2.2.2.2). The reproducibility of HBI and sterol concentrations obtained using both methods is assessed in section 2.5.

2.2.2.1 The DCM-methanol method

Upon addition of 9-OHD IS, enough dichloromethane/methanol (2:1 *v/v*) was added to submerge the sediment (typically 2 mL). The vials were sealed using aluminium-lined polypropylene screw caps, ultrasonicated (30°C, 15 min) and

centrifugated (2500 rpm, 2 min). The supernatant solvent layer was extracted into new 7 ml glass vials using rinsed (2:1 *v/v* DCM/methanol) Pasteur pipettes. Three further extractions were carried out in order to maximize analyte recoveries. The DCM/methanol solvent was evaporated from the TOEs using a gentle stream of N_2 at 25°C. A schematic representation of the initial extraction procedure using DCM/methanol is illustrated in Figure 2.2.

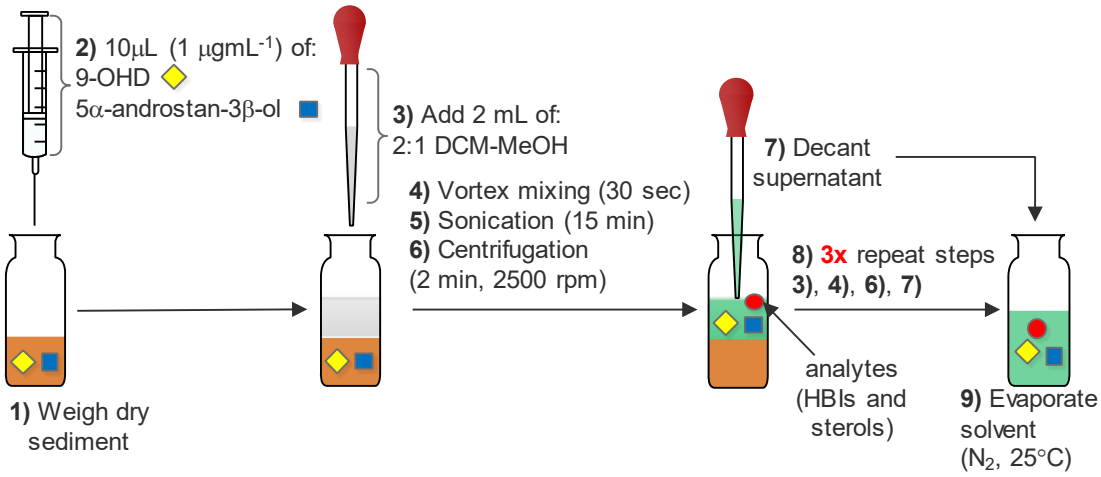

Figure 2.2: a scheme illustrating the method used for obtaining TOEs from marine sediments via the DCM/MeOH extraction procedure.

2.2.2.2 The KOH saponification method

Following 5α-androstan-3β-ol IS addition, *ca.* 3 mL of methanolic 5% (*m/v*) potassium hydroxide (KOH; 9:1 *v/v* MeOH:milliQ water) were added to sediment samples, which were then sealed using aluminium-lined polypropylene screw caps, vortex-mixed (30 sec) and saponified (70°C for 60 min). Approximately 1 mL of hexane was subsequently added to each vial via Pasteur pipette, followed by vortex mixing (60 sec) and centrifugation (2500 rpm; 2 min). The supernatant hexane layer was decanted into separate 7 mL glass vials via Pasteur pipette; three further extractions into hexane (1 mL × 3) were carried out to maximize recovery. Finally, the hexane was evaporated under N_2 (25°C), yielding dry TOEs. The KOH saponification-based procedure is represented in Figure 2.3. Note that for the purpose of assessing

reproducibility between biomarker concentrations obtained via the DCM/methanol extraction- and KOH saponification-based methods (section 2.5), HBIs were also extracted from selected sediments using the latter.

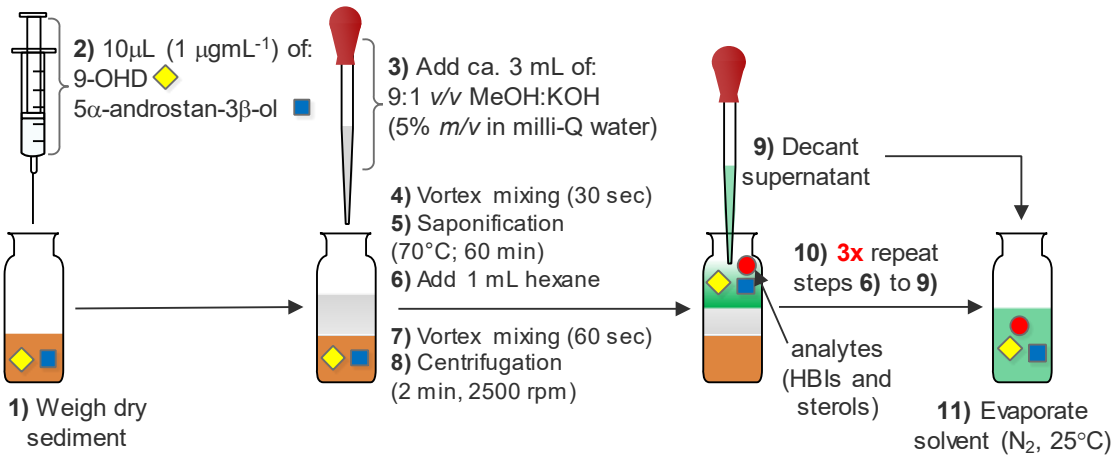

Figure 2.3: a schematic representation of the KOH saponification-based method of obtaining TOEs from marine sediments.

2.2.3 Removal of elemental sulphur

In contrast to direct KOH saponification, the TOEs obtained using DCM/methanol extraction required a further partial purification step to remove elemental sulphur, which was significantly more abundant relative to the analytes of interest and exhibited a retention time very similar to that of IP_{25}, hindering sample pre-concentration capacity and interfering with quantification (e.g. Belt and Cabedo-Sanz, 2015; Smik, 2016). In order to minimize potential influence of elemental sulphur on the quality of chromatographic analysis, a previously described, non-destructive removal procedure was employed for all samples (Jensen et al., 1977), based on the following reaction:

$$(TBA^{+})_2SO_3^{2-} + S_{(s)} \rightleftharpoons 2TBA^{+} + S_2O_3^{2-}$$

The tetrabutylammonium sulphite reagent – $(TBA^{+})_2SO_3^{2-}$ (3.39% *m/v*), hereafter TBA – was prepared via addition of approximately 6.78 g of

tetrabutylammonium hydrogen sulphate to 200 mL of ultra-pure (milli-Q) water, followed by saturation with ca. 50 g of anhydrous sodium sulphate. Dry TOEs were re-suspended in 1mL of hexane, sealed and sonicated (30°C, 5 min). Subsequently, ca. 1 mL of TBA and 2 mL of isopropanol were added to each sample by Pasteur pipette. The vials were sealed and shaken vigorously for at least one minute, or until the appearance of persistent white sodium sulphite ($Na_2SO_{3(s)}$) crystals; 3 mL of milli-Q water were then added, each vial was shaken (1 min) and centrifugated (2500 rpm; 2 min), resulting in a two-phase system. The supernatant hexane layer, containing the analytes of interest, was transferred into new 7 ml glass vials. The extraction procedure was repeated thrice more using 3 × 1 mL aliquots of hexane. Finally, the solvent was evaporated to dryness under a gentle stream of $N_{2\,(g)}$ at 25°C. The sulphur removal procedure is illustrated in Figure 2.4.

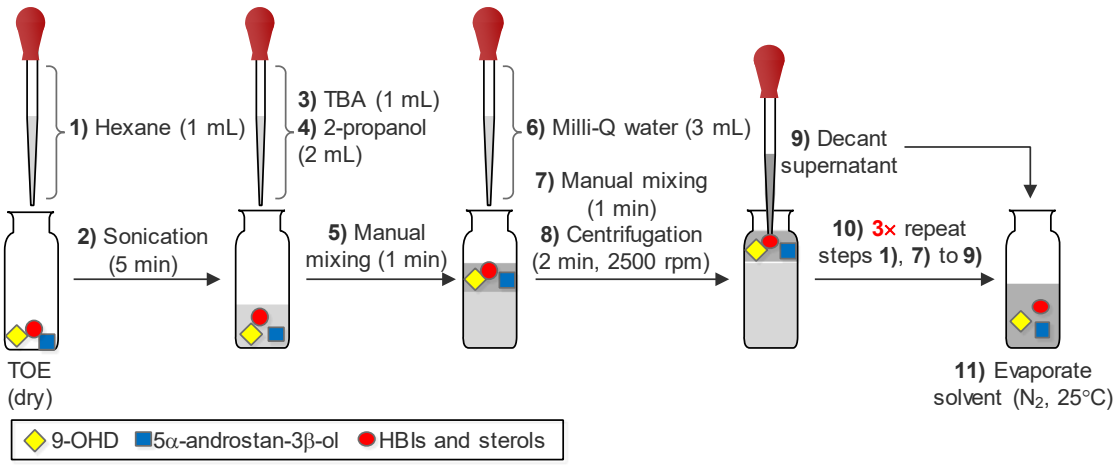

Figure 2.4: Removal of sulphur (S_8) from dry TOEs after DCM/methanol extraction.

The KOH saponification method did not require elemental sulphur removal via TBA due to the reaction of $S_{8(s)}$ with $KOH_{(aq)}$ to produce a mixture of potassium sulphides and thiosulphate, which are soluble in methanol and could be successfully separated from the relatively less polar HBIs and sterols using hexane (Tartar, 1913; Bates and Carpenter, 1979):

$$S_{8(s)} + 6KOH_{(aq)} \rightleftharpoons 2K_2S_3 + K_2S_2O_3 + 3H_2O_{(l)}$$

2.2.4 Partial purification by silica chromatography

Column chromatography was carried out on sulphur-free sediment TOEs (Fig. 2.5) to remove mixtures of unwanted compounds that may interfere with analyte identification and quantification. Dry extracts were re-suspended in 1 mL of hexane, sealed and sonicated (30°C, 5 min). Chromatography columns were assembled using Pasteur pipettes plugged with DCM-cleaned cotton wool, filled with chromatography-grade silica gel (ca. 0.7 g; 60–200 µm particle size) and conditioned with 2 × 1 mL of hexane. Sediment extracts were adsorbed onto individual columns (4 × 1 mL of hexane) and a total of *ca.* 6 mL of hexane eluate were collected into 7 mL glass vials for HBI analysis. A second fraction was collected (*ca.* 6 mL) into separate 7 mL vials for sterol analysis, using a higher-polarity 4:1 *v/v* hexane/methyl acetate mixture as an eluent.

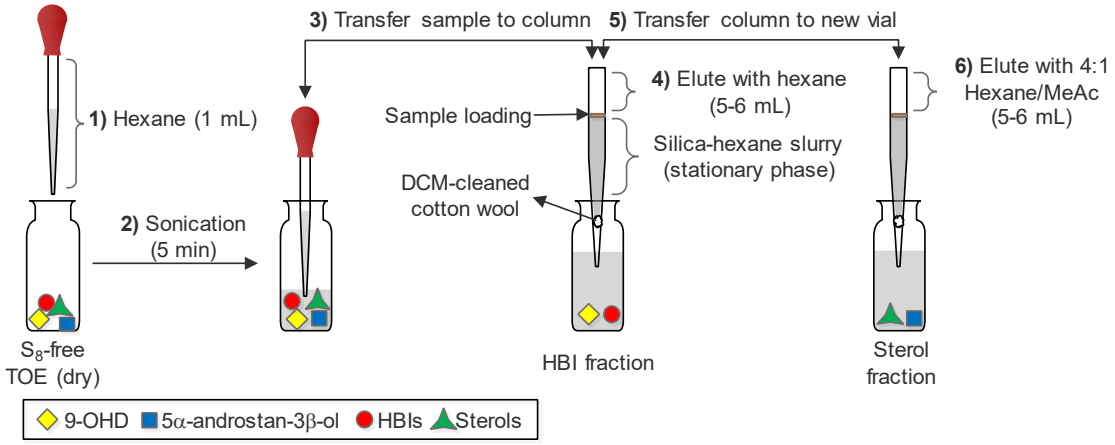

Figure 2.5: Schematic showing partial purification of sediment TOEs via silica column chromatography.

2.2.5 Removal of saturated hydrocarbons by silver-ion chromatography

Following column chromatography, a further purification procedure was carried out exclusively on the non-polar, HBI-containing hexane fraction of the sediment extract. The method was previously developed by Cabedo-Sanz (2013) and allows for chromatographic separation of saturated and unsaturated hydrocarbons, resulting in a higher signal-to-noise ratio and, therefore, a lower detection limit for HBIs.

The hexane (non-polar) fractions of partially purified sediment extracts were placed under an $N_{2(g)}$ stream and the solvent was evaporated until ca. >0.5 mL remained. Small-scale chromatography columns were prepared (section 2.2.4), with substitution of deactivated silica (0.7 g) for the Supelco Discovery® Ag-Ion stationary phase (ca. 100 mg). Column conditioning was carried out with 3 × 1 mL of acetone, followed by 2 mL (ca. 1 column volume) of hexane. The non-polar sediment extract fractions were loaded onto the columns (4 × 400 µL of hexane); saturated hydrocarbon impurities were eluted with 2 mL of hexane and discarded. HBIs were subsequently eluted into 7 ml vials using 3 mL of acetone, which was then evaporated under a gentle $N_{2(g)}$ stream. The Ag-Ion chromatographic purification method is shown in Figure 2.6.

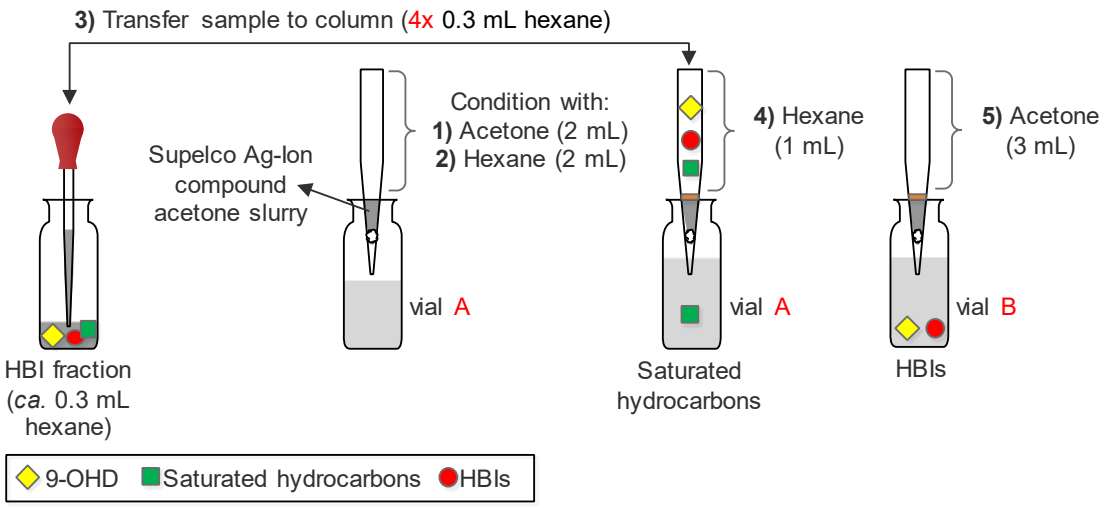

Figure 2.6: schematic representation of the Ag-Ion chromatography method used for fractionation of saturated and unsaturated hydrocarbons.

2.3 Sample analysis, identification, and quantification

2.3.1 Sample preparation and derivatisation

The $N_{2(g)}$-dried, partially-purified HBI fractions were transferred into amber GC vials (Chromacol; 300 µL). The fractions were subsequently concentrated to ca. <50 µL under $N_{2(g)}$ for GC-MS analysis.

To increase the volatility of sterol fractions, these were derivatised with N,O-bis(trimethylsilyl)trifluoroacetamide (BSTFA; 100 µL; 70°C for 60 min) and transferred to GC vials (300 µL) in DCM immediately prior to analysis.

2.3.2 Gas Chromatography-Mass Spectrometry

GC-MS analysis was carried out using an Agilent Tech 7890A series gas chromatograph coupled to a 5975A series quadrupole mass selective detector and equipped with the HP5-MS fused silica column (30m length; 0.25 mm internal diameter; 0.25 µm film thickness). Injection was carried out at 300°C using an Agilent series 7683B auto-injector in split/splitless configuration. Helium carrier gas was utilized at a constant flow rate of 1 mL min^{-1}. Initial identification of the analytes of interest based on retention times (RTs), Kovats Retention Indices (RIs), and electron ionisation mass spectra was carried out using Total Ion Current (TIC) chromatograms, while Selected Ion Monitoring (SIM) was used for quantification of HBIs, in particular, due to its higher sensitivity (sections 2.3.3). In order to maximize sample introduction and analyte signal, HBI samples were injected in splitless mode and the detection window was narrowed to ca. 18–22 minutes (Cabedo-Sanz, 2013). This methodology was not used for sterols due to their considerably higher sedimentary abundances relative to HBIs (e.g. Belt et al., 2013). The instrumental parameters used for HBI and sterol analysis by GC-MS are summarised in Table 2.1.

Table 2.1: GC-MS instrumental parameters used for analysis of HBIs and sterols.

Analytes of interest:	HBIs	Sterols
Column:	HP5-MS fused silica	HP5-MS fused silica
Carrier gas:	Helium (1.0 mL min^{-1})	Helium (1.0 mL min^{-1})
Temperature program:	40 °C–300 °C at 10 °C/min, held for 10 min	40 °C–300 °C at 10 °C/min, held for 10 min
Ionisation energy:	70 eV	70 eV
Detection window	18.7–19.9 and 21.2–21.6	20–36
Mass range (*m/z*):	90–360	50–500
SIM target ions (*m/z*):	350.3, 348.3, 346.3, 344.3, 342.3, 99	333, 343, 372, 382, 396, 458, 470, 472, 500
Injector parameters:	1 µL injected at 300°C	1 µL injected at 300°C

2.3.3 Identification and quantification of HBIs

The identification of HBIs was carried out using a combination of TIC mass spectra and RI values, with respective comparisons to their counterparts reported in literature. Specifically, where sufficiently resolved and abundant signal was present, electron ionization mass spectra of peaks were compared to those reported for authentic compounds. However, due to the generally low naturally-occurring abundances of HBIs in marine sediments (Belt et al., 2013), a mass spectrum was not always obtainable. In such cases, peak identity was assigned by comparing the calculated Retention Index (RI) value of an unknown peak to literature values reported for HBIs using the same instrumental configuration and parameters. An example RI calculation method is shown in Equation 2.1, which compares the RT value of a given HBI to those of adjacent *n*-alkanes obtained from a nC_{19}–nC_{29} reference mixture:

$$RI = \frac{RT_{HBI} - RT_{nC_{20}}}{(RT_{nC_{21}} - RT_{nC_{20}})/100} + 2000 \qquad (2.1)$$

Additionally, a marine sediment sourced from Franklin Bay in the Canadian Arctic Archipelago (hereafter CAA reference sediment), with known concentrations of

HBIs (Cabedo-Sanz, 2013; Navarro-Rodriguez, 2014), was extracted and analysed with every batch of 15–20 samples in order to assess method reproducibility and aid analyte peak assignment via comparison of RT values. The initial determination and summary statistics of HBI concentrations in CAA reference sediment replicates are available in Appendix B (Table B.1). The comparison of observed RIs for all HBIs described in the current study to literature values, as well as the integration technique used to obtain peak areas, are shown in Figure 2.7. TIC mass spectra are shown in Figure 2.8.

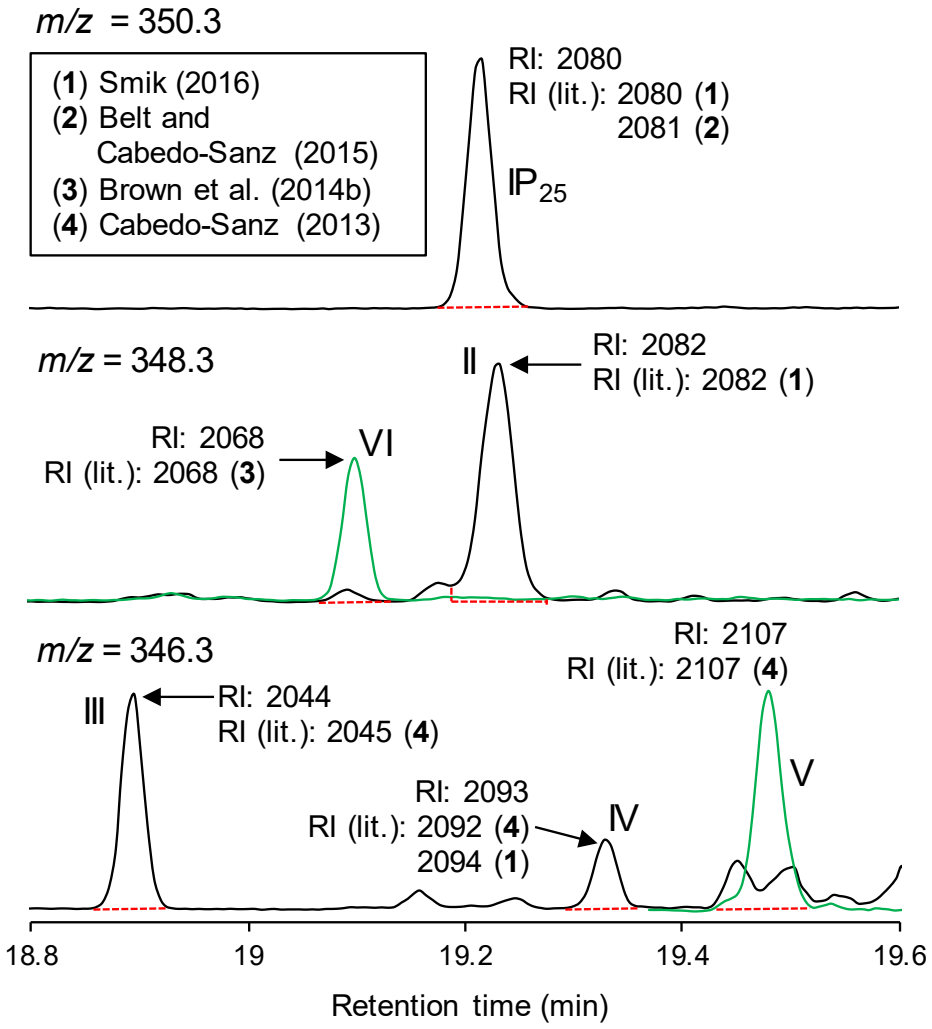

Figure 2.7: GC-MS SIM chromatograms showing the elution order, observed and previously reported retention indices of $C_{25:1}$ (*m/z* 350.3), $C_{25:2}$ (*m/z* 348.3), and $C_{25:3}$ (*m/z* 346.3) HBIs. The integration technique is shown (dashed red lines). Black lines correspond to the CAA reference sediment; green lines are SIM chromatograms of Barents Sea surface sediment extracts added to better illustrate V and VI (Fig. 1.8).

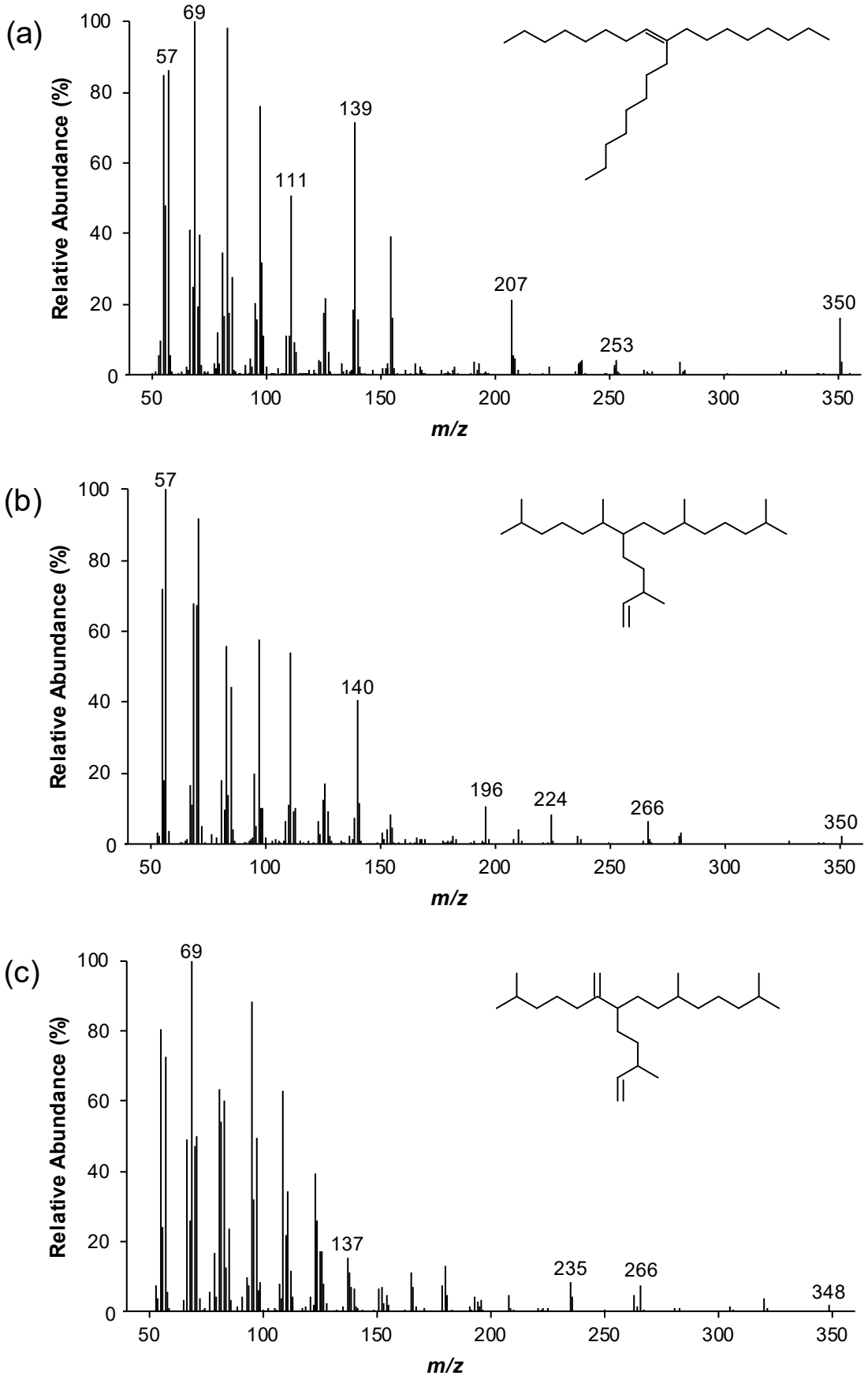

Figure 2.8: Background-corrected TIC mass spectra of: (a) 9-OHD; (b) IP_{25}; (c) II.

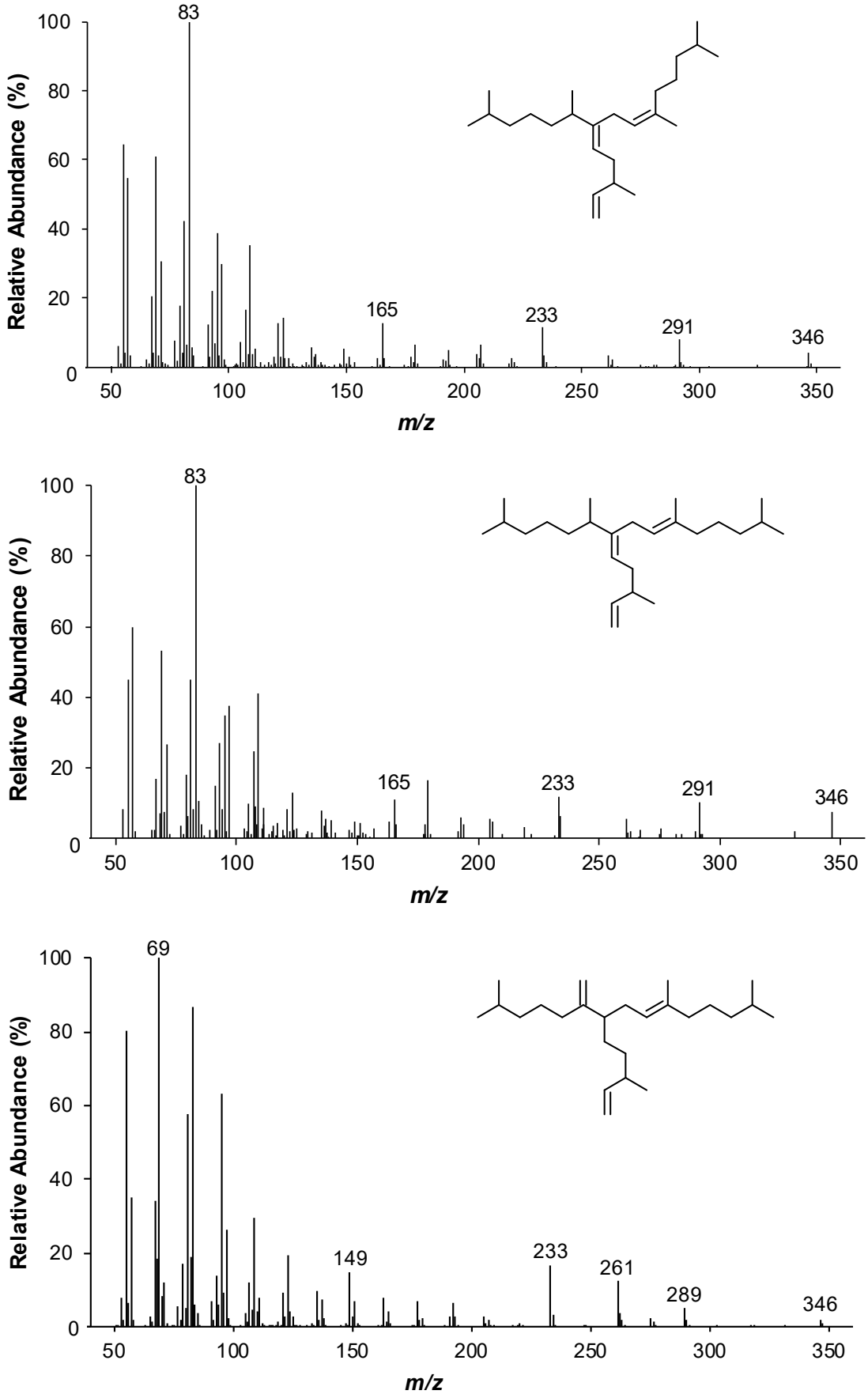

Figure 2.8 (*continued*): Background-corrected TIC mass spectra of: (d) III; (e) IV; (f) V.

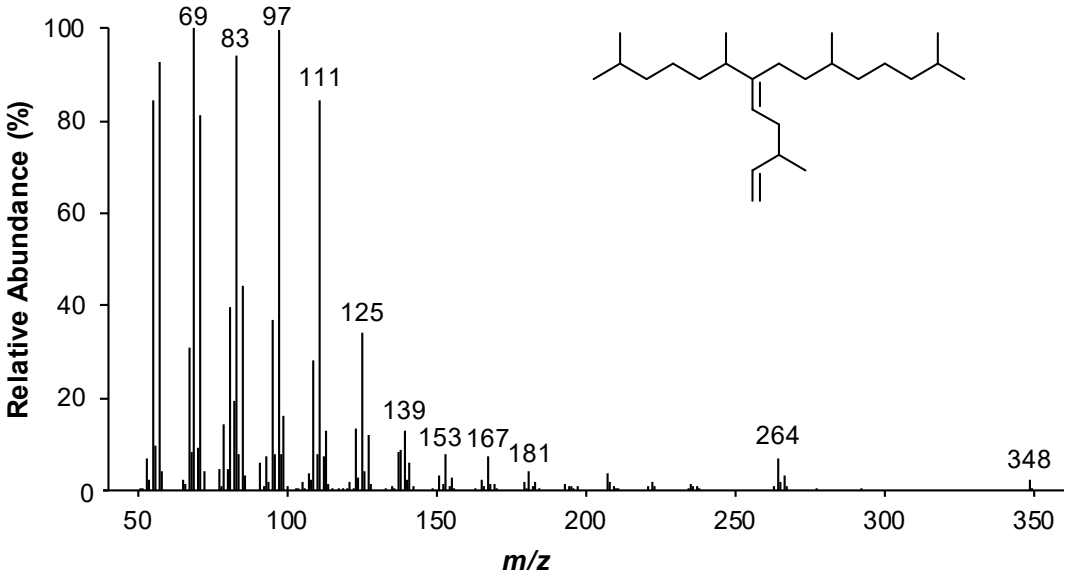

Figure 2.8 (*continued*): Background-corrected TIC mass spectrum of: (g) VI.

Once identified, HBIs were quantified from GC-MS chromatograms in SIM mode using manual integration provided with the ChemStation software (ver. E.02.02). Differences in efficiency of mass spectral fragmentation between various HBIs and the 9-OHD internal standard were accounted for via calculation of Response Factors (RF). While the RFs of IP_{25}, diene II, and trienes III, IV were determined experimentally in previous studies, the values were reported to vary considerably over time, and periodic reassessment was deemed necessary to maintain precise and reproducible records of HBI concentrations (Brown, 2011; Cabedo-Sanz, 2013; Navarro-Rodriguez, 2014). To this end, a range of external calibration series with known concentrations of HBIs I to IV (0.1, 0.2, 0.4, 0.6, 0.8, and 1.0 µg mL^{-1}) and an equal concentration of the 9-OHD internal standard were analysed periodically, depending on the frequency of sample extraction. For each HBI, the RF was calculated as a ratio of concentration-corrected HBI peak area in SIM mode to that of the 9-OHD internal standard. Once an RF value was calculated, the integrated peak area of a given HBI (PA_{HBI}) was corrected for that of the internal standard (PA_{IS}), the corresponding RF, mass of sediment (m_{sed}; in g) and the internal standard (m_{IS}; in µg) using Equation 2.2:

$$HBI\ (\mu g\ g^{-1} dry\ sed.) = \frac{PA_{HBI}/PA_{IS} \times RF}{m_{sed}} \times m_{IS} \quad (2.2)$$

For HBIs V and VI, which were not routinely quantified until 2018, relative response factors (RRFs) were calculated using standards of all six HBIs analysed at the same time (Eq. 2.3, where reference HBIs were IP_{25}, II, and III together with IV). These RRFs were then used to estimate RF values for HBIs V and VI (Eq. 2.4; Table 2.2).

$$RRF_{reference\ HBI} = \frac{RF_{V\ or\ VI}}{RF_{reference\ HBI}} \quad (2.3)$$

$$RF_{estimate} = \frac{(RRF_{IP25} \times RF_{IP25}) + (RRF_{II} \times RF_{II}) + (RRF_{III,IV} \times RF_{III,IV})}{3} \quad (2.4)$$

Thus, RRF values relative to IP_{25}, II, III (and IV) were 2.23, 0.98, 5.95, respectively for HBI V, and 1.84, 0.81, 4.92, respectively for HBI VI.

Table 2.2: GC-MS RFs for HBIs, with associated percentage deviations. Red asterisks denote $RF_{estimate}$ values (Eq. 2.4) estimated using RRFs calculated via Eq. 2.3.

HBI	Response Factor (RF) by date of calibration (day.month.year)								RSD (%)
	16.12.15	16.1.16	10.2.16	23.2.16	14.3.16	25.3.16	28.1.17	07.12.18	
IP_{25}	6.0	6.7	6.3	6.1	6.2	5.7	5.4	6.0	6.3
II	12.1	13.8	13.8	12.5	11.8	12.8	12.1	13.5	6.2
III / IV	1.7	1.9	2.3	1.7	1.9	1.9	1.8	2.2	11.5
V	11.7*	13.2*	13.6*	11.9*	12.1*	12.1*	11.4*	13.3	6.6
VI	9.7*	10.9*	11.2*	9.9*	10.0*	10.0*	9.4*	11.0	6.6

2.3.4 Identification and quantification of sterols

Sterol trimethylsilyl (TMS) ethers were identified by comparing their TIC mass spectra (Fig. 2.9), which were obtainable from most sediment samples, to those reported in the literature (Boon et al., 1979; Combaut, 1986; Volkman, 1986).

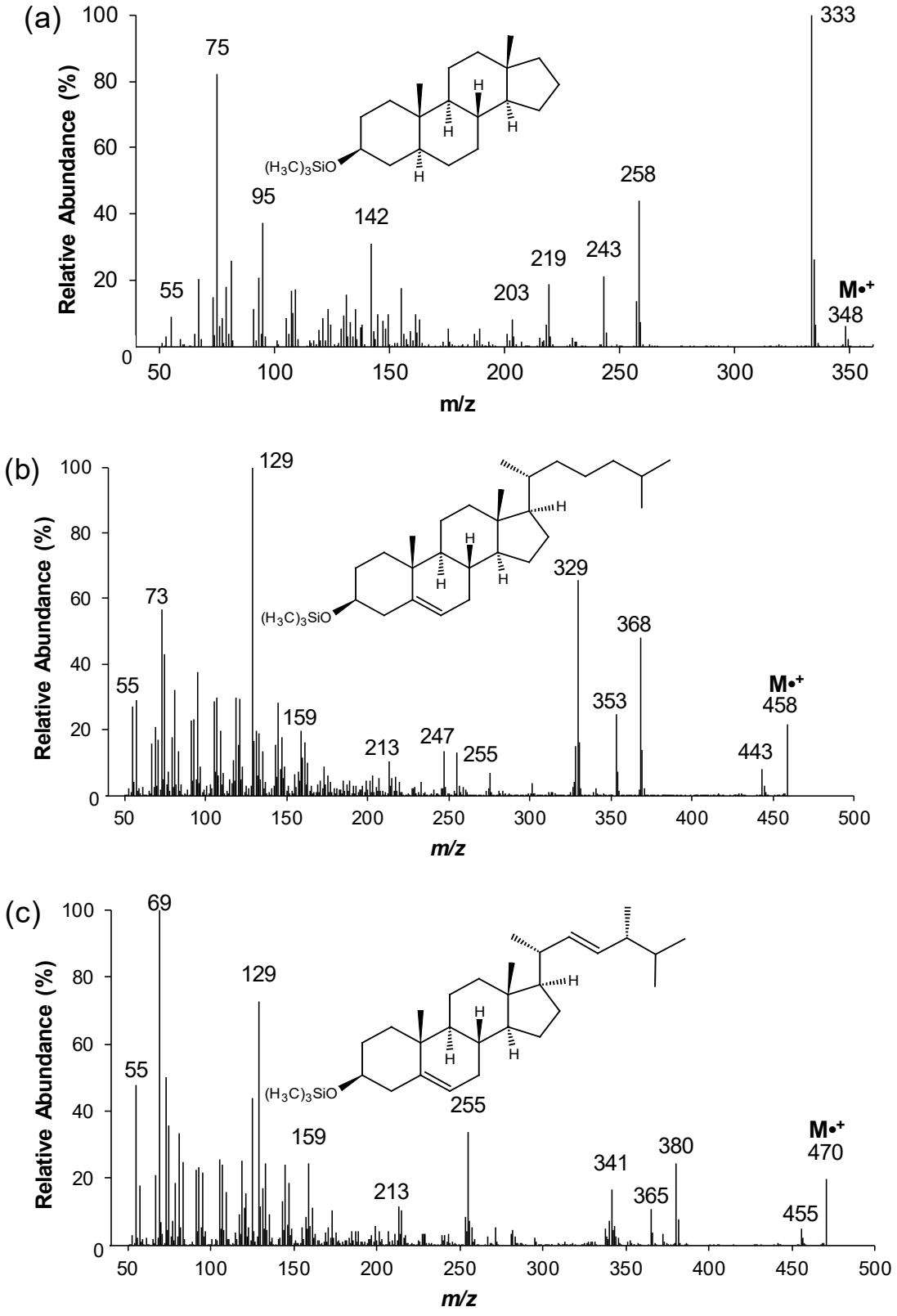

Figure 2.9: Background-corrected TIC mass spectra and structures of internal standard and sterol TMS ethers in sediment extracts: (a) 5α-androstan-3β-ol; (b) Cholesterol; (c) Brassicasterol.

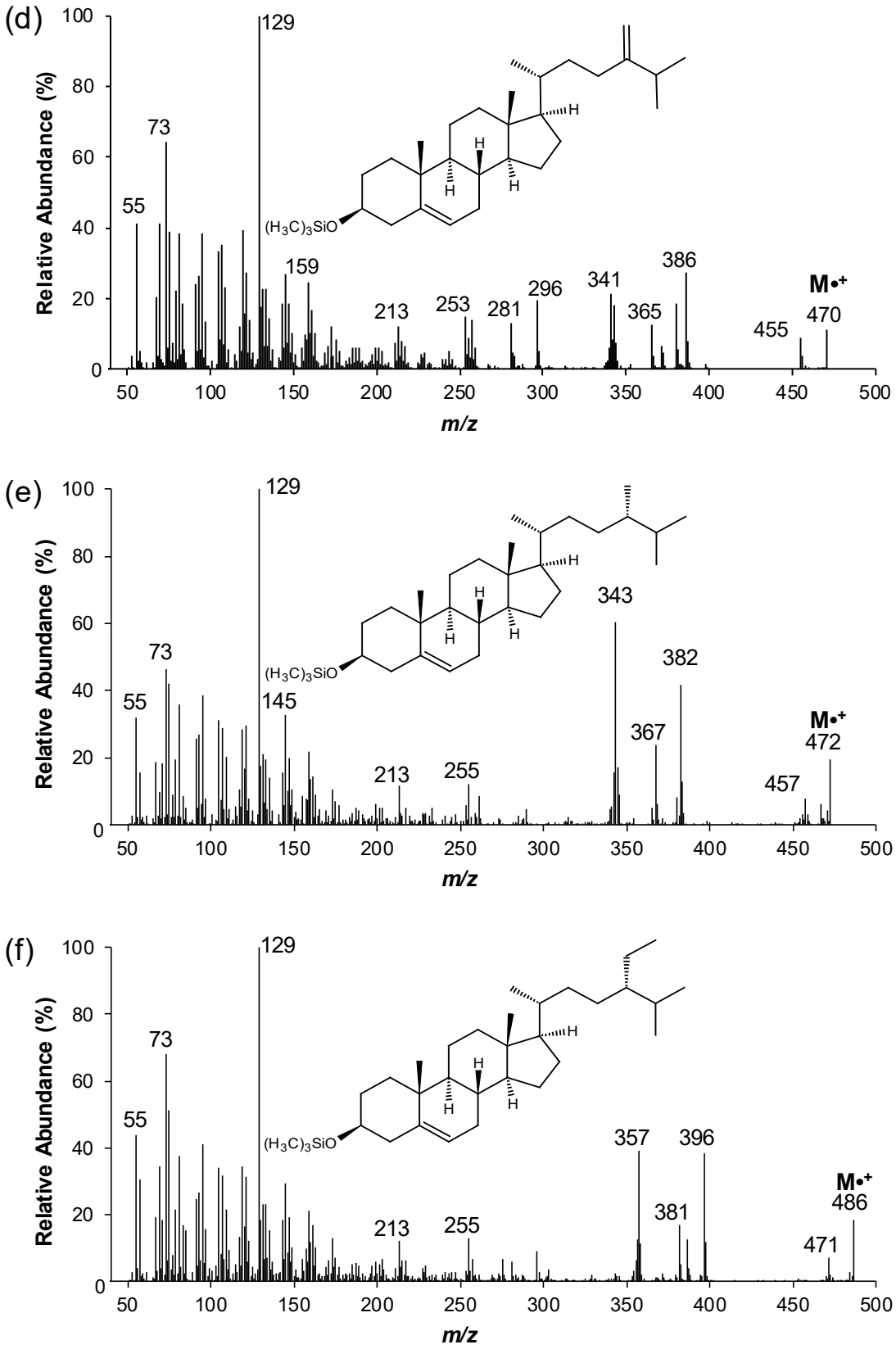

Figure 2.9 (*continued*): Background-corrected TIC mass spectra and structures of sterol TMS ethers in sediment extracts: (d) 24-methylenecholesterol; (e) Campesterol; (f) β-sitosterol.

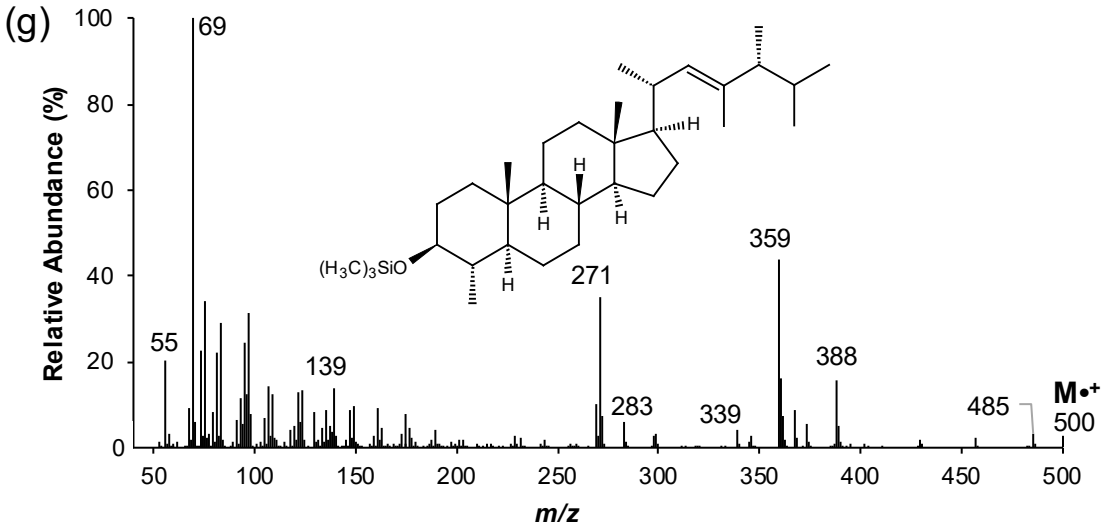

Figure 2.9 (*continued*): Background-corrected TIC mass spectrum and TMS ether structure of: (g) Dinosterol.

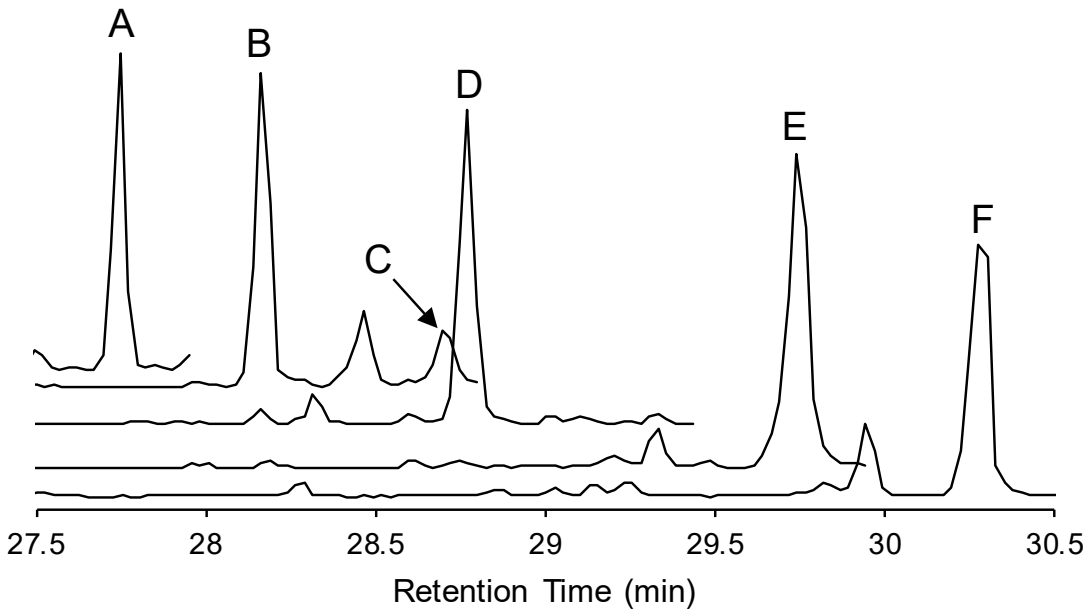

Figure 2.10: EICs of sterols, showing the elution order of cholesterol (A), brassicasterol (B), 24-methylenecholesterol (C), campesterol (D), β-sitosterol (E), and dinosterol (F).

Quantification was carried out by manual integration of characteristic ion signals extracted from the TIC (m/z 458 for cholesterol; m/z 470 for brassicasterol and 24-methylenecholesterol, i.e. chalinasterol; m/z 382 for campesterol; m/z 396 for β-sitosterol; m/z 359 for dinosterol; Sangiorgi et al., 2005). Integrated peak areas were normalised using a method analogous to HBI quantification (Eq. 2.5).

$$Sterol\ (\mu g\ g^{-1} dry\ sed.) = \frac{PA_{Sterol}/PA_{IS} \times RF}{m_{sed}} \times m_{IS} \qquad (2.5)$$

RF values for Eq. 2.5 were calculated via external standard calibrations of derivatised sterols (brassicasterol, RF value of 13.0; cholesterol, RF value of 14.8) and the internal standard at a range of concentrations (0.1, 0.2, 0.4, 0.6, 0.8, 1.0, and 2.0 µg mL^{-1}). However, authentic calibration standards were not available for 24-methylenecholesterol (i.e. chalinasterol), campesterol, β-sitosterol, and dinosterol. In such cases, the percentage intensity of ions used for quantification (I_a) relative to the total intensity of fragment ions in TIC mass spectra (TI_a) was calculated (Fig. 2.9); these percentages were then compared to those of calibrated sterols in the same sample (I_{ref} and TI_{ref}); finally, the results using brassicasterol and cholesterol as reference sterols were averaged in order to estimate an RF value (RF_{est}):

$$RF_{est} = \frac{RF}{(\frac{I_a}{TI_a} / \frac{I_{ref}}{TI_{ref}})} \qquad (2.6)$$

Example calculations of RF estimates for 24-methylenecholesterol, campesterol, β-sitosterol, and dinosterol obtained using Eq. 2.6 are shown in Table 2.3.

Table 2.3: example calculation steps to obtain RF estimates for sterols in the absence of an authentic standard calibration.

Sterol	Reference sterol	*RF*	$I_{ref} \div TI_{ref}$ (%)	$I_a \div TI_a$ (%)	RF_{est}	Mean RF_{est}
24-methylenecholesterol (chalinasterol)	Brassicasterol	13.0	1.38	0.50	36.0	39.1
	Cholesterol	14.8	1.42		42.0	
Campesterol	Brassicasterol	13.0	1.38	1.58	11.4	12.4
	Cholesterol	14.8	1.42		13.4	
β-sitosterol	Brassicasterol	13.0	1.38	1.91	9.4	10.2
	Cholesterol	14.8	1.42		11.1	
Dinosterol	Brassicasterol	13.0	1.38	2.32	7.8	8.4
	Cholesterol	14.8	1.42		9.1	

Sterols were extracted for a downcore record presented in Chapter 5, and RF_{est} values were calculated using Eq. 2.6 for a range of 15 core horizons spanning the investigated depth interval (the reader is referred to Chapter 5 and Table 5.2 for details).

Finally, in some cases, absolute sterol concentrations were normalised to Total Organic Carbon (TOC, % wt.) using Eq. 2.7 to account for differences in sedimentation rates within paleo-records versus those found in younger (e.g. surface) sediments representing the contemporary Barents Sea.

$$Sterol\ (\mu g\ g^{-1}\ TOC) = \frac{sterol\ (\mu g\ g^{-1}\ dry\ sed.)}{TOC\ (\%\ wt.)} \times 100 \qquad (2.7)$$

2.4 Calculations and statistical procedures

2.4.1 Calculation of $P_{III}IP_{25}$ indices

$P_{III}IP_{25}$ indices for downcore records (Eq. 2.8) were derived as the fractional abundance of IP_{25} (ng g^{-1}) relative to its sum with an open-water phytoplankton biomarker produced by pelagic diatoms, HBI III (Belt et al., 2015). To account for differences between IP_{25} and III concentration ranges, a regional concentration balance factor (*c*-factor; Eq. 2.9) of 0.63 was used for the Barents Sea (Smik et al., 2016).

$$P_{III}IP_{25} = \frac{[IP_{25}]}{([IP_{25}] + [III] \times c)} \qquad (2.8)$$

$$c = \frac{average\ [IP_{25}]}{average\ [III]} \qquad (2.9)$$

2.4.2 Classification trees

To facilitate easier interpretation of decision tree output (presented as part of Chapter 3), the method is described in section 2.4.2.1, while its specific application to sedimentary HBI data in the current study is presented in section 2.4.2.2.

2.4.2.1 An overview of decision tree methodology

The primary objective of decision trees is the prediction of a target (dependent) variable based on responses from a multivariate set of descriptive (independent) variables (for reviews, see Rokach and Maimon, 2005; Hastie et al., 2009; Sammut and Webb, 2017). Classification Tree (CT) models describe and predict discrete target variables with a limited number of unique values (representing classes or groups of data). Because trees are supervised classification methods, CTs are trained on a dataset of observations (e.g. surface sediments) with known classes of a target variable (e.g. SpSIC) prior to predictions on new data (e.g. downcore records).

CTs recursively partition a dataset of samples with known values of the target variable (known as a 'training set') into disjoint regions (nodes) by splitting samples on threshold values of individual descriptive variables (e.g. HBI abundances). Every splitting rule estimates target variable values for further samples in the dataset. While the variable and threshold value that achieves the highest classification rate (i.e. the primary split) is chosen at each partitioning step, competing splits (those that achieve comparable classification accuracy) and surrogate splits (those that closely mimic the exact classification outcomes of the primary split) are also recorded. The partitioning process continues until no further information explaining the correlation between descriptors and the target variable can be derived (Breiman et al., 1984). The typical nodal structure of a CT (Fig. 2.11a) consists of a root node, which represents the entire dataset prior to partitioning, as well as internal nodes and terminal (or leaf) nodes,

which represent intermediate decisions made by the algorithm throughout the partitioning process and final assignments of sample target variable values, respectively. Essentially, the tree model visualisation represents a hierarchical structure of algorithm-derived splitting decisions, which are successively applied from the root node to leaf nodes. The best possible splitting decisions, including the descriptive variable and the appropriate threshold value to split on, are determined at each stage of the partitioning process based on how well the target variable assignments of the resulting nodes fit those pre-determined for the training set, i.e. the degree of node heterogeneity (known as 'impurity'). Each subsequent split further reduces node impurity until the terminal nodes are 100% homogeneous and fit the training data perfectly. Various measures of node impurity have been developed, including the Gini Index (Breiman et al., 1984) and information gain (Quinlan, 1986), among others (Rokach and Maimon, 2005). Notably, comparative studies of such splitting criteria generally show insignificant performance differences for a given dataset (Buntine and Niblett, 1992; Shih, 1999; Raileanu and Stoffel, 2004).

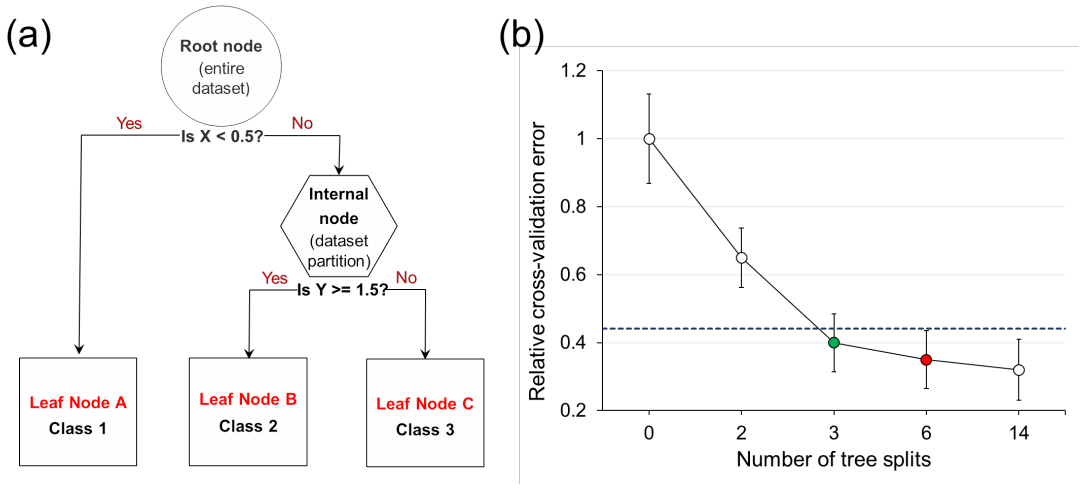

Figure 2.11: (a) A typical nodal structure of a binary classification tree. Left and right branches represent cases where the splitting condition is true and false, respectively; (b) An example of a cost-complexity analysis used to select the optimal tree size based on the relative misclassification error from *k*-fold cross validation. Red and green points represent the appropriate number of splits chosen based on the minimum cross-validated classification error (where +1SD is represented by the dashed line) and the 1-SE rule, respectively (Breiman et al., 1984).

An accurate CT model should describe the trends within the training data well and avoid interpreting random variability (i.e. have low bias, or training error), and have sufficient predictive capability to accurately classify previously unseen samples (i.e. have low variance, or test error). While a fully-grown tree classifies the training dataset perfectly, by definition, it is not well suited for making class predictions on new, unseen data. Such a tree over-interprets (i.e. overfits) the structure of the training data, assigning predictive power to random variability. Thus, while the bias is zero, the variance when making predictions on new data is high (Breiman et al., 1984).

Various stopping criteria can be specified to halt tree growth and prevent overfitting, such as the minimum number of samples within terminal nodes. However, manually setting accurate stopping criteria is challenging and may introduce bias to the model, resulting in an insufficiently complex tree structure that does not capture important trends of (i.e. underfits) the training data (Rokach and Maimon, 2005; Hastie et al., 2009). Tree pruning is an alternative approach to finding the optimal bias-variance trade-off. Cost-complexity pruning achieves this by *k*-fold cross validation (Breiman et al., 1984). A given dataset is divided into *k* random subsets of equal sample size (where *k* is an integer) and a sequence of differently-sized classification trees is induced using *k*-1 subsets. The resulting trees are tested on the final, unused sample partition in order to obtain a less biased estimate of the test error. The procedure is sequentially repeated until every *k*-fold partition is used for model testing. A cost-complexity plot of the resulting cross-validation test errors against tree size (Fig. 2.11b) is then used to choose the least complex tree with minimum test error, or that within 1 standard error of the minimum; the latter approach is known as the 1-SE rule (Breiman et al., 1984). Once a pruned tree is obtained, model performance may be evaluated further, e.g. by repeated *k*-fold cross validation (Breiman et al., 1984). The pruned and

tested classification tree derived from the training dataset can subsequently be used for class prediction in new, unseen samples.

2.4.2.2 Application of CT models in the current study

CT models were constructed using satellite sea ice concentration data from Nimbus-7 SMMR and DMSP SSM/I-SSMIS passive microwave sensors (Cavalieri et al., 1996; Fetterer et al., 2017) as a target variable, and either absolute HBI concentrations (ng g^{-1}) or relative abundances (%) of individual HBIs within an assemblage (e.g. IP_{25}, II, III, and IV; Eq. 2.10) as descriptive variables.

$$HBI\ (\%) = \frac{[HBI]}{[Total\ sum\ of\ HBIs]} \times 100 \qquad (2.10)$$

Tree models were induced using the Classification and Regression Trees (CART) algorithm of Breiman et al. (1984) and information gain as the splitting criterion. Tree structures were pruned using both the minimum cross-validation error and the 1–standard error (1–SE) rule to avoid overfitting and increase interpretability; 10-fold cross validation of the training set was used to estimate model performance. Specifics of the CT implementation to HBI data are described in Chapter 3, and associated code developed via the R Package (R Core Team, 2018) is included in Appendix A.

2.5 Biomarker extraction with and without KOH saponification

The direct KOH saponification procedure used for sterol extraction (section 2.2.2.2) significantly shortened GC-MS sample preparation due to the redundancy of TBA-based elemental sulphur clean-up (Tartar, 1913; Bates and Carpenter, 1979) and reduced N_2 blowdown. The main reason for substituting the DCM-MeOH extraction (Belt et al., 2012a), however, was the ability of KOH to hydrolyse bound (e.g. as esters)

sterols, liberating them for extraction into hexane (e.g. Zhang et al., 2014). The omission of bound sterols may affect paleoceanographic reconstructions, considering the generally high variability of bound versus "free" (i.e. extractable into organic solvents) sterol concentrations in sediments, of which the former are often several times more abundant (Birk et al., 2012). Therefore, the reproducibility of HBI (Tables 2.4, 2.5; Fig. 2.12) and sterol (Tables 2.6, 2.7; Fig. 2.13) concentrations was assessed using both methods to determine whether saponification could substitute solvent extraction.

Table 2.4: Comparison of HBI concentrations in two reference surface sediments extracted in triplicate directly into DCM-MeOH or via KOH saponification.

ID	Method	HBI concentrations ± SD (ng g^{-1})			
		IP_{25}	Diene II	Triene III	Triene IV
1	DCM-MeOH	67.8 ± 0.1	259.3 ± 1.8	12.8 ± 0.5	4.3 ± 0.1
	KOH	71.3 ± 1.8	271.5 ± 4.4	13.3 ± 0.5	4.3 ± 0.2
2	DCM-MeOH	612.6 ± 8.0	1106.2 ± 20.2	12.1 ± 0.7	18.0 ± 1.2
	KOH	634.0 ± 13.5	1149.9 ± 22.5	12.9 ± 0.5	18.1 ± 0.7

Table 2.5: Comparison of HBI concentrations in downcore sediments (JR142-11GC core; Chapter 4) following DCM-MeOH extraction and KOH saponification (M_A and M_B, respectively); factor difference between concentrations is denoted by Δ_{rel}.

Depth	IP_{25} (ng g^{-1})			Diene II (ng g^{-1})			Triene III (ng g^{-1})			Triene IV (ng g^{-1})		
(cm)	$\mathbf{M_A}$	$\mathbf{M_B}$	$\mathbf{\Delta_{rel}}$	$\mathbf{M_A}$	$\mathbf{M_B}$	$\mathbf{\Delta_{rel}}$	$\mathbf{M_A}$	$\mathbf{M_B}$	$\mathbf{\Delta_{rel}}$	$\mathbf{M_A}$	$\mathbf{M_B}$	$\mathbf{\Delta_{rel}}$
15.5	5.7	5.7	1.00	32.8	34.0	0.96	1.0	1.1	0.89	1.0	1.0	0.93
25.5	3.3	2.8	1.21	20.9	19.1	1.09	0.7	0.8	0.86	0.9	0.9	0.97
35.5	4.1	4.3	0.96	26.9	28.5	0.94	1.2	1.4	0.80	1.2	1.4	0.90
45.5	3.2	3.4	0.95	26.0	26.0	1.00	1.6	1.7	0.96	1.5	1.5	1.02
55.5	1.9	2.0	0.99	16.6	19.2	0.87	2.0	1.7	1.15	2.1	1.6	1.32
65.5	1.8	1.8	1.03	15.4	14.5	1.06	2.4	2.5	0.96	2.4	2.4	1.02
75.5	1.7	2.1	0.80	13.9	12.2	1.14	6.3	7.0	0.90	6.2	6.2	0.99
85.5	2.1	2.6	0.84	19.1	18.7	1.02	7.8	9.1	0.86	11.3	11.7	0.96
95.5	3.4	3.0	1.11	25.0	24.4	1.03	7.5	8.8	0.85	10.7	11.4	0.94
114.5	2.9	3.1	0.93	28.5	29.4	0.97	9.8	10.7	0.91	15.6	15.1	1.03
121.5	3.0	3.1	0.97	26.9	27.8	0.97	20.1	20.0	1.00	31.8	29.7	1.07
132.5	3.5	4.1	0.86	34.6	34.2	1.01	13.5	14.6	0.93	19.5	20.0	0.98
139.5	5.0	4.7	1.08	33.3	34.9	0.96	6.5	7.3	0.89	9.1	9.4	0.96
143.5	7.1	6.9	1.03	51.0	43.2	1.18	3.4	4.3	0.80	4.2	4.8	0.88
148.5	4.8	4.8	1.00	14.1	15.1	0.93	0.5	0.4	1.24	0.6	0.5	1.20
Mean	-	-	0.99	-	-	1.01	-	-	0.93	-	-	1.01
SD	-	-	0.10	-	-	0.08	-	-	0.12	-	-	0.11

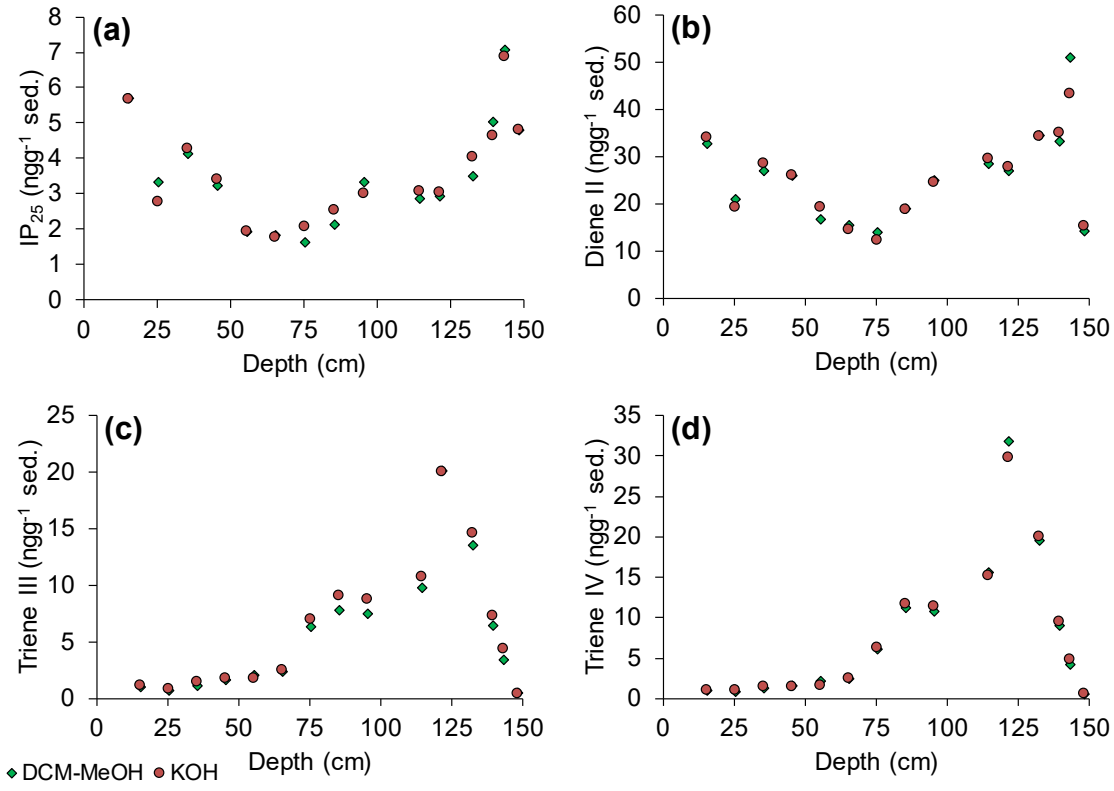

Figure 2.12: A comparison of HBI concentrations obtained via the DCM-MeOH and KOH methods for core JR142-11GC (Chapter 4): (a) IP_{25}; (b) II; (c) III; (d) IV.

Surface and downcore sediments exhibited similar HBI concentrations regardless of the extraction method used, with values within ca. 10% of each other, although the KOH saponification yielded slightly more variable concentrations in surface sediments (Table 2.4). The overall consistency of concentrations highlights the potential of KOH saponification as a viable alternative to DCM-MeOH extraction.

Table 2.6: Sterol concentrations in surface sediments extracted via the DCM-MeOH and KOH saponification methods (analogous to data in Table 2.4). Factor differences between concentrations (Δ_{rel}) are also shown.

ID	Method	Cholesterol ± SD (µg g^{-1})		Brassicasterol ± SD (µg g^{-1})	
		Mean	Δ_{rel}	Mean	Δ_{rel}
1	DCM-MeOH	0.52 ± 0.01	15.40 ± 0.41	0.28 ± 0.01	19.65 ± 0.32
	KOH	8.02 ± 0.08		5.45 ± 0.07	
2	DCM-MeOH	1.51 ± 0.07	19.16 ± 1.58	0.30 ± 0.01	27.60 ± 2.05
	KOH	28.82 ± 1.07		8.22 ± 0.28	

Table 2.7: Sterol concentrations in core JR142-11GC (Chapter 4) obtained via the DCM-MeOH (M_A) and KOH (M_B) methods; Δ_{rel} denote factor differences, with mean and standard deviation calculated across all horizons (analogous to data in Table 2.5). A comparison of 5α-androstan-3β-ol peak areas (PA) is also shown.

Depth	Cholesterol (μg g^{-1})			Brassicasterol (μg g^{-1})			PA of 5α-androstan-3β-ol (e^6)		
(cm)	M_A	M_B	Δ_{rel}	M_A	M_B	Δ_{rel}	M_A	M_B	Δ_{rel}
65.5	0.34	2.94	8.6	0.29	4.32	15.1	1.78	1.79	1.00
75.5	0.48	5.90	12.3	0.46	9.07	19.9	1.69	1.78	1.05
85.5	0.57	6.39	11.2	0.47	6.95	14.9	2.07	1.87	0.90
95.5	0.92	8.60	9.4	0.53	8.74	16.3	1.68	1.82	1.08
114.5	0.49	5.12	10.5	0.34	4.32	12.6	1.73	2.07	1.19
121.5	0.37	3.43	9.3	0.25	2.98	11.8	1.74	1.69	0.97
132.5	0.37	2.54	6.9	0.18	1.77	9.8	1.77	1.74	0.98
139.5	0.36	2.32	6.5	0.23	1.80	7.7	1.70	1.79	1.06
148.5	0.08	0.24	3.1	0.04	0.17	4.7	1.83	1.76	1.15
Mean	-	-	12.5	-	-	8.6	-	-	1.0
SD	-	-	4.7	-	-	2.8	-	-	0.1

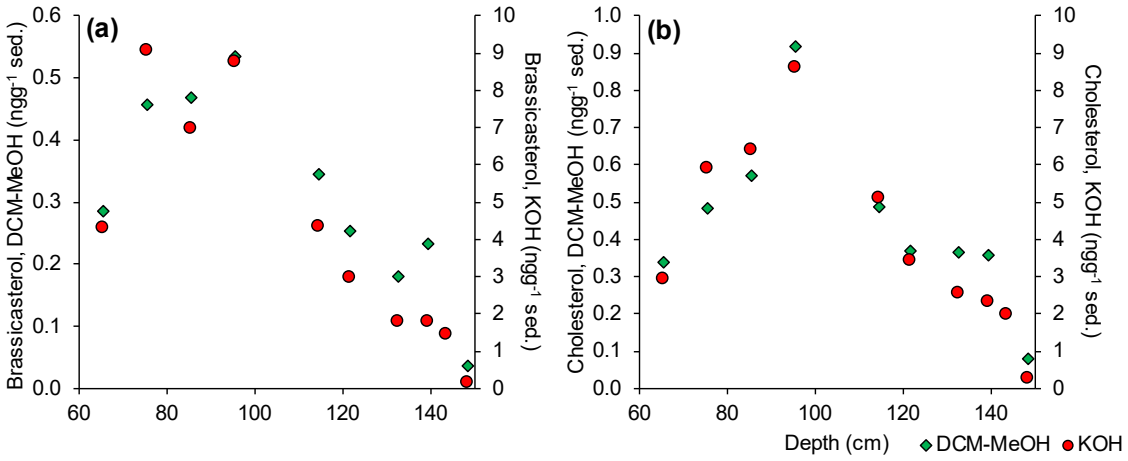

Figure 2.13: Brassicasterol (a) and cholesterol (b) concentrations in core JR142-11GC obtained via direct extraction into DCM-MeOH or KOH saponification.

The sterol concentrations were, on average, between a factor of 15.4–27.6 and 8.6–12.5 higher when extracted via KOH saponification from surface sediments and a downcore record, respectively. Further, loss of internal standard is unlikely to have caused this discrepancy, given similar integrated peak areas of the 5α-androstan-3β-ol internal standard in BSTFA/TMS-silylated extracts (at ca. 250 μL) regardless of the extraction method (mean factor difference of 1.0 ± 0.1). Finally, triplicate surface

sediment analysis revealed similar reproducibility of both methods, with percentage deviations ranging from 1.0–4.7%. Together, these data potentially suggest significantly higher yields of sterols when using direct KOH saponification prior to solvent extraction – a finding supported by the ability of alkaline hydrolysis to release bound (and therefore solvent-unextractable) sterols from sediments. However, despite such significant and variable differences in concentration, the overall temporal sterol variability in a marine sediment core was preserved (Figure 2.12), which tentatively supports the use of saponification for extracting higher amounts of sterols with increased sample throughput. However, robust confirmation of sterol distribution reproducibility using solvent extraction with or without prior saponification implies investigation of free and bound sterol content in further sedimentary records.

CHAPTER THREE

3. Biomarker-based multivariate classification of recent sea ice and productivity conditions in the Barents Sea

3.1 Introduction

The initial discovery of the biomarker IP_{25} as a qualitative proxy for Arctic sea ice, with subsequent introduction of the PIP_{25} index has advanced our understanding of long-term paleo Arctic sea ice conditions over the past decade by providing more detailed descriptions of past sea ice concentrations (section 1.3.2.3). A further development of PIP_{25} constituted the substitution of the pelagic biomarker counterpart of IP_{25} from less source-specific sterols (section 1.3.2.2) to III (Fig. 1.8), a tri-unsaturated HBI thought to originate from pelagic, but similarly minor diatom producers to those of IP_{25} (Brown et al., 2014c) – a hypothesis supported by its recent detection in *Rhizosolenia setigera* from western Svalbard (Belt et al., 2017) and enhanced abundance in the Barents Sea MIZ (Belt et al., 2015; Smik and Belt, 2017). Similar sources and concentration ranges of IP_{25} and III reduced the influence of the *c*-factor on PIP_{25}-based paleo-estimates of SpSIC (e.g. Belt et al., 2015; Cabedo-Sanz and Belt, 2016; Smik et al., 2016; Berben et al., 2017). Despite this, several challenges inherent to the PIP_{25} index persist. Objective selection of optimal biomarkers that best describe spring sea ice conditions remains problematic, not least due to the PIP_{25} index being limited to one pelagic phytoplankton biomarker. Additionally, the broad PIP_{25} thresholds previously used to classify regions of variable sea ice conditions, ranging from open water (P_BIP_{25} <0.1) to extensive sea ice cover (P_BIP_{25} > 0.75, $P_{III}IP_{25}$ > 0.80) were not based on a reproducible classification procedure, but were instead determined using approximate data ranges obtained via linear regression of PIP_{25} and SpSIC

(Müller et al., 2011; Smik et al., 2016). Multivariate HBI analysis could conceivably address these challenges and validate the PIP_{25} approach. The incorporation of HBIs not routinely used for paleo sea ice reconstruction (e.g. II and IV; Fig. 1.8) could provide further insights into the influence of environmental conditions on their distribution. The Barents Sea is key for investigating sea ice and productivity influences on biomarker production, as it exhibits increased sea ice variability and inter-annual decline in winter (Fig. 1.6), is one of the most productive high-latitude shelf seas, and cools Central Arctic-bound AW (section 1.2; Sakshaug et al., 2009).

Data mining algorithms incorporate a variety of parametric and non-parametric methods for multivariate analysis in order to characterise and visualise data structure (e.g. Hastie et al., 2009). Parametric algorithms, including cluster and factor analyses (e.g. Reimann et al., 2002; Templ et al., 2008), make distributional assumptions, such as data normality. This limits the applicability of such methods to geochemical data, which is seldom normally distributed due to strong spatial dependence, statistical outliers, and missing data (Reimann and Filzmoser, 2000). In contrast, non-parametric methods, such as classification trees (CTs), make no distributional assumptions and often allow for intuitive visualisation of implicit trends (e.g. Aitchison, 1986; Vayssières et al., 2000).

The principal aim of the current investigation, therefore, was to ascertain whether a CT model based on the variable distribution of certain biomarkers in Barents Sea sediments could be used to accurately classify the overlying sea ice conditions and provide a potentially more robust approach to paleo sea ice reconstruction. CT models were constructed using six HBI biomarkers (Fig. 1.8) in 198 surface sediments spanning the western and central Barents Sea and the Svalbard margins (Fig. 3.1a). An optimized CT model was used to reconstruct sea ice conditions in four well-dated short sediment cores retrieved from sites of contrasting sea ice conditions (Fig. 3.1b), and for which centennial observational records were available (Divine and Dick, 2006; Vare et al.,

2010; Walsh et al., 2017). CT results were then compared to SpSIC estimates obtained from regionally calibrated $P_{III}IP_{25}$ indices. The availability of a multivariate HBI set facilitated a further investigation into the relationship of satellite-derived oceanographic parameters (e.g. temperature and salinity) and primary productivity indicators versus the ratio of two tri-unsaturated HBIs (III and IV; Fig 1.8), which are the most common sedimentary HBI diastereoisomers (Belt et al., 2000) co-produced by pelagic diatoms (Rowland et al., 2001; Belt et al., 2017) and were previously suggested to be indicative of Atlantic (AW) and Arctic (ArW) waters (Navarro-Rodriguez, 2014).

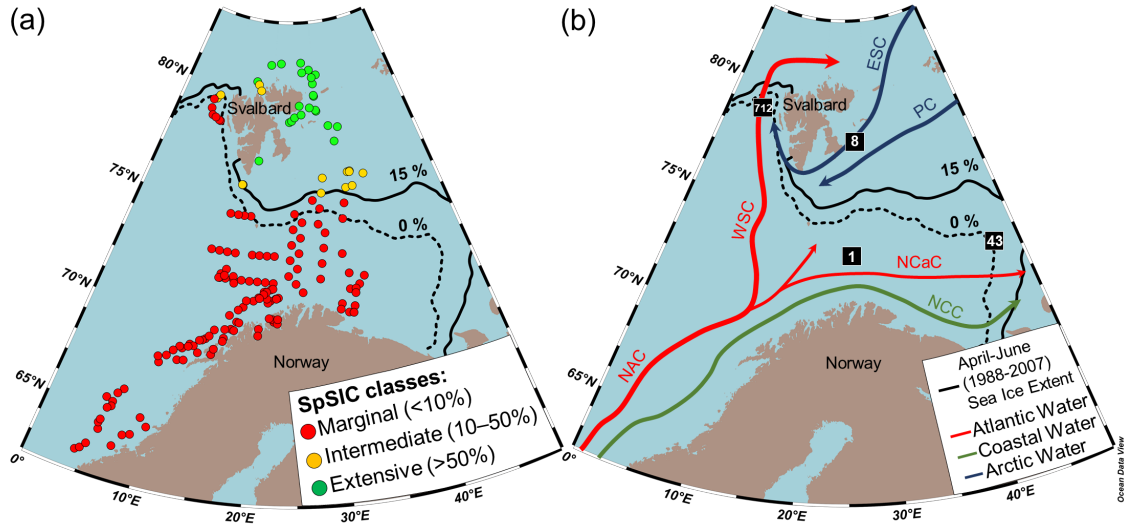

Figure 3.1: Barents Sea maps showing: (a) Surface sediments characterised by marginal (<10% SpSIC), intermediate (10–50% SpSIC), and extensive (>50% SpSIC) satellite-based sea ice conditions (Cavalieri et al., 1996); (b) Downcore records (numbered black squares) and a representation of surface currents carrying major water masses (NAC: North Atlantic Current; WSC: West Spitsbergen Current; NCaC: North Cape Current; ESC: East Spitsbergen Current; PC: Persey Current; NCC: Norwegian Coastal Current). The average April–June 1988–2007 sea ice extent (≥15% SpSIC) and the ice edge (>0% SpSIC) are shown by solid and dashed black lines, respectively.

3.2 Materials and methods

3.2.1 Surface sediment material

A total of 198 surface sediment sub-samples were examined from a range of multicores, box cores and gravity cores reflecting regions of variable sea ice cover (Fig. 3.1b). Most of the sediment material has been described elsewhere (Knies and Martinez, 2009; Navarro-Rodriguez et al., 2013; Belt et al., 2015; Smik et al., 2016); 55 samples described previously (Navarro-Rodriguez et al., 2013) and 96 further sediments from the MAREANO program (Knies and Martinez, 2009) were re-extracted using fresh material sub-sampled at the Geological Survey of Norway. These were supplemented by 47 surface sediments from other sources (Belt et al., 2015), including material collected during the Centre for Arctic Gas Hydrate, Environment, and Climate (CAGE; UiT–Arctic University of Norway) cruises 15-2 and 16-5 aboard the RV Helmer Hanssen in 2015 and 2016, respectively (n = 10). Upon arrival, freeze-dried samples were stored at -20°C to avoid HBI degradation. A depth interval of 0–1 cm was sampled for the majority of the sediments (n = 189), while variable depths ranging from 0–3 cm were only used for 10 samples. Detailed grain size distributions were not available for every sample, although published data from the MAREANO programme (Knies et al., 2006) for 73 sediments indicate that most samples from the central and northern Barents Sea included a variable (40–85%) mud fraction (summed silt and clay particles ≤63μm), while sediment coarsening was observed towards coastal areas along the northern and north-western Norwegian coast, where silt and clay fractions were as low as 5%, with an enhanced sand (63–2000 μm) content. Sampling locations and biomarker data are summarised in Appendix C (Table C.3).

3.2.2 Downcore sediment material

Downcore data were obtained from four short sediment cores (Fig. 3.1b) described elsewhere (Vare et al., 2010; Cabedo-Sanz and Belt, 2016). Cores BASICC 1 (73.13°N, 25.63°W; 425 m water depth), BASICC 8 (77.98°N, 26.83°W; 136 m water depth), and BASICC 43 (72.54°N, 45.74°W; 285 m water depth), henceforth referred to as cores 1, 8, and 43, were recovered aboard the RV *Ivan Petrov* in August 2003 as part of the "Barents Sea Ice Edge in a Changing Climate" (BASICC) project (Cochrane et al., 2009). Previously reported grain-size distributions indicated high mud content for cores 1 and 8 (ca. 89% and 77% summed silt and clay fraction, respectively), while core 43 exhibited a higher proportion of sand (ca. 47%; Cochrane et al., 2009). The age models for all three cores have been described elsewhere (Vare et al., 2010) and span the last ca. 250–300 years. Core MSM5/5-712-1 (78.92°N, 6.77°W; 1490.5 m water depth), hereafter referred to as core 712, was collected in 2007 on board the RV *Maria S. Merian* during the MSM5/5 cruise, and was described previously in both paleo-temperature and sea ice reconstructions (Spielhagen et al., 2011; Cabedo-Sanz and Belt, 2016; Matul et al., 2018). The uppermost 7.5 cm of core 712 presented herein consist of fine-grained mud, with a consistently low content (ca. 5±1%) of sediment coarser than 0.63 μm (Werner et al., 2011). The age model spans the last ca. 2000 years (Spielhagen et al., 2011). The cores were chosen to represent open water (core 1), as well as intermediate (cores 43, 712) and extensive (core 8) seasonal sea ice conditions, at least during recent centuries (Divine and Dick, 2006). Sedimentation rates for cores 1, 8 and 43 ranged from 1.1–1.3 mm y^{-1}, and were considerably lower (0.18 mm y^{-1}) for core 712, resulting in respective temporal resolutions of ca. 8–9 years and 56 years per 1.0 cm horizon. Downcore biomarker data are presented in Appendix C (Table C.4).

3.2.3 Analysis of HBI biomarkers

The extraction of HBI lipids (Fig. 1.8) was carried out according to methods described previously (Belt et al., 2012a; Belt and Cabedo-Sanz, 2015), with detailed descriptions of all steps available in section 2.2. Internal standard (9-octylheptadec-8-ene; 0.1 µg) was added to freeze-dried sediments (ca. 1.5–2.5 g), which were then extracted (3×2 mL) by ultrasonication and centrifugation (2500 rpm; 2 min) using DCM/MeOH (2:1 v/v) to obtain TOEs. Solvent was evaporated from the TOEs (N_2; 25°C) and elemental sulphur was removed as described in section 2.2. The non-polar fraction containing HBI lipids was collected using open column silica chromatography (ca. 1 g silica; 6–7 mL hexane; Belt et al., 2012a). Following solvent evaporation under N_2 (25°C), further purification of the extracts was carried out using Ag-ion column chromatography as described in section 2.2.5. Analysis of HBI-containing fractions was carried out using gas chromatography–mass spectrometry (GC–MS) using methods outlined in section 2.3. Chromatographic data from surface sediment material described by Belt et al. (2015) were re-examined to quantify HBIs not measured previously (II, IV, V, and VI; Fig. 1.8).

3.2.4 Statistical procedure

3.2.4.1 Satellite data processing

SpSIC data (April–June, 1988–2007) for CT induction were obtained on a 25×25 km grid from Nimbus-7 SMMR and DMSP SSM/I-SSMIS passive microwave datasets (Cavalieri et al., 1996), used previously for biomarker-based pan-Arctic and regional sea ice calibrations via the PIP_{25} index (Xiao et al., 2015a; Smik et al., 2016). Sediment sampling dates and regional accumulation rates supported the selection of an appropriate time interval covered by the satellite data. The majority of surface sediment material was collected from 2003–2006 (Navarro-Rodriguez et al., 2013; Belt et al.,

2015), while Barents Sea sedimentation rates in ice-covered regions are typically 0.7±0.4 mm y^{-1} (Zaborska et al., 2008), but can reach 1.1±0.4 mm y^{-1} (Maiti et al., 2010). A 20-year time interval was therefore chosen for satellite SpSIC to represent accumulation of 1.0 cm of sediment at 0.5 mm y^{-1}, which is the median of the 0.2–0.8 mm y^{-1} range reported for the MIZ around Svalbard (Zaborska et al., 2008). For time-series of annual SIC development in the Barents Sea, daily NOAA/NSIDC Climate Data Record of Passive Microwave Sea Ice Concentration (25×25 km) data was averaged for the years 1988–2017 (Peng et al., 2013; Meier et al., 2017). Surface (ca. 0 m depth) chlorophyll *a* concentrations (Chl *a*; mg m^{-3}), particulate inorganic carbon (PIC; mol m^{-3}), photosynthetically available radiation (PAR; E m^{-2} d^{-1}), and sea surface temperatures (SST; °C) were retrieved on a 9×9 km grid from the Moderate Resolution Imaging Spectroradiometer (MODIS) installed on the Aqua (EOS PM) satellite (NASA, 2018a–d). For spatial representation, monthly data from April–September were individually averaged for the 2003–2017 period. Aggregates for April–May (Chl *a* data only), April–June (all data), and July–September (SST, SSS, PAR, PIC data only) were also created. For mean annual time series, daily PAR, SST, SIC, and Chl *a* data were averaged for all available years throughout the satellite record (2003–2017). Regional daily-resolution time series of Chl *a* were also derived for the north-eastern, north-western, south-western, and south-eastern quadrants of the Barents Sea to showcase differences in primary productivity in these areas (region shapefiles used are in Appendix C, Fig. C.1). Sea surface salinity (SSS, psu; 1955–2012 mean; 0–30m water depth) was obtained on a 25×25 km grid from World Ocean Atlas 2013 (Boyer et al., 2014). Distances to the nearest coastline (km) were obtained from the Pacific Islands Observing System (NASA, 2012). A 9 nearest-point neighbourhood mean was used to derive satellite parameters at surface sediment locations using the R package sf (Pebesma, 2018). All R code for satellite data processing is available in Appendix A.

3.2.4.2 $P_{III}IP_{25}$, HBI triene ratio, and data transformation for CT models

$P_{III}IP_{25}$ indices were calculated using Eq. 2.8 as described in section 2.4.1, with III used as the pelagic biomarker counterpart to IP_{25}, and a regional *c*-factor (c=0.63) determined from a previous least-squares regression (Smik et al., 2016). Square brackets denote absolute HBI concentrations (ng g^{-1} dry sed.) in all equations. Estimates of SpSIC (%) and associated standard errors were calculated using Eq. 3.1 and the root-mean-square error (RMSE; ca. 11%) of a previously presented regional calibration, respectively (Cabedo-Sanz and Belt, 2016; Smik et al., 2016).

$$SpSIC\ (\%) = \frac{(P_{III}IP_{25} - 0.0692)}{0.0107} \tag{3.1}$$

Prior to classification tree induction, the optimal number of classes representing different sea ice conditions was estimated via complete linkage Agglomerative Hierarchical Clustering (AHC; Sørensen, 1948) of satellite-derived SpSIC estimates and coordinates of surface sediments (Fig. 3.2). Squared Euclidean distance was used as a mathematical distance measure. Thus, three classes representing marginal (0–10%), intermediate (10–50%) and extensive (50–100%) SpSIC were identified (Fig. 3.1a).

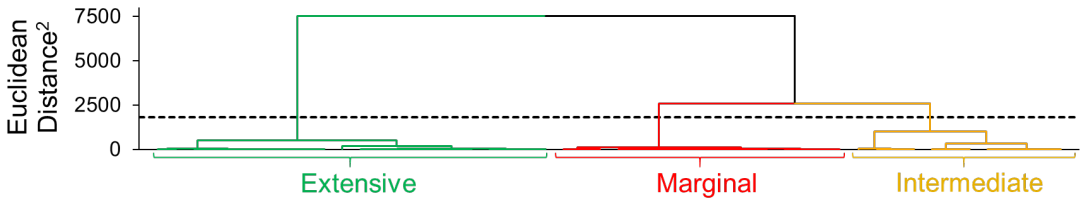

Figure 3.2: Complete linkage agglomerative hierarchical clustering of satellite-derived spring sea ice concentrations (SpSIC) estimates for surface sediment samples. Ice-free locations did not provide information about the SpSIC distribution and were excluded.

HBI concentrations were converted into relative abundances (0–100%) via individual normalisation (Eq. 2.10, section 2.4.2) to four HBI assemblages shown in Eq. 3.2–3.5. Biomarkers I–IV were included in all four assemblages (A to D) due to the contrasting influences of sea ice conditions on their production. HBIs I (IP_{25}) and II

have known sympagic diatom sources (Brown et al., 2014c; Belt et al., 2016), while III and IV are co-produced by ubiquitous pelagic diatoms (Belt et al., 2001a, 2017; Rowland et al., 2001). Minor quantities of IV have been observed in sea ice (Belt et al., 2007; Brown, 2011; Ringrose, 2012). For Assemblage B, HBI V was also included as it has been identified in Arctic sea ice (Belt et al., 2007) and represents a further, although likely less specific (He et al., 2016), sympagic influence. An additional pelagic influence was investigated using VI (Assemblage C), an HBI reported in the diatom *Berkeleya rutilans*, a species abundant within (at least) brackish coastal waters (Brown et al., 2014b). Both V and VI were tested as SpSIC classifiers in Assemblage D.

$$HBI\ Assemblage\ A = \sum([I], [II], [III], [IV]) \tag{3.2}$$

$$HBI\ Assemblage\ B = \sum([I], [II], [III], [IV], [V]) \tag{3.3}$$

$$HBI\ Assemblage\ C = \sum([I], [II], [III], [IV], [VI]) \tag{3.4}$$

$$HBI\ Assemblage\ D = \sum([I], [II], [III], [IV], [V], [VI]) \tag{3.5}$$

Finally, the HBI triene ratio for comparison with satellite Chl *a*, SST, SSS, PAR, and PIC data was calculated as percentage abundance of III relative to the sum of III and IV using Eq. 3.6. Complete linkage AHC using squared Euclidean distance (Sørensen, 1948), and Principal Component Analysis (PCA) were carried out on satellite data and the HBI triene ratio using XLSTAT (Addinsoft, 2018).

$$HBI\ Triene\ Ratio = [III]/([III] + [IV]) \tag{3.6}$$

3.2.4.3 CT induction from sedimentary HBI composition

CT models were built from the surface sediment dataset following the method of Breiman et al. (1984) – see also section 2.4.2.1 (Chapter 2) for a detailed overview. Specifically, the ‘rpart’ (Therneau et al., 2015), ‘caret’ (Kuhn et al., 2016), ‘MLmetrics’

(Yan, 2016), and 'DMwR' (Torgo, 2010) libraries were utilised as part of the R Statistical Package (R Core Team, 2018) for induction and performance evaluation of four CT models using both absolute HBI concentrations or compositional abundances within assemblages A–D (Eq. 3.2–3.5) as descriptive variables, and classes of sea ice cover assigned to each sample using satellite SpSIC data (Fig. 3.1a) as the target variable. First, fully-grown trees were induced using no stopping criteria and information gain as the splitting criterion (Quinlan, 1986, 1993). Cost-complexity pruning and the 1-SE rule were applied to each CT model to counter overfitting. Positive bias in model performance due to class imbalance was reduced by calculating precision (percentage of accurate predictions) and sensitivity (proportion of correct classifications in the training set) metrics for each SpSIC class (example calculations are available in Table C.5 and Eq. C.1–C.9 of Appendix C). The F1 score was calculated as the weighted average of precision and sensitivity. Finally, Cohen's Kappa was used to confirm that model accuracy significantly improved over than that obtained by random chance, with values >0.80 indicating good performance (Landis and Koch, 1977). Variable importance for classification was obtained both after cross-validation and using the Random Forest (RF) algorithm (n = 300 trees; Breiman, 2001). The CT model that best classified sea ice conditions was chosen based on the expected performance of each pruned tree on unseen data (i.e. new samples not used in model construction) using repeated 10-fold cross validation (n = 5; Breiman et al., 1984), variable importance, model complexity and interpretability. Standard deviations (SD) of decision rules were approximated for the optimal CT model only using the C5.0 algorithm (Quinlan, 1993), and probabilities of class predictions were then calculated by linear interpolation between the upper and lower SD bounds. All R code used for CT model building is available in Appendix A.

3.3 Results

3.3.1 Classification tree models and $P_{III}IP_{25}$

3.3.1.1 CTs in surface sediments

CT models created from relative HBI abundances within assemblages A–D using Eq. 2.10 and 3.2–3.5 are henceforth referred to as models A–D, respectively. Models A–D yielded a high classification rate for the training data, with 186–194 samples classified correctly (ca. 94–98%; Table 3.1). Comparably high accuracy was observed following repeated (n = 5) 10-fold cross validation (89–92 ± 6%; Table 3.1), with 172–185 correctly classified samples (Fig. 3.3 and 3.4). Upon examining performance for individual classes of sea ice conditions, the lowest sensitivity (56–76%) and precision (53–69%) were observed for samples with intermediate SpSIC. The loss of sensitivity corresponded to 5–8 samples being misclassified into both marginal (n = 3–6) and extensive (n = 1–2) sea ice classes. Similarly, precision suffered due to the misclassification of 9–12 samples from the marginal to the intermediate sea ice class (Fig. 3.3). In contrast, locations with marginal and extensive SpSIC were correctly classified with higher confidence, exhibiting sensitivity values of 92–95% (marginal SpSIC) and 89–97% (extensive SpSIC), as well as corresponding precision values of 96–98% and 81–85%. The highest overall sensitivity of 88 ± 11% was observed for models C and D, while model A was the most precise (87 ± 12%) and accurate after cross-validation (92 ± 6%). CT models built using absolute HBI concentrations within assemblages A–D only used IP_{25} and IV as primary splitting variables after pruning (Fig. 3.5), while II and III were the top competing and surrogate variables (Table 3.3). Overall, all pruned trees showed comparable (high) performance, with IP_{25}, II, III, and IV used as primary splitting variables (Table 3.1 and Fig. 3.3–3.6). Conversely, V and VI exhibited low relative importance for CT models with both CART and RF algorithms (Fig. 3.7–3.9). Thus, following rationalisation of model outcomes in surface

sediments (Fig. 3.10–3.12), Model A was chosen to predict discrete sea ice conditions for cores 1, 8, 43 and 712 (the reader is referred to section 3.5.1 for associated discussion). Ranges of splitting rule thresholds within standard deviations (Quinlan, 1993) were estimated to be 4.4–8.4% for IP_{25} and 4.1–5.2% for IV (Fig. 3.6a).

Table 3.1: Summary of performance metrics for classification tree (CT) models obtained using percentage HBI abundances with assemblages A–D. Abbreviations represent classes of sea ice conditions (Fig. 3.1a): MAR = marginal; INT = intermediate; EXT = extensive. Kappa and F1 score were 0.8 ± 0.1 and 0.9 ± 0.1 for models A, C, and D; model C exhibited values of 0.7 ± 0.2 and 0.8 ± 0.1, respectively.

	Training Accuracy (%)	10-fold CV accuracy (%)	Per-class sensitivity (%)			Mean sensitivity (%)	Per-class precision (%)			Mean precision (%)
			MAR	INT	EXT		MAR	INT	EXT	
A	94	92 ± 6	95	72	96	87 ± 11	97	69	85	87 ± 12
B	94	89 ± 5	93	56	89	80 ± 13	96	53	81	80 ± 13
C	97	91 ± 6	92	76	93	88 ± 11	98	59	84	84 ± 11
D	98	91 ± 6	92	73	97	88 ± 11	98	59	85	83 ± 12

Model A predictions	Known data classes MAR	INT	EXT
MAR	145	4	0
INT	7	17	1
EXT	2	1	22

Model B predictions	Known data classes MAR	INT	EXT
MAR	143	6	0
INT	9	12	3
EXT	2	3	20

Model C predictions	Known data classes MAR	INT	EXT
MAR	141	3	0
INT	10	17	2
EXT	2	2	21

Model D predictions	Known data classes MAR	INT	EXT
MAR	141	3	0
INT	11	16	1
EXT	1	3	22

Figure 3.3: Confusion matrices for CT models A–D created from percentage HBI abundances. Rows and columns represent known and model-predicted classes of sea ice conditions (MAR = marginal, INT = intermediate, EXT = extensive) after repeated cross-validation. Off-diagonal values highlighted in red represent misclassified samples.

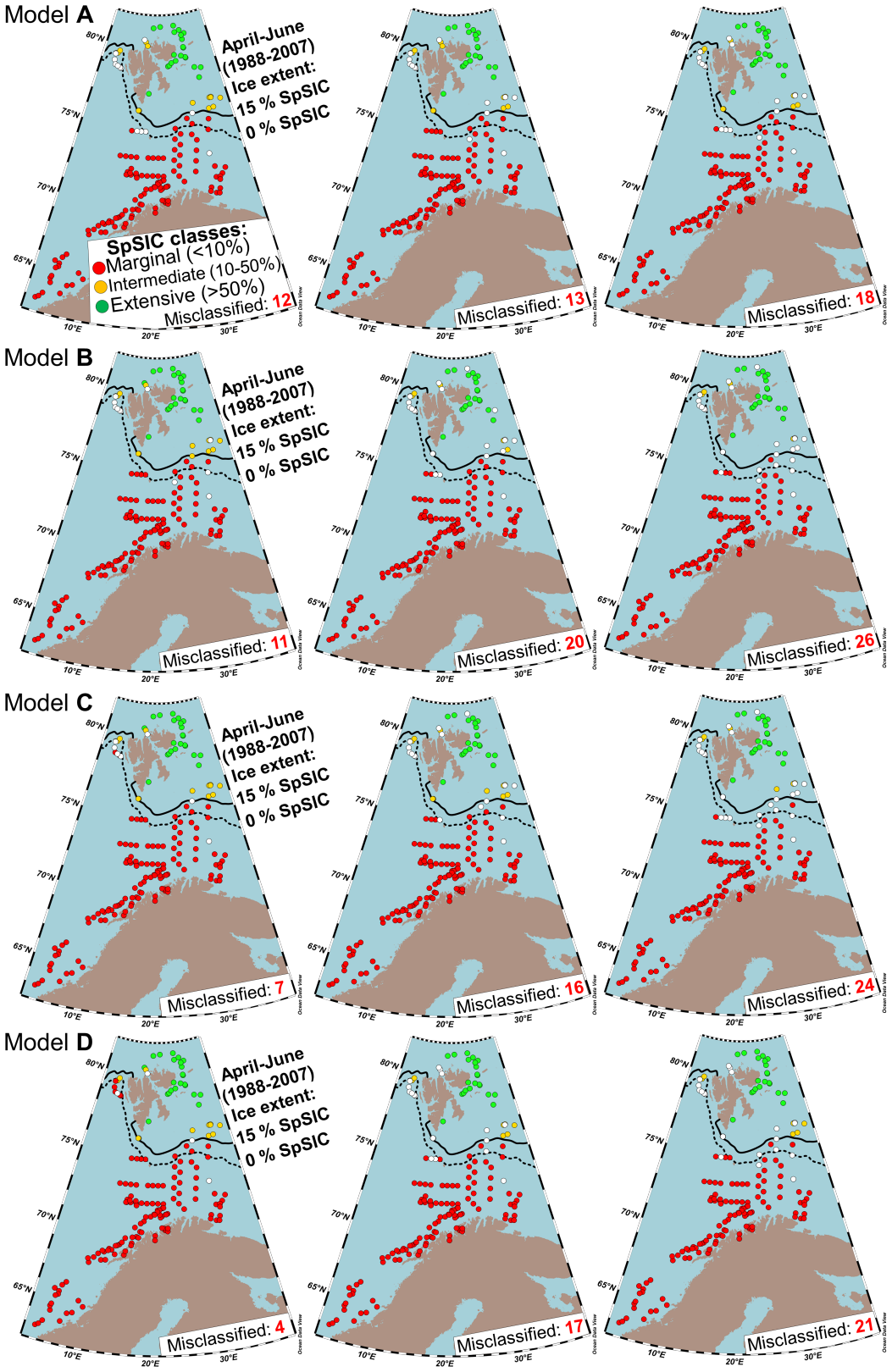

Figure 3.4: Classification of marginal, intermediate, or extensive sea ice conditions by CT models A–D for the surface sediment training set (left); white circles denote misclassified samples. The best (center) and worst (right) performance after 10-fold cross-validation is also shown.

Table 3.2: Top competing variables and surrogate splits corresponding to splitting rules (in %) for derived from relative abundance-based1SE-pruned CT models A–D (Fig. 3.6). The classification improvement and agreement metrics represent a relative performance measure of competing variables and level of similarity (scaled from 0–1) between surrogate and primary splitting rules, respectively.

Model	Primary split (% of total)		Competing split (% of total)		Surrogate split (% of total)	
	Rule	Improvement	Rule	Improvement	Rule	Agreement
A	$IP_{25} < 5.3$	75.0	IV ≥ 25.0	68.4	II < 16.9	0.944
	IV ≥ 4.8	29.5	III ≥ 7.4	28.4	III ≥ 5.3	0.963
B	$IP_{25} < 2.1$	72.4	II < 13.6	71.0	II < 7.0	0.960
	II < 54.2	30.7	$IP_{25} < 12.8$	28.9	$IP_{25} < 12.8$	0.983
	II < 13.6	6.3	IV ≥ 13.2	3.7	$IP_{25} < 3.0$	0.912
C	$IP_{25} < 3.2$	75.0	II < 34.6	70.2	II < 8.9	0.960
	III ≥ 6.3	28.4	IV ≥ 3.7	26.5	IV ≥ 5.7	0.963
	IV ≥ 21.8	7.9	III ≥ 32.0	4.2	III ≥ 32.0	0.929
D	$IP_{25} < 1.8$	76.8	II < 7.6	69.7	II < 7.4	0.960
	II < 49.0	31.6	III ≥ 4.5	28.6	III ≥ 4.4	0.965
	IV ≥ 15.0	4.9	III < 4.8	3.5	VI < 3.0	0.938
	III < 4.8	4.8	VI ≥ 4.8	3.2	-	-
	$IP_{25} < 2.2$	4.7	II < 7.6	4.2	II < 8.3	0.960

Table 3.3: Top competing variables and surrogate splits corresponding to splitting rules (in ng g^{-1}) for 1SE-pruned CT models derived from absolute HBI concentrations of assemblages A–D (Fig. 3.5). The top two primary splits were common to all assemblages.

Model	Primary split (ng g^{-1})		Competing split (ng g^{-1})		Surrogate split (ng g^{-1})	
	Rule	Improvement	Rule	Improvement	Rule	Agreement
A–D	$IP_{25} < 0.6$	72.4	II < 3.3	70.3	II < 1.8	0.985
	IV ≥ 0.5	22.3	III ≥ 0.7	21.1	III ≥ 0.6	0.983
B	$IP_{25} < 4.2$	11.2	II < 19.3	11.2	II < 15.0	0.949
	IV ≥ 4.0	9.0	III ≥ 4.6	6.5	III ≥ 3.0	0.938

3.3.1.2 CT and $P_{III}IP_{25}$–based sea ice estimates in downcore records

Within the time period represented by the core sub-samples (ca. 1750 AD–present), all horizons from cores 43 and 712 were classified into the intermediate sea ice class (10–50% SpSIC), while cores 1 and 8 were characterised as having experienced marginal (<10%) and extensive (50–100%) sea ice cover, respectively. Extensive SpSIC (ca. 84–85%) was also inferred for core 8 from $P_{III}IP_{25}$-based SpSIC estimates, while

ice-free conditions prevailed at the core 1 site. In contrast, cores 43 and 712 were characterised by intermediate and more variable SpSIC (13–30% and 29–41%, respectively; Fig. 3.13a). A gradual decline in SpSIC was apparent for cores 43 and 712 after ca. 1900 AD (Vare et al., 2010; Cabedo-Sanz and Belt, 2016).

3.3.2 HBI triene ratio

3.4.2.1 Comparisons with satellite-derived parameters in surface sediments

Based on PCA, the HBI triene ratio (Eq. 3.6) exhibited a positive or negligible association with Chl *a* during April–May or June–August, respectively (Fig. 3.14). AHC analysis of the ratio resulted in two clusters within areas of well-defined spring bloom seasonality and less productive regions characterised by strong AW inflow and continuous upwelling (Fig. 3.15d, e). Good agreement was observed with Chl *a* during spring (April, May, April–May, April–June), where the April–May aggregate exhibited the least mismatched cluster memberships (n = 28) relative to those of the HBI triene ratio. Averaging the triene ratio AHC centroids yielded an approximate threshold value of ca. 0.62 (i.e. 62% dominance of III) to separate regions of high and low Chl *a*. Some agreement of HBI triene ratio clusters with July–September PIC was also observed (n = 36 mismatches). Conversely, no significant association with SST, PAR, April–June PIC, or SSS data was observed, with 61–75, 60–87, 68, and 75–81 mismatched cluster memberships, respectively (Fig. 3.16e, 3.17–3.19).

3.4.2.2 HBI triene ratio-based productivity inferences in downcore records

Cores 712 and 8, characterised by low overlying Chl *a*, exhibited HBI triene ratio values consistently below the threshold value of 0.62 (0.38–0.57). Since ca. 1850, a gradual decrease and increase of the HBI triene ratio was observed for cores 712 and 8, respectively. Ratios of 0.64–0.71 characterised core 43, located at the highly-

productive ice-edge of the eastern Barents Sea. Finally, core 1, characterised by ice-free conditions and strongly influenced by the NCaC (Fig. 3.1b), exhibited values closer to the threshold and ranging between 0.57–0.63 (Fig. 3.20).

3.4 Discussion

3.4.1 Evaluation of HBI variable importance for sea ice classification

The choice of an appropriate tree model for classification of sea ice conditions among HBI assemblages A–D was based on comparisons of cross-validated performance metrics (Table 3.1 and Fig. 3.4), relative variable importance (Fig. 3.7–3.9), and tree structures obtained with both relative abundances (%) and absolute concentrations (ng g^{-1}) of HBIs. Tree structures of models A–D pruned using the 1-SE rule only used IP_{25}, II, III and IV as the primary splitting variables (Fig. 3.6), while V and VI were only incorporated within the full tree structures prior to pruning, or as low-level competing and surrogate variables, failing to achieve comparable classification improvement (Table 3.2). The variability of tree structures based on relative HBI abundances (Fig. 3.6) is potentially attributable to the presence of spurious correlations within the data following incorporation of V and VI as descriptive variables. Compositional HBI abundances are subject to a constant sum constraint, such that any alteration in one variable inevitably causes an opposing change in those remaining; this imposes spurious correlations between all HBIs, potentially obscuring true associations between biomarkers (e.g. Aitchison, 1986; Pawlowsky-Glahn and Egozcue, 2006; Gibert et al., 2016). Thus, while compositional % abundances of HBIs (Eq. 2.10 and 3.2–3.5) were used for downcore predictions since modern absolute concentration ranges are unlikely to be represented in sedimentary paleo-archives (Stoynova et al., 2013; Xiao et al., 2015a, b), it is arguably more appropriate, at least in the first instance, to derive tree structures for a classification task using absolute (i.e. more independent)

values. Accordingly, absolute concentration-based CT models showed more consistent tree structures, where IP_{25} and IV classified >90% of the training dataset correctly using two splitting rules (Fig. 3.5), and II and III were used as surrogate and competing variables (Table 3.3). This agreed with compositional abundance-based CT models (Fig. 3.6 and Table 3.2) and suggested that V and VI were of low importance to the classification task. However, more generally, the utility of individual HBIs for classification cannot be comprehensively assessed from tree structures alone due to potential masking of similarly important variables – this arises from the "greedy" nature of CT models, which only select one descriptive variable per split during model building. Final tree structures should thus be treated with some circumspection. Relative variable importance incorporates competing and surrogate variables (Tables 3.2–3.3) and is potentially a more robust indicator of HBI utility for classification (Breiman et al., 1984; Grömping, 2009; Tuv et al., 2009).

Relative variable importance values calculated after cross-validation using compositional HBI abundances and absolute concentrations were both in agreement with tree structures, consistently showing lowest importance for V and VI (Fig. 3.7). Concordant results were obtained from the Random Forest method (Fig. 3.8), which constructs a large number of decision trees on 2/3 of the training dataset with random subsets of descriptive variables, and estimates variable importance by testing the resulting forest of trees on the remaining 1/3 of the dataset not used for tree construction (Breiman, 2001). This method provided a further non-parametric measure of variable importance which was potentially less susceptible to spurious correlations within the data (Ishwaran and Lu, 2017). Finally, a comparison of variable importance measures including and excluding competing and surrogate splitting rules indicated that some limited importance of V and VI for classification was mostly attributable to their use as secondary splitting variables, which were unused in final pruned trees (Fig. 3.9).

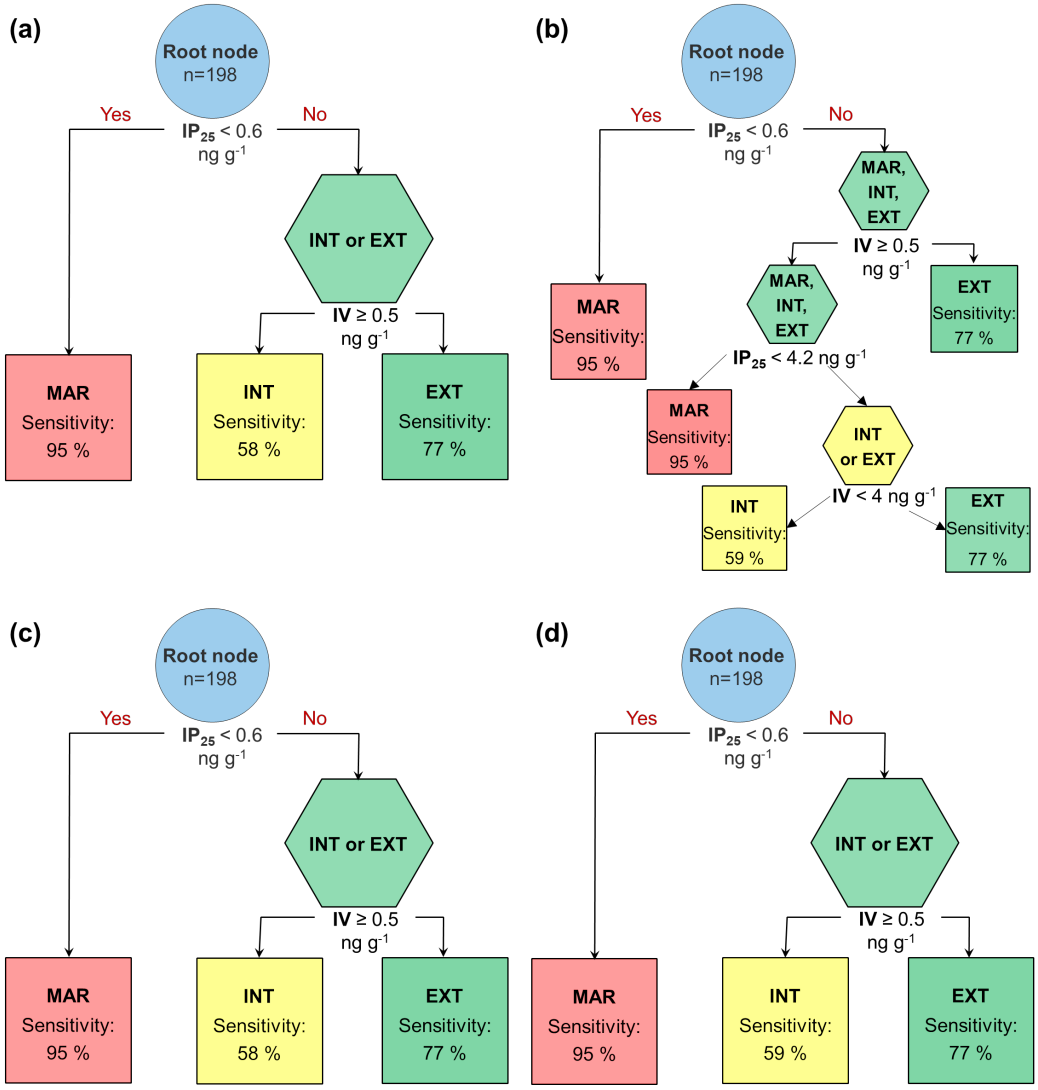

Figure 3.5: Pruned classification tree (CT) structures obtained using the absolute HBI concentrations (ng g^{-1}) in surface sediments (n = 198) and following application of the 1-SE rule to HBI assemblage: (a) A; (b) B; (c) C; (d) D. Abbreviations denote CT-assigned classes of marginal (MAR), intermediate (INT) and extensive (EXT) sea ice conditions (Fig. 3.1a).

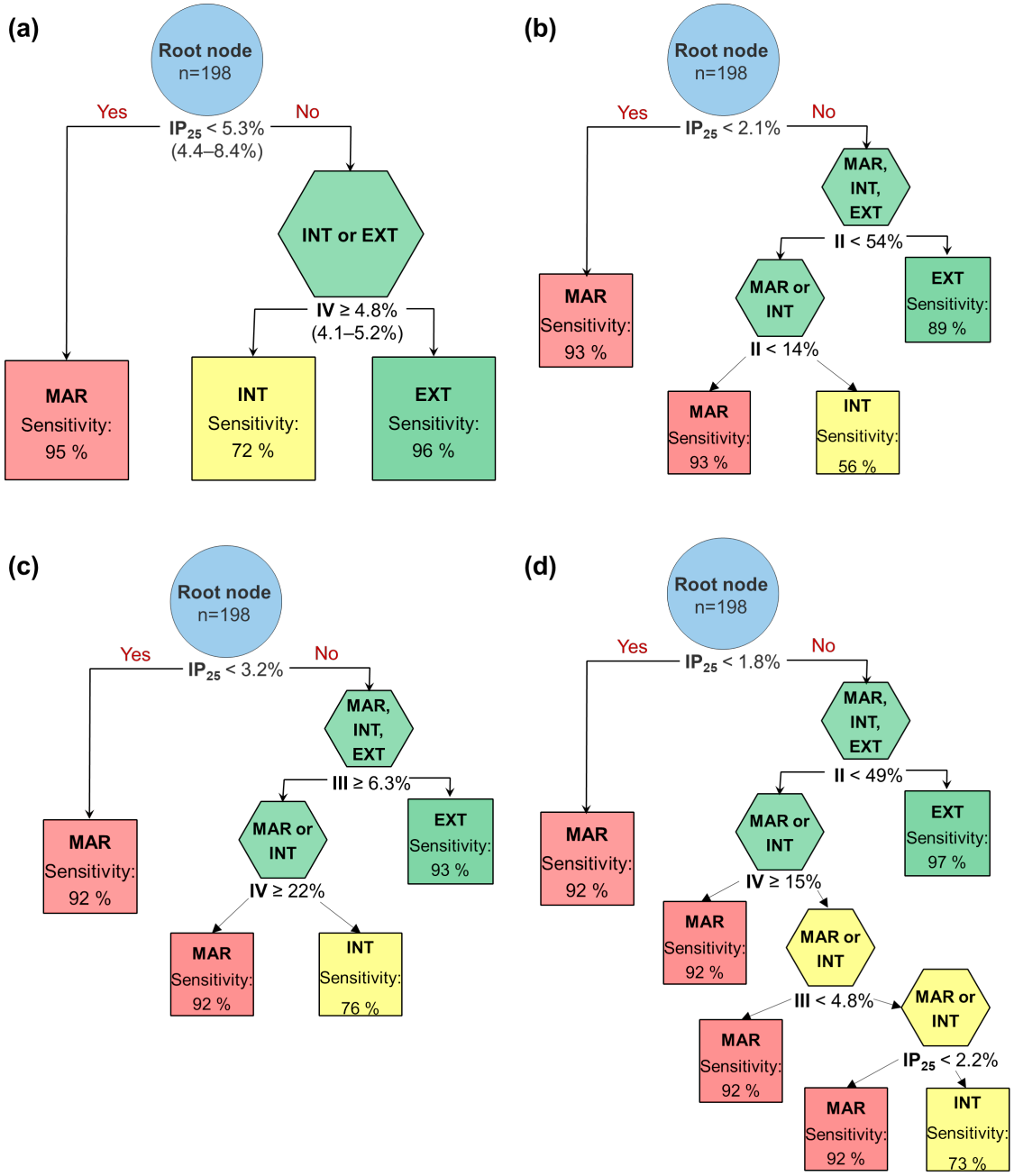

Figure 3.6: Pruned classification tree (CT) structures obtained using HBI percentage abundances (Eq. 3.2–3.5) in the surface sediment training dataset (n = 198) and following application of the 1-SE rule to: (a) Model A; (b) Model B; (c) Model C; (d) Model D. For (a), bracketed values represent ranges of splitting rule thresholds within ±1 standard deviation estimated using the method of Quinlan (1993).

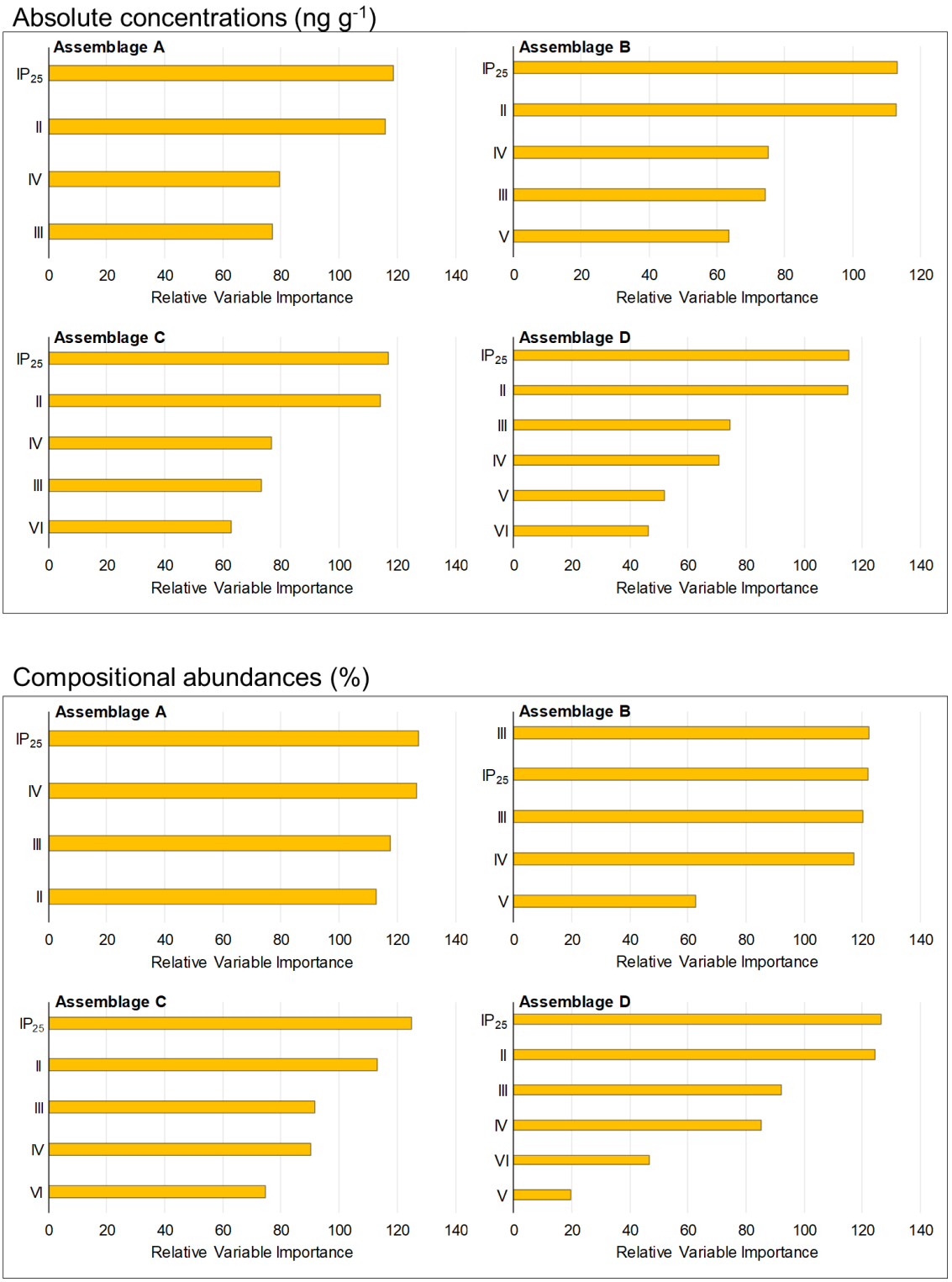

Figure 3.7: Relative HBI importance for models built using absolute concentrations (ng g^{-1}) and compositional abundances (%) within assemblages A–D after cross-validation (Breiman et al., 1984).

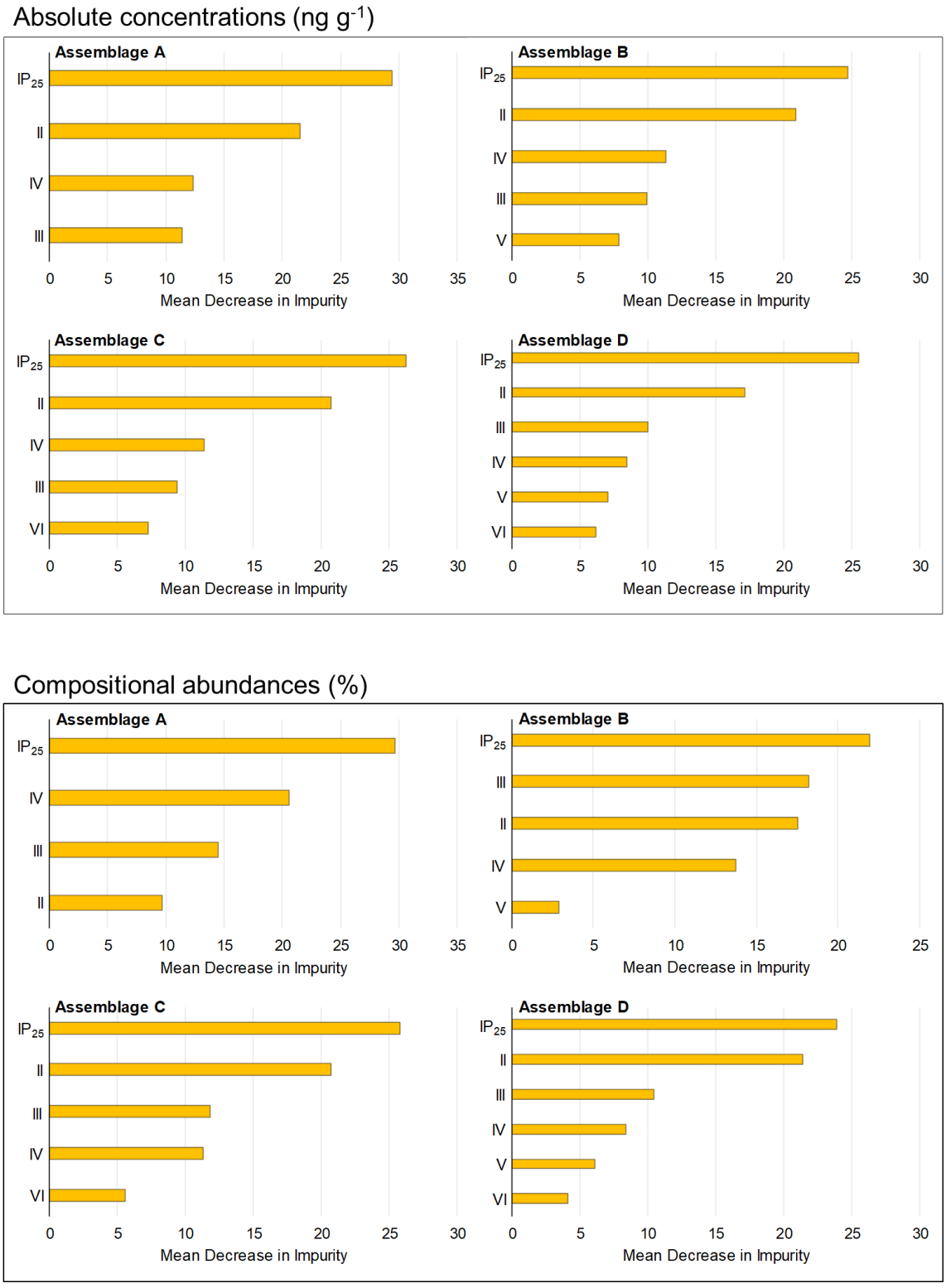

Figure 3.8: Relative HBI importance for models built using absolute concentrations (ng g^{-1}) and compositional abundances (%) within assemblages A–D using the Random Forest algorithm (n = 300 trees; Breiman, 2001).

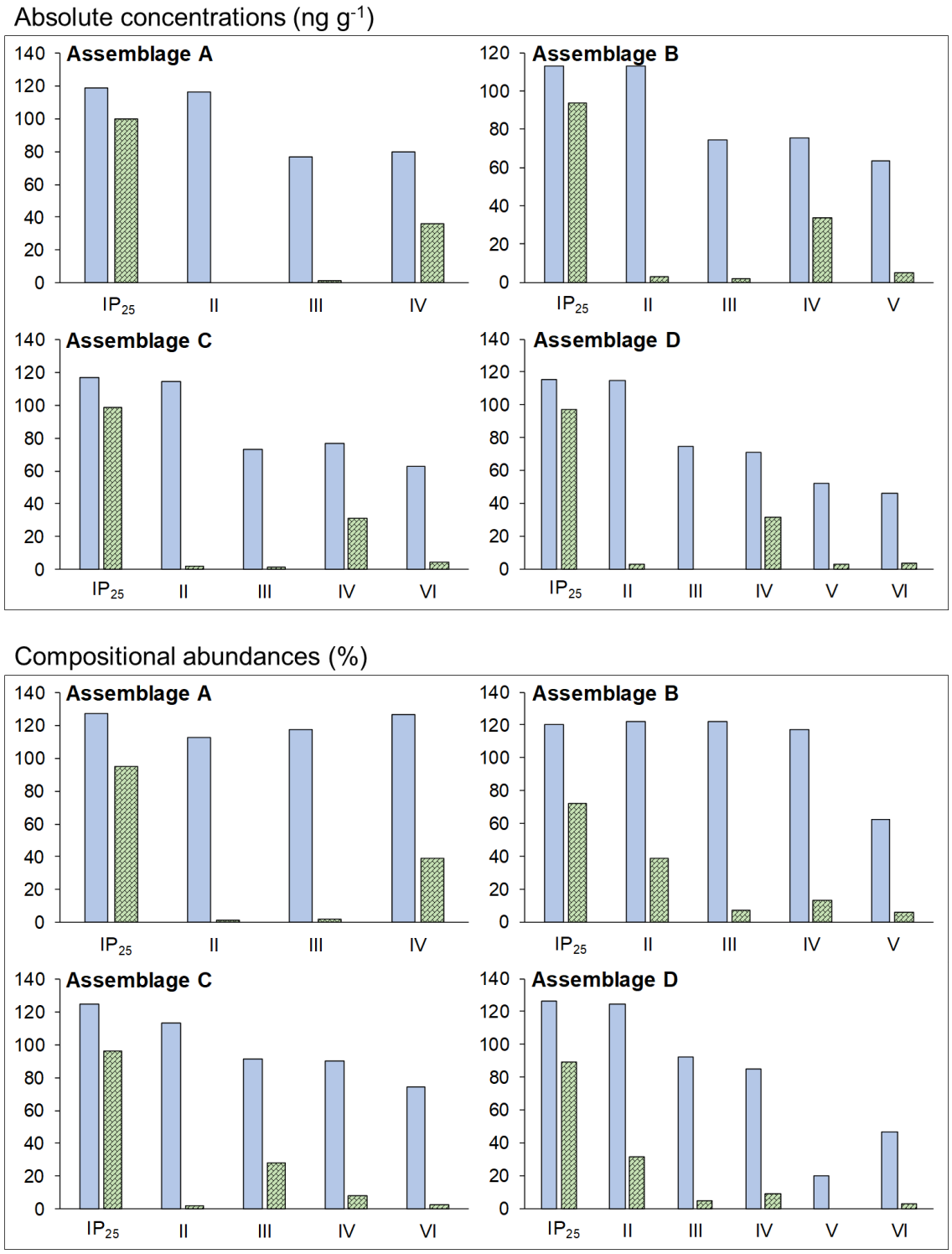

Figure 3.9: Deconstructed HBI importance for models built using absolute concentrations (ng g^{-1}) and compositional abundances (%) within assemblages A–D. Values including or excluding secondary splits (i.e. competing and surrogate variables) are shown by solid blue and shaded green bars, respectively.

Finally, performance metrics for models A–D were considerably similar, and were largely indistinguishable within the associated standard deviations after cross-validation (Table 3.1). Indeed, model A, which used HBIs I–IV only, achieved the highest overall classification rate and precision, with 13–18 samples misclassified after cross-validation (Fig. 3.4). In contrast, models B–D exhibited slightly lower classification rates, particularly for the intermediate sea ice class (10–50% satellite-based SpSIC), despite the incorporation of HBIs V and VI. This is perhaps to be expected since the coastal pelagic diatom source of VI entails elevated abundances in brackish coastal areas, such as fjords (Brown et al., 2014b), while V has previously been detected in contrasting settings of sea ice cover (Belt et al., 2007) and ice-free temperate regions (He et al., 2016), and thus may not be especially environment-specific. Overall, together with low variable importance and limited usage of V and VI within CT structures (Fig. 3.5–3.9), comparable performance metrics for assemblages A–D support the choice of model A as the least complex, yet effective model for classification of sea ice conditions in the Barents Sea. Indeed, addition of V or VI into the compositional assemblage appears to degrade performance and could exacerbate potential issues associated with multicollinearity, such as tree structure instability (Aluja-Banet and Nafria, 2003).

3.4.2 Rationalising CT model outcomes in surface sediments

The identification of IP_{25} as a primary splitting variable in all CT models to differentiate ice–covered and ice–free settings (Fig. 3.5–3.6) is consistent with its sympagic source (Belt et al., 2007; Brown et al., 2014c). Additionally, model A effectively classified locations characterised by intermediate (extensive) sea ice cover using high (low) contribution from the pelagic HBI biomarker IV (Fig. 3.10). The high importance of II and III was attributed to their use as competing or surrogate split

variables (Breiman et al., 1984) for IP_{25} and IV, and is consistent with their sympagic and pelagic sources, respectively (Tables 3.2–3.3; Brown et al., 2014c; Belt et al., 2017).

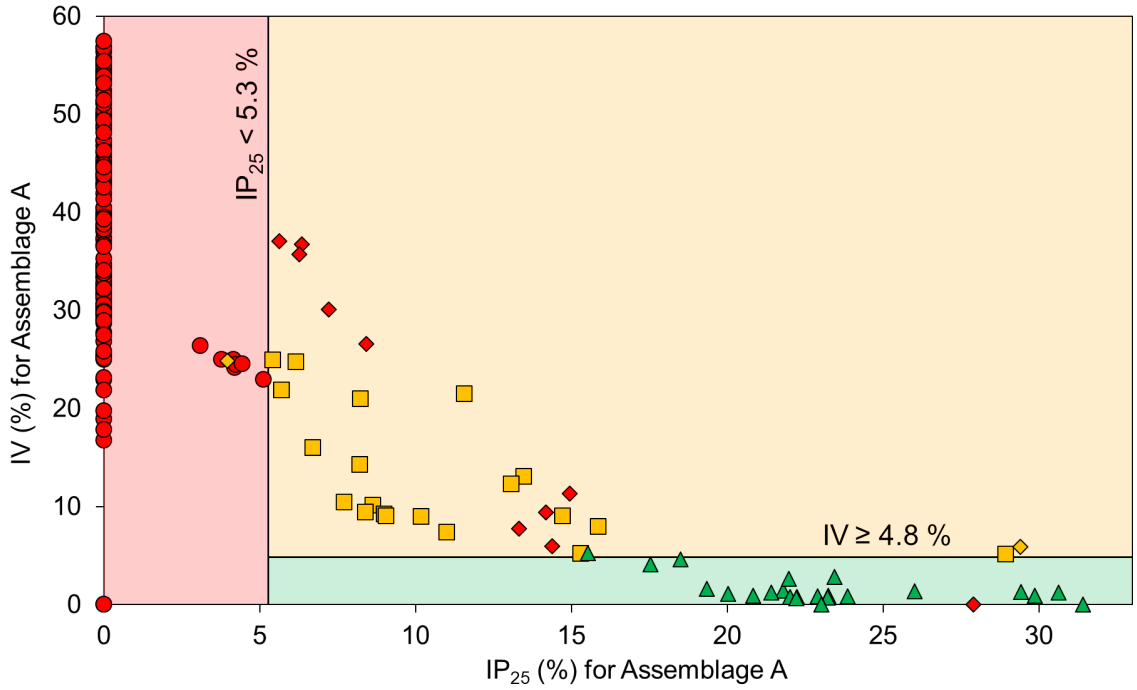

Figure 3.10: Scatter plot showing the distribution of surface sediments within the data space of CT model A. Classes of marginal, intermediate, and extensive sea ice conditions determined using satellite SpSIC data (Fig. 3.1a) are shown by red circles, yellow squares, and green triangles, respectively. The coloured regions represent areas within the data space classified by CT model A as marginal (red), intermediate (yellow), and extensive (green) sea ice conditions. The regions are separated by model-determined decision boundaries (annotated black lines), which show the chosen HBI biomarkers and corresponding relative abundance thresholds used for splitting rules. Misclassified samples (n = 12) are represented by diamond symbols and mostly correspond to sites from west Svalbard and the central Barents Sea MIZ.

More specific classification outcomes predicted by the CT models can be rationalised by considering the markedly different HBI productivity regimes across the study area and their link to the highly variable spatial distribution of seasonal sea ice (e.g. Navarro-Rodriguez et al., 2013; Belt et al., 2015). The physical properties and spatial variability of sea ice are intimately linked to light penetration and stratification of the underlying waters, which are the crucial drivers of primary productivity during the spring and summer blooms (e.g. Wassmann et al., 2006). For example, locations that

experience extensive SpSIC (>50%) in the current dataset are characterised by a bloom of sympagic algae inhabiting the underside of the ice, triggered primarily by the rapid increase of solar radiation and favourable light incidence angle in March–April (e.g. Strass and Nöthig, 1996; Signorini and McClain, 2009; Leu et al., 2011; Fig. 3.11). In the Barents Sea, such blooms are likely supported by upwelling of nutrient-rich AW, e.g. west and north of Svalbard (e.g. Ivanov et al., 2012), and are dominated by diatoms (Wassmann et al., 1999). This is consistent with high relative abundance of IP_{25} (Fig. 3.10), which accumulates mostly in March–April, with a subsequent gradual decline of ice algal production due to the progressive ice desalination over the course of the melt season, at least in the Canadian Arctic (Brown et al., 2011, 2016). Conversely, the productivity of pelagic phytoplankton remains low during this time, and instead follows the highly stratified waters within 20–50 km of the receding ice edge during the ice melt season in May–July (Fig. 3.11), starting approximately two months after the ice algal bloom (Signorini and McClain, 2009; Leu et al., 2011; Janout et al., 2016). However, although pelagic phytoplankton productivity is also possible beneath dense sea ice cover (e.g. Strass and Nöthig, 1996; Wassmann et al., 1999; Leu et al., 2011; Arrigo et al., 2012; Assmy et al., 2017) and can be initiated by light penetration through leads and polynya in the Barents Sea (Willmes and Heinemann, 2016), the highly-productive ice edge conditions do not reach north and east of Svalbard until ca. July–August (Fetterer et al., 2017). This shortens the pelagic bloom duration in these areas, prior to the October ice advance, and probably explains the low relative abundance of IV. Similarly, high model performance for the marginal sea ice class attests to the source specificity of IP_{25}, which was absent at nearly all ice-free locations, and in relatively low abundance at locations with <10% SpSIC. Such source selectivity permitted the separation of most samples belonging to the marginal class with a single CT decision rule (Fig. 3.10). The high range of HBI IV relative abundance in this area reflects the regional productivity

variability (e.g. Olsen et al., 2003; Signorini and McClain, 2009), including the well-known enhancement proximal to the stratified waters of the MIZ (Wassmann et al., 1999; Belt et al., 2015). Overall, the results for extensive and marginal SpSIC classes demonstrated the ability of CT models to effectively classify locations characterised by relatively stable interannual sea ice conditions, with clearly defined variations in ice algal and pelagic phytoplankton productivity (Falk-Petersen et al., 2000; Søreide et al., 2013; Cormier et al., 2016).

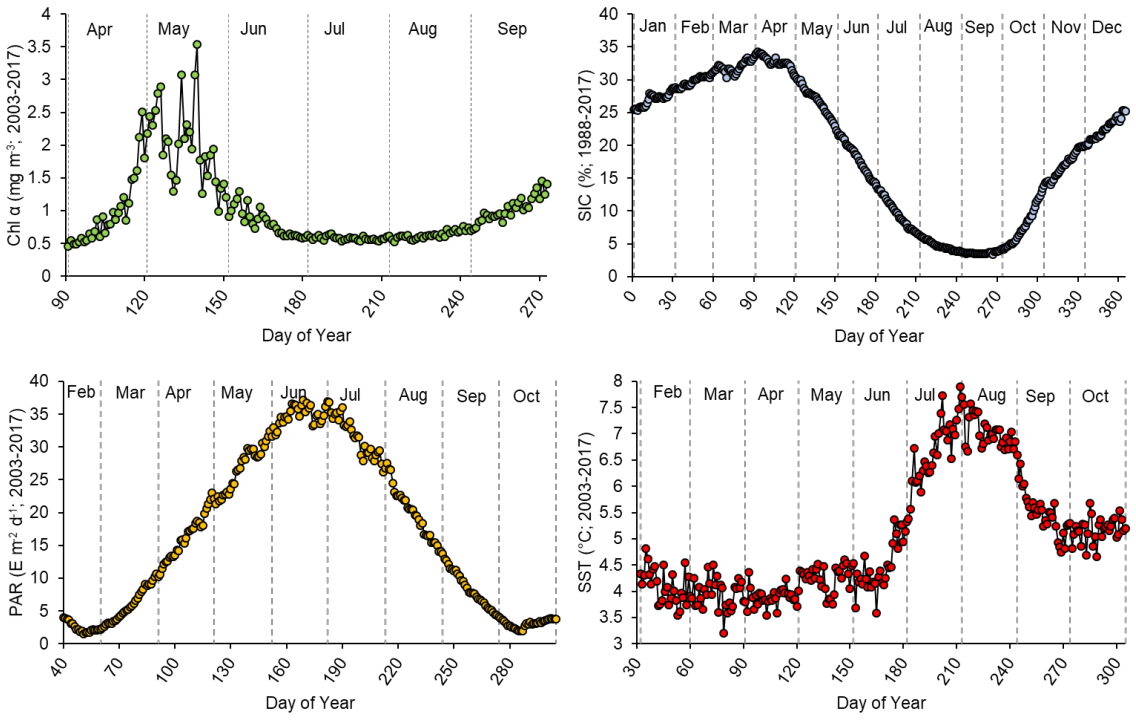

Figure 3.11: Daily-resolution annual development of Chl *a* (mg m^{-3}), SIC (%), PAR (E m^{-2} d^{-1}), and SST (°C) in the Barents Sea based on satellite data from MODIS Aqua (NASA, 2018a–d) and NSIDC (Peng et al., 2013; Meier et al., 2017).

The majority of samples belonging to the intermediate SpSIC class were also correctly classified. In such settings, HBI composition, with lower relative contribution of IP_{25} compared to the extensively sea ice-covered sites, is consistent with a short duration of the under-ice algal bloom before the onset of ice melt in May, whereupon the meltwater discharge triggers strong stratification of the upper water column and stops the vertical mixing of phytoplankton, triggering an intense pelagic bloom (Janout et al., 2016) which results in increased relative abundance of IV (and III; Belt et al.,

2015). Lower performance was observed for the MIZ west of Svalbard, however, an area at the boundary between marginal and intermediate SpSIC (Fig. 3.3–3.4 and Table 3.1). This is potentially attributable to the highly variable sea ice conditions that characterise the region. While the continental slope often remains ice-free throughout the year due to the direct inflow of warm AW with the WSC, sea ice is present on the shelf during winter due to the topographically-steered inflow of colder ArW with the ESC, resulting in a density gradient preventing significant AW intrusion to the shelf (Fig. 3.1b; Walczowski and Piechura, 2011). Similar conditions characterise Whalers Bay north of Svalbard, which is often ice-free, even in February (Ivanov et al., 2012). Such influence of contrasting water masses and sea ice regimes likely favours simultaneous production of sympagic and pelagic biomarkers by ice-algal and open-water phytoplankton communities, respectively (e.g. Søreide et al., 2013; Belt et al., 2015; Smik et al., 2016), previously suggested to manifest as a positive correlation between IP_{25} (or II) and III (e.g. Collins et al., 2013; Smik and Belt, 2017; Detlef et al., 2018). Accordingly, the current dataset shows high relative abundances of both IP_{25} and IV in western Svalbard locations which exhibit marginal satellite-based SpSIC (Fig. 3.10). Nonetheless, elevated abundance of IP_{25} may also result from allochthonous input from the Svalbard shelf (e.g. via ice rafting) to the relatively ice-free margin, especially given the considerable deposition of terrigenous organic matter west of Spitsbergen (e.g. Knies et al., 2007; Knies and Martinez, 2009). Additionally, southward transport of ca. 300 $km^3\ y^{-1}$ of drift ice from the Nansen Basin into the Barents Sea may represent a further allochthonous source of sympagic production (Kwok et al., 2005).

Some misclassification, although less prominent, was also observed in the eastern part of the study region (Fig. 3.4), potentially due to an increase in seasonal and annual sea ice variability in this area compared to the MIZ of the central Barents Sea with consequential influence on the balance between sympagic and pelagic production.

Specifically, in contrast to the western Barents Sea, which exhibits a longer, but less pronounced primary productivity season, a significant phytoplankton bloom is observed in April–May at and south of the ice margin (Fig. 3.12; Wassmann et al., 1999, 2006; Sakshaug et al., 2009; Søreide et al., 2013). Thus, the more frequent misclassification of samples located along the highly dynamic sea ice edge, more generally, is likely a result of spatial shifts in sympagic and pelagic productivity regimes, and underlines the difficulty in characterising the MIZ using geochemical biomarkers alone.

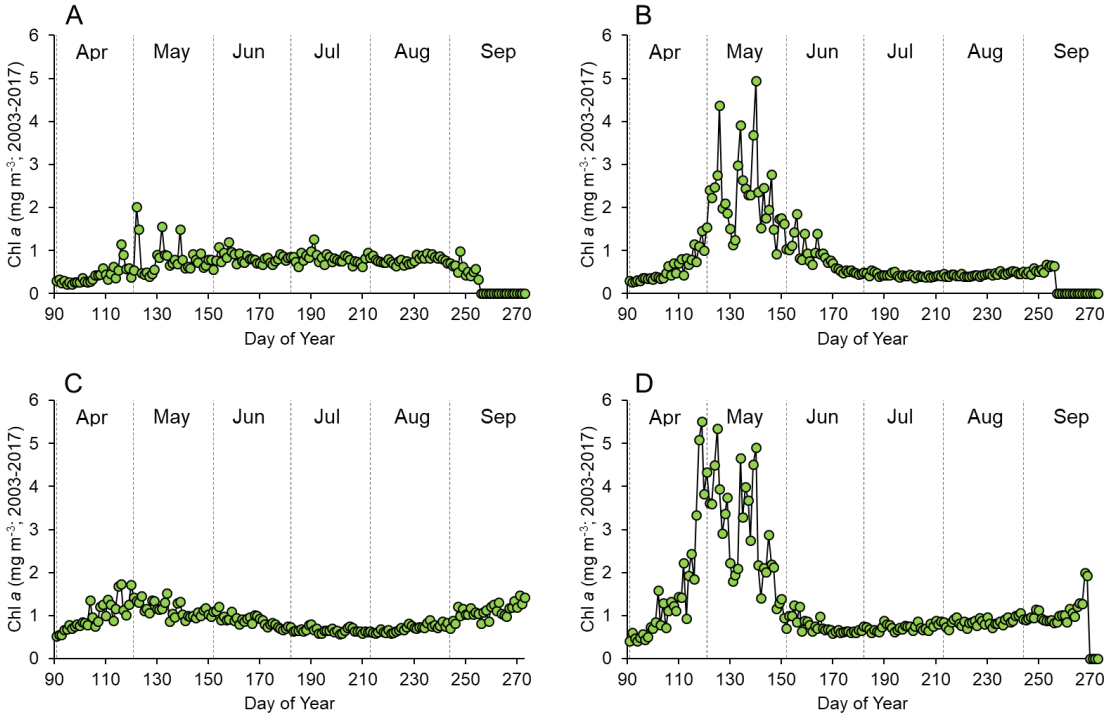

Figure 3.12: Satellite Chl *a* (2003–2017; mg m^{-3}) for the north-western (A), north-eastern (B), south-western (C), and south-eastern (D) Barents Sea.

On the other hand, the use of different coring techniques, as well as variable sediment accumulation rates and diverse depositional settings observed in the Barents Sea (e.g. Boitsov et al., 2009; Knies and Martinez, 2009; Maiti et al., 2010) potentially represent additional sources of misclassification error in CT model output. For example, several surface sediments in the current dataset were collected via gravity coring, which is a potential cause of uppermost sediment distortion (Leonard, 1990). Additionally, integrated proxy signals from surface sediments correspond to variable timescales,

which are potentially different from the 20 years covered by the database of satellite-derived SpSIC presented herein, at least in some locations. While sediment accumulation rates in the seasonal sea ice zone around Svalbard are typically 0.7±0.4 mm y^{-1} (Zaborska et al., 2008), they may reach up to 1.1±0.4 mm y^{-1} closer to the sea ice edge (Maiti et al., 2010), and are higher in fjords and areas of sediment erosion south of Spitsbergen (Boitsov et al., 2009). Thus, a sediment depth of 1.0 cm may represent ca. 5–30 years of deposition. Further, a low number of sediments in the current dataset (n = 10) were sampled at variable depths (ranging from 1–3 cm). Thus, some surface sediment data described herein may not be equally representative of the 20-year satellite SpSIC record. In practice, achieving complete temporal comparability of surface sediment signals is problematic without detailed accumulation rates for all locations. Nevertheless, the distribution of certain individual HBIs (IP_{25} and III) in Barents Sea sediments has been shown previously to be broadly consistent with modern sea ice conditions (Navarro-Rodriguez et al., 2013; Belt et al., 2015; Smik et al., 2016).

3.4.3 Downcore CT predictions and comparison to PIP_{25}-based SpSIC

The downcore records presented herein represent regions of contrasting modern sea ice conditions. Site 8 has consistently experienced extensive SpSIC (ca. 80%) for the last 300 years (at least), in stark contrast to site 1, which has been ice-free during this period (Divine and Dick, 2006; Vare et al., 2010). Site 43 is located in the south-eastern Barents Sea at the modern winter sea ice margin, while site 712, despite being located farther north, is influenced by direct northward inflow of warm AW from the WSC and therefore also experiences low SpSIC. The downcore semi-quantitative SpSIC estimates derived from $P_{III}IP_{25}$ indices (Smik et al., 2016) reflected this variability of modern sea ice conditions, with high values for core 8, similarly low values for cores 43 and 712, and ice-free conditions inferred for core 1 (Fig. 3.13a).

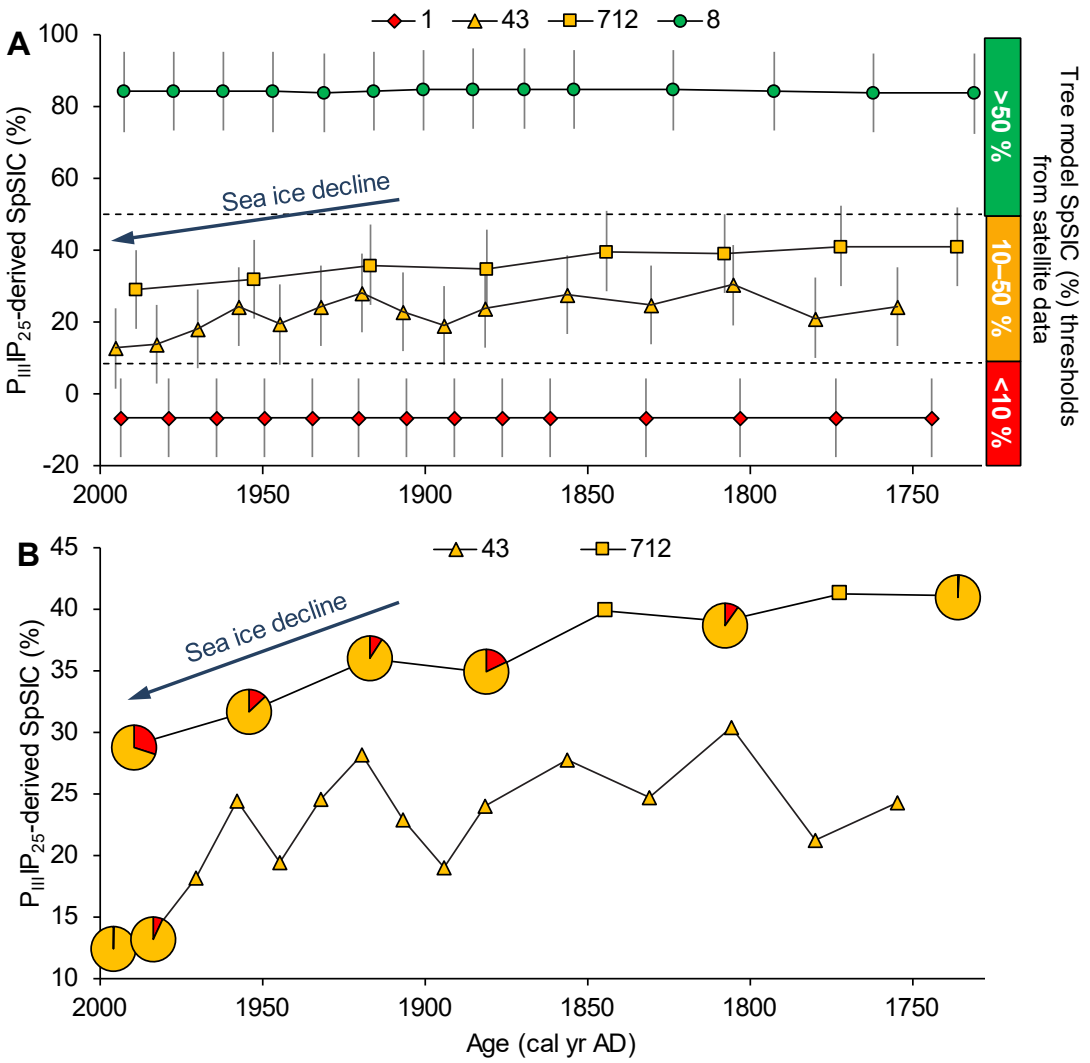

Figure 3.13: (A) Comparison of $P_{III}IP_{25}$- and CT-based sea ice conditions from four dated short cores (cores 1, 8, 43 and 712) from the study region representing contrasting modern-day sea ice cover (Fig. 3.1b). The magnitude of each data point (left-hand axis) corresponds to the $P_{III}IP_{25}$-derived SpSIC and associated standard error estimates based on the regional calibration of Smik et al. (2016). The colours of each data point indicate the CT model A predictions of marginal (red), intermediate (yellow) and green (extensive) sea ice conditions (Fig. 3.1a); (B) A magnification of plot A, where pie charts show the estimated probability of classification (Quinlan, 1993) into the marginal and intermediate sea ice class for samples where percentage abundances of IP_{25} and IV were within the SD boundaries of CT model A (Fig. 3.6a).

The decline in $P_{III}IP_{25}$-derived SpSIC estimates seen for cores 43 and 712 from ca. 1900 yr AD and 1850 yr AD, respectively (Vare et al., 2010; Cabedo-Sanz and Belt, 2016) is consistent with observational sea ice records for the region (Divine and Dick, 2006; Walsh et al., 2017), and previous investigations (Cabedo-Sanz and Belt, 2016; Matul et al., 2018). An overall agreement with the marginal, intermediate and extensive sea ice class predictions obtained using CT model A was also observed. However, due

to the broader scale of sea ice classifications, the CT did not capture the gradual decline of sea ice cover observed in the $P_{III}IP_{25}$-derived SpSIC record of cores 43 and 712 (Fig. 3.13). Despite this, the sea ice classes inferred for downcore records are entirely consistent with both the overlying sea ice conditions and the classification of surface sediments (Fig. 3.4) representing extensive sea ice conditions near east and north Svalbard, the highly-variable intermediate sea ice cover of the MIZ in the central Barents Sea, and largely ice-free conditions south of ca. 75°N. Further, for core 712 (western Svalbard), relative abundances of both IP_{25} and IV were often within the standard deviations of model A splitting rule thresholds (Fig. 3.6a), and increasing probabilities of classifying horizons into the marginal sea ice class mirrored the sea ice decline since ca. 1900 AD (Fig. 3.13b). Nonetheless, both $P_{III}IP_{25}$- and CT-based methods somewhat overestimated the sea ice cover near site 712. Specifically, semi-quantitative SpSIC estimates for site 712 were higher relative to site 43, which experiences similarly low modern SpSIC (ca. 5%), while model A misclassified the majority of surface sediments in close proximity to site 712 from marginal to the intermediate sea ice class (Fig. 3.4), probably due to the highly variable sea ice dynamics that characterise the west Svalbard margin, as outlined earlier. Indeed, IP_{25} and III (used to calculate $P_{III}IP_{25}$) in surface sediments from western Svalbard do not exhibit the same opposing distribution that is observed for the central Barents Sea and eastern Svalbard (Belt et al., 2015; Smik and Belt, 2017), likely as a result of a contrast in seasonal sea ice dynamics and prolonged annual pelagic production (Cabedo-Sanz and Belt, 2016). The latter is further supported by depleted ^{13}C isotopic composition of surface sediments reported for north-western Svalbard relative to that of northern and eastern sites influenced by ArW (Søreide et al., 2013). Thus, the $P_{III}IP_{25}$- and CT-based methods may be more suitable for regions (or downcore temporal windows) where sea ice conditions are better defined or, at least, more consistent in terms of seasonal or

annual advance/retreat cycles, including areas of relatively stable winter maximum sea ice extent and Polar Front (PF) position in the central Barents Sea (Loeng and Drinkwater, 2007). Such consistency likely results in biomarker distributions that best reflect their production by sympagic and pelagic diatoms – information that may be lost when sea ice conditions exhibit greater short-term variability (Smik and Belt, 2017).

3.4.4 General comparison between CT and PIP_{25} methods

The suitability of CT models as a complementary approach to PIP_{25}-based methods for palaeo-reconstruction of sea ice conditions is summarised in terms of perceived advantages and potential limitations of both methods (Table 3.4).

Table 3.4: Summary of advantages and limitations of PIP_{25}- and CT-based methods for estimating spring sea ice conditions.

Method	Advantages	Limitations	Selected references
PIP_{25}	Intuitive scale (0–1), transferable between study sites; Provides semi-quantitative sea ice concentration estimates, including SpSIC (%) in some cases; Potentially able to capture subtle changes in sea ice conditions; Requires quantification of two variables only.	Calculation and interpretation can be problematic when IP_{25}=0 or both biomarkers are absent; Univariate measure affected by regional and downcore variability of the *c*-factor; Objective selection of an appropriate pelagic biomarker can be challenging.	Belt and Müller, 2013 Belt et al., 2015 Müller et al., 2011 Smik et al., 2016
CT	Multivariate method that is not affected by *c*-factor variability; Automatic selection of the most appropriate variables for classification; Model performance on future samples can be quantitatively estimated.	Provides discrete qualitative SpSIC class predictions only; Requires quantification of multiple variables within large datasets; Model structure can be affected by small changes in the training data.	Breiman et al., 1984, 2001 Quinlan, 1986, 1993

The principal advantage of the PIP_{25} approach is the ability, in some cases, to provide quantitative SpSIC information and hence identify relatively subtle trends in temporal data as shown here, especially for cores 43 and 712 (Fig. 3.13). However, as a univariate measure, PIP_{25} is dependent on the *c*-factor, whose magnitude is sensitive to both the chosen pelagic biomarker and its concentration range, which itself varies between regions and temporal windows within downcore records (e.g. Müller et al., 2011; Belt and Müller, 2013; Belt et al., 2015; Cabedo-Sanz and Belt, 2016). While the latter limitation has been circumvented to some extent in the Barents Sea by using a regional *c*-factor obtained from a calibration based on surface sediments (Smik et al., 2016), objective choice of an appropriate pelagic biomarker in other Arctic regions potentially remains a challenge. Additionally, the value of the *c*-factor obtained previously for the Barents Sea (Smik et al., 2016) is unlikely to extend to other Arctic regions, especially given the large circum-Arctic variability of HBI concentration ranges in regions of similar sea ice concentration (e.g. Stoynova et al., 2013; Xiao et al., 2015a, b). Further regional calibrations, potentially based on IP_{25} and III, are needed before this aspect can be fully resolved.

In contrast, classification trees, while only able to provide discrete categorical output, automatically select descriptive variables most relevant to the classification based on class separation via splitting rules, and do not use redundant variables. Further, tree models are not dependent on the *c*-factor due to their multivariate nature, and provide performance metrics that may be used to assign a confidence level to classification (Hastie et al., 2009). Consequently, classification trees can potentially provide results that are more compatible when making comparisons between downcore records located within the geographical region of a model training dataset, and offer intuitive visualisation of trends (Fig. 3.5–3.6) even when used with highly multivariate datasets containing statistical outliers or redundant variables (Breiman et al., 1984). In

addition, classes of sea ice conditions may be assigned to new samples, such as those from downcore records (Fig. 3.13), with a degree of mathematical certainty derived from model evaluation (Table 3.1 and Fig. 3.3–3.4). In contrast, the univariate PIP_{25} approach does not allow for iterative analysis of multiple variables while preserving the possibility for intuitive visualisation, and lacks a quantitative assessment framework. Variables most significant for CT model-derived classification are also more likely to hold geochemical significance. Thus, CT model-based selection of percentage compositions of IP_{25} and triene IV as primary classifiers, as well as diene II and triene III as surrogate classifiers of sea ice cover was concordant with their different (i.e. sympagic and pelagic) diatom sources (Belt et al., 2000, 2017; Rowland et al., 2001; Brown et al., 2014c) and, in turn, their contrasting distributions in Barents Sea surface sediments and some downcore records (Belt et al., 2015; Berben et al., 2017). Further, the choice of triene IV as a classifier variable was consistent with the use of triene III as the phytoplankton biomarker for calculation of the $P_{III}IP_{25}$ index (Belt et al., 2015; Smik, 2016), given the co-production and strong positive correlation of trienes III and IV in the Barents Sea (Belt et al., 2000; Rowland et al., 2001; Navarro-Rodriguez, 2014), as well as the high importance of III observed for CT models (Fig. 3.7–3.8). Finally, the insensitivity of CT models to the *c*-factor or any other monotonic data transformation (Breiman et al., 1984) avoids the potentially considerable influence of the *c*-factor on PIP_{25}-derived SpSIC estimates (e.g. Cabedo-Sanz and Belt, 2016), caused by the sensitivity of the former to variations of relative biomarker concentrations within temporal windows of downcore records (Belt and Müller, 2013; Belt, 2018).

It is important to also note the limitations of classification trees, some of which may be amplified by the data structure used in the current study. The conversion of absolute HBI concentrations to percentage contributions was used to confine the data to a uniform scale and make classification of temporal data possible, since the data ranges

of absolute HBI concentrations in downcore records are often not represented in modern settings and exhibit strong regional dependence (Belt and Müller, 2013; Stoynova et al., 2013; Xiao et al., 2015a). The resulting multicollinearity of HBI abundances associated with compositional data may make CTs unstable, such that a small change in the training data could result in a different tree structure (e.g. Aluja-Banet and Nafria, 2003). Such influence of the training set on tree structure also implies that, like with PIP_{25}, separate models should be constructed for new study regions on a case-by-case basis, especially given the likely variability of circum-Arctic HBI concentrations, as demonstrated previously for IP_{25} (e.g. Stoynova et al., 2013; Xiao et al., 2015a). Additionally, the use of compositional input variables negates the ability of classification trees to handle missing data, because absence of any one variable can profoundly influence the distribution of all remaining variables, some of which would be used for surrogate splitting rules (Breiman et al., 1984). It is recommended, therefore, that sea ice class predictions only be carried out for samples where holistic data for IP_{25}, II, III and IV are available. The potentially lowered stability of CT models when using multicollinear compositional data (Aitchison, 1986; Aluja-Banet and Nafria, 2003) also highlights the importance of excluding variables which are irrelevant to the classification task, despite the capacity of classification trees for automatic variable selection (Breiman et al., 1984). In the current context, this was achieved by using different combinations of biomarkers with known sympagic or pelagic diatom sources (Fig. 1.8 and Eq. 3.2–3.5) as classifiers of ice cover (with exclusion of biomarkers of lower source specificity, including sterols) and selecting the simplest combination of HBIs (Fig. 3.6a, Eq. 3.2) that removed redundant variables (V and VI; Fig. 3.7–3.8) without compromising classification performance (Table 3.1 and Fig 3.5). Finally, compositional data only provide information about the relative distribution of components, without any regard for absolute values (Aitchison, 1986). Analogously,

coeval variation in IP_{25} and III may provide extremely similar SpSIC estimates irrespective of absolute concentrations with the $P_{III}IP_{25}$ approach (Müller et al., 2011, 2012; Belt and Müller, 2013). Construction of models from training sets spanning different Arctic regions, and comparison to PIP_{25} and other proxy methods within further downcore records is required to assess the potential of CT models further.

3.4.5 The HBI triene ratio as a spring bloom indicator

3.4.5.1 Triene ratio comparisons with surface oceanography and productivity

The identification of triene diastereoisomers IV and III as important and largely interchangeable variables within the CT models (Fig. 3.7–3.8 and Tables 3.2–3.3) motivated an investigation into the relationship between the two HBIs in order to identify potential links with contemporary climate in the Barents Sea. This was incentivised further by the previously suggested function of III as a pelagic productivity indicator due to its enhancement near the Barents Sea MIZ (Belt et al., 2015) and identification (alongside IV) in the diatom *Rhizosolenia setigera* (Belt et al., 2017). Spatially-represented abundance of IV relative to both isomers (Eq. 3.6), termed the HBI triene ratio herein, was previously suggested to be broadly consistent with AW and ArW in the region (Navarro-Rodriguez, 2014). The defining characteristics of both water masses include temperature and salinity (e.g. Loeng, 1991, 1997; Sakshaug et al., 2009). However, no association was observed between either the spring-summer satellite SST, PAR (2003–2017) or SSS (1955–2012) record and the HBI triene ratio in surface sediments presented herein (Fig. 3.15g–i, 3.17), which suggests the influence of these is either absent or obscured by competing effects. In contrast, Chl *a* data as an indicator of standing phytoplankton stocks showed a strong correlation with the ratio (Fig. 3.15d–e, 3.16a–d), but only during the spring bloom (April–May; Fig. 3.12, 3.14). This was further supported by similar clustering of the HBI triene ratio and April–May

Chl *a*. Interestingly, the most consistent clusters were obtained with April–May and May (i.e. annual maximum) Chl *a* (Fig. 3.16b–c, 3.18b–c). This is likely due to the highly dynamic nature of phytoplankton bloom development in the central Barents Sea. In April, only the ice-free south-eastern Barents Sea shows significant increases in Chl *a* (Fig. 3.16a), which propagate north-eastwards by early May with the retreating sea ice edge (Fig. 3.16b). Phytoplankton biomass sharply declines by June (Fig. 3.12) due to nutrient (e.g. nitrate and silica) depletion and limited replenishment through the meltwater-established pycnocline in the MIZ (e.g. Signorini and McClain, 2009; Leu et al., 2011), with subsequent summer blooms dominated by coccolithophores (Hopkins et al., 2015) and foraminifera (Skirbekk et al., 2016). Thus, while some consistency between July–September PIC and the HBI triene ratio was evident in this study (Fig. 3.14, 3.16f), this is attributable to the more temperature- and stratification-constrained blooms of calcareous species (Signorini and McClain, 2009), which occur only in the warmer, thermocline-dominated areas south of the PF, are completely temporally decoupled from the earlier diatom bloom in the Barents Sea (Hopkins et al., 2015), and are hence highly unlikely to influence HBI production by diatoms. Therefore, the HBI triene ratio appears to be more representative of the overall, or maximum, spatial and temporal coverage of the pelagic spring bloom throughout April–May. More specifically, III is prevalent (ca. >70%) in the eastern/central Barents Sea characterised by Chl *a* in excess of 2 mg m^{-3}, while the western Barents Sea, where concentrations remain between 0.5–2 mg m^{-3} and bloom seasonality is not as pronounced (Fig. 3.12), is characterised by relatively increased IV (ca. 55–60%). Similarly, low HBI triene ratio values are also evident in extensively ice-covered areas north and east of Svalbard, where the productive season is time- and nutrient-limited due to the late seasonal sea ice retreat throughout July–August (Signorini and McClain, 2009; Becagli et al., 2016).

This further supports the tentative conclusion that the HBI triene ratio is predominantly influenced by spring bloom development in the Barents Sea.

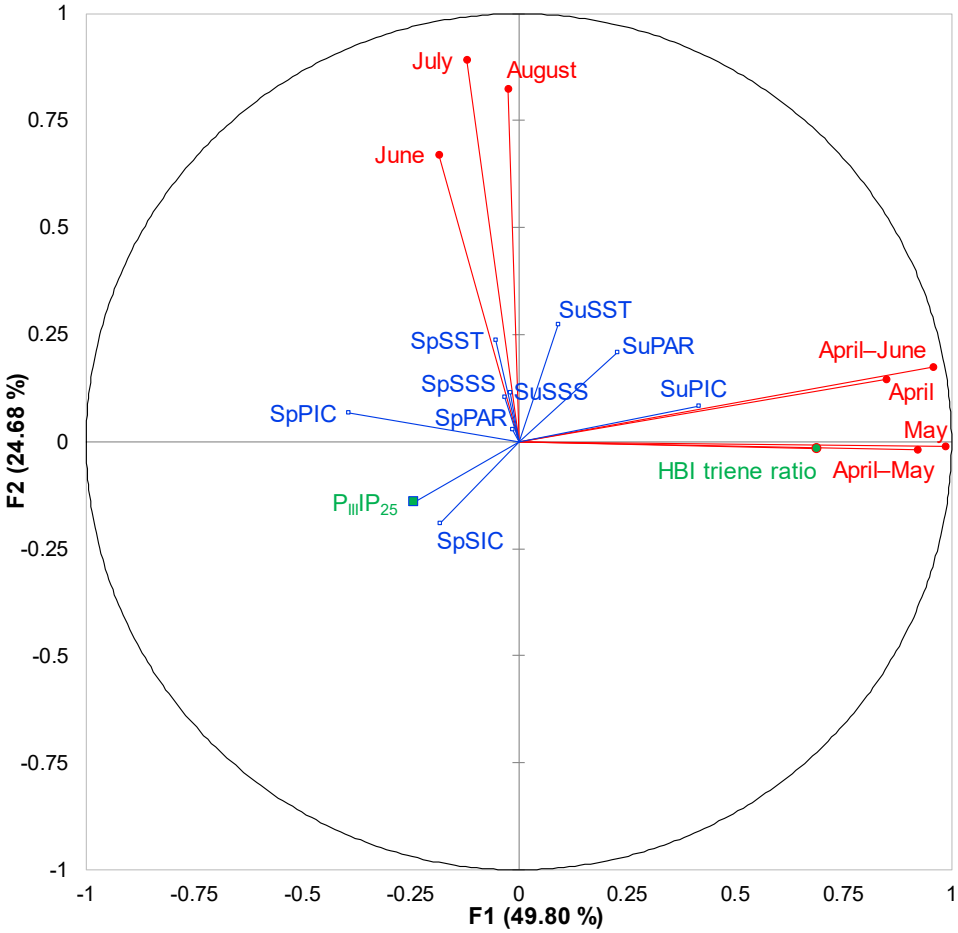

Figure 3.14: Scaled factor loadings of various primary (red lines) and secondary (blue lines) variables with the HBI triene ratio III/(III+IV) at surface sediment locations. Red labels denote months of averaged (2003–2017) satellite-derived Chl *a* (mg m^{-3}). Blue labels represent average (2003–2017) sea surface temperature (SST; °C), photo-available radiation (PAR; E m^{-2} d^{-1}), particulate inorganic carbon (PIC; mol m^{-3}), 1955–2012 sea surface salinity (SSS; psu), as well as 1988–2017 sea ice concentration (SIC; %); prefixes "Su" and "Sp" denote summer (July–September) and spring (April–June). $P_{III}IP_{25}$ index and the HBI triene ratio are shown in green.

There is an interesting discrepancy between the HBI triene ratio being seemingly indicative of the spatially expansive spring bloom, while absolute concentrations of III and IV show a significant enhancement only within the MIZ (Fig. 3.15a–e) (Belt et al., 2015; Smik, 2016). This is potentially attributable to the increasing prevalence of diatoms (as principal HBI sources) relative to other microalgae closer to the well-stratified waters near the ice edge (e.g. Syvertsen, 1991; Wassmann et al., 1999; Ratkova and Wassmann, 2005; Sakshaug et al., 2009). In contrast, the HBI triene ratio

is potentially driven by the spring bloom duration (rather than productivity) and the characteristic diatom assemblage (rather than abundance).

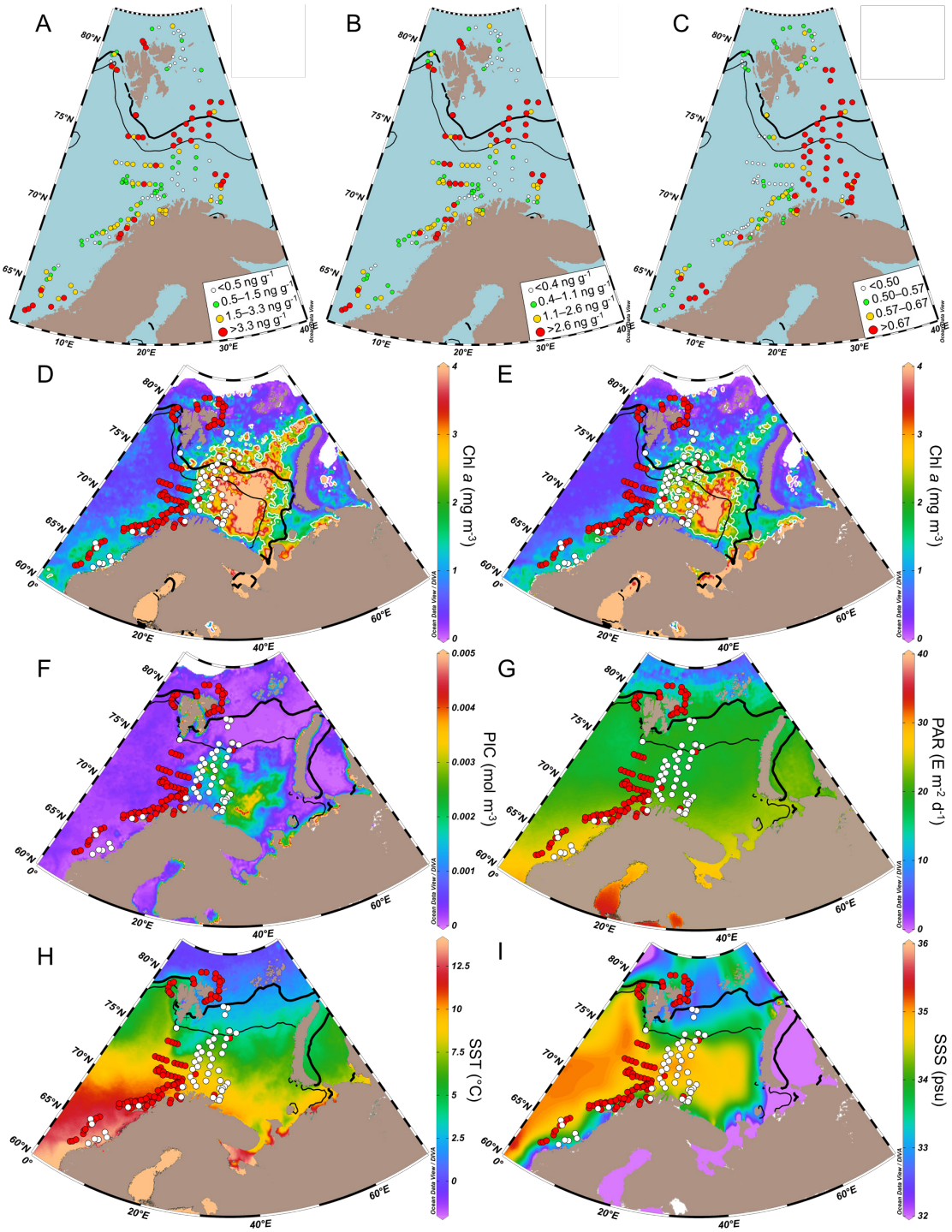

Figure 3.15: Quartile distributions of: (A) III; (B) IV; (C) HBI triene ratio. (D)–(I) show complete linkage AHC of the HBI triene ratio, where red and white circles represent two clusters, overlaid onto averaged (2003–2017) satellite data for: (D) May Chl *a*; (E) April–May Chl *a*; (F) July–September PIC; (G) July–September PAR; (H) July–September SST; (I) shows mean July–September SSS for 1955–2012. The thin (thicker) black lines represent the 0% (15%) contours of average SIC spanning 1988–2017 in all maps; 2 mg m^{-3} contours for Chl *a* are shown as solid white lines in (D), (E).

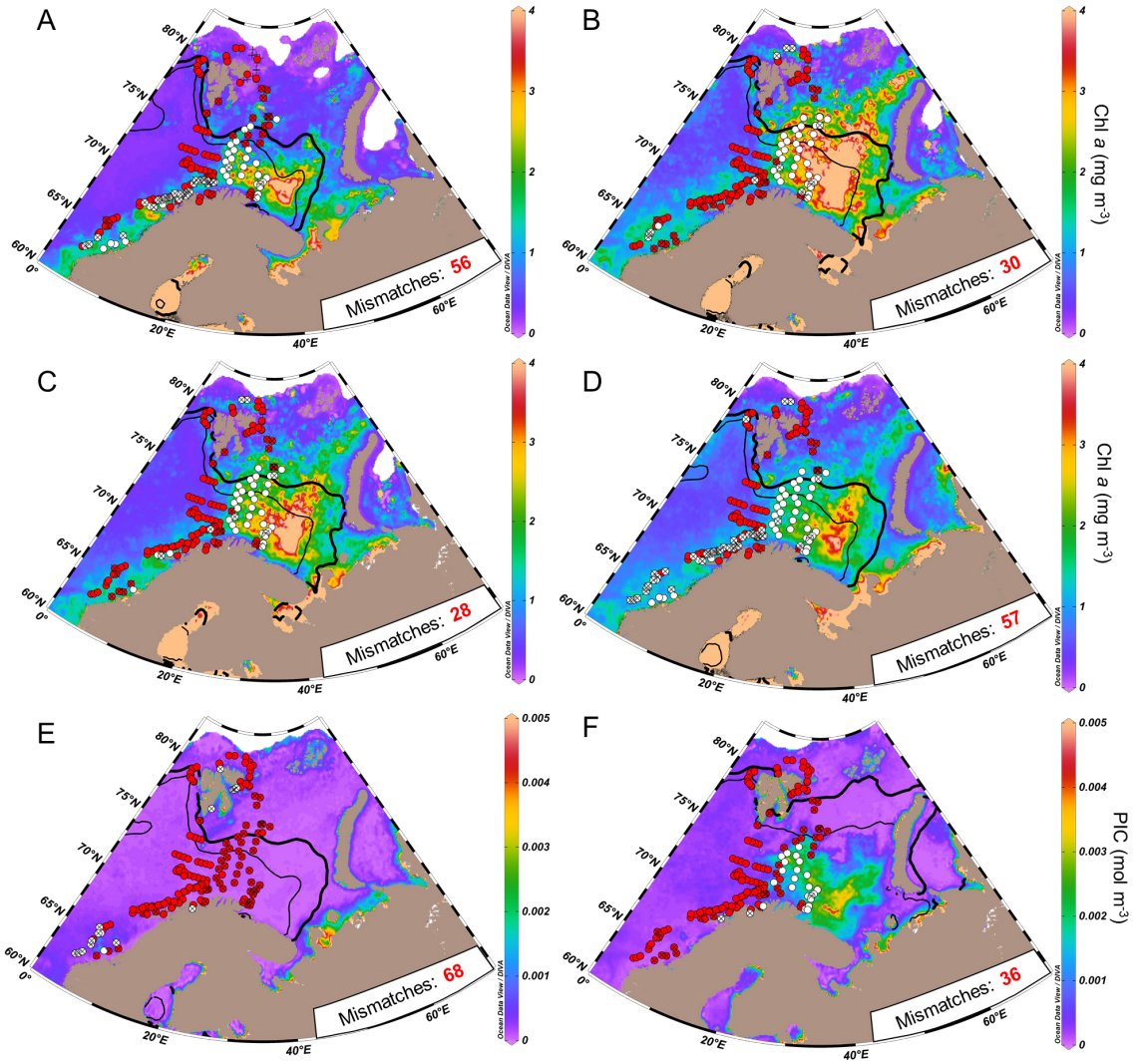

Figure 3.16: Temporally averaged (2003–2017) satellite-derived parameters and associated results of complete linkage AHC clustering at surface sediment locations for: (A) April Chl *a*; (B) May Chl *a*; (C) April–May Chl *a*; (D) April–June Chl *a*; (E) April–June PIC; (F) July–September PIC. Crossed-out sample locations represent AHC cluster memberships mismatching those of the HBI triene ratio III/(III+IV) in Fig. 3.15. The total number of such mismatches is shown in red at the bottom-right corner of each map. The thin (thicker) black lines represent the 0% (15%) contours of average SIC spanning 1988–2017 in all maps.

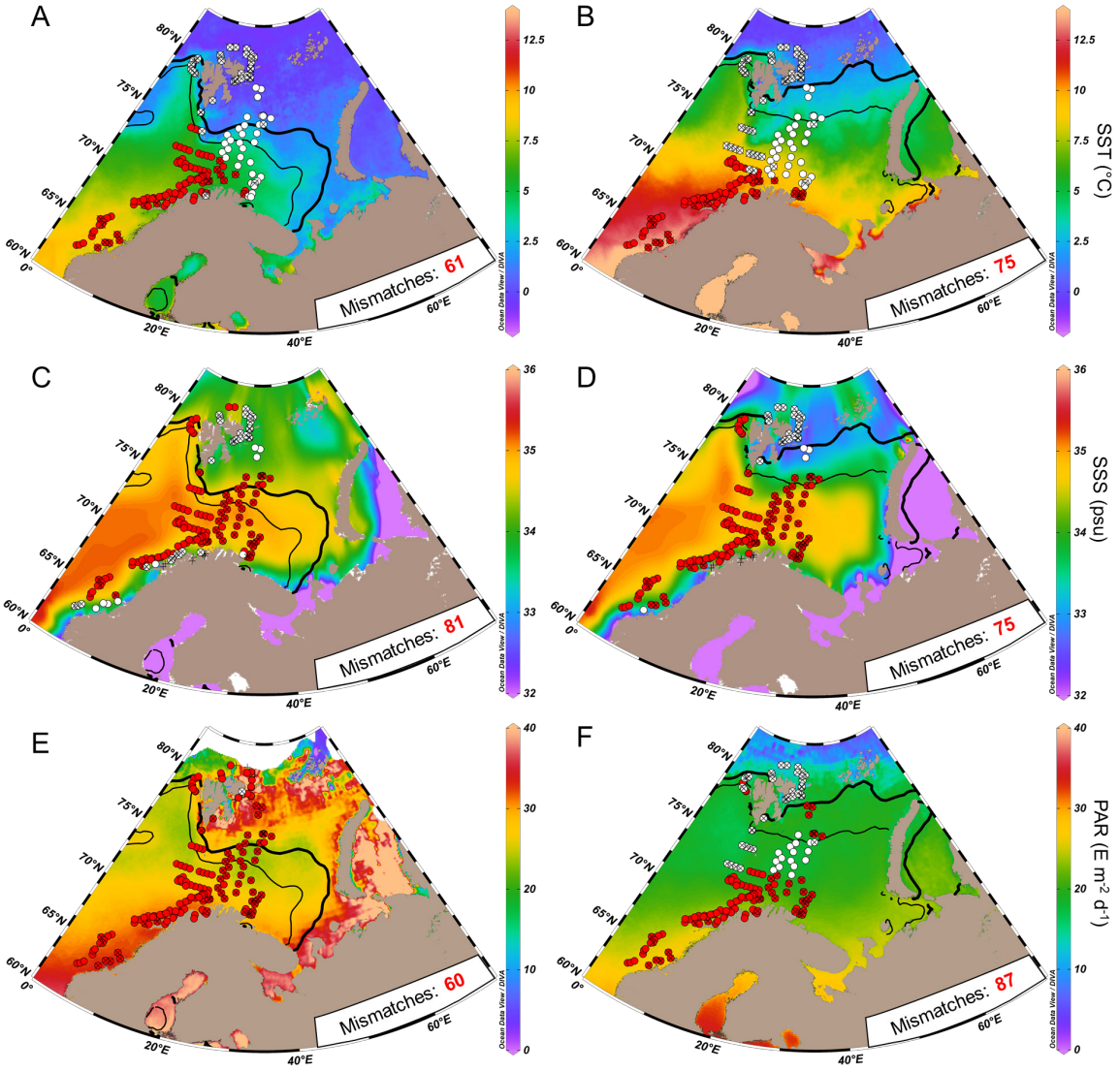

Figure 3.17: Temporally averaged satellite-derived parameters and associated results of complete linkage AHC clustering at surface sediment locations for: (A) April–June SST; (B) July–September SST; (C) April–June SSS; (D) July–September SSS; (E) April–June PAR; (F) July–September PAR. Crossed-out sample locations represent AHC cluster memberships mismatching those of the HBI triene ratio III/(III+IV) in Fig. 3.15. The total number of such mismatches is shown in red at the bottom-right corner of each map. The thin (thicker) black lines represent the 0% (15%) contours of average SIC spanning 1988–2017 in all maps.

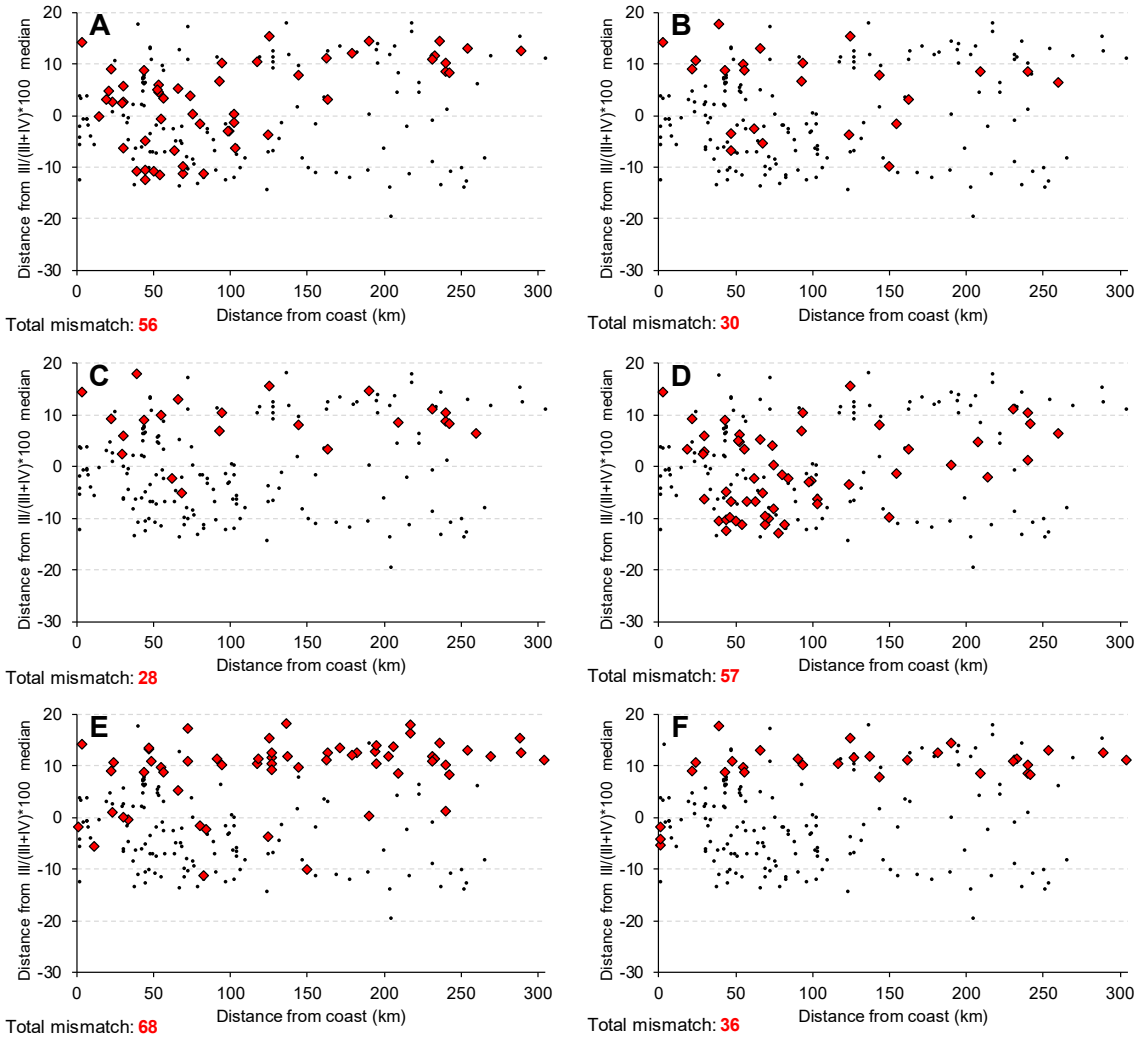

Figure 3.18: Distance (km) of surface sediment locations from the nearest coastline, highlighting matched (black dots) and mismatched (red diamond markers) AHC cluster memberships between the III/(III+IV) triene ratio and: (A) April Chl *a*; (B) May Chl *a*; (C) April–May Chl *a*; (D) April–June Chl *a*; (E) April–June PIC; (F) July–September PIC. The total number of cluster mismatches (Fig. 3.16, 3.17) is shown in the bottom left corner of each plot. Proximity of each triene ratio value to the dataset median (*ca.* 0.57 or 57%) is shown on the ordinate axis.

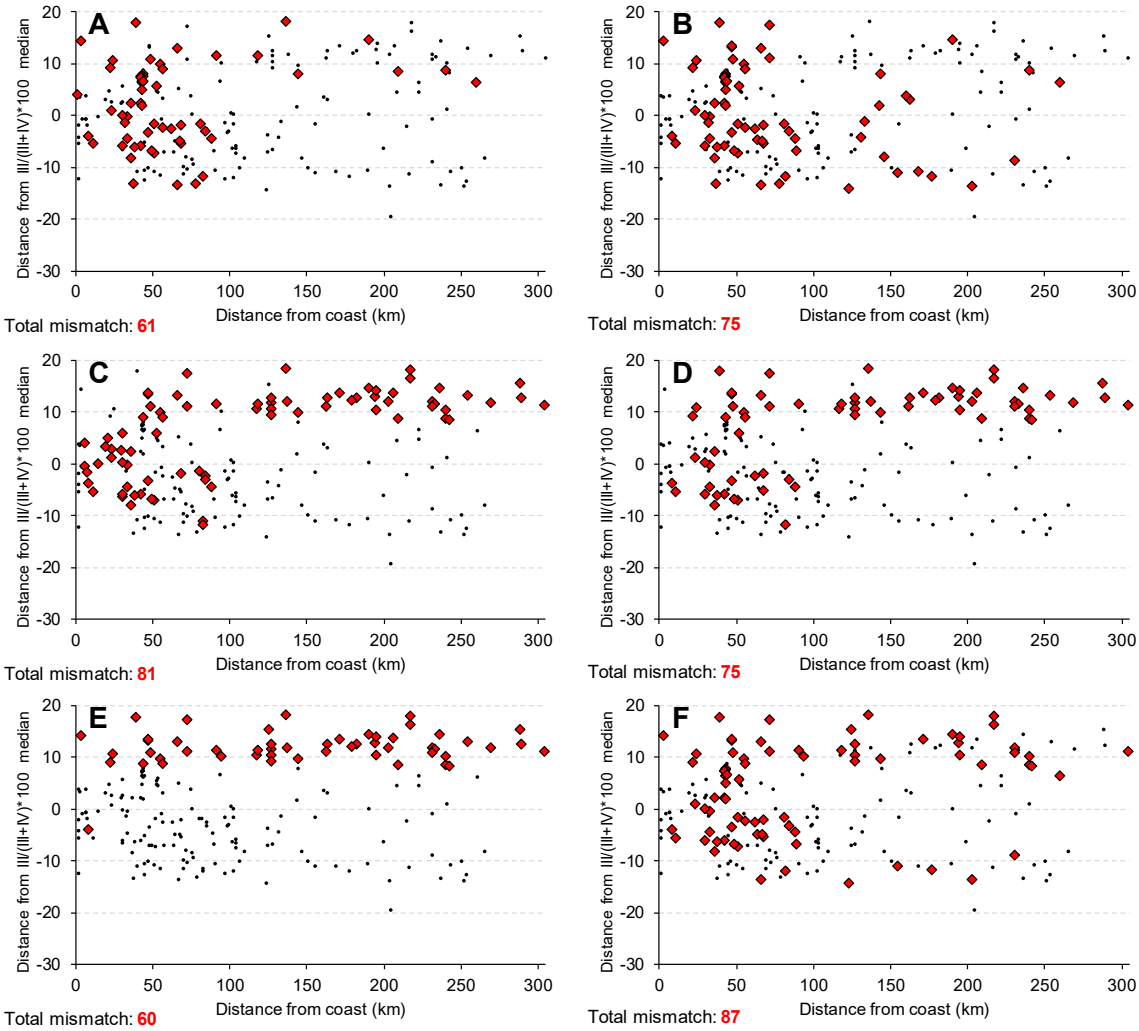

Figure 3.19: Distance (km) of surface sediment locations from the nearest coastline, highlighting matched (black dots) and mismatched (red diamond markers) AHC cluster memberships between the HBI triene ratio and: (A) April–June SST; (B) July–September SST; (C) April–June SSS; (D) July–September SSS; (E) April–June PAR; (F) July–September PAR. The total number of cluster mismatches (Fig. 3.16, 3.17) is shown in the bottom left corner of each plot. Proximity of each triene ratio value to the dataset median (*ca.* 0.57 or 57%) is shown on the ordinate axis.

Despite the findings of cluster analysis, specific reasons for similar distributions of the HBI triene ratio and Chl *a* are unclear at this point. Species characteristic of colder, nutrient-replete waters in the Barents Sea, such as *Thalassiosira* or *Fragilariopsis* spp. (von Quillfeldt, 2000), could preferentially produce III over IV. Conversely, selective removal of IV in areas of high Chl *a* (e.g. due to increased grazing; Kvile et al., 2016) cannot be discounted, although previous food web studies showed no significant change to HBI composition after consumption (Brown and Belt, 2017; Schmidt et al., 2018), even by higher trophic levels (Brown et al., 2014a).

Notably, a considerable number of mismatches in AHC cluster memberships of Chl *a* and the HBI triene ratio occurred along the south-western Barents and Norwegian Sea coastlines, in samples no further than ca. 50–100 km from the nearest coastline (Fig. 3.16 and 3.18). These locations also generally exhibited uncharacteristically high HBI triene ratio values, which could be a consequence of local effects associated with coastal water masses flowing inshore of the NAC. One suggestion would be the presence of a significantly different diatom assemblage within the NCC relative to locations further offshore. For example, the pelagic diatom *Rhizosolenia setigera*, which co-synthesizes III and IV (Rowland et al., 2001), mainly produces the former at the western Svalbard shelf in July (Belt et al., 2017), and has the potential to overtake other species under strong upwelling and nutrient-replete conditions (e.g. Yoder et al., 1994). Moreover, the NCC flowing inshore of the NAC (Fig. 3.1b) carries brackish coastal waters from the Baltic Sea, where increasing dominance of *Rhizosolenia setigera* and other cold-water species during spring and early summer blooms has been reported in recent years (e.g. Wasmund et al., 2008). It is therefore possible that Baltic Sea diatom assemblages are affecting HBI triene ratios along the Norwegian coast in favour of III; lateral transport of coastal water could further propagate this influence off-shore (Sætre et al., 1988). More generally, average Baltic Sea productivity is higher (per unit area) and peaks approximately simultaneously with that of the Barents Sea (e.g. Purina et al., 2018), although bloom productivity may be overestimated by remote Chl *a* sensing (Lyngsgaard et al., 2017). Increased amounts of III relative to IV characteristic of such productivity could also be advected with the NCC. However, such inferences remain speculative and highlight the need for identification of further diatom sources for III and IV, as well as time-series monitoring of their production in areas of well-defined primary productivity. In any case, the initial identification of a potential link between

the HBI triene ratio and primary productivity supports pelagic diatom source-specificity of III and IV and is a viable avenue for future research.

3.5.5.2 Spring bloom occurrence and intensity in downcore records

In agreement with contemporary trends derived from cluster analysis of surface sediments, HBI triene ratio trends in downcore records were generally consistent with the occurrence of phytoplankton-driven and sea ice-influenced spring blooms in the Barents Sea (Fig. 3.20). Thus, cores 712 and 8, characterised by lower Chl *a*, exhibited consistently lower triene ratio values relative to cores 1 and 43, which are located within the spring bloom boundaries (Fig. 3.21). There are more specific differences that can be distinguished for core 712, in particular. The core is located at the largely ice-free western Svalbard margin (Walczowski and Piechura, 2011) and influenced by the strongest inflow of AW with the NAC (Fig. 3.1b, 3.21). The ice edge duration at site 712 is limited, and stratification necessary for rapid spring bloom development is weaker due to continuous AW overturning (Loeng et al., 1997; Smedsrud et al., 2013). However, instrumental records show that ice cover at the Svalbard margin was more extensive until ca. 1850 AD (Divine and Dick, 2006; Walsh et al., 2017), which is supported by the combined CT and $P_{III}IP_{25}$ record in this study (Fig. 3.13). Interestingly, a gradual decrease in the HBI triene ratio at site 712, indicative of decreased spring bloom intensity (and Chl *a*), coincides with the recent sea ice decline (Fig. 3.13, 3.21). Accordingly, increased phytoplankton stocks at site 712 prior to 1850 AD could be attributable to longer annual sea ice duration, when increased stratification potentially stabilised phytoplankton in the photic zone more effectively, facilitating quicker growth approaching that of the contemporary MIZ in the central Barents Sea. Recent increases in AW inflow and atmospheric temperatures (Kinnard et al., 2011; Årthun et al., 2012) subsequently shifted the Svalbard margins towards less productive, predominantly ice-

free conditions dominated by continuous upwelling (Ivanov et al., 2012), explaining the gradual HBI triene ratio decrease at site 712 (Fig. 3.20). This conclusion compares favourably with that of Pathirana et al. (2015), who linked reduced MIZ duration in the Barents Sea to decreasing primary productivity over the last ca. 500 years.

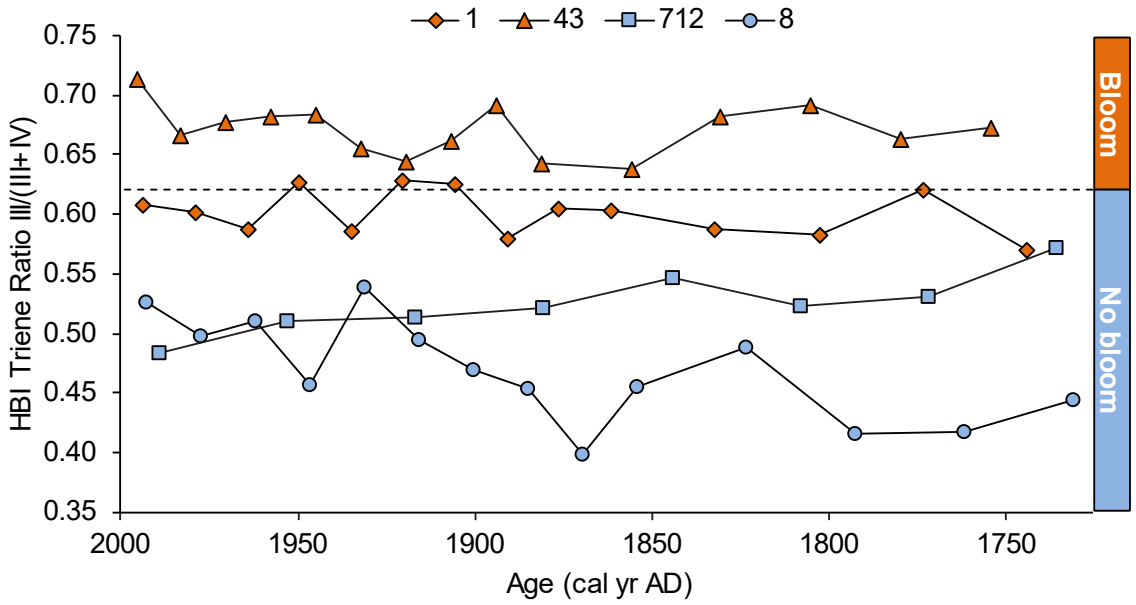

Figure 3.20: HBI triene ratio trends at core sites 1, 8, 43, and 712 throughout the last 250 years. The dashed line represents a tentative threshold value of 0.62 separating the spring phytoplankton bloom from reduced productivity conditions in the Barents Sea.

Core 8 exhibits similar HBI triene ratios as core 712, but is located in a significantly different setting of increased SpSIC north of the central Barents Sea MIZ, which is predominantly influenced by colder ArW. The triene ratio values are therefore potentially attributable to reduced productivity in areas of prolonged seasonal sea ice duration, where the melt season is conversely shortened (Fig. 1.4, Chapter 1). Coupled with potential nutrient depletion within the surrounding waters as a consequence of rapid spring bloom development south of the core site (e.g. Wassmann et al., 2006; Signorini and McClain, 2009), the extensive sea ice cover potentially limits primary production at site 8, explaining lower HBI triene ratio values. Notably, while site 8 appears to be more productive than site 712, such comparisons are compromised by

significant inter-annual variability and small sample size of Chl *a* data (n = 2; Table 3.5), which was unavailable for most of the satellite record due to cloud cover.

Table 3.5: Descriptive statistics of April–May Chl *a* (mg m^{-3}) averaged for the 2003–2017 period at core sites 1, 8, 43, and 712. Note the small sample size for core site 8.

Core ID	Chl *a* concentration (mg m^{-3}) statistics				
	Mean (±SD)	Median	Range	Sample Size	RSD (%)
43	2.2 ± 2.2	1.9	0.3–9.3	15	101
1	1.6 ± 1.6	0.8	0.2–5.5	15	98
712	1.0 ± 1.9	0.4	0.3–7.7	15	195
8	1.6 ± 1.4	1.4	0.4–2.4	2	87

Cores 1 and 43 are characterised by consistently higher Chl *a* and HBI triene ratio values relative to 712 and 8 (Table 3.5, Fig. 3.20–3.21). The latter core site is located firmly within the spring bloom zone, with Chl *a* values >2 mg m^{-3}, which is in good agreement with the highest HBI triene ratios observed in the current dataset. The productivity is potentially increased further by the presence of a proximal ice edge, which would aid stratification during the melt season (e.g. Sundfjord et al., 2007; Meier et al., 2014). Conversely, the absence of seasonal sea ice at site 1 could reduce productivity and contribute to slightly lower HBI triene ratio values (Fig. 3.20–3.21). While lower triene ratios could also arise simply due to the close proximity of site 1 to the spring bloom boundary, Chl *a* values at the core site are also considerably lower than those of the immediate surrounding waters of the southern Barents Sea (Table 3.5 and Fig 3.22). This may be a consequence of the direct influence of the NCaC; intensified AW upwelling could have reduced the stability of the water column at the core site, causing locally lower productivity and HBI triene ratios at site 1 (Fig. 3.21). Overall, while the HBI triene ratio is broadly representative of spring bloom occurrence, at least in recent centuries, evaluation of further sedimentary archives is required to assess its potential as a phytoplankton paleo-productivity tracer.

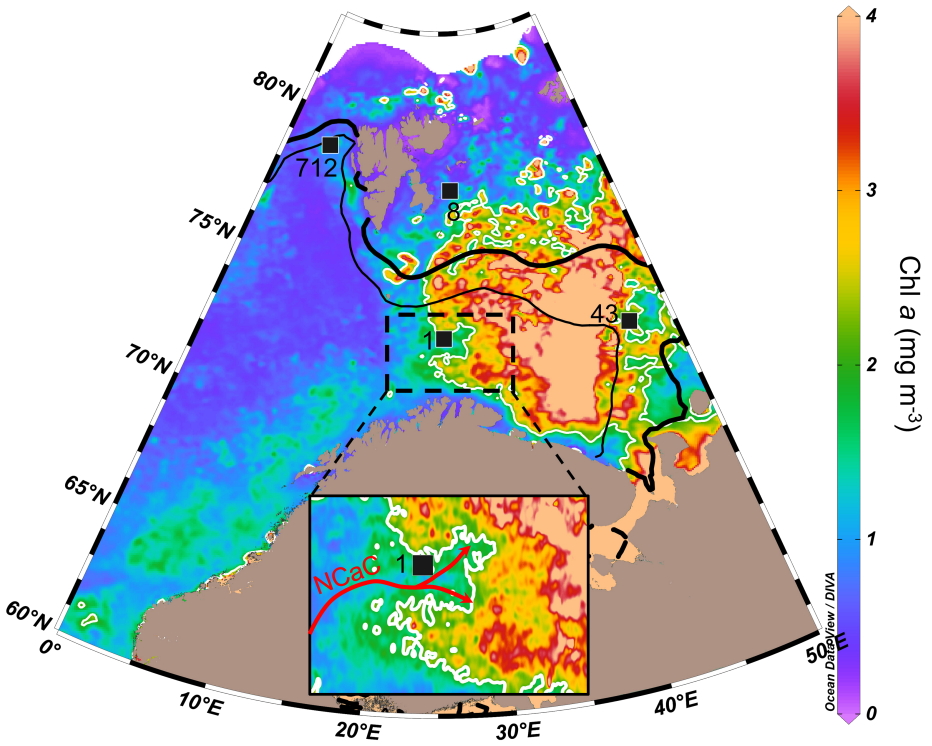

Figure 3.21: Map of the Barents Sea showing the locations of cores 1, 8, 43, and 712 overlaid onto a 2003–2017 average May Chl *a* grid. The surrounding setting of core 1 is magnified, with a suggested NCaC pathway shown. Thin and thick solid black lines represent the average ice edge (0% SpSIC) and ice extent (15% SpSIC) boundaries for the 1988–2017 period. The 2 mg m^{-3} Chl *a* contour is shown by a solid white line.

3.5 Conclusions

Analysis of HBI biomarkers in 198 surface sediments from the Barents Sea and neighbouring regions revealed the potential of classification tree (CT) models as a complementary proxy method for characterising Arctic sea ice conditions. Consistent with known sympagic and pelagic diatom sources, and outcomes from previous studies in the region, CT models constructed using different HBI assemblages revealed that the sea ice diatom derived biomarkers IP_{25} and II, as well as pelagic HBI trienes III and IV were the most appropriate variables used for classification of sea ice conditions in the Barents Sea. Additionally, in agreement with a pelagic source, a link between the ratio of III and IV and maximum spring (April–May) Chl *a* was tentatively identified, and the variability of this HBI triene ratio in downcore records was broadly consistent with

overlying Chl *a* and known sea ice variability throughout recent centuries. Further assessment of the triene ratio as a spring bloom indicator requires investigation of the sources and distributions of HBI trienes in different regions and downcore records.

Semi-quantitative estimates of SpSIC in four downcore records based on a recent calibration using the $P_{III}IP_{25}$ index provided reasonable spatial and temporal agreement with known sea ice trends obtained from satellite and observational records, and a general consistency was also identified in outcomes from the $P_{III}IP_{25}$ and CT approaches. However, compared to the main Barents Sea sites, the agreement between the proxy and observational records was poorer for a core from the western Svalbard margin, and the qualitative predictions of sea ice variability obtained from the CT model did not fully capture trends of ice decline over the last ca. 150 years that could be identified via the semi-quantitative $P_{III}IP_{25}$ approach. Due to the dependence of model structure on changes in the training dataset, construction of separate models for different Arctic regions and the use of comprehensive training data should be carried out in the future. Despite some potential limitations of CTs, automatic selection of appropriate HBI biomarkers for sea ice classification, quantitative model assessment via performance metrics, and insensitivity to the *c*-factor (PIP_{25}) and statistical outliers, make it a potentially useful tool for providing discrete categorical assessment of paleo sea ice conditions to be employed alongside complementary biomarker (e.g. the PIP_{25} index) or other proxy methods. However, the wider applicability of the CT method for paleo sea ice reconstruction requires evaluation of further surface sediments and downcore records from different Arctic and sub-Arctic regions.

CHAPTER FOUR

4. Further assessment and application of CT models, the $P_{III}IP_{25}$ index, and the HBI triene ratio for millennial-scale paleo sea ice and productivity reconstruction

4.1 Introduction

Despite the perceived advantages and good agreement of classification with the $P_{III}IP_{25}$ approach and observational records (ca. last 300 years) of sea ice conditions in the Barents Sea, the CT approach presented in Chapter 3 requires further evaluation before its wider applicability as a statistical tool for classification of sea ice conditions can be established. Specifically, the agreement of CT model-derived categorical assessment of sea ice conditions and $P_{III}IP_{25}$-derived semi-quantitative SpSIC estimates needs to be determined across longer timescales encompassing major changes in sea ice dynamics, such as those occurring during the Younger Dryas–Holocene transition (e.g. Rasmussen et al., 2007; Cabedo-Sanz et al., 2013; Klitgaard-Kristensen et al., 2013) and the Holocene cooling (e.g. Duplessy et al., 2005; Risebrobakken et al., 2011). Potential error sources that could impact accuracy and applicability of both methods also require discussion, such as the influence of the *c*-factor or distributional changes within the HBI assemblage that are not reproducible in contemporary settings. An additional challenge involves determining whether the agreement of the HBI triene ratio (Chapter 3) with occurrence and relative intensity (and/or duration) of diatom-dominated spring blooms in the Barents Sea during the last 300 years (Chapter 3) extends to millennial time scales. This could provide further insight into the use of III and IV as tracers of spring bloom occurrence, duration, and/or intensity in the Arctic.

To achieve these aims, the agreement of $P_{III}IP_{25}$-based SpSIC estimates (Smik et al., 2016) and CT model predictions, as well as HBI triene ratio variability were assessed in four marine sediment cores located at sites of contrasting contemporary sea ice and productivity conditions in the Barents Sea (Fig. 4.1) and spanning periods of both abrupt and gradual climate shifts throughout the last ca. 16 cal kyr BP.

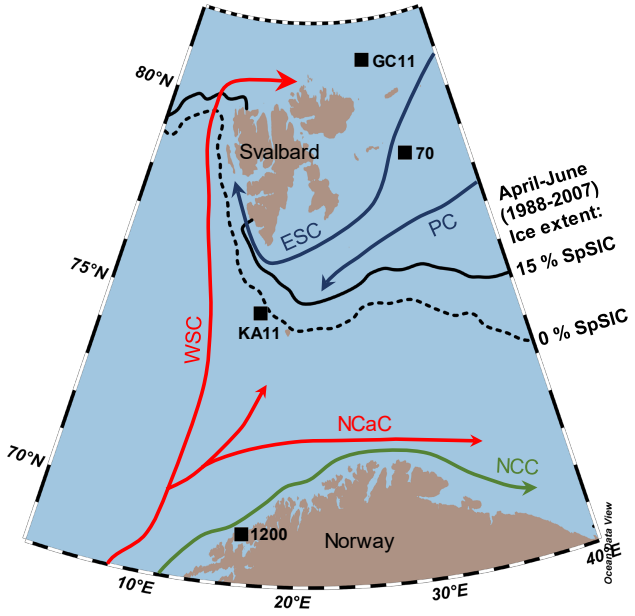

Figure 4.1: Map of the Barents Sea showing locations of downcore records 1200, KA11, GC11, and 70 (black squares). Solid and dotted black lines represent the average April–June sea ice extent (1988–2007) corresponding to SpSIC thresholds of 15% and 0%, respectively. A simplified representation of surface Atlantic Water (AW; red arrows), Arctic Water (ArW; blue arrows) and Coastal Water (CW; green arrows) currents is also shown, with abbreviations analogous to those in Fig. 3.1 (Chapter 3).

Three of the core sites were chosen based on the availability of previous climatological reconstructions (Cabedo-Sanz et al., 2013; Berben et al., 2014, 2017), a comprehensive set of HBI concentrations (Belt et al., 2015), and surface sediment-based regional calibrations for both $P_{III}IP_{25}$ and CT approaches (Smik et al., 2016; Chapter 3). This facilitated efficient identification of the causes of discrepancies between the CT and $P_{III}IP_{25}$ methods and recommendations regarding their complementary application to downcore records, as well as the suitability of the HBI triene ratio for tracing spring bloom intensity. Additionally, HBI biomarker concentrations (IP_{25}, II, III, and IV in Fig.

1.8), $P_{III}IP_{25}$ data, CT predictions, and HBI triene ratio trends for a new sedimentary record from the Kvitøya Trough (north-east off Svalbard) spanning the Younger Dryas (YD) and the Holocene (Hogan et al., 2010, 2017) allowed for a semi-quantitative reconstruction of SpSIC (%), categorical assessment of sea ice cover, and a tentative primary productivity assessment at the north-eastern Barents Sea margin, an area mainly influenced by cold ArW (Gammelsrød et al., 2009) where paleo-reconstructions are relatively scarce (e.g. Duplessy et al., 2001, 2005; Lubinski et al., 2001; Risebrobakken et al., 2011; Klitgaard-Kristensen et al., 2013; Chauhan et al., 2016; Eilertsen, 2016). Thus, in combination with additional data, such as Atlantic Meridional Overturning Circulation (AMOC) and insolation variability, scenarios for sea ice evolution along the northern Barents Sea margin (Kvitøya Trough) throughout the last 13 cal. kyr BP were proposed, and the outcomes contextualised further using previous paleoceanographic reconstructions throughout the Barents Sea and the Svalbard margin.

4.2 Materials and methods

4.2.1 Downcore sediment material

Four sediment cores from sites characterised by different modern sea ice conditions in the Barents Sea were selected for this study. Core NP05-11-70GC (78.67°N, 32.70°E; 293 m water depth), referred to as core 70 (Fig. 4.1), was collected from the Olga Basin to the South of Kong Karls Land (East Svalbard) aboard the RV *Lance* in August 2005. Core chronology is based on three calibrated ^{14}C Accelerator Mass Spectrometry (AMS) dates from mixed foraminifera (Berben et al., 2017). Concentrations of IP_{25} and III (Fig. 1.8), $P_{III}IP_{25}$ indices, and associated semi-quantitative SpSIC estimates of core 70 for the last ca. 9.4 cal kyr BP were presented previously (Belt et al., 2015; Berben et al., 2017). Core JM09-KA11-GC (74.87°N, 16.48°E; 345 m water depth), referred to as core KA11 (Fig. 4.1), was obtained from

the Kveithola Trough (South off Svalbard) aboard RV *Jan Mayen* in 2009. The age model spans ca. 16 cal kyr BP presented in Belt et al. (2015) and is based on merged ^{14}C AMS dates from previous studies (Rüther et al., 2012; Berben et al., 2014). Micropaleontological distributions, stable isotope analyses (Dylmer et al., 2013; Groot et al., 2014), IP_{25} and III concentrations (and $P_{III}IP_{25}$ values) were presented previously for core KA11 (Belt et al., 2015), but not SpSIC estimates. Piston core JM99-1200 (69.27°N, 16.42°E; 475 m water depth), referred to as core 1200 (Fig. 4.1), was retrieved from the Andfjord (northern Norway) aboard the RV *Jan Mayen* in November 1999. Herein, the age model of Cabedo-Sanz et al. (2013) corresponding to ca. 14.0–7.0 cal kyr BP (Bølling-Allerød to middle Holocene) was used. Concentrations of IP_{25} and III and $P_{III}IP_{25}$ values (but not $P_{III}IP_{25}$-derived SpSIC) of core 1200 were reported previously (Cabedo-Sanz et al., 2013; Belt et al., 2015), in addition to sedimentological, isotopic and micropaleontological analyses (Knies et al., 2003; Ebbesen and Hald, 2004). Finally, core JR142-11GC (81.08°N, 28.93°E; 359 m water depth), hereafter GC11 (Fig. 4.1), was collected in the Kvitøya Trough (north-eastern Barents Sea) in June 2006 during cruise JR142 aboard the RRS *James Clark Ross*. The ^{14}C AMS chronology presented in Hogan et al. (2017) was supplemented by 3 further radiocarbon dates obtained at the Poznan Radiocarbon Laboratory in Poland (Fig. 4.2).

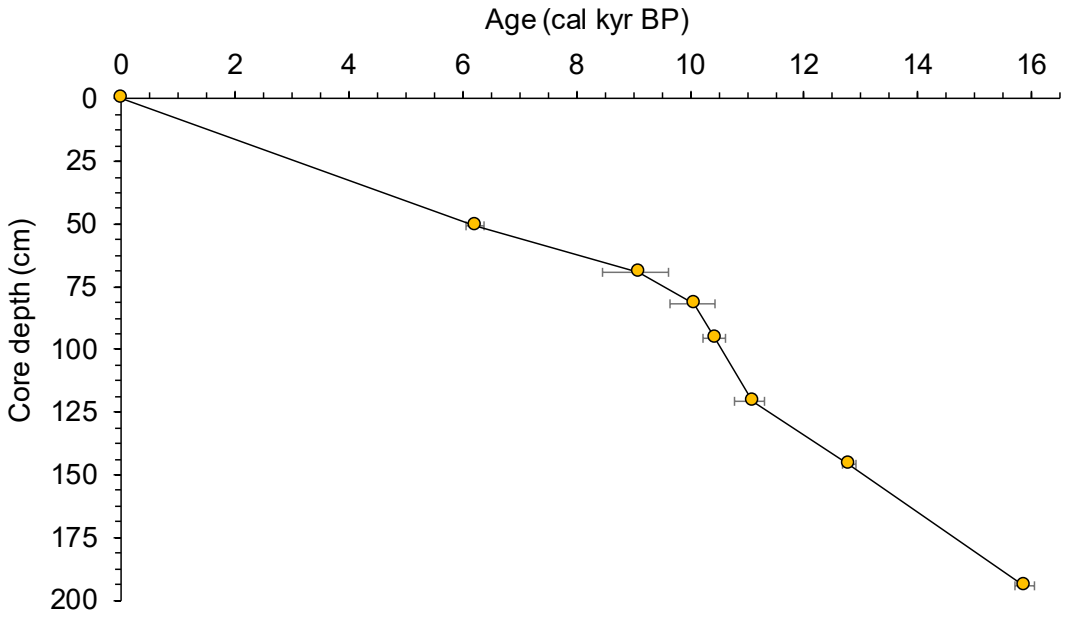

Figure 4.2: Age model for core GC11, showing median calibrated ^{14}C AMS dates (orange markers) and corresponding 2σ standard error ranges (black bars).

^{14}C AMS ages were calibrated within the OxCal 4.3 software (Bronk Ramsey, 2009) using the IntCal13 calibration curve (Reimer et al., 2013) with regional reservoir corrections (ΔR) of 200±50 and 105±25 years applied to dates older and younger than 10 ^{14}C kyr, respectively (Katrine Husum, personal communication). The age model between calibrated ages was constructed via a Poisson process deposition model, assuming a modern (ca. 1900–2010 AD) core top. Dated sample material, associated core depth intervals, initial and calibrated ^{14}C AMS dates for core GC11 are summarised in Appendix D (Table D.6), while specific descriptions and chronologies of cores 70, 1200, and KA11 are available elsewhere (Ebbesen and Hald, 2004; Rüther et al., 2012; Berben et al., 2014, 2017; Belt et al., 2015). CT output and HBI triene ratios for cores 70, KA11 and 1200, and all data for GC11 are presented here for the first time.

4.2.2 HBI lipid extraction and analysis

The exact extraction and partial purification procedures used to obtain new chromatographic data for IP_{25}, II, III and IV (Fig. 1.8) in core GC11 are described in detail in Chapter 2 (sections 2.2–2.3) and Chapter 3 (section 3.3.3). Extraction of TOEs

(section 2.2.2.1) and 3-step purification by elemental sulphur removal (section 2.2.3), silica column chromatography (section 2.2.4), and Ag-Ion chromatography (section 2.2.5) were all carried out, and samples were prepared, analysed via GC-MS, and quantified in SIM mode as described in sections 2.3.1–2.3.3.

4.2.3 Proxy and statistical methods

Modern SpSIC (April-June; 1988–2007) for each core site was inferred from the Nimbus-7 SMMR and DMSP SSM/I-SSMIS satellite dataset (Cavalieri et al., 1996; Chapter 3). Previously published concentrations of IP_{25} and III for cores 1200 (Cabedo-Sanz et al., 2013) and KA11 (Belt et al., 2015) were re-examined to calculate $P_{III}IP_{25}$ indices (Eq. 2.8, Chapter 2; Müller et al., 2011) and derive SpSIC estimates (Eq. 3.1, Chapter 3) using the regional *c*-factor (c = 0.63) and $P_{III}IP_{25}$–SpSIC calibration of Smik et al. (2016), respectively. Additionally, a threshold $P_{III}IP_{25}$ value of 0.8, corresponding to a SpSIC of 68% (Eq. 3.1), was used to qualitatively indicate the occurrence of at least some (>5%) sea ice cover during July–September (Smik et al., 2016). Previously obtained chromatographic and mass spectrometric (MS) data were re-examined to quantify additional HBI lipids (i.e. II and IV; Fig. 1.8) required to obtain CT model predictions of sea ice conditions, which were calculated following the method described in sections 3.3.4.2–3.3.4.3 (Chapter 3). Briefly, percentage abundances of each IP_{25} and HBIs II, III and IV to their total were calculated for each core horizon from absolute concentrations (ng g^{-1}) using Eq. 4.1, where these are denoted by square brackets. Subsequently, the CT model (model A in Chapter 3) constructed from a Barents Sea surface sediment dataset via the R Statistical Package (R Core Team, 2018) was used to classify each core horizon into one of three classes representing marginal (<10% satellite SpSIC), intermediate (10–50% SpSIC), and extensive (>50% SpSIC) spring sea ice conditions (Fig. 3.1a). Finally, probabilities of classification into a particular sea ice

class were estimated for samples where relative abundances (%) of HBIs were close to CT model splitting rule thresholds (Fig. 3.7a in Chapter 3) using a simplified C5.0 algorithm (Quinlan, 1993).

$$HBI\ (\%) = \frac{[HBI]}{\sum([IP_{25}], [II], [III], [IV])} \times 100 \qquad (4.1)$$

HBI triene ratio values were calculated for each horizon using Eq. 3.6 (Chapter 3). Biomarker concentrations, $P_{III}IP_{25}$-derived SpSIC and CT model outcomes, and HBI triene ratios for all cores are available in Appendix D (Table D.7). Additional statistical analyses were carried out to supplement the comparison of CT and $P_{III}IP_{25}$-based sea ice assessments. Thus, Pearson's correlations for IP_{25} versus HBI II and III versus IV were calculated from surface sediment data (Fig. 3.1a, Chapter 3). The biomarker pairings for correlation were chosen due to previous evidence of co-production of sympagic HBIs IP_{25} and II (Navarro-Rodriguez et al., 2013; Brown et al., 2014c; Belt et al., 2016), pelagic HBIs III and IV (Belt et al., 2000; Rowland et al., 2001), as well as significant correlation of these biomarker pairs in the Barents Sea and other Arctic regions (Navarro-Rodriguez et al., 2013; Navarro-Rodriguez, 2014). Thus, the product-moment correlation coefficient *r* was used to distinguish between negative and positive linear relationships and identify periods of anomalously deteriorated correlations in downcore records compared to those characteristic of relatively modern settings represented by surface sediments. Rolling Pearson's correlations were also calculated for all downcore records using a sampling window of nine horizons, corresponding to ca. 0.5–2.0 cal kyr BP. All analyses were implemented in R (R Core Team, 2018; Appendix A).

4.3 Results and discussion

4.4.1 Comparison of CT and $P_{III}IP_{25}$-based sea ice inferences since the YD

4.3.1.1 Core 70 (northern Barents Sea)

The core 70 site is characterised by extensive modern sea ice conditions (≈80% SpSIC) and the downcore record represents a gradual evolution of sea ice cover in the northern Barents Sea from ice-free conditions during the early Holocene to prolonged seasonal sea ice presence prevalent in the region today. The primarily insolation-controlled southward expansion of sea ice cover previously inferred for the core site throughout the Holocene (Belt et al., 2015; Berben et al., 2017) is reflected in the CT model assessment (Fig. 4.3a) and individual HBI profiles (Fig. 4.4a, b). Consistent with the onset of the HCO and the resulting proximity of the annual maximum sea ice edge to the core site between ca. 9.5–8.5 cal kyr BP evident from low $P_{III}IP_{25}$-derived SpSIC (ca. 5–15%), the CT model predicts mostly marginal sea ice conditions during this interval. Similarly, the southward migration of sea ice beginning ca. 8.5 cal kyr BP (to SpSIC of ca. 30 ± 4 % SpSIC) as a response to decreasing summer insolation (Berben et al., 2017) is also reflected by a switch of CT model assessment from marginal to intermediate sea ice conditions. A further southward migration of the ice edge between ca. 6.5–5.9 cal kyr BP, previously attributed to continued decreases of summer insolation and reduced AW influence (Berben et al., 2017), is reflected by an associated shift of CT model predictions from intermediate to extensive sea ice conditions at ca. 6.0 cal kyr BP. This trend agrees with Neoglaciation onset, when glacier advances and increased ice export via the FS helped re-establish modern-type oceanic circulation (Werner et al., 2013, 2016; Rasmussen and Thomsen, 2015).

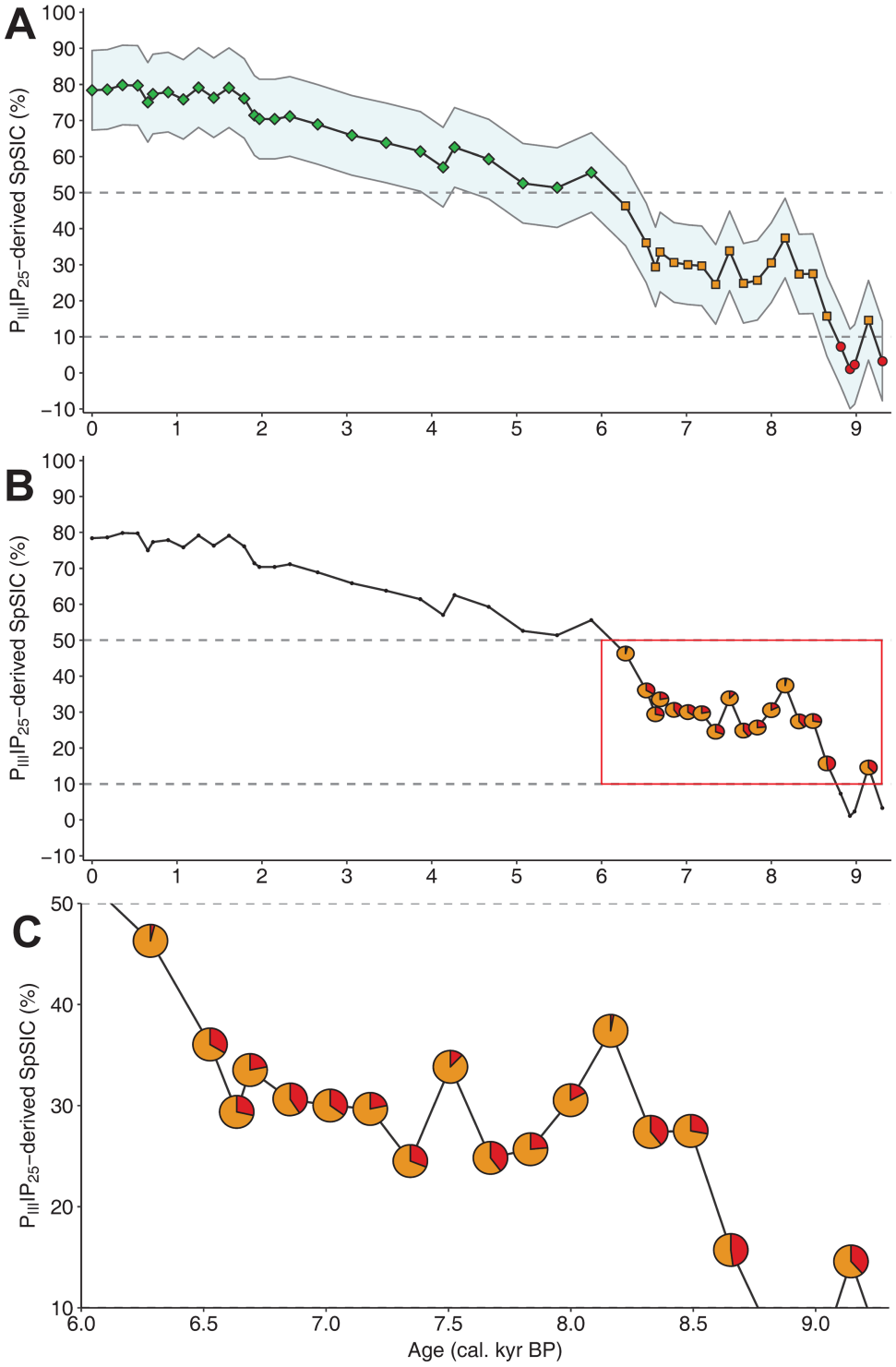

Figure 4.3: Sea ice proxy data for core 70 showing the $P_{III}IP_{25}$-based % SpSIC profile (black line) with: (A) An RMSE error of ca. 11% (blue bands; Smik et al., 2016) and superimposed CT predictions of marginal (red circles), intermediate (yellow squares), and extensive (green diamonds) sea ice cover. Dashed horizontal lines represent the 10% and 50% satellite SpSIC boundaries separating sea ice classes in the CT model (Fig. 3.1a, Chapter 3); (B) The probabilities of classification estimated from SD boundaries of CT model splitting rules (Quinlan, 1993) shown as pie charts for samples where the probability of classification into a single class was not certain (i.e. not =100%). Colours within pie charts correspond to the red, yellow, and green colours of SpSIC classes in plot A. The portion of plot B contained within the red square was magnified in plot C.

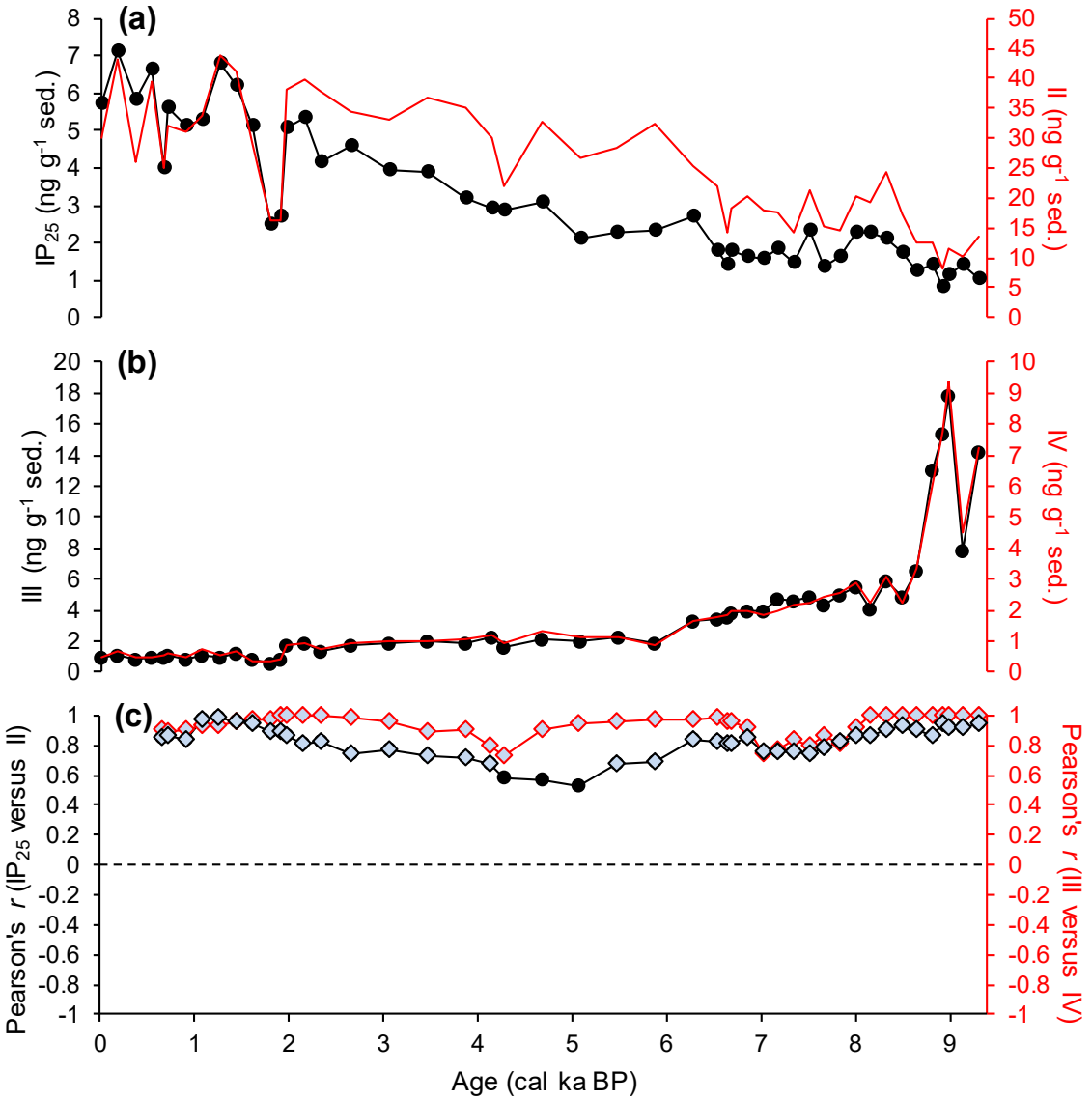

Figure 4.4: HBI concentrations and correlations for core 70 (northern Barents Sea), where black lines (with circle markers) and red lines correspond to primary (left) and secondary (right) colour-coded y-axes: (a) Concentrations of IP_{25} and II; (b) Concentrations of III and IV; (c) Running correlations (window of 9 horizons) for IP_{25} versus II (black line with circle markers) and III versus IV (red line). Grey diamonds represent significant correlations ($p = 0.05$). The dashed line separates positive ($r > 0$) and negative ($r < 0$) correlations.

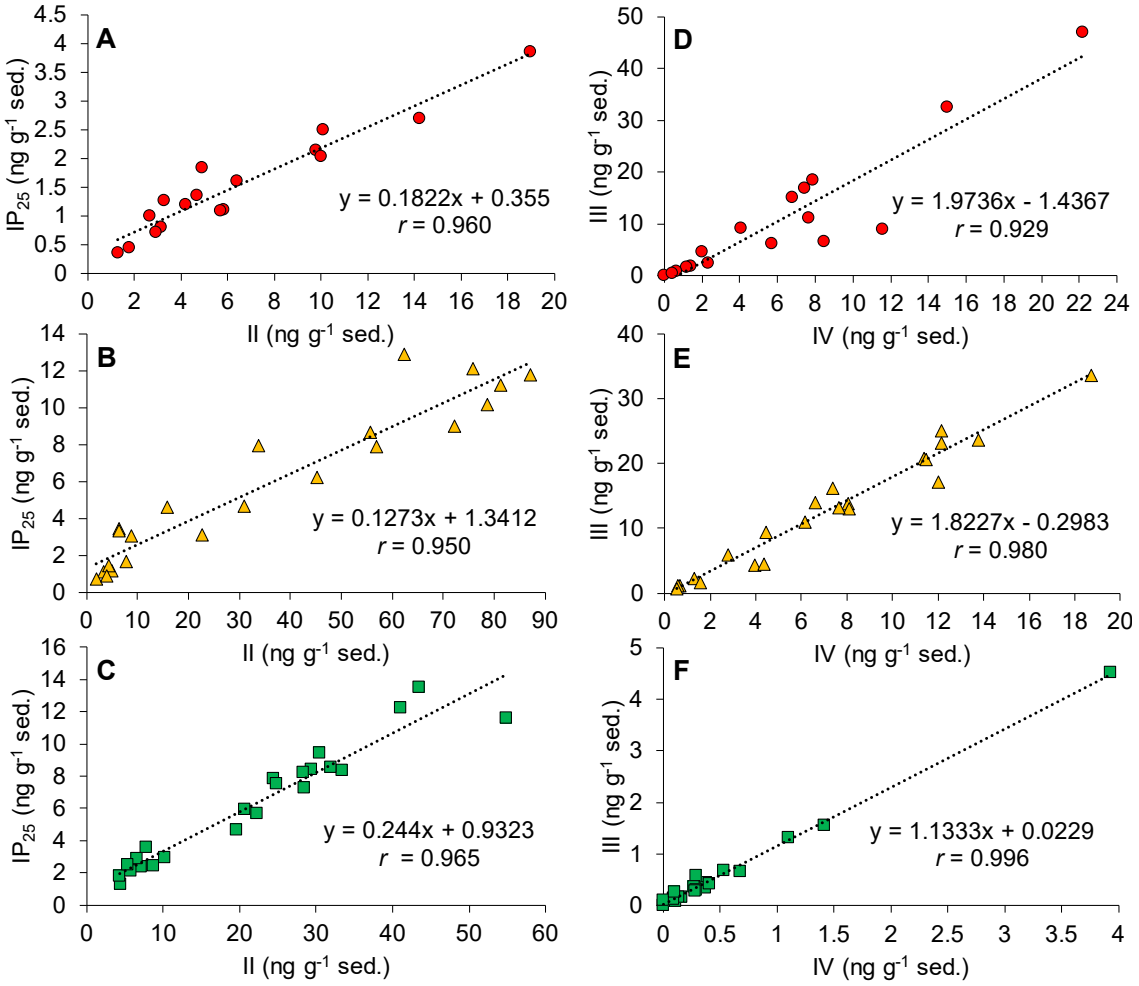

Figure 4.5: Pearson's correlations of IP_{25} versus II (panels A–C) and III versus IV (panels D–F) in Barents Sea surface sediments with marginal (<10% SpSIC; red circles), intermediate (10–50% SpSIC; yellow triangles), and extensive (>50% SpSIC; green squares) overlying sea ice conditions. Only surface sediments (Fig. 3.1a, Chapter 3) where holistic data for IP_{25}, II, III and IV was available were used to avoid influencing the best-fit line towards zero.

Overall, the timing of CT prediction shifts was consistent with previously inferred climate evolution at the core 70 site (Berben et al., 2017), and no discrepancies from semi-quantitative SpSIC estimates were observed, with all horizons consistently classified within the satellite SpSIC boundaries defined in the CT model training set (Fig. 4.3a). This supports the complementary application of both approaches when describing gradual changes in sea ice conditions at millennial timescales, where CT predictions have the potential to identify the timing of switches between distinct sea ice conditions, as hypothesized previously (Chapter 3). Notably, however, the CT model is limited by the class boundaries assigned to the training set (Fig. 3.1a), which may result

in insufficiently detailed assessment of changing sea ice conditions. In this case, a distinct ice expansion ca. 2.8–2.7 cal kyr BP (SpSIC values of ca. 80%; Fig. 4.3a) previously linked to insolation decreases (Berben et al., 2017) and reflected in another record south of Storfjorden (Pathirana et al., 2015) was not identified by the CT model since the 50–100% SpSIC range is only represented by a single class within the training set (Fig. 3.1a). Such limitations, in this case driven by reduced sample density around Svalbard, should be considered when interpreting model output. More generally, potential uncertainties of the CT when classifying samples into the intermediate sea ice class are also highlighted by relative probability values, which are never certain (i.e. never =100%) for samples between 10–50% $P_{III}IP_{25}$-based SpSIC in core 70 (Fig. 4.3b); this is a consequence of a relatively large confidence interval of splitting rule threshold based on relative contribution of IP_{25} to the HBI assemblage (4.4–8.4%; Fig. 3.7a). Indeed, the CT model was shown to lose performance (Chapter 3) in areas characterised by highly variable sea ice and primary productivity regimes, such as the MIZ of western Svalbard and the central Barents Sea. The otherwise high agreement with the $P_{III}IP_{25}$ approach is potentially attributable, at least in part, to significantly similar HBI distributions and data structure between the surface sediment training set and core 70. Like most supervised classification methods, CTs rely on distributional similarity of predictive variables (e.g. HBI percentages) between the training set and new samples to be classified. Thus, in this study, the model is only likely to function correctly when the overall relative abundance ranges and relationships between HBIs observed in the surface sediment training set (Fig. 3.1a) are reproduced in downcore records. This is the case for core 70, where consistently significant positive correlations are observed for IP_{25} versus II and III versus IV biomarker pairs (Fig. 4.4c), also evident in surface sediments with different overlying SpSIC (Fig. 4.5) used to build the CT model. Absolute concentrations and relative HBI abundances (Eq. 4.1) are also broadly

comparable and generally dominated by sympagic biomarkers in both datasets (Table 4.1); although it should be stressed that inherent HBI variability in surface sediments and core 70 prevent any detailed interpretation of spatially and temporally averaged values. Nonetheless, such visualisations of data ranges and structure help inform the expected CT performance for a given dataset and suggest that the model is likely to perform well for core 70.

Table 4.1: Mean absolute concentrations of HBIs (ng g^{-1} ± 1 SD) and relative abundances (%) calculated from these in surface sediments used to build the CT model, as well as in downcore records 70, 1200, KA11, and GC11.

Dataset	HBI concentration in ng g^{-1} ± 1 SD (relative abundance in %)			
	IP_{25}	II	III	IV
Surface	4.8 ± 3.9 (12)	22.1 ± 23.1 (57)	7.6 ± 10.1 (20)	4.4 ± 5.2 (11)
70	3.2 ± 1.8 (9)	25.2 ± 9.9 (74)	3.8 ± 3.9 (11)	1.9 ± 2.0 (6)
1200	8.5 ± 8.8 (13)	47.0 ± 47.2 (71)	4.9 ± 6.0 (7)	6.2 ± 8.3 (9)
KA11	4.9 ± 6.9 (6)	37.2 ± 41.7 (42)	21.8 ± 29.5 (25)	24.3 ± 41.3 (28)
GC11	3.9 ± 1.9 (8)	29.3 ± 9.3 (60)	6.4 ± 6.0 (13)	9.3 ± 9.7 (19)

4.3.1.2 Core 1200 (southwestern Barents Sea)

In contrast to contemporary ice-free conditions that characterise the core 1200 site, harsh glacial conditions with short ice-free summers during most of the YD cold stadial spanning ca. 13.0–11.9 cal kyr BP were previously inferred (Cabedo-Sanz et al., 2013; Belt et al., 2015). Accordingly, the record shows elevated $P_{III}IP_{25}$-derived SpSIC values (>75%) accompanied by CT model predictions of extensive sea ice conditions during this period (Fig. 4.6a). Subsequently, ameliorated conditions are evident during the YD–Holocene transition, with precipitous decrease of SpSIC estimates (to ca. 10–40%) and a switch of CT model assessment from extensive to marginal (<10% SpSIC) sea ice conditions. In core 1200, the ice retreat is characterised by rapid fluctuations of SpSIC estimates, consistent with switching of CT model assessment between intermediate and marginal classification of sea ice cover during the 11.9–11.5 cal kyr

BP period, which is followed by ice-free conditions for the remainder of the record (Fig. 4.6a). Similar unstable conditions, likely attributable to the return of thermohaline circulation during this period (e.g. Bakke et al., 2009), were previously inferred for core 1200 from PIP_{25} records (Cabedo-Sanz et al., 2013; Belt et al., 2015), as well as sea surface temperature (SST) and sea surface salinity (SSS) reconstructions based on stable isotope measurements of planktic foraminifera (Ebbesen and Hald, 2004).

The apparent consistency of CT predictions and $P_{III}IP_{25}$-derived SpSIC in core 1200 suggests that both methods respond similarly to extremes of sea ice conditions observed both during (ca. 13.0–12.0 cal kyr BP) and after (11.5 cal kyr BP onwards) the YD stadial. However, while the CT model also detected rapid fluctuations of sea ice cover during the climatically unstable YD–Holocene transition (11.9–11.5 cal kyr BP), several horizons (n = 7) were classified outside of the categorical sea ice boundaries based on satellite SpSIC thresholds (Fig. 4.6). Nonetheless, such discrepancies with the $P_{III}IP_{25}$-based SpSIC record were always within the RMSE of the regional $P_{III}IP_{25}$–SpSIC calibration (ca. ±11% SpSIC; Smik et al., 2016), and are potentially attributable to various error sources associated with $P_{III}IP_{25}$-based SpSIC estimates and CT models. For example, the dependence of $P_{III}IP_{25}$ values on the c-factor may significantly influence the regional comparability of the resulting SpSIC estimates. While the general trends of $P_{III}IP_{25}$-derived SpSIC were previously shown to be unaffected by the magnitude of the c-factor (Belt et al., 2015; Smik et al., 2016), $P_{III}IP_{25}$ values (and associated SpSIC estimates) may vary by ca. 10% when omitting the c-factor (c = 1; Smik et al., 2016). Further, the c-factor used in the current study (c = 0.63) was calculated based on average IP_{25} and III concentrations from a wide range of Barents Sea locations characterised by different sea ice conditions (Smik et al., 2016). Thus, the regional applicability of a spatially averaged c-factor remains a challenge, and the same value may not provide fully comparable SpSIC estimates for all downcore locations

presented herein. In contrast, the CT approach is based on a multivariate set of HBI biomarkers, is therefore independent of the *c*-factor, and probably provides results that are more comparable between locations within the geographical coverage of the surface sediment dataset used for model training (Chapter 3). In any case, 4 out of 7 samples where a discrepancy between CT and $P_{III}IP_{25}$ approaches was observed were not classified into the marginal sea ice class with complete certainty (Fig. 4.6b–c) due to relative abundances of IP_{25} similar to the CT splitting rule threshold (5.3%; Fig. 3.7a). Together, these caveats imply that the interpretation of $P_{III}IP_{25}$-derived SpSIC variability and any discrepancies with CT model predictions within the associated RMSE (±11 % SpSIC) should be avoided, and broader changes beyond this error range should instead be considered. Additionally, unlike core 70, the data structure in core 1200 is significantly unstable during rapid climate fluctuations, with correlations degrading to near-zero values (Fig. 4.7). This potentially hinders CT performance due to unpredictable data structure differences with the surface sediment training set. The period of high misclassification spanning 11.9–11.5 cal kyr BP in core 1200 was characterised by the return of enhanced biogenic production (Knies, 2005), fluctuating AW inflow, and similarly variable sea ice conditions resulting from meltwater and nutrient input from waning ice sheets (Cabedo-Sanz et al., 2013). It is possible that CT performance suffered during this interval of significantly unstable sea ice cover and primary productivity regimes, of which the latter could potentially have contributed to degraded correlations observed in the record (Fig. 4.7c) due to inconsistent, variable HBI production.

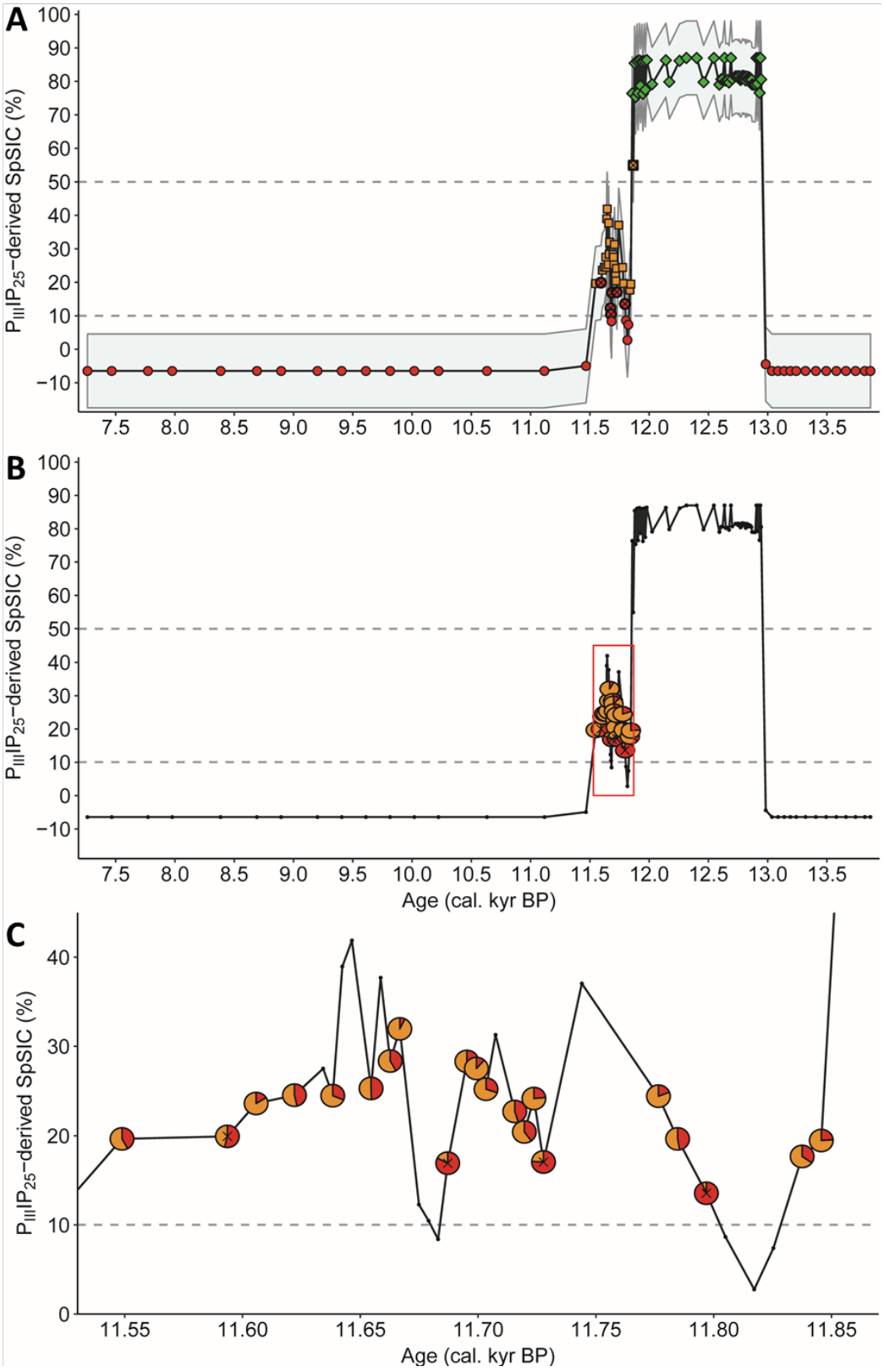

Figure 4.6: Sea ice proxy data for core 1200, where plots A, B, and C are analogous to those presented in Fig 4.3. Diagonal crosses represent horizons where any discrepancy between CT predictions and $P_{III}IP_{25}$ estimates (c=0.63) was observed.

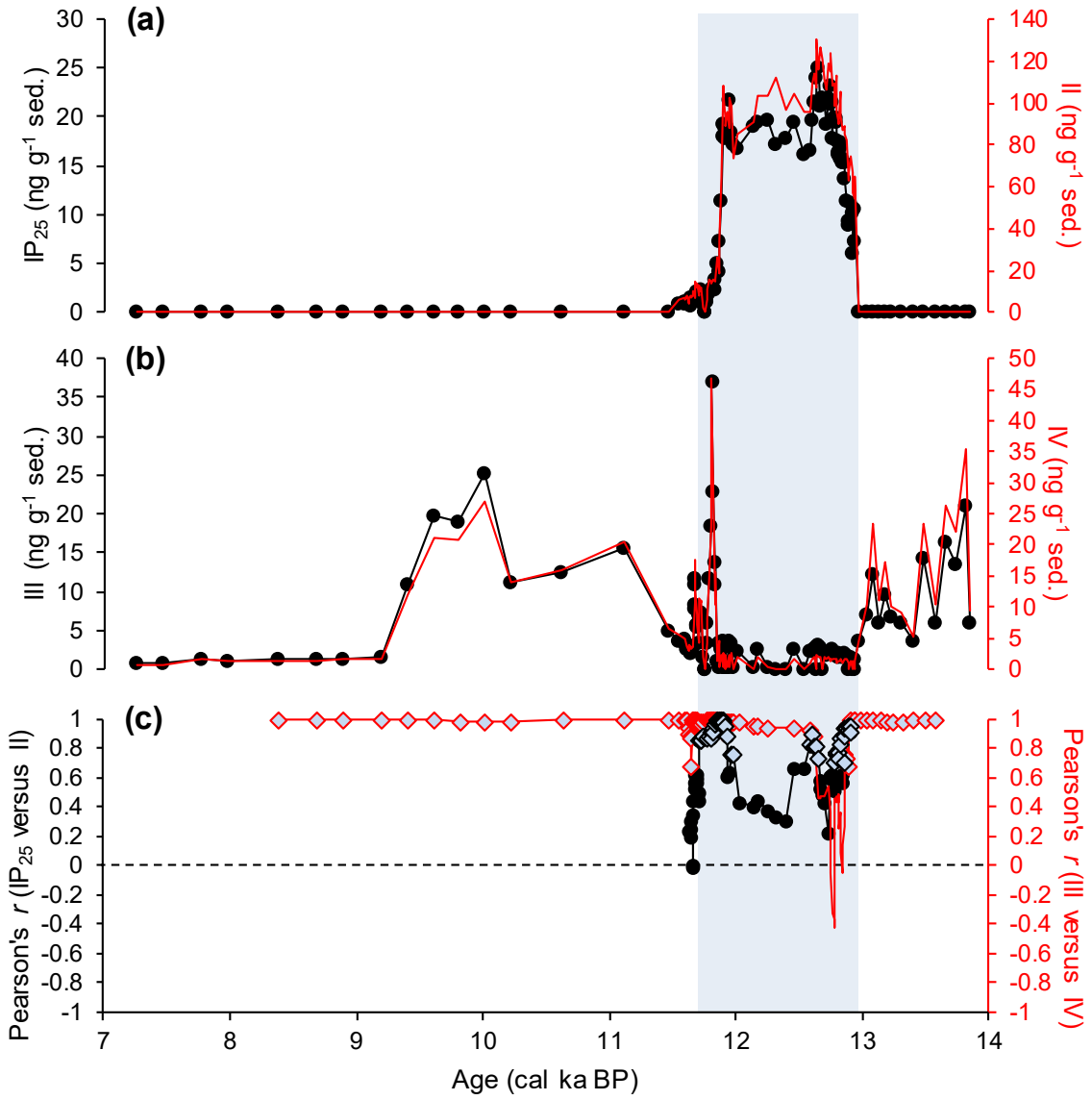

Figure 4.7: HBI concentrations and correlations for core 1200 (southwestern Barents Sea). The illustrated profiles are analogous to those shown in Fig 4.4. The light blue vertical bar highlights the YD (12.95–11.70 cal kyr BP).

Overall, the results suggest that CT predictions potentially become more prone to misclassification, and therefore less consistent with semi-quantitative SpSIC estimates, in rapidly shifting climate conditions observed during stadial-interstadial transitions. Finally, misclassification errors may also be associated with information loss due to insufficient representation of the SpSIC range (0–100%) in the CT model. Specifically, the surface sediment dataset used for model construction contains no samples with modern overlying SpSIC of 16–22% and 56–67% (Fig. 3.1a, Chapter 3), potentially resulting in an incomplete model definition near the marginal-intermediate

(10% satellite SpSIC) and intermediate-extensive (50% satellite SpSIC) sea ice class boundaries, respectively. Such potential error sources may be mitigated by expansion of the model training set to increase sample density and include such under-represented SpSIC ranges. In the meantime, shifts in CT model class predictions are probably more realistically interpreted as broader changes between sea ice regimes, rather than between definitive SpSIC threshold values of 10% and 50%. Thus, the marginal, intermediate, and extensive sea ice classes included in the model likely represent ice-free or proximal maximum ice edge conditions, the highly-productive MIZ during the spring melt season, and more northern regions where ice cover persists until ca. August–September (e.g. North-East of Svalbard), respectively.

4.3.1.3 Core KA11 (western Barents Sea)

The core KA11 site is presently characterised by marginal SpSIC (<5%) with a proximal spring sea ice edge (Fig. 4.1). As seen for core 1200, the site experienced SpSIC values of ca. 80% during the YD (ca. 13.0–12.0 cal kyr BP), but exhibited a more gradual ice retreat and a step-wise switch of CT model predictions from extensive towards marginal sea ice conditions during the 12.0–11.5 cal kyr BP period (Fig. 4.8a). A period of highly unstable sea ice cover is instead observed between ca. 11.0–10.0 cal kyr BP, with fluctuating SpSIC estimates (ca. 0–65%) and CT model predictions. This is consistent with the return of enhanced sub-surface AW inflow to the core site after ca. 11.5 cal kyr BP inferred from benthic foraminiferal census data (Groot et al., 2014), with a contrastingly colder surface water layer dominated by ArW inferred from reduced SSTs (Berben et al., 2014). From ca. 10.0–1.5 cal kyr BP, ice-free conditions characterised the core KA11 site, as evidenced by consistently low SpSIC (ca. <10%) and marginal sea ice conditions predicted by the CT model, and further supported by an enhancement of AW inflow to the core site from ca. 9.8 cal kyr BP (Groot et al., 2014).

Finally, re-emergence of highly fluctuating sea ice cover during the last ca. 0.9–0.6 cal kyr BP (Berben et al., 2014; Belt et al., 2015), despite increasing AW inflow (Dylmer et al., 2013), was also captured by the CT model, which switches from marginal to intermediate sea ice conditions at this time (Fig. 4.8a).

Consistent with outcomes from core 1200, several horizons (n = 20) from core KA11 were classified outside of the sea ice class boundaries based on satellite SpSIC thresholds. The majority of these differences correspond to samples with ca. 10–20% $P_{III}IP_{25}$-based SpSIC being classified into the marginal sea ice class, and not with certain probability (Fig. 4.8b). However, in contrast to core 1200, some discrepancies also exceeded the standard RMSE (±11% SpSIC) of the regional $P_{III}IP_{25}$-SpSIC calibration (Smik et al., 2016) for four horizons, where marginal sea ice cover (<10% satellite SpSIC) was inferred for $P_{III}IP_{25}$-derived SpSIC values in excess of ca. 40% (Fig. 4.8). These discrepancies persist even when the c-factor is omitted (c = 1), and occur during periods of high climatic variability (11.5–10.0 and 0.9–0.6 cal kyr BP), coincident with the return of variable sub-surface AW inflow. As with core 1200, the discrepancies likely stem from considerably different distributions and data structure of HBIs in the misclassified horizons compared to those of surface sediments used for model construction, potentially caused by climate fluctuations during intervals of rapid climate change. Indeed, running correlations between IP_{25} and II severely degrade towards negative r values during the 11.5–10.0 cal kyr BP interval and the last 0.7 cal kyr BP (Fig. 4.9c), thus deviating from the consistently high positive associations observed in the surface training set (Fig. 4.5). Indeed, these distributional changes coincide with CT misclassification beyond the $P_{III}IP_{25}$-based SpSIC error of 11% and are better illustrated when considering individual concentration profiles of IP_{25} and II, as well as rolling correlations of corresponding relative differences (Fig. 4.10).

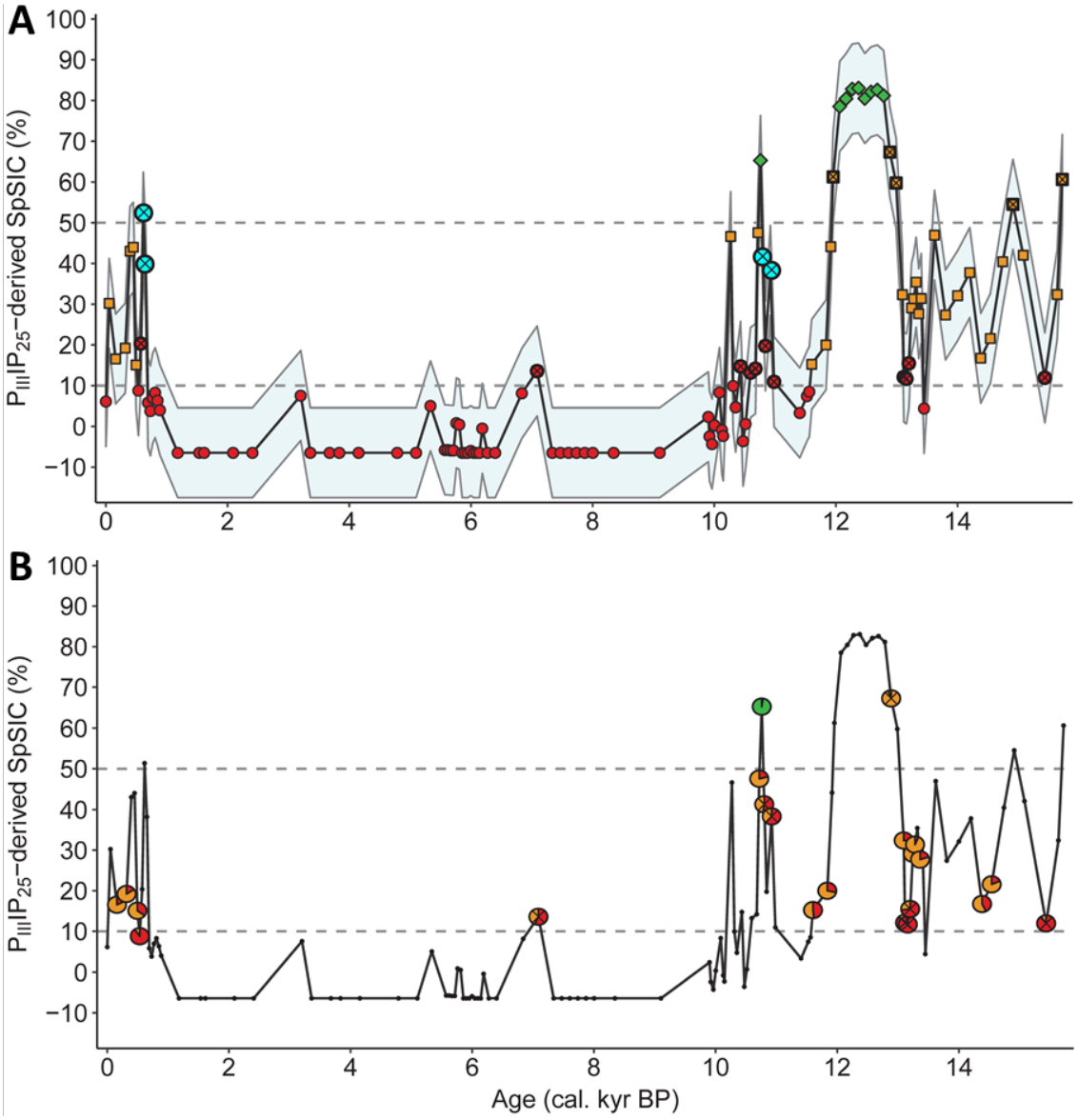

Figure 4.8: Sea ice proxy data for core KA11 analogous to that shown for cores 70 and 1200 in Fig. 4.3 and 4.6, respectively. In plot A, crossed light-blue circle markers represent horizons where the discrepancy between CT predictions and $P_{III}IP_{25}$-based SpSIC estimates exceeded the $P_{III}IP_{25}$ versus SpSIC calibration RMSE of ca. 11% (Smik et al., 2016) irrespective of the *c*-factor used to calculate $P_{III}IP_{25}$.

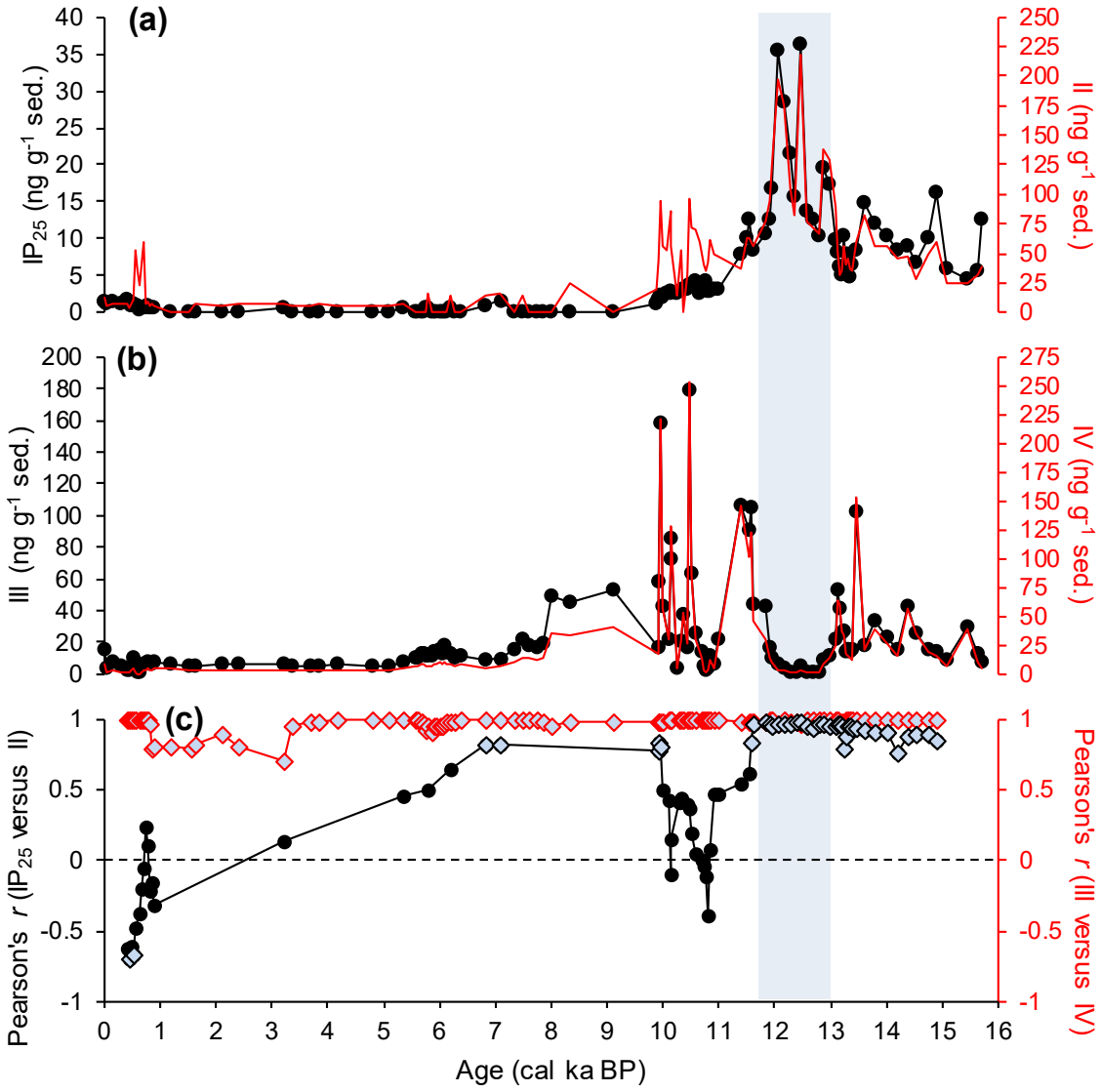

Figure 4.9: HBI concentrations and correlations for core KA11 (western Barents Sea). The illustrated profiles are analogous to those shown in Fig. 4.4, 4.7. The light blue vertical bar highlights the YD (12.95–11.70 cal kyr BP).

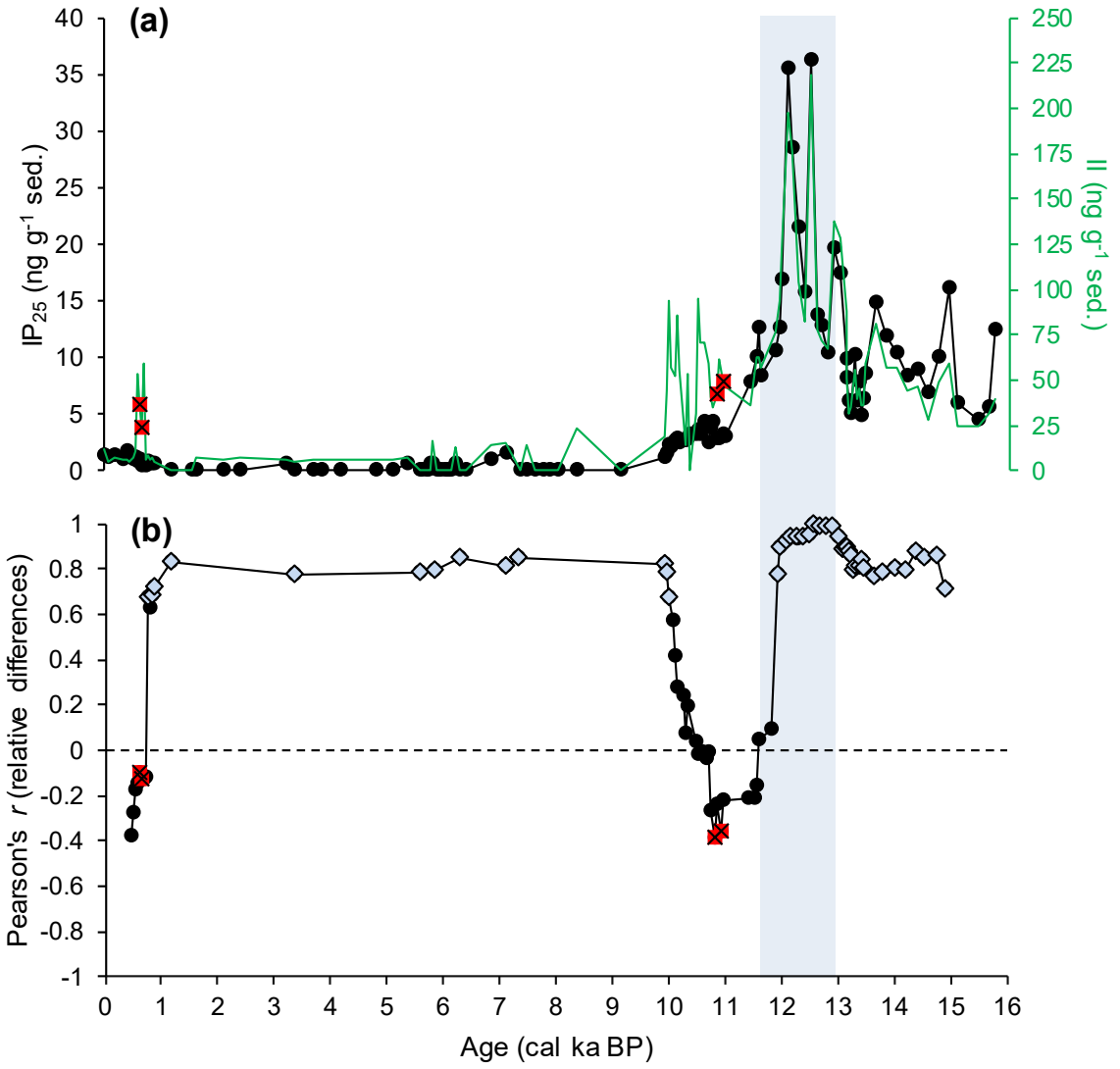

Figure 4.10: Biomarker profiles and correlations for core KA11: (a) Concentrations of IP_{25} and II represented by black (with circle markers) and green lines, respectively; (b) Running correlation of first relative (%) differences, with a sampling window of 9 horizons. Positive and negative correlations are separated by a dashed horizontal line, while grey diamonds show correlations significant at a 95% confidence level. In both (a) and (b), crossed red squares represent samples for which CT model predictions significantly differed from $P_{III}IP_{25}$-derived % SpSIC values, with a discrepancy exceeding the RMSE of the $P_{III}IP_{25}$–SpSIC calibration (ca. ±11% SpSIC) irrespective of the *c*-factor used to calculate $P_{III}IP_{25}$. The light blue vertical bar highlights the YD (12.95–11.70 cal kyr BP).

It is evident that disproportional increases of II relative to IP_{25} contribute to the correlation reduction. Similar increases in the II/IP_{25} ratio (i.e. DIP_{25}) were previously observed across the Arctic during periods of increased warm water inflow from the North Atlantic and North Pacific (e.g. Fahl and Stein, 2012; Hörner et al., 2016; Ruan et al., 2017), conditions that also characterised the KA11 site during intervals of elevated

HBI II concentration (Berben et al., 2014; Belt et al., 2015). Overall, the data support the results from core 1200 and suggest that CT performance and consistency with the $P_{III}IP_{25}$ approach suffer when HBI distributions included in the model training set are not represented in downcore records characterised by different or unstable climate. Visualisation of the variables used in the CT assessment (Fig. 4.8–4.10) is essential when identifying such cases. It is important to acknowledge that this limitation is potentially amplified as variations in relative abundances of any biomarker included in the model inherently affect the overall HBI composition due to data normalisation used for the CT (Eq. 4.1). The dependence of CT performance and viability on the consistency of data distribution in the training set with that of new samples highlights the necessity of constructing separate training sets for different Arctic regions, which often exhibit significantly different HBI distributions despite similar seasonal ice conditions (Stoynova et al., 2013; Xiao et al., 2015a). Ideally, downcore records to be classified should be within the geographical coverage of the surface sediment training set, as is the case in this study. Further, the choice of an optimal time interval for the satellite SpSIC data is potentially problematic due to the frequent unavailability of accumulation rates for surface sediments. Thus, the integrated biomarker signal at each surface location potentially corresponds to a variable temporal window (Chapter 3) and some surface sediments may not even represent recent accumulation. This is likely to influence the accuracy of both the CT model and $P_{III}IP_{25}$-based SpSIC estimates.

4.3.1.4 Core GC11 (Kvitøya Trough proximal to the northern Barents Sea shelf)

4.3.1.4.1 Paleo-sea ice variability throughout the last 13 cal kyr BP

The 13.0–12.0 cal. kyr BP period in the GC11 record is characterised by the highest, most variable IP_{25} concentrations (2.4–13.5 ng g^{-1}) and relatively low concentrations of triene III (0.3–6.5 ng g^{-1}). Peak abundance of IP_{25} and high $P_{III}IP_{25}$-

derived SpSIC (ca. >80%) indicate harsh glacial conditions with more extensive than modern spring sea ice cover, position of the sea ice edge south of the core site, and summer sea ice occurrence until ca. 12.7 cal. kyr BP (Fig. 4.11b, d). Perennial sea ice cover is unlikely, given the high sympagic diatom productivity evidenced by maximum IP_{25} concentrations during this period (Brown et al., 2014c), which exceed the 5.5 ± 3.3 ng g^{-1} observed in proximal surface sediments (Belt et al., 2015). A gradual decrease of SpSIC to ca. 50% is evident between 12.6–12.0 cal. kyr BP. The reconstructed $P_{III}IP_{25}$-based SpSIC trend is generally consistent with CT assessment of sea ice conditions, which shows extensive sea ice cover until 12.7 cal. kyr BP, followed by a switch to milder, intermediate sea ice conditions (Fig. 4.11d). This 1000-year period of relatively stable seasonal sea ice cover likely corresponds to the YD stadial evident throughout the Arctic Ocean and the Northern North Atlantic (e.g. Broecker, 2006; Bakke et al., 2009). This interval is characterised by increased sea ice and meltwater export through the Fram Strait (Bradley and England, 2008), sea level rise after the final collapse of the ice sheets, including the BSIS (Peltier and Fairbanks, 2006; Clark et al., 2009), and a hampered AMOC (Fig. 4.11a; McManus et al., 2004; Ritz et al., 2013). Accordingly, stable seasonal sea ice cover (ca. 50–80% SpSIC) observed at the GC11 site during 13.0–12.0 cal kyr BP was likely caused by the expansion of sea ice during the YD, which is relatively well-constrained in the Barents Sea (Fig. 4.12a). However, the ice conditions appear to be less extensive, with more seasonally open waters after 12.7 cal kyr BP relative to sites KA11 and 1200, for which extensive SpSIC of over 70% was present until ca. 11.9 cal. kyr BP (Fig. 4.6, 4.8; Cabedo-Sanz et al., 2013; Berben et al., 2014; Belt et al., 2015).

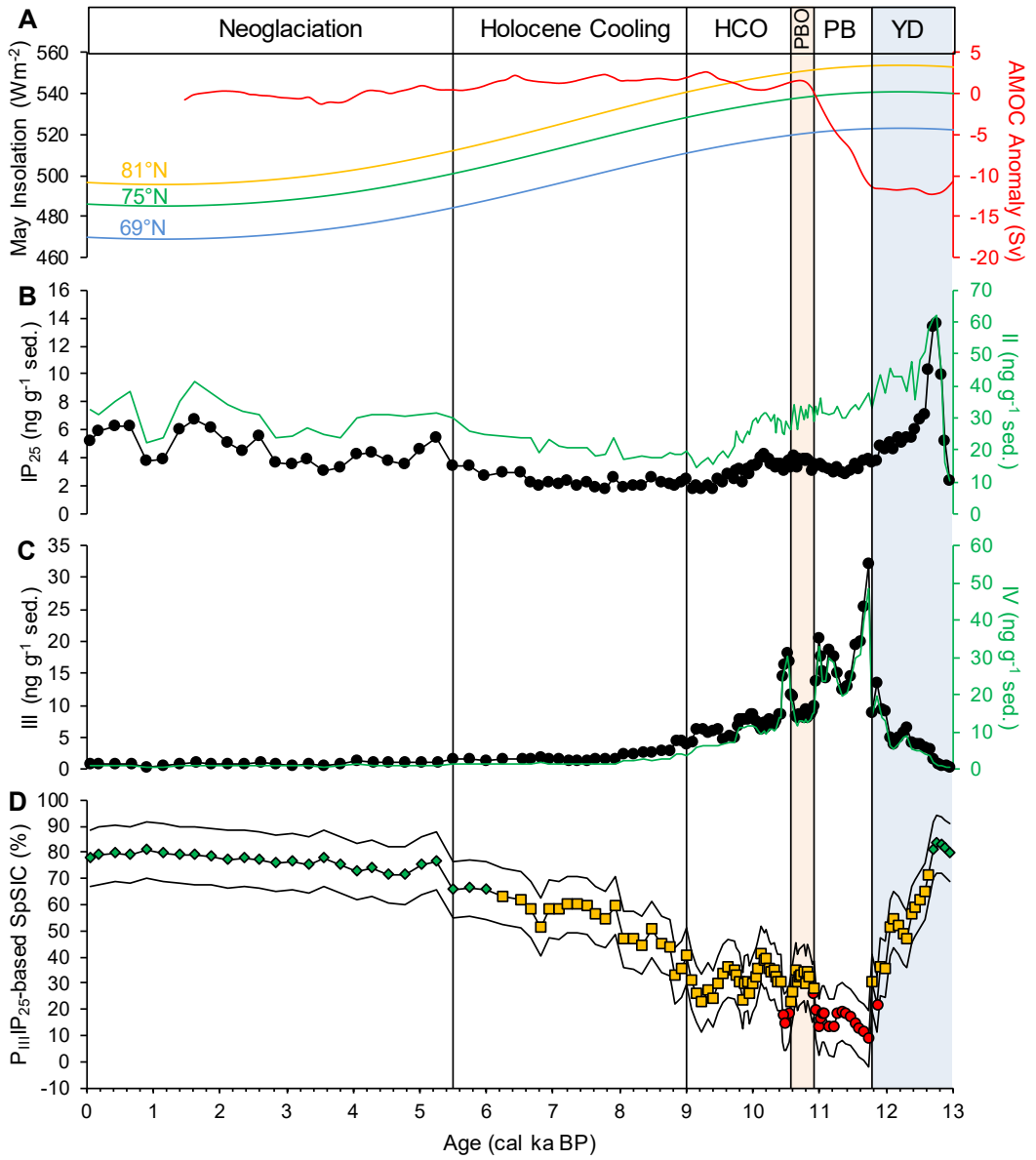

Figure 4.11: Proxies of core GC11, and modelled climate data spanning the last 13 cal. kyr BP: (A) Modelled AMOC anomaly describing the global oceanic overturning (Ritz et al., 2013), and average May insolation values (Laskar et al., 2004) at several latitudes; (B) Sympagic IP_{25} and II concentrations (ng g^{-1}); (C) Pelagic HBI III and IV concentrations (ng g^{-1}); (D) $P_{III}IP_{25}$-based SpSIC profile with CT model classification of core horizons analogous to Fig. 4.3a, 4.6a, 4.8a. Periods of distinct climate conditions are delineated by black lines. Abbreviations denote: YD – Younger Dryas; PB – Preboreal; PBO – Preboreal Oscillation; HCO – Holocene Climatic Optimum.

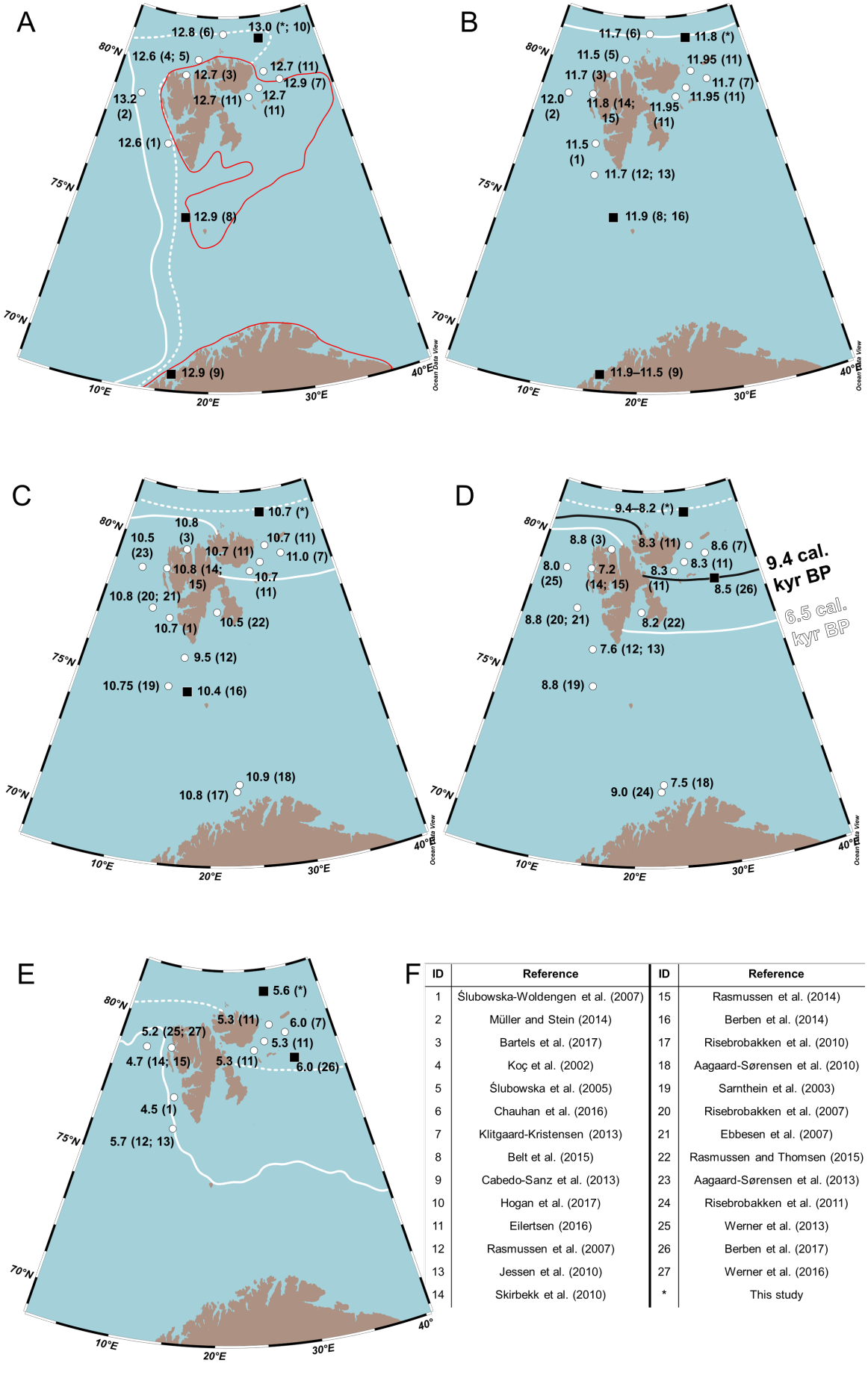

F

ID	Reference	ID	Reference
1	Ślubowska-Woldengen et al. (2007)	15	Rasmussen et al. (2014)
2	Müller and Stein (2014)	16	Berben et al. (2014)
3	Bartels et al. (2017)	17	Risebrobakken et al. (2010)
4	Koç et al. (2002)	18	Aagaard-Sørensen et al. (2010)
5	Ślubowska et al. (2005)	19	Sarnthein et al. (2003)
6	Chauhan et al. (2016)	20	Risebrobakken et al. (2007)
7	Klitgaard-Kristensen (2013)	21	Ebbesen et al. (2007)
8	Belt et al. (2015)	22	Rasmussen and Thomsen (2015)
9	Cabedo-Sanz et al. (2013)	23	Aagaard-Sørensen et al. (2013)
10	Hogan et al. (2017)	24	Risebrobakken et al. (2011)
11	Eilertsen (2016)	25	Werner et al. (2013)
12	Rasmussen et al. (2007)	26	Berben et al. (2017)
13	Jessen et al. (2010)	27	Werner et al. (2016)
14	Skirbekk et al. (2010)	*	This study

Figure 4.12: Proposed spatio-temporal development of sea ice conditions at core sites examined herein (black squares) and in previous investigations (white circles), where black numbering represents the timing of: (A) The YD (ca. 13.0–11.7 cal. kyr BP) onset. The extent of Svalbard and Fennoscandian ice sheets at ca. 13 cal kyr BP is shown in red (Bradley and England, 2008); (B) The YD–Preboreal transition (ca. 11.7–10.8 cal. kyr BP); (C) The onset of increased AW inflow during the Early Holocene and HCO (ca. 10.8–10.4 cal. kyr BP); (D) The Mid-Holocene Cooling onset (MHC; ca. 9.4–6.5 cal. kyr BP). Southward ice expansion from 9.4 cal. kyr BP to ca. 6.5 cal. kyr BP is shown by solid black and white lines, respectively; (E) Continued cooling (i.e. Neoglaciation) and ice expansion over the last ca. 6.0 cal. kyr BP. Bracketed numbers denote data sources, summarised in (F). In maps A–E, the suggested annual maximum and minimum sea ice extent is shown by solid and dotted white lines, respectively.

There are several possible explanations for this disparity. First, the known producers of HBI biomarkers presented herein include diatoms which inhabit relatively shallow depths of the photic zone (e.g. Brown et al., 2014c; Belt et al., 2017), and are probably susceptible to solar insolation changes during the spring sympagic and pelagic diatom blooms (Jansen et al., 2009; Signorini and McClain, 2009; Leu et al., 2011). May–June solar insolation was approaching maximum values during the 13.0–12.0 cal. kyr BP period (Fig. 4.11a) and was ca. 10% higher than today (Laskar et al., 2004). The insolation increase potentially hastened the melting of sea ice prior to the spring diatom bloom, increasing the heat budget of the surface waters and delaying ice formation in autumn. This could have caused a long-term albedo decrease and thinning of the sea ice cover via a positive feedback mechanism (e.g. Perovich and Polashenski, 2012; Smedsrud et al., 2013). Recent results of model studies (e.g. Berger et al., 2013; Stranne et al., 2014) emphasize the potential of such radiative forcing to decrease the extent and thickness of sea ice over time, creating a regime dominated by seasonally open waters. It is possible that such radiative forcing could have gradually reduced the sea ice cover at the GC11 site after 12.7 cal. kyr BP. Further, the effect of rising insolation was potentially more pronounced in the Kvitøya Trough, since May–June insolation values were higher at the GC11 core location relative to sites KA11 and 1200 (Fig. 4.11a). Additionally, sub-surface inflow of AW with the WSC could have further contributed to

less severe spring sea ice conditions at the site during the YD. Winter upwelling of AW at the core site would bring nutrients to the photic zone and enhance phytoplankton productivity during the spring bloom, as well as reduce ice thickness via heat-induced underside melting (e.g. Ivanov et al., 2012; Meier et al., 2014, and references therein). Further, increased light penetration through leads and polynya in the ice during this time could have triggered pelagic blooms directly underneath the ice (e.g. Arrigo et al., 2012; Assmy et al., 2017). Wollenburg et al. (2004) observed a paleoproductivity peak in the nearby core PS2138-1 north of the Kvitøya Trough after 12.5 cal. kyr BP, and attributed this increase to the influence of Atlantic-derived water along the northern Barents Sea margin. Further, seasonal sea ice conditions and proximal, highly-productive oceanic fronts during the YD were also inferred in several studies along the western and northern Svalbard margin, at sites directly influenced by AW (e.g. Koç et al., 2002; Ślubowska et al., 2005; Ślubowska-Woldengen et al., 2007, 2008). This also agrees with an early (ca. 12.5 cal kyr BP) increase in surface water salinities inferred from heavier $\delta^{18}O$ values of planktic foraminifera and increased biogenic production at the Yermak Plateau (Nørgaard-Pedersen et al., 2003; Birgel and Hass, 2004), as well as farther along the NAC inflow path in the Laptev Sea (Fahl and Stein, 2012). Decreased influence of cold surface waters was also inferred at ca. 12.2 cal kyr BP in the Greenland Seas (Pearce et al., 2013, 2014). More recently, Bartels et al. (2017) attributed similar conditions in a core from the Woodfjorden mouth (North Svalbard) to periodic upwelling of AW during the early YD. Such a mechanism of AW upwelling could have enhanced the pelagic phytoplankton productivity and contributed to slightly reduced SpSIC at the GC11 site after 12.7 cal kyr BP (Fig. 4.11d). Conversely, localised meltwater discharges from, or outward expansion of the Fennoscandian (Vorren and Plassen, 2002) and Svalbard (Hormes et al., 2013) ice sheets to core sites 1200 and KA11, respectively, could have strengthened water column stratification,

promoting sea ice formation and hampering AW upwelling in the Kveithola Trough and Andfjord. Similar scenarios of contrasting perennial and seasonal sea ice conditions at the western and northern Svalbard shelves were potentially a recurrent feature throughout the last glaciation (Kremer et al., 2018a, b). While the inference of seasonal sea ice in the GC11 record also agrees with an early sea ice decline after 12.6 cal. kyr BP inferred from decreasing PIP_{25} values in a record from the Western Svalbard margin (Müller and Stein, 2014), where a similarly short period of 13.2–12.6 cal. kyr BP was attributed to the YD sea ice expansion, this may be attributable to potential caveats of the age model. Nonetheless, seasonally open sea ice conditions in the Kvitøya Trough during the YD are supported by the clay-mineral assemblage analysis by Hogan et al. (2017), who noted the presence of coarse-grained sediment in core GC11 as contrasting to a record south of Kvitøya, which exhibited a distinct lack of IRD and was therefore characterised by closed/perennial sea ice cover during the YD (Klitgaard-Kristensen et al., 2013).

The YD–Holocene transition (ca. 12.0–11.7 cal. kyr BP) in core GC11 is characterised by a significant retreat of $P_{III}IP_{25}$-derived SpSIC to 10–20% (Fig. 4.11d). An associated shift of CT predictions from intermediate to marginal sea ice conditions is observed at ca. 11.7 cal. kyr BP, consistent with the termination of the YD in the NGRIP ice core (Rasmussen et al., 2006). This period corresponds to the general amelioration of environmental conditions, coincident with maximum summer insolation and gradual AMOC recovery (Fig. 4.11a; Ritz et al., 2013), which rejuvenated AW inflow (Bakke et al., 2009) and increased primary production and SSTs throughout the Svalbard margins and the central Barents Sea by ca. 11.7 cal kyr BP (Fig. 4.12b). Accordingly, the combined effect of the maximum May-June insolation since 12.0 cal. kyr BP and an early AMOC recovery (Fig. 4.11a) likely caused a rapid northward migration of the sea ice margin to the GC11 site between 12.0–11.7 cal. kyr BP, as

evidenced by the decrease of $P_{III}IP_{25}$-derived SpSIC estimates and a switch of CT model predictions from intermediate to marginal ice cover (Fig. 4.11d). This agrees with the position of sea ice edge at the northern Svalbard margin at ca. 11.7 cal. kyr BP proposed by Chauhan et al. (2016) (Fig. 4.12b). Additionally, the maximum concentration of triene III at ca. 11.7 cal. kyr BP (32.0 ng g^{-1}; Fig. 4.11c) is considerably higher than that observed in proximal surface sediments (13.0 ± 8.3 ng g^{-1}; Belt et al., 2015), potentially indicating more productive than modern MIZ conditions in the Kvitøya Trough during the Earliest Holocene. This is consistent with the findings of Wollenburg et al. (2004), who reconstructed approximately two-fold higher than modern primary productivity during the YD–Holocene transition, which approached the contemporary production in the Barents Sea MIZ (Pathirana et al., 2015), in a proximal core north of the GC11 site. The input of coarser sediments at site GC11 between ca. 12–11 cal. kyr BP indicates possible iceberg rafting (Hogan et al., 2017) and is potentially a response to the terminal deglaciation of remaining glaciers on Svalbard during this period (e.g. Hormes et al., 2013; Chauhan et al., 2016).

Ameliorated conditions of the Earliest Holocene persisted until ca. 11.0 cal. kyr BP, with relatively low IP_{25} content (2.9–3.9 ng g^{-1}), peak concentrations of triene III (12.5–25.4 ng g^{-1}), and low SpSIC values (11–20%) indicating highly productive MIZ conditions with a proximal spring sea ice edge. Accordingly, the CT model predicts marginal sea ice conditions throughout this interval (Fig. 4.11d). The warm conditions are interrupted by a northward expansion of the sea ice edge between ca. 11.0–10.7 cal. kyr BP. The period is characterised by a slight increase of IP_{25} (3.1–4.1 ng g^{-1}) and a concurrent decrease of HBI III concentrations (8.2–9.9 ng g^{-1}) (Fig. 4.11b, c). Increased, consistent SpSIC values (26–35%) indicate a stable position of the sea ice margin south of the core site. The increase of SpSIC values is consistent with a switch in the CT assessment, which predicts intermediate sea ice conditions throughout the period. This

short-term extension of sea ice cover potentially corresponds to the Preboreal Oscillation (PBO), when a North Atlantic meltwater intrusion facilitated an increase in ice formation (Fisher et al., 2002; Husum and Hald, 2002; Hald et al., 2007). This is consistent with the sudden increase of $P_{III}IP_{25}$-derived SpSIC and a switch of CT predictions from marginal to intermediate ice conditions from 11.0–10.7 cal. kyr BP in the record (Fig. 4.11d). Similar timing and duration of the PBO have been identified in various records from the western and northern Svalbard margins (e.g. Ślubowska et al., 2005; Skirbekk et al., 2010; Aagaard-Sørensen et al., 2013; Rasmussen et al., 2014; Bartels et al., 2017), southern Spitsbergen shelf (e.g. Berben et al., 2014) and the southwestern Barents Sea (e.g. Aagaard-Sørensen et al., 2010). Small temporal discrepancies between the records (ca. 0.2 cal. kyr BP) are probably attributable to chronological uncertainty due to regional variability of reservoir ages in the Barents Sea and Svalbard regions (e.g. Bondevik et al., 2006; Austin et al., 2011; Rasmussen and Thomsen, 2015).

Following the cessation of the PBO at ca. 10.7 cal. kyr BP, another rapid northward migration of the sea ice edge towards the core site is evidenced by a significant increase of triene III (11.4–18.2 ng g^{-1}) and a concurrent decrease of IP_{25} concentrations (3.1–4.0 ng g^{-1}) (Fig. 4.11b–c). Relatively low $P_{III}IP_{25}$-derived sea ice estimates (15–27%) and CT predictions of marginal sea ice cover indicate the close proximity of the winter maximum sea ice margin to the core site during ca. 10.7–10.5 cal. kyr BP (Fig. 4.11d). This period is potentially attributable to the onset of warmer conditions due to maximum insolation and resumed AW overturning at the onset of the HCO (Fig. 4.11a). WSC-derived AW was likely present as a surface water mass as far the northern Barents Sea margin by 10.8 cal. kyr BP and likely contributed to resurgence of planktic and benthic foraminifera (Ebbesen et al., 2007; Jessen et al., 2010; Rasmussen and Thomsen, 2015; Werner et al., 2016) and increased temperatures

of the summer mixed layer (Sarnthein et al., 2003; Spielhagen, 2012; Rasmussen et al., 2014; Werner et al., 2016; Bartels et al., 2017), which could have accelerated the spring ice melt and contributed to SpSIC retreat and increasing HBI III concentrations observed in the GC11 record at approximately the same time. Conversely, an expansion of sea ice cover after 10.5 cal. kyr BP evident at the GC11 site from increasing SpSIC (from ca. 22% to 41%) and intermediate ice cover predicted by the CT model (Fig. 4.11d) is potentially linked to the sinking of AW beneath the photic zone after 10.5 cal. kyr BP reported for northern Svalbard (e.g. Bartels et al., 2017; van der Bilt et al., 2018). Intermediate, stable sea ice conditions persisted from 10.5–9.1 cal. kyr BP, with the ice margin located south of the core site (Fig. 4.12c). Moreover, from at least 9.4 cal. kyr BP onwards, the maximum spring sea ice edge was probably located in close proximity to core 70 from the Olga Basin, where SpSIC values and CT model assessment indicate productive MIZ conditions with minimal sea ice cover during 9.4–8.5 cal. kyr BP (Fig. 4.3a). The overall succession of the PB and HCO conditions, characterised by minimum SpSIC estimates and potentially punctuated by the PBO in core GC11 agrees well with reports of a two-step warming due to AW intrusion towards Svalbard, such as those occurring at 11.8–11.3 and 10.8 cal kyr BP in the Kongsfjorden Trough (Skirbekk et al., 2010), similar timings in the Hinlopen Trough (Koç et al., 2002) and southwestern Svalbard shelf (Rasmussen et al., 2007), and slightly earlier warming at ca. 11.4 and 11.1 cal kyr BP in the northeastern Norwegian Sea (Hald and Hagen, 1998).

Gradual sea ice expansion is observed over the 9.1–6.5 cal. kyr BP period. The initial increase of SpSIC to ca. 43–50% at 9.1 cal kyr BP coincides with decreased summer insolation (Fig. 4.11a) and reports of widespread surface water cooling at ca. 9.0–8.8 cal. kyr BP (e.g. Ebbesen et al., 2007; Risebrobakken et al., 2010, 2011; Spielhagen, 2012; Werner et al., 2016), which could have resulted in decreased diatom

productivity evidenced by concurrently low IP_{25} and HBI III concentrations during this time (1.8–3.5 ng g^{-1} and 1.3–4.6 ng g^{-1}, respectively) (Fig. 4.11b–c). Another abrupt southward ice expansion is also evident between 8.4–8.2 cal. kyr BP, with SpSIC values of ca. 60% are consistently observed until ca. 6.0 cal. kyr BP. A similar SpSIC increase is also observed in the Olga Basin record (Fig. 4.3a), indicating a position of the spring sea ice edge south of 78.7°N after ca. 8.4 cal. kyr BP (Berben et al., 2017). The timing of the southward ice edge migration is broadly consistent with the 8.2 cal. kyr BP cold event associated with freshwater discharge from Lake Agassiz (e.g. Werner et al., 2016). The resulting stratification of the water column could have contributed to the long-term sea ice expansion at the GC11 core site (Fig. 4.11d and 4.12d), which was likely further reinforced by reducing solar insolation (Fig. 4.11a) and decreased poleward AW advection caused by increasingly frequent occurrences of negative NAO (Aagaard-Sørensen et al., 2010, 2013; Rasmussen et al., 2014). Glacier expansion on the Svalbard shelf was also indicated after ca. 7.6 cal. kyr BP (Jessen et al., 2010).

A further increase in SpSIC to values >70% at ca. 5.6 cal. kyr BP, and an accompanying shift of CT model assessment from intermediate to extensive sea ice conditions at ca. 6 cal. kyr BP (Fig. 4.11d) indicate generally colder conditions with presence of at least some sea ice at the GC11 site during the summer months (July–September; Smik et al., 2016). Additionally, the lowest concentrations of pelagic HBI III observed throughout the record (0.9 ± 0.2 ng g^{-1}) and gradually increasing IP_{25} concentrations (4.7 ± 1.1 ng g^{-1}) similar to values obtained from proximal surface sediments (5.5 ± 3.3 ng g^{-1}; Belt et al., 2015) suggest an increase (decrease) in sympagic (pelagic) diatom productivity associated with longer (shorter) seasonal ice duration. Similarly, extensive SpSIC (>60%) also prevailed at core site 70 south of Kvitøya Trough from ca. 5.9 cal. kyr BP (Berben et al., 2017) (Fig. 4.3a), and the ice edge reached site KA11 in south-western Spitsbergen at ca. 1.1 cal. kyr BP (Berben et al.,

2014) (Fig. 4.12e). The timing of south-westward expansion of ice cover at core sites presented herein agrees with that of the Neoglaciation onset, and is potentially due to an initial freshening and cooling of the surface waters as a result of weakened AW inflow (Klitgaard-Kristensen et al., 2013; Berben et al., 2014, 2017; Groot et al., 2014; Rasmussen et al., 2014; Werner et al., 2016) and increased drift ice transport to the Barents Sea (Werner et al., 2013), followed by gradual long-term thickening and prolonged annual duration of sea ice cover as a result of decreasing insolation (Fig. 4.11a). Although no evidence of further SpSIC increase was observed at the GC11 site, the ice edge probably advanced farther south after 2.8 cal kyr BP in the central Barents Sea (Knies et al., 2016; Berben et al., 2017), coincident with widespread surface and sub-surface water temperature decreases (e.g. Balascio and Bradley, 2012) and reduced productivity (Pathirana et al., 2015), despite somewhat contrasting reports of ice retreat and warmer bottom water on the western Svalbard margin (Werner et al., 2014).

4.4.1.4.2 Critical comparison between $P_{III}IP_{25}$- and CT-based sea ice inferences

As described in section 4.4.1.4.1, broadly consistent results were obtained from the combined use of CT and $P_{III}IP_{25}$ methods in core GC11, in agreement with inferences from cores 70, 1200, and KA11. Generally, the GC11 record (Fig. 4.11, 4.13, 4.14) mirrors the gradual insolation- and ArW-mediated cooling observed in core 70 (Fig. 4.3; Navarro-Rodriguez, 2014; Berben et al., 2017) and extends to the YD stadial. Nevertheless, discrepancies are observed for multiple samples (n = 40) and correspond to CT classification of horizons with >50% and >10% $P_{III}IP_{25}$-based SpSIC into intermediate (n = 19) and marginal (n = 21) sea ice classes, respectively (Fig. 4.14a). As with cores KA11 and 1200, some of these discrepancies may potentially be attributed to periods of reduced correlations between IP_{25} and II during the climatically unstable YD–Holocene transition (Fig. 4.13c) or horizons where classification probability is not

certain (n = 10; Fig. 4.14b, c). However, these considerations alone still fail to explain the majority of discrepancies (n = 30), including samples classified into the intermediate sea ice class during the mid-Holocene ice expansion at ca. 8–6 cal kyr BP, in particular (Fig. 4.14a). This highlights the fact that explaining differences between CT- and $P_{III}IP_{25}$-based inferences of sea ice conditions is not always straightforward, and may not always be related to unexpected HBI distributions in downcore records relative to those characterising the CT surface sediment training set. Instead, as mentioned in section 4.4.1.2, inconsistencies may arise due to $P_{III}IP_{25}$-related influences, the most significant of which is potentially that of the c-factor on SpSIC estimates. Within the Barents Sea surface sediment dataset (Fig. 3.1a, Chapter 3), the c-factor varies considerably from ca. 0.1 for samples with 1–10% overlying SpSIC to over 10 in the near-perennial ice conditions of northeastern Svalbard. For core GC11, even a relatively small change in the c-factor (from c = 0.63 to c = 1) results in a significant increase in consistency between CT predictions and $P_{III}IP_{25}$-based SpSIC, with the number of discrepancies reduced from 40 to 28, of which 9 were not classified with certain probability. Similarly, optimizing the c-factor (c = 1.17) to maximize the least-squares correlation coefficient (r = 0.95) of $P_{III}IP_{25}$ and SpSIC data presented by Smik et al. (2016) further decreased the number of discrepancies to 23. In particular, only 5 horizons exhibited discrepancies during ca. 8–6 cal kyr BP, instead of 12 observed with c = 0.63. At the same time, the overall variability of SpSIC estimates is preserved throughout the record for all values of c (Fig. 4.15). This highlights the difficulty in determining an appropriate c-factor value when dealing with a spatially expansive dataset characterised by pronounced sea ice seasonality (Fig. 3.1a), and reinforces the previous recommendation of omitting inflexible SpSIC thresholds of 10% and 50% when comparing CT predictions to $P_{III}IP_{25}$-based SpSIC (section 4.4.1.2). In any case,

attaining complete agreement using either approach as a reference may not be desirable, given their significantly different assumptions (Table 3.4, Chapter 3).

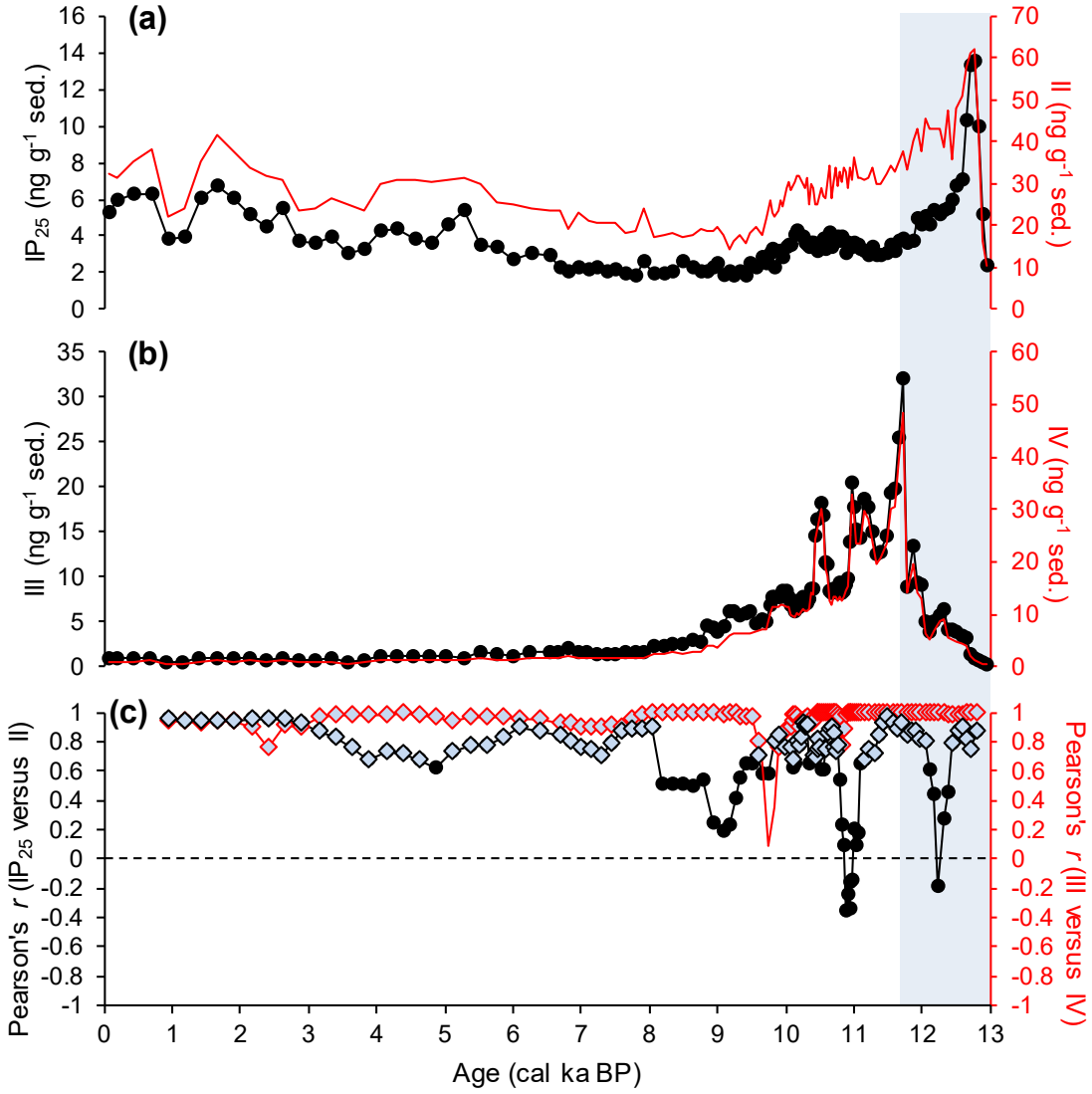

Figure 4.13: HBI concentrations and correlations for core GC11 (north-eastern Barents Sea margin). The illustrated profiles are analogous to those shown in Fig. 4.4, 4.7, and 4.9. The light blue vertical bar highlights the YD (12.95–11.70 cal kyr BP).

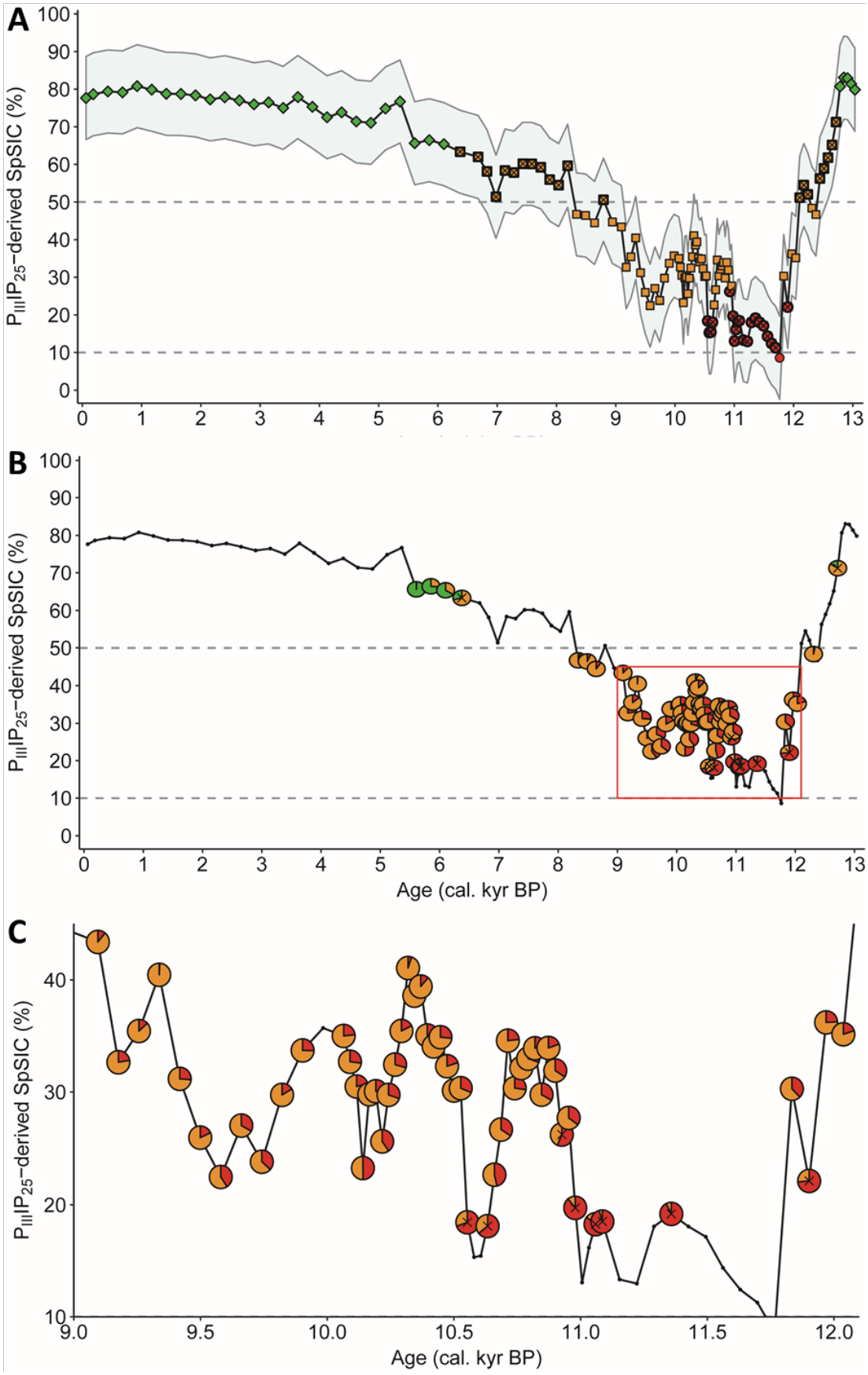

Figure 4.14: Sea ice proxy data for core GC11 analogous to that shown for other cores in Fig. 4.3, 4.6, and 4.8.

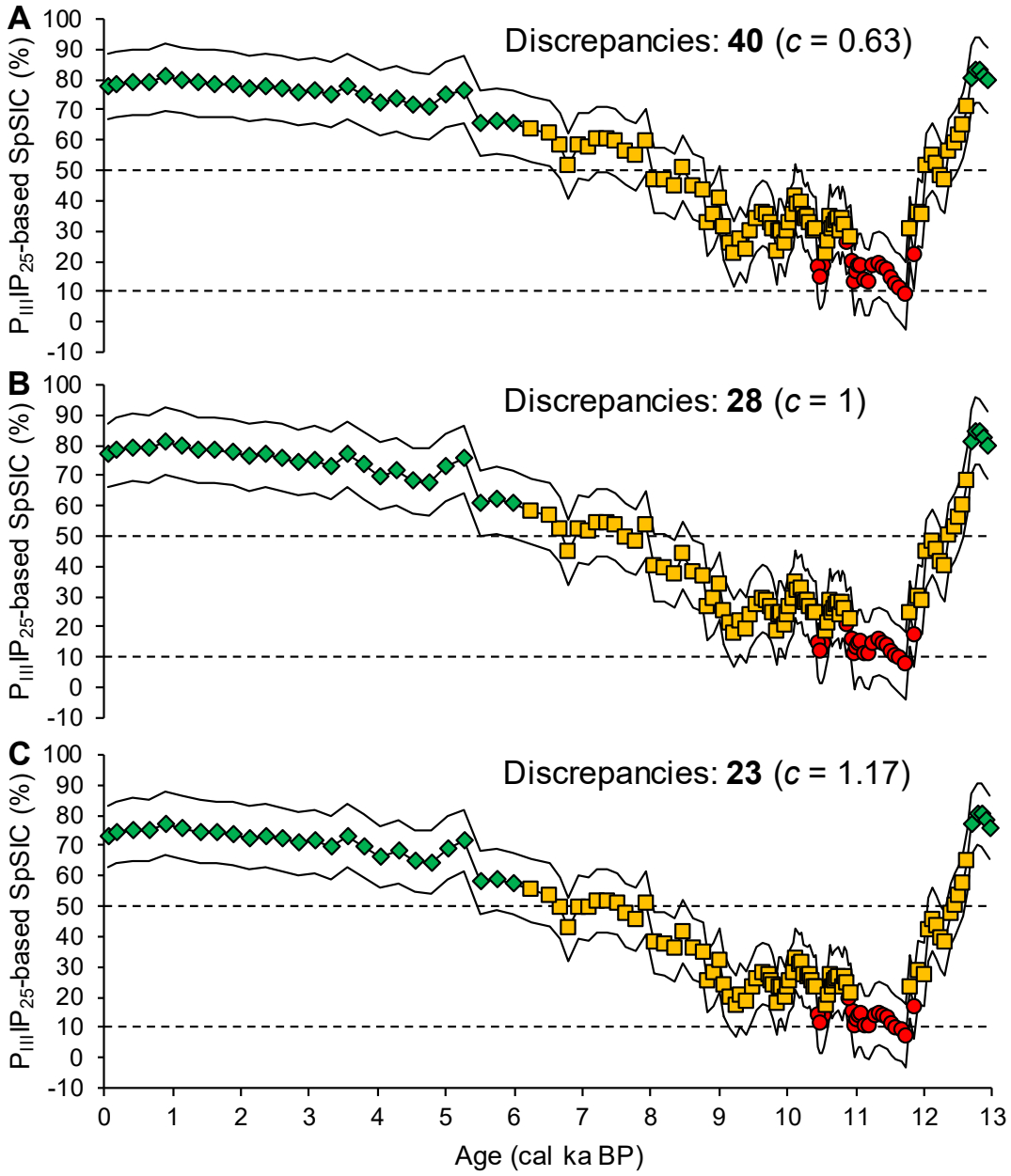

Figure 4.15: A comparison of the number of discrepancies of at least 1% between CT model predictions and $P_{III}IP_{25}$-based SpSIC estimates obtained using *c*-factor values of 0.63 (A), 1 (B), and 1.17 (C), where the latter was obtained by optimising the $P_{III}IP_{25}$–SpSIC regression of Smik et al. (2016) for a maximum correlation coefficient *r*.

Another important consideration is the consistent quantification of all biomarkers between the training set and new samples. Accurate quantification of HBIs via mass spectrometric techniques involves the use of an instrumental Response Factor (RF), usually obtained external standard calibration, to account for mass spectral fragmentation efficiency differences between individual biomarkers and the internal standard (Belt et al., 2012a). Moreover, HBIs usually exhibit different RF values (Belt

et al., 2014), necessitating instrument calibration via separate standard series for each biomarker and subsequent quality monitoring using a reference sediment material of known HBI concentration. Any RF changes thus affect the HBI distribution and resulting CT model rules, such that the use of different quantification methods (RF values) for the model training set and new (e.g. downcore) samples will cause the model to fail when classifying the latter. In this study, assigning the same value to all RFs shifts the HBI composition towards higher relative abundances of III and IV (Fig. 4.16a). When these modified downcore distributions are classified using the CT model trained with correctly quantified surface sediments, the model fails to identify the extensive sea ice class completely and exhibits a high discrepancy with $P_{III}IP_{25}$-based SpSIC. Directly comparable quantification is therefore necessary for the training and new sample sets, and the CT must be re-built with a new training set should a change in quantification methods occur.

Finally, the relatively high susceptibility of more unsaturated HBIs, particularly those with trisubstituted double bonds (III and IV, in this case), towards degradative processes could also alter biomarker distributions in downcore sedimentary sequences relative to those in surface sediments. The lower stability of HBI trienes towards photodegradation and autoxidation in sea ice and the water column (Rontani et al., 2014a, b) possibly implies their increased potential for aerobic degradation in upper oxic sediments, which was shown recently to affect even the more diagenetically stable IP_{25} (Rontani et al., 2018b, b). Thus, selective removal of III and IV from the HBI distribution may adversely affect $P_{III}IP_{25}$-based SpSIC estimates and CT model performance, especially under conditions of high light penetration, long residence times of algal cells in the photic zone, and low sedimentation rates, where diagenetic processes are more likely to have an effect. While it is not feasible to analytically diagnose the relative impacts of climate change and selective HBI degradation due to

the extremely high reactivity of associated photo- and oxidation products (Rontani et al., 2014a, b), examination of HBI triene concentration profiles suggests a prevailing influence of climate on the data presented herein. Specifically, the concentrations of pelagic HBI III reach and surpass those of IP_{25} (Fig. 4.4b, 4.7b, 4.9b, and 4.13b) during periods of reduced sea ice cover and generally ameliorated climate conditions inferred in previous studies, while reduced concentrations only coincide with harsh glacial conditions of the YD and the late Holocene ice expansion (Cabedo-Sanz et al., 2013; Berben et al., 2014, 2017). Moreover, downcore concentrations of III and IV are often higher than maximum values observed in surface sediments from the highly-productive MIZ, which are ca. 40 ng g^{-1} and 20 ng g^{-1} for III and IV, respectively (Belt et al., 2015). This suggests that, in this case, sedimentary aerobic degradation or other processes prior to deposition are unlikely to significantly alter downcore HBI content relative to that of proximal surface sediments. Finally, as noted previously, the alteration of HBI distributions and data structure due to disproportional and even opposing concentration increases of II relative to those of IP_{25} is the likely cause of discrepancies between $P_{III}IP_{25}$- and CT-based methods for cores 1200 and KA11, in particular (Fig. 4.7c, 4.9c, 4.10). Nonetheless, a diagenetic influence on downcore HBI concentrations cannot be discounted, particularly in older core sections or when overlying climate conditions are more likely to promote accelerated or prolonged oxidation and photodegradation. Thus, where possible, HBI distributions are probably best combined with degradation proxies, such as the recently utilized ratio of brassicasterol to 24-methylenecholesterol in near-surface sediments (Rontani et al., 2018b), and uncharacteristically low concentrations of III and IV relative to otherwise inferred climate conditions (e.g. using other proxies) should be interpreted with caution.

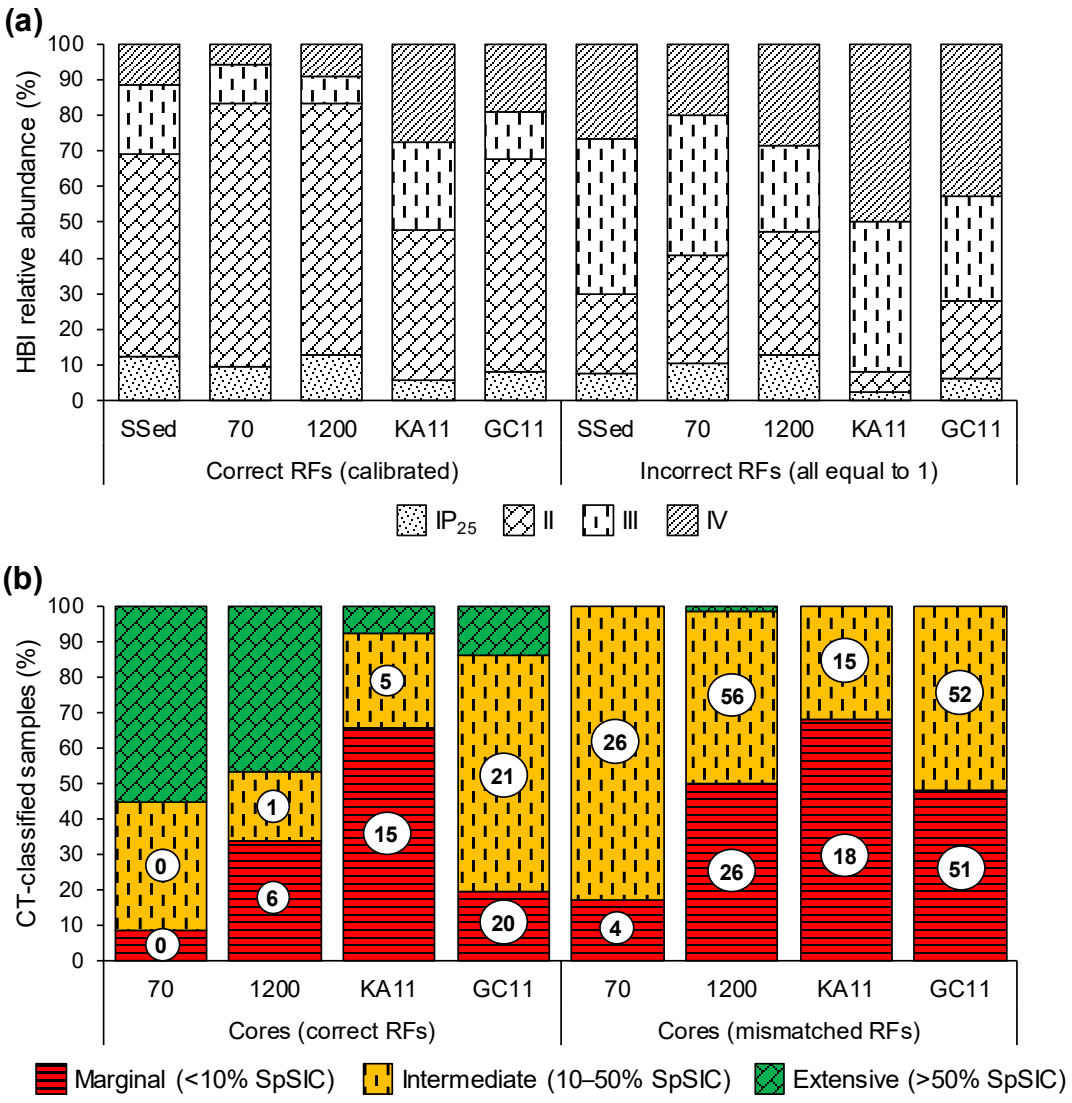

Figure 4.16: Biomarker composition and CT model output for cores 70, 1200, KA11, and GC11 using different RF combinations: (a) Averaged relative abundances of IP_{25} and HBIs II, III and IV in surface sediments and cores using calibrated and arbitrarily equated (uncalibrated) RFs; (b) Percentage distribution of core horizons classified into three categories of sea ice conditions by the CT model. "Correct RFs" are those calibrated externally, whereas "mismatched RFs" denotes the use of calibrated and uncalibrated RFs (equated to 1) for the CT training set and downcore records, respectively. Values within white circles correspond to the number of horizons classified into a given category of sea ice conditions where a discrepancy with $P_{III}IP_{25}$-based SpSIC estimates was observed. No samples were misclassified into the extensive (>50% SpSIC) sea ice category.

4.3.2 Millennial-scale HBI triene ratio variability as a bloom indicator

In contrast to the generally consistent sea ice reconstructions obtained using the CT and $P_{III}IP_{25}$ methods, HBI triene ratio values showed variable consistency with paleo-productivity inferences based on the cores presented herein (Fig. 4.1) and other investigations in the Barents Sea. Interestingly, all inconsistencies appear during the YD and the Early Holocene prior to ca. 10 cal kyr BP. The remainder of the record (ca. 10 cal kyr BP–present) is in good agreement with Holocene paleoceanography. Simultaneous ratio increases observed at ca. 10 cal kyr BP in cores 1200, KA11, and GC11 (Fig. 4.17b–d) coincide with the return of planktic and benthic foraminifera, reduced influence of IRD and meltwater, and continuous surface AW presence with resumed overturning throughout Svalbard waters between by ca. 10–9.6 cal kyr BP (Risebrobakken et al., 2011; Rasmussen et al., 2014; Łącka et al., 2015). Thereafter, core 1200 exhibits relatively low HBI triene ratios consistent with continuous AW upwelling and ice-free conditions which prevent rapid development of ice-edge spring blooms in the contemporary Barents Sea (Chapter 3). Consistent triene ratio variability characterises cores 70 and GC11 in the extensively ice-covered northern Barents Sea. Both records display higher ratios from ca. 9–6 cal kyr BP, with slightly decreased values thereafter. This generally agrees with the onset of increased sea ice cover (Fig. 4.17) and Svalbard glacier expansions during colder conditions less influenced by AW and driven by decreasing insolation in the Barents Sea (e.g. Hald et al., 2007; Ślubowska-Woldengen et al., 2007; Jessen et al., 2010; Rasmussen et al., 2014), as previously inferred for core 70 (Belt et al., 2015; Berben et al., 2017). Notably, while the relative HBI triene ratio variability is similar for cores 70 and GC11, which both experienced a southward ice advance during the last 6 cal kyr BP, the generally higher ratios for core 70 (>0.62; Fig. 4.17a) suggest it was characterised by productive and/or prolonged spring blooms throughout the Holocene, which were less pronounced in core

GC11 throughout this interval. This is not surprising given the more northern location of the latter, where reduced annual duration of stratification and light availability relative to core 70 potentially reduced phytoplankton productivity during the Holocene. Interestingly, a reverse trend is observed in core KA11, where the HBI triene ratio gradually increased since 10 cal kyr BP, with values >0.62 indicating spring blooms since the onset of the Neoglacial at ca. 6 cal kyr BP (Fig. 4.17c). Unlike cores 70 and GC11, the KA11 site was relatively ice-free during the Holocene (Berben et al., 2014; Belt et al., 2015). However, a highly-productive ice edge likely remained proximal to the Kveithola Trough following the Neoglacial ice advance, as previously suggested for Storfjorden (Rasmussen and Thomsen, 2015; Knies et al., 2016). High productivity fuelled by seasonal sea ice-induced stratification and AW upwelling could have propagated towards the KA11 site at 6 cal kyr BP, inducing spring blooms and causing slight increases in the HBI triene ratio. This is in agreement with a final triene ratio increase (>0.65) when the ice edge reached the core site at ca. 1.1 cal kyr BP (Fig. 4.17c; Belt et al., 2015), coincident with a productivity increase inferred from higher foraminiferal content and $CaCO_3$ (Berben et al., 2014; Groot et al., 2014).

Despite the consistency of HBI triene ratio increases with spring bloom and sea ice dynamics since ca. 10 cal kyr BP–present, cores 1200 and KA11 are characterised by sharp, unexpected triene ratio increases throughout the YD, with a similar, but much less prominent trend observed in core GC11. Ratio excursions to values >0.62 coincide with heavy sea ice cover during this period inferred from both CT and $P_{III}IP_{25}$. Conversely, the time-transgressive YD–Holocene transition (ca. 11.9–11.5 cal kyr BP) and the Early Holocene (11.5–10 cal kyr BP), characterised by rapid ice retreat, exhibited the lowest HBI triene ratio values throughout the records (Fig. 4.17). On one hand, neither observation is consistent with primary productivity (and, more specifically, bloom intensity) conditions inferred from previous investigations in the

Barents Sea. Specifically, in addition to extensive sea ice cover, the YD stadial was characterised by cold, meltwater-influenced conditions with severely reduced productivity inferred from high IRD input, planktic $\delta^{18}O$ depletions and undetectable foraminifera in core KA11 (e.g. Berben et al., 2014; Groot et al., 2014), with similar observations of low biogenic calcite and marine organic matter in core 1200 (Knies et al., 2003; Ebbesen and Hald, 2004; Knies, 2005; Cabedo-Sanz et al., 2013). Together with low concentrations of sterols and HBIs (Belt et al., 2015; Fig. 4.7a–b and 4.9a–b), this does not support an HBI triene ratio increase during the YD, and a decrease would instead be expected under the assumption that the triene ratio is dependent on bloom intensity (i.e. productivity). On the other hand, the HBI triene ratio could be associated with spring bloom occurrence in salinity- and/or temperature-stratified surface waters (e.g. Wassmann et al., 2006; Signorini and McClain, 2009; Leu et al., 2011; Wiedmann et al., 2017), rather than bloom intensity (productivity). Indeed, numerous records indicate the existence of seasonally open sea ice conditions, albeit of limited annual duration, along the AW inflow path during the YD (e.g. Koç et al., 2002; Ślubowska et al., 2005; Ślubowska-Woldengen et al., 2007, 2008; Bartels et al., 2017). Meltwater-induced haloclines and increasing insolation (Laskar et al., 2004) at this time could have facilitated a mechanism of spring bloom development similar (but more time-limited) to that characterising the modern Barents Sea shelf, increasing HBI triene ratio values despite low absolute HBI concentrations. Nonetheless, neither scenario explains reduced triene ratios during the MIZ-like conditions of the YD-Holocene transition (Fig. 4.17b–d), characterised by intermediate SpSIC, high concentrations of pelagic HBIs III and IV (Fig. 4.4b, 4.7b, 4.9b, 4.13b, and 4.17), and a clear return of biogenic production supported by sub-surface AW throughout the study area (e.g. Knies et al., 2003; Wollenburg et al., 2004; Aagaard-Sørensen et al., 2010; Risebrobakken et al., 2011; Rasmussen and Thomsen, 2015), albeit meltwater and IRD input likely persisted

until ca. 10 cal kyr BP, at least on the western and northern Svalbard shelves (Hald et al., 2007; Rasmussen et al., 2014).

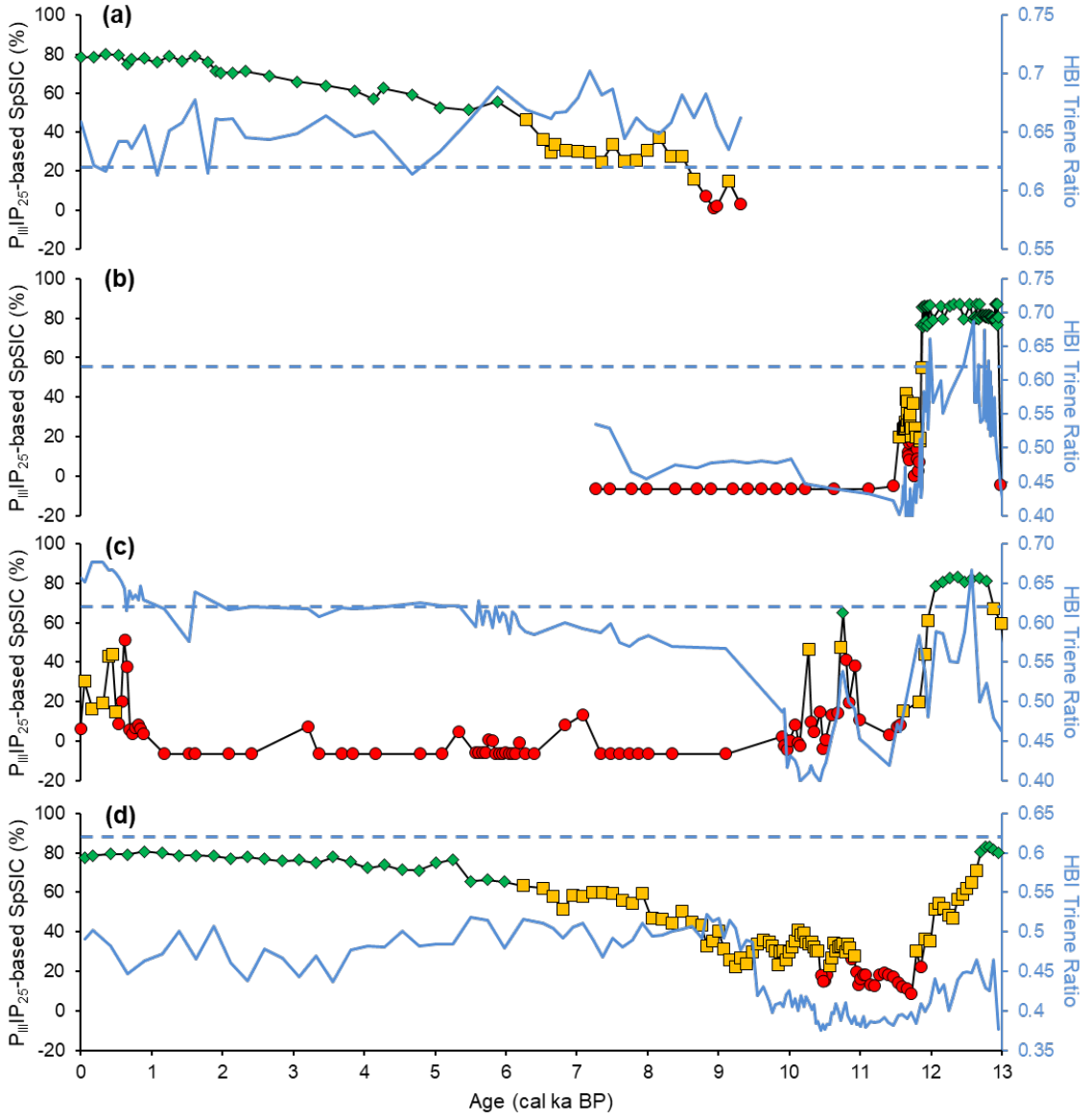

Figure 4.17: $P_{III}IP_{25}$-based SpSIC estimates (black line; left-hand y-axis) with overlaid CT predictions of sea ice conditions, and HBI triene ratios (blue line; right-hand y-axis) for core: (a) 70; (b) 1200; (c) KA11; (d) GC11. The dashed blue line is a tentative HBI triene ratio threshold (Chapter 3) separating areas of phytoplankton blooms in well-stratified waters (>0.62) from areas of reduced production due to slower development of weaker stratification (<0.62), such as the contemporary western Barents Sea.

Overall, the HBI triene ratio is seemingly consistent with shifts in pelagic bloom productivity (and/or duration) and sea ice conditions inferred from previous studies following the retreat of Svalbard glaciers and, therefore, reduced meltwater influence since the Early Holocene after ca. 10 cal kyr BP (Risebrobakken and Berben, 2018).

Conversely, the YD and initial transition into the Earliest Holocene, characterised by unstable fluctuations in sea ice, meltwater, and AW influence (Aagaard-Sørensen et al., 2010; Cabedo-Sanz et al., 2013; Bartels et al., 2017), exhibit unexpected increases in the HBI triene ratio during periods of near-perennial sea ice conditions and low absolute concentrations of III and IV (ca. 13–12 cal kyr BP), and decreases during productive intervals of variable, but seasonal sea ice (ca. 11.9–10 cal kyr BP). One potential reason for these disparities encompasses changes in diatom assemblage during cold stadials and glacial-interglacial transitions, which were not reproduced during interstadials (e.g. the Holocene, in particular) or in contemporary settings. Diatom assemblages in the Arctic exhibit decreasing biodiversity in more inhospitable conditions, where thick, perennial ice cover and consequential low light availability prevents winter survival of most species (e.g. Zhang et al., 1995). The contemporary Barents Sea exhibits significantly different diatom assemblages in areas of different sea ice conditions. A wealth of centric diatoms, such as those belonging to the *Thalassiosira* and *Chaetoceros* genera (von Quillfeldt, 2000; Ratkova and Wassmann, 2005; Luddington et al., 2016) are observed south of and within the MIZ, with some species characteristic of AW inflow (e.g. certain *Thalassionema*, *Paralia* and *Proboscia* spp.; Koç-Karpuz and Schrader, 1990). April–June under-ice assemblages farther north are dominated by a reduced diversity of cold-water species, such as *Flagilariopsis cylindricus*, *F. oceanica*, *Fossula arctica* (Falk-Petersen et al., 2000), *Nitzschia frigida* (Falk-Petersen et al., 1998; Henderson et al., 1998) and *Melosira arctica* (Syvertsen, 1991). The latter also drives Central Arctic spring blooms (e.g. Boetius et al., 2013; Poulin et al., 2014) as one of the most productive centric diatoms (Stecher et al., 2016) uniquely adapted to the sea ice environment through alteration of ice morphology (Krembs et al., 2011). Such reduction of diatom species richness in colder, darker conditions that limit photosynthetic activity is also apparent in paleo-records during periods of abrupt

climate change, such as the cold Heinrich Stadials (e.g. Cermeño et al., 2012) and Dansgaard–Oeschger cycles (e.g. Ampel et al., 2010). Under the assumption that the HBI triene ratio is controlled by diatom assemblage (at least in part), similar limitation of diatom biodiversity during harsh glacial conditions of the YD could have unexpectedly influenced the ratio towards higher values of III despite reduced annual duration and intensity of the spring phytoplankton bloom. However, this scenario implies that the HBI triene ratio is potentially more influenced by diatom composition variability than spring bloom intensity, and does not explain reduced HBI triene ratios during the highly-productive YD–Holocene transition and the Earliest Holocene prior to 10 cal kyr BP. A more general speculation involves the presence of yet unidentified competing influence(s) on the HBI triene ratio, which may either contradict or coincide with, and therefore potentially be masked by, spring bloom intensity and/or duration. Rapid phytoplankton growth in the central Barents Sea co-occurs with density- and temperature-based stratification within and without the MIZ, respectively (Oziel et al., 2017). Diatoms thriving in such environments often possess several morphological and biochemical adaptations, such as large cell size, relatively low surface area, structural protrusions, and efficient active buoyancy control, which allows these species to travel to areas of higher nutrient concentrations within, and avoid sinking below, the photic zone (Gemmell et al., 2016; Kemp and Villareal, 2018). Conversely, turbulent and nutrient-replete waters (such as the NAC-mediated AW) preferentially host smaller-celled, needle-shaped diatoms capable of higher nutrient uptake rates and able to survive under intense upwelling (e.g. Fragoso et al., 2018). Thus, higher HBI triene ratio values in the central Barents Sea (Fig. 3.16c–e, Chapter 3) and during the YD (Fig. 4.17b–d) may be associated with stratification and nutrient concentration adaptability of the diatom community, rather than spring bloom occurrence, duration and/or intensity. This represents one example of important influences on the diatom species composition

(and, possibly, the HBI triene ratio) that may be masked by the spring bloom. However, limited insight into the biological functions and species-specific distributions of HBIs preclude any conclusive association of stratification-based (or other) adaptations in key diatom genera with the HBI triene ratio. Such considerations, together with some inconsistencies of HBI triene ratio variability with diatom productivity and spring bloom occurrence in downcore records (Fig. 4.17) limit paleoceanographic inferences to speculation, and highlight the importance of determining HBI distributions in a wider range of cultured or *in-situ* diatom assemblages whose traits (e.g. nutrient uptake rate, cell size and shape) facilitate adaptability under contrasting conditions.

4.4 Conclusions

Downcore records encompassing different modern sea ice conditions in the Barents Sea were used to assess the spatio-temporal consistency between CT model predictions and $P_{III}IP_{25}$-based SpSIC estimates, and to further assess the potential of the HBI triene ratio to reconstruct spring bloom dynamics. The latter approach showed variable consistency with previous multi-proxy inferences of highly-productive, MIZ-like conditions in the Barents Sea. Throughout the last ca. 10 cal kyr BP, increases and decreases of the HBI triene ratio agreed with those of seasonal open water duration and pelagic productivity generally mediated by movement of the spring sea ice margin. Conversely, interpreting increases of the HBI triene ratio during extended annual sea ice duration of the YD is challenging, despite the absence of perennial sea ice cover and, therefore, the possibility of short-lived spring bloom development during this period. Similarly, excursions to lower triene ratio values during otherwise productive, intermediate sea ice conditions characterising the YD–Holocene transition and the Earliest Holocene (ca. 11.9–10 cal kyr BP) remain unexplained. The presence of yet unidentified environmental influences on the HBI triene ratio, and the consistency of its

agreement with spring bloom occurrence (and/or intensity) in other regions are also unknowns. These need to be resolved before the ratio can be confidently interpreted in downcore records by analysing HBI distributions pre- and post-sedimentation in regions of well-defined bloom seasonality, both within the polar oceans and at lower latitudes.

In contrast to HBI triene ratio-related challenges, a good overall agreement between CT- and $P_{III}IP_{25}$-based inferences of sea ice conditions was observed for all cores. The CT was able to capture both abrupt and fluctuating shifts in sea ice regimes, such as those evident during the YD stadial, as well as more gradual trends in sea ice conditions during the Holocene. However, shifts of CT model predictions occurred at variable threshold values of $P_{III}IP_{25}$-based SpSIC estimates in different downcore records.

This variability was attributed partially to the occurrence of downcore HBI distributions which are not represented in the model training dataset, most notably during intervals of unstable and rapid climate change characterising stadial-interstadial transitions. While it is not feasible to avoid this limitation, examination of data structure and distribution may pinpoint intervals where CT performance is likely to decrease. First, a consequence of CT dependency on HBI distributional changes is the necessity to use consistent quantification methods for model training and new (downcore) samples, and to use separate training sets for different Arctic regions. Second, selective removal of more unsaturated HBIs via degradation processes represents another potential error source, although this was likely not the case herein.

Further potential error sources of both methods were also identified, including the uncertain regional applicability of a uniform *c*-factor and insufficient sample density for representation of the entire SpSIC range (0–100%) within the CT model. It is therefore advised that only variations of $P_{III}IP_{25}$-based SpSIC exceeding the associated

RMSE of 11% be considered significant, and that CT model predictions should be interpreted in terms of broader changes in sea ice regimes (i.e. open water or proximal ice edge, MIZ conditions, and stable sea ice cover) rather than inflexible satellite-based numeric SpSIC thresholds (i.e. 10% and 50% SpSIC).

Despite these caveats, the complementary application of CT- and $P_{III}IP_{25}$-based approaches facilitated reconstruction of sea ice conditions near the northern Barents Sea margin spanning the last 13 cal. kyr BP. Sea ice evolution during the YD showed a shift from extensive ice cover to more seasonally open waters between 12.7–12.4 cal. kyr BP, while near-perennial ice cover is evident in records located farther south until ca. 12 cal. kyr BP. The results compound previous suggestions that long-term weakening of the ice cover as a result of maximum summer insolation and upwelling of AW may have resulted in a regional amelioration of conditions in areas influenced by the NAC, while the surrounding regions remained cold. Following the YD, ameliorated conditions persisted from ca. 12–10.7 cal. kyr BP, when the maximum sea ice edge was likely proximal to the site and coincided with the widely-reported strengthening of AW inflow and increased productivity following AMOC recovery. The ice edge likely advanced towards the Olga Basin after ca. 9.4 cal. kyr BP, controlled by decreasing summer insolation and the previously reported return of surface ArW to the region. The return of extensive spring sea ice to the core site after ca. 6.0 cal. kyr BP agrees with the well-documented glacier advances, increased ice export via the Fram Strait, and further decreases in summer insolation that characterised the Neoglaciation in the Barents Sea. Despite being grounded in HBI data alone, the complementary results obtained from CT and $P_{III}IP_{25}$-based inferences of sea ice conditions core GC11 showcase the potential of multivariate proxy methods based on distributions of several biomarkers. Additionally, the initial paleo-sea ice interpretation provided here serves as a framework for multi-proxy investigations at the core site and, more generally, in the northern Barents Sea.

CHAPTER FIVE

5. Multi-proxy characterisation of seasonal sea ice and productivity regimes at the western Barents Sea continental slope during the late Weichselian glaciation

5.1 Introduction

One of the major drivers of precipitous and accelerating Arctic sea ice decline (section 1.1.2, Chapter 1), in addition to GHG-induced anthropogenic warming (Stroeve et al., 2007; Notz and Marotzke, 2012), is the increasing inflow and temperature of Atlantic Water (AW) (Kinnard et al., 2011). This is most evident in the seasonally ice-covered Barents Sea (Fig. 1.6 and Table 1.1, Chapter 1; Fig. 5.1a), where increasing AW volume transport and temperature (Årthun et al., 2012; Oziel et al., 2016; Barton et al., 2018), coupled with recession of the Barents Sea ice cover over the last decades (e.g. Onarheim et al., 2018), have already changed the local ecosystem. Earlier ice melt and increased incidence of leads and polynyas (Willmes and Heinemann, 2016) has hastened and spatially expanded the spring phytoplankton blooms (Fig. 1.4 and Table 1.2) (Arrigo et al., 2012; Maksimovich and Vihma, 2012; Stroeve et al., 2014; Assmy et al., 2017), with potential consequences including intrusion of pelagic species northwards at the expense of ice-obligate algae (Hegseth and Sundfjord, 2008; Assmy et al., 2017; Hoppe et al., 2018), and considerable overall increases in pelagic primary productivity (Arrigo and van Dijken, 2015). Despite the latter, the reduction in sympagic organic matter deposition accompanying sea ice decline is likely to negatively affect the survivability and biodiversity of pelagic and benthic communities, at least in the Barents Sea (Søreide et al., 2010, 2013). Moreover, increasing stratification due to Arctic freshening could weaken AW overturning (e.g. Yang et al., 2016), limit nutrient

upwelling and promote smaller-celled phytoplankton (e.g. Arrigo et al., 2008; Hodal and Kristiansen, 2008). Finally, the spread of unprecedented ocean acidification (Sosdian et al., 2018) due to rising atmospheric GHGs is likely exacerbated due to increased open water area available for CO_2 sequestration (e.g. Harada, 2016), and holds potentially catastrophic implications for calcareous marine fauna (Azevedo et al., 2015). The motivation of understanding such implications and forecasting future development of high-latitude oceans in a warming climate implies paleo-reconstruction of sea ice conditions and associated responses of sympagic and pelagic biota over longer timescales.

Such paleo reconstructions can potentially be obtained through the analysis of proxy measures of sympagic and pelagic primary production in sedimentary records whose temporal coverage includes significant shifts in oceanographic and sea ice conditions. The largely consistent results of CT predictions and $P_{III}IP_{25}$-based SpSIC estimates since at least the Last Deglaciation (Chapter 4) and, in particular, opposing trends between pelagic (III and IV) and sympagic (IP_{25} and II) HBIs in regions of seasonal ice-influenced primary productivity (Chapter 3) suggest they are indicative of contrasting (i.e. sympagic versus pelagic) primary production sources. Thus, multivariate HBI distributions, supplemented by additional lipid biomarkers indicative of productivity, such as sterols (Volkman, 1986, 2006; Rampen et al., 2010), may be used to reconstruct sea ice variability and decouple primary productivity regimes over temporal windows spanning significant climate shifts. For example, the Last Glacial Maximum (LGM) in the Barents Sea between ca. 23–19 cal kyr BP (Clark et al., 2009) and eventual collapse of the Barents Sea Ice Sheet (BSIS) post ca. 18 cal kyr BP are relevant time intervals for investigating the interactions between AW inflow, Atlantic Meridional Overturning Circulation (AMOC), sea ice concentration, and primary productivity. Geochemical evidence suggests that the LGM and post-deglaciation intervals exhibited heavy

seasonal sea ice and near ice-free conditions, respectively, and were punctuated by the Heinrich Stadial 1 (HS1), when harsh glaciomarine conditions and weakened AW inflow prevented growth of biota (e.g. Müller et al., 2009; Müller and Stein, 2014; Jennings et al., 2017, 2018; Knies et al., 2018). Such contrasting conditions that characterised these time intervals, coupled with the direct interaction of AW inflow with both the maximum-extent BSIS and the adjacent sea ice margin, make the Late Weichselian Barents Sea key for elucidating the interactions between oceanographic conditions, the sea ice regime, and the associated interplay of sympagic and pelagic primary productivity. Relatively few biomarker-based sea ice reconstructions covering this time interval have been conducted in the Barents Sea (Müller et al., 2009; Müller and Stein, 2014; Knies et al., 2018), with most efforts focusing on the Younger Dryas and Holocene period spanning the last ca. 13 cal kyr BP (for a review, see Belt, 2018).

The focus of this study was, therefore, to reconstruct sea ice conditions and associated changes in primary productivity at the western Barents Sea continental slope throughout extreme climate shifts spanning ca. 25.8–15.4 cal kyr BP. To achieve this, a multivariate set of 10 geochemical biomarkers (Table 5.1) representing ice-algal and marine phytoplankton input was quantified in a marine sediment core (Fig. 5.1b) to assess the roles of ice cover and coastal polynya proximal to the Barents Sea Ice Sheet (BSIS) in sustaining both sympagic and pelagic primary productivity during three climatically contrasting periods. These can be summarised as: (i) The LGM and initial ice sheet destabilisation (ca. 25.8–18 cal kyr BP); (ii) HS1 following final BSIS collapse (ca. 18.0–16.3 cal kyr BP); (iii) The retreat of sea ice cover (ca. 16.3 cal kyr BP) preceding AMOC recovery and the onset of the Bølling-Allerød (BA) interstadial. Downcore biomarker distributions were compared to those of proximal surface sediments to determine whether data characteristic of contemporary sea ice and productivity conditions remained broadly representative over geological timescales.

Table 5.1: A list of HBI and sterol lipids utilized as biomarkers of sea ice and primary productivity regimes in the current study, with associated uses and potential limitations.

HBIs	Common use(s)	Potential limitation(s)	Present interpretation	References
IP_{25} and II	Source-specific, co-produced diatom proxies of seasonal Arctic sea ice[1, 2]. Stable within sedimentary record and resistant to photodegradation and autoxidation[3].	Require concurrent analysis of an open-water biomarker(s) to distinguish perennial ice and open water settings[4, 5, 6, 7]. Only represent productivity of minor sympagic diatoms[1, 2].	Used as indicators of sympagic diatom productivity within sea ice, where absolute concentrations and relative abundances increase with longer seasonal sea ice duration.	Belt et al. (2015[5], 2016[2], 2017[9]) Brown et al. (2014b)[1] Köseoğlu et al. (2018a,b)[7] Müller et al. (2011)[4] Ringrose (2012)[8] Rontani et al. (2011, 2014b)[3] Smik et al. (2016)[6]
III and IV	Ubiquitous pelagic diatom proxies vastly enhanced during the spring MIZ phytoplankton bloom, and limited under extensive ice conditions[5, 6, 7]. III used to derive $P_{III}IP_{25}$-based SpSIC estimates[5, 6], and IV used for CT predictions of sea ice cover[7].	Increased degradation rates relative to IP_{25} and II, at least under laboratory conditions[3]. IV (<10%) detected in sea ice, while all but one *in-situ* sources in the Arctic (*Rhizosolenia setigera*) are still unknown[9].	Used as indicators of pelagic diatom productivity in the photic zone of the water column. Absolute concentrations and relative abundances increase under highly-productive conditions.	**Reviews:** Belt and Müller (2013) Belt (2018)
Sterols				
Brassicasterol	A major constituent of marine algae and indicative of general productivity[10].	Present in sea ice[11].	Due to their reduced source-specificity, variability of all absolute sterol concentrations was interpreted as a general indicator of changes in marine productivity. Comparison of sterol relative abundance distributions downcore to those of surface sediments was used to identify similarities and differences between paleo and more recent/contemporary settings characterised by contrasting sea ice and/or productivity conditions.	Belt et al. (2013, 2018)[11] Boon et al. (1979)[15] Hassett and Crockett (2009)[19] Huang and Meinschein (1976)[14] Mühlebach et al. (1999)[18] Nichols et al. (1990)[16] Rampen et al. (2010)[10] Rontani et al. (2014a, 2016)[12] Volkman et al. (1993)[17] **Review:** Volkman (1986)[13]
Chalinasterol	An indicator of marine diatom productivity as the dominant sterol in many centric and pennate diatoms[10].	Susceptible to photodegradation and autoxidation[12]; Found in other algae (e.g. cryptomonads), and in sea ice[11, 13].		
Campesterol and β-sitosterol	Commonly associated with terrigenous input from vascular plants[14].	Found in many diatoms, where β-sitosterol often dominates the sterol assemblage[10].		
Dinosterol	A common biomarker of dinoflagellate productivity[15].	Detected as a minor constituent of diatoms (including sympagic) in polar settings[16] and cultures[17].		
Cholesterol	High proportional abundance can indicate increased marine faunal productivity[13].	Ubiquitous amongst vertebrates[18, 19] and diatoms[10].		

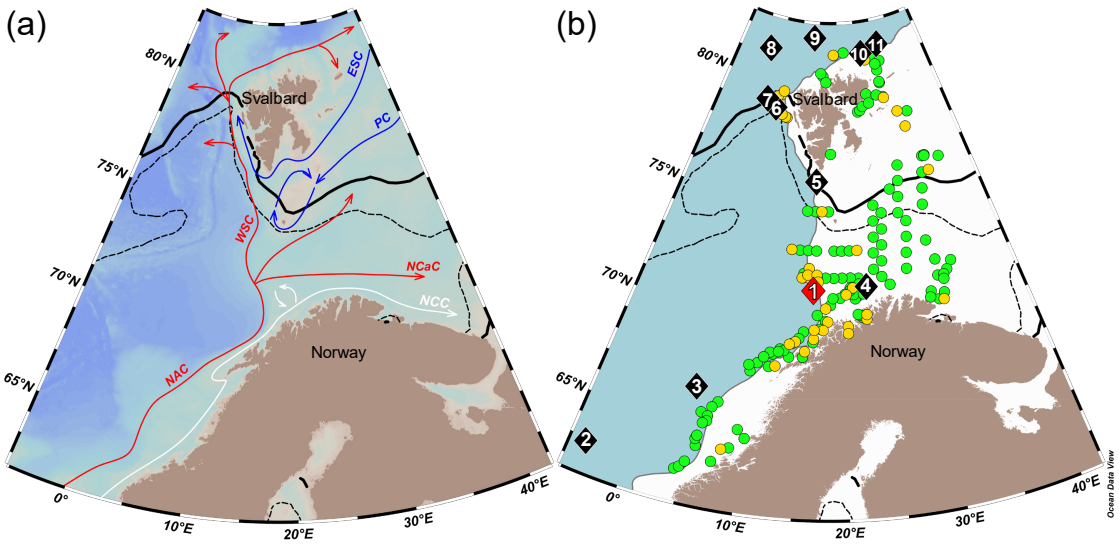

Figure 5.1: Maps of the Barents Sea showing: (a) The main inflow currents carrying AW (via the NAC, NCaC, and WSC), ArW (PC and ESC), and CW (NCC); (b) Surface and downcore sample locations. Green and orange circles correspond to surface sediment locations where HBI with or without additional sterol data were available for comparison with downcore records, respectively. Both the investigated site and referenced downcore locations are shown by numbered diamond markers: (1) GS14-190-PC01 (this study); (2) JM11-F1-19PC (Hoff et al., 2016); (3) MD95-2010 (Marcott et al., 2011); (4) JM05-85-GC (Aagaard-Sørensen et al., 2010); (5) JM02-460 GC/PC (Rasmussen et al., 2007); (6) MSM5/5-712-2 (Müller and Stein, 2014); (7) PS93/006-1 (Kremer et al., 2018a); (8) PS2837-5 (Wollenburg et al., 2004; Müller et al., 2009); (9) PS92/039-2 (Kremer et al., 2018b); (10) HH11-09GC (Chauhan et al., 2016); (11) PS2138-1 (e.g. Knies and Stein, 1998; Nørgaard-Pedersen et al., 2003). Maximum BSIS extent throughout the LGM (at ca. 21 cal kyr BP) is shown by a white polygon (Hughes et al., 2016). In both maps, dashed and solid black lines correspond to averaged SpSIC contours (April–June; 1988–2017) of 0% and 15%, respectively.

5.2 Biomarker interpretation rationale

The $P_{III}IP_{25}$ index (Belt et al., 2015; Smik et al., 2016) and CT model predictions described in Chapters 3–4 were both used alongside absolute concentrations of IP_{25} and II (Fig. 1.8, Chapter 1) as sea ice and, more generally, sympagic diatom productivity indicators (Belt and Müller, 2013; Belt, 2018). Conversely, the recent detection of HBI III and its diastereoisomer (HBI IV; Table 5.1) in the pelagic diatom *Rhizosolenia setigera* near Western Svalbard (Belt et al., 2017), together with high correlation and clear enhancement of both biomarkers near the receding spring sea ice edge (Belt et al.,

2015; Chapter 3), supported their use as indicators of pelagic diatom productivity in the Barents Sea marginal ice zone (MIZ). Overall, both the CT model and HBI concentration database in Barents Sea surface sediments presented in Chapter 3 provided an opportunity to determine whether, and to what extent, HBI distributions characteristic of different sea ice and productivity regimes in the modern Barents Sea are reproduced within the Late Weichselian sedimentary sequence.

Several sterol lipids were also analysed to complement the HBI data. Despite the use of sterols as indicators of different (e.g. marine and terrigenous) organic matter sources, many clades of microalgae, as well as vascular plants, produce the same sterols (Chapter 1, section 1.3.2). The possibility of a significant sea ice source for sterols cannot be excluded given their ubiquity in marine algae (e.g. Yunker et al., 2005; Rampen et al., 2010) and detection in sea ice algal aggregates (Belt et al., 2013), including those in the northern Barents Sea (Belt et al., 2018), where β-sitosterol, (epi-)brassicasterol, and cholesterol were the major constituents. Even 4-methyl C_{30} sterols, such as dinosterol, traditionally considered to be exclusive to dinoflagellates (e.g. Boon et al., 1979) and more specific to marine productivity (e.g. Knies, 2005), have been detected in both sea ice (Nichols et al., 1990) and diatom cultures (e.g. *Navicula* spp.; Volkman et al., 1993). Such observations highlight the possibility of overlap between sterol and more source-specific sympagic HBI producers, such that assignment of individual sterol profiles to specific organic matter sources or productivity regimes should either be avoided or treated with considerable circumspection. The current study instead focuses on downcore relative abundance distributions of a multivariate sterol set (Table 5.1), and compares these with surface sediment sterol distributions representative of contrasting sea ice (and productivity) conditions in the contemporary Barents and Norwegian Seas.

5.3 Materials and methods

5.3.1 Sediment material

The 1384 cm long GS14-190-PC01 piston core (71.475° N, 16.165°E; 949 m water depth), hereafter GS14, was recovered aboard the *Georg Ossian Sars* research vessel on June 3rd, 2014 at the southwestern Barents Sea slope (Fig. 5.1b). A detailed core chronology for the upper 694 cm of the core is available in Knies et al. (2018) and is based on six accelerator mass spectrometry (AMS) ^{14}C measurements of planktonic and benthic microfossils, including foraminifera and bivalves. This is supported by an additional six radiocarbon dates transferred to a common depth scale from the nearby 33-GC08 core (hereafter GC08) using tie-points inferred from the XRF Ca records. A total of 131 1.0 cm sediment horizons, corresponding to core depths of 11.5–523 cm (ca. 25.8–15.4 cal kyr BP), were sampled with 10 mL cut-barrel plastic syringes, freeze-dried for 24–48 hours (1 µbar; -80°C) and frozen in plastic bags at -20°C to preserve sample integrity prior to lipid extraction. While HBIs were extracted and analysed for all 131 horizons, sterol analysis was carried out separately using the same depth interval, but a lower sampling frequency (95 horizons) due to limited availability of material. The average temporal resolution between analysed horizons therefore ranged from 8–282 yr BP and 24–492 cal yr BP for HBIs and sterols, respectively. To supplement the GS14 core analysis, several Barents Sea surface sediments (n = 144; Fig. 5.1b) representing contrasting contemporary sea ice conditions, and for which HBI data was reported in Chapter 3, were re-extracted to obtain sterol distributions. Barents and Norwegian Seas were delineated using the International Council for the Exploration of the Sea (ICES) Ecoregions shapefiles (http://gis.ices.dk/geonetwork/srv/metadata/4745e824-a612-4a1f-bc56-b540772166eb). All surface and downcore data are available in Appendix E.

5.3.2 Lipid extraction and analysis

HBI extraction (IP_{25}, II, III, and IV; Table 5.1) and analysis were carried out using methods identical to those described in Chapters 2–4. Specifically, TOE extraction into DCM–MeOH (section 2.2.2.1, Chapter 2) was followed by removal of elemental sulphur (section 2.2.3), silica column chromatography (section 2.2.4), and Ag-Ion chromatography to remove saturated hydrocarbons (section 2.2.5). Samples were subsequently prepared for GC–MS, analysed, and HBIs quantified in SIM mode (section 2.3.1–2.3.3, Chapter 2).

Sterols were also extracted using the procedures described in Chapter 2. Briefly, an internal standard was added to sediments (5α-androstan-3β-ol; 0.1 μg), which were then saponified with 5% (m/v) methanolic potassium hydroxide (5% m/v $KOH_{(aq)}$; 9:1 v/v MeOH : milliQ water; 70°C for 60 min), as described in section 2.2.2.2. Impurities were partially removed by elution via 7:3 DCM:hexane (6 mL) on silica chromatography columns (ca. 1 g of hexane-conditioned silica) and sterols were subsequently collected using 4:1 (v/v) hexane:methyl acetate (ca. 7 mL). Following N_2 blowdown (25°C), sterol-containing fractions were derivatised with BSTFA (100 μL; 70°C for 60 min; section 2.3.1) and transferred to GC vials (300 μL) in DCM prior to GC–MS analysis following the methods described in section 2.3.2 (Chapter 2). Sterols were identified in total ion current (TIC) mode by comparison of peak retention times and mass spectra to authentic standards (for brassicasterol and cholesterol) and published data (Boon et al., 1979; Combaut, 1986; Volkman, 1986). Quantification was also carried out in TIC mode (section 2.3.4), and the resulting peak areas were corrected according to internal standard responses, instrumental response factors (RFs), and sediment mass (Eq. 2.5, Chapter 2). While RF values were calculated using external standard calibrations for all HBIs, brassicasterol, and cholesterol, authentic standards were unavailable for chalinasterol, campesterol, β-sitosterol, and dinosterol. As outlined in section 2.3.4, RFs

for these four sterols were estimated (via Eq. 2.6) by comparing relative intensities of MS fragment ions used for quantification to those of brassicasterol and cholesterol, for which RF values were known. Such RF estimates (RF_{est}) were derived from several GS14 core horizons (n = 15) spanning depths of 11.5–475.0 cm, and averaged. A summary of all RF_{est} values calculated using Eq. 2.6 is presented in Table 5.2, with example calculation steps shown in Table 2.3 (Chapter 2).

Table 5.2: RF_{est} values for chalinasterol, campesterol, β-sitosterol, and dinosterol estimated using Eq. 2.6 (Chapter 2) with both externally calibrated reference sterols (brassicasterol and cholesterol). The final averaged RF_{est} values used for sterol quantification in core GS14 are highlighted in bold.

Depth (cm)	Reference sterol	Estimated RF values (RF_{est}) based on reference sterols			
		chalinasterol	campesterol	β-sitosterol	dinosterol
11.5	Brassicasterol	36.0	11.4	9.4	7.8
	Cholesterol	42.2	13.4	11.1	9.1
18.5	Brassicasterol	38.1	10.5	9.9	7.8
	Cholesterol	48.4	13.4	12.6	10.0
27.8	Brassicasterol	32.2	11.3	9.4	7.0
	Cholesterol	40.9	14.3	11.9	8.9
122.5	Brassicasterol	40.9	8.1	8.5	8.7
	Cholesterol	45.6	9.0	9.4	9.7
135.5	Brassicasterol	37.2	9.1	7.8	10.2
	Cholesterol	45.0	11.0	9.4	12.3
157.5	Brassicasterol	31.5	8.4	8.2	8.1
	Cholesterol	38.3	10.2	9.9	9.9
160.5	Brassicasterol	38.9	9.8	8.2	8.5
	Cholesterol	51.0	12.8	10.8	11.1
176.5	Brassicasterol	32.4	9.5	8.9	8.3
	Cholesterol	35.2	10.3	9.6	9.0
202.0	Brassicasterol	36.6	9.1	7.6	7.7
	Cholesterol	50.1	12.5	10.3	10.5
252.0	Brassicasterol	32.4	8.7	7.9	6.2
	Cholesterol	48.3	12.9	11.7	9.3
282.5	Brassicasterol	32.0	8.9	8.1	7.6
	Cholesterol	40.9	11.4	10.3	9.8
322.5	Brassicasterol	38.6	8.7	8.7	7.8
	Cholesterol	42.4	9.6	9.6	8.6
350.5	Brassicasterol	37.4	10.7	8.7	6.8
	Cholesterol	50.6	14.5	11.8	9.3
401.2	Brassicasterol	36.6	8.4	7.5	6.1
	Cholesterol	44.2	10.1	9.1	7.4
475.0	Brassicasterol	29.8	9.9	7.7	5.4
	Cholesterol	40.3	13.4	10.4	7.3
Mean ± SD (brassicasterol)		35.4 ± 3.4	9.5 ± 1.1	8.4 ± 0.7	7.6 ± 1.2
Mean ± SD (cholesterol)		44.2 ± 4.8	11.9 ± 1.8	10.5 ± 1.1	9.5 ± 1.3
Mean ± SD (overall)		**39.8 ± 6.1**	**10.7 ± 1.9**	**9.5 ± 1.4**	**8.5 ± 1.5**

5.3.3 Statistical analysis

Divisive changepoint analysis from the R package ECP (James and Matteson, 2013) was used on individual biomarker timeseries to identify significant shifts (p = 0.005) in biomarker profiles within the investigated temporal window (Fig. 5.2–5.3). $P_{III}IP_{25}$ values for each horizon were derived using a regional concentration balance factor for the Barents Sea (c-factor = 0.63; Eq. 2.8) with non-zero absolute concentrations (ng g^{-1} dry sed., shown in square brackets in all equations) of IP_{25} and III. Semi-quantitative estimates of spring sea ice concentrations (SpSIC, %; April–June) were subsequently calculated using the Barents Sea SpSIC–$P_{III}IP_{25}$ calibration (Eq. 3.1, Chapter 3) of Smik et al. (2016). The occurrence of summer sea ice (SuSIC, %; July–September) was tentatively inferred using a $P_{III}IP_{25}$-based SpSIC threshold of ca. 70% ($P_{III}IP_{25}$>0.8; Smik et al., 2016). Semi-quantitative SpSIC estimates were supplemented with categorical classification of each horizon into marginal (near ice-free waters; <10% SpSIC), intermediate (MIZ conditions with ca. 10–50% SpSIC), and extensive (heavy ice cover characteristic of north-eastern Svalbard; >50% SpSIC) sea ice conditions using the multivariate classification tree (CT) model A presented in Chapter 3 (Fig. 3.7a). CT predictions were derived from percentage contributions of each HBI (IP_{25}, II, III and IV) to the total (Eq. 4.1, Chapter 4) and were not carried out for samples where no HBIs were detected. The annotated R code for all statistical analyses, including changepoint detection and CT-based assessment of sea ice conditions is available in Appendix A.

In addition to examining downcore profiles (Fig. 5.2–5.3), the absolute concentration (ng g^{-1} sed.) and compositional distributions (%) of all biomarkers were examined for three temporal windows, including the LGM (ca. 25.8–18.0 cal kyr BP), HS1 (ca. 18.0–16.3 cal kyr BP) and the Deglaciation (after ca. 16.3 cal kyr BP), in order to identify significant distributional shifts and further assess the general variability of

each biomarker throughout the record (Fig. 5.4 and 5.5). Relative distributional changes were additionally compared to modern assemblages observed in Barents Sea surface sediments characterised by contrasting overlying SpSIC and annual open water duration (Fig. 5.1b and 5.5) (Chapter 3; Belt et al., 2015).

5.4 Results

5.4.1 LGM (ca. 25.8–18.0 cal kyr BP)

After an initial increase from ca. 25.8 cal kyr BP, IP_{25} and II concentrations reached their respective peak values of 7.5 and 43.7 ng g^{-1} by ca. 23.7 cal kyr BP (Fig 5.2). This coincided with a similar increase of all six sterols during the same period, which culminated between 24.7–23.7 cal kyr BP (Fig. 5.3). Both sympagic HBIs (i.e. IP_{25} and II) and all sterols remained at relatively high, but variable concentrations for most of the LGM (Fig. 5.2–5.4), with a second distinct maximum of IP_{25} and II at ca. 20.7 cal kyr BP (6.4 ng g^{-1} and 38.4 ng g^{-1}, respectively). Conversely, concentrations of trienes III and IV remained low throughout the LGM (0.7 ± 0.5 ng g^{-1} and 0.6 ± 0.5 ng g^{-1}, respectively; Fig. 5.4a). Accordingly, the HBI assemblage was dominated by IP_{25} and II during the LGM, with respective percentage contributions of 13 ± 2% and 80 ± 5%, while III and IV were only minor constituents (Fig. 5.5a). This was accompanied by average $P_{III}IP_{25}$ SpSIC estimates of 74 ± 9% and consistently extensive sea ice conditions predicted by the CT model (Fig. 5.2c). However, SpSIC values < 60% with sporadic summer sea ice occurrence ca. 19.2–18.7 cal kyr BP and CT predictions of intermediate (MIZ-like) sea ice conditions accompanied slight, but abrupt decreases in sympagic HBI and sterol concentrations, with the more distinct changes also highlighted by changepoint analysis ($p < 0.005$; Fig. 5.2a,b and 5.3). Finally, examination of the sterol distribution revealed the prevalence of β-sitosterol (23 ± 6%)

and brassicasterol (23 ± 5%), with moderate cholesterol (18 ± 3%) and chalinasterol (19 ± 4%), and relatively minor campesterol (10 ± 2%) and dinosterol (7 ± 2%; Fig. 5.5b).

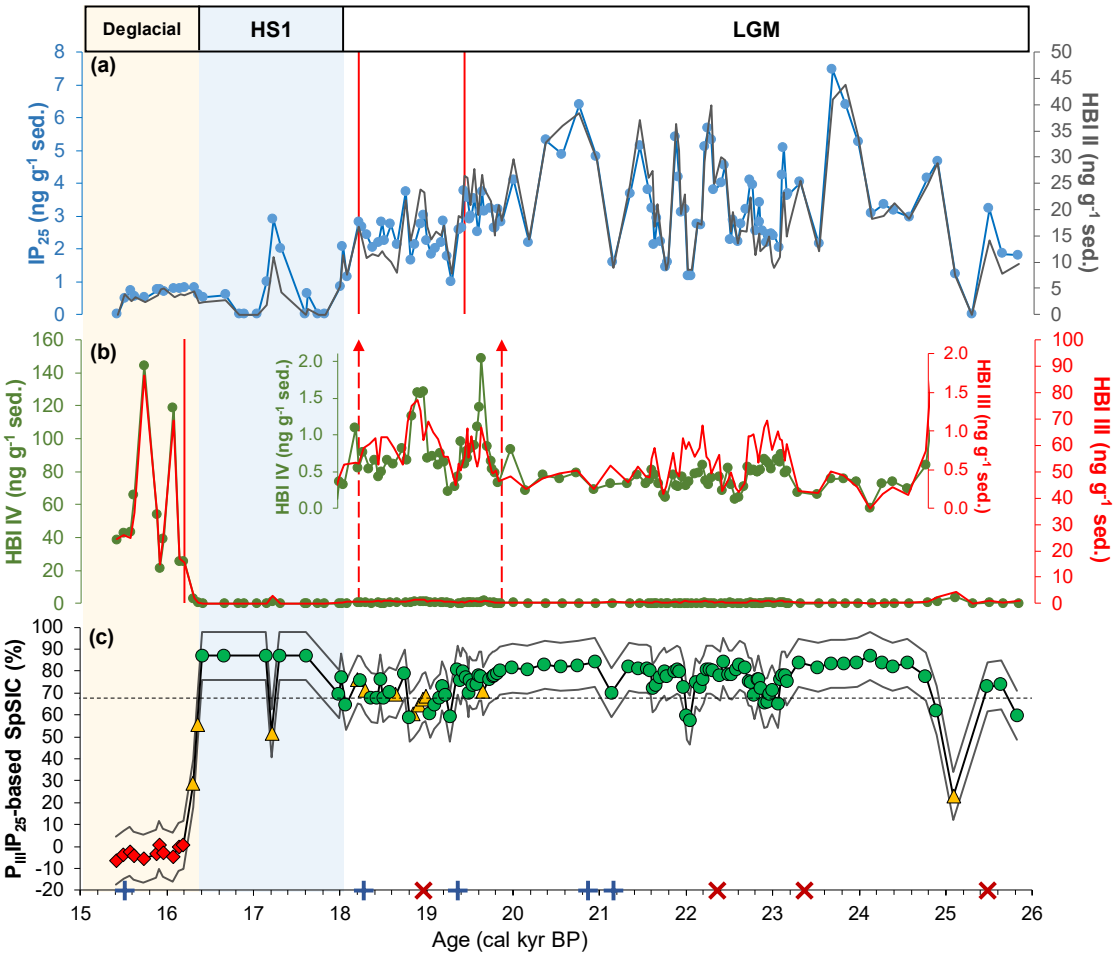

Figure 5.2: HBI concentration profiles for core GS14: (a) IP_{25} and HBI II, indicative of sympagic diatom productivity; (b) HBIs III and IV, showing pelagic diatom productivity. A zoomed-in version of the profile spanning ca. 25–18 cal kyr BP is also shown; (c) $P_{III}IP_{25}$-based SpSIC (%) estimates with confidence limits (grey lines) corresponding to the standard error of calibration (ca. ±11%; Smik et al., 2016), and superimposed categorical CT predictions of marginal (ca. <10% SpSIC), intermediate (ca. 10–50% SpSIC), and extensive (>50% SpSIC) sea ice regimes denoted by red diamonds, yellow triangles, and green circles, respectively. The threshold for summer sea ice occurrence is shown by the horizontal dashed line. In all plots, coloured background bands constrain the LGM (25.8–18.0 cal kyr BP), HS1 (18.0–16.3 cal kyr BP) and Deglacial (after 16.3 cal kyr BP) intervals – a rationale for dividing the GS14 record into time slices is provided in the Discussion. Changepoints significant at a 99.5% confidence level ($p < 0.005$) are shown by vertical red lines, where upward-pointing dashed arrows apply to the left y-axis only, while a solid line applies to both the left and right y-axes. Red and blue crosses highlight GS14 and GC08 ^{14}C AMS dates on the age scale, respectively.

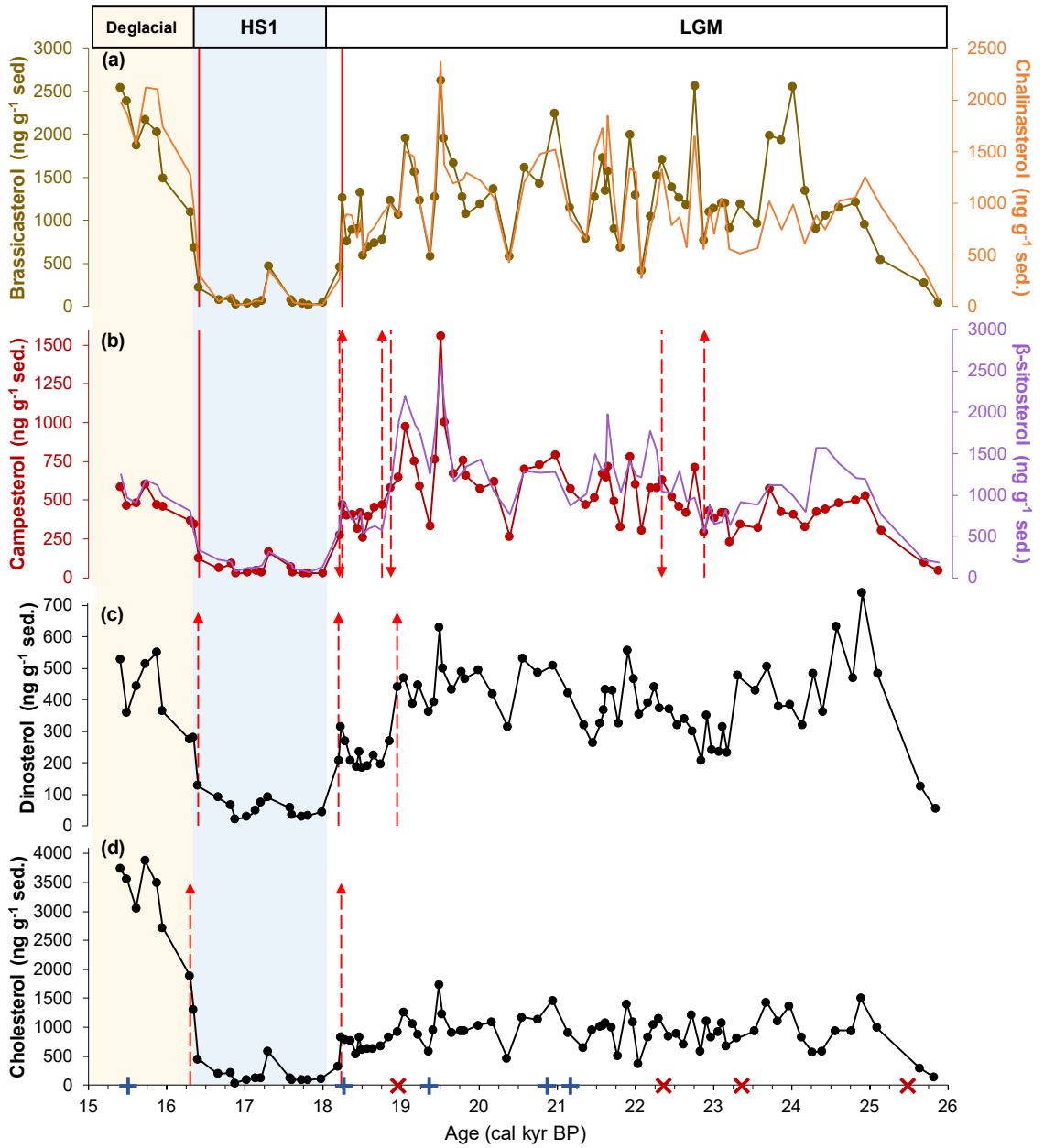

Figure 5.3: Sterol concentration profiles for core GS14: (a) Brassicasterol and chalinasterol; (b) Campesterol and β-sitosterol; (c) Dinosterol; (d) Cholesterol. In all plots, coloured background bands constrain the LGM (25.8–18.0 cal kyr BP), HS1 (18.0–16.3 cal kyr BP) and Deglacial (after 16.3 cal kyr BP) time slices. Changepoints significant at a 99.5% confidence level ($p < 0.005$) are shown by vertical red lines, where upward or downward pointing dashed arrows apply to the left and right y-axis, respectively, while a solid line applies to both left and right y-axes. Red and blue crosses highlight GS14 and GC08 ^{14}C AMS dates on the age scale, respectively.

5.4.2 HS1 (ca. 18.0–16.3 cal kyr BP)

Precipitous and abrupt decreases of all biomarker concentrations characterise this period, with averaged HBI and sterol concentrations ranging from 0.2–2.2 ng g^{-1} and 57–182 ng g^{-1}, respectively (Fig. 5.4). Despite brief increases in IP_{25} and II to 2.9 ng g^{-1} and 10.9 ng g^{-1}, respectively (Fig. 5.2a), biomarker depletions were also detected via changepoint analysis across all temporal profiles (Fig. 5.2a,b and 5.3). Nonetheless, biomarker percentage distributions remained similar to those observed during the LGM, albeit with more variability and, in case of sterols, prevalence of β-sitosterol alongside cholesterol (Fig. 5.5). The HS1 was also characterised by the highest SpSIC estimates (ca. 90%), summer sea ice occurrence, and CT predictions of extensive sea ice conditions.

5.4.3 Deglaciation (after 16.3 cal kyr BP)

An abrupt increase of biomarker concentrations, with significant shifts in percentage distributions and sea ice conditions are evident after ca. 16.3 cal kyr BP. $P_{III}IP_{25}$-derived SpSIC values dropped to a minimum of 4 ± 11%, and the CT model consistently predicted marginal ice cover or open water conditions (Fig. 5.2c). HBIs III and IV increased by ca. 2 orders of magnitude to the highest values observed throughout the record (29.1 ± 24.4 ng g^{-1} and 48.2 ± 41.8 ng g^{-1}, respectively), while IP_{25} and II remained at respective minimum values of 0.6 ± 0.2 ng g^{-1} and 3.3 ± 1.3 ng g^{-1}. Consequently, III and IV dominated the HBI distribution during this period, with relative abundances of 33 ± 8% and 53 ± 14%, respectively (Fig. 5.5). The sterols experienced a similar, but less pronounced resurgence, with most exhibiting concentrations similar to those observed during the LGM (Fig. 5.3 and 5.4b). The greatest concentration increase was observed for cholesterol, which reached a mean value of ca. 2957 ± 930 ng g^{-1} (Fig. 5.3d and 5.4b), a factor ca. three higher than the

LGM average (904 ± 302 ng g^{-1}). Cholesterol therefore dominated the sterol assemblage with 36 ± 1% relative abundance instead of brassicasterol and β-sitosterol, which contributed 22 ± 2% and 12 ± 1%, respectively (Fig. 5.5b). Similar to the LGM and HS1, chalinasterol abundance (21 ± 2%) was comparable to that of brassicasterol, while campesterol (6 ± 1%) and dinosterol (5 ± 1%) remained minor components.

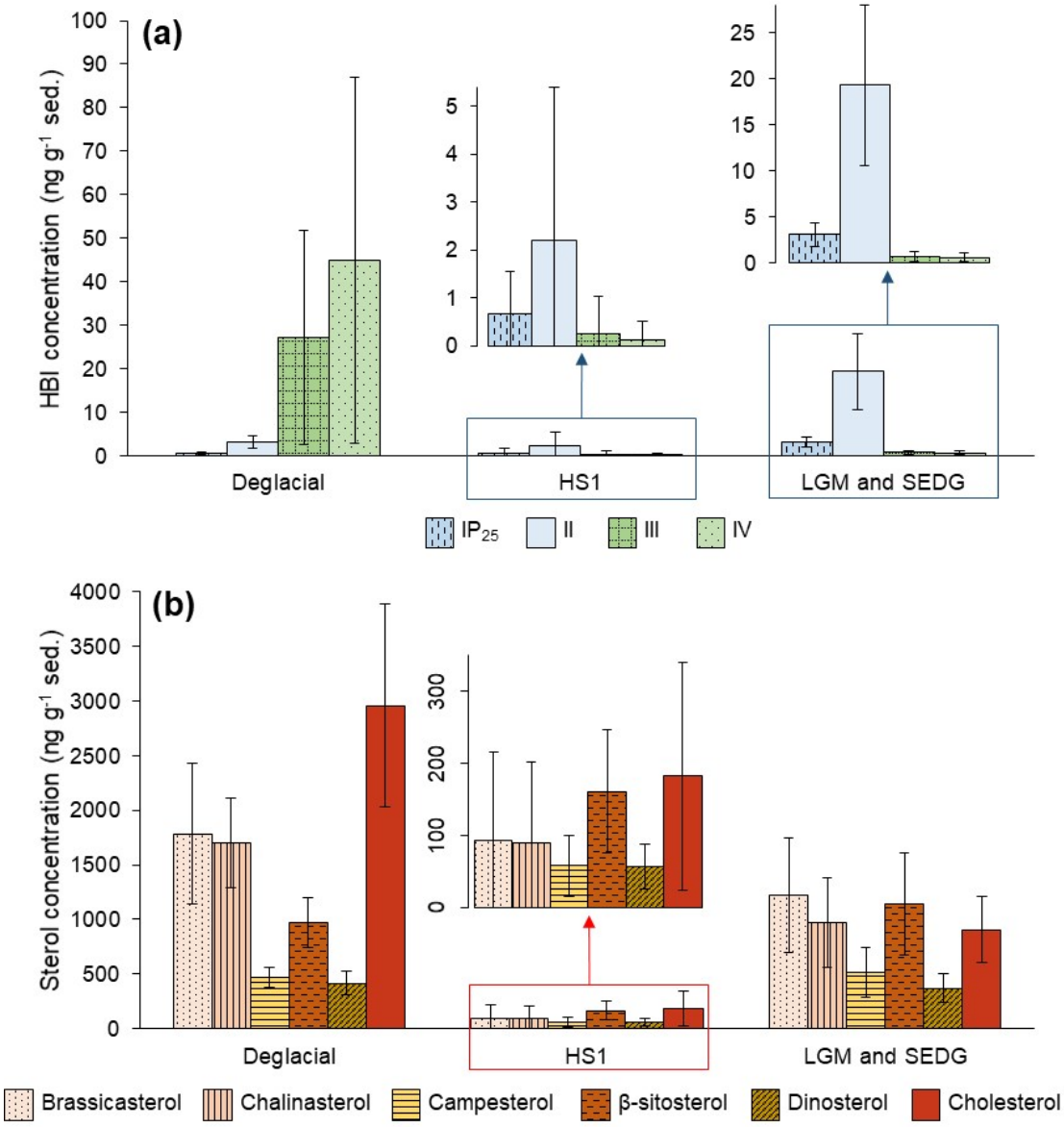

Figure 5.4: Concentration distributions during the LGM, HS1 and Deglacial for: (a) HBIs; (b) Sterols. Error bars denote ± 1 sample SD in each case. Blue and red boxes with outgoing arrows show plot areas zoomed in for clarity for HBIs and sterols, respectively.

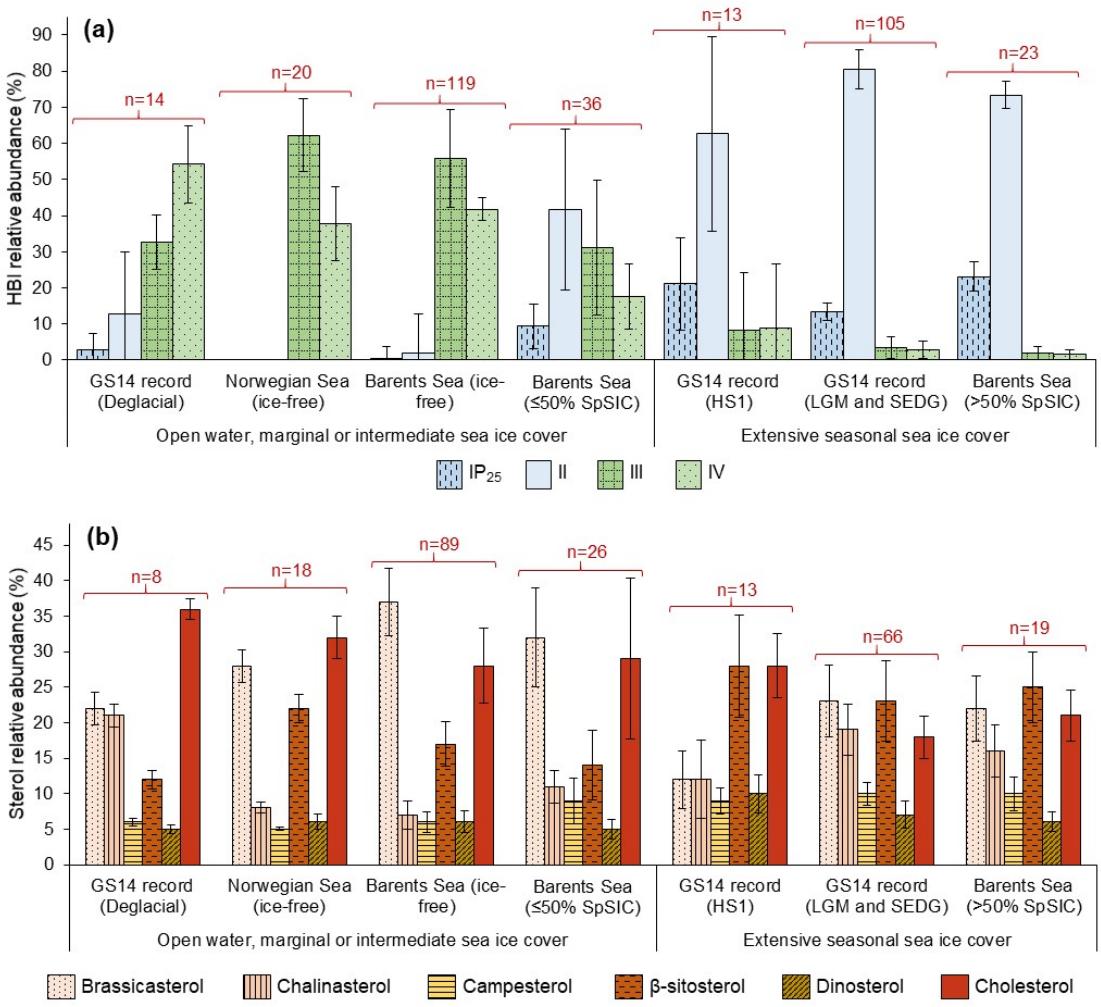

Figure 5.5: Relative abundance distributions during the LGM, HS1, and Deglacial for: (a) HBIs, with comparisons to modern distributions reported in Barents and Norwegian Sea surface sediments characterised by contrasting sea ice regimes (Fig. 1b); (b) Sterols, with comparisons to surface sedimentary distributions analogous to those in (a). Error bars denote ± 1 sample SD for each biomarker, while the sample size *n* is shown in red above each distribution.

5.4.4 Surface sediment biomarker distributions

HBI distributions in surface sediments (Fig. 7a) experiencing extensive sea ice cover (>50% SpSIC; n = 23) were characterised by a distinct prevalence of IP_{25} and HBI II within the assemblage (23 ± 4% and 73 ± 4%, respectively), with minor contribution from HBIs III and IV (2 ± 2% and 2 ± 1%, respectively). The contribution of sympagic biomarkers was lower and more variable in the central Barents Sea MIZ (≤50% SpSIC; n = 36), with respective percentage abundances of 9 ± 6% and 42 ± 22% observed for IP_{25} and HBI II. Accordingly, pelagic HBIs III and IV comprised a higher 31 ± 19% and

18 ± 9% of the assemblage, respectively. Ice-free Barents (n = 119) and Norwegian Sea (n = 20) locations were characterised almost entirely by HBIs III (56 ± 14% and 62 ± 10%, respectively) and IV (42 ± 3% and 38 ± 10%, respectively), while only 4 locations close to the annual maximum sea ice edge in the Barents Sea exhibited non-zero IP_{25} and HBI II.

Sterol distributions were mainly defined by the variability of β-sitosterol, epibrassicasterol, and cholesterol in all surface sediments. Conversely, chalinasterol, campesterol, and dinosterol remained minor components (Fig. 7b). Extensively ice-covered locations showed a prevalence of β-sitosterol (25 ± 5%), with comparable, but slightly lower abundances of cholesterol (21 ± 4%) and epibrassicasterol (22 ± 5%). Conversely, MIZ and ice-free Barents Sea locations (n = 26 and n = 89, respectively) exhibited decreased β-sitosterol abundance (14–17 ± 3–5%), with epibrassicasterol (32–37 ± 5–7%) and cholesterol (28–29 ± 5–11%) comprising most of the assemblage. Norwegian Sea sediments (n = 18) showed consistent prevalence of cholesterol (32 ± 3%), with similar epibrassicasterol content (28 ± 2%) and lower β-sitosterol (22 ± 2%).

5.5 Discussion

5.5.1 BSIS-adjacent productive SIZ during the LGM (25.8–18 cal kyr BP)

The LGM HBI assemblage was dominated by sympagic IP_{25} and II (ca. 96% total contribution) with a relatively minor contribution from pelagic trienes III and IV (ca. 4%), which was in excellent agreement with the relative HBI distribution observed in surface sediments north-east off Svalbard (Fig. 5.5a) characterised by extensive seasonal sea ice duration (ca. 10 months per year; Fetterer et al., 2017) and high SpSIC (ca. 80–90%) throughout the last 250 cal yr BP, at least (Chapter 3; Vare et al., 2010). In combination with high $P_{III}IP_{25}$-based SpSIC (ca. 65–80%) and extensive sea ice conditions inferred from CT assessment until ca. 19.8 cal kyr BP (Fig. 5.2c), the HBI

assemblage suggests harsh glacial conditions with near-perennial sea ice cover and an annual maximum sea ice margin situated further south from the core site. Thicker, longer-lasting ice cover potentially lengthened the ice algal bloom while conversely reducing the annual duration of pelagic productivity in well-stratified water near the retreating ice margin, facilitating dominance of IP_{25} and II with severely reduced contribution from III and IV (Fig. 5.2a, b and 5.5b). The inferred presence of extensive sea ice at the core site broadly agrees with the widespread advance of Northern Hemisphere (NH) ice sheets, including the BSIS, to their maximum positions since ca. 33–32 cal kyr BP (e.g. Jessen et al., 2010; Eldevik et al., 2014; Jakobsson et al., 2014). The BSIS advance, driven by low solar insolation, atmospheric CO_2 concentrations and sea surface temperatures (Clark et al., 2009; Shakun et al., 2012), was already proximal to the western margin by ca. 29–26 cal kyr BP (e.g. Clark et al., 2009; Hughes et al., 2016) and culminated at the continental shelf break at ca. 24–22.7 cal kyr BP (Jessen et al., 2010; Patton et al., 2015, 2016), while the north-eastern Svalbard margin may have already been fully glaciated with a grounded BSIS by ca. 27.4–27.2 cal kyr BP (e.g. Knies et al., 2000, 2001), with recent results indicative of a contemporaneous maximum BSIS extent west and north off Svalbard at ca. 24 cal kyr BP (Chauhan et al., 2016). At approximately the same time, BSIS merged with the Fennoscandian Ice Sheet (FIS) ca. 26–24.5 cal kyr BP (e.g. Elverhøi et al., 1993; Patton et al., 2016). Maximum BSIS extent timing agrees with rising sedimentation rate in core GS14, culminating at 23–22 cal kyr BP (Knies et al., 2018).

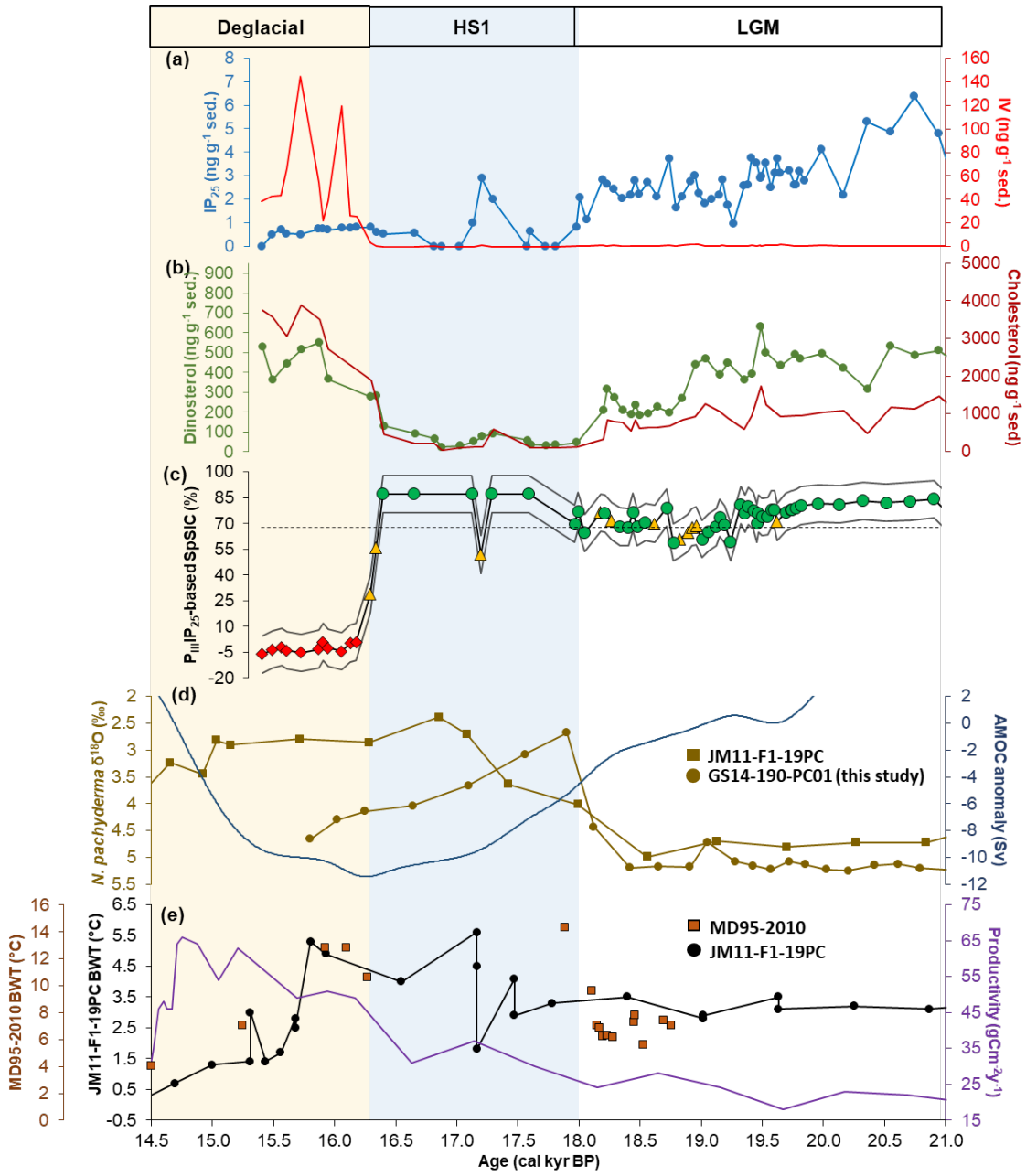

Figure 5.6: Comparison of GS14 data with other paleo-reconstructions: (a) GS14 IP_{25} and IV concentrations; (b) GS14 dinosterol and cholesterol concentrations; (c) $P_{III}IP_{25}$-derived SpSIC with CT predictions of sea ice conditions (as in Fig. 5.2c); (d) $\delta^{18}O$ of *N. pachyderma* (sin.) for GS14 (Knies et al., 2018) and the Norwegian Sea core J11-F1-19PC (Hoff et al., 2016), with the modelled North Atlantic AMOC anomaly on the right y-axis (Ritz et al., 2013); (e) Foraminiferal Mg/Ca-based bottom water temperature (BWT) at Norwegian Sea sites MD95-2010 (Marcott et al., 2011) and J11-F1-19PC (Ezat et al., 2014), with paleoproductivity north off Svalbard (Wollenburg et al., 2004).

In addition to near-zero concentrations of pelagic HBIs characteristic of minimal seasonal duration of MIZ conditions at the core site throughout the LGM due to heavy ice cover, the strongly fluctuating profiles of sympagic HBIs (ca. ±41–45% RSD; Fig.

5.2a), and high concentrations of sterols (>1 $\mu g g^{-1}$ sed.) representing general marine production (Fig. 5.3) both support the existence of variable seasonal ice extent, as well as vertical phytoplankton and nutrient stabilisation necessary to maintain pelagic spring and summer blooms (e.g. Wassmann et al., 1999; Falk-Petersen et al., 2000; Signorini and McClain, 2009; Janout et al., 2016). This is corroborated by previous inferences of continuous surface AW inflow in the Nordic Seas throughout ca. 27–22.5 cal kyr BP, at least (Rørvik et al., 2013), which progressively cooled and submerged due to increasingly fresher and colder ArW influence along the western and northern BS and Svalbard shelves (Knies et al., 1999; Vogt et al., 2001; Nørgaard-Pedersen et al., 2003; Rasmussen et al., 2007; Chauhan et al., 2016). Further, based on increased dinosterol and IP_{25} concentrations, Knies et al. (2018) previously inferred the presence of highly-productive coastal polynyas at the GS14 site initiated by NAC-carried AW upwelling and maintained by powerful offshore katabatic winds from the maximum-extent BSIS. Such polynyas were previously suggested to significantly influence the LGM sea ice and primary productivity regimes across the western (Müller et al., 2009; Müller and Stein, 2014; Xiao et al., 2015b; Kremer et al., 2018a) and northern Barents Sea margin (Knies et al., 1999, 2018; Nørgaard-Pedersen et al., 2003; Chauhan et al., 2016; Kremer et al., 2018b), reaching as far north as the Laptev Sea shelf (Taldenkova et al., 2008). The katabatic winds and lithogenic fluxes from the BSIS could have aided AW upwelling and provided a continuous nutrient supply (e.g. Knies and Stein, 1998; Knies et al., 1999, 2018), while the ocean-atmosphere heat exchange during the open water season was an important moisture source for maintaining the BSIS mass and equilibrium (e.g. Patton et al., 2015, and references therein). In addition to the conclusions of Knies et al. (2018), the characteristically low concentrations of pelagic HBIs III and IV in this study suggest that coastal polynyas probably exhibited short seasonal duration (ca. 1–2 months per year) at the core site (Fig. 5.2b, 5.4a). Locations

farther north along the AW path were previously shown to exhibit relatively low LGM productivity with alternating periods of open water and perennial sea ice conditions throughout ca. 26–20 cal kyr BP, inferred from minimum biomarker (e.g. sterol) concentrations and linked to progressive northward cooling and temporal variability of the NAC (Müller et al., 2009; Müller and Stein, 2014). NAC-controlled lead and polynya formation is also observed in the contemporary Barents Sea, where AW fluxes cause underside melting of sea ice and considerably reduce sea ice concentration West off Svalbard and in the Nansen Basin, particularly in winter (Walczowski and Piechura, 2011; Ivanov et al., 2012), also contributing to the high lead fraction in the region (Willmes and Heinemann, 2016). Light penetration through such polynyas facilitates the development of pelagic phytoplankton blooms directly under the ice cover (e.g. Arrigo et al., 2012; Assmy et al., 2017), with weak stratification provided from salinity decreases due to AW-induced underside melting (Strass and Nöthig, 1996), a mechanism that could also have contributed to considerable marine productivity observed in the GS14 record during the LGM (Fig 5.3; Knies et al., 2018). Accordingly, several investigations report high primary productivity with seasonally open waters controlled by AW inflow, evident from coevally high pelagic and sympagic biomarker concentrations along western Svalbard and the Yermak Plateau (e.g. Rasmussen et al., 2007; Müller et al., 2009; Müller and Stein, 2014; Kremer et al., 2018a, b), presence of temperate benthic foraminifera, such as *I. norcrossi*, west and north off Svalbard (Chauhan et al., 2016), and decreasing planktonic foraminiferal and IRD abundances from the Fram Strait towards the central Arctic Ocean (e.g. Nørgaard-Pedersen et al., 2003). Overall, incidence of seasonal coastal polynyas along the western Barents Sea shelf (Knies et al., 2018) likely improved the survivability of biota in harsh surrounding conditions (Thatje et al., 2008), aided deep water ventilation (e.g. Thornalley et al.,

2015) and increased snowfall over the BSIS, providing an insulating effect (Gildor et al., 2014).

Interesting decreases in both sympagic HBIs and sterols (Fig. 5.2–5.3), with more variable SpSIC and fluctuating CT-based sea ice conditions (Fig. 5.2c) centred around ca. 19.5 cal kyr BP indicate reduced primary productivity, and a potentially slightly shortened seasonal sea ice duration at the core site. At this time, continued warming of northern latitudes since ca. 21.5–19 cal kyr BP (Shakun et al., 2012; Siegert and Dowdeswell, 2002) due to increasing summer insolation (Berger and Loutre, 1991; Laskar et al., 2004) and strong sub-surface influx of warm AW (McManus et al., 2004; Ritz et al., 2013) facilitated progressive thinning and initial retreat of NH ice sheets (e.g. Hormes et al., 2013; Patton et al., 2015, 2017). Significant ice outflow from the eroding BSIS at the western (Winsborrow et al., 2010) and northern Barents Sea margins (Hogan et al., 2010; Hormes et al., 2013), together with associated meltwater discharge at 20–18.5 cal kyr BP (Clark et al., 2004; Chauhan et al., 2016), contributed to a significant sea level rise since ca. 21 cal kyr BP following a global lowstand (Peltier and Fairbanks, 2006; Clark et al., 2009), and may have increased the calving potential of the BSIS further via positive feedback (Winsborrow et al., 2010). Indeed, iceberg release from the destabilised BSIS is evidenced by increased IRD content and debris flow deposits at ca. 19.1–18.5 cal kyr BP along the northern Svalbard margin (e.g. Knies et al., 1999, 2000, 2001; Vogt et al., 2001; Chauhan et al., 2016), with an earlier interval of ca. 20.5–18.7 cal kyr BP inferred for the lower latitudes of southwestern Barents Sea and Svalbard (Rasmussen et al., 2007; Aagaard-Sørensen et al., 2010; Jessen et al., 2010; Junttila et al., 2010; Winsborrow et al., 2010; Łącka et al., 2015; Pope et al., 2016). Accordingly, the GS14 record exhibits distinct IRD and Zr/Al maxima with increased sedimentation rates at ca. 20 cal kyr BP, which was attributed to the onset of insolation- and AW-induced glacial erosion of the BSIS in the southwestern Barents

Sea (Knies et al., 2018). The timing of this BSIS retreat is in good agreement with depleted $\delta^{18}O$ values of benthic foraminifera in the Nordic Seas and the North Atlantic since ca. 19 cal kyr BP (Bauch et al., 2001; Knies et al., 2001, 2018), which may represent gradual AMOC weakening resulting from deglacial meltwater-induced stratification and cooling of surface waters (e.g. Benway et al., 2010), and is further corroborated by $^{231}Pa/^{230}Th$ measurements (McManus et al., 2004) and model studies (Fig. 5.6d; Ritz et al., 2013). The presented data suggests that insolation-induced BSIS destabilisation at the GS14 site began at ca. 19.4 cal kyr BP. Thus, meltwater fluxes from the retreating BSIS probably strongly stratified the water column during this interval, and the resulting weakening of AW inflow potentially hampered upwelling-based nutrient replenishment to the photic zone, resulting in the slightly decreased sympagic (e.g. IP_{25}) and pelagic (sterols) primary productivity at the core site (Fig. 5.2). Moreover, insolation increases and associated long-term sea ice thinning via radiative forcing (Berger et al., 2013; Loutre et al., 2014) could have hastened the seasonal ice melt and shortened the ice algal bloom (Wassmann et al., 1999; Signorini and McClain, 2009; Leu et al., 2011). Nonetheless, extensive sea ice conditions that characterised the early LGM (26.0–19.8 cal kyr BP) persisted, with frequent summer sea ice occurrence (Fig. 5.2c).

5.5.2 Productivity termination during the HS1 (18–16.3 cal kyr BP)

Precipitous decreases of all biomarker concentrations to minimum values observed throughout the record (Fig. 5.2–5.4) and maximum $P_{III}IP_{25}$-derived SpSIC with extensive sea ice conditions predicted by the CT model (Fig. 5.2c) support the presence of closed perennial sea ice cover with near-zero primary productivity at the core site between ca. 18–16.3 cal kyr BP. While a brief increase in sympagic HBIs to late LGM levels at 17.2 cal kyr BP potentially indicates sufficient thinning of ice cover

to initiate photosynthesis during the summer (Fig. 5.2a), the overall onset of harsh conditions agrees with the widespread collapse of NH ice sheets at ca. 17.5 cal kyr BP following continued increases of summer insolation and sea level (e.g. Clark et al., 2009; Shakun et al., 2012), strong ice stream activity (e.g. Winsborrow et al., 2010) and warm AW-induced weathering of the BSIS grounding line (Hormes et al., 2013; Patton et al., 2015). Contemporaneous massive meltwater discharges from icebergs are evidenced between ca. 17.5–16.9 cal kyr BP by severely depleted planktic $\delta^{18}O$ and dominance of cold-adapted *N. pachyderma* (sin.) across the Norwegian Sea (Rasmussen and Thomsen, 2008; Thornalley et al., 2015; Hoff et al., 2016), southwestern Barents Sea (Rasmussen et al., 2007) and around Svalbard (Koç et al., 2002; Jessen et al., 2010; Chauhan et al., 2016). Accordingly, the significantly decreased planktic $\delta^{18}O$ values observed in the GS14 record at ca. 17.9 cal kyr BP (Fig. 5.6d) were previously attributed to meltwater-induced cooling and freshening of surface waters (Knies et al., 2018), which probably strongly stratified the water column, promoting rapid sea ice re-expansion in the Barents Sea. Moreover, the strength of such meltwater-induced temperature and density gradients significantly hampered the AMOC (Fig. 5.6d; McManus et al., 2004; Benway et al., 2010; Ritz et al., 2013), causing a reduction in NAC-bound AW inflow evident from depleted benthic $\delta^{18}O$ values across the Nordic Seas (Bauch et al., 2001; Knies et al., 2001; Rasmussen and Thomsen, 2008). Thus, the results support the conclusion that the combined influence of cold, low-salinity surface waters, a strongly stratified water column, and a hindered AW inflow into the Barents Sea following BSIS disintegration facilitated perennial sea ice formation and limited the volume and upwelling of deep nutrient-rich waters to the photic zone (Fig. 5.7b). Thus, insufficient nutrient replenishment combined with reduced light penetration through thick multi-year ice following the closing of coastal polynya potentially caused a catastrophic collapse of microalgal stocks, resulting in near-zero biomarker

concentrations observed in core GS14 from ca. 18.0–16.3 cal kyr BP (Fig. 5.2–5.4). Indeed, similarly to the LGM, the relative distributions of HBIs (Fig. 5.5a) remain consistent with modern assemblages indicative of extensive sea ice conditions East off Svalbard (Chapter 3), which suggests that primary productivity was still controlled by sea ice. The sterol distribution, however, slightly deviates from that of the north-eastern Svalbard surface sediments (Fig. 5.5b) and the Nansen Basin sympagic algal aggregate (Belt et al., 2018) due to pronounced dominance of β-sitosterol and cholesterol. The inhospitable conditions of thick, perennial ice cover during the HS1 likely reduced algal biodiversity – a trend observed at higher latitudes of the contemporary Arctic Ocean (Zhang et al., 1995; Falk-Petersen et al., 1998; Henderson et al., 1998). Thus, the change in sterol distribution probably reflects a shift in the algal assemblage, especially given the ubiquity of sterols in marine microorganisms (Volkman, 2003; Belt et al., 2013). For instance, spring blooms in the Central Arctic ocean are often dominated by the cold-adapted diatom *Melosira arctica* (Syvertsen, 1991; Boetius et al., 2013), while at least some Melosirales produce both β-sitosterol and cholesterol as the two major sterols (Rampen et al., 2010). In any case, the presence of perennial ice overlying the study area is further substantiated by the absence of significant IRD input and low sedimentation rates throughout the 18.0–16.3 cal kyr BP interval (Knies et al., 2018). Global ice sheet retreat and the resulting release of iceberg armadas resulted in distinct IRD deposits in the northern North Atlantic and the Nordic Seas, known as Heinrich Events, the most recent of which occurred at ca. 16.8 cal kyr BP (e.g. Bond and Lotti, 1995; Hemming, 2004). Contrastingly low or moderate IRD input observed at ca. 17 cal kyr BP at the western (e.g. Jessen et al., 2010) and northern Svalbard margins (e.g. Vogt et al., 2001) was attributed to the presence of extensive sea ice with cold surface waters; similar conditions at the GS14 site could have re-suspended coarse particles into ice, preventing deposition.

5.5.3 Ice retreat and productivity recovery after 16.3 cal kyr BP

Considerable increases in absolute concentrations of pelagic HBIs (Fig. 5.2b and 5.4a) and sterols (Fig. 5.3 and 5.4b), accompanied by shifts in respective percentage distributions (Fig. 5.5) indicated a general climate amelioration with enhanced primary productivity and SpSIC < 10% (Fig. 5.2c) between ca. 16.3–15.4 cal kyr BP. Comparatively low concentrations of sympagic IP_{25} and II therefore shifted the relative HBI distribution to favour III and IV, which agrees with the modern HBI assemblage representing nearly ice-free settings with prolonged open water duration (Fig. 5.5a). Together with decreased $P_{III}IP_{25}$-derived SpSIC with CT predictions of marginal sea ice conditions (Fig. 5.2c; Smik et al., 2016; Chapter 3) and an abrupt increase of IRD at ca. 16.3 cal kyr BP (Knies et al., 2018), the evidence suggests limited annual sea ice cover (<10% SpSIC) and sympagic productivity (e.g. Belt et al., 2007; Brown et al., 2014c; Belt, 2018), with favourable conditions for pelagic blooms in the postglacial Barents Sea (Belt et al., 2015; Belt et al., 2017). Rapid sea ice and areal BSIS retreat is also apparent throughout the Barents Sea continental shelves between ca. 16.5–15.5 cal kyr BP, inferred from the abundance of opportunistic benthic foraminifera characteristic of productive waters (Chauhan et al., 2016; Pau and Hammer, 2016), increased IRD deposition and meltwater release from sea ice and icebergs (e.g. Knies and Stein, 1998; Vogt et al., 2001; Jessen et al., 2010; Chauhan et al., 2016), as well as high biomarker concentrations (e.g. Müller and Stein, 2014) around Svalbard. Since ca. 17.5 cal kyr BP, gradual increases in insolation (Berger and Loutre, 1991; Laskar et al., 2004) and atmospheric GHGs (e.g. Monnin et al., 2001; Shakun et al., 2012) probably contributed to the areal retreat of the BSIS and rejuvenation of the AMOC following HS1 at ca. 16 cal kyr BP (Fig. 5.6d; McManus et al., 2004; Ritz et al., 2013). The deglaciation was potentially also triggered by progressive aridification of the Arctic during HS1 due to limited ocean-atmosphere heat and moisture exchange through perennial ice cover (e.g.

Liu et al., 2009; Hormes et al., 2013), which reduced the moisture supply for ice sheet build-up. Ice streams retreated from the western Barents Sea margin due to a shifting BSIS mass balance after ca. 17 cal kyr BP (Winsborrow et al., 2010), which contributed to a separation of the BSIS and FIS in the central Barents Sea (e.g. Bjarnadóttir et al., 2014; Newton and Huuse, 2017; Patton et al., 2017). Thus, precipitous sea ice retreat from the western Barents Sea continental slope at ca. 16.3 cal kyr BP potentially coincided with eastbound areal deglaciation of the BSIS (Fig. 5.7c).

Conspicuous enhancement of pelagic HBI concentrations (Fig. 5.2b and 5.4a) towards values >140 ng g^{-1} is unprecedented both within the GS14 record and the contemporary Barents Sea, where maximum sedimentary concentrations of III and IV detected in the highly-productive MIZ do not exceed ca. 47 and 22 ng g^{-1}, respectively (Chapter 3; Belt et al., 2015). Such a remarkable increase in pelagic diatom productivity at the GS14 site after ca. 16.3 cal kyr agrees with the reconstruction of Wollenburg et al. (2004), who also found that paleoproductivity in relatively fresh surface waters surpassed modern averages at the northern Svalbard margin during this period (Fig. 5.6e). Moreover, benthic foraminiferal assemblages along the continental margin adapted to warm AW and increased nutrient availability (e.g. Chauhan et al., 2016). Together, these data suggest the existence of significantly more productive post-HS1 conditions compared to those spanning at least the last several decades of sedimentation in the MIZ (Chapter 3; Belt et al., 2015), and are unlikely to be solely attributable to sea ice retreat and establishment of a time-limited, but productive post-HS1 ice margin.

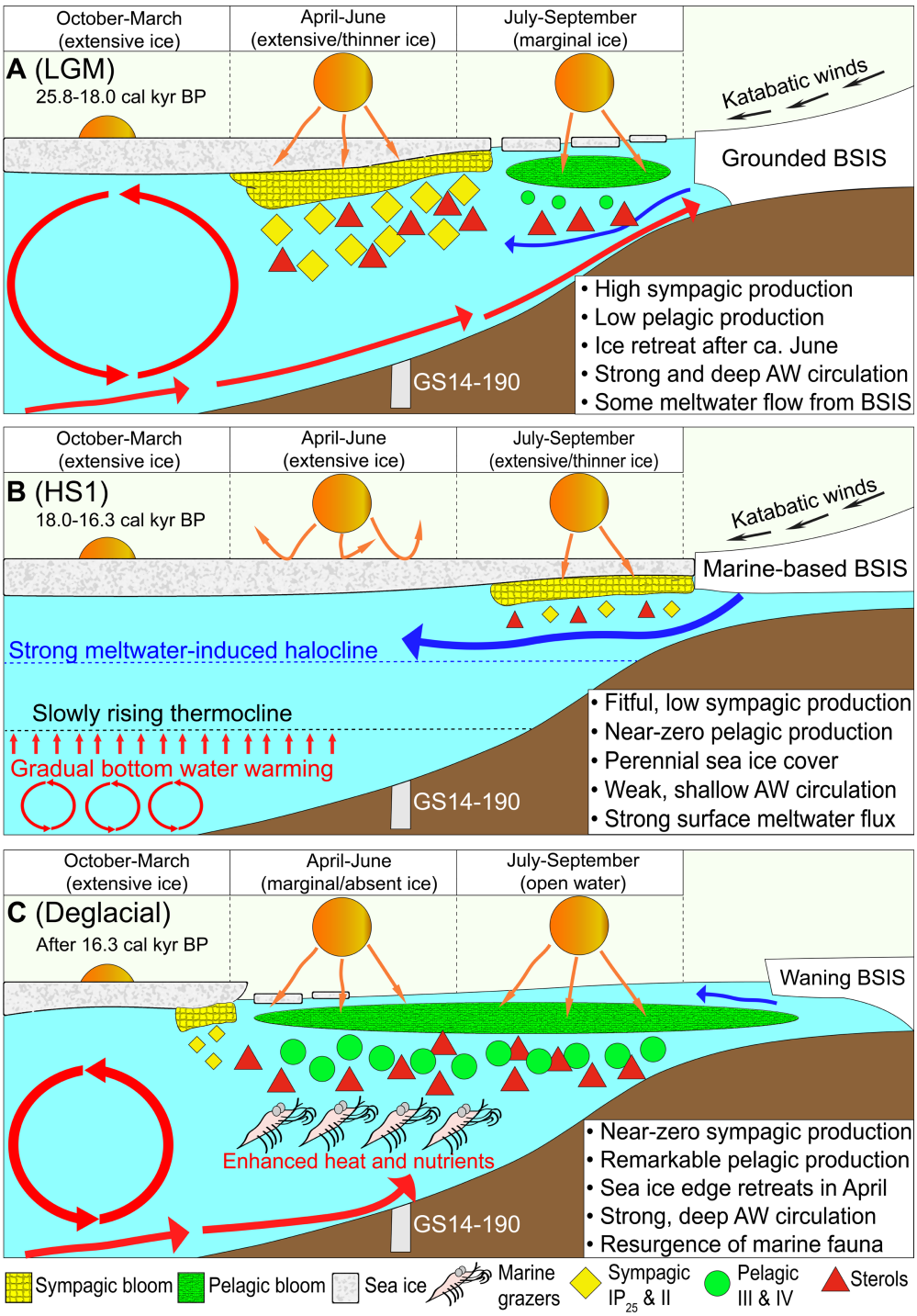

Figure 5.7: A representation of sea ice and productivity conditions at the southwestern Barents Sea slope throughout: (A) The LGM (25.8–18.0 cal kyr BP); (B) The HS1 (18.0–16.3 cal kyr BP); (C) The Deglacial (16.3 cal kyr BP onwards). Seasonal sea ice conditions inferred from SpSIC (%) and the CT model are illustrated during winter (October–March), spring (April–June) and summer (July-September). Red and blue arrows correspond to AW and meltwater fluxes, respectively, where line width increases with flow strength. Orange arrows represent solar insolation.

Several factors could have renewed pelagic productivity. The stratified water column in the Arctic throughout HS1 was initially salinity-controlled due to deglacial

meltwater input since ca. 20–19 cal kyr BP (e.g. Rasmussen et al., 2007; Rasmussen and Thomsen, 2008; Jessen et al., 2010; Chauhan et al., 2016; Hoff et al., 2016; Jennings et al., 2017, 2018), which hampered the AMOC and NADW formation (McManus et al., 2004; Gherardi et al., 2009). The shallow thermohaline circulation drastically slowed deepwater ventilation, evidenced by decreases of planktic-benthic radiocarbon ratios in the North Atlantic and the Nordic Seas (Thiagarajan et al., 2014; Thornalley et al., 2015). As a result, a combination of reduced convective heat loss from northbound bottom waters due to strong salinity-driven stratification, and geothermal heating (e.g. Adkins et al., 2005) potentially caused a basin-wide increase of subsurface water temperatures (Liu et al., 2009). Indeed, millennial sub-surface warming of 2–3°C since ca. 19 cal kyr BP is supported by foraminiferal transfer function reconstructions (Rørvik et al., 2013), Δ_{47} clumped isotope data, increased Mg/Ca ratios (Cronin et al., 2012; Thiagarajan et al., 2014; Thornalley et al., 2015), benthic $\delta^{18}O$ depletions (Rasmussen and Thomsen, 2004), and model simulations of ice sheet destabilisation (Álvarez-Solas et al., 2011) across the Nordic and Norwegian Seas (Fig. 5.6e). Similar warming along the Barents Sea and Svalbard margins is indicated by intrusion of temperate benthic foraminifera adapted to reduced productivity immediately prior to and throughout the HS1 (Wollenburg et al., 2004; Rasmussen et al., 2007; Chauhan et al., 2016), which potentially affected the GS14 site and contributed to the basal melting and debuttressing of the BSIS that triggered glacial conditions at the onset of HS1 (e.g. Marcott et al., 2011; Hormes et al., 2013). Such accumulation of sub-surface heat in a stable salinity-stratified water column lowers the density of deep waters – an effect which positively scales with pressure due to oceanic thermobaricity – and gradually destabilises the column by reducing the depth threshold at which the cold surface waters become denser than the warm, saline waters below. Once the depth threshold is breached, overturning resumes as the cold surface waters accelerate downwards, while the heat and salt

accumulated in the deep waters is rapidly released to the surface ocean, deepening the thermocline (e.g. Adkins et al., 2005; Stewart and Haine, 2016). Such phenomena have been recorded by paleotemperature proxies in the Norwegian Sea, where subsurface temperatures rapidly decreased between ca. 18–15 cal kyr BP following a period of millennial warming (Rørvik et al., 2013; Thornalley et al., 2015), which could have contributed to the return of deepwater convection and AMOC recovery after 16 cal kyr BP (Ritz et al., 2013; Lynch-Stieglitz et al., 2014). Intense, thermobaric instability- or buoyancy-driven upwelling of warm and saline subsurface waters at the GS14 site could therefore have made massive surface reservoirs of heat and nutrients available (Fig. 5.7c) for seasonal ice melting after 16.3 cal kyr BP (Fig. 5.2c) and the subsequent development of unprecedented pelagic productivity (Fig. 5.2b), respectively. Increased nutrient availability and efficient surface enrichment activated by this overturning resumption was potentially maintained by the deepening and intensification of the AMOC towards the Bølling-Allerød warming at ca. 15 cal kyr BP (McManus et al., 2004; Shakun et al., 2012; Ritz et al., 2013). Additionally, in contrast to the slow development of stratification and pelagic productivity in the ice-free southwestern Barents Sea today due to strong NAC-driven vertical mixing (Chapter 3; Loeng and Drinkwater, 2007; Oziel et al., 2017), the post-HS1 productive season at the GS14 site could have been prolonged and hastened by both an earlier and stronger stratification due to meltwater input from sea ice and BSIS retreat (Hormes et al., 2013). Finally, as the BSIS reached northern Norway by ca. 15 cal kyr BP (Winsborrow et al., 2010), the influx of ice and iceberg-entrained terrigenous material from coastal erosion could have provided an additional nutrient supply to the surface ocean, as previously noted for the postgalcial western (Aagaard-Sørensen et al., 2010) and northern Barents Sea (Knies and Stein, 1998). Thus, a combination of marginal seasonal sea ice presence, surface warming, hastened meltwater-fuelled stratification, and an augmented nutrient input

from terrigenous material and intense upwelling potentially stabilised pelagic species longer in the euphotic zone and reduced nutritional limitation during the peak bloom phase, explaining the productivity trends observed herein (Fig. 5.7c). Although it is not feasible to decouple the relative influences of individual factors, site GS14 was likely characterised by a significantly different productivity regime relative to the ephemeral, nutrient-limited blooms of the modern Barents Sea (e.g. Sakshaug et al., 2009; Signorini and McClain, 2009), where the phytoplankton productivity increase of recent years is mainly driven by a strengthening of AW inflow (Årthun et al., 2012; Barton et al., 2018) and increased open water area due to melting sea ice (Arrigo and van Dijken, 2015; Assmy et al., 2017), rather than by deglacial meltwater and terrigenous fluxes.

High sterol concentrations after ca. 16 cal kyr BP resemble the trend of abruptly increasing pelagic HBI concentrations (Fig. 5.2b, 5.4a) and support the assumption of renewed primary productivity following precipitous ice retreat (Fig. 5.2c, 5.7c). Though absolute sterol concentrations are lower relative to those of surface sediments, this is at least partly attributable to higher organic matter content of the latter. Indeed, post-HS1 concentrations are more comparable to those of surface sediments when normalised to TOC (Fig. E.2, Appendix E). While the combination of lower sterol and significantly higher pelagic HBI concentrations in core GS14 relative to surface sediments may be due to prevalence of diatoms within the post-HS1 algal assemblage, diagenetic influences on sterols (e.g. Wakeham, 1989; Rontani et al., 2012) cannot be discounted. Hence, absolute sterol concentrations are interpreted solely within the GS14 record.

While most sterols only reach pre-HS1 values at the core site (Fig. 5.3), cholesterol concentrations increase by a factor of 3 relative to LGM values and dominate the percentage distribution at 36% relative abundance instead of β-sitosterol (Fig. 5.4b, 5.5b). Similarly to HS1, this is potentially attributable to a switch in the algal assemblage to favour cholesterol production (e.g. by centric diatoms; Rampen et al.,

2010), or to a resurgence of marine fauna (Volkman, 1986, 2003) after sea ice retreat. One explanation is the efficient conversion of algal sterols to cholesterol by auxotrophic consumers, including zooplankton, which potentially flourished after the HS1 due to renewed deep circulation (McManus et al., 2004; Gherardi et al., 2009; Ritz et al., 2013), as well as global atmospheric and oceanic warming (Shakun et al., 2012). Zooplankton at lower trophic levels extensively feed on pelagic and sympagic algae for growth and reproduction, with increased grazing rates characteristic of warm and highly-productive conditions with large phytoplankton stocks (Falk-Petersen et al., 2000; Verity et al., 2002; Tamelander et al., 2008; Søreide et al., 2010). Contemporary zooplankton communities in the Barents Sea MIZ during peak blooms are dominated by crustaceans, including copepods (ca. 80% abundance in spring; Aarflot et al., 2017) and krill (Eriksen et al., 2017), which require a continuous source of cholesterol to maintain their phospholipid membranes and produce offspring (e.g. Hassett, 2004; Hassett and Crockett, 2009; Kohlbach et al., 2016). Accordingly, cholesterol is invariably the major constituent (usually >50%) of sterol distributions in Arctic and Antarctic crustaceans (Mühlebach et al., 1999; Hamm et al., 2001). Herbivorous and omnivorous arthropods largely rely on chemical conversion of phytosterols to cholesterol, which they cannot biosynthesize (e.g. Martin-Creuzburg and Elert, 2009) or obtain in sufficient quantity from an algal diet. Therefore, it is possible that the nutrient-replete and diatom-rich conditions inferred from high pelagic HBI (III and IV) concentrations at the GS14 site after HS1 (Fig. 5.2b) revitalised zooplankton production and phytosterol to cholesterol bioconversion, leading to the proportionally larger increases of the latter sterol (Fig. 5.3 and 5.5b). Additionally, the suggestion of a warming water column due to intensive post-HS1 circulation of sub-surface heat and increasing atmospheric GHGs could have accelerated zooplankton metabolism, switching from temperature-limited to nutrient-limited growth with increased nutritional and reproductive cholesterol requirements

(Hassett and Crockett, 2009), as well as accelerated oogenesis (Dvoretsky and Dvoretsky, 2014). Overall, increased phytosterol conversion rates and zooplankton stocks following the post-HS1 climate amelioration represent a plausible mechanism for the switch from a phytosterol- to cholesterol-defined sterol assemblage after 16 cal kyr BP. Notably, however, such a cholesterol-dominated sterol distribution is not reproduced in the contemporary Barents Sea, where epibrassicasterol abundances increase alongside those of cholesterol, and are often higher. Consistent cholesterol prevalence is only observed in the warmer Norwegian Sea (Fig. 5.5b) characterised by significant transport of copepods and krill with the NAC (Falk-Petersen et al., 2000), contributing to their role as major pelagic food web components in the Barents Sea (Aarflot et al., 2017; Eriksen et al., 2017). These observations potentially indicate that the highly-productive post-HS1 interval in the GS14 record is unique and not reproduced in the contemporary Barents Sea, supporting similar suggestions based on the unprecedented increase of pelagic HBIs III and IV, which overshadows that of cholesterol (Fig. 5.2b, 5.3). In contrast to sterols, HBI distributions appear to be relatively unaffected by grazing and were shown to be effective tracers of pelagic and benthic food web interactions in the Arctic (Brown and Belt, 2012, 2017; Brown et al., 2015, 2017). Thus, a tentative explanation is that III and IV were less affected by grazing relative to sterols and proportionally higher amounts therefore achieved sedimentation. Nonetheless, the unknown biological significance and metabolic reactivities of HBIs during trophic transfer highlight the need to consider selective consumer-mediated modification of algal lipids when assessing productivity trends in marine sediments.

5.6 Conclusions

Geochemical biomarkers in a marine sediment core provided new insights into the shifting seasonal sea ice and primary productivity conditions on the southwestern Barents Sea slope during ca. 25.8–15.4 cal kyr BP. The outcomes drawn were:

1) Once the BSIS reached the shelf edge by ca. 24 cal kyr BP, the LGM interval was characterised by extensive sea ice covering the site, with limited seasonal duration of coastal polynya. Sympagic productivity was variable, but high, while pelagic phytoplankton remained a minor contributor until 16.3 cal kyr BP. However, as the ice sheet thinned and destabilised at ca. 19.8 cal kyr BP under the influence of increasing insolation, aridification, warm sub-surface AW and sea level rise, annual sea ice duration and sympagic production declined slightly.

2) The onset of perennial sea ice cover during HS1 coincides with widespread NH ice sheet collapse and large meltwater influx at ca. 18.0 cal kyr BP as a result of AW-induced basal melting, atmospheric aridification and increased iceberg calving due to sea level rise. Thus, overall productivity plummeted until ca. 16.3 cal kyr BP as a result of a pan-Arctic meltwater-induced pycnocline, abrupt AMOC weakening and reduced light penetration through perennial sea ice. The BSIS probably did not contribute to the Heinrich Events observed as IRD deposits in the North Atlantic. The data corroborate a similar collapse of primary production projected for the eventual debuttressing of the contemporary WAIS.

3) Coincident with a rapid sea ice retreat to values <10% SpSIC between ca. 16.3–16.1 cal kyr BP, pelagic diatom productivity exceeded the most productive contemporary conditions in the Barents Sea MIZ. This feature is likely uniquely deglacial and attributable to heat and nutrients released to the surface waters due to thermobaric and/or buoyancy-triggered instabilities following sub-surface

warming under weak thermohaline circulation of the HS1. This probably vastly increased pelagic algal biomass and revitalised the marine fauna, with meltwater input and coastal erosion from the BSIS providing additional nutrients.

4) A consistency of relative biomarker distributions downcore with those observed in contrasting sea ice and primary productivity regimes of the contemporary Barents Sea was noted. Sympagic and pelagic primary production was distinguishable using HBI biomarkers of ice algal and pelagic diatoms, which indicate that LGM productivity was predominantly ice-based, while post-HS1 production relied on free-floating pelagic algae with minor contribution from sympagic sources. In contrast to dramatically increased pelagic HBI concentrations post-HS1 in response to ice retreat, sterol concentrations remained similar under more extensive sea ice conditions of the LGM and the post-HS1 deglaciation, likely due to their mixed algal sources. Despite this, relative sterol distributions strongly differed between extensive (LGM) and near-zero (post-HS1) ice conditions, with higher cholesterol and lower phytosterol abundances observed for the latter and possibly indicative of abundant marine grazers. This showcases some capacity of multivariate analysis of less source-specific biomarkers to decipher contrasting sea ice and productivity regimes.

CHAPTER SIX

6. Conclusions and future work

6.1 Conclusions

The overall aim of this project was to improve HBI-based proxy methods for paleoclimate reconstruction by exploring associations between multiple sedimentary HBIs and overlying environmental conditions, and to utilize insights obtained from such investigations within a multi-proxy framework to describe sea ice and productivity regimes encompassing intervals of significant climate change in the Barents Sea. To this end, the following was achieved:

1) A multivariate method involving CTs was implemented to classify Barents Sea ice conditions alongside $P_{III}IP_{25}$-based SpSIC estimates (Chapter 3). CTs offered several advantages over the $P_{III}IP_{25}$ approach, while associated caveats (Chapter 4) were mostly traceable to specific features within the data used (section 6.1.1).

2) A relationship between a pelagic HBI triene ratio (Eq. 3.6, Chapters 3 and 4) and spring Chl *a* was identified in surface and centennial-scale downcore sediments, and broadly agreed with overlying spring bloom dynamics (and sea ice conditions), despite some caveats identified in longer-term archives (section 6.1.2).

3) CT and $P_{III}IP_{25}$ methods were both utilised for paleoclimatological reconstructions during the late Weichselian glaciation (ca. 26–15 cal kyr BP; Chapter 5) and since the YD (last ca. 13 cal kyr BP; Chapter 4). In addition to providing new paleo-information, the findings also highlighted the potential of multivariate HBI distributions to distinguish between sympagic and pelagic primary production, as well as the potential of less source-specific biomarkers to exhibit distributions characteristic of specific (e.g. ice-covered versus ice-free) settings (section 6.1.3).

6.1.1 CT model development and comparison to the $P_{III}IP_{25}$ approach

The first objective was to implement multivariate HBI distributions for the purposes of Arctic sea ice reconstruction to both alleviate certain challenges associated with the $P_{III}IP_{25}$ index and, more generally, explore new potential relationships of sympagic and pelagic HBIs with both contemporary and paleo-sea ice and productivity regimes. This was achieved by building a CT model using HBI abundances relative to their total in a Barents Sea surface sediment dataset encompassing seasonal sea ice variability, and testing the CT in centennial-scale downcore records (Chapter 3). In both datasets, CT-based discrete class predictions favourably agreed with known sources of various HBIs and indicated the prevalence of pelagic HBIs III and IV (Fig. 1.8, Chapter 1) in highly-productive MIZ conditions (10–50% SpSIC), while sympagic IP_{25} and II were enhanced in areas North-East off Svalbard experiencing extensive sea ice cover (>50% SpSIC) until July–August. As expected, largely ice-free areas (<10% SpSIC) were characterised by very low or absent IP_{25}. These findings were consistent with the basic principle of $P_{III}IP_{25}$, which relies on the opposing responses of sympagic and pelagic diatoms (and, therefore, HBIs) to changes in sea ice cover. However, the CT model offered several potential advantages over the PIP_{25} approach. Thus, while HBIs IP_{25}, II, III, and IV were extensively utilised by the CT model, the addition of coastal diatom-produced VI and likely less source-specific V did not improve and arguably deteriorated model performance, showcasing the capacity of CTs to both aid the selection of appropriate biomarkers for sea ice classification (provided appropriate prior knowledge about their sources) and quantitatively assess performance. Additionally, due to the multivariate nature of CTs, they do not require a *c*-factor used by PIP_{25}-based methods to correct for different IP_{25} and pelagic biomarker concentration ranges. Nonetheless, the arguably more robust categorical nature of CT predictions is potentially also more limiting compared to the semi-quantitative $P_{III}IP_{25}$-based SpSIC estimates.

The different methodologies governing $P_{III}IP_{25}$-based SpSIC and CT predictions (Table 3.4, Chapter 3) did not prevent general consistency of outcome between these methods in millennial-scale downcore records (Chapter 4). Specifically, both the gradual ice expansion throughout the Holocene and abrupt shifts between glacial – interglacial conditions at the end of the YD were detected by corresponding changes of CT predictions and $P_{III}IP_{25}$-based SpSIC. Despite this, there were discrepancies between $P_{III}IP_{25}$ SpSIC estimates and CT classification (based on satellite SpSIC), which could usually be identified as:

- Disproportionately large increases in sympagic HBI II relative to IP_{25}, biomarkers which are otherwise highly correlated in the modern Barents Sea. Such discrepancies may also extend to other correlated HBIs, such as III and IV, as well as additional descriptive variables potentially used in future CT models. Identification of these inconsistencies (e.g. by rolling correlation and changepoint analysis) and other features of downcore HBI distributions that are not represented by a given training set should be carried out routinely, with identified samples either treated with caution or removed from analysis to ensure accurate CT predictions.
- Less traceable discrepancies associated with with selection of an appropriate *c*-factor for the $P_{III}IP_{25}$-based approach, which significantly varies spatially and can alter SpSIC estimates by as much as ca. 10% in the Barents Sea, thereby altering the agreement between CT and $P_{III}IP_{25}$ approaches. It is therefore not appropriate to seek complete agreement (based on definitive numerical SpSIC thresholds) between CT and $P_{III}IP_{25}$ approaches to sea ice reconstruction, especially since the $P_{III}IP_{25}$ approach is unlikely to reproduce overlying SpSIC with complete accuracy. Instead, CT predictions should be interpreted independently, while only changes (but not absolute values) of $P_{III}IP_{25}$-based SpSIC beyond the RMSE error of calibration (ca. ±11%) should be considered significant.

- Potentially insufficient coverage of the entire SpSIC range (0–100%) by the CT training set), which emphasizes the need for expansive training sets and also implies construction of separate models for different Arctic regions characterised by temporally and/or mechanistically unique sea ice seasonality. Similarly, separate SpSIC–$P_{III}IP_{25}$ calibrations should also be constructed for each region, since these will also likely be governed by different spatially-averaged *c*-factors depending on the relative production of IP_{25} and its chosen pelagic counterpart (e.g. HBI III).

6.1.2 Association between the HBI triene ratio and spring bloom dynamics

In addition to reconstructing sea ice conditions, the relationship between an HBI triene ratio of III against the sum of III and IV, and various satellite-derived oceanographic parameters was investigated via cluster and principal component analyses of surface and downcore sediment locations in the Barents Sea. Contrary to the previously hypothesized relationship between the HBI triene ratio and surface water mass (AW and ArW) distribution in the Barents Sea (Navarro-Rodriguez, 2014), no association was found with either SST or SSS. In contrast, the HBI triene ratio was positively associated with surface April–May Chl *a*, and could therefore potentially serve as an indicator of spring diatom blooms in the Barents Sea. Moreover, while absolute pelagic HBI concentrations were most enhanced in the central MIZ due to increased bloom intensity (and, therefore, organic matter deposition) at the retreating ice edge, the HBI triene ratio was also enhanced south of the ice edge. These findings tentatively suggested that the HBI triene ratio may be associated with a diatom response to the mechanism of spring bloom development (e.g. strong surface stratification, high nutrient stocks with limited vertical replenishment) or bloom duration, rather that net bloom productivity (or, at least, production of HBIs). Centennial downcore records also showed HBI triene ratio variability consistent with the likely spring bloom dynamics

controlled by overlying sea ice conditions. Thus, core sites located within the spring bloom zone at and south of the MIZ exhibited higher triene ratios relative to locations characterised by either extended annual sea ice duration or slow development of stratification due to continuous AW upwelling and absence of sea ice. Further, core sites that experienced decreasing and increasing proximity of the productive spring sea ice edge due to ice retreat since ca. 1850 exhibited a contrasting decrease and increase of the HBI triene ratio, respectively (section 3.5.5.2 and Fig. 3.21–3.22, Chapter 3). While the outcomes from surface sediments and centennial downcore records showcased the potential of the HBI triene ratio as a proxy of spring bloom occurrence and/or intensity, several caveats emerged when investigating millennial-scale cores (Chapter 4). HBI triene ratio variability was generally consistent with paleoproductivity-related inferences in these records throughout the Holocene (ca. 10 cal kyr BP–present), yet increased and decreased unexpectedly during the cold YD (when spring bloom duration was probably very limited) and the warm YD–Holocene transition (characterised by ice-free or MIZ conditions with high pelagic HBI concentrations), respectively. These uncertainties may be due to as yet unidentified influences on the HBI triene ratio within paleo-records, which may or may not be reproducible within the contemporary ocean.

6.1.3 A distributional approach to paleo-reconstruction in the Barents Sea

The second objective of the project was to use the investigated biomarker-based methods (sections 6.1.1–6.1.2) to characterise sea ice conditions and productivity regimes in the Barents Sea during intervals of significant climate change. Thus, CT and $P_{III}IP_{25}$ approaches to sea ice reconstruction provided insights into sea ice dynamics governing the northern Barents Sea shelf (section 4.4.1.4.1, Chapter 4), currently characterised by extensive seasonal ice cover. The Holocene section of the record (ca. 11.7 cal kyr BP–present) followed the insolation-mediated, gradual southward ice

advance widely reported in previous studies (Fig. 4.17). Interestingly, an earlier and more gradual ice retreat was observed throughout the YD stadial relative to sites on the western Barents Sea shelf, where abrupt ice decline following persistently extensive sea ice conditions was instead inferred. This suggested locally ameliorated conditions at the northern Barents Sea shelf during the YD, possibly due to a combination of AW inflow with (at least) periodic upwelling and/or a more distant BSIS relative to the western margin. This agrees with previous inferences of perennial ice cover in western and central Barents Sea at a time of seasonally open waters at the northern margin.

A multi-proxy examination of a southwestern Barents Sea core located on the continental slope (Chapter 5) revealed the prevalence of similar seasonally ice-covered conditions during the otherwise cold LGM (ca. 26–19 cal kyr BP). The presence of marginal ice was likely facilitated by the formation of coastal polynya supported by a combination of west-bound katabatic winds from a proximal BSIS, and upwelling of AW flowing within the NAC. Low concentrations of pelagic $C_{25:3}$ HBIs and conversely high sympagic IP_{25} and II during this period suggested that presence of MIZ conditions at the core site was likely time-limited, and that extensive sea ice cover prevailed for most of the annual cycle. This showcased the ability of HBIs produced by sea ice and open-water diatoms to distinguish sympagic and pelagic primary productivity. Meanwhile, concentrations of sterols remained high throughout the LGM – likely a consequence of their reduced source-specificity relative to pelagic HBIs, such that a wider range of sterol producers survived LGM conditions. In any case, presence of significant primary productivity unequivocally indicated survival of biota and absence of either a grounded BSIS or inhospitable, closed sea ice cover at the southwestern Barents Sea slope. In contrast, the subsequent HS1 event (ca. 18–16 cal kyr BP) was characterised by near-zero concentrations of all biomarkers signifying perennial conditions which could not support significant primary production; these coincided with

massive meltwater injections and an IRD pulse from the collapsing BSIS, which likely promoted ice formation at the surface and hampered AW overturning. The latter potentially resulted in multicentennial sub-surface warming and the eventual resumption of AW overturning by ca. 16 cal kyr BP mediated by release of warm water to the surface and reduced meltwater influence from the increasingly distant BSIS. At this time, rapid sea ice retreat (very low IP_{25} and II, <10% $P_{III}IP_{25}$-based SpSIC, and CT predictions of marginal sea ice conditions) and highly-productive MIZ conditions conducive to pelagic diatom growth (very high III and IV) prevailed. Overall, the ecosystem rapidly recovered despite the collapse of microalgal stocks triggered by the final collapse of a marine-based BSIS at the start of HS1. The resurgence of pelagic HBIs at this time overshadowed that of sterols, which only increased to pre-HS1 concentrations. As pointed out previously, this is probably indicative of the reduced source-specificity of sterols, which were likely produced by a similarly wide range of flora and fauna before and after HS1. In contrast, pelagic HBI occurrence was solely indicative of diatom productivity, which flourished during extended annual duration of MIZ conditions at the site at ca. 16 cal kyr BP. Importantly, however, while absolute sterol concentrations were unable to distinguish more extensive LGM sea ice cover from ameliorated MIZ conditions post-HS1, relative distributions of various sterols within a multivariate set were unique in these settings, and compared favourably to sterol distributions in proximal surface sediments representative of contrasting contemporary ice conditions. The most striking feature was the shift from C_{28}–C_{29} phytosterol-dominated distributions during the LGM to a prevalence of cholesterol, potentially as a consequence of a marine fauna resurgence in highly-productive, diatom-dominated conditions. This highlighted the ability of distributional sterol analysis to distinguish contrasting environmental settings despite their reduced source-specificity relative to that of HBIs.

6.2 Future work

Despite initial introduction of the multivariate CT approach (Chapter 3) and its consistency with $P_{III}IP_{25}$-based SpSIC, the application of both methods is currently limited to the Barents Sea, which is defined by a stable seasonality of ice advance and retreat. Investigating the potential of multivariate classification methods based on HBI distributions further requires analyses of additional surface sediment datasets encompassing contrasting seasonal sea ice conditions in other Arctic seas. Moreover, CT models targeting parameters other than sea ice may be built – for example, the influence of HBI VI produced by the coastal diatom *B. rutilans* could be investigated in regions of considerable fluvial input.

The identification of a potential influence of the Barents Sea spring diatom bloom on the pelagic HBI triene ratio is not fully resolved at present. First, the consistency of the association between Chl *a* and the triene ratio needs to be confirmed in other regions characterised by spring blooms – the ubiquity of HBI trienes allows for such investigations in both temperate and polar environments. Second, uncertainties remain as to whether the HBI triene ratio is controlled by changes in diatom assemblage to favour species adapted to productive halocline-stratified conditions, or by biological influences common to all HBI-producing diatoms (such as the principal producer of III and IV, *R. setigera*). Deciphering this requires comparison of HBI distributions with diatom traits (e.g. morphology, nutrient uptake and growth rates) in both strongly-stratified spring bloom conditions and less productive areas controlled by weaker (e.g. thermal) stratification and turbulent mixing. Such comparisons may elucidate whether particular diatom types preferentially produce one HBI triene, while investigations of HBI production under variable conditions influencing growth rates (e.g. nutrient availability and temperature) will be useful when determining biological controls on relative triene

production. Third, unexpected changes of the HBI triene ratio during ca. 13–10 cal kyr BP require analysis of further cores to ascertain the extent of its applicability to paleo-records.

Finally, new insights into paleo-sea ice and productivity conditions obtained during the YD and the Late Weichselian glaciation suggested not only that HBIs can decouple sympagic and pelagic productivity, but that multivariate analysis of the less source-specific sterols could also be beneficial, with unique distributions observed during glacial and interglacial conditions. Both HBI and sterol distributions were also comparable to those observed in extensively ice-covered and MIZ conditions in the contemporary Barents Sea. The confirmation of these findings will require biomarker-based examination of other cores encompassing glacial-interglacial transitions.

Appendix A

This Appendix contains web links to the R source code used for the statistical analyses:

1) Functions for downloading, analysing, and plotting satellite data (Chapters 1 and 3) are available at: https://github.com/Deniz-Koseoglu/ClimMap_Toolkit.
2) Functions for training and testing CT models (Chapter 3), as well as calculating and plotting rolling correlations (Chapter 4) with changepoint analysis (Chapter 5) are available at: https://github.com/Deniz-Koseoglu/CT-Toolkit.

Appendix B

To determine HBI and sterol concentrations used for reproducibility monitoring, several replicates of the CAA reference sediment (section 2.3.3, Chapter 2) were extracted via the DCM–MeOH (section 2.2.2.1) and KOH (section 2.2.2.2) methods, respectively. The results for HBIs and sterols are shown in Tables B.1 and B.2.

Table B.1: Absolute concentrations (ng g^{-1} sed.) of HBIs (Fig. 1.8, Chapter 1) in the CAA reference sediment. Red asterisks denote values derived using $RF_{estimate}$ values (Eq. 2.4) calculated from RRFs (Eq. 2.3).

Replicate	HBI concentrations (ng g^{-1} sed.) with mean, SD, and RSD (%) values					
	IP_{25}	II	III	IV	V*	VI*
1	66.13	262.17	13.42	4.51	20.41	8.29
2	66.07	249.11	13.11	4.18	23.71	8.38
3	67.95	263.86	13.81	5.18	22.48	8.46
4	62.44	250.70	12.02	3.88	20.81	7.72
5	62.00	252.90	13.81	4.73	22.26	7.71
6	63.09	267.78	12.80	4.82	22.80	7.67
7	64.64	259.61	12.97	4.62	22.84	8.59
8	66.11	262.20	13.21	4.58	20.71	8.37
9	63.82	272.69	12.75	4.66	22.64	7.83
10	65.81	275.39	12.19	4.73	21.96	8.56
Mean	**64.81**	**261.64**	**13.01**	**4.59**	**22.06**	**8.16**
SD (RSD)	**1.93 (2.9)**	**8.89 (3.4)**	**0.60 (4.6)**	**0.35 (7.7)**	**1.08 (4.9)**	**0.38 (4.7)**

Table B.2: Absolute concentrations (μg g^{-1} sed.) of sterols (Fig. 2.9, Chapter 2) in the CAA reference sediment. Red asterisks denote values obtained using RF estimates calculated via Eq. 2.6 (Chapter 2) and shown in Table 5.2 (Chapter 5). Abbreviations denote brassicasterol (A), chalinasterol (B), campesterol (C), β-sitosterol (D); dinosterol (E), and cholesterol (F).

Replicate	Sterol concentrations (μg g^{-1} sed.) with mean, SD, and RSD (%) values					
	A	B*	C*	D*	E*	F
1	5.11	12.67	4.37	4.92	1.59	7.49
2	5.04	12.07	4.43	4.97	1.58	7.36
3	4.91	12.90	4.78	5.25	1.68	7.78
4	5.11	12.98	4.44	4.89	1.75	7.75
5	4.84	12.61	4.39	4.70	1.42	7.68
Mean	**5.00**	**12.65**	**4.48**	**4.95**	**1.60**	**7.61**
SD	**0.12**	**0.36**	**0.17**	**0.20**	**0.12**	**0.18**
RSD	**2.5**	**2.8**	**3.8**	**4.0**	**7.7**	**2.3**

Appendix C

Various data relevant to Chapter 3 of this thesis are presented herein. These include HBI concentrations (ng g^{-1} sed.), $P_{III}IP_{25}$-derived SpSIC estimates (%), CT model predictions of sea ice conditions, and HBI triene ratios in surface sediments (Table C.3) and downcore records 1, 8, 43, and 712 (Table C.4). Also included is a map showing the region shapefiles used for averaging of satellite data (Fig. C.1) to create daily timeseries shown in Fig. 3.12–3.13 (Chapter 3). Finally, example calculations of the performance metrics used for CT model assessment (Table 3.1, Chapter 3) are shown in Table C.5 and Eq. C.1–C.9.

Table C.3: HBI concentrations (ng g^{-1} sed.), $P_{III}IP_{25}$-based SpSIC estimates (%), HBI triene ratios (abbreviated to TRa), and classes of marginal (M), intermediate (I), or extensive (E) sea ice conditions assigned using CT models A–D (Fig. 3.7, Chapter 3) in Barents Sea surface sediments.

ID	°N	°E	HBIs (ng g^{-1} sed.)						Proxy data		CT output			
			IP_{25}	II	III	IV	V	VI	SpSIC	TRa	A	B	C	D
625	71.72	21.76	0.0	0.0	0.2	0.2	0.0	2.0	-6.5	0.51	M	M	M	M
627	72.32	24.06	0.0	0.0	0.1	0.0	0.0	1.9	-6.5	0.75	M	M	M	M
629	73.01	24.25	0.0	0.0	0.7	0.4	1.4	3.7	-6.5	0.65	M	M	M	M
631	73.67	24.47	0.0	0.0	1.0	0.4	1.6	5.6	-6.5	0.69	M	M	M	M
633	74.34	24.69	0.5	1.8	4.6	2.0	3.8	13.8	6.2	0.69	I	M	M	M
635	75	24.94	3.9	19.0	46.9	22.2	54.4	53.4	4.3	0.68	M	M	M	M

Table C.3 (*continued*)

ID	°N	°E	HBIs (ng g^{-1} sed.)						Proxy data		CT output			
			IP_{25}	II	III	IV	V	VI	SpSIC	TRa	A	B	C	D
639	75.57	27.9	2.5	10.1	32.5	15.0	28.0	51.3	3.7	0.68	M	M	I	M
643	76.49	29.91	3.0	8.9	25.1	12.2	10.3	37.8	8.6	0.67	M	M	I	M
645	75.86	29.46	1.2	5.0	16.2	7.4	6.0	28.3	3.2	0.69	M	M	M	M
647	75.2	29.01	0.8	3.1	15.1	6.8	5.3	0.0	0.8	0.69	M	M	M	I
649	74.54	28.58	0.0	1.5	8.8	3.5	2.9	32.4	-6.5	0.71	M	M	M	M
651	74.64	26.08	0.7	2.9	9.0	4.1	10.5	25.5	3.9	0.69	M	M	M	M
653	73.97	25.81	0.0	0.0	3.2	1.3	3.1	15.5	-6.5	0.70	M	M	M	M
655	73.31	25.54	0.0	0.0	1.0	0.4	2.3	6.1	-6.5	0.69	M	M	M	M
657	72.64	25.27	0.0	0.0	0.2	0.2	0.0	2.9	-6.5	0.60	M	M	M	M
659	71.98	25.06	0.0	0.0	0.3	0.1	0.0	5.9	-6.5	0.68	M	M	M	M
661	71.37	22.76	0.0	0.0	0.2	0.1	0.0	2.4	-6.5	0.67	M	M	M	M
663	71.61	25.99	0.0	0.0	0.2	0.1	0.0	4.0	-6.5	0.68	M	M	M	M
665	72.17	28.41	0.0	0.0	0.4	0.2	0.0	6.5	-6.5	0.68	M	M	M	M
667	72.84	28.76	0.0	0.0	0.6	0.3	0.0	9.3	-6.5	0.70	M	M	M	M
669	73.5	29.15	0.0	0.0	1.4	0.7	0.9	12.1	-6.5	0.69	M	M	M	M
671	74.15	29.55	0.0	0.0	3.2	1.2	0.0	18.3	-6.5	0.72	M	M	M	M
673	74.67	32.49	1.4	4.7	16.9	7.5	0.0	31.3	4.1	0.69	M	M	I	M
675	75.33	33.07	1.2	4.2	18.4	7.9	0.0	51.0	2.3	0.70	M	M	M	M
677	75.97	33.73	1.1	3.4	6.0	2.8	0.0	16.2	14.5	0.68	I	M	I	I
679	76.62	34.45	4.6	15.8	9.4	4.5	4.8	7.5	34.5	0.68	I	I	I	I
681	76.43	37.17	1.4	4.4	14.1	6.6	0.0	18.2	6.6	0.68	M	M	M	I
690	71.02	30.96	0.0	0.0	0.3	0.3	0.0	3.5	-6.5	0.50	M	M	M	M
692	70.62	31.72	0.0	0.0	0.2	0.0	0.0	1.4	-6.5	1.00	M	M	M	M
R3 MC110	71.33	22.42	0.0	0.0	0.5	0.3	0.0	6.6	-6.5	0.63	M	M	M	M
R4 MC107	71.33	22.49	0.0	0.0	0.4	0.2	0.0	4.0	-6.5	0.61	M	M	M	M
R10 MC96	71.21	21.45	0.0	0.0	0.3	0.3	0.0	1.5	-6.5	0.50	M	M	M	M
R11 MC105	71.22	21.72	0.0	0.0	0.2	0.2	0.0	1.0	-6.5	0.50	M	M	M	M
R14 MC94	71.13	21.44	0.0	0.0	0.5	0.4	0.0	3.9	-6.5	0.56	M	M	M	M
R18 MC98	71.31	21.28	0.0	0.0	0.1	0.1	0.0	0.8	-6.5	0.57	M	M	M	M
R37 MC115	70.31	22.26	0.0	0.0	2.3	1.5	0.0	80.8	-6.5	0.60	M	M	M	M
R49 MC128	70.42	22.1	0.0	0.0	1.6	1.2	0.0	53.9	-6.5	0.56	M	M	M	M
R68 MC149	71.32	22.5	0.0	0.0	1.2	0.8	0.0	15.3	-6.5	0.62	M	M	M	M
R68A MC136	71.32	22.49	0.0	0.0	0.2	0.0	0.0	2.6	-6.5	1.00	M	M	M	M
R77 MC001	69.96	20.44	0.0	0.0	2.0	1.6	0.0	54.0	-6.5	0.56	M	M	M	M
R80 MC004	69.66	20.43	0.0	0.0	1.8	1.5	0.0	46.8	-6.5	0.55	M	M	M	M
R81 MC002	71.16	18.65	0.0	0.0	0.3	0.2	0.0	2.4	-6.5	0.57	M	M	M	M
R96 MC008	69.71	15.2	0.0	0.0	1.3	0.8	0.0	20.0	-6.5	0.60	M	M	M	M
R104 MC011	70.19	17.73	0.0	0.0	0.6	0.4	0.0	11.7	-6.5	0.60	M	M	M	M
R112 MC007	69.81	17.42	0.0	0.0	4.2	2.8	0.0	76.8	-6.5	0.60	M	M	M	M
R117 MC005	69.85	17.13	0.0	0.0	0.5	0.5	0.0	6.3	-6.5	0.50	M	M	M	M
R184 BX065	69.41	16.4	0.0	0.0	2.3	1.7	0.0	51.8	-6.5	0.57	M	M	M	M
R223 MC005	69.26	16.33	0.0	0.0	1.8	1.4	0.0	43.7	-6.5	0.56	M	M	M	M
R231 MC008	69.26	14.33	0.0	0.0	1.9	2.2	0.0	2.8	-6.5	0.46	M	M	M	M
R243 GR037	68.58	13.71	0.0	0.0	0.3	0.1	0.0	5.1	-6.5	0.68	M	M	M	M
R248 GR039	68.78	12.53	0.0	0.0	2.1	2.5	0.0	1.6	-6.5	0.46	M	M	M	M
R259 GR041	69.18	13.98	0.0	0.0	1.5	1.7	0.0	1.2	-6.5	0.46	M	M	M	M
R259 MC011	69.18	13.98	0.0	0.0	1.1	1.4	0.0	0.8	-6.5	0.44	M	M	M	M

Table C.3 (*continued*)

ID	°N	°E	HBIs (ng g^{-1} sed.)						Proxy data		CT output			
			IP_{25}	II	III	IV	V	VI	SpSIC	TRa	A	B	C	D
R259 MC011	69.18	13.98	0.0	0.0	1.1	1.4	0.0	0.8	-6.5	0.44	M	M	M	M
R276 BX049	68.48	10.97	0.0	0.0	0.3	0.4	0.0	0.0	-6.5	0.45	M	M	M	M
R280A MC016	68.14	12.3	0.0	0.0	0.8	0.5	0.0	11.1	-6.5	0.63	M	M	M	M
R291 MC020	68.61	15.24	0.0	0.0	4.9	4.6	0.0	234.5	-6.5	0.51	M	M	M	M
R291 MC022	68.61	15.24	0.0	0.0	7.2	6.5	0.0	294.5	-6.5	0.53	M	M	M	M
R297 BX056	68.65	11.91	0.0	0.0	0.4	0.4	0.0	0.3	-6.5	0.48	M	M	M	M
R301 MC023	68.71	11.59	0.0	0.0	1.0	1.1	0.0	0.4	-6.5	0.46	M	M	M	M
R311 BX059	68.9	12.67	0.0	0.0	1.5	1.7	0.0	0.8	-6.5	0.47	M	M	M	M
R351 BX065	68.85	13.1	0.0	0.0	0.3	0.4	0.0	0.7	-6.5	0.45	M	M	M	M
R359 BX067	68.09	11.6	0.0	0.0	0.2	0.1	0.0	3.7	-6.5	0.66	M	M	M	M
R406 MC0	72.19	14.83	0.0	0.0	0.6	0.6	0.0	1.1	-6.5	0.49	M	M	M	M
R754 MC021	67.8	9.71	0.0	0.0	0.5	0.7	0.0	0.0	-6.5	0.45	M	M	M	M
R776 MC004	68.19	10.36	0.0	0.0	0.5	0.5	0.0	0.0	-6.5	0.51	M	M	M	M
R782 MC007	68.06	9.47	0.0	0.0	0.6	0.6	0.0	0.0	-6.5	0.50	M	M	M	M
R889 MC025	64.29	8.8	0.0	0.0	5.6	1.7	0.0	0.0	-6.5	0.77	M	M	M	M
R911 MC022	63.55	7.41	0.0	0.0	8.9	2.1	0.0	0.0	-6.5	0.81	M	M	M	M
R932 BX029-1	64.11	5.73	0.0	0.0	2.6	2.3	0.0	1.9	-6.5	0.53	M	M	M	M
R942 BX026-1	64.41	5.57	0.0	0.0	3.3	3.8	0.0	2.4	-6.5	0.47	M	M	M	M
R949 MC028-4	65.16	9.35	0.0	0.0	1.7	0.7	0.0	0.0	-6.5	0.70	M	M	M	M
R949 MC028-2	65.16	9.35	0.0	0.0	0.8	0.5	0.0	0.0	-6.5	0.62	M	M	M	M
R961 MC024-1	64.17	8.1	0.0	0.0	2.8	1.0	0.0	0.0	-6.5	0.75	M	M	M	M
R973 BX025-1	64.57	5.67	0.0	0.0	1.8	1.4	0.0	0.0	-6.5	0.55	M	M	M	M
R1080 BX010	66.21	7	0.0	0.0	0.4	0.3	0.0	0.0	-6.5	0.55	M	M	M	M
R1096 MC002-1	65.95	6.51	0.0	0.0	0.6	0.3	0.0	0.0	-6.5	0.63	M	M	M	M
R1096 MC002-4	65.95	6.51	0.0	0.0	0.5	0.3	0.0	0.0	-6.5	0.61	M	M	M	M
R1114 MC003-2	65.63	5.57	0.0	0.0	2.5	1.3	0.0	0.0	-6.5	0.65	M	M	M	M
R1114 MC003-6	65.63	5.57	0.0	0.0	1.2	0.8	0.0	0.0	-6.5	0.58	M	M	M	M
R1119 MC004	65.51	6.28	0.0	0.0	0.7	0.4	0.0	0.0	-6.5	0.61	M	M	M	M
R1129 MC005	65.29	6.28	0.0	0.0	1.9	0.8	0.0	0.0	-6.5	0.71	M	M	M	M
R1133 MC006	65.17	5.93	0.0	0.0	1.1	0.8	0.0	0.0	-6.5	0.57	M	M	M	M
R1139 MC010-2	72.31	32.35	0.0	0.0	6.4	2.7	0.0	43.1	-6.5	0.71	M	M	M	M
R1139 MC010-1	72.31	32.35	0.0	0.0	2.6	1.3	0.0	73.1	-6.5	0.67	M	M	M	M
R1146 MC011-2	72.11	34.33	0.0	0.0	8.1	3.0	0.0	68.8	-6.5	0.73	M	M	M	M
R1146 MC011-4	72.11	34.33	0.0	0.0	9.3	3.1	0.0	93.1	-6.5	0.75	M	M	M	M
R1165 MC012	71.78	33.53	0.0	0.0	6.5	2.7	0.0	76.3	-6.5	0.70	M	M	M	M
R1174 MC013	71.62	32.22	0.0	0.0	2.5	1.2	0.0	42.6	-6.5	0.67	M	M	M	M
R1180 MC014	71.61	32.99	0.0	0.0	3.3	1.7	0.0	49.1	-6.5	0.67	M	M	M	M
R1180 MC014	71.61	32.99	0.0	0.0	4.3	2.3	0.0	61.2	-6.5	0.65	M	M	M	M
R1186 MC015-1	71.42	32.87	0.0	0.0	2.4	1.2	0.0	41.3	-6.5	0.66	M	M	M	M
R1186 MC015-6	71.42	32.87	0.0	0.0	2.5	1.1	0.0	37.8	-6.5	0.69	M	M	M	M
R1200 MC016-1	70.86	32.52	0.0	0.0	2.6	1.2	0.0	29.0	-6.5	0.68	M	M	M	M
R1200 MC016-2	70.86	32.52	0.0	0.0	1.6	0.6	0.0	20.9	-6.5	0.74	M	M	M	M
R1205 MC017-4	70.58	32.28	0.0	0.0	1.0	0.4	0.0	16.8	-6.5	0.70	M	M	M	M
R1205 MC017-6	70.58	32.28	0.0	0.0	1.1	0.5	0.0	16.2	-6.5	0.70	M	M	M	M
R1213 MC018	70.78	30.72	0.0	0.0	2.1	1.1	0.0	41.2	-6.5	0.66	M	M	M	M
R1257 GR681	62.89	4.3	0.0	0.0	3.7	3.1	0.0	1.7	-6.5	0.54	M	M	M	M
R1261 MC020	63.03	4.69	0.0	0.0	7.7	9.2	0.0	6.6	-6.5	0.46	M	M	M	M

Table C.3 (*continued*)

ID	°N	°E	HBIs (ng g^{-1} sed.)						Proxy data		CT output			
			IP_{25}	II	III	IV	V	VI	SpSIC	TRa	A	B	C	D
R1271 MC021	63.31	5.09	0.0	0.0	4.6	3.8	0.0	1.9	-6.5	0.55	M	M	M	M
R1284 MC027	64.81	10.12	0.0	0.0	2.5	0.8	0.0	1.3	-6.5	0.77	M	M	M	M
St01	72	22	0.0	0.0	0.9	0.9	0.0	3.2	-6.5	0.50	M	M	M	M
St02	72.02	20.92	0.0	0.0	1.0	1.1	0.0	2.2	-6.5	0.49	M	M	M	M
St03	72.03	19.85	0.0	0.0	1.8	2.1	0.0	1.2	-6.5	0.46	M	M	M	M
St04	72.02	18.77	0.0	0.0	3.6	4.1	0.0	0.7	-6.5	0.46	M	M	M	M
St05	72.03	17.7	0.0	0.0	1.7	2.9	0.0	0.0	-6.5	0.37	M	M	M	M
St06	72.02	16.62	0.0	0.0	2.7	3.2	0.0	0.6	-6.5	0.46	M	M	M	M
St07	72.02	15.52	0.0	0.0	1.0	1.2	0.0	0.7	-6.5	0.44	M	M	M	M
St08	72.01	14.73	0.0	0.0	0.8	1.1	0.0	0.2	-6.5	0.43	M	M	M	M
St09	72.01	14.62	0.0	0.0	1.5	1.9	0.0	0.8	-6.5	0.44	M	M	M	M
St11	73.17	12.94	0.0	0.0	2.4	2.6	0.0	0.5	-6.5	0.48	M	M	M	M
St12	73.17	14.09	0.0	0.0	0.4	0.5	0.0	0.0	-6.5	0.43	M	M	M	M
St13	73.17	15.23	0.0	0.0	2.4	2.9	0.0	0.4	-6.5	0.45	M	M	M	M
St14	73.17	16.38	0.0	0.0	2.2	2.6	2.2	1.1	-6.5	0.46	M	M	M	M
St16	73.17	18.82	0.0	0.0	1.5	1.3	2.8	1.6	-6.5	0.53	M	M	M	M
St17	73.17	19.86	0.0	0.0	2.3	1.8	4.4	2.6	-6.5	0.56	M	M	M	M
St18	73.17	20.95	0.0	0.0	3.5	2.5	4.5	3.9	-6.5	0.59	M	M	M	M
St19	73.17	22.01	0.0	0.0	2.0	1.3	3.7	3.8	-6.5	0.61	M	M	M	M
St20	74.82	18.02	1.8	4.9	11.1	7.7	112.9	5.5	13.0	0.59	M	I	I	M
St21	74.82	17	1.0	2.7	6.2	5.7	35.5	2.6	12.4	0.52	M	I	M	I
St22	74.82	16.03	0.4	1.3	2.4	2.4	8.2	0.9	11.7	0.50	M	M	M	I
St23	74.82	14.79	0.0	0.0	3.4	4.5	0.0	0.7	-6.5	0.43	M	M	M	M
St34	71.75	22	0.0	0.0	0.6	0.6	0.0	2.2	-6.5	0.50	M	M	M	M
St35	71.62	21.07	0.0	0.0	0.4	0.4	0.0	0.7	-6.5	0.47	M	M	M	M
St36	71.6	20.86	0.0	0.0	1.0	1.1	0.0	1.1	-6.5	0.49	M	M	M	M
St37	71.6	21.19	0.0	0.0	0.8	0.8	0.0	1.4	-6.5	0.51	M	M	M	M
St38	71.49	20.82	0.0	0.0	0.7	0.5	0.0	1.1	-6.5	0.57	M	M	M	M
St39	71.34	20.19	0.0	0.0	0.4	0.4	0.0	0.6	-6.5	0.54	M	M	M	M
St40	71.18	19.56	0.0	0.0	0.4	0.3	0.0	1.3	-6.5	0.54	M	M	M	M
St42	70.87	18.34	0.0	0.0	0.7	0.4	0.0	2.6	-6.5	0.61	M	M	M	M
St43	70.72	17.75	0.0	0.0	2.9	3.0	0.0	6.1	-6.5	0.49	M	M	M	M
St45	70.44	16.75	0.0	0.0	1.2	1.2	0.0	1.9	-6.5	0.49	M	M	M	M
JR142-GC10	80.49	29.65	8.4	33.5	0.7	0.7	4.5	2.8	82.5	0.50	E	E	E	E
JR142-GC11	81.08	28.93	6.0	20.7	0.4	0.4	3.5	1.7	82.9	0.54	E	E	E	E
JR142-GC12	81.39	26.94	5.7	22.3	1.6	1.4	9.8	3.2	73.3	0.52	E	I	I	E
JR142-GC13	81.35	21.63	1.3	4.4	0.2	0.2	1.5	0.6	80.0	0.52	E	E	E	E
JR142-GC19	81.26	19.02	4.7	19.7	1.3	1.1	5.3	3.3	73.0	0.54	E	E	E	E
JR142-GC20	79.59	26.19	1.9	4.3	0.1	0.1	0.0	0.8	84.2	0.53	E	E	E	E
JR142-GC21	78.57	34.06	2.4	7.1	0.6	0.3	1.2	1.8	74.6	0.67	E	I	E	E
JR142-GC22	79.33	29.9	8.6	31.9	0.4	0.4	5.1	2.0	84.6	0.49	E	E	E	E
JR142-GC23	79.38	29.77	8.5	29.4	0.3	0.3	5.4	1.9	85.0	0.51	E	E	E	E
JR142-GC4	78.9	23.98	13.6	43.6	0.7	0.5	8.8	4.1	84.1	0.57	E	E	E	E
JR142-GC5	78.95	24.45	9.4	30.5	0.4	0.3	4.8	2.5	84.7	0.57	E	E	E	E
JR142-GC6	79.1	25.1	7.9	24.4	0.4	0.3	4.1	1.9	84.3	0.58	E	E	E	E
JR142-GC7	79.21	26.54	8.3	28.3	0.3	0.3	3.5	2.3	84.9	0.51	E	E	E	E
JR142-GC8	79.49	28.44	7.6	24.9	0.3	0.3	3.4	1.7	84.9	0.50	E	E	E	E

Table C.3 (*continued*)

ID	°N	°E	HBIs (ng g^{-1} sed.)						Proxy data		CT output			
			IP_{25}	II	III	IV	V	VI	SpSIC	TRa	A	B	C	D
JR142-GC9	79.96	29.65	7.3	28.4	0.4	0.4	4.1	2.0	83.7	0.51	E	E	E	E
PS2111-2	76.64	34.88	3.4	6.3	1.3	0.7	0.0	3.9	69.3	0.65	I	E	I	I
PS2113-1	76	34.9	0.7	1.8	2.2	1.3	0.0	14.3	24.6	0.63	I	I	I	I
PS2115-1	77.2	18.33	12.3	41.0	0.0	0.0	13.0	2.2	87.0	0.00	E	E	E	E
PS2131-1	80.98	27.1	2.9	6.6	0.2	0.1	0.0	0.5	84.0	0.63	E	E	E	E
PS2142-3	80.85	30.64	2.1	5.8	0.1	0.1	0.0	0.4	84.6	0.45	E	E	E	E
PS2144-3	80.75	29.47	2.5	8.8	0.2	0.1	0.0	0.6	83.1	0.55	E	E	E	E
PS2148-1	80.01	29.6	3.0	10.2	0.1	0.1	0.0	0.7	84.5	0.59	E	E	E	E
PS2149-1	73.18	31.73	1.3	3.2	0.0	0.0	0.0	0.0	85.2	1.00	E	E	E	E
PS2150-1	78.67	32.13	3.6	7.8	0.1	0.0	0.0	0.0	85.4	1.00	E	E	E	E
PS2151-1	77.99	32.94	2.5	5.4	0.3	0.1	0.0	0.5	81.3	0.72	E	E	E	E
PS2153-1	76.61	34.81	3.3	6.4	1.2	0.6	0.0	4.5	69.7	0.67	E	E	E	E
R1 MC85	70.46	21.68	0.0	0.0	2.8	2.3	0.0	55.2	-6.5	0.55	M	M	M	M
R100 MC010	70.16	18.02	0.0	0.0	2.5	1.7	0.0	42.2	-6.5	0.60	M	M	M	M
R111 MC004	69.8	17.5	0.0	0.0	2.5	1.6	0.0	45.0	-6.5	0.62	M	M	M	M
R178 MC010	68.86	15.44	0.0	0.0	9.0	11.2	0.0	346.4	-6.5	0.45	M	M	M	M
R209 MC003	69.8	16.42	0.0	0.0	3.0	2.8	0.0	14.2	-6.5	0.52	M	M	M	M
R223 MC006	69.26	16.33	0.0	0.0	3.4	2.2	0.0	70.5	-6.5	0.61	M	M	M	M
R229 MC007	69.14	13.68	0.0	0.0	1.6	1.8	0.0	2.1	-6.5	0.46	M	M	M	M
R232 MC009	69.41	14.7	0.0	0.0	1.6	1.8	0.0	0.0	-6.5	0.47	M	M	M	M
R248 MC010	68.78	12.53	0.0	0.0	2.3	2.6	0.0	0.0	-6.5	0.47	M	M	M	M
R276 BX049	68.48	10.97	0.0	0.0	0.5	0.4	0.0	0.0	-6.5	0.55	M	M	M	M
R280 MC018	68.14	12.31	0.0	0.0	0.9	0.6	0.0	15.3	-6.5	0.59	M	M	M	M
R35 MC114	70.23	22.71	0.0	0.0	3.2	2.1	0.0	113.3	-6.5	0.61	M	M	M	M
R35 MC118	70.43	22.75	0.0	0.0	2.4	1.0	0.0	116.4	-6.5	0.71	M	M	M	M
R367 MC026	72.42	15.5	0.0	0.0	0.8	1.0	0.0	1.8	-6.5	0.46	M	M	M	M
R405 MC031	72.14	15.35	0.0	0.0	1.2	1.4	0.0	2.5	-6.5	0.47	M	M	M	M
R421 MC033	72.15	16.55	0.0	0.0	0.5	0.4	0.0	0.0	-6.5	0.56	M	M	M	M
R431 MC035	71.86	16.75	0.0	0.0	0.7	0.7	0.0	3.6	-6.5	0.51	M	M	M	M
R81 MC002	71.16	18.65	0.0	0.0	0.4	0.3	0.0	5.6	-6.5	0.55	M	M	M	M
R87 MC006	71.31	20.32	0.0	0.0	0.5	0.3	0.0	0.0	-6.5	0.64	M	M	M	M
04GC	78.58	9.42	2.1	9.8	1.8	1.4	20.9	2.5	55.1	0.56	I	I	I	I
10BC	78.6	9.12	2.7	14.2	6.5	8.5	13.5	3.2	30.4	0.44	I	I	I	I
12GC	79.46	7.4	1.7	7.8	1.7	1.6	9.9	2.5	50.5	0.52	I	I	I	I
13GC	79.39	6.77	1.1	5.8	0.8	0.6	8.1	1.4	58.1	0.55	I	I	I	I
15GC	79.63	7.92	0.9	4.0	0.7	0.6	4.5	1.4	57.5	0.55	I	I	I	I
26GC	79.01	6.9	1.1	5.7	0.4	0.5	6.9	1.3	71.3	0.44	E	E	E	I
28GC	78.74	7.49	2.0	10.0	8.9	11.6	9.1	0.8	18.5	0.43	I	I	I	I
33GC	78.68	8.27	1.6	6.4	1.5	1.2	8.1	1.1	52.4	0.55	I	I	I	I
GC14	80.39	16.44	8.0	33.8	4.4	4.0	13.4	7.9	63.0	0.52	I	I	I	E
GC15	80.51	15.9	11.6	54.9	4.5	3.9	14.1	11.6	68.7	0.53	I	I	I	I
GC17	80.15	17.18	12.9	62.3	4.6	4.4	9.2	13.6	69.8	0.51	I	E	E	E
921GC	76.11	16.00	11.8	87.0	23.7	13.8	218.3	15.1	34.7	0.63	I	I	I	I
1070GC	76.11	16.00	3.1	22.6	17.1	12.0	73.8	6.7	14.5	0.59	I	M	I	M
914GC	76.11	16.03	10.2	78.7	20.9	11.4	158.3	14.0	34.3	0.65	I	I	I	I
932MC	76.11	15.97	7.9	56.9	33.8	18.7	210.7	13.7	18.8	0.64	I	M	I	I
1036GC	76.11	16.08	11.2	81.3	20.7	11.5	182.0	13.4	36.8	0.64	I	I	I	I

Table C.3 (*continued*)

ID	°N	°E	HBIs (ng g^{-1} sed.)						Proxy data		CT output			
			IP_{25}	II	III	IV	V	VI	SpSIC	TRa	A	B	C	D
914GC	76.11	16.03	9.0	72.3	23.3	12.2	148.3	13.0	29.1	0.66	I	I	I	I
1048GC	76.11	16.00	12.1	75.9	13.9	8.1	152.4	12.9	47.8	0.63	I	I	I	I
1069GC	76.11	16.01	4.7	30.9	13.1	8.1	91.1	6.7	27.3	0.62	I	I	I	I
1081GC	76.12	16.04	6.2	45.2	11.0	6.2	121.1	8.1	37.7	0.64	I	I	I	I
1082GC	76.11	15.95	8.7	55.7	13.2	7.6	134.4	9.6	41.2	0.63	I	I	I	I

Table C.4: HBI concentrations (ng g^{-1} sed.), $P_{III}IP_{25}$-based SpSIC estimates (%), HBI triene ratios (abbreviated to TRa), and classes of marginal (M), intermediate (I), or extensive (E) sea ice conditions assigned using CT model A (Fig. 3.7a, Chapter 3) in Barents Sea cores 1, 8, 43, and 712.

ID	Coordinates		Depth	Age (cal	HBIs (ng g^{-1} sed.)				Proxy data		CT output
	°N	°E	(cm)	yr AD)	IP_{25}	II	III	IV	SpSIC	TRa	(Model A)
1	73.10	25.63	0.5	1994	0	0	3.6	2.3	-6.5	0.61	M
1	73.10	25.63	1.5	1979	0	0	3.2	2.1	-6.5	0.60	M
1	73.10	25.63	2.5	1964	0	0	3.9	2.8	-6.5	0.59	M
1	73.10	25.63	3.5	1950	0	0	3.1	1.8	-6.5	0.63	M
1	73.10	25.63	4.5	1935	0	0	3.2	2.3	-6.5	0.59	M
1	73.10	25.63	5.5	1920	0	0	3.1	1.8	-6.5	0.63	M
1	73.10	25.63	6.5	1906	0	0	2.8	1.7	-6.5	0.62	M
1	73.10	25.63	7.5	1891	0	0	2.3	1.6	-6.5	0.58	M
1	73.10	25.63	8.5	1876	0	0	3.4	2.2	-6.5	0.61	M
1	73.10	25.63	9.5	1862	0	0	3.5	2.3	-6.5	0.60	M
1	73.10	25.63	11	1832	0	0	2.3	1.6	-6.5	0.59	M
1	73.10	25.63	13	1803	0	0	2.4	1.7	-6.5	0.58	M
1	73.10	25.63	15	1774	0	0	2.8	1.7	-6.5	0.62	M
1	73.10	25.63	17	1744	0	0	4.7	3.5	-6.5	0.57	M
8	77.98	26.79	0.5	1993	13.1	45.3	0.6	0.6	84.2	0.53	E
8	77.98	26.79	1.5	1978	15.5	60.1	0.7	0.7	84.3	0.50	E
8	77.98	26.79	2.5	1962	17.6	74.9	0.9	0.8	84.2	0.51	E
8	77.98	26.79	3.5	1947	16.9	78.1	0.9	1.0	84.1	0.46	E
8	77.98	26.79	4.5	1931	16.9	87.1	1.0	0.8	83.8	0.54	E
8	77.98	26.79	5.5	1916	16.6	82.3	0.8	0.8	84.2	0.49	E
8	77.98	26.79	6.5	1901	16.3	80.8	0.7	0.8	84.6	0.47	E
8	77.98	26.79	7.5	1885	17.8	90.5	0.6	0.8	85.0	0.45	E
8	77.98	26.79	8.5	1870	15.3	79.0	0.5	0.8	85.0	0.40	E
8	77.98	26.79	9.5	1854	13.4	64.9	0.5	0.6	84.7	0.45	E
8	77.98	26.79	11	1824	13.4	69.2	0.6	0.6	84.6	0.49	E
8	77.98	26.79	13	1793	14.2	76.8	0.6	0.9	84.5	0.42	E
8	77.98	26.79	15	1762	13.5	78.4	0.7	1.0	84.0	0.42	E
8	77.98	26.79	17	1731	15.9	86.1	0.9	1.2	83.7	0.44	E
43	72.54	45.74	0.5	1996	1.9	4.4	11.5	4.6	12.8	0.71	I
43	72.54	45.74	1.5	1983	2.2	6.6	12.6	6.3	13.9	0.67	I
43	72.54	45.74	2.5	1970	2.5	7.4	11.1	5.3	18.2	0.68	I

Table C.4 (*continued*)

ID	Coordinates		Depth	Age (cal	HBIs (ng g^{-1} sed.)				Proxy data		CT output
	°N	°E	(cm)	yr AD)	IP_{25}	II	III	IV	SpSIC	TRa	(Model A)
43	72.54	45.74	3.5	1958	2.8	6.3	8.9	4.2	24.4	0.68	I
43	72.54	45.74	4.5	1945	2.0	5.2	8.3	3.8	19.4	0.68	I
43	72.54	45.74	5.5	1932	2.5	8.3	8.1	4.3	24.6	0.65	I
43	72.54	45.74	6.5	1920	2.4	5.6	6.5	3.6	28.1	0.64	I
43	72.54	45.74	7.5	1907	2.5	6.8	8.6	4.4	22.9	0.66	I
43	72.54	45.74	8.5	1894	2.8	6.9	11.8	5.3	19.0	0.69	I
43	72.54	45.74	9.5	1881	2.1	6.2	6.9	3.8	24.0	0.64	I
43	72.54	45.74	11	1856	1.7	3.7	4.7	2.7	27.8	0.64	I
43	72.54	45.74	13	1831	2.5	6.5	7.9	3.7	24.7	0.68	I
43	72.54	45.74	15	1805	1.9	4.8	4.5	2.0	30.4	0.69	I
43	72.54	45.74	17	1780	1.2	3.5	4.4	2.2	21.2	0.66	I
43	72.54	45.74	19	1755	1.2	3.2	3.8	1.8	24.3	0.67	I
712	78.92	6.77	0.5	1989	1.7	15.6	4.5	4.8	29.0	0.48	I
712	78.92	6.77	1.5	1953	1.9	14.3	4.2	4.1	31.8	0.51	I
712	78.92	6.77	2.5	1917	1.9	15.2	3.6	3.4	36.0	0.51	I
712	78.92	6.77	3.5	1881	2.2	19.3	4.4	4.0	34.9	0.52	I
712	78.92	6.77	4.5	1844	2.3	15.8	3.8	3.1	39.8	0.55	I
712	78.92	6.77	5.5	1808	1.6	14.2	2.7	2.5	39.0	0.52	I
712	78.92	6.77	6.5	1772	1.8	13.1	2.7	2.4	41.2	0.53	I
712	78.92	6.77	7.5	1736	1.7	14.1	2.6	2.0	41.0	0.57	I

Spatial averaging of daily-resolution satellite data

The exact regions used to derive daily time series of satellite data (Fig. 3.12–3.13, Chapter 3) are shown in Fig. C.1.

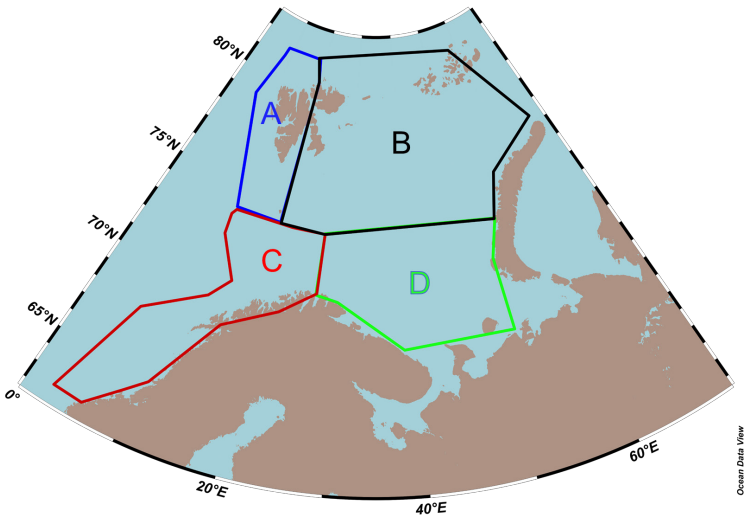

Figure C.1: quadrants used to derive daily time-series of satellite data for the north-western (A), north-eastern (B), south-western (C), and south-eastern (D) Barents Sea.

Example calculations of CT model performance metrics

In order to facilitate easier interpretation of model performance presented in Table 3.1 as part of Chapter 3, the definitions of performance metrics used for CT model evaluation are provided, and their derivation illustrated using results from CT model A (Fig. 3.7a, Chapter 3) obtained from the training set.

The distribution of sample classification for an individual model is easily represented using a confusion matrix (Table C.5), which tabulates known data classes manually assigned in the training set (e.g. marginal, intermediate, and extensive sea ice conditions) against classifications obtained by the model. Thus, the rows correspond to model predictions, and columns represent known classes of, in this case, sea ice conditions. Performance metrics may be calculated from the confusion matrix.

Table C.5: Confusion matrix results for CT model A obtained using the training set. Abbreviations represent classes of sea ice conditions based on satellite SpSIC (Fig. 3.1a): MAR = marginal; INT = intermediate; EXT = extensive.

Model predictions	Known data classes		
	MAR	INT	EXT
MAR	143	1	0
INT	9	21	1
EXT	1	0	22

Accuracy – the proportion of correct model predictions, hereafter referred to as A_{obs}, calculated by dividing the sum of correctly-classified samples by the sample size of the training set. In this case, overall model accuracy for the training set is 94 %.

$$A_{obs} = \frac{(143 + 21 + 22)}{198} \times 100 = 94\,\% \qquad (C.1)$$

Sensitivity (i.e. recall) – the proportion of samples assigned to a class in the training set that was correctly classified by the model. In this case, the sensitivity was

96 % for the intermediate (INT) sea ice class, while the averaged (i.e. total) sensitivity for the entire dataset was 95 %.

$$Sensitivity\ (INT\ class, \%) = \frac{21}{22} \times 100 = 96\ \% \qquad (C.2)$$

$$Total\ sensitivity\ (\%) = \frac{\left(\frac{143}{153} + \frac{21}{22} + \frac{22}{23}\right)}{3} \times 100 = 95\ \% \qquad (C.3)$$

Precision (i.e. positive predictive value, or PPV) – the percentage of samples of a given class correctly classified versus the total number of samples assigned to that class by the model. In the current context, the precision for the intermediate class was 68 %, while the class-averaged precision was 88 %. It is evident that class-averaged precision obscures the reduced performance for the intermediate class of sea ice conditions.

$$Precision\ (INT\ class, \%) = \frac{21}{(9 + 21 + 1)} \times 100 = 68\ \% \qquad (C.4)$$

$$Total\ precision\ (\%) = \frac{\left(\frac{143}{144} + \frac{21}{31} + \frac{22}{23}\right)}{3} \times 100 = 88\ \% \qquad (C.5)$$

F1 score – the weighted average (i.e. harmonic mean) of precision and sensitivity that is usually represented as a decimal fraction.

$$F1\ score = \frac{2 \times 88 \times 95}{(88 + 95)} \div 100 = 0.9 \qquad (C.6)$$

Kappa statistic – a measure of comparing actual accuracy of a model to that expected by random chance (e.g. from a trivial classifier which assigns all samples to the majority class). The Kappa statistics accounts for class imbalance and allows quantitative comparison between different models due to a standardised scale (0–1). Calculation of the Kappa statistic requires the marginal frequencies to be determined for each class of

data, herein referred to as MF_{MAR}, MF_{INT} and MF_{EXT} for the marginal, intermediate, and extensive classes of sea ice conditions, respectively. The MF is calculated by multiplying the number of samples assigned to a given class by the model with the number of samples assigned to that class in the training set, and dividing the product by the total sample size of the training set. Thus, the marginal frequency MF_{INT} for the intermediate sea ice class was calculated to be *ca.* 3.44. Once the marginal frequency of each class is determined, their sum is divided by the total sample size of the training set to calculate the expected accuracy (referred to as A_{exp} herein). Finally, the Kappa statistic may then be calculated using A_{exp} and the actual accuracy obtained by the model (A_{obs}). Thus, for the training set of CT model A, Kappa was found to be 0.85.

$$MF_{INT} = \frac{22 \times (21 + 9 + 1)}{198} = 3.44 \qquad (C.7)$$

$$A_{exp} = \frac{MF_{MAR} + MF_{INT} + MF_{EXT}}{198} \times 100 = \frac{111.3 + 3.44 + 2.67}{198} \times 100 = 59\% \qquad (C.8)$$

$$Kappa = \frac{A_{obs} - A_{exp}}{100 - A_{exp}} \div 100 = \frac{94 - 59}{100 - 59} \div 100 = 0.85 \qquad (C.9)$$

Appendix D

Data pertaining to Chapter 4 is presented here, including age model data for core GC11 (Table D.6), HBI concentrations (ng g^{-1} sed.), $P_{III}IP_{25}$-derived SpSIC (%), HBI triene ratios, and CT model A (Fig. 3.7a) predictions of sea ice conditions in cores 70, 1200, KA11, and GC11 (Table D.7).

Table D.6: Age model data for core GC11 (Katrine Husum, personal communication), including ^{14}C AMS-dated core depths, carbonate sources, ^{14}C (yr BP ± SD) and calibrated (cal yr BP) ages with associated 2σ error ranges.

Sample code	Depth (cm)	Carbonate source	^{14}C age (cal yr BP) ± SD	Calibrated ages (cal yr BP)	2σ range (cal yr BP)
ETH-55693.1.1	50.5	MBF	5803 ± 71	6224	6046–6383
ETH-55693.3.1	69.5	*N. labradorica*	5667 ± 137	9095	8456–9628
Poz-89011	81.5	*N. labradorica*	8500 ± 240	10065	9650–10445
Poz-89012	95.5	*N. labradorica*	9280 ± 140	10420	10220–10618
ETH-55694.1.1	120.5	*N. labradorica*	9557 ± 83	11086	10778–11290
ETH-55694.3.1	145.5	MBF	9566 ± 187	12785	12670–12908
Poz-89013	194.5	MBF	10100 ± 100	15861	15694–16041

Table D.7: HBI concentrations (ng g^{-1} sed.), $P_{III}IP_{25}$-based SpSIC estimates (%), HBI triene ratios (abbreviated to TRa), and classes of marginal (M), intermediate (I), or extensive (E) sea ice conditions assigned using CT model A (Fig. 3.7a, Chapter 3) in Barents Sea cores 70, 1200, KA11, and GC11.

ID	Coordinates		Depth	Age (cal	HBIs (ng g^{-1} sed.)				Proxy data		CT
	°N	°E	(cm)	yr BP)	IP_{25}	II	III	IV	SpSIC	TRa	**A**
70	78.40	32.42	10.5	0	5.7	30.1	0.9	0.5	78.4	0.66	E
70	78.40	32.42	13.5	179	7.1	43.2	1.1	0.7	78.6	0.62	E
70	78.40	32.42	16.5	358	5.8	26.0	0.8	0.5	79.8	0.62	E
70	78.40	32.42	19.5	538	6.7	39.6	0.9	0.5	79.7	0.64	E
70	78.40	32.42	21.5	657	4.0	24.9	0.9	0.5	75.0	0.64	E
70	78.40	32.42	22.5	717	5.6	32.0	1.0	0.6	77.3	0.64	E
70	78.40	32.42	25.5	896	5.1	31.0	0.9	0.5	77.8	0.66	E
70	78.40	32.42	28.5	1075	5.3	33.7	1.1	0.7	75.8	0.61	E
70	78.40	32.42	31.5	1254	6.8	43.7	1.0	0.5	79.1	0.65	E
70	78.40	32.42	34.5	1433	6.2	41.0	1.3	0.7	76.3	0.66	E
70	78.40	32.42	37.5	1613	5.1	29.1	0.8	0.4	79.1	0.68	E
70	78.40	32.42	40.5	1792	2.5	16.4	0.5	0.3	76.1	0.61	E
70	78.40	32.42	42.5	1911	2.7	16.4	0.9	0.4	71.4	0.66	E
70	78.40	32.42	43.5	1971	5.1	38.2	1.7	0.9	70.4	0.66	E
70	78.40	32.42	46.5	2150	5.3	40.0	1.8	0.9	70.4	0.66	E
70	78.40	32.42	49.5	2329	4.2	37.9	1.4	0.7	71.1	0.65	E
70	78.40	32.42	52.5	2658	4.6	34.4	1.7	1.0	68.9	0.64	E
70	78.40	32.42	55.5	3060	4.0	33.1	1.8	1.0	65.9	0.65	E
70	78.40	32.42	58.5	3463	3.9	36.9	2.0	1.0	63.8	0.66	E
70	78.40	32.42	61.5	3866	3.2	35.2	1.9	1.0	61.4	0.65	E
70	78.40	32.42	63.5	4134	3.0	29.9	2.2	1.2	57.0	0.65	E
70	78.40	32.42	64.5	4269	2.9	22.1	1.6	0.9	62.5	0.64	E
70	78.40	32.42	67.5	4672	3.1	32.7	2.1	1.3	59.3	0.61	E
70	78.40	32.42	70.5	5074	2.1	26.7	2.0	1.1	52.6	0.63	E
70	78.40	32.42	73.5	5477	2.3	28.4	2.2	1.1	51.4	0.66	E
70	78.40	32.42	76.5	5880	2.3	32.5	1.9	0.8	55.6	0.69	E
70	78.40	32.42	79.5	6283	2.7	25.4	3.3	1.6	46.3	0.67	I

Table D.7 (*continued*)

ID	Coordinates		Depth	Age (cal	HBIs (ng g^{-1} sed.)				Proxy data		CT
	°N	°E	(cm)	yr BP)	IP_{25}	II	III	IV	SpSIC	TRa	**A**
70	78.40	32.42	82.5	6526	1.8	21.8	3.5	1.7	36.0	0.66	I
70	78.40	32.42	84.5	6635	1.4	14.4	3.6	1.8	29.4	0.66	I
70	78.40	32.42	85.5	6690	1.8	18.3	3.9	1.9	33.5	0.67	I
70	78.40	32.42	88.5	6853	1.6	20.5	4.0	2.0	30.6	0.67	I
70	78.40	32.42	91.5	7017	1.6	18.1	3.9	1.9	30.0	0.68	I
70	78.40	32.42	94.5	7181	1.9	17.8	4.7	2.0	29.7	0.70	I
70	78.40	32.42	97.5	7344	1.4	14.2	4.6	2.2	24.5	0.68	I
70	78.40	32.42	100.5	7508	2.3	21.2	4.9	2.2	33.8	0.69	I
70	78.40	32.42	103.5	7672	1.4	15.2	4.3	2.4	24.8	0.64	I
70	78.40	32.42	106.5	7835	1.6	14.6	5.0	2.5	25.7	0.66	I
70	78.40	32.42	109.5	7999	2.3	20.2	5.5	2.9	30.5	0.65	I
70	78.40	32.42	112.5	8162	2.3	19.3	4.1	2.2	37.4	0.65	I
70	78.40	32.42	115.5	8326	2.1	24.3	5.9	3.1	27.4	0.66	I
70	78.40	32.42	118.5	8490	1.7	17.3	4.8	2.3	27.5	0.68	I
70	78.40	32.42	121.5	8653	1.3	12.5	6.5	3.3	15.7	0.66	I
70	78.40	32.42	124.5	8817	1.4	12.5	13.0	6.0	7.3	0.68	M
70	78.40	32.42	126.5	8926	0.9	8.1	15.3	7.8	1.1	0.66	M
70	78.40	32.42	127.5	8981	1.2	11.6	17.8	9.3	2.3	0.66	M
70	78.40	32.42	130.5	9144	1.4	10.2	7.9	4.5	14.6	0.64	I
70	78.40	32.42	133.5	9308	1.0	13.7	14.2	7.2	3.3	0.66	M
1200	69.27	16.42	105	7262	0.0	0.0	0.9	0.8	-6.5	0.54	M
1200	69.27	16.42	115	7467	0.0	0.0	0.8	0.7	-6.5	0.53	M
1200	69.27	16.42	130	7773	0.0	0.0	1.3	1.5	-6.5	0.47	M
1200	69.27	16.42	140	7977	0.0	0.0	1.1	1.3	-6.5	0.46	M
1200	69.27	16.42	160	8386	0.0	0.0	1.3	1.4	-6.5	0.47	M
1200	69.27	16.42	175	8692	0.0	0.0	1.2	1.4	-6.5	0.47	M
1200	69.27	16.42	185	8896	0.0	0.0	1.4	1.5	-6.5	0.48	M
1200	69.27	16.42	200	9203	0.0	0.0	1.5	1.7	-6.5	0.48	M
1200	69.27	16.42	210	9407	0.0	0.0	11.0	12.0	-6.5	0.48	M
1200	69.27	16.42	220	9611	0.0	0.0	19.7	21.3	-6.5	0.48	M
1200	69.27	16.42	230	9815	0.0	0.0	19.0	20.7	-6.5	0.48	M
1200	69.27	16.42	240	10019	0.0	0.0	25.3	27.0	-6.5	0.48	M
1200	69.27	16.42	250	10224	0.0	0.0	11.3	14.0	-6.5	0.45	M
1200	69.27	16.42	270	10632	0.0	0.0	12.5	16.0	-6.5	0.44	M
1200	69.27	16.42	290	11117	0.0	0.0	15.6	20.5	-6.5	0.43	M
1200	69.27	16.42	310	11468	0.1	0.0	4.9	6.7	-5.0	0.42	M
1200	69.27	16.42	330	11549	0.9	5.6	3.8	5.6	19.6	0.40	I
1200	69.27	16.42	341	11594	0.9	7.4	3.5	4.9	19.9	0.42	M
1200	69.27	16.42	344	11606	1.2	6.0	4.0	5.0	23.6	0.44	I
1200	69.27	16.42	348	11622	0.8	8.3	2.7	3.6	24.5	0.43	I
1200	69.27	16.42	351	11634	0.9	4.5	2.6	2.9	27.5	0.47	I
1200	69.27	16.42	352	11638	1.0	7.2	3.2	4.1	24.5	0.44	I
1200	69.27	16.42	353	11642	1.3	8.2	2.2	3.6	39.0	0.38	I
1200	69.27	16.42	354	11646	1.5	7.7	2.2	3.3	41.9	0.40	I
1200	69.27	16.42	356	11655	0.7	6.9	2.1	3.1	25.3	0.40	I
1200	69.27	16.42	357	11659	1.4	8.3	2.5	3.8	37.7	0.40	I
1200	69.27	16.42	358	11663	1.0	9.8	2.7	3.7	28.4	0.42	I

Table D.7 (*continued*)

ID	Coordinates		Depth	Age (cal	HBIs (ng g^{-1} sed.)				Proxy data		CT
	°N	°E	(cm)	yr BP)	IP_{25}	II	III	IV	SpSIC	TRa	**A**
1200	69.27	16.42	359	11667	1.3	7.8	3.0	4.4	32.0	0.40	I
1200	69.27	16.42	361	11675	1.2	10.6	7.8	10.8	12.3	0.42	M
1200	69.27	16.42	362	11679	1.5	6.7	11.0	17.2	10.5	0.39	M
1200	69.27	16.42	363	11683	1.4	10.6	11.6	17.5	8.4	0.40	M
1200	69.27	16.42	364	11687	1.8	14.4	8.4	12.8	16.9	0.40	M
1200	69.27	16.42	366	11695	2.1	12.7	5.6	8.8	28.3	0.39	I
1200	69.27	16.42	367	11699	2.0	11.4	5.5	7.1	27.5	0.44	I
1200	69.27	16.42	368	11703	1.8	13.4	5.7	7.3	25.2	0.44	I
1200	69.27	16.42	369	11707	1.4	7.7	3.3	4.4	31.3	0.43	I
1200	69.27	16.42	371	11716	1.7	13.0	6.0	10.2	22.7	0.37	I
1200	69.27	16.42	372	11720	1.8	10.4	7.1	11.4	20.4	0.38	I
1200	69.27	16.42	373	11724	2.2	12.1	7.3	10.6	24.2	0.41	I
1200	69.27	16.42	374	11728	1.5	11.7	7.2	11.2	17.0	0.39	M
1200	69.27	16.42	378	11744	0.8	2.6	1.5	2.0	37.1	0.42	I
1200	69.27	16.42	381	11756	0.0	0.0	0.0	0.0	-	-	M
1200	69.27	16.42	383	11764	0.0	0.0	0.0	0.0	-	-	M
1200	69.27	16.42	386	11777	1.1	6.2	3.5	4.3	24.4	0.45	I
1200	69.27	16.42	388	11785	1.4	10.9	5.9	8.2	19.6	0.42	I
1200	69.27	16.42	391	11797	2.0	15.7	11.7	14.7	13.5	0.44	M
1200	69.27	16.42	393	11805	2.3	14.7	18.6	23.0	8.6	0.45	M
1200	69.27	16.42	396	11817	2.6	13.9	37.1	46.7	2.8	0.44	M
1200	69.27	16.42	398	11825	2.5	15.7	23.0	28.5	7.4	0.45	M
1200	69.27	16.42	401	11838	2.4	14.7	10.9	10.4	17.7	0.51	I
1200	69.27	16.42	403	11846	3.3	15.5	13.8	15.7	19.5	0.47	I
1200	69.27	16.42	406	11858	5.0	26.5	1.0	1.4	76.4	0.43	E
1200	69.27	16.42	408	11866	4.2	18.7	3.5	4.4	54.9	0.44	I
1200	69.27	16.42	411	11878	7.3	33.8	0.2	0.2	85.4	0.50	E
1200	69.27	16.42	413	11886	11.5	63.2	2.6	2.2	75.4	0.54	E
1200	69.27	16.42	416	11899	19.3	107.9	0.3	0.2	86.1	0.57	E
1200	69.27	16.42	418	11907	18.1	104.0	3.6	2.6	76.5	0.58	E
1200	69.27	16.42	421	11919	18.9	92.5	0.2	0.2	86.3	0.57	E
1200	69.27	16.42	423	11927	17.8	89.3	2.8	2.2	78.7	0.55	E
1200	69.27	16.42	426	11939	19.0	96.0	0.3	0.2	86.0	0.58	E
1200	69.27	16.42	428	11947	17.8	88.0	3.7	2.2	76.3	0.63	E
1200	69.27	16.42	431	11960	21.8	102.7	0.3	0.3	86.1	0.53	E
1200	69.27	16.42	433	11968	18.4	98.8	3.3	2.5	77.5	0.57	E
1200	69.27	16.42	436	11980	17.2	73.4	0.2	0.1	86.4	0.66	E
1200	69.27	16.42	438	12025	16.8	84.9	2.4	1.9	79.1	0.57	E
1200	69.27	16.42	442	12141	19.1	90.9	0.2	0.1	86.3	0.60	E
1200	69.27	16.42	443	12170	19.5	103.8	2.6	2.1	79.8	0.55	E
1200	69.27	16.42	446	12257	19.6	103.5	0.3	0.2	86.1	0.58	E
1200	69.27	16.42	448	12315	17.1	112.4	0.0	0.0	87.0	-	E
1200	69.27	16.42	451	12402	17.8	96.6	0.0	0.0	87.0	-	E
1200	69.27	16.42	453	12460	19.5	104.7	2.6	1.6	79.8	0.62	E
1200	69.27	16.42	456	12546	16.1	95.8	0.0	0.0	87.0	-	E
1200	69.27	16.42	458	12593	16.6	95.4	2.5	1.1	79.0	0.69	E
1200	69.27	16.42	461	12609	19.8	108.9	2.3	1.7	80.6	0.57	E

Table D.7 (*continued*)

ID	Coordinates		Depth	Age (cal	HBIs (ng g^{-1} sed.)				Proxy data		CT
	°N	°E	(cm)	yr BP)	IP_{25}	II	III	IV	SpSIC	TRa	**A**
1200	69.27	16.42	463	12620	21.5	114.3	2.5	1.9	80.6	0.57	E
1200	69.27	16.42	466	12636	21.4	107.0	0.0	0.0	87.0	-	E
1200	69.27	16.42	468	12647	23.9	130.0	3.0	2.3	80.2	0.57	E
1200	69.27	16.42	471	12663	25.0	116.3	3.0	1.8	80.4	0.62	E
1200	69.27	16.42	473	12674	21.2	126.1	2.9	2.0	79.7	0.58	E
1200	69.27	16.42	476	12690	21.9	121.2	0.0	0.0	87.0	-	E
1200	69.27	16.42	478	12701	21.3	111.4	2.4	2.1	80.7	0.54	E
1200	69.27	16.42	483	12728	19.3	105.8	1.9	1.6	81.5	0.54	E
1200	69.27	16.42	486	12744	22.0	118.9	2.2	1.8	81.5	0.54	E
1200	69.27	16.42	487	12750	23.2	115.4	2.5	1.2	81.1	0.67	E
1200	69.27	16.42	488	12755	21.8	123.5	2.4	1.7	81.0	0.58	E
1200	69.27	16.42	489	12761	21.2	123.0	2.1	1.5	81.5	0.59	E
1200	69.27	16.42	491	12772	17.9	107.8	2.2	1.8	80.4	0.55	E
1200	69.27	16.42	492	12777	21.6	109.0	2.5	1.6	80.6	0.61	E
1200	69.27	16.42	493	12782	20.0	109.2	2.2	1.7	81.0	0.56	E
1200	69.27	16.42	494	12788	19.7	98.3	1.9	1.6	81.7	0.54	E
1200	69.27	16.42	496	12799	20.0	113.2	2.1	1.7	81.2	0.56	E
1200	69.27	16.42	497	12804	19.5	113.3	1.9	1.7	81.6	0.53	E
1200	69.27	16.42	498	12809	17.7	95.4	1.8	1.1	81.4	0.63	E
1200	69.27	16.42	499	12815	16.2	90.7	2.0	1.3	80.3	0.61	E
1200	69.27	16.42	501	12826	16.5	89.8	1.6	1.4	81.5	0.54	E
1200	69.27	16.42	502	12831	16.8	105.0	1.9	1.2	80.7	0.61	E
1200	69.27	16.42	503	12837	15.7	93.6	1.8	1.4	80.6	0.57	E
1200	69.27	16.42	504	12842	17.4	93.8	1.8	1.7	81.2	0.52	E
1200	69.27	16.42	506	12853	15.4	87.4	1.7	1.2	81.0	0.59	E
1200	69.27	16.42	507	12858	15.7	86.6	1.8	1.6	80.7	0.52	E
1200	69.27	16.42	508	12864	15.4	88.8	1.8	1.6	80.5	0.53	E
1200	69.27	16.42	509	12869	13.7	85.3	2.0	1.7	79.0	0.55	E
1200	69.27	16.42	513	12885	11.5	82.2	1.7	1.6	79.0	0.52	E
1200	69.27	16.42	517	12895	9.4	62.8	1.4	1.0	79.0	0.57	E
1200	69.27	16.42	521	12906	8.8	66.8	0.0	0.0	87.0	-	E
1200	69.27	16.42	524	12914	11.3	74.1	1.6	1.5	79.3	0.52	E
1200	69.27	16.42	528	12924	10.2	66.4	0.0	0.0	87.0	-	E
1200	69.27	16.42	531	12932	6.1	56.7	1.2	1.3	76.6	0.48	E
1200	69.27	16.42	534	12940	7.2	54.1	0.0	0.0	87.0	-	E
1200	69.27	16.42	536	12945	10.6	64.5	1.2	1.3	80.6	0.48	E
1200	69.27	16.42	551	12984	0.1	0.0	3.6	4.5	-4.4	0.44	M
1200	69.27	16.42	571	13036	0.0	0.0	7.0	10.3	-6.5	0.40	M
1200	69.27	16.42	591	13088	0.0	0.0	12.1	23.3	-6.5	0.34	M
1200	69.27	16.42	611	13140	0.0	0.0	6.1	10.9	-6.5	0.36	M
1200	69.27	16.42	631	13192	0.0	0.0	9.5	17.1	-6.5	0.36	M
1200	69.27	16.42	650	13241	0.0	0.0	6.7	10.2	-6.5	0.40	M
1200	69.27	16.42	670	13319	0.0	0.0	5.9	9.0	-6.5	0.40	M
1200	69.27	16.42	690	13407	0.0	0.0	3.7	5.3	-6.5	0.41	M
1200	69.27	16.42	710	13494	0.0	0.0	14.4	23.5	-6.5	0.38	M
1200	69.27	16.42	730	13579	0.0	0.0	5.9	10.3	-6.5	0.36	M
1200	69.27	16.42	750	13661	0.0	0.0	16.5	26.3	-6.5	0.39	M

Table D.7 (*continued*)

ID	Coordinates		Depth	Age (cal	HBIs (ng g^{-1} sed.)				Proxy data		CT
	°N	°E	(cm)	yr BP)	IP_{25}	II	III	IV	SpSIC	TRa	**A**
1200	69.27	16.42	770	13742	0.0	0.0	13.5	22.2	-6.5	0.38	M
1200	69.27	16.42	790	13820	0.0	0.0	21.0	35.3	-6.5	0.37	M
1200	69.27	16.42	810	13867	0.0	0.0	6.0	9.6	-6.5	0.38	M
KA11	74.87	16.48	0	0	1.46	11.8	14.9	7.8	6.11	0.66	M
KA11	74.87	16.48	0.5	53	1.22	5.6	3.0	1.6	30.19	0.65	I
KA11	74.87	16.48	1.5	159	1.42	7.8	6.9	3.3	16.54	0.68	I
KA11	74.87	16.48	3.25	317	1.05	6.6	4.4	2.1	19.21	0.68	I
KA11	74.87	16.48	3.75	397	1.70	6.6	2.4	1.2	43.00	0.67	I
KA11	74.87	16.48	4.25	450	1.33	4.6	1.8	0.9	43.98	0.67	I
KA11	74.87	16.48	4.75	496	1.00	7.1	5.3	2.7	15.07	0.66	I
KA11	74.87	16.48	5.25	535	1.23	10.3	10.0	5.2	8.80	0.66	M
KA11	74.87	16.48	5.75	574	0.76	53.4	3.0	1.6	20.34	0.65	M
KA11	74.87	16.48	6.25	614	0.92	35.9	0.9	0.5	51.35	0.64	M
KA11	74.87	16.48	6.75	653	0.46	23.1	0.8	0.5	38.13	0.62	M
KA11	74.87	16.48	7.25	692	0.61	59.0	6.4	3.6	5.81	0.64	M
KA11	74.87	16.48	7.75	731	0.49	6.6	6.3	3.7	3.80	0.63	M
KA11	74.87	16.48	8.25	770	0.77	9.0	7.3	4.2	6.94	0.63	M
KA11	74.87	16.48	8.75	809	0.72	6.3	6.1	3.6	8.28	0.63	M
KA11	74.87	16.48	9.25	849	0.64	7.2	6.4	3.5	6.34	0.65	M
KA11	74.87	16.48	9.75	888	0.62	5.0	7.8	4.6	4.00	0.63	M
KA11	74.87	16.48	13.5	1181	0.00	0.0	6.8	4.2	-6.47	0.62	M
KA11	74.87	16.48	16.5	1536	0.00	0.0	5.3	3.9	-6.47	0.58	M
KA11	74.87	16.48	16.75	1615	0.00	7.1	5.3	3.0	-6.47	0.64	M
KA11	74.87	16.48	18.25	2091	0.00	5.8	6.1	3.8	-6.47	0.62	M
KA11	74.87	16.48	19.25	2409	0.00	7.2	6.2	3.8	-6.47	0.62	M
KA11	74.87	16.48	21.75	3202	0.70	6.8	6.3	3.9	7.54	0.62	M
KA11	74.87	16.48	22.25	3361	0.00	5.5	5.1	3.3	-6.47	0.61	M
KA11	74.87	16.48	23.25	3678	0.00	5.8	5.2	3.2	-6.47	0.62	M
KA11	74.87	16.48	23.75	3837	0.00	6.7	5.5	3.4	-6.47	0.62	M
KA11	74.87	16.48	24.75	4155	0.00	6.4	5.7	3.5	-6.47	0.62	M
KA11	74.87	16.48	26.75	4789	0.00	6.2	5.0	3.0	-6.47	0.63	M
KA11	74.87	16.48	28.25	5098	0.00	6.2	5.1	3.1	-6.47	0.62	M
KA11	74.87	16.48	30.75	5335	0.61	7.3	6.9	4.2	5.03	0.62	M
KA11	74.87	16.48	33.25	5572	0.05	0.0	10.6	7.2	-5.77	0.60	M
KA11	74.87	16.48	33.75	5619	0.05	0.0	10.6	6.3	-5.77	0.63	M
KA11	74.87	16.48	34.25	5667	0.05	0.0	12.5	8.4	-5.88	0.60	M
KA11	74.87	16.48	34.75	5714	0.05	0.0	12.5	7.8	-5.88	0.62	M
KA11	74.87	16.48	35.25	5761	0.63	0.0	11.8	7.4	0.83	0.61	M
KA11	74.87	16.48	35.75	5809	0.56	16.5	11.1	7.6	0.46	0.59	M
KA11	74.87	16.48	36.25	5856	0.00	0.0	11.9	7.3	-6.47	0.62	M
KA11	74.87	16.48	36.75	5903	0.00	0.0	13.9	9.2	-6.47	0.60	M
KA11	74.87	16.48	37.25	5951	0.00	0.0	14.4	9.1	-6.47	0.61	M
KA11	74.87	16.48	37.75	5998	0.05	0.0	15.4	9.9	-5.99	0.61	M
KA11	74.87	16.48	38.25	6046	0.00	0.0	12.6	8.9	-6.47	0.59	M
KA11	74.87	16.48	38.75	6093	0.00	0.0	17.3	10.9	-6.47	0.61	M
KA11	74.87	16.48	39.25	6140	0.00	0.0	13.5	8.6	-6.47	0.61	M
KA11	74.87	16.48	39.75	6188	0.56	13.7	13.0	8.8	-0.49	0.60	M

Table D.7 (*continued*)

ID	Coordinates		Depth	Age (cal	HBIs (ng g^{-1} sed.)				Proxy data		CT
	°N	°E	(cm)	yr BP)	IP_{25}	II	III	IV	SpSIC	TRa	**A**
KA11	74.87	16.48	40.25	6274	0.00	0.0	10.3	7.2	-6.47	0.59	M
KA11	74.87	16.48	40.75	6399	0.00	0.0	11.7	8.3	-6.47	0.59	M
KA11	74.87	16.48	42.5	6838	1.02	14.4	8.7	5.8	8.14	0.60	M
KA11	74.87	16.48	43.5	7088	1.82	15.6	10.6	7.3	13.59	0.59	M
KA11	74.87	16.48	44.5	7339	0.00	0.0	15.1	10.6	-6.47	0.59	M
KA11	74.87	16.48	46.5	7472	0.00	14.0	21.9	14.7	-6.47	0.60	M
KA11	74.87	16.48	48.5	7605	0.00	0.0	18.4	13.6	-6.47	0.58	M
KA11	74.87	16.48	50.5	7738	0.00	0.0	17.2	13.0	-6.47	0.57	M
KA11	74.87	16.48	52.5	7871	0.00	0.0	19.2	14.0	-6.47	0.58	M
KA11	74.87	16.48	54.5	8004	0.00	0.0	49.5	35.3	-6.47	0.58	M
KA11	74.87	16.48	59.5	8346	0.00	24.0	44.6	33.6	-6.47	0.57	M
KA11	74.87	16.48	70.5	9103	0.00	0.0	52.7	40.1	-6.47	0.57	M
KA11	74.87	16.48	83.25	9902	1.11	19.3	16.9	17.8	2.36	0.49	M
KA11	74.87	16.48	83.75	9923	1.64	44.7	57.8	60.0	-2.44	0.49	M
KA11	74.87	16.48	84.75	9964	2.35	94.0	158.8	222.0	-4.32	0.42	M
KA11	74.87	16.48	85.75	10004	2.10	56.9	42.7	56.3	0.30	0.43	M
KA11	74.87	16.48	87.75	10086	2.63	52.2	22.2	30.0	8.33	0.43	M
KA11	74.87	16.48	88.75	10127	2.89	85.9	72.1	101.4	-0.88	0.42	M
KA11	74.87	16.48	89.25	10147	2.51	56.1	85.6	128.6	-2.31	0.40	M
KA11	74.87	16.48	92.25	10270	2.65	14.7	3.2	4.6	46.61	0.41	I
KA11	74.87	16.48	93.25	10310	2.83	53.0	21.1	29.3	9.94	0.42	M
KA11	74.87	16.48	94.25	10351	3.15	0.0	36.8	53.2	4.71	0.41	M
KA11	74.87	16.48	96.25	10433	3.18	32.0	17.2	25.9	14.74	0.40	M
KA11	74.87	16.48	97.25	10474	3.55	95.6	178.7	253.3	-3.61	0.41	M
KA11	74.87	16.48	98.25	10514	3.28	71.1	63.4	86.5	0.62	0.42	M
KA11	74.87	16.48	100.25	10596	4.32	70.4	25.7	30.6	13.22	0.46	M
KA11	74.87	16.48	102.25	10678	2.43	59.6	13.6	14.4	14.18	0.49	M
KA11	74.87	16.48	103.25	10718	3.71	40.6	4.3	3.8	47.55	0.53	I
KA11	74.87	16.48	104.25	10759	4.37	35.2	2.1	1.8	65.27	0.54	E
KA11	74.87	16.48	105.25	10800	2.76	41.8	4.2	3.9	41.25	0.52	M
KA11	74.87	16.48	106.25	10841	2.90	62.2	11.8	11.8	19.76	0.50	M
KA11	74.87	16.48	108.25	10922	3.24	49.0	5.6	5.8	38.27	0.49	M
KA11	74.87	16.48	109.75	10983	3.06	47.1	21.2	25.6	10.95	0.45	M
KA11	74.87	16.48	119.5	11406	7.80	36.8	105.8	146.5	3.32	0.42	M
KA11	74.87	16.48	122.5	11523	10.0	62.9	90.9	101.5	7.43	0.47	M
KA11	74.87	16.48	123.5	11562	12.7	62.6	105.5	122.7	8.53	0.46	M
KA11	74.87	16.48	124.5	11602	8.4	56.9	44.1	46.9	15.23	0.48	I
KA11	74.87	16.48	130.5	11836	10.6	76.6	42.6	30.3	19.99	0.58	I
KA11	74.87	16.48	132.5	11915	12.7	94.1	17.1	14.8	44.10	0.54	I
KA11	74.87	16.48	133.5	11954	16.9	122.3	10.2	11	61.24	0.48	I
KA11	74.87	16.48	136.5	12062	35.5	198.0	5.6	3.9	78.54	0.59	E
KA11	74.87	16.48	139.5	12165	28.5	175.4	3.4	2.4	80.46	0.59	E
KA11	74.87	16.48	142.5	12268	21.5	104.5	1.6	1.3	82.81	0.55	E
KA11	74.87	16.48	145.5	12371	15.8	82.2	1.1	0.9	83.06	0.55	E
KA11	74.87	16.48	148.5	12474	36.3	218.7	4.3	3	80.51	0.59	E
KA11	74.87	16.48	151.5	12577	13.7	77.3	1.2	0.6	82.11	0.67	E
KA11	74.87	16.48	154.5	12680	12.7	71.6	1	1	82.59	0.50	E

Table D.7 (*continued*)

ID	Coordinates		Depth	Age (cal	HBIs (ng g^{-1} sed.)				Proxy data		CT
	°N	°E	(cm)	yr BP)	IP_{25}	II	III	IV	SpSIC	TRa	**A**
KA11	74.87	16.48	157.5	12783	10.5	67.1	1.1	1	81.20	0.52	E
KA11	74.87	16.48	160.5	12886	19.6	137.9	8.3	9	67.30	0.48	I
KA11	74.87	16.48	163.5	12989	17.5	128.6	11.4	13.2	59.76	0.46	I
KA11	74.87	16.48	166.5	13092	9.8	88.5	21.9	23.8	32.34	0.48	I
KA11	74.87	16.48	170.5	13116	8.3	51.3	52.8	64.8	12.11	0.45	M
KA11	74.87	16.48	181.5	13160	6.3	32.2	41.2	59.6	11.69	0.41	M
KA11	74.87	16.48	191.5	13199	5.1	35.6	26.1	36.4	15.50	0.42	M
KA11	74.87	16.48	202.5	13243	10.3	55.9	26.6	33.4	29.08	0.44	I
KA11	74.87	16.48	211.5	13278	6.3	39.7	14.6	17.5	31.34	0.45	I
KA11	74.87	16.48	221.5	13318	7.9	45.4	15.4	16.4	35.38	0.48	I
KA11	74.87	16.48	232.5	13362	4.9	36.8	13.5	13.2	27.66	0.51	I
KA11	74.87	16.48	242.5	13401	6.4	35.7	14.9	11.6	31.40	0.56	I
KA11	74.87	16.48	254.5	13449	8.5	58.8	102.5	153.8	4.41	0.40	M
KA11	74.87	16.48	264.5	13620	14.87	81.5	17.7	20.5	46.94	0.46	I
KA11	74.87	16.48	274.5	13801	11.94	56.7	33.4	38.3	27.36	0.47	I
KA11	74.87	16.48	285.5	14000	10.39	56.7	23.5	26.2	32.08	0.47	I
KA11	74.87	16.48	296.5	14199	8.31	44.9	14.7	16.2	37.74	0.48	I
KA11	74.87	16.48	306.5	14381	8.97	47.1	43.1	57.4	16.74	0.43	I
KA11	74.87	16.48	315.5	14538	6.86	27.8	25.4	34.6	21.58	0.42	I
KA11	74.87	16.48	327.5	14741	10.02	48.6	15.8	19.9	40.41	0.44	I
KA11	74.87	16.48	337.5	14910	16.19	59.5	13.7	15.4	54.49	0.47	I
KA11	74.87	16.48	347.5	15079	5.98	24.4	8.8	6.5	42.02	0.58	I
KA11	74.87	16.48	368.5	15434	4.53	25.1	29.3	39.3	11.95	0.43	M
KA11	74.87	16.48	380.5	15637	5.55	31.9	12.4	9.6	32.37	0.56	I
KA11	74.87	16.48	385.5	15721	12.50	39.5	7.8	5.2	60.62	0.60	I
GC11	81.08	28.93	0.5	58	5.2	32.5	0.9	1.0	77.6	0.49	E
GC11	81.08	28.93	1.5	178	5.9	31.2	0.9	0.9	78.7	0.50	E
GC11	81.08	28.93	3.5	421	6.3	35.1	0.9	1.0	79.4	0.48	E
GC11	81.08	28.93	5.5	662	6.3	38.2	0.9	1.1	79.1	0.45	E
GC11	81.08	28.93	7.5	904	3.8	22.2	0.4	0.5	80.8	0.46	E
GC11	81.08	28.93	9.5	1146	3.9	24.0	0.5	0.6	79.9	0.47	E
GC11	81.08	28.93	11.5	1388	6.1	35.2	0.9	0.9	78.8	0.50	E
GC11	81.08	28.93	13.5	1629	6.8	41.5	1.0	1.2	78.7	0.47	E
GC11	81.08	28.93	15.5	1873	6.1	37.9	1.0	1.0	78.4	0.51	E
GC11	81.08	28.93	17.5	2115	5.1	33.9	0.9	1.1	77.3	0.46	E
GC11	81.08	28.93	19.5	2355	4.5	32.1	0.8	1.0	77.9	0.44	E
GC11	81.08	28.93	21.5	2598	5.5	30.9	1.1	1.1	77.0	0.48	E
GC11	81.08	28.93	23.5	2840	3.7	23.7	0.8	0.9	76.0	0.47	E
GC11	81.08	28.93	25.5	3082	3.6	24.1	0.7	0.9	76.5	0.44	E
GC11	81.08	28.93	27.5	3323	3.9	26.7	0.9	1.0	75.0	0.47	E
GC11	81.08	28.93	29.5	3565	3.1	24.8	0.5	0.7	77.9	0.44	E
GC11	81.08	28.93	31.5	3807	3.3	23.6	0.8	0.8	75.3	0.48	E
GC11	81.08	28.93	33.5	4050	4.3	30.0	1.3	1.3	72.5	0.48	E
GC11	81.08	28.93	35.5	4290	4.4	31.0	1.2	1.2	73.9	0.48	E
GC11	81.08	28.93	37.5	4532	3.8	31.0	1.2	1.2	71.4	0.50	E
GC11	81.08	28.93	39.5	4774	3.6	30.6	1.2	1.2	71.1	0.48	E
GC11	81.08	28.93	41.5	5014	4.6	30.9	1.1	1.2	74.9	0.48	E

Table D.7 (*continued*)

ID	Coordinates		Depth	Age (cal	HBIs (ng g^{-1} sed.)				Proxy data		CT
	°N	°E	(cm)	yr BP)	IP_{25}	II	III	IV	SpSIC	TRa	**A**
GC11	81.08	28.93	43.5	5258	5.4	31.4	1.1	1.1	76.7	0.48	E
GC11	81.08	28.93	45.5	5499	3.5	30.1	1.6	1.5	65.6	0.52	E
GC11	81.08	28.93	47.5	5742	3.4	25.6	1.5	1.4	66.4	0.51	E
GC11	81.08	28.93	49.5	5983	2.7	25.0	1.3	1.4	65.4	0.48	E
GC11	81.08	28.93	51.5	6243	3.0	24.2	1.6	1.5	63.4	0.52	I
GC11	81.08	28.93	53.5	6524	2.9	23.6	1.7	1.6	62.0	0.51	I
GC11	81.08	28.93	54.5	6662	2.3	23.6	1.6	1.6	58.1	0.50	I
GC11	81.08	28.93	55.5	6803	2.1	19.2	2.0	2.1	51.4	0.49	I
GC11	81.08	28.93	56.5	6942	2.3	23.0	1.6	1.6	58.4	0.51	I
GC11	81.08	28.93	57.5	7081	2.1	21.2	1.5	1.5	57.8	0.51	I
GC11	81.08	28.93	58.5	7222	2.3	20.5	1.5	1.5	60.2	0.49	I
GC11	81.08	28.93	59.5	7361	2.0	20.7	1.3	1.5	60.1	0.47	I
GC11	81.08	28.93	60.5	7500	2.2	20.6	1.5	1.5	59.2	0.49	I
GC11	81.08	28.93	61.5	7640	2.0	18.1	1.5	1.7	56.0	0.48	I
GC11	81.08	28.93	62.5	7780	1.8	18.5	1.6	1.6	54.5	0.49	I
GC11	81.08	28.93	63.5	7921	2.5	23.9	1.7	1.6	59.6	0.51	I
GC11	81.08	28.93	64.5	8060	1.9	17.2	2.3	2.4	46.7	0.50	I
GC11	81.08	28.93	65.5	8200	2.0	17.8	2.4	2.4	46.4	0.50	I
GC11	81.08	28.93	66.5	8338	2.0	18.1	2.6	2.6	44.5	0.50	I
GC11	81.08	28.93	67.5	8478	2.6	17.4	2.6	2.6	50.6	0.50	I
GC11	81.08	28.93	68.5	8619	2.2	17.7	2.9	2.9	44.7	0.51	I
GC11	81.08	28.93	69.5	8758	2.1	19.0	2.9	3.0	43.4	0.49	I
GC11	81.08	28.93	70.5	8838	2.1	18.7	4.6	4.2	32.7	0.52	I
GC11	81.08	28.93	71.5	8917	2.2	18.7	4.4	4.1	35.4	0.51	I
GC11	81.08	28.93	72.5	8997	2.5	19.6	3.9	3.6	40.5	0.52	I
GC11	81.08	28.93	73.5	9077	2.0	17.6	4.6	4.7	31.2	0.49	I
GC11	81.08	28.93	74.5	9157	2.1	14.3	6.2	5.8	26.0	0.51	I
GC11	81.08	28.93	75.5	9235	1.8	16.1	6.3	6.2	22.5	0.51	I
GC11	81.08	28.93	76.5	9316	2.0	17.6	5.7	6.2	27.0	0.48	I
GC11	81.08	28.93	77.5	9394	1.8	15.5	6.0	6.2	23.8	0.49	I
GC11	81.08	28.93	78.5	9474	2.5	18.2	6.2	6.5	29.8	0.49	I
GC11	81.08	28.93	79.5	9554	2.3	19.7	4.8	6.7	33.7	0.42	I
GC11	81.08	28.93	80.5	9634	2.8	17.8	5.4	7.1	35.7	0.43	I
GC11	81.08	28.93	81.5	9714	2.5	21.4	5.0	7.1	35.0	0.41	I
GC11	81.08	28.93	82.5	9754	3.1	25.9	6.8	10.3	32.7	0.40	I
GC11	81.08	28.93	83.5	9794	3.2	23.3	7.9	11.4	30.5	0.41	I
GC11	81.08	28.93	84.5	9835	2.3	22.0	7.8	11.3	23.2	0.41	I
GC11	81.08	28.93	85.5	9876	3.1	23.8	7.8	11.2	29.8	0.41	I
GC11	81.08	28.93	86.5	9916	3.2	26.1	7.9	11.6	30.1	0.40	I
GC11	81.08	28.93	87.5	9956	2.8	24.7	8.5	11.7	25.6	0.42	I
GC11	81.08	28.93	88.5	9997	3.4	28.7	8.5	11.5	29.8	0.43	I
GC11	81.08	28.93	89.5	10037	3.5	30.2	7.7	11.3	32.5	0.41	I
GC11	81.08	28.93	90.5	10078	3.5	28.3	6.9	9.7	35.5	0.42	I
GC11	81.08	28.93	91.5	10118	4.0	30.5	6.2	9.3	41.1	0.40	I
GC11	81.08	28.93	92.5	10159	4.3	31.6	7.3	10.1	38.6	0.42	I
GC11	81.08	28.93	93.5	10199	4.0	31.7	6.6	9.6	39.4	0.41	I
GC11	81.08	28.93	94.5	10240	3.9	30.0	7.8	10.9	35.1	0.42	I

Table D.7 (*continued*)

ID	Coordinates		Depth	Age (cal	HBIs (ng g^{-1} sed.)				Proxy data		CT
	°N	°E	(cm)	yr BP)	IP_{25}	II	III	IV	SpSIC	TRa	**A**
GC11	81.08	28.93	95.5	10280	3.6	28.9	7.5	10.7	34.1	0.41	I
GC11	81.08	28.93	96.5	10312	3.5	31.2	7.1	10.5	34.9	0.40	I
GC11	81.08	28.93	97.5	10343	3.4	25.2	7.5	10.9	32.3	0.41	I
GC11	81.08	28.93	98.5	10375	3.5	29.8	8.7	14.0	30.2	0.38	I
GC11	81.08	28.93	99.5	10407	3.6	29.2	8.7	13.7	30.4	0.39	I
GC11	81.08	28.93	100.5	10439	3.3	25.2	14.6	24.4	18.4	0.38	M
GC11	81.08	28.93	101.5	10470	3.1	24.9	16.3	26.3	15.3	0.38	M
GC11	81.08	28.93	102.5	10502	3.5	29.1	18.2	30.1	15.4	0.38	M
GC11	81.08	28.93	103.5	10534	3.8	27.1	16.8	27.1	18.1	0.38	M
GC11	81.08	28.93	104.5	10565	3.3	26.6	11.6	18.7	22.7	0.38	I
GC11	81.08	28.93	105.5	10597	4.0	30.4	11.4	17.3	26.7	0.40	I
GC11	81.08	28.93	106.5	10629	4.1	34.3	8.4	12.7	34.6	0.40	I
GC11	81.08	28.93	107.5	10661	3.4	26.6	8.2	11.8	30.4	0.41	I
GC11	81.08	28.93	108.5	10692	3.9	30.5	8.7	13.2	32.2	0.40	I
GC11	81.08	28.93	109.5	10724	3.8	33.8	8.4	13.2	33.0	0.39	I
GC11	81.08	28.93	110.5	10756	3.9	29.3	8.2	12.4	33.9	0.40	I
GC11	81.08	28.93	111.5	10787	3.8	32.7	9.4	13.5	29.8	0.41	I
GC11	81.08	28.93	112.5	10819	3.9	30.2	8.2	12.6	33.9	0.39	I
GC11	81.08	28.93	113.5	10851	3.7	34.1	8.5	13.3	31.9	0.39	I
GC11	81.08	28.93	114.5	10882	3.1	33.0	9.1	14.6	26.2	0.38	M
GC11	81.08	28.93	115.5	10914	3.6	28.9	9.9	15.3	27.7	0.39	I
GC11	81.08	28.93	116.5	10946	3.4	33.8	13.9	22.4	19.7	0.38	M
GC11	81.08	28.93	117.5	10978	3.4	30.8	20.4	32.8	13.1	0.38	M
GC11	81.08	28.93	118.5	11009	3.6	36.2	17.7	28.8	16.2	0.38	M
GC11	81.08	28.93	119.5	11041	3.5	31.4	15.3	23.6	18.2	0.39	M
GC11	81.08	28.93	120.5	11073	3.3	31.5	14.3	23.4	18.5	0.38	M
GC11	81.08	28.93	121.5	11138	3.2	31.1	18.7	29.6	13.3	0.39	M
GC11	81.08	28.93	122.5	11203	2.9	31.4	17.8	28.3	13.0	0.39	M
GC11	81.08	28.93	123.5	11268	3.4	33.8	15.0	23.7	18.1	0.39	M
GC11	81.08	28.93	124.5	11333	3.0	30.1	12.5	19.4	19.2	0.39	M
GC11	81.08	28.93	125.5	11397	2.9	30.0	12.9	20.6	18.0	0.38	M
GC11	81.08	28.93	126.5	11463	3.1	32.5	14.5	23.6	17.1	0.38	M
GC11	81.08	28.93	127.5	11529	3.5	34.4	19.5	30.0	14.4	0.39	M
GC11	81.08	28.93	128.5	11594	3.2	32.8	19.9	30.5	12.4	0.39	M
GC11	81.08	28.93	129.5	11658	3.8	35.4	25.4	39.7	11.3	0.39	M
GC11	81.08	28.93	130.5	11724	3.9	37.9	32.0	48.4	8.6	0.40	M
GC11	81.08	28.93	131.5	11788	3.6	33.3	8.9	14.2	30.3	0.38	I
GC11	81.08	28.93	132.5	11853	3.7	40.0	13.5	19.5	22.1	0.41	M
GC11	81.08	28.93	133.5	11918	4.9	43.2	9.3	14.0	36.2	0.40	I
GC11	81.08	28.93	134.5	11984	4.6	37.6	9.1	13.1	35.2	0.41	I
GC11	81.08	28.93	135.5	12049	5.1	45.5	5.0	6.4	51.2	0.44	I
GC11	81.08	28.93	136.5	12113	4.6	42.9	3.9	5.3	54.5	0.42	I
GC11	81.08	28.93	137.5	12179	5.4	43.0	5.1	6.7	52.0	0.43	I
GC11	81.08	28.93	138.5	12245	5.1	42.9	5.7	8.6	48.4	0.40	I
GC11	81.08	28.93	139.5	12309	5.4	38.5	6.5	9.1	46.7	0.42	I
GC11	81.08	28.93	140.5	12375	5.5	47.4	4.3	5.4	56.3	0.44	I
GC11	81.08	28.93	141.5	12441	6.0	35.9	4.1	5.0	58.9	0.45	I

Table D.7 (*continued*)

ID	Coordinates		Depth	Age (cal	HBIs (ng g^{-1} sed.)				Proxy data		CT
	°N	°E	(cm)	yr BP)	IP_{25}	II	III	IV	SpSIC	TRa	**A**
GC11	81.08	28.93	142.5	12505	6.7	48.1	3.9	4.8	61.8	0.45	I
GC11	81.08	28.93	143.5	12571	7.1	51.0	3.4	4.2	65.2	0.45	I
GC11	81.08	28.93	144.5	12636	10.3	57.7	3.3	3.8	71.3	0.46	I
GC11	81.08	28.93	145.5	12701	13.3	61.2	1.5	1.9	80.7	0.45	E
GC11	81.08	28.93	146.5	12763	13.5	62.2	0.9	1.2	83.1	0.43	E
GC11	81.08	28.93	147.5	12824	9.9	42.8	0.7	1.0	82.9	0.43	E
GC11	81.08	28.93	148.5	12886	5.2	16.3	0.5	0.6	81.4	0.46	E
GC11	81.08	28.93	149.5	12948	2.4	10.3	0.3	0.5	79.8	0.38	E

Appendix E

This contains data for Chapter 5: HBI concentrations (ng g^{-1} sed.), $P_{III}IP_{25}$-based SpSIC (%), and CT model A (Fig. 3.7a, Chapter 3) predictions of sea ice conditions in core GS14 (Table E.8). Downcore and surface sedimentary sterol concentrations (ng g^{-1} sed.) are included in Tables E.9 and E.10, respectively. A visual comparison between sterol concentrations before and after TOC normalisation (Eq. 2.7) is presented (Fig. E.2).

Table E.8: HBI concentrations (ng g^{-1} sed.), $P_{III}IP_{25}$-based SpSIC estimates (%), and classes of marginal (M), intermediate (I), or extensive (E) sea ice conditions assigned using CT model A (Fig. 3.7a, Chapter 3) in Barents Sea core GS14.

ID	Coordinates		Depth	Age (cal	HBIs (ng g^{-1} sed.)				$P_{III}IP_{25}$	CT
	°N	°E	(cm)	kyr BP)	IP_{25}	II	III	IV	SpSIC	**A**
GS14	71.48	16.16	11.5	15.413	0.0	0.0	24.5	38.8	-6.47	M
GS14	71.48	16.16	14.5	15.495	0.5	3.9	26.0	43.0	-3.77	M
GS14	71.48	16.16	17	15.570	0.7	2.6	24.9	43.8	-3.77	M
GS14	71.48	16.16	18.5	15.614	0.5	3.3	34.5	66.1	-2.28	M
GS14	71.48	16.16	22.5	15.730	0.5	2.3	86.6	144.7	-4.17	M
GS14	71.48	16.16	27.8	15.878	0.7	3.6	35.0	54.3	-5.60	M
GS14	71.48	16.16	29	15.911	0.8	4.8	14.7	21.8	-3.43	M
GS14	71.48	16.16	30.5	15.952	0.7	5.0	27.5	39.4	0.59	M
GS14	71.48	16.16	34.5	16.066	0.8	3.3	69.5	119.2	-2.80	M
GS14	71.48	16.16	37	16.137	0.8	3.8	17.2	25.9	-4.82	M
GS14	71.48	16.16	38.8	16.188	0.8	3.8	15.5	25.5	-0.08	M
GS14	71.48	16.16	42.8	16.301	0.8	4.5	2.1	3.3	0.74	M
GS14	71.48	16.16	44	16.350	0.6	2.2	0.5	0.6	28.72	M
GS14	71.48	16.16	45.5	16.407	0.5	2.3	0.0	0.0	55.78	I
GS14	71.48	16.16	51.5	16.662	0.6	2.8	0.0	0.0	86.99	I

Table E.8 (*continued*)

ID	Coordinates		Depth	Age (cal	HBIs (ng g^{-1} sed.)				$P_{III}IP_{25}$	CT
	°N	°E	(cm)	kyr BP)	IP_{25}	II	III	IV	SpSIC	**A**
GS14	71.48	16.16	55	16.823	0.0	0.0	0.1	0.1	86.99	E
GS14	71.48	16.16	56.3	16.880	0.0	0.0	0.0	0.0	-	E
GS14	71.48	16.16	59.5	17.029	0.0	0.0	0.0	0.0	-	M
GS14	71.48	16.16	62	17.140	1.0	1.8	0.0	0.0	-	M
GS14	71.48	16.16	63.5	17.211	2.9	10.9	2.8	1.3	86.99	M
GS14	71.48	16.16	65.5	17.301	2.0	4.3	0.0	0.0	51.66	E
GS14	71.48	16.16	71.5	17.584	0.0	0.0	0.0	0.0	86.99	I
GS14	71.48	16.16	72	17.608	0.6	1.1	0.0	0.0	-	E
GS14	71.48	16.16	74.8	17.734	0.0	0.0	0.0	0.0	86.99	M
GS14	71.48	16.16	77	17.812	0.0	0.0	0.0	0.0	-	E
GS14	71.48	16.16	84.8	17.986	0.8	5.5	0.3	0.1	-	M
GS14	71.48	16.16	86.1	18.014	2.1	11.4	0.4	0.4	69.39	M
GS14	71.48	16.16	88.5	18.067	1.1	7.5	0.6	0.3	76.92	E
GS14	71.48	16.16	94.5	18.200	2.8	16.7	0.6	1.1	64.36	E
GS14	71.48	16.16	96.1	18.234	2.7	14.6	0.6	0.6	76.03	E
GS14	71.48	16.16	98.5	18.290	2.4	10.8	0.8	0.8	75.64	I
GS14	71.48	16.16	101.5	18.359	2.0	11.6	0.8	0.5	71.19	E
GS14	71.48	16.16	104.5	18.429	2.2	11.2	0.9	0.7	67.83	I
GS14	71.48	16.16	106.1	18.466	2.8	12.1	0.6	0.4	67.48	E
GS14	71.48	16.16	107.5	18.500	2.2	11.2	0.9	0.5	76.34	E
GS14	71.48	16.16	110.5	18.569	2.7	10.0	0.9	0.7	67.64	E
GS14	71.48	16.16	113.8	18.644	2.1	8.1	0.8	0.6	70.55	E
GS14	71.48	16.16	118.1	18.744	3.7	21.7	0.6	0.8	69.39	E
GS14	71.48	16.16	120.5	18.801	1.6	14.1	1.1	0.7	78.80	I
GS14	71.48	16.16	122.5	18.848	2.1	17.4	1.3	1.3	58.69	E
GS14	71.48	16.16	125.5	18.917	2.8	23.8	1.4	1.6	60.62	E
GS14	71.48	16.16	127.1	18.954	3.0	23.4	1.3	1.6	64.35	I
GS14	71.48	16.16	128.5	18.988	2.2	16.7	0.9	1.6	67.42	I
GS14	71.48	16.16	130.5	19.037	1.8	14.3	1.1	0.7	68.35	I
GS14	71.48	16.16	132.8	19.090	2.0	15.8	1.0	0.7	60.73	I
GS14	71.48	16.16	135.5	19.153	2.2	15.1	0.9	0.6	64.76	E
GS14	71.48	16.16	137.1	19.181	2.8	16.9	0.8	0.7	67.65	E
GS14	71.48	16.16	139.3	19.220	1.8	13.0	0.7	0.6	73.20	E
GS14	71.48	16.16	142.5	19.269	1.0	7.8	0.7	0.2	68.89	E
GS14	71.48	16.16	148.1	19.354	2.6	18.7	0.3	0.3	59.03	E
GS14	71.48	16.16	150.5	19.388	2.6	18.4	0.6	0.4	80.49	E
GS14	71.48	16.16	152.5	19.417	3.8	26.3	0.5	0.9	75.61	E
GS14	71.48	16.16	155.5	19.460	3.5	26.1	0.7	0.6	79.83	E
GS14	71.48	16.16	157.5	19.489	2.9	20.8	1.0	0.8	77.08	E
GS14	71.48	16.16	158.1	19.497	3.0	22.6	0.7	0.7	69.85	E
GS14	71.48	16.16	160.5	19.532	3.5	27.8	0.9	0.8	75.57	E
GS14	71.48	16.16	163.5	19.576	2.5	19.0	0.6	0.9	73.63	E
GS14	71.48	16.16	165.5	19.606	3.1	23.3	0.5	1.1	73.88	E
GS14	71.48	16.16	167.1	19.630	3.7	26.7	0.7	1.4	77.77	E
GS14	71.48	16.16	168.5	19.651	3.1	24.0	1.0	2.0	77.68	E
GS14	71.48	16.16	173.5	19.725	3.2	21.6	0.7	0.8	70.68	E
GS14	71.48	16.16	176.5	19.770	2.6	15.0	0.5	0.6	76.24	I

Table E.8 (*continued*)

ID	Coordinates		Depth	Age (cal	HBIs (ng g^{-1} sed.)				$P_{III}IP_{25}$	CT
	°N	°E	(cm)	kyr BP)	IP_{25}	II	III	IV	SpSIC	**A**
GS14	71.48	16.16	177.1	19.778	2.6	18.0	0.5	0.5	77.69	E
GS14	71.48	16.16	179.5	19.813	3.2	20.9	0.5	0.5	77.89	E
GS14	71.48	16.16	182	19.848	2.8	17.9	0.4	0.4	78.64	E
GS14	71.48	16.16	192	19.991	4.1	29.6	0.4	0.8	80.12	E
GS14	71.48	16.16	202	20.165	2.2	14.3	0.3	0.3	81.37	E
GS14	71.48	16.16	212	20.362	5.3	32.8	0.4	0.5	80.69	E
GS14	71.48	16.16	222	20.552	4.9	36.0	0.5	0.4	82.87	E
GS14	71.48	16.16	232	20.749	6.4	38.4	0.5	0.5	81.84	E
GS14	71.48	16.16	242	20.945	4.8	29.6	0.3	0.3	82.61	E
GS14	71.48	16.16	252	21.138	1.6	8.9	0.6	0.3	84.00	E
GS14	71.48	16.16	262	21.337	3.7	24.8	0.3	0.3	70.11	E
GS14	71.48	16.16	268	21.449	5.1	37.1	0.5	0.5	81.88	E
GS14	71.48	16.16	273.5	21.546	3.8	26.1	0.4	0.3	81.15	E
GS14	71.48	16.16	276	21.589	3.2	27.3	0.4	0.4	81.03	E
GS14	71.48	16.16	277.5	21.613	2.1	16.8	0.6	0.5	80.16	E
GS14	71.48	16.16	279.5	21.646	2.9	21.0	0.8	0.5	72.04	E
GS14	71.48	16.16	282.5	21.695	2.2	14.7	0.4	0.3	73.61	E
GS14	71.48	16.16	286	21.751	1.4	8.5	0.2	0.2	77.08	E
GS14	71.48	16.16	287.5	21.775	1.6	10.1	0.3	0.1	79.70	E
GS14	71.48	16.16	292.5	21.861	5.4	36.4	0.7	0.5	77.57	E
GS14	71.48	16.16	294.5	21.896	4.2	31.3	0.5	0.3	79.78	E
GS14	71.48	16.16	296	21.924	3.1	19.2	0.4	0.3	80.65	E
GS14	71.48	16.16	298.5	21.969	3.2	22.9	0.9	0.4	79.71	E
GS14	71.48	16.16	300.5	22.006	1.2	8.4	0.8	0.3	72.77	E
GS14	71.48	16.16	302.5	22.043	1.2	8.6	0.9	0.4	59.81	E
GS14	71.48	16.16	306	22.110	2.8	17.5	0.7	0.5	57.61	E
GS14	71.48	16.16	308.5	22.158	2.7	17.1	0.8	0.5	74.70	E
GS14	71.48	16.16	310.5	22.197	5.1	29.0	1.1	0.6	72.57	E
GS14	71.48	16.16	312.5	22.236	5.7	36.1	0.7	0.4	76.07	E
GS14	71.48	16.16	314.5	22.274	5.3	39.8	0.6	0.3	80.56	E
GS14	71.48	16.16	316	22.303	3.8	25.0	0.5	0.4	80.65	E
GS14	71.48	16.16	320.5	22.389	4.0	30.0	0.7	0.4	80.36	E
GS14	71.48	16.16	322.5	22.427	4.6	29.4	0.2	0.2	77.81	E
GS14	71.48	16.16	326	22.494	2.3	15.8	0.4	0.6	84.08	E
GS14	71.48	16.16	327.5	22.523	2.9	19.6	0.5	0.3	78.46	E
GS14	71.48	16.16	330.5	22.578	2.2	13.6	0.3	0.1	78.22	E
GS14	71.48	16.16	332.5	22.615	2.7	16.1	0.2	0.1	80.45	E
GS14	71.48	16.16	336	22.677	3.2	15.8	0.3	0.3	82.70	E
GS14	71.48	16.16	338.5	22.721	4.1	22.2	0.9	0.6	81.38	E
GS14	71.48	16.16	340.5	22.753	3.9	16.8	0.9	0.5	75.28	E
GS14	71.48	16.16	342.5	22.784	2.6	11.3	1.0	0.5	74.83	E
GS14	71.48	16.16	345.5	22.831	3.4	15.4	0.7	0.5	69.09	E
GS14	71.48	16.16	346	22.838	2.8	12.1	0.6	0.5	76.09	E
GS14	71.48	16.16	347.5	22.861	2.6	12.5	0.8	0.5	76.05	E
GS14	71.48	16.16	350.5	22.908	2.2	13.2	1.1	0.7	72.18	E
GS14	71.48	16.16	352.5	22.939	2.4	14.9	1.1	0.6	65.26	E
GS14	71.48	16.16	354.5	22.970	2.5	10.0	0.9	0.6	65.68	E

Table E.8 (*continued*)

ID	Coordinates		Depth	Age (cal	HBIs (ng g^{-1} sed.)				$P_{III}IP_{25}$	CT
	°N	°E	(cm)	kyr BP)	IP_{25}	II	III	IV	SpSIC	**A**
GS14	71.48	16.16	356	22.993	2.4	8.9	0.8	0.5	69.66	E
GS14	71.48	16.16	360.5	23.062	2.0	11.0	1.0	0.7	71.45	E
GS14	71.48	16.16	362.5	23.092	4.2	18.1	0.9	0.6	64.94	E
GS14	71.48	16.16	363.5	23.108	5.1	23.3	0.9	0.7	75.95	E
GS14	71.48	16.16	366	23.144	3.6	14.9	0.6	0.5	77.78	E
GS14	71.48	16.16	367.5	23.167	3.7	16.8	0.8	0.5	77.88	E
GS14	71.48	16.16	376.2	23.300	4.0	25.6	0.2	0.2	75.31	E
GS14	71.48	16.16	391.2	23.522	2.2	12.1	0.2	0.2	83.86	E
GS14	71.48	16.16	401.2	23.675	7.5	40.9	0.5	0.4	81.71	E
GS14	71.48	16.16	411.2	23.825	6.4	43.7	0.4	0.4	83.34	E
GS14	71.48	16.16	421.2	23.974	5.3	33.9	0.3	0.4	83.19	E
GS14	71.48	16.16	431.2	24.125	3.1	18.3	0.0	0.0	83.93	E
GS14	71.48	16.16	441.2	24.269	3.4	18.8	0.2	0.3	86.99	E
GS14	71.48	16.16	449.2	24.385	3.2	21.2	0.3	0.4	83.83	E
GS14	71.48	16.16	459.2	24.559	3.0	18.3	0.2	0.3	82.05	E
GS14	71.48	16.16	469.2	24.769	4.2	24.8	0.7	0.6	83.66	E
GS14	71.48	16.16	475	24.889	4.7	28.9	2.7	1.7	77.55	E
GS14	71.48	16.16	485	25.092	1.2	7.5	4.2	3.9	62.08	E
GS14	71.48	16.16	495	25.287	0.0	0.0	0.0	0.0	23.00	E
GS14	71.48	16.16	505	25.482	3.2	14.2	0.9	0.7	-	I
GS14	71.48	16.16	513	25.639	1.9	7.7	0.5	0.3	72.89	M
GS14	71.48	16.16	523	25.825	1.8	9.7	1.2	0.5	73.78	E

Table E.9: Sterol concentrations (µg g^{-1} sed.) in core GS14. Abbreviations denote brassicasterol (A), chalinasterol (B), campesterol (C), β-sitosterol (D), dinosterol (E), and cholesterol (F).

ID	Coordinates		Depth	Age (cal	Sterols (µg g^{-1} sed.)					
	°N	°E	(cm)	kyr BP)	A	B	C	D	E	F
GS14	71.48	16.16	11.5	15.413	2.54	1.98	0.58	1.24	0.53	3.74
GS14	71.48	16.16	14.5	15.495	2.39	1.87	0.46	0.97	0.36	3.56
GS14	71.48	16.16	18.5	15.614	1.87	1.57	0.48	0.90	0.44	3.06
GS14	71.48	16.16	22.5	15.730	2.17	2.12	0.60	1.18	0.51	3.88
GS14	71.48	16.16	27.8	15.878	2.02	2.10	0.47	1.12	0.55	3.49
GS14	71.48	16.16	30.5	15.952	1.49	1.75	0.45	0.99	0.36	2.72
GS14	71.48	16.16	42.8	16.301	1.10	1.28	0.37	0.80	0.27	1.89
GS14	71.48	16.16	44	16.350	0.68	0.96	0.34	0.55	0.28	1.31
GS14	71.48	16.16	45.5	16.407	0.22	0.31	0.12	0.34	0.13	0.45
GS14	71.48	16.16	51.5	16.662	0.08	0.05	0.06	0.22	0.09	0.20
GS14	71.48	16.16	55	16.823	0.09	0.12	0.09	0.19	0.06	0.21
GS14	71.48	16.16	56.3	16.880	0.03	0.01	0.03	0.08	0.02	0.04
GS14	71.48	16.16	59.5	17.029	0.03	0.03	0.03	0.12	0.03	0.10
GS14	71.48	16.16	62	17.140	0.04	0.06	0.04	0.12	0.05	0.12
GS14	71.48	16.16	63.5	17.211	0.06	0.05	0.03	0.15	0.07	0.12
GS14	71.48	16.16	65.5	17.301	0.46	0.35	0.16	0.32	0.09	0.58
GS14	71.48	16.16	71.5	17.584	0.08	0.08	0.07	0.16	0.06	0.13

Table E.9 (*continued*)

ID	Coordinates		Depth	Age (cal	Sterols (µg g^{-1} sed.)					
	°N	°E	(cm)	kyr BP)	A	B	C	D	E	F
GS14	71.48	16.16	72	17.608	0.04	0.04	0.04	0.11	0.03	0.09
GS14	71.48	16.16	74.8	17.734	0.03	0.02	0.03	0.09	0.03	0.10
GS14	71.48	16.16	77	17.812	0.02	0.02	0.03	0.07	0.03	0.10
GS14	71.48	16.16	84.8	17.986	0.04	0.02	0.03	0.13	0.04	0.12
GS14	71.48	16.16	94.5	18.200	0.46	0.27	0.27	0.58	0.21	0.33
GS14	71.48	16.16	96.1	18.234	1.26	0.80	0.47	0.94	0.31	0.83
GS14	71.48	16.16	98.5	18.290	0.75	0.89	0.40	0.86	0.27	0.79
GS14	71.48	16.16	101.5	18.359	0.89	0.89	0.41	0.70	0.21	0.77
GS14	71.48	16.16	104.5	18.429	0.90	0.67	0.32	0.71	0.19	0.54
GS14	71.48	16.16	106.1	18.466	1.32	0.84	0.42	0.79	0.23	0.83
GS14	71.48	16.16	107.5	18.500	0.59	0.50	0.25	0.54	0.18	0.61
GS14	71.48	16.16	110.5	18.569	0.70	0.71	0.39	0.59	0.19	0.63
GS14	71.48	16.16	113.8	18.644	0.73	0.76	0.45	0.63	0.22	0.63
GS14	71.48	16.16	118.1	18.744	0.78	0.89	0.47	0.58	0.20	0.68
GS14	71.48	16.16	122.5	18.848	1.23	1.00	0.58	1.13	0.27	0.83
GS14	71.48	16.16	127.1	18.954	1.07	0.88	0.64	1.89	0.44	0.92
GS14	71.48	16.16	130.5	19.037	1.95	1.51	0.97	2.20	0.47	1.26
GS14	71.48	16.16	135.5	19.153	1.56	1.45	0.75	1.86	0.39	1.07
GS14	71.48	16.16	139.3	19.220	1.23	1.02	0.59	1.74	0.45	0.88
GS14	71.48	16.16	148.1	19.354	0.58	0.52	0.33	1.26	0.36	0.58
GS14	71.48	16.16	152.5	19.417	1.27	1.22	0.76	1.78	0.39	0.95
GS14	71.48	16.16	157.5	19.489	2.63	2.37	1.56	2.59	0.63	1.73
GS14	71.48	16.16	160.5	19.532	1.95	1.38	1.00	2.11	0.50	1.24
GS14	71.48	16.16	168.5	19.651	1.66	1.20	0.67	1.16	0.43	0.91
GS14	71.48	16.16	176.5	19.770	1.28	1.23	0.75	1.28	0.49	0.94
GS14	71.48	16.16	179.5	19.813	1.08	1.30	0.66	1.34	0.47	0.94
GS14	71.48	16.16	192	19.991	1.19	1.22	0.57	1.44	0.49	1.04
GS14	71.48	16.16	202	20.165	1.37	1.06	0.62	1.05	0.42	1.09
GS14	71.48	16.16	212	20.362	0.58	0.43	0.26	0.76	0.31	0.47
GS14	71.48	16.16	222	20.552	1.61	1.20	0.70	1.30	0.53	1.17
GS14	71.48	16.16	232	20.749	1.42	1.48	0.72	1.27	0.49	1.14
GS14	71.48	16.16	242	20.945	2.25	1.52	0.79	1.28	0.51	1.47
GS14	71.48	16.16	252	21.138	1.15	0.85	0.57	0.87	0.42	0.91
GS14	71.48	16.16	262	21.337	0.79	0.65	0.47	1.01	0.32	0.64
GS14	71.48	16.16	268	21.449	1.28	1.49	0.52	1.50	0.26	0.95
GS14	71.48	16.16	273.5	21.546	1.73	1.72	0.67	1.29	0.32	1.02
GS14	71.48	16.16	276	21.589	1.35	1.34	0.65	1.35	0.37	1.03
GS14	71.48	16.16	277.5	21.613	1.57	1.85	0.71	1.97	0.43	1.07
GS14	71.48	16.16	282.5	21.695	0.90	1.09	0.49	1.33	0.43	1.00
GS14	71.48	16.16	287.5	21.775	0.68	0.55	0.32	1.03	0.33	0.51
GS14	71.48	16.16	294.5	21.896	2.00	1.34	0.78	1.41	0.56	1.40
GS14	71.48	16.16	298.5	21.969	1.29	1.30	0.60	1.23	0.47	1.09
GS14	71.48	16.16	302.5	22.043	0.42	0.27	0.30	1.21	0.35	0.37
GS14	71.48	16.16	308.5	22.158	1.05	0.76	0.58	1.77	0.39	0.83
GS14	71.48	16.16	312.5	22.236	1.52	0.98	0.58	1.55	0.44	1.05
GS14	71.48	16.16	316	22.303	1.70	1.33	0.63	1.04	0.37	1.15
GS14	71.48	16.16	322.5	22.427	1.38	0.79	0.52	1.02	0.37	0.85

Table E.9 (*continued*)

ID	Coordinates		Depth	Age (cal	Sterols (μg g^{-1} sed.)					
	°N	°E	(cm)	kyr BP)	A	B	C	D	E	F
GS14	71.48	16.16	338.5	22.721	2.56	1.65	0.71	0.97	0.30	1.22
GS14	71.48	16.16	346	22.838	0.77	0.56	0.29	0.56	0.21	0.59
GS14	71.48	16.16	350.5	22.908	1.10	0.94	0.43	0.88	0.35	1.11
GS14	71.48	16.16	354.5	22.970	1.14	0.70	0.38	0.64	0.24	0.84
GS14	71.48	16.16	360.5	23.062	1.20	1.05	0.42	0.68	0.24	0.93
GS14	71.48	16.16	363.5	23.108	1.20	0.98	0.42	0.82	0.31	1.08
GS14	71.48	16.16	367.5	23.167	0.91	0.56	0.23	0.64	0.23	0.68
GS14	71.48	16.16	376.2	23.300	1.19	0.52	0.34	0.92	0.48	0.81
GS14	71.48	16.16	391.2	23.522	0.96	0.56	0.32	0.88	0.43	0.93
GS14	71.48	16.16	401.2	23.675	1.99	1.02	0.57	1.12	0.50	1.43
GS14	71.48	16.16	411.2	23.825	1.94	0.75	0.43	1.12	0.38	1.11
GS14	71.48	16.16	421.2	23.974	2.55	0.99	0.41	0.99	0.38	1.37
GS14	71.48	16.16	431.2	24.125	1.35	0.61	0.33	0.80	0.32	0.82
GS14	71.48	16.16	441.2	24.269	0.91	0.89	0.42	1.57	0.48	0.57
GS14	71.48	16.16	449.2	24.385	1.06	0.75	0.44	1.57	0.36	0.59
GS14	71.48	16.16	459.2	24.559	1.14	1.02	0.48	1.38	0.63	0.94
GS14	71.48	16.16	469.2	24.769	1.21	1.06	0.50	1.20	0.47	0.94
GS14	71.48	16.16	475	24.889	0.95	1.26	0.53	1.19	0.74	1.50
GS14	71.48	16.16	485	25.092	0.55	0.97	0.30	0.77	0.48	1.00
GS14	71.48	16.16	513	25.639	0.27	0.36	0.09	0.21	0.12	0.30
GS14	71.48	16.16	523	25.825	0.04	0.07	0.05	0.19	0.05	0.14

Table E.10: Sterol concentrations (μg g^{-1} sed.) in Barents Sea surface sediments. Abbreviations are analogous to those in Table E.9.

ID	Coordinates		Sterols (μg g^{-1} sed.)					
	°N	°E	A	B	C	D	E	F
631	73.67	24.47	10.30	1.89	1.95	4.56	1.88	8.19
St. 1	72.00	22.00	6.97	0.96	0.77	2.89	0.84	3.31
St. 2	72.02	20.92	6.31	0.76	0.68	2.39	0.66	4.16
St. 3	72.03	19.85	8.81	1.27	1.15	4.62	0.95	5.90
St. 4	72.02	18.77	11.83	2.01	1.58	6.48	1.36	8.08
St. 5	72.03	17.70	10.06	3.34	1.91	5.90	0.95	11.21
St. 6	72.02	16.62	2.52	0.43	0.42	1.50	0.57	1.87
St. 8	72.01	14.73	4.11	1.26	0.49	1.23	0.40	3.06
St. 12	73.17	14.09	2.70	0.38	0.22	0.99	0.27	1.35
St. 13	73.17	15.23	3.65	0.51	0.39	1.68	0.48	1.78
St. 14	73.17	16.38	5.80	1.12	0.61	2.58	0.78	3.70
St. 16	73.17	18.82	5.69	1.09	0.69	2.37	0.84	3.47
St. 17	73.17	19.86	7.16	1.39	0.95	3.11	1.04	5.12
St. 18	73.17	20.95	10.53	1.70	2.18	4.74	1.43	16.84
St. 22	74.82	16.03	4.65	1.12	0.61	2.04	0.66	3.88
St. 23	74.82	14.79	8.56	1.48	1.02	4.19	0.96	4.21
St.34	71.75	22.00	4.36	0.60	0.48	1.64	0.59	2.75
St.35	71.62	21.07	3.35	0.41	0.38	1.57	0.47	2.02

Table E.10 *(continued)*

ID	Coordinates		Sterols (μg g^{-1} sed.)					
	°N	°E	A	B	C	D	E	F
St.36	71.60	20.86	5.98	0.86	0.66	2.90	0.57	3.69
St.38	71.49	20.82	6.71	0.99	0.85	3.01	0.75	4.69
St.39	71.34	20.19	3.70	0.45	0.40	1.61	0.51	2.32
St.40	71.18	19.56	7.94	1.08	0.99	3.01	0.83	5.68
St.42	70.87	18.34	6.74	1.13	0.91	2.55	0.88	6.33
St. 45	70.44	16.75	4.50	0.79	0.51	1.94	0.51	2.66
625	71.72	21.76	4.19	0.53	0.50	1.55	0.52	2.77
627	72.32	24.06	3.70	0.56	0.52	1.17	0.48	2.51
629	73.01	24.25	7.83	0.87	1.26	3.32	1.35	6.17
653	73.97	25.81	12.47	2.57	2.60	7.33	2.95	7.99
655	73.31	25.54	8.64	1.71	1.52	4.20	1.74	8.18
657	72.64	25.27	3.96	0.50	0.50	1.56	0.59	2.46
659	71.98	25.06	6.34	0.85	0.92	2.08	0.56	10.89
661	71.37	22.76	3.21	0.45	0.42	1.18	0.50	2.19
663	71.61	25.99	3.54	0.47	0.39	1.05	0.37	2.46
665	72.17	28.41	5.12	0.73	0.62	1.93	0.80	3.65
667	72.84	28.76	2.02	0.29	0.29	1.01	0.50	1.46
669	73.50	29.15	4.46	0.95	0.79	1.96	1.00	3.62
671	74.15	29.55	5.25	0.99	0.91	2.41	1.13	3.59
690	71.02	30.96	2.92	0.65	0.73	1.82	0.65	3.24
692	70.62	31.72	1.66	0.42	0.26	0.59	0.32	1.79
R1 MC85	70.46	21.68	19.57	3.49	2.52	5.94	3.18	15.55
R3 MC110	71.33	22.42	3.91	0.53	0.73	1.35	0.53	2.76
R4 MC107	71.33	22.49	4.34	0.62	0.62	1.83	0.65	3.11
R5 MC112	71.30	22.53	4.89	0.77	0.85	2.08	0.81	3.57
R7 MC89	71.32	22.20	3.31	0.46	0.57	1.21	0.61	2.76
R8 MC88	71.27	22.13	1.68	0.26	0.27	0.70	0.23	1.37
R10 MC96	71.21	21.45	4.93	0.67	0.83	2.43	0.66	4.17
R11 MC105	71.22	21.72	2.31	0.43	0.36	1.00	0.32	2.02
R14 MC94	71.13	21.44	5.79	0.94	1.40	2.64	0.62	4.48
R18 MC98	71.31	21.28	2.16	0.36	0.31	0.77	0.27	1.31
R37 MC115	70.31	22.26	37.25	6.48	12.10	9.41	4.92	21.72
R49 MC128	70.42	22.10	34.80	7.26	5.88	10.16	5.69	21.14
R68 MC149	71.32	22.50	9.67	1.53	2.38	4.85	1.18	8.35
R68A MC136	71.32	22.49	4.13	0.59	0.44	1.46	0.65	4.10
R81 MC002	71.16	18.65	5.74	1.00	0.76	2.63	0.95	4.26
R96 MC008	70.14	18.15	13.68	2.85	1.90	3.91	1.39	8.12
R104 MC010	70.19	17.73	5.91	1.27	0.91	2.21	0.61	4.30
R112 MC007	69.81	17.42	32.28	7.36	5.30	13.62	4.17	20.95
R117 MC005	69.85	17.13	6.43	0.93	0.84	2.36	0.89	4.21
R223 MC005	69.26	16.33	40.72	7.56	9.24	19.98	4.91	23.86
R232 MC009	69.41	14.70	8.95	2.26	1.39	6.54	1.12	8.53
R243 GR037	68.58	13.71	3.20	0.50	0.43	0.89	0.33	1.99
R248 GR039	68.78	12.53	14.19	3.68	1.92	8.25	2.65	11.05
R259 GR041	69.18	13.98	8.98	2.17	1.25	5.38	1.63	7.46
R259 MC011	69.18	13.98	9.30	2.32	1.35	6.25	1.47	7.24
R276 BX049	68.48	10.97	2.76	0.75	0.42	2.22	0.45	2.82

Table E.10 *(continued)*

ID	Coordinates		Sterols (µg g^{-1} sed.)					
	°N	°E	A	B	C	D	E	F
R280A MC016	68.14	12.30	5.58	1.46	0.95	3.06	0.82	4.28
R291 MC020	68.61	15.24	31.74	8.53	5.89	13.15	4.89	22.05
R291 MC022	68.61	15.24	49.93	13.03	9.92	24.11	7.77	32.67
R297 BX056	68.65	11.91	3.57	0.87	0.48	2.22	0.65	3.29
R301 MC023	68.71	11.59	6.03	1.89	0.86	4.39	1.00	5.05
R311 BX059	68.90	12.67	10.64	2.53	1.46	6.67	1.89	8.23
R351 BX065	68.85	13.10	4.25	0.84	0.53	2.16	0.55	3.15
R359 BX067	68.09	11.60	4.08	0.86	0.66	2.33	0.68	3.66
R406 MC0	72.19	14.83	7.03	1.34	0.90	4.19	0.66	5.96
R754 MC021	67.80	9.71	4.63	2.34	1.21	3.61	0.59	15.30
R776 MC004	68.19	10.36	4.57	1.09	0.68	3.27	0.72	3.93
R782 MC007	68.06	9.47	6.53	1.92	0.91	5.18	0.80	7.91
R889 MC025	64.29	8.80	7.07	1.85	1.38	6.45	1.75	9.80
R911 MC022	63.55	7.41	5.12	1.36	0.79	4.33	1.20	5.15
R932 BX029-1	64.11	5.73	7.59	1.91	1.25	5.43	1.93	7.46
R942 BX026-1	64.41	5.57	9.54	2.64	1.46	6.84	2.34	11.13
R949 MC028-4	65.16	9.35	4.97	1.40	0.84	4.48	1.16	5.15
R949 MC028-2	65.16	9.35	3.89	1.03	0.74	3.51	0.83	4.66
R973 BX025-1	64.57	5.67	4.21	1.31	0.75	3.20	0.93	4.86
R1080 BX010	66.21	7.00	3.16	0.91	0.50	2.32	0.48	3.51
R1096 MC002-1	65.95	6.51	3.80	1.07	0.52	2.41	0.57	3.36
R1096 MC002-4	65.95	6.51	3.05	0.74	0.46	2.08	0.48	3.44
R1114 MC003-2	65.63	5.57	4.82	1.55	0.87	3.74	0.81	8.16
R1114 MC003-6	65.63	5.57	3.86	1.15	0.67	2.67	0.66	4.37
R1119 MC004	65.51	6.28	2.61	0.90	0.43	2.23	0.46	2.97
R1129 MC005	65.29	6.28	4.17	1.15	0.67	3.08	0.72	4.54
R1133 MC006	65.17	5.93	2.98	0.86	0.49	2.29	0.74	3.39
R1139 MC010-2	72.31	32.35	12.64	1.76	1.96	4.93	2.84	7.43
R1139 MC010-1	72.31	32.35	19.61	2.78	4.76	11.75	3.85	18.30
R1146 MC011-4	72.11	34.33	16.99	2.75	3.33	7.23	3.91	11.09
R1165 MC012	71.78	33.53	15.75	3.01	3.64	7.70	4.47	16.57
R1174 MC013	71.62	32.22	9.15	1.49	1.62	3.92	1.97	5.74
R1180 MC014	71.61	32.99	10.98	1.79	1.91	4.72	2.74	7.03
R1180 MC014	71.61	32.99	12.80	1.89	2.38	6.21	3.20	9.16
R1186 MC015-6	71.42	32.87	9.99	1.91	1.93	5.33	2.10	6.51
R1200 MC016-1	70.86	32.52	14.93	3.30	3.26	7.43	2.31	12.61
R1200 MC016-2	70.86	32.52	9.79	1.73	1.79	4.37	2.21	6.24
R1213 MC018	70.78	30.72	14.16	2.48	2.21	8.69	2.68	8.94
R1257 GR681	62.89	4.30	6.24	1.78	0.98	4.95	1.30	5.81
R1261 MC020	63.03	4.69	11.47	3.41	1.90	8.28	3.14	13.00
R1284 MC027	64.81	10.12	3.98	1.20	0.87	4.68	1.06	5.90
PS2149-1	73.18	31.73	1.65	1.61	0.72	1.12	0.27	2.80
633	74.34	24.69	5.83	1.36	2.01	3.36	1.21	9.11
649	74.54	28.58	13.06	3.12	2.87	5.76	2.83	15.61
673	74.67	32.49	7.85	2.93	2.33	2.98	1.11	7.10
St. 20	74.82	18.02	18.95	5.48	2.47	6.46	2.09	11.35
647	75.20	29.01	15.01	3.68	3.18	5.38	2.70	8.98

Table E.10 *(continued)*

ID	Coordinates		Sterols (μg g^{-1} sed.)					
	°N	°E	A	B	C	D	E	F
651	74.64	26.08	12.84	3.09	2.27	5.12	2.37	7.58
635	75.00	24.94	20.55	7.00	4.77	6.93	2.59	14.19
675	75.33	33.07	15.52	6.98	7.24	6.45	2.41	59.76
639	75.57	27.90	15.35	4.99	4.55	6.57	2.97	11.56
645	75.86	29.46	10.18	3.31	1.95	3.37	1.33	6.52
677	75.97	33.73	7.24	2.29	1.14	1.94	0.73	4.51
643	76.49	29.91	10.45	3.71	3.30	4.17	1.45	12.04
681	76.43	37.17	5.85	2.28	2.09	2.47	0.72	6.91
PS2111-2	76.64	34.88	5.64	2.02	1.81	3.02	1.02	3.85
PS2153-1	76.61	34.81	6.59	2.20	4.60	3.71	1.22	4.37
JR142-GC17	80.15	17.18	18.40	8.34	5.80	17.53	2.34	10.54
JR211-GC14	80.39	16.44	8.17	3.70	2.48	6.42	1.08	5.00
679	76.62	34.45	9.02	4.34	6.05	5.31	1.11	24.75
JR211-GC15	80.51	15.90	11.56	5.57	3.73	10.84	1.59	6.78
PS2115-1	77.20	18.33	4.63	2.89	2.08	2.80	0.71	4.21
PS2148-1	80.01	29.60	2.28	1.65	1.79	2.51	0.71	2.63
JR142-GC09	79.96	29.65	3.46	3.09	1.95	5.12	0.87	3.10
JR142-GC18	81.26	19.05	2.78	1.08	0.67	2.16	0.70	2.13
JR142-GC21	78.57	34.06	1.05	0.50	0.26	1.01	0.31	0.95
JR142-GC08	79.49	28.44	2.18	2.87	1.55	3.41	0.77	3.61
JR142-GC07	79.21	26.54	2.09	2.04	1.13	3.24	0.71	2.12
JR142-GC23	79.38	29.77	1.83	1.53	1.16	3.40	0.54	2.06
JR142-GC10	80.49	29.65	2.65	2.70	1.15	2.61	0.48	2.49
PS2144-3	80.75	29.47	2.17	1.30	0.97	1.95	0.69	2.10
PS2142-3	80.85	30.64	1.67	1.30	0.56	0.96	0.33	1.29
JR142-GC20	79.59	26.19	1.12	1.29	1.23	2.75	0.29	1.16
JR142-GC4	78.90	23.98	1.89	1.76	0.78	2.26	0.53	1.95
JR142-GC13	81.35	21.63	0.37	0.22	0.19	0.51	0.18	0.68
JR142-GC06	79.10	25.10	1.43	1.48	0.68	1.75	0.47	1.60
JR142-GC05	78.95	24.45	1.80	1.70	0.76	1.93	0.64	1.81
JR142-GC11	81.08	28.93	1.79	1.38	0.82	2.42	0.58	1.61
JR142-GC12	81.39	26.94	3.89	1.56	1.20	4.42	0.81	2.64

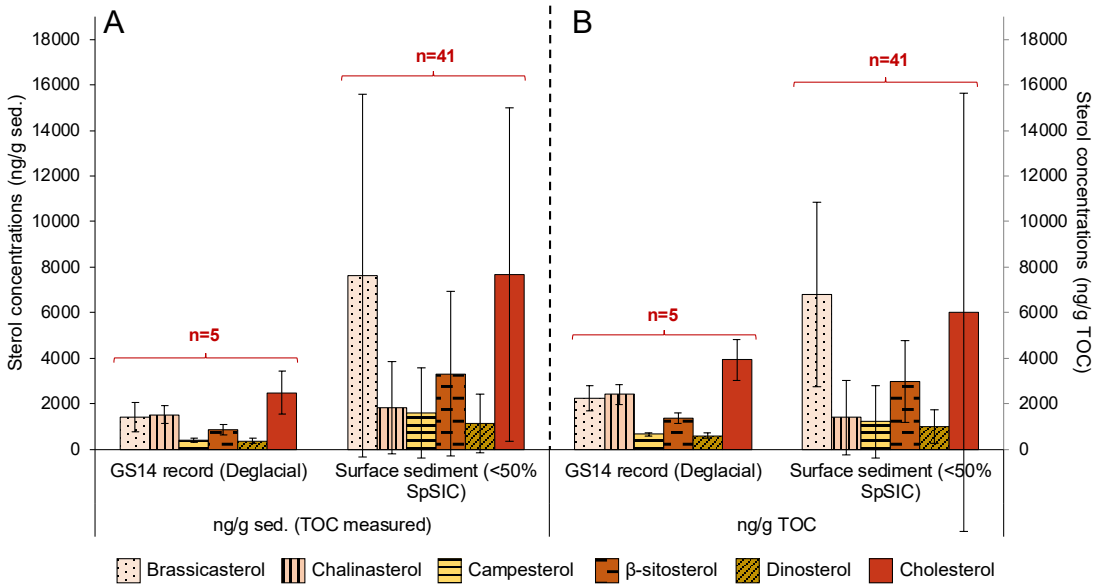

Figure E.2: Absolute sterol concentrations before (A) and after (B) normalisation to TOC during the Deglacial period (after 16.3 cal kyr BP) of the GS14 record, and in surface sediments characterised by <50% SpSIC in the modern Barents Sea (Chapter 5).

References

Aagaard, K., Woodgate, R.A. (2001), 'Some thoughts on the freezing and melting of sea ice and their effects on the ocean', *Ocean Modelling* **3**, pp. 127–135.

Aagaard-Sørensen, S., Husum, K., Hald, M., Knies, J. (2010), 'Paleoceanographic development in the SW Barents Sea during the Late Weichselian–Early Holocene transition', *Quaternary Science Reviews* **29**, pp. 3442–3456.

Aagaard-Sørensen, S., Husum, K., Hald, M., Marchitto, T.M., Godtliebsen, F. (2013), 'Sub sea surface temperatures in the Polar North Atlantic during the Holocene: Planktic foraminiferal Mg/Ca temperature reconstructions', *The Holocene* **24**, pp. 93–103.

Aarflot, J.M., Skjoldal, H.R., Dalpadado, P., Skern-Mauritzen, M. (2017), 'Contribution of Calanus species to the mesozooplankton biomass in the Barents Sea', *ICES Journal of Marine Science* **75**, pp. 2342–2354.

Addinsoft (2018), *XLSTAT: Data Analysis and Statistical Solution for Microsoft Excel*, Paris, France.

Adkins, J.F., Ingersoll, A.P., Pasquero, C. (2005), 'Rapid climate change and conditional instability of the glacial deep ocean from the thermobaric effect and geothermal heating', *Quaternary Science Reviews* **24**, pp. 581–594.

Aitchison, J. (1986), *The Statistical Analysis of Compositional Data*. Chapman & Hall Ltd., London, UK.

Aluja-Banet, T., Nafria, E. (2003), 'Stability and scalability in decision trees', *Computational Statistics* **18**, pp. 505–520.

Álvarez-Solas, J., Montoya, M., Ritz, C., Ramstein, G., Charbit, S., Dumas, C., Nisancioglu, K., Dokken, T., Ganopolski, A. (2011), 'Heinrich event 1: an example of dynamical ice-sheet reaction to oceanic changes', *Climate of the Past* **7**, pp. 1297–1306.

Ampel, L., Wohlfarth, B., Risberg, J., Veres, D., Leng, M.J., Tillman, P.K. (2010), 'Diatom assemblage dynamics during abrupt climate change: the response of lacustrine diatoms to Dansgaard–Oeschger cycles during the last glacial period', *Journal of Paleolimnology* **44**, pp. 397–404.

Andreassen, K., Winsborrow, M. (2009), 'Signature of ice streaming in Bjørnøyrenna, Polar North Atlantic, through the Pleistocene and implications for ice-stream dynamics', *Annals of Glaciology* **50**, pp. 17–27.

Andrews, J.T. (2000), 'Icebergs and iceberg rafted detritus (IRD) in the North Atlantic: Facts and assumptions ', *Oceanography* **13**, pp. 100–108.

Andrews, J.T., Tedesco, K. (1992), 'Detrital carbonate-rich sediments, northwestern Labrador Sea: Implications for ice-sheet dynamics and iceberg rafting (Heinrich) events in the North Atlantic', *Geology* **20**, pp. 1087–1090.

Arrigo, K.R., Perovich, D.K., Pickart, R.S., Brown, Z.W., van Dijken, G.L., Lowry, K.E., Mills, M.M., Palmer, M.A., Balch, W.M., Bahr, F., Bates, N.R., Benitez-Nelson, C., Bowler, B., Brownlee, E., Ehn, J.K., Frey, K.E., Garley, R., Laney, S.R., Lubelczyk,

L., Mathis, J., Matsuoka, A., Mitchell, B.G., Moore, G.W.K., Ortega-Retuerta, E., Pal, S., Polashenski, C.M., Reynolds, R.A., Schieber, B., Sosik, H.M., Stephens, M., Swift, J.H. (2012), 'Massive Phytoplankton Blooms Under Arctic Sea Ice', *Science* **336**, p. 1408.

Arrigo, K.R., van Dijken, G., Pabi, S. (2008), 'Impact of a shrinking Arctic ice cover on marine primary production', *Geophysical Research Letters* **35**, article L19603.

Arrigo, K.R., van Dijken, G.L. (2015), 'Continued increases in Arctic Ocean primary production', *Progress in Oceanography* **136**, pp. 60–70.

Årthun, M., Eldevik, T., Smedsrud, L.H., Skagseth, Ø., Ingvaldsen, R.B. (2012), 'Quantifying the Influence of Atlantic Heat on Barents Sea Ice Variability and Retreat', *Journal of Climate* **25**, pp. 4736–4743.

Assmy, P., Fernández-Méndez, M., Duarte, P., Meyer, A., Randelhoff, A., Mundy, C.J., Olsen, L.M., Kauko, H.M., Bailey, A., Chierici, M., Cohen, L., Doulgeris, A.P., Ehn, J.K., Fransson, A., Gerland, S., Hop, H., Hudson, S.R., Hughes, N., Itkin, P., Johnsen, G., King, J.A., Koch, B.P., Koenig, Z., Kwasniewski, S., Laney, S.R., Nicolaus, M., Pavlov, A.K., Polashenski, C.M., Provost, C., Rösel, A., Sandbu, M., Spreen, G., Smedsrud, L.H., Sundfjord, A., Taskjelle, T., Tatarek, A., Wiktor, J., Wagner, P.M., Wold, A., Steen, H., Granskog, M.A. (2017), 'Leads in Arctic pack ice enable early phytoplankton blooms below snow-covered sea ice', *Scientific Reports* **7**, article 40850.

Austin, W.E.N., Telford, R.J., Ninnemann, U.S., Brown, L., Wilson, L.J., Small, D.P., Bryant, C.L. (2011), 'North Atlantic reservoir ages linked to high Younger Dryas atmospheric radiocarbon concentrations', *Global and Planetary Change* **79**, pp. 226–233.

Azevedo, L.B., De Schryver, A.M., Hendriks, A.J., Huijbregts, M.A.J. (2015), 'Calcifying Species Sensitivity Distributions for Ocean Acidification', *Environmental Science & Technology* **49**, pp. 1495–1500.

Bakke, J., Lie, Ø., Heegaard, E., Dokken, T., Haug, G.H., Birks, H.H., Dulski, P., Nilsen, T. (2009), 'Rapid oceanic and atmospheric changes during the Younger Dryas cold period', *Nature Geoscience* **2**, pp. 202–205.

Bakker, A.M.R., Wong, T.E., Ruckert, K.L., Keller, K. (2017), 'Sea-level projections representing the deeply uncertain contribution of the West Antarctic ice sheet', *Scientific Reports* **7**, article 3880.

Balascio, N.L., Bradley, R.S. (2012), 'Evaluating Holocene climate change in northern Norway using sediment records from two contrasting lake systems', *Journal of Paleolimnology* **48**, pp. 259–273.

Barbara, L., Crosta, X., Leventer, A., Schmidt, S., Etourneau, J., Domack, E., Massé, G. (2016), 'Environmental responses of the Northeast Antarctic Peninsula to the Holocene climate variability', *Paleoceanography* **31**, pp. 131–147.

Barker, S., Cacho, I., Benway, H., Tachikawa, K. (2005), 'Planktonic foraminiferal Mg/Ca as a proxy for past oceanic temperatures: a methodological overview and data compilation for the Last Glacial Maximum', *Quaternary Science Reviews* **24**, pp. 821–834.

Bartels, M., Titschack, J., Fahl, K., Stein, R., Seidenkrantz, M.S., Hillaire-Marcel, C., Hebbeln, D. (2017), 'Atlantic Water advection vs. glacier dynamics in northern Spitsbergen since early deglaciation', *Climate of the Past* **13**, pp. 1717–1749.

Barton, B.I., Lenn, Y.-D., Lique, C. (2018), 'Observed Atlantification of the Barents Sea Causes the Polar Front to Limit the Expansion of Winter Sea Ice', *Journal of Physical Oceanography* **48**, pp. 1849–1866.

Bates, T.S., Carpenter, R. (1979), 'Determination of organosulfur compounds extracted from marine sediments', *Analytical Chemistry* **51**, pp. 551–554.

Bauch, H.A., Erlenkeuser, H., Spielhagen, R.F., Struck, U., Matthiessen, J., Thiede, J., Heinemeier, J. (2001), 'A multiproxy reconstruction of the evolution of deep and surface waters in the subarctic Nordic seas over the last 30,000yr', *Quaternary Science Reviews* **20**, pp. 659–678.

Becagli, S., Lazzara, L., Marchese, C., Dayan, U., Ascanius, S.E., Cacciani, M., Caiazzo, L., Di Biagio, C., Di Iorio, T., di Sarra, A., Eriksen, P., Fani, F., Giardi, F., Meloni, D., Muscari, G., Pace, G., Severi, M., Traversi, R., Udisti, R. (2016), 'Relationships linking primary production, sea ice melting, and biogenic aerosol in the Arctic', *Atmospheric Environment* **136**, pp. 1–15.

Bekryaev, R.V., Polyakov, I.V., Alexeev, V.A. (2010), 'Role of Polar Amplification in Long-Term Surface Air Temperature Variations and Modern Arctic Warming', *Journal of Climate* **23**, pp. 3888–3906.

Belt, S.T. (2018), 'Source-specific biomarkers as proxies for Arctic and Antarctic sea ice', *Organic Geochemistry* **125**, pp. 277–298.

Belt, S.T., Allard, W.G., Massé, G., Robert, J.-M., Rowland, S.J. (2000), 'Highly branched isoprenoids (HBIs): identification of the most common and abundant sedimentary isomers', *Geochimica et Cosmochimica Acta* **64**, pp. 3839–3851.

Belt, S.T., Brown, T.A., Ampel, L., Cabedo-Sanz, P., Fahl, K., Kocis, J.J., Massé, G., Navarro-Rodriguez, A., Ruan, J., Xu, Y. (2014), 'An inter-laboratory investigation of the Arctic sea ice biomarker proxy IP_{25} in marine sediments: key outcomes and recommendations', *Climate of the Past* **10**, pp. 155–166.

Belt, S.T., Brown, T.A., Ringrose, A.E., Cabedo-Sanz, P., Mundy, C.J., Gosselin, M., Poulin, M. (2013), 'Quantitative measurement of the sea ice diatom biomarker IP_{25} and sterols in Arctic sea ice and underlying sediments: Further considerations for palaeo sea ice reconstruction', *Organic Geochemistry* **62**, pp. 33–45.

Belt, S.T., Brown, T.A., Rodriguez, A.N., Sanz, P.C., Tonkin, A., Ingle, R. (2012a), 'A reproducible method for the extraction, identification and quantification of the Arctic sea ice proxy IP_{25} from marine sediments', *Analytical Methods* **4**, pp. 705–713.

Belt, S.T., Brown, T.A., Sanz, P.C., Rodriguez, A.N. (2012b), 'Structural confirmation of the sea ice biomarker IP_{25} found in Arctic marine sediments', *Environmental Chemistry Letters* **10**, pp. 189–192.

Belt, S.T., Brown, T.A., Smik, L., Assmy, P., Mundy, C.J. (2018), 'Sterol identification in floating Arctic sea ice algal aggregates and the Antarctic sea ice diatom *Berkeleya adeliensis*', *Organic Geochemistry* **118**, pp. 1–3.

Belt, S.T., Brown, T.A., Smik, L., Tatarek, A., Wiktor, J., Stowasser, G., Assmy, P., Allen, C.S., Husum, K. (2017), 'Identification of C_{25} highly branched isoprenoid (HBI) alkenes in diatoms of the genus *Rhizosolenia* in polar and sub-polar marine phytoplankton', *Organic Geochemistry* **110**, pp. 65–72.

Belt, S.T., Cabedo-Sanz, P. (2015), 'Characterisation and isomerisation of mono- and di-unsaturated highly branched isoprenoid (HBI) alkenes: Considerations for palaeoenvironment studies', *Organic Geochemistry* **87**, pp. 55–67.

Belt, S.T., Cabedo-Sanz, P., Smik, L., Navarro-Rodriguez, A., Berben, S.M.P., Knies, J., Husum, K. (2015), 'Identification of paleo Arctic winter sea ice limits and the marginal ice zone: Optimised biomarker-based reconstructions of late Quaternary Arctic sea ice', *Earth and Planetary Science Letters* **431**, pp. 127–139.

Belt, S.T., Cooke, D.A., Robert, J.-M., Rowland, S. (1996), 'Structural characterisation of widespread polyunsaturated isoprenoid biomarkers: A C_{25} triene, tetraene and pentaene from the diatom *Haslea ostrearia* simonsen', *Tetrahedron Letters* **37**, pp. 4755–4758.

Belt, S.T., Massé, G., Allard, W.G., Robert, J.-M., Rowland, S.J. (2001a), 'C_{25} highly branched isoprenoid alkenes in planktonic diatoms of the *Pleurosigma* genus', *Organic Geochemistry* **32**, pp. 1271–1275.

Belt, S.T., Massé, G., Allard, W.G., Robert, J.-M., Rowland, S.J. (2001b), 'Identification of a C_{25} highly branched isoprenoid triene in the freshwater diatom *Navicula sclesvicensis*', *Organic Geochemistry* **32**, pp. 1169–1172.

Belt, S.T., Massé, G., Rowland, S.J., Poulin, M., Michel, C., LeBlanc, B. (2007), 'A novel chemical fossil of palaeo sea ice: IP_{25}', *Organic Geochemistry* **38**, pp. 16–27.

Belt, S.T., Massé, G., Vare, L.L., Rowland, S.J., Poulin, M., Sicre, M.-A., Sampei, M., Fortier, L. (2008), 'Distinctive ^{13}C isotopic signature distinguishes a novel sea ice biomarker in Arctic sediments and sediment traps', *Marine Chemistry* **112**, pp. 158–167.

Belt, S.T., Müller, J. (2013), 'The Arctic sea ice biomarker IP_{25}: a review of current understanding, recommendations for future research and applications in palaeo sea ice reconstructions', *Quaternary Science Reviews* **79**, pp. 9–25.

Belt, S.T., Smik, L., Brown, T.A., Kim, J.H., Rowland, S.J., Allen, C.S., Gal, J.K., Shin, K.H., Lee, J.I., Taylor, K.W.R. (2016), 'Source identification and distribution reveals the potential of the geochemical Antarctic sea ice proxy $IPSO_{25}$', *Nature Communications* **7**, article 12655.

Bendle, J., Rosell-Melé, A. (2004), 'Distributions of U^{K}_{37} and $U^{K}_{37'}$ in the surface waters and sediments of the Nordic Seas: Implications for paleoceanography', *Geochemistry, Geophysics, Geosystems* **5**, article Q11013.

Benveniste, P. (2002), 'Sterol metabolism', *The Arabidopsis Book* **1**, article e0004.

Benway, H.M., McManus, J.F., Oppo, D.W., Cullen, J.L. (2010), 'Hydrographic changes in the eastern subpolar North Atlantic during the last deglaciation', *Quaternary Science Reviews* **29**, pp. 3336–3345.

Berben, S.M.P., Husum, K., Cabedo-Sanz, P., Belt, S.T. (2014), 'Holocene sub-centennial evolution of Atlantic water inflow and sea ice distribution in the western Barents Sea', *Climate of the Past* **10**, pp. 181–198.

Berben, S.M.P., Husum, K., Navarro-Rodriguez, A., Belt, S.T., Aagaard-Sørensen, S. (2017), 'Semi-quantitative reconstruction of early to late Holocene spring and summer sea ice conditions in the northern Barents Sea', *Journal of Quaternary Science* **32**, pp. 587–603.

Berger, A., Loutre, M.F. (1991), 'Insolation values for the climate of the last 10 million years', *Quaternary Science Reviews* **10**, pp. 297–317.

Berger, M., Brandefelt, J., Nilsson, J. (2013), 'The sensitivity of the Arctic sea ice to orbitally induced insolation changes: a study of the mid-Holocene Paleoclimate Modelling Intercomparison Project 2 and 3 simulations', *Climate of the Past* **9**, pp. 969–982.

Bhatt, U.S., Walker, D.A., Walsh, J.E., Carmack, E.C., Frey, K.E., Meier, W.N., Moore, S.E., Parmentier, F.-J.W., Post, E., Romanovsky, V.E., Simpson, W.R. (2014), 'Implications of Arctic Sea Ice Decline for the Earth System', *Annual Review of Environment and Resources* **39**, pp. 57–89.

Birgel, D., Hass, H.C. (2004), 'Oceanic and atmospheric variations during the last deglaciation in the Fram Strait (Arctic Ocean): a coupled high-resolution organic-geochemical and sedimentological study', *Quaternary Science Reviews* **23**, pp. 29–47.

Birk, J.J., Dippold, M., Wiesenberg, G.L.B., Glaser, B. (2012), 'Combined quantification of faecal sterols, stanols, stanones and bile acids in soils and terrestrial sediments by gas chromatography–mass spectrometry', *Journal of Chromatography A* **1242**, pp. 1–10.

Bjarnadóttir, L.R., Winsborrow, M.C.M., Andreassen, K. (2014), 'Deglaciation of the central Barents Sea', *Quaternary Science Reviews* **92**, pp. 208–226.

Bluhm, B.A., Gradinger, R. (2008), 'Regional variability in food availability for Arctic marine mammals', *Ecological Applications* **18**, pp. S77–S96.

Boetius, A., Albrecht, S., Bakker, K., Bienhold, C., Felden, J., Fernández-Méndez, M., Hendricks, S., Katlein, C., Lalande, C., Krumpen, T., Nicolaus, M., Peeken, I., Rabe, B., Rogacheva, A., Rybakova, E., Somavilla, R., Wenzhöfer, F. (2013), 'Export of Algal Biomass from the Melting Arctic Sea Ice', *Science* **339**, pp. 1430–1432.

Bogus, K., Harding, I.C., King, A., Charles, A.J., Zonneveld, K.A.F., Versteegh, G.J.M. (2012), 'The composition and diversity of dinosporin in species of the *Apectodinium* complex (Dinoflagellata)', *Review of Palaeobotany and Palynology* **183**, pp. 21–31.

Boitsov, S., Jensen, H.K.B., Klungsøyr, J. (2009), 'Natural background and anthropogenic inputs of polycyclic aromatic hydrocarbons (PAH) in sediments of South-Western Barents Sea', *Marine Environmental Research* **68**, pp. 236–245.

Bond, G.C., Lotti, R. (1995), 'Iceberg Discharges into the North Atlantic on Millennial Time Scales During the Last Glaciation', *Science* **267**, pp. 1005–1010.

Bondevik, S., Mangerud, J., Birks, H.H., Gulliksen, S., Reimer, P. (2006), 'Changes in North Atlantic Radiocarbon Reservoir Ages During the Allerød and Younger Dryas', *Science* **312**, pp. 1514–1517.

Boon, J.J., Rijpstra, W.I.C., De Lange, F., De Leeuw, J.W., Yoshioka, M., Shimizu, Y. (1979), 'Black Sea sterol — a molecular fossil for dinoflagellate blooms', *Nature* **277**, pp. 125–127.

Boon, J.J., van der Meer, F.W., Schuyl, P.J.W., de Leeuw, J.W., Schenk, P.A. (1978), 'Organic geochemical analyses of core samples from Site 362, Walvis Ridge, DSDP Leg 40', *Initial Reports of the Deep Sea Drilling Project* **40**, pp. 627–637.

Boulton, G.S. (1979), 'Glacial history of the Spitsbergen archipelago and the problem of a Barents Shelf ice sheet', *Boreas* **8**, pp. 31–57.

Boyer, T.P., Garcia, H.E., Locarnini, R.A., Zweng, M.M., Mishonov, A.V., Reagan, J.R., Antonov, J.I., Baranova, O.K., Biddle, M.M., Johnson, D.R., Paver, C.R. (2014), '2013 World Ocean Atlas Aids High-Resolution Climate Studies', *Eos, Transactions American Geophysical Union* **95**, pp. 369–370.

Bradley, R.S., England, J.H. (2008), 'The Younger Dryas and the Sea of Ancient Ice', *Quaternary Research* **70**, pp. 1–10.

Brassell, S.C., Dumitrescu, M. (2004), 'Recognition of alkenones in a lower Aptian porcellanite from the west-central Pacific', *Organic Geochemistry* **35**, pp. 181–188.

Brassell, S.C., Eglinton, G., Marlowe, I.T., Pflaumann, U., Sarnthein, M. (1986), 'Molecular stratigraphy: a new tool for climatic assessment', *Nature* **320**, pp. 129–133.

Breiman, L. (2001), 'Random Forests', *Machine Learning* **45**, pp. 5–32.

Breiman, L., Friedman, J., Stone, C.J., Olshen, R.A. (1984), *Classification and Regression Trees*. CRC Press, New York, USA.

Broecker, W., Bond, G., Klas, M., Clark, E., McManus, J. (1992), 'Origin of the northern Atlantic's Heinrich events', *Climate Dynamics* **6**, pp. 265–273.

Broecker, W.S. (1998), 'Paleocean circulation during the Last Deglaciation: A bipolar seesaw?', *Paleoceanography* **13**, pp. 119–121.

Broecker, W.S. (2006), 'Was the Younger Dryas Triggered by a Flood?', *Science* **312**, pp. 1146–1148.

Brown, T.A. (2011). *Productin and preservation of the Arctic sea ice diatom biomarker IP_{25}*. Ph.D. thesis, University of Plymouth, Plymouth, UK.

Brown, T.A. (2018), 'Stability of the lipid biomarker H-Print within preserved animals', *Polar Biology* **41**, pp. 1901–1905.

Brown, T.A., Alexander, C., Yurkowski, D.J., Ferguson, S.H., Belt, S.T. (2014a), 'Identifying variable sea ice carbon contributions to the Arctic ecosystem: A case study

using highly branched isoprenoid lipid biomarkers in Cumberland Sound ringed seals', *Limnology and Oceanography* **59**, pp. 1581–1589.

Brown, T.A., Assmy, P., Hop, H., Wold, A., Belt, S.T. (2017), 'Transfer of ice algae carbon to ice-associated amphipods in the high-Arctic pack ice environment', *Journal of Plankton Research* **39**, pp. 664–674.

Brown, T.A., Belt, S.T. (2012), 'Identification of the sea ice diatom biomarker IP_{25} in Arctic benthic macrofauna: direct evidence for a sea ice diatom diet in Arctic heterotrophs', *Polar Biology* **35**, pp. 131–137.

Brown, T.A., Belt, S.T. (2017), 'Biomarker-based H-Print quantifies the composition of mixed sympagic and pelagic algae consumed by *Artemia* sp', *Journal of Experimental Marine Biology and Ecology* **488**, pp. 32–37.

Brown, T.A., Belt, S.T., Cabedo-Sanz, P. (2014b), 'Identification of a novel di-unsaturated C_{25} highly branched isoprenoid in the marine tube-dwelling diatom *Berkeleya rutilans*', *Environmental Chemistry Letters* **12**, pp. 455–460.

Brown, T.A., Belt, S.T., Gosselin, M., Levasseur, M., Poulin, M., Mundy, C.J. (2016), 'Quantitative estimates of sinking sea ice particulate organic carbon based on the biomarker IP_{25}', *Marine Ecology Progress Series* **546**, pp. 17–29.

Brown, T.A., Belt, S.T., Philippe, B., Mundy, C.J., Massé, G., Poulin, M., Gosselin, M. (2011), 'Temporal and vertical variations of lipid biomarkers during a bottom ice diatom bloom in the Canadian Beaufort Sea: further evidence for the use of the IP_{25} biomarker as a proxy for spring Arctic sea ice', *Polar Biology* **34**, pp. 1857–1868.

Brown, T.A., Belt, S.T., Piepenburg, D. (2012), 'Evidence for a pan-Arctic sea-ice diatom diet in *Strongylocentrotus* spp', *Polar Biology* **35**, pp. 1281–1287.

Brown, T.A., Belt, S.T., Tatarek, A., Mundy, C.J. (2014c), 'Source identification of the Arctic sea ice proxy IP_{25}', *Nature Communications* **5**, article 4197.

Brown, T.A., Galicia, M.P., Thiemann, G.W., Belt, S.T., Yurkowski, D.J., Dyck, M.G. (2018), 'High contributions of sea ice derived carbon in polar bear (*Ursus maritimus*) tissue', *PLoS ONE* **13**, article e0191631.

Brown, T.A., Hegseth, E.N., Belt, S.T. (2015), 'A biomarker-based investigation of the mid-winter ecosystem in Rijpfjorden, Svalbard', *Polar Biology* **38**, pp. 37–50.

Brown, T.A., Yurkowski, D.J., Ferguson, S.H., Alexander, C., Belt, S.T. (2014d), 'H-Print: a new chemical fingerprinting approach for distinguishing primary production sources in Arctic ecosystems', *Environmental Chemistry Letters* **12**, pp. 387–392.

Buntine, W., Niblett, T. (1992), 'A Further Comparison of Splitting Rules for Decision-Tree Induction', *Machine Learning* **8**, pp. 75–85.

Cabedo-Sanz, P. (2013). *Identification of variability in sub-Arctic sea ice conditions during the Younger Dryas and Holocene*. Ph.D. thesis, University of Plymouth, Plymouth, UK.

Cabedo-Sanz, P., Belt, S.T. (2016), 'Seasonal sea ice variability in eastern Fram Strait over the last 2000 years', *Arktos* **2**, article 22.

Cabedo-Sanz, P., Belt, S.T., Knies, J., Husum, K. (2013), 'Identification of contrasting seasonal sea ice conditions during the Younger Dryas', *Quaternary Science Reviews* **79**, pp. 74–86.

Cavalieri, D.J., Parkinson, C.L., Gloersen, P., Zwally, H.J. (1996, updated yearly), *Sea ice concentrations from Nimbus-7 SMMR and DMSP SSM/I-SSMIS passive microwave data, version 1.1*. NASA DAAC at the National Snow and Ice Data Center, Boulder, Colorado, USA. doi: https://doi.org/10.5067/8GQ8LZQVL0VL (accessed 20.01.2019)

Cermeño, P., Marañón, E., Romero, O.E. (2012), 'Response of marine diatom communities to Late Quaternary abrupt climate changes', *Journal of Plankton Research* **35**, pp. 12–21.

Chauhan, T., Rasmussen, T.L., Noormets, R. (2016), 'Palaeoceanography of the Barents Sea continental margin, north of Nordaustlandet, Svalbard, during the last 74 ka', *Boreas* **45**, pp. 76–99.

Chauhan, T., Rasmussen, T.L., Noormets, R., Jakobsson, M., Hogan, K.A. (2014), 'Glacial history and paleoceanography of the southern Yermak Plateau since 132 ka BP', *Quaternary Science Reviews* **92**, pp. 155–169.

Clark, P.U., Dyke, A.S., Shakun, J.D., Carlson, A.E., Clark, J., Wohlfarth, B., Mitrovica, J.X., Hostetler, S.W., McCabe, A.M. (2009), 'The Last Glacial Maximum', *Science* **325**, pp. 710–714.

Clark, P.U., McCabe, A.M., Mix, A.C., Weaver, A.J. (2004), 'Rapid Rise of Sea Level 19,000 Years Ago and Its Global Implications', *Science* **304**, pp. 1141–1144.

Clotten, C., Stein, R., Fahl, K., De Schepper, S. (2018), 'Seasonal sea ice cover during the warm Pliocene: Evidence from the Iceland Sea (ODP Site 907)', *Earth and Planetary Science Letters* **481**, pp. 61–72.

Cochrane, S.K.J., Denisenko, S.G., Renaud, P.E., Emblow, C.S., Ambrose, W.G., Ellingsen, I.H., Skarðhamar, J. (2009), 'Benthic macrofauna and productivity regimes in the Barents Sea – Ecological implications in a changing Arctic', *Journal of Sea Research* **61**, pp. 222–233.

Cohen, J., Foster, J., Barlow, M., Saito, K., Jones, J. (2010), 'Winter 2009–2010: A case study of an extreme Arctic Oscillation event', *Geophysical Research Letters* **37**, article L17707.

Cohen, J.L., Furtado, J.C., Barlow, M.A., Alexeev, V.A., Cherry, J.E. (2012), 'Arctic warming, increasing snow cover and widespread wintertime boreal cooling', *Environmental Research Letters* **7**, article 014007.

Collins, L.G., Allen, C.S., Pike, J., Hodgson, D.A., Weckström, K., Massé, G. (2013), 'Evaluating highly branched isoprenoid (HBI) biomarkers as a novel Antarctic sea-ice proxy in deep ocean glacial age sediments', *Quaternary Science Reviews* **79**, pp. 87–98.

Colony, R., Thorndike, A.S. (1984), 'An estimate of the mean field of Arctic sea ice motion', *Journal of Geophysical Research: Oceans* **89**, pp. 10623–10629.

Combaut, G. (1986), 'GC-MS of Plant Sterol Analysis', in: Linskens, H.F., Jackson, J.F. (eds.), *Gas Chromatography/Mass Spectrometry*. Springer Berlin Heidelberg, Berlin, Heidelberg, pp. 121–133.

Comiso, J.C. (2012), 'Large Decadal Decline of the Arctic Multiyear Ice Cover', *Journal of Climate* **25**, pp. 1176–1193.

Condron, A., Winsor, P. (2012), 'Meltwater routing and the Younger Dryas', *Proceedings of the National Academy of Sciences* **109**, pp. 19928–19933.

Conte, M.H., Eglinton, G., Madureira, L.A.S. (1992), 'Long-chain alkenones and alkyl alkenoates as palaeotemperature indicators: their production, flux and early sedimentary diagenesis in the Eastern North Atlantic', *Organic Geochemistry* **19**, pp. 287–298.

Conte, M.H., Sicre, M.-A., Rühlemann, C., Weber, J.C., Schulte, S., Schulz-Bull, D., Blanz, T. (2006), 'Global temperature calibration of the alkenone unsaturation index ($U^{K'37}$) in surface waters and comparison with surface sediments', *Geochemistry, Geophysics, Geosystems* **7**, article Q02005.

Cormier, M.-A., Rochon, A., de Vernal, A., Gélinas, Y. (2016), 'Multi-proxy study of primary production and paleoceanographical conditions in northern Baffin Bay during the last centuries', *Marine Micropaleontology* **127**, pp. 1–10.

Cronin, T.M., Dwyer, G.S., Farmer, J., Bauch, H.A., Spielhagen, R.F., Jakobsson, M., Nilsson, J., Briggs Jr, W.M., Stepanova, A. (2012), 'Deep Arctic Ocean warming during the last glacial cycle', *Nature Geoscience* **5**, pp. 631–634.

Cronin, T.M., Gemery, L., Briggs, W.M., Jakobsson, M., Polyak, L., Brouwers, E.M. (2010), 'Quaternary Sea-ice history in the Arctic Ocean based on a new Ostracode sea-ice proxy', *Quaternary Science Reviews* **29**, pp. 3415–3429.

Cronin, T.M., Polyak, L.V., Reed, D., Kandiano, E.S., Marzen, R.E., Council, E.A. (2013), 'A 600-ka Arctic sea-ice record from Mendeleev Ridge based on ostracodes', *Quaternary Science Reviews* **79**, pp. 157–167.

Crosta, X., Koç, N. (2007), 'Chapter Eight Diatoms: From Micropaleontology to Isotope Geochemistry', in: Hillaire–Marcel, C., De Vernal, A. (eds.), *Developments in Marine Geology*. Elsevier, pp. 327–369.

D'Andrea, W.J., Huang, Y. (2005), 'Long chain alkenones in Greenland lake sediments: Low $\delta^{13}C$ values and exceptional abundance', *Organic Geochemistry* **36**, pp. 1234–1241.

Dalpadado, P., Arrigo, K.R., Hjøllo, S.S., Rey, F., Ingvaldsen, R.B., Sperfeld, E., van Dijken, G., Stige, L.C., Olsen, A., Ottersen, G. (2014), 'Productivity in the Barents Sea - Response to Recent Climate Variability', *PLoS ONE* **9**, article e95273.

Darby, D.A., Ortiz, J., Polyak, L., Lund, S., Jakobsson, M., Woodgate, R.A. (2009), 'The role of currents and sea ice in both slowly deposited central Arctic and rapidly deposited Chukchi–Alaskan margin sediments', *Global and Planetary Change* **68**, pp. 58–72.

de Leeuw, J.W., v.d. Meer, F.W., Rijpstra, W.I.C., Schenck, P.A. (1980), 'On the occurrence and structural identification of long chain unsaturated ketones and hydrocarbons in sediments', *Physics and Chemistry of the Earth* **12**, pp. 211–217.

de Vernal, A., Gersonde, R., Goosse, H., Seidenkrantz, M.-S., Wolff, E.W. (2013a), 'Sea ice in the paleoclimate system: the challenge of reconstructing sea ice from proxies – an introduction', *Quaternary Science Reviews* **79**, pp. 1–8.

de Vernal, A., Hillaire-Marcel, C., Rochon, A., Fréchette, B., Henry, M., Solignac, S., Bonnet, S. (2013b), 'Dinocyst-based reconstructions of sea ice cover concentration during the Holocene in the Arctic Ocean, the northern North Atlantic Ocean and its adjacent seas', *Quaternary Science Reviews* **79**, pp. 111–121.

de Vernal, A., Rochon, A. (2011), 'Dinocysts as tracers of sea-surface conditions and sea-ice cover in polar and subpolar environments', *IOP Conference Series: Earth and Environmental Science* **14**, article 012007.

Derocher, A.E., Andersen, M., Wiig, Ø., Aars, J., Hansen, E., Biuw, M. (2011), 'Sea ice and polar bear den ecology at Hopen Island, Svalbard', *Marine Ecology Progress Series* **441**, pp. 273–279.

Detlef, H., Belt, S.T., Sosdian, S.M., Smik, L., Lear, C.H., Hall, I.R., Cabedo-Sanz, P., Husum, K., Kender, S. (2018), 'Sea ice dynamics across the Mid-Pleistocene transition in the Bering Sea', *Nature Communications* **9**, article 941.

Dickson, B. (1999), 'All change in the Arctic', *Nature* **397**, pp. 389–391.

Divine, D.V., Dick, C. (2006), 'Historical variability of sea ice edge position in the Nordic Seas', *Journal of Geophysical Research: Oceans* **111**, article C01001.

Duplessy, J.C., Cortijo, E., Ivanova, E., Khusid, T., Labeyrie, L., Levitan, M., Murdmaa, I., Paterne, M. (2005), 'Paleoceanography of the Barents Sea during the Holocene', *Paleoceanography* **20**, article PA4004.

Duplessy, J.C., Ivanova, E., Murdmaa, I., Paterne, M., Labeyrie, L. (2001), 'Holocene paleoceanography of the northern Barents Sea and variations of the northward heat transport by the Atlantic Ocean', *Boreas* **30**, pp. 2–16.

Dvoretsky, V.G., Dvoretsky, A.G. (2014), 'Egg production rates of two common copepods in the Barents Sea in summer', *Polar Science* **8**, pp. 298–305.

Dylmer, C.V., Giraudeau, J., Eynaud, F., Husum, K., De Vernal, A. (2013), 'Northward advection of Atlantic water in the eastern Nordic Seas over the last 3000 yr', *Climate of the Past* **9**, pp. 1505–1518.

Ebbesen, H., Hald, M. (2004), 'Unstable Younger Dryas climate in the northeast North Atlantic', *Geology* **32**, pp. 673–676.

Ebbesen, H., Hald, M., Eplet, T.H. (2007), 'Lateglacial and early Holocene climatic oscillations on the western Svalbard margin, European Arctic', *Quaternary Science Reviews* **26**, pp. 1999–2011.

Eden, P. (2011), 'December 2010 Coldest December since 1890', *Weather* **66**, pp. i–iv.

Eglinton, T.I., Eglinton, G. (2008), 'Molecular proxies for paleoclimatology', *Earth and Planetary Science Letters* **275**, pp. 1–16.

Eilertsen, T.V. (2016). Reconstructions of paleoceanography and ice retreat based on benthic foraminifera, stable isotopes and sedimentological investigations from the northwestern Barents Sea south of Nordaustlandet, Svalbard. M.Sc. thesis, UiT The Arctic University of Norway, Tromsø, Norway.

Eisenman, I., Wettlaufer, J.S. (2009), 'Nonlinear threshold behavior during the loss of Arctic sea ice', *Proceedings of the National Academy of Sciences* **106**, pp. 28–32.

Eldevik, T., Risebrobakken, B., Bjune, A.E., Andersson, C., Birks, H.J.B., Dokken, T.M., Drange, H., Glessmer, M.S., Li, C., Nilsen, J.E.Ø., Otterå, O.H., Richter, K., Skagseth, Ø. (2014), 'A brief history of climate – the northern seas from the Last Glacial Maximum to global warming', *Quaternary Science Reviews* **106**, pp. 225–246.

Elverhøi, A., Fjeldskaar, W., Solheim, A., Nyland-Berg, M., Russwurm, L. (1993), 'The Barents Sea Ice Sheet — A model of its growth and decay during the last ice maximum', *Quaternary Science Reviews* **12**, pp. 863–873.

Eriksen, E., Skjoldal, H.R., Gjøsæter, H., Primicerio, R. (2017), 'Spatial and temporal changes in the Barents Sea pelagic compartment during the recent warming', *Progress in Oceanography* **151**, pp. 206–226.

Ezat, M.M., Rasmussen, T.L., Groeneveld, J. (2014), 'Persistent intermediate water warming during cold stadials in the southeastern Nordic seas during the past 65 k.y', *Geology* **42**, pp. 663–666.

Fahl, K., Stein, R. (2012), 'Modern seasonal variability and deglacial/Holocene change of central Arctic Ocean sea-ice cover: New insights from biomarker proxy records', *Earth and Planetary Science Letters* **351–352**, pp. 123–133.

Falk-Petersen, S., Hop, H., Budgell, W.P., Hegseth, E.N., Korsnes, R., Løyning, T.B., Børre Ørbæk, J., Kawamura, T., Shirasawa, K. (2000), 'Physical and ecological processes in the marginal ice zone of the northern Barents Sea during the summer melt period', *Journal of Marine Systems* **27**, pp. 131–159.

Falk-Petersen, S., Sargent, J.R., Henderson, J., Hegseth, E.N., Hop, H., Okolodkov, Y.B. (1998), 'Lipids and fatty acids in ice algae and phytoplankton from the Marginal Ice Zone in the Barents Sea', *Polar Biology* **20**, pp. 41–47.

Fetterer, F., Knowles, K., Meier, W., Savoie, M., Windnagel, A.K. (2017, updated daily), *Sea Ice Index, Version 3*. NSIDC: National Snow and Ice Data Center, Boulder, Colorado, USA. doi: https://doi.org/10.7265/N5K072F8 (accessed 09.02.2018).

Fetterer, F., Savoie, M., Helfrich, S., Clemente-Colón (2010, updated daily), *Multisensor Analyzed Sea Ice Extent - Northern Hemisphere (MASIE-NH), Version 1*. NSIDC: National Snow and Ice Data Center, Boulder, Colorado, USA. doi: https://doi.org/10.7265/N5GT5K3K (accessed 11.01.2018).

Fisher, T.G., Smith, D.G., Andrews, J.T. (2002), 'Preboreal oscillation caused by a glacial Lake Agassiz flood', *Quaternary Science Reviews* **21**, pp. 873–878.

Fragoso, G.M., Poulton, A.J., Yashayaev, I.M., Head, E.J.H., Johnsen, G., Purdie, D.A. (2018), 'Diatom Biogeography From the Labrador Sea Revealed Through a Trait-Based Approach', *Frontiers in Marine Science* **5**, doi: https://doi.org/10.3389/fmars.2018.00297.

Francis, J.A., Hunter, E. (2006), 'New insight into the disappearing Arctic sea ice', *Eos, Transactions American Geophysical Union* **87**, pp. 509–511.

Francis, J.A., Vavrus, S.J. (2012), 'Evidence linking Arctic amplification to extreme weather in mid-latitudes', *Geophysical Research Letters* **39**, article L06801.

Freeman, K.H., Wakeham, S.G. (1992), 'Variations in the distributions and isotopic composition of alkenones in Black Sea particles and sediments', *Organic Geochemistry* **19**, pp. 277–285.

Gammelsrød, T., Leikvin, Ø., Lien, V., Budgell, W.P., Loeng, H., Maslowski, W. (2009), 'Mass and heat transports in the NE Barents Sea: Observations and models', *Journal of Marine Systems* **75**, pp. 56–69.

Gearing, P., Gearing, J.N., Lytle, T.F., Lytle, J.S. (1976), 'Hydrocarbons in 60 northeast Gulf of Mexico shelf sediments: a preliminary survey', *Geochimica et Cosmochimica Acta* **40**, pp. 1005–1017.

Gemery, L., Cronin, T.M., Briggs, W.M., Brouwers, E.M., Schornikov, E.I., Stepanova, A., Wood, A.M., Yasuhara, M. (2017), 'An Arctic and Subarctic ostracode database: biogeographic and paleoceanographic applications', *Hydrobiologia* **786**, pp. 59–95.

Gemmell, B.J., Oh, G., Buskey, E.J., Villareal, T.A. (2016), 'Dynamic sinking behaviour in marine phytoplankton: rapid changes in buoyancy may aid in nutrient uptake', *Proceedings of the Royal Society B: Biological Sciences* **283**, article 20161126.

Gherardi, J.-M., Labeyrie, L., Nave, S., Francois, R., McManus, J.F., Cortijo, E. (2009), 'Glacial-interglacial circulation changes inferred from $^{231}Pa/^{230}Th$ sedimentary record in the North Atlantic region', *Paleoceanography* **24**, article PA2204.

Gibert, K., Sànchez–Marrè, M., Izquierdo, J. (2016), 'A survey on pre-processing techniques: Relevant issues in the context of environmental data mining', *AI Communications* **29**, pp. 627–663.

Gildor, H., Ashkenazy, Y., Tziperman, E., Lev, I. (2014), 'The role of sea ice in the temperature-precipitation feedback of glacial cycles', *Climate Dynamics* **43**, pp. 1001–1010.

Gosselin, M., Levasseur, M., Wheeler, P.A., Horner, R.A., Booth, B.C. (1997), 'New measurements of phytoplankton and ice algal production in the Arctic Ocean', *Deep Sea Research Part II: Topical Studies in Oceanography* **44**, pp. 1623–1644.

Grobe, H. (1987), 'A simple method for the determination of Ice-Rafted Debris in sediment cores', *Polarforschung* **57**, pp. 123–126.

Grömping, U. (2009), 'Variable Importance Assessment in Regression: Linear Regression versus Random Forest', *The American Statistician* **63**, pp. 308–319.

Groot, D.E., Aagaard-Sørensen, S., Husum, K. (2014), 'Reconstruction of Atlantic water variability during the Holocene in the western Barents Sea', *Climate of the Past* **10**, pp. 51–62.

Grossi, V., Beker, B., Geenevasen, J.A.J., Schouten, S., Raphel, D., Fontaine, M.-F., Sinninghe Damsté, J.S. (2004), 'C_{25} highly branched isoprenoid alkenes from the marine benthic diatom *Pleurosigma strigosum*', *Phytochemistry* **65**, pp. 3049–3055.

Hald, M., Andersson, C., Ebbesen, H., Jansen, E., Klitgaard-Kristensen, D., Risebrobakken, B., Salomonsen, G.R., Sarnthein, M., Sejrup, H.P., Telford, R.J. (2007), 'Variations in temperature and extent of Atlantic Water in the northern North Atlantic during the Holocene', *Quaternary Science Reviews* **26**, pp. 3423–3440.

Hald, M., Ebbesen, H., Forwick, M., Godtliebsen, F., Khomenko, L., Korsun, S., Ringstad Olsen, L., Vorren, T.O. (2004), 'Holocene paleoceanography and glacial history of the West Spitsbergen area, Euro-Arctic margin', *Quaternary Science Reviews* **23**, pp. 2075–2088.

Hald, M., Hagen, S. (1998), 'Early Preboreal cooling in the Nordic seas region triggered by meltwater', *Geology* **26**, pp. 615–618.

Hald, M., Korsun, S. (2008), 'The 8200 cal. yr BP event reflected in the Arctic fjord, Van Mijenfjorden, Svalbard', *The Holocene* **18**, pp. 981–990.

Hamm, C., Reigstad, M., Riser, C.W., Mühlebach, A., Wassmann, P. (2001), 'On the trophic fate of *Phaeocystis pouchetii*. VII. Sterols and fatty acids reveal sedimentation of *P. pouchetii*-derived organic matter via krill fecal strings', *Marine Ecology Progress Series* **209**, pp. 55–69.

Hansen, E., Gerland, S., Granskog, M.A., Pavlova, O., Renner, A.H.H., Haapala, J., Løyning, T.B., Tschudi, M. (2013), 'Thinning of Arctic sea ice observed in Fram Strait: 1990–2011', *Journal of Geophysical Research: Oceans* **118**, pp. 5202–5221.

Hansen, J., Ruedy, R., Sato, M., Lo, K. (2010), 'Global Surface Temperature Change', *Reviews of Geophysics* **48**, article RG4004.

Harada, N. (2016), 'Review: Potential catastrophic reduction of sea ice in the western Arctic Ocean: Its impact on biogeochemical cycles and marine ecosystems', *Global and Planetary Change* **136**, pp. 1–17.

Hassett, R.P. (2004), 'Supplementation of a diatom diet with cholesterol can enhance copepod egg-production rates', *Limnology and Oceanography* **49**, pp. 488–494.

Hassett, R.P., Crockett, E.L. (2009), 'Habitat temperature is an important determinant of cholesterol contents in copepods', *Journal of Experimental Biology* **212**, pp. 71–77.

Hastie, T., Tibshirani, R., Friedman, J. (2009), 'Additive Models, Trees, and Related Methods', *The Elements of Statistical Learning: Data Mining, Inference, and Prediction*. Springer New York, New York, NY, pp. 295–336.

Hastings, D.W., Russell, A.D., Emerson, S.R. (1998), 'Foraminiferal magnesium in *Globeriginoides sacculifer* as a paleotemperature proxy', *Paleoceanography* **13**, pp. 161–169.

He, D., Simoneit, B.R.T., Xu, Y., Jaffé, R. (2016), 'Occurrence of unsaturated C_{25} highly branched isoprenoids (HBIs) in a freshwater wetland', *Organic Geochemistry* **93**, pp. 59–67.

Hebbeln, D. (2000), 'Flux of ice-rafted detritus from sea ice in the Fram Strait', *Deep Sea Research Part II: Topical Studies in Oceanography* **47**, pp. 1773–1790.

Hegseth, E.N., Sundfjord, A. (2008), 'Intrusion and blooming of Atlantic phytoplankton species in the high Arctic', *Journal of Marine Systems* **74**, pp. 108–119.

Heinrich, H. (1988), 'Origin and consequences of cyclic ice rafting in the Northeast Atlantic Ocean during the past 130,000 years', *Quaternary Research* **29**, pp. 142–152.

Hemming, S.R. (2004), 'Heinrich events: Massive late Pleistocene detritus layers of the North Atlantic and their global climate imprint', *Reviews of Geophysics* **42**, article RG1005.

Henderson, R.J., Hegseth, E.N., Park, M.T. (1998), 'Seasonal variation in lipid and fatty acid composition of ice algae from the Barents Sea', *Polar Biology* **20**, pp. 48–55.

Hertzberg, J.E., Schmidt, M.W., Bianchi, T.S., Smith, R.W., Shields, M.R., Marcantonio, F. (2016), 'Comparison of eastern tropical Pacific TEX_{86} and *Globigerinoides ruber* Mg/Ca derived sea surface temperatures: Insights from the Holocene and Last Glacial Maximum', *Earth and Planetary Science Letters* **434**, pp. 320–332.

Ho, S.L., Laepple, T. (2016), 'Flat meridional temperature gradient in the early Eocene in the subsurface rather than surface ocean', *Nature Geoscience* **9**, pp. 606–610.

Hodal, H., Kristiansen, S. (2008), 'The importance of small-celled phytoplankton in spring blooms at the marginal ice zone in the northern Barents Sea', *Deep Sea Research Part II: Topical Studies in Oceanography* **55**, pp. 2176–2185.

Hoff, U., Rasmussen, T.L., Stein, R., Ezat, M.M., Fahl, K. (2016), 'Sea ice and millennial-scale climate variability in the Nordic seas 90 kyr ago to present', *Nature Communications* **7**, article 12247.

Hogan, K.A., Dowdeswell, J.A., Hillenbrand, C.-D., Ehrmann, W., Noormets, R., Wacker, L. (2017), 'Subglacial sediment pathways and deglacial chronology of the northern Barents Sea Ice Sheet', *Boreas* **46**, pp. 750–771.

Hogan, K.A., Dowdeswell, J.A., Noormets, R., Evans, J., Ó Cofaigh, C., Jakobsson, M. (2010), 'Submarine landforms and ice-sheet flow in the Kvitøya Trough, northwestern Barents Sea', *Quaternary Science Reviews* **29**, pp. 3545–3562.

Hopkins, J., Henson, S.A., Painter, S.C., Tyrrell, T., Poulton, A.J. (2015), 'Phenological characteristics of global coccolithophore blooms', *Global Biogeochemical Cycles* **29**, pp. 239–253.

Hopkinson, B.M., Dupont, C.L., Allen, A.E., Morel, F.M.M. (2011), 'Efficiency of the CO_2-concentrating mechanism of diatoms', *Proceedings of the National Academy of Sciences* **108**, pp. 3830–3837.

Hoppe, C.J.M., Flintrop, C.M., Rost, B. (2018), 'The Arctic picoeukaryote *Micromonas pusilla* benefits synergistically from warming and ocean acidification', *Biogeosciences* **15**, pp. 4353–4365.

Hormes, A., Gjermundsen, E.F., Rasmussen, T.L. (2013), 'From mountain top to the deep sea – Deglaciation in 4D of the northwestern Barents Sea ice sheet', *Quaternary Science Reviews* **75**, pp. 78–99.

Hörner, T., Stein, R., Fahl, K. (2017), 'Evidence for Holocene centennial variability in sea ice cover based on IP_{25} biomarker reconstruction in the southern Kara Sea (Arctic Ocean)', *Geo-Marine Letters* **37**, pp. 515–526.

Hörner, T., Stein, R., Fahl, K., Birgel, D. (2016), 'Post-glacial variability of sea ice cover, river run-off and biological production in the western Laptev Sea (Arctic Ocean) – A high-resolution biomarker study', *Quaternary Science Reviews* **143**, pp. 133–149.

Howe, J.A., Harland, R., Cottier, F.R., Brand, T., Willis, K.J., Berge, J., Grosfjeld, K., Eriksson, A. (2010), 'Dinoflagellate cysts as proxies for palaeoceanographic conditions in Arctic fjords', *Fjord Systems and Archives* **344**, pp. 61–74.

Huang, W.Y., Meinschein, W.G. (1976), 'Sterols as source indicators of organic materials in sediments', *Geochimica et Cosmochimica Acta* **40**, pp. 323–330.

Hudson, E.D., Parrish, C.C., Helleur, R.J. (2001), 'Biogeochemistry of sterols in plankton, settling particles and recent sediments in a cold ocean ecosystem (Trinity Bay, Newfoundland)', *Marine Chemistry* **76**, pp. 253–270.

Hughes, A.L.C., Gyllencreutz, R., Lohne, Ø.S., Mangerud, J., Svendsen, J.I. (2016), 'The last Eurasian ice sheets – a chronological database and time-slice reconstruction, DATED-1', *Boreas* **45**, pp. 1–45.

Huguet, C., Kim, J.-H., Sinninghe Damsté, J.S., Schouten, S. (2006), 'Reconstruction of sea surface temperature variations in the Arabian Sea over the last 23 kyr using organic proxies (TEX_{86} and $U^{K'37}$)', *Paleoceanography* **21**, article PA3003.

Hulbe, C. (2017), 'Is ice sheet collapse in West Antarctica unstoppable?', *Science* **356**, pp. 910–911.

Husum, K., Hald, M. (2002), 'Early Holocene cooling events in Malangenfjord and the adjoining shelf, north-east Norwegian Sea', *Polar Research* **21**, pp. 267–274.

Ingvaldsen, R.B., Asplin, L., Loeng, H. (2004), 'Velocity field of the western entrance to the Barents Sea', *Journal of Geophysical Research: Oceans* **109**, article C03021.

Ishwaran, H., Lu, M. (2017), 'Standard errors and confidence intervals for variable importance in random forest regression, classification, and survival', *Statistics in Medicine* **2018**, pp. 1–25.

Ivanov, V.V., Alexeev, V.A., Repina, I., Koldunov, N.V., Smirnov, A. (2012), 'Tracing Atlantic Water Signature in the Arctic Sea Ice Cover East of Svalbard', *Advances in Meteorology* **2012**, article 201818.

J. Wraige, E., T. Belt, S., A. Lewis, C., A. Cooke, D., Robert, J.M., Massé, G., Rowland, S.J. (1997), 'Variations in structures and distributions of C_{25} highly branched

isoprenoid (HBI) alkenes in cultures of the diatom, *Haslea ostrearia* (Simonsen)', *Organic Geochemistry* **27**, pp. 497–505.

Jakobsson, M., Andreassen, K., Bjarnadóttir, L.R., Dove, D., Dowdeswell, J.A., England, J.H., Funder, S., Hogan, K., Ingólfsson, Ó., Jennings, A., Krog Larsen, N., Kirchner, N., Landvik, J.Y., Mayer, L., Mikkelsen, N., Möller, P., Niessen, F., Nilsson, J., O'Regan, M., Polyak, L., Nørgaard-Pedersen, N., Stein, R. (2014), 'Arctic Ocean glacial history', *Quaternary Science Reviews* **92**, pp. 40–67.

James, N.A., Matteson, D.S. (2013), 'ecp: An R Package for Nonparametric Multiple Change Point Analysis of Multivariate Data', *Journal of Statistical Software* **62**, pp. 1–25.

Janout, M.A., Hölemann, J., Waite, A.M., Krumpen, T., von Appen, W.-J., Martynov, F. (2016), 'Sea-ice retreat controls timing of summer plankton blooms in the Eastern Arctic Ocean', *Geophysical Research Letters* **43**, pp. 12,493–412,501.

Jansen, E., Andersson, C., Moros, M., Nisancioglu, K.H., Nyland, B.F., Telford, R. (2009), 'The Early to Mid-Holocene Thermal Optimum in the North Atlantic', in: Battarbee, R.W., Binney, H.A. (eds.), *Natural Climate Variability and Global Warming*, doi: https://doi.org/10.1002/9781444300932.ch5.

Jenkyns, H.C., Schouten-Huibers, L., Schouten, S., Sinninghe-Damsté, J.S. (2012), 'Warm Middle Jurassic–Early Cretaceous high-latitude sea-surface temperatures from the Southern Ocean', *Climate of the Past* **8**, pp. 215–226.

Jennings, A.E., Andrews, J.T., Ó Cofaigh, C., Onge, G.S., Sheldon, C., Belt, S.T., Cabedo-Sanz, P., Hillaire-Marcel, C. (2017), 'Ocean forcing of Ice Sheet retreat in central west Greenland from LGM to the early Holocene', *Earth and Planetary Science Letters* **472**, pp. 1–13.

Jennings, A.E., Andrews, J.T., Ó Cofaigh, C., St-Onge, G., Belt, S., Cabedo-Sanz, P., Pearce, C., Hillaire-Marcel, C., Calvin Campbell, D. (2018), 'Baffin Bay paleoenvironments in the LGM and HS1: Resolving the ice-shelf question', *Marine Geology* **402**, pp. 5–16.

Jensen, S., Renberg, L., Reutergardh, L. (1977), 'Residue analysis of sediment and sewage sludge for organochlorines in the presence of elemental sulfur', *Analytical Chemistry* **49**, pp. 316–318.

Jessen, S.P., Rasmussen, T.L., Nielsen, T., Solheim, A. (2010), 'A new Late Weichselian and Holocene marine chronology for the western Svalbard slope 30,000–0 cal years BP', *Quaternary Science Reviews* **29**, pp. 1301–1312.

Ji, R., Stegert, C., Davis, C.S. (2012), 'Sensitivity of copepod populations to bottom-up and top-down forcing: a modeling study in the Gulf of Maine region', *Journal of Plankton Research* **35**, pp. 66–79.

Johannesen, E., Ingvaldsen, R.B., Bogstad, B., Dalpadado, P., Eriksen, E., Gjøsæter, H., Knutsen, T., Skern-Mauritzen, M., Stiansen, J.E. (2012), 'Changes in Barents Sea ecosystem state, 1970–2009: climate fluctuations, human impact, and trophic interactions', *ICES Journal of Marine Science* **69**, pp. 880–889.

Johannessen, O.M., Bengtsson, L., Miles, M.W., Kuzmina, S.I., Semenov, V.A., Alekseev, G.V., Nagurnyi, A.P., Zakharov, V.F., Bobylev, L.P., Pettersson, L.H., Hasselmann, K., Cattle, H.P. (2004), 'Arctic climate change: observed and modelled temperature and sea-ice variability', *Tellus A* **56**, pp. 328–341.

Johns, L., Wraige, E.J., Belt, S.T., Lewis, C.A., Massé, G., Robert, J.M., Rowland, S.J. (1999), 'Identification of a C_{25} highly branched isoprenoid (HBI) diene in Antarctic sediments, Antarctic sea-ice diatoms and cultured diatoms', *Organic Geochemistry* **30**, pp. 1471–1475.

Jonas, A.S., Schwark, L., Bauersachs, T. (2017), 'Late Quaternary water temperature variations of the Northwest Pacific based on the lipid paleothermometers TEX^{H86}, $U^{K'37}$ and LDI', *Deep Sea Research Part I: Oceanographic Research Papers* **125**, pp. 81–93.

Junttila, J., Aagaard-Sørensen, S., Husum, K., Hald, M. (2010), 'Late Glacial–Holocene clay minerals elucidating glacial history in the SW Barents Sea', *Marine Geology* **276**, pp. 71–85.

Justwan, A., Koç, N. (2008), 'A diatom based transfer function for reconstructing sea ice concentrations in the North Atlantic', *Marine Micropaleontology* **66**, pp. 264–278.

Kahru, M., Lee, Z., Mitchell, B.G., Nevison, C.D. (2016), 'Effects of sea ice cover on satellite-detected primary production in the Arctic Ocean', *Biology letters* **12**, article 20160223.

Kaiser, J., Belt, S.T., Tomczak, M., Brown, T.A., Wasmund, N., Arz, H.W. (2016), 'C_{25} highly branched isoprenoid alkenes in the Baltic Sea produced by the marine planktonic diatom *Pseudosolenia calcar-avis*', *Organic Geochemistry* **93**, pp. 51–58.

Kaltin, S., Anderson, L.G., Olsson, K., Fransson, A., Chierici, M. (2002), 'Uptake of atmospheric carbon dioxide in the Barents Sea', *Journal of Marine Systems* **38**, pp. 31–45.

Karner, M.B., DeLong, E.F., Karl, D.M. (2001), 'Archaeal dominance in the mesopelagic zone of the Pacific Ocean', *Nature* **409**, pp. 507–510.

Kay, J.E., Holland, M.M., Jahn, A. (2011), 'Inter-annual to multi-decadal Arctic sea ice extent trends in a warming world', *Geophysical Research Letters* **38**, article L15708.

Kemp, A.E.S., Villareal, T.A. (2018), 'The case of the diatoms and the muddled mandalas: Time to recognize diatom adaptations to stratified waters', *Progress in Oceanography* **167**, pp. 138–149.

Kerr, R.A. (2007), 'Is Battered Arctic Sea Ice Down For the Count?', *Science* **318**, pp. 33–34.

Kim, J.-H., Crosta, X., Willmott, V., Renssen, H., Bonnin, J., Helmke, P., Schouten, S., Sinninghe Damsté, J.S. (2012), 'Holocene subsurface temperature variability in the eastern Antarctic continental margin', *Geophysical Research Letters* **39**, article L06705.

Kim, J.-H., Schouten, S., Hopmans, E.C., Donner, B., Sinninghe Damsté, J.S. (2008), 'Global sediment core-top calibration of the TEX_{86} paleothermometer in the ocean', *Geochimica et Cosmochimica Acta* **72**, pp. 1154–1173.

Kim, J.-H., van der Meer, J., Schouten, S., Helmke, P., Willmott, V., Sangiorgi, F., Koç, N., Hopmans, E.C., Damsté, J.S.S. (2010), 'New indices and calibrations derived from the distribution of crenarchaeal isoprenoid tetraether lipids: Implications for past sea surface temperature reconstructions', *Geochimica et Cosmochimica Acta* **74**, pp. 4639–4654.

Kinnard, C., Zdanowicz, C.M., Fisher, D.A., Isaksson, E., de Vernal, A., Thompson, L.G. (2011), 'Reconstructed changes in Arctic sea ice over the past 1,450 years', *Nature* **479**, pp. 509–512.

Klitgaard-Kristensen, D., Rasmussen, T.L., Koç, N. (2013), 'Palaeoceanographic changes in the northern Barents Sea during the last 16 000 years – new constraints on the last deglaciation of the Svalbard–Barents Sea Ice Sheet', *Boreas* **42**, pp. 798–813.

Knies, J. (2005), 'Climate-induced changes in sedimentary regimes for organic matter supply on the continental shelf off northern Norway', *Geochimica et Cosmochimica Acta* **69**, pp. 4631–4647.

Knies, J., Brookes, S., Schubert, C.J. (2007), 'Re-assessing the nitrogen signal in continental margin sediments: New insights from the high northern latitudes', *Earth and Planetary Science Letters* **253**, pp. 471–484.

Knies, J., Hald, M., Ebbesen, H., Mann, U., Vogt, C. (2003), 'A deglacial–middle Holocene record of biogenic sedimentation and paleoproductivity changes from the northern Norwegian continental shelf', *Paleoceanography* **18**, article 1096.

Knies, J., Jensen, H.K.B., Finne, T.E., Lepland, A., Saether, O.M. (2006), *Sediment composition and heavy metal distribution in Barents Sea surface samples: results from Institute of Marine Research 2003 and 2004 cruises.* NGU rapport 2006.067, Trondheim, Norway.

Knies, J., Kleiber, H.-P., Matthiessen, J., Müller, C., Nowaczyk, N. (2001), 'Marine ice-rafted debris records constrain maximum extent of Saalian and Weichselian ice-sheets along the northern Eurasian margin', *Global and Planetary Change* **31**, pp. 45–64.

Knies, J., Köseoğlu, D., Rise, L., Baeten, N., Bellec, V.K., Bøe, R., Klug, M., Panieri, G., Jernas, P.E., Belt, S.T. (2018), 'Nordic Seas polynyas and their role in preconditioning marine productivity during the Last Glacial Maximum', *Nature Communications* **9**, article 3959.

Knies, J., Martinez, P. (2009), 'Organic matter sedimentation in the western Barents Sea region: terrestrial and marine contribution based on isotopic composition and organic nitrogen content', *Norwegian Journal of Geology* **89**, pp. 79–89.

Knies, J., Nowaczyk, N., Müller, C., Vogt, C., Stein, R. (2000), 'A multiproxy approach to reconstruct the environmental changes along the Eurasian continental margin over the last 150, 000 years', *Marine Geology* **163**, pp. 317–344.

Knies, J., Pathirana, I., Cabedo-Sanz, P., Banica, A., Fabian, K., Rasmussen, T.L., Forwick, M., Belt, S.T. (2016), 'Sea-ice dynamics in an Arctic coastal polynya during the past 6500 years', *Arktos* **3**, article 1.

Knies, J., Stein, R. (1998), 'New aspects of organic carbon deposition and its paleoceanographic implications along the northern Barents Sea margin during the last 30,000 years', *Paleoceanography* **13**, pp. 384–394.

Knies, J., Vogt, C., Stein, R. (1998), 'Late Quaternary growth and decay of the Svalbard/Barents Sea ice sheet and paleoceanographic evolution in the adjacent Arctic Ocean', *Geo-Marine Letters* **18**, pp. 195–202.

Koç, N., Klitgaard-Kristensen, D., Hasle, K., Forsberg, C.F., Solheim, A. (2002), 'Late glacial palaeoceanography of Hinlopen Strait, northern Svalbard', *Polar Research* **21**, pp. 307–314.

Koç-Karpuz, N., Schrader, H. (1990), 'Surface sediment diatom distribution and Holocene paleotemperature variations in the Greenland, Iceland and Norwegian Sea', *Paleoceanography* **5**, pp. 557–580.

Kohlbach, D., Graeve, M., A. Lange, B., David, C., Peeken, I., Flores, H. (2016), 'The importance of ice algae-produced carbon in the central Arctic Ocean ecosystem: Food web relationships revealed by lipid and stable isotope analyses', *Limnology and Oceanography* **61**, pp. 2027–2044.

Köseoğlu, D., Belt, S.T., Husum, K., Knies, J. (2018a), 'An assessment of biomarker-based multivariate classification methods versus the PIP_{25} index for paleo Arctic sea ice reconstruction', *Organic Geochemistry* **125**, pp. 82–94.

Köseoğlu, D., Belt, S.T., Smik, L., Yao, H., Panieri, G., Knies, J. (2018b), 'Complementary biomarker-based methods for characterising Arctic sea ice conditions: A case study comparison between multivariate analysis and the PIP_{25} index', *Geochimica et Cosmochimica Acta* **222**, pp. 406–420.

Kovacs, K.M., Lydersen, C., Overland, J.E., Moore, S.E. (2011), 'Impacts of changing sea-ice conditions on Arctic marine mammals', *Marine Biodiversity* **41**, pp. 181–194.

Krembs, C., Eicken, H., Deming, J.W. (2011), 'Exopolymer alteration of physical properties of sea ice and implications for ice habitability and biogeochemistry in a warmer Arctic', *Proceedings of the National Academy of Sciences* **108**, pp. 3653–3658.

Kremer, A., Stein, R., Fahl, K., Bauch, H., Mackensen, A., Niessen, F. (2018a), 'A 190-ka biomarker record revealing interactions between sea ice, Atlantic Water inflow and ice sheet activity in eastern Fram Strait', *Arktos* **4**, article 22.

Kremer, A., Stein, R., Fahl, K., Ji, Z., Yang, Z., Wiers, S., Matthiessen, J., Forwick, M., Löwemark, L., O'Regan, M., Chen, J., Snowball, I. (2018b), 'Changes in sea ice cover and ice sheet extent at the Yermak Plateau during the last 160 ka – Reconstructions from biomarker records', *Quaternary Science Reviews* **182**, pp. 93–108.

Krumpen, T., Gerdes, R., Haas, C., Hendricks, S., Herber, A., Selyuzhenok, V., Smedsrud, L.H., Spreen, G. (2016), 'Recent summer sea ice thickness surveys in Fram Strait and associated ice volume fluxes', *The Cryosphere* **10**, pp. 523–534.

Kucera, M. (2007), 'Chapter Six Planktonic Foraminifera as Tracers of Past Oceanic Environments', in: Hillaire–Marcel, C., De Vernal, A. (eds.), *Developments in Marine Geology*. Elsevier, pp. 213–262.

Kucera, M., Weinelt, M., Kiefer, T., Pflaumann, U., Hayes, A., Weinelt, M., Chen, M.-T., Mix, A.C., Barrows, T.T., Cortijo, E., Duprat, J., Juggins, S., Waelbroeck, C. (2005), 'Reconstruction of sea-surface temperatures from assemblages of planktonic foraminifera: multi-technique approach based on geographically constrained calibration data sets and its application to glacial Atlantic and Pacific Oceans', *Quaternary Science Reviews* **24**, pp. 951–998.

Kuhn, M., Wing, J., Weston, S., Williams, A., Keefer, C., Engelhardt, A., Cooper, T., Mayer, Z., Kenkel, B., Benesty, M., Lescarbeau, R., Ziem, A., Scrucca, L., Tang, Y., Candan, C., Hunt, T. (2016), *Caret: Classification and Regression Training*, ver. 6.0-73, url: https://cran.r-project.org/package=caret (accessed 07.05.2018).

Kumar, A., Perlwitz, J., Eischeid, J., Quan, X., Xu, T., Zhang, T., Hoerling, M., Jha, B., Wang, W. (2010), 'Contribution of sea ice loss to Arctic amplification', *Geophysical Research Letters* **37**, article L21701.

Kvile, K.Ø., Langangen, Ø., Prokopchuk, I., Stenseth, N.C., Stige, L.C. (2016), 'Disentangling the mechanisms behind climate effects on zooplankton', *Proceedings of the National Academy of Sciences* **113**, pp. 1841–1846.

Kwok, R., Cunningham, G.F. (2015), 'Variability of Arctic sea ice thickness and volume from CryoSat-2', *Philosophical Transactions of the Royal Society A: Mathematical, Physical and Engineering Sciences* **373**, article 20140157.

Kwok, R., Maslowski, W., Laxon, S.W. (2005), 'On large outflows of Arctic sea ice into the Barents Sea', *Geophysical Research Letters* **32**, article L22503.

Kwok, R., Rothrock, D.A. (2009), 'Decline in Arctic sea ice thickness from submarine and ICESat records: 1958–2008', *Geophysical Research Letters* **36**, article L15501.

Kwok, R., Spreen, G., Pang, S. (2013), 'Arctic sea ice circulation and drift speed: Decadal trends and ocean currents', *Journal of Geophysical Research: Oceans* **118**, pp. 2408–2425.

Kwok, R., Untersteiner, N. (2011), 'The thinning of Arctic sea ice', *Physics Today* **64**, pp. 36–41.

Łącka, M., Zajączkowski, M., Forwick, M., Szczuciński, W. (2015), 'Late Weichselian and Holocene palaeoceanography of Storfjordrenna, southern Svalbard', *Climate of the Past* **11**, pp. 587–603.

Lalande, C., Nöthig, E.-M., Bauerfeind, E., Hardge, K., Beszczynska-Möller, A., Fahl, K. (2016), 'Lateral supply and downward export of particulate matter from upper waters to the seafloor in the deep eastern Fram Strait', *Deep Sea Research Part I: Oceanographic Research Papers* **114**, pp. 78–89.

Landis, J.R., Koch, G.G. (1977), 'The Measurement of Observer Agreement for Categorical Data', *Biometrics* **33**, pp. 159–174.

Landvik, J.Y., Bondevik, S., ElverhØI, A., Fjeldskaar, W., Mangerud, J.A.N., Salvigsen, O., Siegert, M.J., Svendsen, J.-I., Vorren, T.O. (1998), 'The Last Glacial Maximum of Svalbard and the Barents Sea area: Ice sheet extent and configuration', *Quaternary Science Reviews* **17**, pp. 43–75.

Laskar, J., Robutel, P., Joutel, F., Gastineau, M., Correia, A.C.M., Levrard, B. (2004), 'A long-term numerical solution for the insolation quantities of the Earth', *Astronomy & Astrophysics* **428**, pp. 261–285.

Lattaud, J., Kirkels, F., Peterse, F., Freymond, C.V., Eglinton, T.I., Hefter, J., Mollenhauer, G., Balzano, S., Villanueva, L., van der Meer, M.T.J., Hopmans, E.C., Sinninghe-Damsté, J.S., Schouten, S. (2018a), 'Long-chain diols in rivers: distribution and potential biological sources', *Biogeosciences* **15**, pp. 4147–4161.

Lattaud, J., Lo, L., Huang, J.-J., Chou, Y.-M., Gorbarenko, S.A., Sinninghe Damsté, J.S., Schouten, S. (2018b), 'A Comparison of Late Quaternary Organic Proxy-Based Paleotemperature Records of the Central Sea of Okhotsk', *Paleoceanography and Paleoclimatology* **33**, pp. 732–744.

Laxon, S.W., Giles, K.A., Ridout, A.L., Wingham, D.J., Willatt, R., Cullen, R., Kwok, R., Schweiger, A., Zhang, J., Haas, C., Hendricks, S., Krishfield, R., Kurtz, N., Farrell, S., Davidson, M. (2013), 'CryoSat-2 estimates of Arctic sea ice thickness and volume', *Geophysical Research Letters* **40**, pp. 732–737.

Lea, D.W. (2014), '8.14 - Elemental and Isotopic Proxies of Past Ocean Temperatures', in: Holland, H.D., Turekian, K.K. (eds.), *Treatise on Geochemistry (Second Edition)*. Elsevier, Oxford, pp. 373–397.

Lea, D.W., Pak, D.K., Spero, H.J. (2000), 'Climate impact of late Quaternary equatorial Pacific sea surface temperature variations', *Science* **289**, pp. 1719–1724.

Leonard, E. (1990), 'An assessment of sediment loss and distortion at the top of short gravity cores', *Sedimentary Geology* **66**, pp. 57–63.

Leu, E., Søreide, J.E., Hessen, D.O., Falk-Petersen, S., Berge, J. (2011), 'Consequences of changing sea-ice cover for primary and secondary producers in the European Arctic shelf seas: Timing, quantity, and quality', *Progress in Oceanography* **90**, pp. 18–32.

Lind, S., Ingvaldsen, R.B. (2012), 'Variability and impacts of Atlantic Water entering the Barents Sea from the north', *Deep Sea Research Part I: Oceanographic Research Papers* **62**, pp. 70–88.

Lindsay, R., Schweiger, A. (2015), 'Arctic sea ice thickness loss determined using subsurface, aircraft, and satellite observations', *The Cryosphere* **9**, pp. 269–283.

Lindsay, R.W., Zhang, J. (2005), 'The Thinning of Arctic Sea Ice, 1988–2003: Have We Passed a Tipping Point?', *Journal of Climate* **18**, pp. 4879–4894.

Liu, J., Curry, J.A., Wang, H., Song, M., Horton, R.M. (2012), 'Impact of declining Arctic sea ice on winter snowfall', *Proceedings of the National Academy of Sciences* **109**, pp. 4074–4079.

Liu, Z., Otto-Bliesner, B.L., He, F., Brady, E.C., Tomas, R., Clark, P.U., Carlson, A.E., Lynch-Stieglitz, J., Curry, W., Brook, E., Erickson, D., Jacob, R., Kutzbach, J., Cheng, J. (2009), 'Transient Simulation of Last Deglaciation with a New Mechanism for Bølling-Allerød Warming', *Science* **325**, pp. 310–314.

Lo, L., Belt, S.T., Lattaud, J., Friedrich, T., Zeeden, C., Schouten, S., Smik, L., Timmermann, A., Cabedo-Sanz, P., Huang, J.-J., Zhou, L., Ou, T.-H., Chang, Y.-P.,

Wang, L.-C., Chou, Y.-M., Shen, C.-C., Chen, M.-T., Wei, K.-Y., Song, S.-R., Fang, T.-H., Gorbarenko, S.A., Wang, W.-L., Lee, T.-Q., Elderfield, H., Hodell, D.A. (2018), 'Precession and atmospheric CO_2 modulated variability of sea ice in the central Okhotsk Sea since 130,000 years ago', *Earth and Planetary Science Letters* **488**, pp. 36–45.

Loeng, H. (1991), 'Features of the physical oceanographic conditions of the Barents Sea', *Polar Research* **10**, pp. 5–18.

Loeng, H., Drinkwater, K. (2007), 'An overview of the ecosystems of the Barents and Norwegian Seas and their response to climate variability', *Deep Sea Research Part II: Topical Studies in Oceanography* **54**, pp. 2478–2500.

Loeng, H., Ozhigin, V., Ådlandsvik, B. (1997), 'Water fluxes through the Barents Sea', *ICES Journal of Marine Science* **54**, pp. 310–317.

Lopes dos Santos, R.A., Spooner, M.I., Barrows, T.T., De Deckker, P., Sinninghe Damsté, J.S., Schouten, S. (2013), 'Comparison of organic ($U^{K'}_{37}$, TEX^{H}_{86}, LDI) and faunal proxies (foraminiferal assemblages) for reconstruction of late Quaternary sea surface temperature variability from offshore southeastern Australia', *Paleoceanography* **28**, pp. 377–387.

Loutre, M.F., Fichefet, T., Goosse, H., Huybrechts, P., Goelzer, H., Capron, E. (2014), 'Factors controlling the last interglacial climate as simulated by LOVECLIM1.3', *Clim. Past* **10**, pp. 1541–1565.

Lubinski, D.J., Polyak, L., Forman, S.L. (2001), 'Freshwater and Atlantic water inflows to the deep northern Barents and Kara seas since ca 13 ^{14}C ka:: foraminifera and stable isotopes', *Quaternary Science Reviews* **20**, pp. 1851–1879.

Lücke, A., Moschen, R., Schleser, G.H. (2005), 'High-temperature carbon reduction of silica: A novel approach for oxygen isotope analysis of biogenic opal', *Geochimica et Cosmochimica Acta* **69**, pp. 1423–1433.

Luddington, I.A., Lovejoy, C., Kaczmarska, I. (2016), 'Species-rich meta-communities of the diatom order Thalassiosirales in the Arctic and northern Atlantic Ocean', *Journal of Plankton Research* **38**, pp. 781–797.

Lynch-Stieglitz, J., Schmidt, M.W., Gene Henry, L., Curry, W.B., Skinner, L.C., Mulitza, S., Zhang, R., Chang, P. (2014), 'Muted change in Atlantic overturning circulation over some glacial-aged Heinrich events', *Nature Geoscience* **7**, pp. 144–150.

Lyngsgaard, M.M., Markager, S., Richardson, K., Møller, E.F., Jakobsen, H.H. (2017), 'How Well Does Chlorophyll Explain the Seasonal Variation in Phytoplankton Activity?', *Estuaries and Coasts* **40**, pp. 1263–1275.

Maiti, K., Carroll, J., Benitez-Nelson, C.R. (2010), 'Sedimentation and particle dynamics in the seasonal ice zone of the Barents Sea', *Journal of Marine Systems* **79**, pp. 185–198.

Makshtas, A., Atkinson, D., Kulakov, M., Shutilin, S., Krishfield, R., Proshutinsky, A. (2007), 'Atmospheric forcing validation for modeling the central Arctic', *Geophysical Research Letters* **34**, article L20706.

Maksimovich, E., Vihma, T. (2012), 'The effect of surface heat fluxes on interannual variability in the spring onset of snow melt in the central Arctic Ocean', *Journal of Geophysical Research: Oceans* **117**, article C07012.

Mangerud, J., Dokken, T., Hebbeln, D., Heggen, B., Ingólfsson, Ó., Landvik, J.Y., Mejdahl, V., Svendsen, J.I., Vorren, T.O. (1998), 'Fluctuations of the Svalbard – Barents Sea ice sheet during the last 150,000 years', *Quaternary Science Reviews* **17**, pp. 11–42.

Manley, T.O. (1995), 'Branching of Atlantic Water within the Greenland-Spitsbergen Passage: An estimate of recirculation', *Journal of Geophysical Research: Oceans* **100**, pp. 20,627–20,634.

Marcott, S.A., Clark, P.U., Padman, L., Klinkhammer, G.P., Springer, S.R., Liu, Z., Otto-Bliesner, B.L., Carlson, A.E., Ungerer, A., Padman, J., He, F., Cheng, J., Schmittner, A. (2011), 'Ice-shelf collapse from subsurface warming as a trigger for Heinrich events', *Proceedings of the National Academy of Sciences* **108**, pp. 13,415–13,419.

Martens, K., Schön, I., Meisch, C., Horne, D.J. (2008), 'Global diversity of ostracods (Ostracoda, Crustacea) in freshwater', *Hydrobiologia* **595**, pp. 185–193.

Martin-Creuzburg, D., von Elert, E. (2009), 'Ecological significance of sterols in aquatic food webs', in: Kainz, M., Brett, M.T., Arts, M.T. (eds.), *Lipids in Aquatic Ecosystems*. Springer New York, New York, NY, pp. 43–64.

Maslanik, J.A., Fowler, C., Stroeve, J., Drobot, S., Zwally, J., Yi, D., Emery, W. (2007), 'A younger, thinner Arctic ice cover: Increased potential for rapid, extensive sea-ice loss', *Geophysical Research Letters* **34**, article L24501.

Massé, G., Belt, S.T., Crosta, X., Schmidt, S., Snape, I., Thomas, D.N., Rowland, S.J. (2011), 'Highly branched isoprenoids as proxies for variable sea ice conditions in the Southern Ocean', *Antarctic Science* **23**, pp. 487–498.

Matthiessen, J., de Vernal, A., Head, M., Okolodkov, Y., Zonneveld, K., Harland, R. (2005), 'Modem organic-walled dinoflagellate cysts in arctic marine environments and their (paleo-) environmental significance', *Paläontologische Zeitschrift* **79**, pp. 3–51.

Matthiessen, J., Knies, J. (2001), 'Dinoflagellate cyst evidence for warm interglacial conditions at the northern Barents Sea margin during marine oxygen isotope stage 5', *Journal of Quaternary Science* **16**, pp. 727–737.

Matul, A., Spielhagen, R.F., Kazarina, G., Kruglikova, S., Dmitrenko, O., Mohan, R. (2018), 'Warm-water events in the eastern Fram Strait during the last 2000 years as revealed by different microfossil groups ', *Polar Research* **37**, article 1540243.

McManus, J.F., Francois, R., Gherardi, J.M., Keigwin, L.D., Brown-Leger, S. (2004), 'Collapse and rapid resumption of Atlantic meridional circulation linked to deglacial climate changes', *Nature* **428**, pp. 834–837.

Méheust, M., Fahl, K., Stein, R. (2013), 'Variability in modern sea surface temperature, sea ice and terrigenous input in the sub-polar North Pacific and Bering Sea: Reconstruction from biomarker data', *Organic Geochemistry* **57**, pp. 54–64.

Meier, W., Fetterer, F., Savoie, M., Mallory, S., Duerr, R., Stroeve, J. (2017, *NOAA/NSIDC Climate Data Record of Passive Microwave Sea Ice Concentration, Version 3*. NSIDC: National Snow and Ice Data Center, Boulder, Colorado, USA. doi: https://doi.org/10.7265/N59P2ZTG (accessed 11.06.2018).

Meier, W.N., Hovelsrud, G.K., van Oort, B.E.H., Key, J.R., Kovacs, K.M., Michel, C., Haas, C., Granskog, M.A., Gerland, S., Perovich, D.K., Makshtas, A., Reist, J.D. (2014), 'Arctic sea ice in transformation: A review of recent observed changes and impacts on biology and human activity', *Reviews of Geophysics* **52**, pp. 185–217.

Meier, W.N., Stroeve, J., Fetterer, F. (2007), 'Whither Arctic sea ice? A clear signal of decline regionally, seasonally and extending beyond the satellite record', *Annals of Glaciology* **46**, pp. 428–434.

Menviel, L., Timmermann, A., Timm, O.E., Mouchet, A. (2010), 'Climate and biogeochemical response to a rapid melting of the West Antarctic Ice Sheet during interglacials and implications for future climate', *Paleoceanography* **25**, article PA4231.

Miettinen, A. (2018), 'Diatoms in Arctic regions: Potential tools to decipher environmental changes', *Polar Science* **18**, pp. 220–226.

Miettinen, A., Divine, D., Koç, N., Godtliebsen, F., Hall, I.R. (2012), 'Multicentennial Variability of the Sea Surface Temperature Gradient across the Subpolar North Atlantic over the Last 2.8 kyr', *Journal of Climate* **25**, pp. 4205–4219.

Miettinen, A., Koç, N., Hall, I.R., Godtliebsen, F., Divine, D. (2011), 'North Atlantic sea surface temperatures and their relation to the North Atlantic Oscillation during the last 230 years', *Climate Dynamics* **36**, pp. 533–543.

Miettinen, A., Koç, N., Husum, K. (2013), 'Appearance of the Pacific diatom Neodenticula seminae in the northern Nordic Seas – An indication of changes in Arctic sea ice and ocean circulation', *Marine Micropaleontology* **99**, pp. 2–7.

Mikaelyan, A.S., Pautova, L.A., Chasovnikov, V.K., Mosharov, S.A., Silkin, V.A. (2015), 'Alternation of diatoms and coccolithophores in the north-eastern Black Sea: a response to nutrient changes', *Hydrobiologia* **755**, pp. 89–105.

Miller, G.H., Alley, R.B., Brigham-Grette, J., Fitzpatrick, J.J., Polyak, L., Serreze, M.C., White, J.W.C. (2010a), 'Arctic amplification: can the past constrain the future?', *Quaternary Science Reviews* **29**, pp. 1779–1790.

Miller, G.H., Brigham-Grette, J., Alley, R.B., Anderson, L., Bauch, H.A., Douglas, M.S.V., Edwards, M.E., Elias, S.A., Finney, B.P., Fitzpatrick, J.J., Funder, S.V., Herbert, T.D., Hinzman, L.D., Kaufman, D.S., MacDonald, G.M., Polyak, L., Robock, A., Serreze, M.C., Smol, J.P., Spielhagen, R., White, J.W.C., Wolfe, A.P., Wolff, E.W. (2010b), 'Temperature and precipitation history of the Arctic', *Quaternary Science Reviews* **29**, pp. 1679–1715.

Miller, K.R., Chapman, M.R. (2013), 'Holocene climate variability reflected in diatom-derived sea surface temperature records from the subpolar North Atlantic', *The Holocene* **23**, pp. 882–887.

Mioduszewski, J., Vavrus, S., Wang, M. (2018), 'Diminishing Arctic Sea Ice Promotes Stronger Surface Winds', *Journal of Climate* **31**, pp. 8101–8119.

Mischke, S., Zhang, C., Börner, A. (2008), 'Bias of ostracod stable isotope data caused by drying of sieve residues from water', *Journal of Paleolimnology* **40**, pp. 567–575.

Monnin, E., Indermühle, A., Dällenbach, A., Flückiger, J., Stauffer, B., Stocker, T.F., Raynaud, D., Barnola, J.-M. (2001), 'Atmospheric CO_2 Concentrations over the Last Glacial Termination', *Science* **291**, pp. 112–114.

Montzka, S.A., Dlugokencky, E.J., Butler, J.H. (2011), 'Non-CO_2 greenhouse gases and climate change', *Nature* **476**, pp. 43–50.

Moreau, R.A., Whitaker, B.D., Hicks, K.B. (2002), 'Phytosterols, phytostanols, and their conjugates in foods: structural diversity, quantitative analysis, and health-promoting uses', *Progress in Lipid Research* **41**, pp. 457–500.

Mori, M., Watanabe, M., Shiogama, H., Inoue, J., Kimoto, M. (2014), 'Robust Arctic sea-ice influence on the frequent Eurasian cold winters in past decades', *Nature Geoscience* **7**, pp. 869–873.

Moros, M., Andrews, J.T., Eberl, D.D., Jansen, E. (2006), 'Holocene history of drift ice in the northern North Atlantic: Evidence for different spatial and temporal modes', *Paleoceanography* **21**, article PA2017.

Mortyn, P.G., Martínez-Botí, M.A. (2008), 'Planktonic foraminifera and their proxies for the reconstruction of surface-ocean climate parameters', *Contributions to Science* **3**, pp. 371–383.

Mudie, P.J., Harland, R., Matthiessen, J., Vernal, A.d. (2001), 'Marine dinoflagellate cysts and high latitude Quaternary paleoenvironmental reconstructions: an introduction', *Journal of Quaternary Science* **16**, pp. 595–602.

Mueller, B.L., Gillett, N.P., Monahan, A.H., Zwiers, F.W. (2018), 'Attribution of Arctic Sea Ice Decline from 1953 to 2012 to Influences from Natural, Greenhouse Gas, and Anthropogenic Aerosol Forcing', *Journal of Climate* **31**, pp. 7771–7787.

Mühlebach, A., Albers, C., Kattner, G. (1999), 'Differences in the sterol composition of dominant antarctic zooplankton', *Lipids* **34**, pp. 45–51.

Müller, J., Massé, G., Stein, R., Belt, S.T. (2009), 'Variability of sea-ice conditions in the Fram Strait over the past 30,000 years', *Nature Geoscience* **2**, pp. 772–776.

Müller, J., Stein, R. (2014), 'High-resolution record of late glacial and deglacial sea ice changes in Fram Strait corroborates ice–ocean interactions during abrupt climate shifts', *Earth and Planetary Science Letters* **403**, pp. 446–455.

Müller, J., Wagner, A., Fahl, K., Stein, R., Prange, M., Lohmann, G. (2011), 'Towards quantitative sea ice reconstructions in the northern North Atlantic: A combined biomarker and numerical modelling approach', *Earth and Planetary Science Letters* **306**, pp. 137–148.

Müller, J., Werner, K., Stein, R., Fahl, K., Moros, M., Jansen, E. (2012), 'Holocene cooling culminates in sea ice oscillations in Fram Strait', *Quaternary Science Reviews* **47**, pp. 1–14.

Müller, P.J., Kirst, G., Ruhland, G., von Storch, I., Rosell-Melé, A. (1998), 'Calibration of the alkenone paleotemperature index $U^{K'37}$ based on core-tops from the eastern South Atlantic and the global ocean (60°N-60°S)', *Geochimica et Cosmochimica Acta* **62**, pp. 1757–1772.

Mundy, C.J., Gosselin, M., Ehn, J., Gratton, Y., Rossnagel, A., Barber, D.G., Martin, J., Tremblay, J.-É., Palmer, M., Arrigo, K.R., Darnis, G., Fortier, L., Else, B., Papakyriakou, T. (2009), 'Contribution of under-ice primary production to an ice-edge upwelling phytoplankton bloom in the Canadian Beaufort Sea', *Geophysical Research Letters* **36**, article L17601.

Naafs, B.D.A., Hefter, J., Stein, R. (2012), 'Application of the long chain diol index (LDI) paleothermometer to the early Pleistocene (MIS 96)', *Organic Geochemistry* **49**, pp. 83–85.

NASA (2018a, updated daily), *Moderate-resolution Imaging Spectroradiometer (MODIS) Aqua L3M CHL Data*. NASA OB.DAAC, Greenbelt, MD, USA. doi: https://doi.org/10.5067/AQUA/MODIS/L3M/CHL/2018 (accessed 17.09.2018).

NASA (2018b, updated daily), *Moderate-resolution Imaging Spectroradiometer (MODIS) Aqua L3M PAR Data*. NASA OB.DAAC, Greenbelt, MD, USA. doi: https://doi.org/10.5067/AQUA/MODIS/L3M/PAR/2018 (accessed 17.09.2018)

NASA (2018c, updated daily), *Moderate-resolution Imaging Spectroradiometer (MODIS) Aqua L3M PIC Data*. NASA OB.DAAC, Greenbelt, MD, USA. doi: https://doi.org/10.5067/AQUA/MODIS/L3M/PIC/2018 (accessed 17.09.2018).

NASA (2018d, updated daily), *Moderate-resolution Imaging Spectroradiometer (MODIS) Aqua L3M SST Data*. NASA OB.DAAC, Greenbelt, MD, USA. doi: https://doi.org/10.5067/AQUA/MODIS/L3M/SST/2014 (accessed 17.09.2018).

NASA Goddard Space Flight Center (GSFC) Ocean Color Group (2012), 'Distance to Nearest Coastline: 0.01-Degree Grid: Ocean', available at: http://www.pacioos.hawaii.edu/metadata/dist2coast_1deg_ocean.html (accessed 22.09.2018).

Navarro-Rodriguez, A. (2014). Reconstruction of recent and palaeo sea ice conditions in the Barents Sea. Ph.D. thesis, University of Plymouth, Plymouth, UK.

Navarro-Rodriguez, A., Belt, S.T., Knies, J., Brown, T.A. (2013), 'Mapping recent sea ice conditions in the Barents Sea using the proxy biomarker IP_{25}: implications for palaeo sea ice reconstructions', *Quaternary Science Reviews* **79**, pp. 26–39.

Nelson, D.M., Tréguer, P., Brzezinski, M.A., Leynaert, A., Quéguiner, B. (1995), 'Production and dissolution of biogenic silica in the ocean: Revised global estimates, comparison with regional data and relationship to biogenic sedimentation', *Global Biogeochemical Cycles* **9**, pp. 359–372.

Nes, W.D. (2011), 'Biosynthesis of cholesterol and other sterols', *Chemical reviews* **111**, pp. 6423–6451.

Newton, A.M.W., Huuse, M. (2017), 'Glacial geomorphology of the central Barents Sea: Implications for the dynamic deglaciation of the Barents Sea Ice Sheet', *Marine Geology* **387**, pp. 114–131.

Nghiem, S.V., Rigor, I.G., Perovich, D.K., Clemente-Colón, P., Weatherly, J.W., Neumann, G. (2007), 'Rapid reduction of Arctic perennial sea ice', *Geophysical Research Letters* **34**, article L19504.

Nichols, P.D., Palmisano, A.C., Rayner, M.S., Smith, G.A., White, D.C. (1990), 'Occurrence of novel C_{30} sterols in Antarctic sea-ice diatom communities during a spring bloom', *Organic Geochemistry* **15**, pp. 503–508.

Nichols, P.D., Palmisano, A.C., Volkman, J.K., Smith, G.A., White, D.C. (1988), 'Ocurrence of an isoprenoid C_{25} diunsaturated alkene and high neutral lipid content in Antarctic sea-ice diatom communities', *Journal of Phycology* **24**, pp. 90–96.

Nørgaard-Pedersen, N., Spielhagen, R.F., Erlenkeuser, H., Grootes, P.M., Heinemeier, J., Knies, J. (2003), 'Arctic Ocean during the Last Glacial Maximum: Atlantic and polar domains of surface water mass distribution and ice cover', *Paleoceanography* **18**, article 1063.

Not, F., Siano, R., Kooistra, W.H.C.F., Simon, N., Vaulot, D., Probert, I. (2012), 'Chapter One - Diversity and Ecology of Eukaryotic Marine Phytoplankton', in: Piganeau, G. (ed.), *Advances in Botanical Research*. Academic Press, pp. 1–53.

Notz, D., Marotzke, J. (2012), 'Observations reveal external driver for Arctic sea-ice retreat', *Geophysical Research Letters* **39**, article L08502.

Ogawa, F., Keenlyside, N., Gao, Y., Koenigk, T., Yang, S., Suo, L., Wang, T., Gastineau, G., Nakamura, T., Cheung, H.N., Omrani, N.-E., Ukita, J., Semenov, V. (2018), 'Evaluating Impacts of Recent Arctic Sea Ice Loss on the Northern Hemisphere Winter Climate Change', *Geophysical Research Letters* **45**, pp. 3255–3263.

Oksman, M., Weckström, K., Miettinen, A., Juggins, S., Divine, D.V., Jackson, R., Telford, R., Korsgaard, N.J., Kucera, M. (2017), 'Younger Dryas ice margin retreat triggered by ocean surface warming in central-eastern Baffin Bay', *Nature Communications* **8**, article 1017.

Olsen, A., Johannessen, T., Rey, F. (2003), 'On the nature of the factors that control spring bloom development at the entrance to the Barents Sea and their interannual variability', *Sarsia* **88**, pp. 379–393.

Olsen, L.M., Laney, S.R., Duarte, P., Kauko, H.M., Fernández-Méndez, M., Mundy, C.J., Rösel, A., Meyer, A., Itkin, P., Cohen, L., Peeken, I., Tatarek, A., Różańska-Pluta, M., Wiktor, J., Taskjelle, T., Pavlov, A.K., Hudson, S.R., Granskog, M.A., Hop, H., Assmy, P. (2017), 'The seeding of ice algal blooms in Arctic pack ice: The multiyear ice seed repository hypothesis', *Journal of Geophysical Research: Biogeosciences* **122**, pp. 1529–1548.

Onarheim, I.H., Eldevik, T., Årthun, M., Ingvaldsen, R.B., Smedsrud, L.H. (2015), 'Skillful prediction of Barents Sea ice cover', *Geophysical Research Letters* **42**, pp. 5364–5371.

Onarheim, I.H., Eldevik, T., Smedsrud, L.H., Stroeve, J.C. (2018), 'Seasonal and Regional Manifestation of Arctic Sea Ice Loss', *Journal of Climate* **31**, pp. 4917–4932.

Osborn, T.J. (2011), 'Winter 2009/2010 temperatures and a record-breaking North Atlantic Oscillation index', *Weather* **66**, pp. 19–21.

Overland, J.E., Wang, M. (2013), 'When will the summer Arctic be nearly sea ice free?', *Geophysical Research Letters* **40**, pp. 2097–2101.

Oziel, L., Neukermans, G., Ardyna, M., Lancelot, C., Tison, J.-L., Wassmann, P., Sirven, J., Ruiz-Pino, D., Gascard, J.-C. (2017), 'Role for Atlantic inflows and sea ice loss on shifting phytoplankton blooms in the Barents Sea', *Journal of Geophysical Research: Oceans* **122**, pp. 5121–5139.

Oziel, L., Sirven, J., Gascard, J.-C. (2016), 'The Barents Sea frontal zones and water masses variability (1980–2011)', *Ocean Science* **12**, pp. 169–184.

Palm, S.P., Strey, S.T., Spinhirne, J., Markus, T. (2010), 'Influence of Arctic sea ice extent on polar cloud fraction and vertical structure and implications for regional climate', *Journal of Geophysical Research: Atmospheres* **115**, article D21209.

Parkinson, C.L., Cavalieri, D.J., Gloersen, P., Zwally, H.J., Comiso, J.C. (1999), 'Arctic sea ice extents, areas, and trends, 1978–1996', *Journal of Geophysical Research: Oceans* **104**, pp. 20837–20856.

Parkinson, C.L., DiGirolamo, N.E. (2016), 'New visualizations highlight new information on the contrasting Arctic and Antarctic sea-ice trends since the late 1970s', *Remote Sensing of Environment* **183**, pp. 198–204.

Pathirana, I., Knies, J., Felix, M., Mann, U., Ellingsen, I. (2015), 'Middle to late Holocene paleoproductivity reconstructions for the western Barents Sea: a model-data comparison', *Arktos* **1**, article 20.

Patton, H., Andreassen, K., Bjarnadóttir, L.R., Dowdeswell, J.A., Winsborrow, M.C.M., Noormets, R., Polyak, L., Auriac, A., Hubbard, A. (2015), 'Geophysical constraints on the dynamics and retreat of the Barents Sea ice sheet as a paleobenchmark for models of marine ice sheet deglaciation', *Reviews of Geophysics* **53**, pp. 1051–1098.

Patton, H., Hubbard, A., Andreassen, K., Auriac, A., Whitehouse, P.L., Stroeven, A.P., Shackleton, C., Winsborrow, M., Heyman, J., Hall, A.M. (2017), 'Deglaciation of the Eurasian ice sheet complex', *Quaternary Science Reviews* **169**, pp. 148–172.

Patton, H., Hubbard, A., Andreassen, K., Winsborrow, M., Stroeven, A.P. (2016), 'The build-up, configuration, and dynamical sensitivity of the Eurasian ice-sheet complex to Late Weichselian climatic and oceanic forcing', *Quaternary Science Reviews* **153**, pp. 97–121.

Pau, M., Hammer, Ø. (2016), 'Sedimentary environments in the south-western Barents Sea during the last deglaciation and the Holocene: a case study outside the Ingøydjupet trough', *Polar Research* **35**, article 23104.

Pawlowsky-Glahn, V., Egozcue, J.J. (2006), 'Compositional data and their analysis: an introduction', *Geological Society, London, Special Publications* **264**, pp. 1–10.

Pearce, C., Seidenkrantz, M.-S., Kuijpers, A., Massé, G., Reynisson, N.F., Kristiansen, S.M. (2013), 'Ocean lead at the termination of the Younger Dryas cold spell', *Nature Communications* **4**, article 1664.

Pearce, C., Seidenkrantz, M.-S., Kuijpers, A., Reynisson, N.F. (2014), 'A multi-proxy reconstruction of oceanographic conditions around the Younger Dryas–Holocene transition in Placentia Bay, Newfoundland', *Marine Micropaleontology* **112**, pp. 39–49.

Pearson, P.N. (2012), 'Oxygen isotopes in foraminifera: Overview and historical review', *The Paleontological Society Papers* **18**, pp. 1–38.

Pebesma, E. (2018), 'Simple Features for R: Standardized Support for Spatial Vector Data', *The R Journal*, available at: https://journal.r-project.org/archive/2018/RJ-2018-009/ (accessed 25.08.2018).

Pegau, W.S., Paulson, C.A. (2001), 'The albedo of Arctic leads in summer', *Annals of Glaciology* **33**, pp. 221–224.

Peltier, W.R., Fairbanks, R.G. (2006), 'Global glacial ice volume and Last Glacial Maximum duration from an extended Barbados sea level record', *Quaternary Science Reviews* **25**, pp. 3322–3337.

Peng, G., Meier, W.N., Scott, D.J., Savoie, M.H. (2013), 'A long-term and reproducible passive microwave sea ice concentration data record for climate studies and monitoring', *Earth System Science Data* **5**, pp. 311–318.

Perovich, D.K., Grenfell, T.C., Light, B., Hobbs, P.V. (2002), 'Seasonal evolution of the albedo of multiyear Arctic sea ice', *Journal of Geophysical Research: Oceans* **107**, article 8044.

Perovich, D.K., Polashenski, C. (2012), 'Albedo evolution of seasonal Arctic sea ice', *Geophysical Research Letters* **39**, article L08501.

Perovich, D.K., Richter-Menge, J.A. (2009), 'Loss of Sea Ice in the Arctic', *Annual Review of Marine Science* **1**, pp. 417–441.

Peterson, B.J., McClelland, J., Curry, R., Holmes, R.M., Walsh, J.E., Aagaard, K. (2006), 'Trajectory Shifts in the Arctic and Subarctic Freshwater Cycle', *Science* **313**, pp. 1061–1066.

Petoukhov, V., Semenov, V.A. (2010), 'A link between reduced Barents-Kara sea ice and cold winter extremes over northern continents', *Journal of Geophysical Research: Atmospheres* **115**, article D21111.

Pfuhl, H.A., Shackleton, N.J. (2004), 'Two proximal, high-resolution records of foraminiferal fragmentation and their implications for changes in dissolution', *Deep Sea Research Part I: Oceanographic Research Papers* **51**, pp. 809–832.

Pieńkowski, A.J., Gill, N.K., Furze, M.F.A., Mugo, S.M., Marret, F., Perreaux, A. (2016), 'Arctic sea-ice proxies: Comparisons between biogeochemical and

micropalaeontological reconstructions in a sediment archive from Arctic Canada', *The Holocene* **27**, pp. 665–682.

Planque, B., Primicerio, R., Michalsen, K., Aschan, M., Certain, G., Dalpadado, P., Gjøsæater, H., Hansen, C., Johannesen, E., Jørgensen, L.L., Kolsum, I., Kortsch, S., Leclerc, L.-M., Omli, L., Skern-Mauritzen, M., Wiedmann, M. (2014), 'Who eats whom in the Barents Sea: a food web topology from plankton to whales', *Ecology* **95**, pp. 1430–1430.

Poirier, R.K., Cronin, T.M., Briggs, W.M., Lockwood, R. (2012), 'Central Arctic paleoceanography for the last 50 kyr based on ostracode faunal assemblages', *Marine Micropaleontology* **88–89**, pp. 65–76.

Polyak, L., Alley, R.B., Andrews, J.T., Brigham-Grette, J., Cronin, T.M., Darby, D.A., Dyke, A.S., Fitzpatrick, J.J., Funder, S., Holland, M., Jennings, A.E., Miller, G.H., O'Regan, M., Savelle, J., Serreze, M., St. John, K., White, J.W.C., Wolff, E. (2010), 'History of sea ice in the Arctic', *Quaternary Science Reviews* **29**, pp. 1757–1778.

Polyak, L., Belt, S.T., Cabedo-Sanz, P., Yamamoto, M., Park, Y.-H. (2016), 'Holocene sea-ice conditions and circulation at the Chukchi-Alaskan margin, Arctic Ocean, inferred from biomarker proxies', *The Holocene* **26**, pp. 1810–1821.

Polyakov, I.V., Walsh, J.E., Kwok, R. (2012), 'Recent Changes of Arctic Multiyear Sea Ice Coverage and the Likely Causes', *Bulletin of the American Meteorological Society* **93**, pp. 145–151.

Pope, E.L., Talling, P.J., Hunt, J.E., Dowdeswell, J.A., Allin, J.R., Cartigny, M.J.B., Long, D., Mozzato, A., Stanford, J.D., Tappin, D.R., Watts, M. (2016), 'Long-term record of Barents Sea Ice Sheet advance to the shelf edge from a 140,000 year record', *Quaternary Science Reviews* **150**, pp. 55–66.

Poulin, M., Daugbjerg, N., Gradinger, R., Ilyash, L., Ratkova, T., von Quillfeldt, C. (2011), 'The pan-Arctic biodiversity of marine pelagic and sea-ice unicellular eukaryotes: a first-attempt assessment', *Marine Biodiversity* **41**, pp. 13–28.

Poulin, M., Underwood, G.J.C., Michel, C. (2014), 'Sub-ice colonial Melosira arctica in Arctic first-year ice', *Diatom Research* **29**, pp. 213–221.

Prahl, F.G., Muehlhausen, L.A., Zahnle, D.L. (1988), 'Further evaluation of long-chain alkenones as indicators of paleoceanographic conditions', *Geochimica et Cosmochimica Acta* **52**, pp. 2303–2310.

Prahl, F.G., Wakeham, S.G. (1987), 'Calibration of unsaturation patterns in long-chain ketone compositions for palaeotemperature assessment', *Nature* **330**, pp. 367–369.

Purina, I., Labucis, A., Barda, I., Jurgensone, I., Aigars, J. (2018), 'Primary productivity in the Gulf of Riga (Baltic Sea) in relation to phytoplankton species and nutrient variability', *Oceanologia* **60**, pp. 544–552.

Quinlan, J.R. (1986), 'Induction of decision trees', *Machine Learning* **1**, pp. 81–106.

Quinlan, J.R. (1993), *C4.5: programs for machine learning*. Morgan Kaufmann Publishers Inc., San Mateo, California, USA.

Radi, T., de Vernal, A. (2008), 'Dinocysts as proxy of primary productivity in mid–high latitudes of the Northern Hemisphere', *Marine Micropaleontology* **68**, pp. 84–114.

Ragueneau, O., Tréguer, P., Leynaert, A., Anderson, R.F., Brzezinski, M.A., DeMaster, D.J., Dugdale, R.C., Dymond, J., Fischer, G., François, R., Heinze, C., Maier-Reimer, E., Martin-Jézéquel, V., Nelson, D.M., Quéguiner, B. (2000), 'A review of the Si cycle in the modern ocean: recent progress and missing gaps in the application of biogenic opal as a paleoproductivity proxy', *Global and Planetary Change* **26**, pp. 317–365.

Raileanu, L.E., Stoffel, K. (2004), 'Theoretical Comparison between the Gini Index and Information Gain Criteria', *Annals of Mathematics and Artificial Intelligence* **41**, pp. 77–93.

Rampal, P., Weiss, J., Marsan, D. (2009), 'Positive trend in the mean speed and deformation rate of Arctic sea ice, 1979–2007', *Journal of Geophysical Research: Oceans* **114**, article C05013.

Rampen, S.W., Abbas, B.A., Schouten, S., Sinninghe Damste, J.S. (2010), 'A comprehensive study of sterols in marine diatoms (Bacillariophyta): Implications for their use as tracers for diatom productivity', *Limnology and Oceanography* **55**, pp. 91–105.

Rampen, S.W., Schouten, S., Sinninghe Damsté, J.S. (2011), 'Occurrence of long chain 1,14-diols in *Apedinella radians*', *Organic Geochemistry* **42**, pp. 572–574.

Rampen, S.W., Schouten, S., Wakeham, S.G., Sinninghe Damsté, J.S. (2007), 'Seasonal and spatial variation in the sources and fluxes of long chain diols and mid-chain hydroxy methyl alkanoates in the Arabian Sea', *Organic Geochemistry* **38**, pp. 165–179.

Rampen, S.W., Willmott, V., Kim, J.-H., Uliana, E., Mollenhauer, G., Schefuß, E., Sinninghe Damsté, J.S., Schouten, S. (2012), 'Long chain 1,13- and 1,15-diols as a potential proxy for palaeotemperature reconstruction', *Geochimica et Cosmochimica Acta* **84**, pp. 204–216.

Rasmussen, S.O., Andersen, K.K., Svensson, A.M., Steffensen, J.P., Vinther, B.M., Clausen, H.B., Siggaard-Andersen, M.-L., Johnsen, S.J., Larsen, L.B., Dahl-Jensen, D., Bigler, M., Röthlisberger, R., Fischer, H., Goto-Azuma, K., Hansson, M.E., Ruth, U. (2006), 'A new Greenland ice core chronology for the last glacial termination', *Journal of Geophysical Research: Atmospheres* **111**, article D06102.

Rasmussen, T.L., Thomsen, E. (2004), 'The role of the North Atlantic Drift in the millennial timescale glacial climate fluctuations', *Palaeogeography, Palaeoclimatology, Palaeoecology* **210**, pp. 101–116.

Rasmussen, T.L., Thomsen, E. (2008), 'Warm Atlantic surface water inflow to the Nordic seas 34–10 calibrated ka B.P', *Paleoceanography* **23**, article PA1201.

Rasmussen, T.L., Thomsen, E. (2015), 'Palaeoceanographic development in Storfjorden, Svalbard, during the deglaciation and Holocene: evidence from benthic foraminiferal records', *Boreas* **44**, pp. 24–44.

Rasmussen, T.L., Thomsen, E., Skirbekk, K., Ślubowska-Woldengen, M., Klitgaard Kristensen, D., Koç, N. (2014), 'Spatial and temporal distribution of Holocene

temperature maxima in the northern Nordic seas: interplay of Atlantic-, Arctic- and polar water masses', *Quaternary Science Reviews* **92**, pp. 280–291.

Rasmussen, T.L., Thomsen, E., Ślubowska, M.A., Jessen, S., Solheim, A., Koç, N. (2007), 'Paleoceanographic evolution of the SW Svalbard margin (76°N) since 20,000 ^{14}C yr BP', *Quaternary Research* **67**, pp. 100–114.

Ratkova, T.N., Wassmann, P. (2005), 'Sea ice algae in the White and Barents seas: composition and origin', *Polar Research* **24**, pp. 95–110.

Ravelo, A.C., Hillaire-Marcel, C. (2007), 'Chapter Eighteen The Use of Oxygen and Carbon Isotopes of Foraminifera in Paleoceanography', in: Hillaire–Marcel, C., De Vernal, A. (eds.), *Developments in Marine Geology*. Elsevier, pp. 735–764.

Rechka, J.A., Maxwell, J.R. (1988), 'Characterisation of alkenone temperature indicators in sediments and organisms', *Organic Geochemistry* **13**, pp. 727–734.

Reimann, C., Filzmoser, P. (2000), 'Normal and lognormal data distribution in geochemistry: death of a myth. Consequences for the statistical treatment of geochemical and environmental data', *Environmental Geology* **39**, pp. 1001–1014.

Reimann, C., Filzmoser, P., Garrett, R.G. (2002), 'Factor analysis applied to regional geochemical data: problems and possibilities', *Applied Geochemistry* **17**, pp. 185–206.

Reimer, P.J., Bard, E., Bayliss, A., Beck, J.W., Blackwell, P.G., Ramsey, C.B., Buck, C.E., Cheng, H., Edwards, R.L., Friedrich, M., Grootes, P.M., Guilderson, T.P., Haflidason, H., Hajdas, I., Hatté, C., Heaton, T.J., Hoffmann, D.L., Hogg, A.G., Hughen, K.A., Kaiser, K.F., Kromer, B., Manning, S.W., Niu, M., Reimer, R.W., Richards, D.A., Scott, E.M., Southon, J.R., Staff, R.A., Turney, C.S.M., van der Plicht, J. (2013), 'IntCal13 and Marine13 Radiocarbon Age Calibration Curves 0–50,000 Years cal BP', *Radiocarbon* **55**, pp. 1869–1887.

Richardson, A.J. (2008), 'In hot water: zooplankton and climate change', *ICES Journal of Marine Science* **65**, pp. 279–295.

Ringrose, A.E. (2012). Temporal and vertical distributions of IP_{25} and other lipid biomarkers in sea ice from Resolute Bay, Nunavut, Canada. M.Phil. thesis, University of Plymouth, Plymouth, UK.

Risebrobakken, B., Berben, S.M.P. (2018), 'Early Holocene Establishment of the Barents Sea Arctic Front', *Frontiers in Earth Science* **6**, doi: https://doi.org/10.3389/feart.2018.00166.

Risebrobakken, B., Dokken, T., Smedsrud, L.H., Andersson, C., Jansen, E., Moros, M., Ivanova, E.V. (2011), 'Early Holocene temperature variability in the Nordic Seas: The role of oceanic heat advection versus changes in orbital forcing', *Paleoceanography* **26**, article PA4206.

Risebrobakken, B., Moros, M., Ivanova, E.V., Chistyakova, N., Rosenberg, R. (2010), 'Climate and oceanographic variability in the SW Barents Sea during the Holocene', *The Holocene* **20**, pp. 609–621.

Ritz, S.P., Stocker, T.F., Grimalt, J.O., Menviel, L., Timmermann, A. (2013), 'Estimated strength of the Atlantic overturning circulation during the last deglaciation', *Nature Geoscience* **6**, pp. 208–212.

Robson, J.N., Rowland, S.J. (1986), 'Identification of novel widely distributed sedimentary acyclic sesterterpenoids', *Nature* **324**, pp. 561–563.

Rodrigo-Gámiz, M., Rampen, S.W., de Haas, H., Baas, M., Schouten, S., Sinninghe-Damsté, J.S. (2015), 'Constraints on the applicability of the organic temperature proxies $U^{K'}_{37}$, TEX_{86} and LDI in the subpolar region around Iceland', *Biogeosciences* **12**, pp. 6573–6590.

Rodriguez-Lazaro, J., Ruiz-Muñoz, F. (2012), 'Chapter 1 - A General Introduction to Ostracods: Morphology, Distribution, Fossil Record and Applications', in: Horne, D.J., Holmes, J.A., Rodriguez-Lazaro, J., Viehberg, F.A. (eds.), *Developments in Quaternary Sciences*. Elsevier, pp. 1–14.

Rokach, L., Maimon, O. (2005), 'Decision Trees', in: Maimon, O., Rokach, L. (eds.), *Data Mining and Knowledge Discovery Handbook*. Springer US, Boston, MA, pp. 165–192.

Rontani, J.-F., Aubert, C., Belt, S.T. (2018a), 'Electron ionization mass spectrometry fragmentation and multiple reaction monitoring quantification of bacterial metabolites of the sea ice biomarker proxy IP_{25} in Arctic sediments', *Rapid Communications in Mass Spectrometry* **32**, pp. 775–783.

Rontani, J.-F., Belt, S.T., Amiraux, R. (2018b), 'Biotic and abiotic degradation of the sea ice diatom biomarker IP_{25} and selected algal sterols in near-surface Arctic sediments', *Organic Geochemistry* **118**, pp. 73–88.

Rontani, J.-F., Belt, S.T., Brown, T.A., Vaultier, F., Mundy, C.J. (2014a), 'Sequential photo- and autoxidation of diatom lipids in Arctic sea ice', *Organic Geochemistry* **77**, pp. 59–71.

Rontani, J.-F., Belt, S.T., Vaultier, F., Brown, T.A. (2011), 'Visible light induced photo-oxidation of highly branched isoprenoid (HBI) alkenes: Significant dependence on the number and nature of double bonds', *Organic Geochemistry* **42**, pp. 812–822.

Rontani, J.-F., Belt, S.T., Vaultier, F., Brown, T.A., Massé, G. (2014b), 'Autoxidative and Photooxidative Reactivity of Highly Branched Isoprenoid (HBI) Alkenes', *Lipids* **49**, pp. 481–494.

Rontani, J.F., Charriere, B., Forest, A., Heussner, S., Vaultier, F., Petit, M., Delsaut, N., Fortier, L., Sempéré, R. (2012), 'Intense photooxidative degradation of planktonic and bacterial lipids in sinking particles collected with sediment traps across the Canadian Beaufort Shelf (Arctic Ocean)', *Biogeosciences* **9**, pp. 4787–4802.

Rontani, J.F., Volkman, J.K., Prahl, F.G., Wakeham, S.G. (2013), 'Biotic and abiotic degradation of alkenones and implications for $U^{K'}_{37}$ paleoproxy applications: A review', *Organic Geochemistry* **59**, pp. 95–113.

Rørvik, K.-L., Rasmussen, T.L., Hald, M., Husum, K. (2013), 'Intermediate water ventilation in the Nordic seas during MIS 2', *Geophysical Research Letters* **40**, pp. 1805–1810.

Rothrock, D.A., Percival, D.B., Wensnahan, M. (2008), 'The decline in arctic sea-ice thickness: Separating the spatial, annual, and interannual variability in a quarter century of submarine data', *Journal of Geophysical Research: Oceans* **113**, article C05003.

Rothrock, D.A., Yu, Y., Maykut, G.A. (1999), 'Thinning of the Arctic sea-ice cover', *Geophysical Research Letters* **26**, pp. 3469–3472.

Rothrock, D.A., Zhang, J. (2005), 'Arctic Ocean sea ice volume: What explains its recent depletion?', *Journal of Geophysical Research: Oceans* **110**, article C01002.

Rowland, S.J., Allard, W.G., Belt, S.T., Massé, G., Robert, J.M., Blackburn, S., Frampton, D., Revill, A.T., Volkman, J.K. (2001), 'Factors influencing the distributions of polyunsaturated terpenoids in the diatom, *Rhizosolenia setigera*', *Phytochemistry* **58**, pp. 717–728.

Ruan, J., Huang, Y., Shi, X., Liu, Y., Xiao, W., Xu, Y. (2017), 'Holocene variability in sea surface temperature and sea ice extent in the northern Bering Sea: A multiple biomarker study', *Organic Geochemistry* **113**, pp. 1–9.

Rüther, D.C., Bjarnadóttir, L.R., Junttila, J., Husum, K., Rasmussen, T.L., Lucchi, R.G., Andreassen, K. (2012), 'Pattern and timing of the northwestern Barents Sea Ice Sheet deglaciation and indications of episodic Holocene deposition', *Boreas* **41**, pp. 494–512.

Sachs, J.P., Lehman, S.J. (1999), 'Subtropical North Atlantic Temperatures 60,000 to 30,000 Years Ago', *Science* **286**, pp. 756–759.

Sachs, J.P., Pahnke, K., Smittenberg, R., Zhang, Z. (2013), 'PALEOCEANOGRAPHY, BIOLOGICAL PROXIES | Biomarker Indicators of Past Climate', in: Elias, S.A., Mock, C.J. (eds.), *Encyclopedia of Quaternary Science (Second Edition)*. Elsevier, Amsterdam, pp. 775–782.

Sætre, R. (2007), *The Norwegian Coastal Current: Oceanography and Climate*. Tapir Academic Press, Trondheim, Norway.

Sætre, R., Aure, J., Ljøen, R. (1988), 'Wind effects on the lateral extension of the Norwegian Coastal Water', *Continental Shelf Research* **8**, pp. 239–253.

Sakshaug, E., Johnsen, G., Kovacs, K.M. (2009), *Ecosystem Barents Sea*. Tapir Academic Press, Trondheim, Norway.

Sakshaug, E., Slagstad, D. (1992), 'Sea ice and wind: Effects on primary productivity in the Barents Sea', *Atmosphere-Ocean* **30**, pp. 579–591.

Sammut, C., Webb, G.I. (2017), *Encyclopedia of Machine Learning and Data Mining: 2nd edition*. Springer Publishing Company, Incorporated, New York, USA.

Sandven, S., Johannessen, O.M., Kloster, K. (2006), 'Sea Ice Monitoring by Remote Sensing', in: Meyers, R.A., Mather, P.M. (eds.), *Encyclopedia of Analytical Chemistry*.

Sangiorgi, F., Fabbri, D., Comandini, M., Gabbianelli, G., Tagliavini, E. (2005), 'The distribution of sterols and organic-walled dinoflagellate cysts in surface sediments of the North-western Adriatic Sea (Italy)', *Estuarine, Coastal and Shelf Science* **64**, pp. 395–406.

Sarnthein, M., Pflaumann, U., Weinelt, M. (2003), 'Past extent of sea ice in the northern North Atlantic inferred from foraminiferal paleotemperature estimates', *Paleoceanography* **18**, article 1047.

Schauer, U., Loeng, H., Rudels, B., Ozhigin, V.K., Dieck, W. (2002), 'Atlantic Water flow through the Barents and Kara Seas', *Deep Sea Research Part I: Oceanographic Research Papers* **49**, pp. 2281–2298.

Schmidt, K., Brown, T.A., Belt, S.T., Ireland, L.C., Taylor, K.W.R., Thorpe, S.E., Ward, P., Atkinson, A. (2018), 'Do pelagic grazers benefit from sea ice? Insights from the Antarctic sea ice proxy $IPSO_{25}$', *Biogeosciences* **15**, pp. 1987–2006.

Schneider, A., Wetterich, S., Schirrmeister, L., Herzschuh, U., Meyer, H., Pestryakova, L.A. (2016), 'Freshwater ostracods (Crustacea) and environmental variability of polygon ponds in the tundra of the Indigirka Lowland, north-east Siberia', *Polar Research* **35**, article 25225.

Schouten, S., Hopmans, E.C., Forster, A., van Breugel, Y., Kuypers, M.M.M., Sinninghe-Damsté, J.S. (2003), 'Extremely high sea-surface temperatures at low latitudes during the middle Cretaceous as revealed by archaeal membrane lipids', *Geology* **31**, pp. 1069–1072.

Schouten, S., Hopmans, E.C., Pancost, R.D., Damsté, J.S.S. (2000), 'Widespread occurrence of structurally diverse tetraether membrane lipids: Evidence for the ubiquitous presence of low-temperature relatives of hyperthermophiles', *Proceedings of the National Academy of Sciences* **97**, pp. 14421–14426.

Schouten, S., Hopmans, E.C., Schefuß, E., Sinninghe Damsté, J.S. (2002), 'Distributional variations in marine crenarchaeotal membrane lipids: a new tool for reconstructing ancient sea water temperatures?', *Earth and Planetary Science Letters* **204**, pp. 265–274.

Schouten, S., Hopmans, E.C., Sinninghe Damsté, J.S. (2013), 'The organic geochemistry of glycerol dialkyl glycerol tetraether lipids: A review', *Organic Geochemistry* **54**, pp. 19–61.

Screen, J.A., Simmonds, I. (2012), 'Declining summer snowfall in the Arctic: causes, impacts and feedbacks', *Climate Dynamics* **38**, pp. 2243–2256.

Serreze, M.C., Barrett, A.P., Slater, A.G., Steele, M., Zhang, J., Trenberth, K.E. (2007), 'The large-scale energy budget of the Arctic', *Journal of Geophysical Research: Atmospheres* **112**, article D11122.

Serreze, M.C., Barry, R.G. (2011), 'Processes and impacts of Arctic amplification: A research synthesis', *Global and Planetary Change* **77**, pp. 85–96.

Setoyama, E., Kaminski, M.A., Tyszka, J. (2011), 'The Late Cretaceous–Early Paleocene palaeobathymetric trends in the southwestern Barents Sea —

Palaeoenvironmental implications of benthic foraminiferal assemblage analysis', *Palaeogeography, Palaeoclimatology, Palaeoecology* **307**, pp. 44–58.

Shakun, J.D., Clark, P.U., He, F., Marcott, S.A., Mix, A.C., Liu, Z., Otto-Bliesner, B., Schmittner, A., Bard, E. (2012), 'Global warming preceded by increasing carbon dioxide concentrations during the last deglaciation', *Nature* **484**, pp. 49–54.

Shemesh, A., Burckle, L.H., Hays, J.D. (1995), 'Late Pleistocene oxygen isotope records of biogenic silica from the Atlantic sector of the Southern Ocean', *Paleoceanography* **10**, pp. 179–196.

Shemesh, A., Charles, C.D., Fairbanks, R.G. (1992), 'Oxygen Isotopes in Biogenic Silica: Global Changes in Ocean Temperature and Isotopic Composition', *Science* **256**, pp. 1434–1436.

Shih, Y.-S. (1999), 'Families of splitting criteria for classification trees', *Statistics and Computing* **9**, pp. 309–315.

Shimokawara, M., Nishimura, M., Matsuda, T., Akiyama, N., Kawai, T. (2010), 'Bound forms, compositional features, major sources and diagenesis of long chain, alkyl mid-chain diols in Lake Baikal sediments over the past 28,000 years', *Organic Geochemistry* **41**, pp. 753–766.

Siegert, M.J., Dowdeswell, J.A. (2002), 'Late Weichselian iceberg, meltwater and sediment production from the Eurasian High Arctic ice sheet: results from numerical ice-sheet modelling', *Marine Geology* **188**, pp. 109–127.

Signorini, S.R., McClain, C.R. (2009), 'Environmental factors controlling the Barents Sea spring-summer phytoplankton blooms', *Geophysical Research Letters* **36**, article L10604.

Sinninghe Damsté, J.S., Schouten, S., Rijpstra, W.I.C., Hopmans, E.C., Peletier, H., Gieskes, W.W.C., Geenevasen, J.A.J. (1999), 'Structural identification of the C_{25} highly branched isoprenoid pentaene in the marine diatom *Rhizosolenia setigera*', *Organic Geochemistry* **30**, pp. 1581–1583.

Skirbekk, K., Hald, M., Marchitto, T.M., Junttila, J., Klitgaard Kristensen, D., Aagaard Sørensen, S. (2016), 'Benthic foraminiferal growth seasons implied from Mg/Ca-temperature correlations for three Arctic species', *Geochemistry, Geophysics, Geosystems* **17**, pp. 4684–4704.

Skirbekk, K., Kristensen, D.K., Rasmussen, T.L., Koç, N., Forwick, M. (2010), 'Holocene climate variations at the entrance to a warm Arctic fjord: evidence from Kongsfjorden trough, Svalbard', *Geological Society, London, Special Publications* **344**, pp. 289–304.

Ślubowska, M.A., Koç, N., Rasmussen, T.L., Klitgaard-Kristensen, D. (2005), 'Changes in the flow of Atlantic water into the Arctic Ocean since the last deglaciation: Evidence from the northern Svalbard continental margin, 80°N', *Paleoceanography* **20**, article PA4014.

Ślubowska-Woldengen, M., Koç, N., Rasmussen, T.L., Klitgaard-Kristensen, D., Hald, M., Jennings, A.E. (2008), 'Time-slice reconstructions of ocean circulation changes on

the continental shelf in the Nordic and Barents Seas during the last 16,000 cal yr B.P', *Quaternary Science Reviews* **27**, pp. 1476–1492.

Ślubowska-Woldengen, M., Rasmussen, T.L., Koç, N., Klitgaard-Kristensen, D., Nilsen, F., Solheim, A. (2007), 'Advection of Atlantic Water to the western and northern Svalbard shelf since 17,500 cal yr BP', *Quaternary Science Reviews* **26**, pp. 463–478.

Sluijs, A., Schouten, S., Donders, T.H., Schoon, P.L., Röhl, U., Reichart, G.-J., Sangiorgi, F., Kim, J.-H., Sinninghe Damsté, J.S., Brinkhuis, H. (2009), 'Warm and wet conditions in the Arctic region during Eocene Thermal Maximum 2', *Nature Geoscience* **2**, pp. 777–780.

Smedsrud, L.H., Esau, I., Ingvaldsen, R.B., Eldevik, T., Haugan, P.M., Li, C., Lien, V.S., Olsen, A., Omar, A.M., Otterå, O.H., Risebrobakken, B., Sandø, A.B., Semenov, V.A., Sorokina, S.A. (2013), 'The role of the Barents Sea in the Arctic climate system', *Reviews of Geophysics* **51**, pp. 415–449.

Smedsrud, L.H., Halvorsen, M.H., Stroeve, J.C., Zhang, R., Kloster, K. (2017), 'Fram Strait sea ice export variability and September Arctic sea ice extent over the last 80 years', *The Cryosphere* **11**, pp. 65–79.

Smedsrud, L.H., Ingvaldsen, R.B., Nilsen, J.E.Ø., Skagseth, Ø. (2010), 'Heat in the Barents Sea: transport, storage, and surface fluxes', *Ocean Science* **6**, pp. 219–234.

Smik, L. (2016). *Development of biomarker-based proxies for paleo sea ice reconstructions*. Ph.D. thesis, University of Plymouth, Plymouth, UK.

Smik, L., Belt, S.T. (2017), 'Distributions of the Arctic sea ice biomarker proxy IP_{25} and two phytoplanktonic biomarkers in surface sediments from West Svalbard', *Organic Geochemistry* **105**, pp. 39–41.

Smik, L., Cabedo-Sanz, P., Belt, S.T. (2016), 'Semi-quantitative estimates of paleo Arctic sea ice concentration based on source-specific highly branched isoprenoid alkenes: A further development of the PIP_{25} index', *Organic Geochemistry* **92**, pp. 63–69.

Smith, W.O., Sakshaug, E. (1990), 'Polar Phytoplankton', in: Smith, W.O. (ed.), *Polar Oceanography*. Academic Press, San Diego, pp. 477–525.

Solomon, S., Plattner, G.-K., Knutti, R., Friedlingstein, P. (2009), 'Irreversible climate change due to carbon dioxide emissions', *Proceedings of the National Academy of Sciences* **106**, pp. 1704–1709.

Søreide, J.E., Carroll, M.L., Hop, H., Ambrose, W.G., Hegseth, E.N., Falk-Petersen, S. (2013), 'Sympagic-pelagic-benthic coupling in Arctic and Atlantic waters around Svalbard revealed by stable isotopic and fatty acid tracers', *Marine Biology Research* **9**, pp. 831–850.

Søreide, J.E., Leu, E., Berge, J., Graeve, M., Falk-Petersen, S. (2010), 'Timing of blooms, algal food quality and Calanus glacialis reproduction and growth in a changing Arctic', *Global Change Biology* **16**, pp. 3154–3163.

Sørensen, T. (1948), 'A method of establishing groups of equal amplitude in plant sociology based on similarity of species and its application to analyses of the vegetation on Danish commons', *Biologiske Skrifter* **5**, pp. 1–34.

Sorteberg, A., Kvingedal, B. (2006), 'Atmospheric Forcing on the Barents Sea Winter Ice Extent', *Journal of Climate* **19**, pp. 4772–4784.

Sosdian, S.M., Greenop, R., Hain, M.P., Foster, G.L., Pearson, P.N., Lear, C.H. (2018), 'Constraining the evolution of Neogene ocean carbonate chemistry using the boron isotope pH proxy', *Earth and Planetary Science Letters* **498**, pp. 362–376.

Spielhagen, R.F. (2012), 'History of Atlantic Water Advection to the Arctic Ocean: A Review of 20 Years of Progress Since the "Oden" - "Polarstern" Expedition ARCTIC 91', *Polarforschung* **82**, pp. 19–36.

Spielhagen, R.F., Baumann, K.-H., Erlenkeuser, H., Nowaczyk, N.R., Nørgaard-Pedersen, N., Vogt, C., Weiel, D. (2004), 'Arctic Ocean deep-sea record of northern Eurasian ice sheet history', *Quaternary Science Reviews* **23**, pp. 1455–1483.

Spielhagen, R.F., Erlenkeuser, H., Siegert, C. (2005), 'History of freshwater runoff across the Laptev Sea (Arctic) during the last deglaciation', *Global and Planetary Change* **48**, pp. 187–207.

Spielhagen, R.F., Werner, K., Sørensen, S.A., Zamelczyk, K., Kandiano, E., Budeus, G., Husum, K., Marchitto, T.M., Hald, M. (2011), 'Enhanced Modern Heat Transfer to the Arctic by Warm Atlantic Water', *Science* **331**, pp. 450–453.

St John, K., Passchier, S., TantillO, B., Darby, D., Kearns, L. (2015), 'Microfeatures of modern sea-ice-rafted sediment and implications for paleo-sea-ice reconstructions', *Annals of Glaciology* **56**, pp. 83–93.

Stecher, A., Neuhaus, S., Lange, B., Frickenhaus, S., Beszteri, B., Kroth, P.G., Valentin, K. (2016), 'rRNA and rDNA based assessment of sea ice protist biodiversity from the central Arctic Ocean', *European Journal of Phycology* **51**, pp. 31–46.

Steele, M., Ermold, W., Zhang, J. (2008), 'Arctic Ocean surface warming trends over the past 100 years', *Geophysical Research Letters* **35**, article L02614.

Stein, R., Fahl, K. (2012), 'A first southern Lomonosov Ridge (Arctic Ocean) 60 ka IP_{25} sea-ice record', *Polarforschung* **82**, pp. 83–86.

Stein, R., Fahl, K. (2013), 'Biomarker proxy shows potential for studying the entire Quaternary Arctic sea ice history', *Organic Geochemistry* **55**, pp. 98–102.

Stein, R., Fahl, K., Müller, J. (2012), 'Proxy reconstruction of Arctic Ocean sea ice history - From IRD to IP_{25}', *Polarforschung* **82**, pp. 37–71.

Stein, R., Fahl, K., Schreck, M., Knorr, G., Niessen, F., Forwick, M., Gebhardt, C., Jensen, L., Kaminski, M., Kopf, A., Matthiessen, J., Jokat, W., Lohmann, G. (2016), 'Evidence for ice-free summers in the late Miocene central Arctic Ocean', *Nature Communications* **7**, article 11148.

Stenson, G.B., Hammill, M.O. (2014), 'Can ice breeding seals adapt to habitat loss in a time of climate change?', *ICES Journal of Marine Science* **71**, pp. 1977–1986.

Stewart, K.D., Haine, T.W.N. (2016), 'Thermobaricity in the Transition Zones between Alpha and Beta Oceans', *Journal of Physical Oceanography* **46**, pp. 1805–1821.

Stickley, C.E., St John, K., Koç, N., Jordan, R.W., Passchier, S., Pearce, R.B., Kearns, L.E. (2009), 'Evidence for middle Eocene Arctic sea ice from diatoms and ice-rafted debris', *Nature* **460**, pp. 376–379.

Stoynova, V., Shanahan, T.M., Hughen, K.A., de Vernal, A. (2013), 'Insights into Circum-Arctic sea ice variability from molecular geochemistry', *Quaternary Science Reviews* **79**, pp. 63–73.

Stranne, C., Jakobsson, M., Björk, G. (2014), 'Arctic Ocean perennial sea ice breakdown during the Early Holocene Insolation Maximum', *Quaternary Science Reviews* **92**, pp. 123–132.

Strass, V.H., Nöthig, E.-M. (1996), 'Seasonal shifts in ice edge phytoplankton blooms in the Barents Sea related to the water column stability', *Polar Biology* **16**, pp. 409–422.

Stroeve, J., Blanchard-Wrigglesworth, E., Guemas, V., Howell, S., Massonnet, F., Tietsche, S. (2015), 'Improving predictions of Arctic sea ice extent', *Eos, Transactions American Geophysical Union* **96**, doi: https://doi.org/10.1029/2015EO031431.

Stroeve, J., Holland, M.M., Meier, W., Scambos, T., Serreze, M. (2007), 'Arctic sea ice decline: Faster than forecast', *Geophysical Research Letters* **34**, article L09501.

Stroeve, J.C., Kattsov, V., Barrett, A., Serreze, M., Pavlova, T., Holland, M., Meier, W.N. (2012a), 'Trends in Arctic sea ice extent from CMIP5, CMIP3 and observations', *Geophysical Research Letters* **39**, article L16502.

Stroeve, J.C., Markus, T., Boisvert, L., Miller, J., Barrett, A. (2014), 'Changes in Arctic melt season and implications for sea ice loss', *Geophysical Research Letters* **41**, pp. 1216–1225.

Stroeve, J.C., Serreze, M.C., Holland, M.M., Kay, J.E., Malanik, J., Barrett, A.P. (2012b), 'The Arctic's rapidly shrinking sea ice cover: a research synthesis', *Climatic Change* **110**, pp. 1005–1027.

Strong, C., Rigor, I.G. (2013), 'Arctic marginal ice zone trending wider in summer and narrower in winter', *Geophysical Research Letters* **40**, pp. 4864–4868.

Stuart, K.M., Long, D.G. (2011), 'Tracking large tabular icebergs using the SeaWinds Ku-band microwave scatterometer', *Deep Sea Research Part II: Topical Studies in Oceanography* **58**, pp. 1285–1300.

Sundfjord, A., Fer, I., Kasajima, Y., Svendsen, H. (2007), 'Observations of turbulent mixing and hydrography in the marginal ice zone of the Barents Sea', *Journal of Geophysical Research: Oceans* **112**, article C05008.

Syvertsen, E.E. (1991), 'Ice algae in the Barents Sea: types of assemblages, origin, fate and role in the ice-edge phytoplankton bloom', *Polar Research* **10**, pp. 277–288.

Taldenkova, E., Bauch, H.A., Stepanova, A., Dem'yankov, S., Ovsepyan, A. (2005), 'Last postglacial environmental evolution of the Laptev Sea shelf as reflected in

molluscan, ostracodal, and foraminiferal faunas', *Global and Planetary Change* **48**, pp. 223–251.

Taldenkova, E., Bauch, H.A., Stepanova, A., Strezh, A., Dem'yankov, S., Ovsepyan, Y. (2008), 'Postglacial to Holocene history of the Laptev Sea continental margin: Palaeoenvironmental implications of benthic assemblages', *Quaternary International* **183**, pp. 40–60.

Tamelander, T., Reigstad, M., Hop, H., Carroll, M.L., Wassmann, P. (2008), 'Pelagic and sympagic contribution of organic matter to zooplankton and vertical export in the Barents Sea marginal ice zone', *Deep Sea Research Part II: Topical Studies in Oceanography* **55**, pp. 2330–2339.

Tarasov, L., Peltier, W.R. (2005), 'Arctic freshwater forcing of the Younger Dryas cold reversal', *Nature* **435**, pp. 662–665.

Tartar, H.V. (1913), 'On the reaction between sulfur and potassium hydroxide in aqueous solution', *Journal of the American Chemical Society* **35**, pp. 1741–1747.

Team, R.C. (2018), *R: A Language and Environment for Statistical Computing*. R Foundation for Statistical Computing, Vienna.

Telford, R.J. (2006), 'Limitations of dinoflagellate cyst transfer functions', *Quaternary Science Reviews* **25**, pp. 1375–1382.

Templ, M., Filzmoser, P., Reimann, C. (2008), 'Cluster analysis applied to regional geochemical data: Problems and possibilities', *Applied Geochemistry* **23**, pp. 2198–2213.

Ternois, Y., Kawamura, K., Keigwin, L., Ohkouchi, N., Nakatsuka, T. (2001), 'A biomarker approach for assessing marine and terrigenous inputs to the sediments of Sea of Okhotsk for the last 27,000 years', *Geochimica et Cosmochimica Acta* **65**, pp. 791–802.

Thatje, S., Hillenbrand, C.-D., Mackensen, A., Larter, R. (2008), 'Life hung by a thread: Endurance of Antarctic fauna in glacial periods', *Ecology* **89**, pp. 682–692.

Therneau, T., Atkinson, B., Ripley, B. (2015), *Rpart: Recursive Partitioning and Regression Trees*, ver. 4.1-10, url: https://cran.r-project.org/package=rpart (accessed 07.05.2018).

Thiagarajan, N., Subhas, A.V., Southon, J.R., Eiler, J.M., Adkins, J.F. (2014), 'Abrupt pre-Bølling–Allerød warming and circulation changes in the deep ocean', *Nature* **511**, pp. 75–78.

Thomas, D.N., Dieckmann, G.S. (2010), *Sea ice: 2nd edition*. Wiley-Blackwell, Oxford, United Kingdom.

Thornalley, D.J.R., Bauch, H.A., Gebbie, G., Guo, W., Ziegler, M., Bernasconi, S.M., Barker, S., Skinner, L.C., Yu, J. (2015), 'A warm and poorly ventilated deep Arctic Mediterranean during the last glacial period', *Science* **349**, pp. 706–710.

Tierney, J.E., Tingley, M.P. (2014), 'A Bayesian, spatially-varying calibration model for the TEX_{86} proxy', *Geochimica et Cosmochimica Acta* **127**, pp. 83–106.

Tierney, J.E., Tingley, M.P. (2015), 'A TEX_{86} surface sediment database and extended Bayesian calibration', *Scientific Data* **2**, article 150029.

Torgo, L. (2010), *Data Mining with R, learning with case studies*. CRC Press, Boca Raton, Florida, USA.

Tschudi, M.A., Stroeve, J.C., Stewart, J.S. (2016), 'Relating the Age of Arctic Sea Ice to its Thickness, as Measured during NASA's ICESat and IceBridge Campaigns', *Remote Sensing* **8**, article 457.

Tuv, E., Borisov, A., Runger, G., Torkkola, K. (2009), 'Feature Selection with Ensembles, Artificial Variables, and Redundancy Elimination', *Journal of Machine Learning Research* **10**, pp. 1341–1366.

Uda, I., Sugai, A., Itoh, Y.H., Itoh, T. (2001), 'Variation in molecular species of polar lipids from Thermoplasma acidophilum depends on growth temperature', *Lipids* **36**, pp. 103–105.

Uttal, T., Curry, J.A., McPhee, M.G., Perovich, D.K., Moritz, R.E., Maslanik, J.A., Guest, P.S., Stern, H.L., Moore, J.A., Turenne, R., Heiberg, A., Serreze, M.C., Wylie, D.P., Persson, O.G., Paulson, C.A., Halle, C., Morison, J.H., Wheeler, P.A., Makshtas, A., Welch, H., Shupe, M.D., Intrieri, J.M., Stamnes, K., Lindsey, R.W., Pinkel, R., Pegau, W.S., Stanton, T.P., Grenfeld, T.C. (2002), 'Surface Heat Budget of the Arctic Ocean', *Bulletin of the American Meteorological Society* **83**, pp. 255–276.

van der Bilt, W.G.M., D'Andrea, W.J., Bakke, J., Balascio, N.L., Werner, J.P., Gjerde, M., Bradley, R.S. (2018), 'Alkenone-based reconstructions reveal four-phase Holocene temperature evolution for High Arctic Svalbard', *Quaternary Science Reviews* **183**, pp. 204–213.

Van Leeuwe, M., Tedesco, L., Arrigo, K.R., Assmy, P., Campbell, K., Meiners, K.M., Rintala, J.-M., Selz, V., Thomas, D.N., Stefels, J. (2018), 'Microalgal community structure and primary production in Arctic and Antarctic sea ice: A synthesis', *Elementa: Science of the Anthropocene* **6**, article 4.

Vance, D.E., Van den Bosch, H. (2000), 'Cholesterol in the year 2000', *Biochimica et Biophysica Acta (BBA) - Molecular and Cell Biology of Lipids* **1529**, pp. 1–8.

Vancoppenolle, M., Meiners, K.M., Michel, C., Bopp, L., Brabant, F., Carnat, G., Delille, B., Lannuzel, D., Madec, G., Moreau, S., Tison, J.-L., van der Merwe, P. (2013), 'Role of sea ice in global biogeochemical cycles: emerging views and challenges', *Quaternary Science Reviews* **79**, pp. 207–230.

Vare, L.L., Massé, G., Belt, S.T. (2010), 'A biomarker-based reconstruction of sea ice conditions for the Barents Sea in recent centuries', *The Holocene* **20**, pp. 637–643.

Vare, L.L., Massé, G., Gregory, T.R., Smart, C.W., Belt, S.T. (2009), 'Sea ice variations in the central Canadian Arctic Archipelago during the Holocene', *Quaternary Science Reviews* **28**, pp. 1354–1366.

Vayssières, M.P., Plant, R.E., Allen-Diaz, B.H. (2000), 'Classification trees: An alternative non-parametric approach for predicting species distributions', *Journal of Vegetation Science* **11**, pp. 679–694.

Vázquez Riveiros, N., Govin, A., Waelbroeck, C., Mackensen, A., Michel, E., Moreira, S., Bouinot, T., Caillon, N., Orgun, A., Brandon, M. (2016), 'Mg/Ca thermometry in planktic foraminifera: Improving paleotemperature estimations for G. bulloides and *N. pachyderma* left', *Geochemistry, Geophysics, Geosystems* **17**, pp. 1249–1264.

Verity, P.G., Wassmann, P., Frischer, M.E., Howard-Jones, M.H., Allen, A.E. (2002), 'Grazing of phytoplankton by microzooplankton in the Barents Sea during early summer', *Journal of Marine Systems* **38**, pp. 109–123.

Vernal, A.d., Marret, F. (2007), 'Chapter Nine Organic-Walled Dinoflagellate Cysts: Tracers of Sea-Surface Conditions', in: Hillaire–Marcel, C., De Vernal, A. (eds.), *Developments in Marine Geology*. Elsevier, pp. 371–408.

Vihma, T. (2014), 'Effects of Arctic Sea Ice Decline on Weather and Climate: A Review', *Surveys in Geophysics* **35**, pp. 1175–1214.

Vogt, C., Knies, J., Spielhagen, R.F., Stein, R. (2001), 'Detailed mineralogical evidence for two nearly identical glacial/deglacial cycles and Atlantic water advection to the Arctic Ocean during the last 90,000 years', *Global and Planetary Change* **31**, pp. 23–44.

Volkman, J. (2003), 'Sterols in microorganisms', *Applied Microbiology and Biotechnology* **60**, pp. 495–506.

Volkman, J.K. (1986), 'A review of sterol markers for marine and terrigenous organic matter', *Organic Geochemistry* **9**, pp. 83–99.

Volkman, J.K. (2006), 'Lipid Markers for Marine Organic Matter', in: Volkman, J.K. (ed.), *Marine Organic Matter: Biomarkers, Isotopes and DNA*. Springer Berlin Heidelberg, Berlin, Heidelberg, pp. 27–70.

Volkman, J.K., Barrerr, S.M., Blackburn, S.I., Sikes, E.L. (1995), 'Alkenones in *Gephyrocapsa oceanica*: Implications for studies of paleoclimate', *Geochimica et Cosmochimica Acta* **59**, pp. 513–520.

Volkman, J.K., Barrett, S.M., Blackburn, S.I. (1999), 'Eustigmatophyte microalgae are potential sources of C_{29} sterols, C_{22}–C_{28} *n*-alcohols and C_{28}–C_{32} *n*-alkyl diols in freshwater environments', *Organic Geochemistry* **30**, pp. 307–318.

Volkman, J.K., Barrett, S.M., Dunstan, G.A. (1994), 'C_{25} and C_{30} highly branched isoprenoid alkenes in laboratory cultures of two marine diatoms', *Organic Geochemistry* **21**, pp. 407–414.

Volkman, J.K., Barrett, S.M., Dunstan, G.A., Jeffrey, S.W. (1993), 'Geochemical significance of the occurrence of dinosterol and other 4-methyl sterols in a marine diatom', *Organic Geochemistry* **20**, pp. 7–15.

Volkman, J.K., Eglinton, G., Corner, E.D.S., Forsberg, T.E.V. (1980a), 'Long-chain alkenes and alkenones in the marine coccolithophorid *Emiliania huxleyi*', *Phytochemistry* **19**, pp. 2619–2622.

Volkman, J.K., Eglinton, G., Corner, E.D.S., Sargent, J.R. (1980b), 'Novel unsaturated straight-chain C_{37}-C_{39} methyl and ethyl ketones in marine sediments and a coccolithophore *Emiliania huxleyi*', *Physics and Chemistry of the Earth* **12**, pp. 219–227.

von Quillfeldt, C.H. (2000), 'Common Diatom Species in Arctic Spring Blooms: Their Distribution and Abundance', *Botanica Marina* **43**, pp. 499–516.

Voronina, E., Polyak, L., Vernal, A.D., Peyron, O. (2001), 'Holocene variations of sea-surface conditions in the southeastern Barents Sea, reconstructed from dinoflagellate cyst assemblages', *Journal of Quaternary Science* **16**, pp. 717–726.

Vorren, T.O., Plassen, L. (2002), 'Deglaciation and palaeoclimate of the Andfjord-Vågsfjord area, North Norway', *Boreas* **31**, pp. 97–125.

Wadhams, P., Hughes, N., Rodrigues, J. (2011), 'Arctic sea ice thickness characteristics in winter 2004 and 2007 from submarine sonar transects', *Journal of Geophysical Research: Oceans* **116**, article C00E02.

Wakeham, S.G. (1989), 'Reduction of stenols to stanols in particulate matter at oxic–anoxic boundaries in sea water', *Nature* **342**, pp. 787–790.

Walczowski, W., Piechura, J. (2011), 'Influence of the West Spitsbergen Current on the local climate', *International Journal of Climatology* **31**, pp. 1088–1093.

Walsh, J.E., Fetterer, F., Scott Stewart, J., Chapman, W.L. (2017), 'A database for depicting Arctic sea ice variations back to 1850', *Geographical Review* **107**, pp. 89–107.

Warren, S.G., Rigor, I.G., Untersteiner, N., Radionov, V.F., Bryazgin, N.N., Aleksandrov, Y.I., Colony, R. (1999), 'Snow Depth on Arctic Sea Ice', *Journal of Climate* **12**, pp. 1814–1829.

Wasmund, N., Göbel, J., Bodungen, B.v. (2008), '100-years-changes in the phytoplankton community of Kiel Bight (Baltic Sea)', *Journal of Marine Systems* **73**, pp. 300–322.

Wassmann, P., Ratkova, T., Andreassen, I., Vernet, M., Pedersen, G., Rey, F. (1999), 'Spring Bloom Development in the Marginal Ice Zone and the Central Barents Sea', *Marine Ecology* **20**, pp. 321–346.

Wassmann, P., Reigstad, M., Haug, T., Rudels, B., Carroll, M.L., Hop, H., Gabrielsen, G.W., Falk-Petersen, S., Denisenko, S.G., Arashkevich, E., Slagstad, D., Pavlova, O. (2006), 'Food webs and carbon flux in the Barents Sea', *Progress in Oceanography* **71**, pp. 232–287.

Weckström, K., Massé, G., Collins, L.G., Hanhijärvi, S., Bouloubassi, I., Sicre, M.-A., Seidenkrantz, M.-S., Schmidt, S., Andersen, T.J., Andersen, M.L., Hill, B., Kuijpers, A. (2013), 'Evaluation of the sea ice proxy IP_{25} against observational and diatom proxy data in the SW Labrador Sea', *Quaternary Science Reviews* **79**, pp. 53–62.

Weeks, W.F., Ackley, S.F. (1986), 'The Growth, Structure, and Properties of Sea Ice', in: Untersteiner, N. (ed.), *The Geophysics of Sea Ice*. Springer US, Boston, MA, pp. 9–164.

Werner, K., Frank, M., Teschner, C., Müller, J., Spielhagen, R.F. (2014), 'Neoglacial change in deep water exchange and increase of sea-ice transport through eastern Fram Strait: evidence from radiogenic isotopes', *Quaternary Science Reviews* **92**, pp. 190–207.

Werner, K., Müller, J., Husum, K., Spielhagen, R.F., Kandiano, E.S., Polyak, L. (2016), 'Holocene sea subsurface and surface water masses in the Fram Strait – Comparisons of temperature and sea-ice reconstructions', *Quaternary Science Reviews* **147**, pp. 194–209.

Werner, K., Spielhagen, R.F., Bauch, D., Hass, H.C., Kandiano, E. (2013), 'Atlantic Water advection versus sea-ice advances in the eastern Fram Strait during the last 9 ka: Multiproxy evidence for a two-phase Holocene', *Paleoceanography* **28**, pp. 283–295.

Wiedmann, I., Tremblay, J.-É., Sundfjord, A., Reigstad, M. (2017), 'Upward nitrate flux and downward particulate organic carbon flux under contrasting situations of stratification and turbulent mixing in an Arctic shelf sea', *Elementa: Science of the Anthropocene* **5**, p. 43.

Willmes, S., Heinemann, G. (2016), 'Sea-Ice Wintertime Lead Frequencies and Regional Characteristics in the Arctic, 2003–2015', *Remote Sensing* **8**, article 4.

Winsborrow, M.C.M., Andreassen, K., Corner, G.D., Laberg, J.S. (2010), 'Deglaciation of a marine-based ice sheet: Late Weichselian palaeo-ice dynamics and retreat in the southern Barents Sea reconstructed from onshore and offshore glacial geomorphology', *Quaternary Science Reviews* **29**, pp. 424–442.

Wollenburg, J.E., Knies, J., Mackensen, A. (2004), 'High-resolution paleoproductivity fluctuations during the past 24 kyr as indicated by benthic foraminifera in the marginal Arctic Ocean', *Palaeogeography, Palaeoclimatology, Palaeoecology* **204**, pp. 209–238.

Wraige, E.J., Belt, S.T., Massé, G., Robert, J.M., Rowland, S.J. (1998), 'Variations in distributions of C_{25} highly branched isoprenoid (HBI) alkenes in the diatom, *Haslea ostrearia*: influence of salinity', *Organic Geochemistry* **28**, pp. 855–859.

Wraige, E.J., Johns, L., Belt, S.T., Massé, G., Robert, J.-M., Rowland, S. (1999), 'Highly branched C_{25} isoprenoids in axenic cultures of *Haslea ostrearia*', *Phytochemistry* **51**, pp. 69–73.

Xiao, X., Fahl, K., Müller, J., Stein, R. (2015a), 'Sea-ice distribution in the modern Arctic Ocean: Biomarker records from trans-Arctic Ocean surface sediments', *Geochimica et Cosmochimica Acta* **155**, pp. 16–29.

Xiao, X., Fahl, K., Stein, R. (2013), 'Biomarker distributions in surface sediments from the Kara and Laptev seas (Arctic Ocean): indicators for organic-carbon sources and sea-ice coverage', *Quaternary Science Reviews* **79**, pp. 40–52.

Xiao, X., Stein, R., Fahl, K. (2015b), 'MIS 3 to MIS 1 temporal and LGM spatial variability in Arctic Ocean sea ice cover: Reconstruction from biomarkers', *Paleoceanography* **30**, pp. 969–983.

Xu, L., Reddy, C.M., Farrington, J.W., Frysinger, G.S., Gaines, R.B., Johnson, C.G., Nelson, R.K., Eglinton, T.I. (2001), 'Identification of a novel alkenone in Black Sea sediments', *Organic Geochemistry* **32**, pp. 633–645.

Yan, Y. (2016), *Machine Learning Evaluation Metrics*, ver. 1.1.1, url: http://github.com/yanyachen/MLmetrics (accessed 05.05.2017).

Yang, H., Wang, K., Dai, H., Wang, Y., Li, Q. (2016), 'Wind effect on the Atlantic meridional overturning circulation via sea ice and vertical diffusion', *Climate Dynamics* **46**, pp. 3387–3403.

Yang, S., Christensen, J.H. (2012), 'Arctic sea ice reduction and European cold winters in CMIP5 climate change experiments', *Geophysical Research Letters* **39**, article L20707.

Yashayaev, I., Seidov, D. (2015), 'The role of the Atlantic Water in multidecadal ocean variability in the Nordic and Barents Seas', *Progress in Oceanography* **132**, pp. 68–127.

Ye, Y., Shokr, M., Heygster, G., Spreen, G. (2016), 'Improving Multiyear Sea Ice Concentration Estimates with Sea Ice Drift', *Remote Sensing* **8**, article 397.

Yoder, J.A., Ackleson, S.G., Barber, R.T., Flament, P., Balch, W.M. (1994), 'A line in the sea', *Nature* **371**, pp. 689–692.

Yunker, M.B., Belicka, L.L., Harvey, H.R., Macdonald, R.W. (2005), 'Tracing the inputs and fate of marine and terrigenous organic matter in Arctic Ocean sediments: A multivariate analysis of lipid biomarkers', *Deep Sea Research Part II: Topical Studies in Oceanography* **52**, pp. 3478–3508.

Zaborska, A., Carroll, J., Papucci, C., Torricelli, L., Carroll, M.L., Walkusz-Miotk, J., Pempkowiak, J. (2008), 'Recent sediment accumulation rates for the Western margin of the Barents Sea', *Deep Sea Research Part II: Topical Studies in Oceanography* **55**, pp. 2352–2360.

Zachos, J.C., Schouten, S., Bohaty, S., Quattlebaum, T., Sluijs, A., Brinkhuis, H., Gibbs, S.J., Bralower, T.J. (2006), 'Extreme warming of mid-latitude coastal ocean during the Paleocene-Eocene Thermal Maximum: Inferences from TEX_{86} and isotope data', *Geology* **34**, pp. 737–740.

Zamelczyk, K., Rasmussen, T.L., Husum, K., Godtliebsen, F., Hald, M. (2014), 'Surface water conditions and calcium carbonate preservation in the Fram Strait during marine isotope stage 2, 28.8–15.4 kyr', *Paleoceanography* **29**, pp. 1–12.

Zhang, Q., Gradinger, R., Spindler, M. (1995), 'Dark Survival of Marine Microalgae in the High Arctic (Greenland Sea)', *Polarforschung* **65**, pp. 111–116.

Zhang, W., Miller, P.A., Jansson, C., Samuelsson, P., Mao, J., Smith, B. (2018), 'Self-Amplifying Feedbacks Accelerate Greening and Warming of the Arctic', *Geophysical Research Letters* **45**, pp. 7102–7111.

Zhang, Z., Metzger, P., Sachs, J.P. (2014), 'Bound lipid biomarkers in sediments from El Junco Lake, Galápagos Islands', *Organic Geochemistry* **75**, pp. 122–128.

Zheng, Y., Huang, Y., Andersen, R.A., Amaral-Zettler, L.A. (2016), 'Excluding the di-unsaturated alkenone in the U^{K}_{37} index strengthens temperature correlation for the common lacustrine and brackish-water haptophytes', *Geochimica et Cosmochimica Acta* **175**, pp. 36–46.

Zonneveld, K.A.F., Sebastian Meier, K.J., Esper, O., Siggelkow, D., Wendler, I., Willems, H. (2005), 'The (palaeo) environmental significance of modern calcareous dinoflagellate cysts: a review', *Paläontologische Zeitschrift* **79**, pp. 61–77.

Zwally, H.J., Gloersen, P. (2008), 'Arctic sea ice surviving the summer melt: interannual variability and decreasing trend', *Journal of Glaciology* **54**, pp. 279–296.

Zygmuntowska, M., Rampal, P., Ivanova, N., Smedsrud, L.H. (2014), 'Uncertainties in Arctic sea ice thickness and volume: new estimates and implications for trends', *The Cryosphere* **8**, pp. 705–720.